
بیست و دومین کنفرانس شیمی فیزیک انجمن شیمی ایران
22nd Iranian Physical Chemistry Conference
۲۹ الی ۳۱ مرداد ۱۳۹۸
گروه شیمی دانشگاه زنجان

Thermodynamic Modeling of Hydrogen Solubility in [MDEA][Cl] Using Sanchez–Lacombe Equation of State

M. Mohammadi*, F. Sabzi
Department of Chemical Engineering, Shiraz University of Technology, Shiraz 71555--313, Iran
Email: moslem238011@gmail.com

Abstract: Solubility of hydrogen in ionic liquid 2-[2-hydroxyethyl (methyl)amino] ethanol chloride ([MDEA][Cl]) was investigated at temperatures ranging from 313.15 to 333.15K and pressures ranging from 1.22 to 8.62 MPa. It was shown that the solubility of H_2 increased with increasing of pressure while decreased with increasing of temperature. The solubility was modeled by the Sanchez–Lacombe Equation of State (SL EoS) and partial molar volume of gas was obtained. The solubility of H_2 in [MDEA][Cl] is low and increases slightly with temperature.

Keywords: Hydrogen solubility, SL Equation of State, Ionic liquid.

I. INTRODUCTION

Today, releasing of the dangerous gases such as CO_2 and CO into atmosphere which is emitted from excessive consumption of fossil materials has changed or destroyed the environment. On the other hand, fossil fuels resources, i.e. gas, oil and their derivatives are also on a steep decline. Hence, scientists and experts are looking for a renewable and safe alternative to reduce the overall dependency on fossil fuels. There are a plenty of energy sources such as solar, geothermal, tidal, wind power, biomass and hydrogen. However due to some technical concerns, hydrogen can be chosen as the ideal energy carrier to resolve the problem [1].

There are several methods to store hydrogen gas including: as a compressed gas in high pressure tanks [2], as a liquid by absorbing within metal hydrides [3], carbon nanotubes [4] and metal organic frameworks [5] or by storing in a chemical solvent. There is currently growing interest in hydrogen storage by ionic liquids.

Ionic liquids (IL), which are also known as liquid electrolytes or liquid salts consist of a small organic or inorganic anion and a large asymmetric organic cation [6]. Ionic liquids are also used as solvents in various areas, for example, in the chemical and petroleum industries. Despite this, there are still some disadvantages that prevent the proceeding of the so-called “hydrogen economy” [7].

II. METHODS

In this study, Sanchez–Lacombe equation of state, a thermodynamic model in terms of lattice fluid theory is presented. The MATLAB programing is used to predict the solubility of hydrogen gas in [MDEA][Cl] at temperature range from 313 to 333 K and pressure range from 1.22 to 8.62 MPa.

$$\tilde{\rho}^2 + \tilde{P} + \tilde{T}\left(\ln(1-\tilde{\rho}) + \left(1-\frac{1}{r}\right)\tilde{\rho}\right) = 0 \qquad (1)$$

$$\tilde{T} = \frac{T}{T^*}, \quad \tilde{P} = \frac{P}{P^*}, \quad \tilde{\rho} = \frac{\rho}{\rho^*}$$

$$\varepsilon^* = RT^*, \quad v^* = \frac{RT^*}{P^*}, \quad r = \frac{MP^*}{RT^*\rho^*} \qquad (2)$$

where T^*, P^* and $\rho*$ are the characteristic parameters of the equation of state for each pure component, *M* is the molecular weight and *R* is the universal gas constant .At first, with the help of PVT experimental data, we obtain these parameters using the fminsearch method in the MATLAB program. Then, the characteristic parameters, $\varepsilon*$, $\nu*$ and r which represent the interaction energy, the characteristic volume and the segment length for pure components, respectively; are obtained from their relation with T^*, P^* and $\rho*$ through Eq. (2) [8].

III. RESULTS AND DISCUSSION

The hydrogen solubility in ionic liquid [MDEA][Cl] have been predicted using SL equation of state and have been demonstrated along with adopted experimental data points in Fig 1. The binary interaction parameter along with the percent of absolute average relative error have been brought in Table1.The results show that the solubility of hydrogen gas decreases with increasing temperature

Table 1. Binary interaction parameter and absolute average relative deviation of hydrogen sorption in [MDEA][Cl].

IL Name	T(K)	P(Mpa)	K_{ij}	%AARD	Ref
[MDEA][Cl]	313.15	1.32-5.44	-0.6300	5.24	[9]
	318.15	1.34-5.77	-0.6172	4.80	
	323.15	1.59-5.85	-0.5720	3.83	
	328.15	1.64-5.88	-0.5679	2.80	
	333.15	1.65-5.86	-0.5638	2.70	

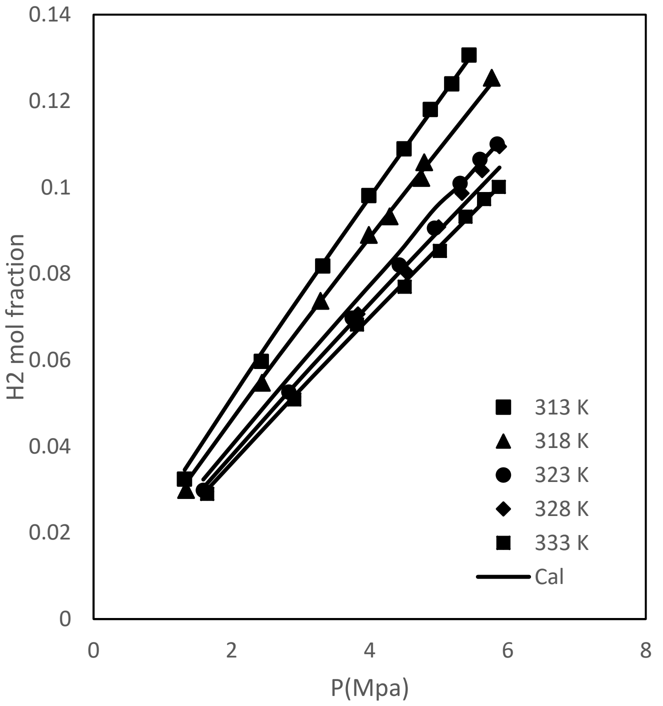

Fig.1: Calculated and experimental [9] hydrogen solubility in [MDEA][Cl] at temperatures range 313 to 333 K.

IV. CONCLUSION

In this work, we studied the SL EoS to quantitatively describe the solubility of hydrogen gas in ionic liquid [MDEA][Cl]. The amount of H_2 solubility increases with increasing pressure and decreases with temperature. It can be concluded that the solubility of hydrogen can be accurately described using SL EoS with AARD percent ranging less than 5%.

REFERENCES

[1] Ogden, Joan M. ,International Journal of Hydrogen Energy ,vol.24,pp .709-730, **1999**.

[2] Dogan, B. ASME 2006 Pressure Vessels and Piping/ICPVT-11 Conference. American Society of Mechanical Engineers, **2006**.

[3] Sakintuna, B., Lamari-Darkrim, F., Hirscher, M., International Journal of Hydrogen energy ,vol. 32,pp. 1121-1140. **2007**.

[4] Hirscher, M., and M. Becher. Journal of Nanoscience and Nanotechnology ,vol.3,pp. 3-17, **2003**.

[5] Langmi, Henrietta W., et al. Electrochimica Acta, vol.128,pp.368-392, **2014**.

[6] Lim, K.L., Kazemian, H., Yaakob, Z. and Daud, W.W.,. Solid-state materials and methods for hydrogen storage, vol.33, pp.213-226, **2010**

[7] Sherif, S. A., Barbir, F., & Veziroglu, T. N.,. Principles of hydrogen energy production, storage and utilization.,**2003**.

[8] Sanchez, I.C. and Lacombe, R.H. Macromolecules, vol.11, pp.1145-1156. **1978**.

[9] Zhao, Y., Zhang, X., Dong, H., Zhen, Y., Li, G., Zeng, S., & Zhang, S. Fluid Phase Equilibria,vol.302, pp. 60-64. **2011**.

بیست و دومین کنفرانس شیمی فیزیک انجمن شیمی ایران
22nd Iranian Physical Chemistry Conference
۲۹ الی ۳۱ مرداد ۱۳۹۸
گروه شیمی دانشگاه زنجان

The Mathematical Modeling of Open Cooling Tower and the Effect of Air Humidity on Outlet Water Temperature

M.Firouz*[a]*, M.R.Talaghat*[a]**
Department of Chemical, Petroleum and Gas Engineering, Shiraz University of Technology, Shiraz, Iran
Email:Talaghat@sutech.ac.ir

Abstract: For mathematical modeling of cooling tower we choose a control volume of length of cooling tower and write the mass balance and heat balance. Eventually we obtain a set of differential equations that are solved by using numerical methods. The fourth order Runge-Kutta and shooting method were employed to solve the Equations by Matlab software. By drawing the water temperature graph, we observed that in lower humidity of the inlet air, will increase the cooling rate of the water and outlet water from the tower will have a lower temperature.

Keywords: Cooling Tower, Open System, Close System, Mathematical Modeling.

I. INTRODUCTION

Cooling towers today are widely used in industries. These devices are generally open and closed. In the open system, air and water are in direct contact with each other and water will be cool, but in the close system, Water flows through a pipe network and cools in contact with the air and spray water. The mathematical modeling of cooling towers is very important. Because with mathematical modeling we can compare different systems together and with actual data.

In the analysis of cooling tower performance, mathematical modeling is used. Merkel [1] in 1925, he was the first to use a mathematical model to analyze the performance of open cooling towers. In the Merkel method, several simplistic assumptions have been made. For example, the Lewis coefficient is considered to be one. In 1984 Pope [2] did not consider Merkel's simplifications. Thus, the temperature of the exhaust air from the tower was more accurately reported.

In this regard, models derived from the combination of mathematical equations with thermodynamic rules are used to predict and calculate the performance of towers, which are known as thermodynamic models, the most credible are Merkel equations by Kloppers and Kröger [3], it was used in 2004. Zubir and Qureishi [4] were studied the effects of sedimentation on open cooling towers by using a mathematical model in 2006 and 2007. In their studies, they wrote the heat and mass transfer equations to analyze the performance of open cooling towers by using the ESS software. In 2015, Ghassem Heydarinejad et al. [5] performed a cooling tower optimization to minimize the cost of operations by using a genetic algorithm. In this research we choose a control volume of cooling tower and after writing the mass balance and energy balance of air and water, we solve the final equations by fourth order Runge-Kutta method.

II. METHODS

In this Research for analyzing the performance of cooling tower, a mathematical modeling is used that does not have the complexity of the CFD method and is easy to apply. The fourth order Runge-Kutta method is employed to solve the Equations by Matlab software.

The fourth order RK-method is:

$y_{i+1} = y_i + 1/6(k_1 + 2k_2 + 2k_3 + k_4)$

$k_1 = hf(x_i, y_i)$

$k_2 = hf(x_i + h/2, y_i + k_1/2)$

$k_3 = hf(x_i + h/2, y_i + k_2/2)$

$k_4 = hf(x_i + h, y_i + k_3)$

III. RESULTS AND DISCUSSION

For modeling, we consider a control volume as in figure 1.

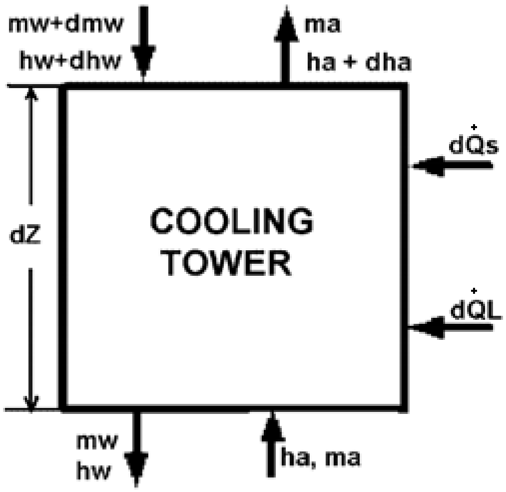

Fig.1: A control volume of cooling tower.

With application of the first law of thermodynamics for the air side, we will have:

$\dot{m}_a dh_a = d\dot{Q}_s + d\dot{Q}_l$ (1)

In the above relation h_a is enthalpy of air, which can be calculated by using the following equation:

$h_a = c_{pa}T_a + W\left(c_{ps}^{sat}T_a + \Delta h_w\right)$ (2)

And $d\dot{Q}_s$ is sensible heat between water and air.
And $d\dot{Q}_l$ is latent heat between water and air.
By writing the energy balance for spray water from the top of the tower, we will have:

$\left(\dot{m}_w + d\dot{m}_w\right)\left(h_w + dh_w\right) = \dot{m}_w h_w + d\dot{Q}_s + d\dot{Q}_l$ (3)

After writing the equations of mass balance and energy balance for water side and air side, we obtain the following differential equations:

$$\frac{dT_a}{dz} = \left(\frac{L\alpha_{LA}}{\dot{m}_a} + c_{ps}^{sat}\frac{dW}{dz}\right)\frac{\left(T_w - T_a\right)}{c_{pm}} \quad (4)$$

$$\frac{dT_w}{dz} = \frac{1}{\dot{m}_w c_{pw}}\left[L\alpha_{LA}\left(T_w - T_a\right) + \dot{m}_a\frac{dW}{dz}\left(c_{ps}^{sat}T_w - c_{pw}T_w + \Delta h_w\right)\right] \quad (5)$$

$$\frac{dW}{dz} = \frac{LK}{\dot{m}_a}\left[W^{sat}\left(T_w\right) - W\right] \quad (6)$$

$$\frac{d\dot{m}_w}{dz} = \dot{m}_a\frac{dW}{dz} \quad (7)$$

The boundary conditions for the above equations are as follows:

$(T_a)_{z=0} = T_{a0}, (T_w)_{z=L} = T_{w0}, (W)_{z=0} = W_0, (m_w)_{z=L} = m_{w0}$

In the above equations, T_a is air temperature and T_w is water temperature and W is air humidity and m_w is water flow rate.

After solving the equations and drawing the temperature of the water output from tower in terms of length of tower in different humidity, according Fig2 we will have:

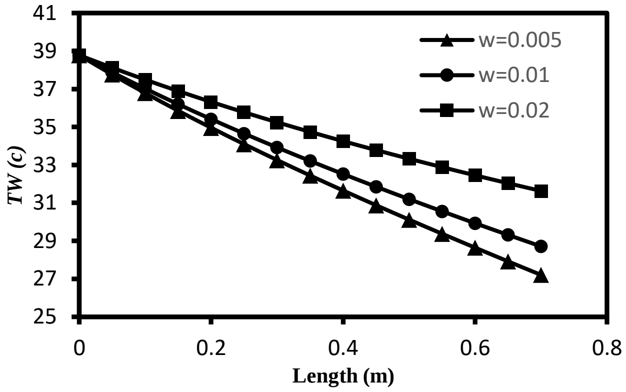

Fig.2: water outlet temperature vs length of tower at different air humidity.

Table1: result of outlet water temperature at three case

Case	Tw_{in}(c)	Ta_{in}(c)	W(kg water/kg dry air)	Tw_{out}(c)	Ta_{out}(c)
Case1	38.76	26.67	0.005	27.2	29.81
Case2	38.76	26.67	0.01	28.71	30.725
Case3	38.76	26.67	0.02	31.63	31.45

As seen from Fig (2) and table (1) with increasing humidity, the temperature of the output water from the tower has increased. Therefore, in low the air humidity, the temperature of the output water is low. Or in other words, the cooling rate of the water is increased.

IV. CONCLUSION

As the results are found, with increasing humidity, the temperature of the water output from the tower has increased. Therefore, the lower the air humidity, the lower the water temperature will be.
Also, the effect of mass flow of the input water on performance of tower has been investigated. And the result is that by increasing the mass flow of the inlet water, the cooling rate of the inlet water decreases.
Also, the effect of temperature of the input air on performance of tower has been investigated. And the result is that by increasing the temperature of the inlet air, the cooling rate of the inlet water decreases.

REFERENCES

[1] Merkel, F., Verdunstungskuehlung, VDI Forschungsarbeiten No. 275, Berlin, 1925.
[2] Poppe, M. & Rogener, H., Berechnung von Ruckkuhlwerken,VDI-WarmeatlasMi 1–Mi 15, 1991.
[3] Kloppers, J. & Kröger, D., "Cooling Tower Performance: A Critical Evaluation of the Merkel Assumptions," R&D Journa, 2004.
[4] Qureshi, B.A & Zubair S.M, A comprehensive design and rating study of evaporative coolers and condensers part I: performance evaluation. International Journal of Refrigeration, vol. 29, pp. 645-658, 2006.
[5] Heidarinejad, G., Miri, S.Z. & Pasdarshahri, H., Optimization of hybrid cooling system including direct evaporative cooler- cooling tower in order to minimize operation cost using genetic algorithm, Modares Mechanical Engineering, Vol. 15, No. 4, pp. 348-354, 2015.

Adsorption of cefixime from aqueous solution using Fenton process in presence of nanostructured magnetic alginate composite and nanostructured alginate-hydroxyapatite composite

M. Nabizad Gharani[a*], A. Dadvand Koohi[b]
(Department of Chemical engineering, Masters student of University of guilan, Rasht, 41996-13776, Iran)[a]
(Department of Chemical engineering, Associate Professor of University of guilan, Rasht, 41996-13776, Iran)[b]
Email: Nabizadmona@yahoo.com[a], b_dadvand@yahoo.com[b]

Abstract*:* The aim of this research was to study efficiency for removal of cefixime from aqueous solution with nanostructured magnetic alginate composites (Alg+m) and nanostructured alginate-hydroxyapatite (Alg+Hap) composites using heterogeneous fenton process. Catalysts were synthesized from hydroxyapatite extracted from fish scales, alginate and magnetic nanoparticles (Fe_3O_4). Catalysts amount, pH, initial concentration of cefixime and initial concentration of hydrogen peroxide were investigated. Based on the results at the optimum pH =3.3, removal percent of cefixime was 80.74% and 67.72% for Alg+m and Alg+Hap, respectively. Experiment results were revealed that removal of cefixime has reduced when the catalysts amount has increased and when the initial concentration of cefixime has enhanced. Degradation of antibiotic has improved until certain level of H_2O_2 concentration while it has decreased after 3mM H_2O_2 concentration for both of catalysts.

Keywords: alginate, cefixime, Fe_3O_4 nanoparticles, fenton process, hydroxyapatite

I. INTRODUCTION

Cefixime has been used in treatment of bacterial infections. Due to widely using cefixime in treatment of human and animals, aqueous source have polluted [1, 2]. Different methods have been offered to remove cefixime from aqueous solution like membrane separation, ion exchange, reverse osmosis, chemical oxidation, adsorption and advanced oxidation process [1, 3]. Advanced oxidation processes (AOPs) have been reported as an interesting technique for degradation and mineralization of organic compounds. AOPs are based on the reaction between H_2O_2 and ferrous ions (Eq 1) [4, 5].

$$Fe^{2+} + H_2O_2 \rightarrow OH^{\bullet} + Fe^{3+} + OH^{-} \quad (1)$$

In classical fenton, the reaction uses iron (Ⅱ) as catalyst. Another possibility is the heterogeneous fenton reactions where the catalyst is immobilized on solid supports. Alginate is a cheap, non-harmful, non-toxic, biodegradable and edible substance [6, 7]. In the homogeneous fenton, the reaction occurs between iron ions and hydrogen peroxide in the liquid phase while the heterogeneous fenton occurs on the surface of the catalyst. Here, we assumed that the degradation reaction of cefixime follows the OH• mediated mechanism. According to this mechanism, OH• radicals are generated as a reaction products between the H_2O_2 and the iron ions that stabilized on the catalyst. Then, these free radicals attack and degrade the cefixime molecules [8].

We used hydroxyapatite to improve catalyst structure. Purpose of this study was to evaluate effect of Alg+m and Alg+Hap as catalyst at heterogeneous fenton to remove cefixime.

II. METHODS

Materials: Cefixime (pars drug), NaOH (merck), Ammonia (Merck), $FeCl_3.6H_2O$ (qatran shimi), $FeSO_4.7H_2O$ (qatran shimi), HCl (Merck), Hydrogen peroxide (Merck), $FeCl_3$ (Merck), sodium alginate (Sigma Aldrich)

Extracting hydroxyapatite from fish scale: Fish scales washed several times with distillated water and dried at room temperature about 24h.The dried scales were washed with HCl (0.1M) for 5 hours and then washed several times with distillated water. washed scales were added to NaOH (5%w/v) and stirred and heated at 70°C for 5h. treated scales powder washed with distillated water and dried at 60°C. In continue, produced white powder mixed and heated at 100°C for 1h with NaOH (50%w/v). Then, the obtained hydroxyapatite nanopowder washed and drie d at 60°C.

Synthesis of magnetic nanoparticles: Fe_3O_4 were synthesized by the chemical co precipitation method. Briefly, 7.76g $FeCl_3.6H_2O$ and 4g $FeSO_4.7H_2O$ were dissolved in 100ml deionized water. The solution heated at 80°C for 15 min. Then, 50ml of ammonia 25% was quickly added into the reaction solution. At this moment the color of mixture changed to dark brown. The solution thoroughly mixed for 40 min. Then, the magnetic nanoparticles separated with centrifuge (5000rpm) and washed several times and dried in an oven at 40°C for 24h.

Synthesis of Alg+m and Alg+Hap composite: sodium alginate solution (2%w/v) was prepared by dissolving sodium alginate salt in distillated water. The suspension mixed for 2h and then Fe_3O_4 or hydroxyapatite nanoparticles were added into solution and mixed for 2h again. The solution drop wised into $FeCl_3$ 0.05M and were kept 24h in the gelling solution. Composites were washed repeatedly and kept stored in distilled water for experiments.

Experimental procedure: The removal of cefixime by composites was measured in batch experiments at different concentrations of cefixime (5, 20 and 30ppm). The solution pH stabilized at 3.3 using HCl (0.4M). The amount of catalysts (50, 72, 90 g/L) was adjusted and finally, the concentration of hydrogen peroxide (1, 2, 3, 10 ppm) was regulated and the suspension was agitated using a shaker (130 rpm) at 25 ° C for 90 min. At different times, the concentration of cefixime was determined by spectrophotometry (Cary 50) at 285 nm according to the calibration curve ($R^2 = 0.995$).

III. RESULTS AND DISCUSSION

Effect of concentration of hydrogen peroxide: Fig.1 shows effect of increasing the concentration of hydrogen peroxide in cefixime removal. It was observed that the removal percentage was improved with increasing of H_2O_2 concentration from 1 to 3mM. The amount of degradation of cefixime increased from 80.74% to 83.32% at 25°C. At high concentration of H_2O_2, it can scavenge amount of hydroxyl radicals by resume of reactive OH• and produce less reactive $HO_2^{\bullet}$ specie (Eq.2). $HO_2^{\bullet}$ can also scavenge hydroxyl radicals (Eq.3), so there were competition between cefixime and $HO_2^{\bullet}$ to react with $OH^{\bullet}$, leading to decrease of reaction rate at 10 mM H_2O_2 concentration [7,9,10].

$$H_2O_2 + OH^{\bullet} \rightarrow HO_2^{\bullet} + H_2O \qquad (2)$$

$$HO_2^{\bullet} + OH^{\bullet} \rightarrow H_2O + O_2 \qquad (3)$$

Effect of amount of catalyst: Fig.2 shows the results of cefixime removal along experiments performed at different of amount of catalysts. In both of catalysts, the cefixime removal has increased when the catalyst contest has enhanced. The removal percentage has measured 83.93% and 71.23% for Alg+m and Alg+Hap at 90g/L catalysts dosage, respectively. This was due to the increasing numbers of active sites that help to decomposition of H_2O_2, that increases the number of radical hydroxyl [7,9,11].

Effect of initial concentration of cefixime: Fig.3 represents the effect of initial concentration of antibiotic. Alg+m and Alg+Hap catalysts have most removal percentage at 5 ppm cefixime concentration about 82.72% and 69.9% respectively. Also removal percentage decreased to 80.37% and 60.56% after enhancing concentration of ceifxime to 30ppm, respectively. It was observed that at high concentrations of cefixime, amount of free hydroxyls available for the reaction of fenton and degradation of cefixime will be inadequate [1, 7, 11].

Effect of pH: As it is shown in Fig.4, solution pH influences on removal cefixime and the highest oxidation activity achieved at pH 3.3. In the alkaline solutions, hydrogen peroxide is unstable and it has the potential to decompose H_2O_2 into water and oxygen which reduces its oxidation properties. At pH below 3.3, according to Eq.1 and Eq.4, increasing water production instead of free hydroxyl decreases the removal efficiency of cefixime [9].

$$OH^{\cdot} + H^{+} + e^{-} \rightarrow H_2O \qquad (4)$$

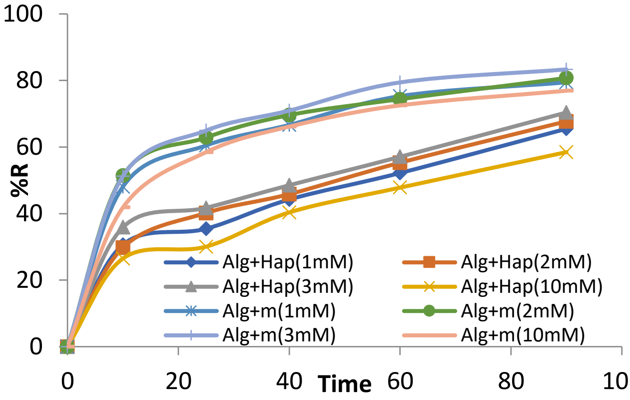

Fig.1: Effect of concentration of H_2O_2 at C_{cfx}=20ppm, pH=3.3 and 72 g/L catalysts.

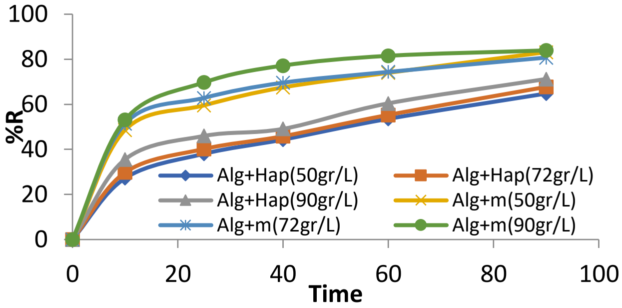

Fig.2: Effect of amount of catalyst at pH=3.3, C_{cfx}=20ppm, C_{H2O2}=2mM.

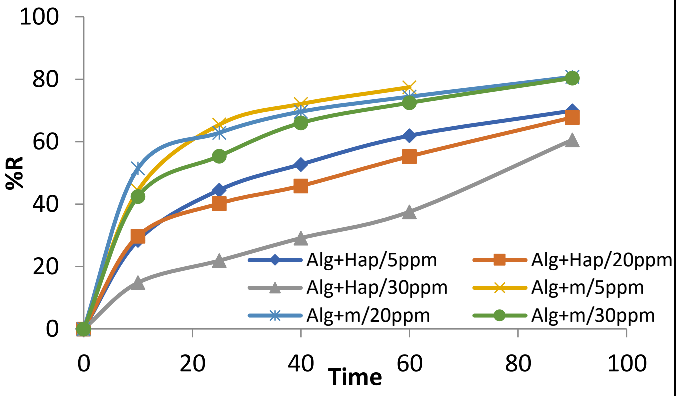

Fig.3: Effect of initial concentration of cefixime at pH=3.3, C_{H2o2}=2 mM, 72 g/L of Catalysts.

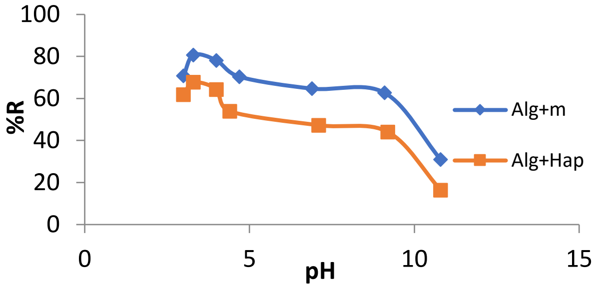

Fig.4: Effect of pH on degradation by fenton process at C_{cfx}=20ppm, C_{H2O2}=2mM, 72g/L Catalysts.

IV. CONCLUSION

The results of this study showed that the heterogeneous fenton process using Alg+m and Alg+Hap catalysts could be a suitable method for the removal of cefixime from aqueous solutions. Alg+m catalyst was better than Alg+Hap catalyst.

REFERENCES

[1] I.Belghadr, Gh.Shams.Kh, H.Godini, M.Almasian., 55 1068–1075, 2015

[2] M. Rasoulifard, S. Khanmohammadi, A. Heidari , Water Science & Technology,1069-1078,2016

[3] S.Zavareh, T.Eghbalazar, Journal of environmental chemical engineering 5.4, 3337-3347, 2017

[4] O. Iglesias, J. Gómez, M. Pazos, & Sanromán, M. Applied Catalysis B: Environmental, 144, 416-424.2014

[5] M.Bayat, M.Sohrabi, & S.J.RoyaeeJournal of Industrial and Engineering Chemistry, 18(3), 957-962. 2012

[6] A.Cruz,L. Couto, S. Esplugas, & C.Sans, Chemical Engineering Journal, 318, 272-280.2017

[7] H.Titouhi, & J.E. Belgaied, Journal of Environmental Sciences, 45, 84-93, 2016

[8] N.Wang,T. Zheng, G.Zhang, & P.Wang, Journal of Environmental Chemical Engineering, 4(1), 762-787, 2016

[9] S. Ben Hammouda, N. Adhoum & L. Monser, Desalination and Water Treatment, 57:15, 6761-6771,2016

[10] M.Ahmadi, H.Rahmani, A.Takdastan, N.Jaafarzadeh & A.Mostoufi, Process safety and environmental protection, 104, 413-421, 2016

[11] S.B.Hammouda,N. Adhoum & L. Monser, Journal of hazardous materials, 294, 128-136, 2015

Study of Reactive Yellow 145 Removal by Ag/GO nanocomposite using Response Surface Methodology

Parvin Gharbani

Department of chemistry, Ahar Branch, Islamic Azad University, Ahar, Iran
Email: parvingharbani@yahoo.com, p-gharbani@iau-ahar.ac.

Abstract : Ag /GO nano composite was used for the removal of Reactive Yellow 145 dye (RY145). The effect of Reactive Yellow 145 dye concentration, Ag /GO dosage, contact time and pH on removal of RY 145 were studied. Results revealed that catalyst dosage and RY145 concentration are more effective parameters than contact time and pH. As results, 38.98% of RY145 removal was obtained. So, it is concluded that Ag /GO nano composite can be used as an efficiency catalyst for removal of Reactive Yellow 145 dye.

Keywords: Reactive Yellow 145 dye, Ag/GO, RSM, Adsorption

I. INTRODUCTION

Azo dyes are organic compounds bearing the functional group R−N=N−R′, in which R and R′ are usually aryl. They are a commercially important family of azo compounds, i.e. compounds containing the linkage C-N=N-C. Azo dyes are widely used to treat textiles, leather articles, and some foods. Chemically related to azo dyes are azo pigments, which are insoluble in water and other solvents. Azo dyes should be removed from water resources since they are highly resistant under aerobic conditions and their anaerobic reduction gives aromatic amines, which are intrinsically carcinogenic and mutagenic [1]. Azo dyes are highly carcinogenic, mutagenic and resistance against biodegradation [2]. Therefore, they must be to remove from water and wastewater. Different physical and chemical processes have been employed to removal of azo dyes [3-4]. Adsorption is a efficiency method to removal of pollutants. In recent years, interest in composite based on graphene oxide (GO) with silver species has increased.

Response surface methodology (RSM) is a useful technique for evaluation of several input variables that affect the efficiency or the qualitative properties of interest. Also, this method is a beneficial tool for optimization studies [5]. RSM proposes a second- or higher-order function to relate the response to the experimental parameters. This study aims to investigate removal of the Reactive Yellow 145 azo (RY 145) dye by the Ag /GO nanocomposite and evaluate the effect of pH, RY 145 concentration, contact time and catalyst dosage on RY 145 removal. Structure of RY 145 is shown in Fig. 1. Performance of the process is predicted and optimized using a second-order equation by RSM.

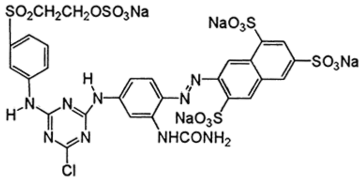

Fig. 1. Structure of RY145 dye

II. METHODS

All chemicals were prepared from Merck compony.

Preparation of Ag NPs / GO

240 mL AgNO3 (0.1 M) and 1.2 g GO were mixed and stirred vigorously for 90 min to prepare Ag/GO suspension. KOH solution (1 M) was used to adjust the pH of the solution at 7. The obtained solid was stirred for 1 h and maintained overnight at room temperature. After the precipitated, particles were washed with deionized water, it dried in an oven at 45 °C.

REMOVAL EFFECIENCY

All experiments were conducted in a batch system at room temperature. 100 mL of a RY145 solution with the desired concentration was added to a reactor, its pH was adjusted using 1 N HCl and/or NaOH and a definite amount of the catalyst was added to it. At the desired reaction intervals, the solution was sampled, filtered and RY145 concentration was measured by a UV-Vis spectrophotometer، Model DR-5000, Hach, USA. Eq. (1) was used to determine the removal percentage (%R). Where, [C]0 and [C]t are the initial and at any time concentration of RY145 (mg/L), respectively.

$$R(\%) = \frac{[C]_0 - [C]_t}{[C]_0} \times 100$$

III. RESULTS AND DISCUSSION

The experiments were performed by the design expert software (DOE 7.0). Initial RY145 concentration, pH, time and catalyst dosage were chosen as the four independent variables at five variable levels.

The results of RY1645 removal shows a significant agreement between the observed and predicted removal efficiencies.

ANOVA results revealed that the linear effects of the variables are more effective than others. Also, the lower P and higher F values of catalyst dosage and RY145 concentration indicate that the response is more influenced by these two variables rather than contact time and pH. The regression (R^2) value, i.e. 99.43%, confirms fitness of the model in the removal of RY145.

To evaluate the effect of the four operational parameters on the response, 3D graphs were plotted. According to Fig. 2 increasing the initial concentration of RY 145 has a positive effect. It might be due to the fact that increasing of RY145 concentration provides a driving force.

As shown, RY145 removal was increased by increasing the dosage of catalyst. Increasing the dosage of the catalyst increases the active surface area and enhancement of RY145 adsorption. consequently, removal of a of RY 145 was increased.

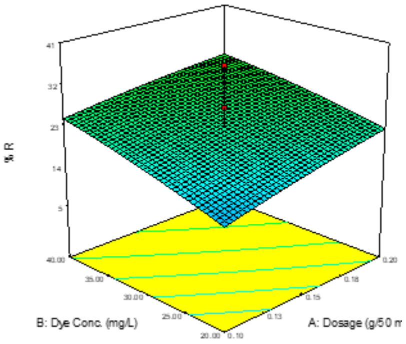

Fig. 2 Effect of initial dye concentration and catalyst dosage

IV. CONCLUSION

In this research, efficiency of Ag/GO nanocomposite on removal of Reactive Yellow 145 dye was evaluated by response surface methodology. The results confirmed the Reactive Yellow 145 dye removal is depended on the Reactive Yellow 145 dye initial concentration and Ag/GO nanocomposite dosage.The maximum removal of Reactive Yellow 145 dye was about 38.98%. As a result, Ag/GO nanocomposite can be applied as a performance adsorbent to remove of Reactive Yellow 145 dye from aqueous solutions

REFERENCES

[1] M.M, Tauber, G. M. Gubitz, and A. Rehorek, Bioresour. Technol. Vol. 99, pp. 4213-4220, **2008**.

[2] A. Pandey, P. Singh, L. Iyengar, Int. Biodeter. Biodegr. Vol. 59, pp. 73–84, **2007**.

[3] F. Ali, J. Ali Khan, N.S. Shah, M. Sayed, H.M. Khan, Process Saf, Environ. Vol. 117, pp. 307-314, **2018.**

[4] Y. P. Chen, S. Y. Liu, H.Q. Yu, H. Yin, R. Li, Chemosphere, vol. 72, pp. 532-536, **2008.**

[5] M.A. Bezerra, R.E. Santelli, E.P., Oliveira, L.S. Villar and L.A. Escaleira, Talanta, vol. 76, pp. 965-977, **2008**.

Investigation of Carbon Dioxide and Hydrogen Sorption in ZSM-5 Using Grand Canonical Monte Carlo Simulation

A. Hassanzadeh*, *F. Sabzi*
Department of Chemical Engineering, Shiraz University of Technology, Shiraz 71555--313, Iran

Abstract*:* The adsorption properties of ZSM-5 zeolite was investigated by Grand Canonical Monte Carlo (GCMC) simulation. The force field of PCFF was used in the GCMC simulation. The sorption isotherms of pure hydrogen and carbon dioxide in ZSM-5 zeolite were calculated. The results illustrate that ZSM-5 zeolite is a nice choice for the sorption of hydrogen and carbon dioxide at vast pressures and low temperatures.

Keywords: GCMC،Simulation،Sorption،Zeolite،ZSM-5

I. INTRODUCTION

Zeolites are considered as ideal systems for studying the structural affect on the gas sorption attributes [1,2]. Investigation of sorption attributes of new zeolite structures is many momentous and noteworthy both from methodical view points and for industrial usage. The Usefulness of the adsorbent materials can be appraised by simulation method [1,3–5]. On the other hand, molecular simulation prepares a perfect and strong means to research the sorption of gases in zeolite substance [5]. Last discussion display that Monte Carlo simulation is an proper and well way for studying the sorption of gases by zeolite substance [1-5].

II. METHODS

All the simulations were accomplished exerting the Accelrys_Material Studio 4.3 simulation software parcel. The force field of PCFF was used in the GCMC simulation.

The partial charges of atoms were appraised by charge-equilibration method and electrostatic energy are calculated by Ewald summation method [6], which is highly accurate in the long range interactions calculation.

The GCMC method is mostly exerted in the simulation of the adsorption isotherm which works in the stable μVT((chemical potential: μ),(volume: V),(temperature : T)) ensemble [7,8]. It is chiefly appropriate for simulations of blend and inhomogeneous apparatuses. The adsorption situations (pressure and temperature) are too steady in the empirical evaluations of sorption method therefore evaluations among simulation conclusions and empirical information are sensible.

The simulations includes of measurement the average number of adsorbate molecules for which the chemical potential of the gas in the bulk phase equalizes the chemical potential of the adsorbed gas at a given pressure and temperature. The partial pressure necessary for measurement of the chemical potential of the adsorbed molecules was measured by exerting the ideal gas law. Pending the cycle of the simulation, sorbate molecules in the zeolite were translated, rotated, created and deleted from the zeolite framework at random with the possibility of 0.225, 0.225, 0.275 and 0.275, sequence.

Atom based method was exerted for the computation of the van der Waals potential energy with a cut-off interval of 1.3 nm. The Ewald aggregate method with Ewald precision of 0.0001 kcal/mol was exerted for the electrostatic potential energy. For getting balance, $5 * 10^5$ steps were implementation out and for computation of the necessary attributes and for information analysis $1 * 10^6$ more steps were exerted.

The structure of hydrogen and carbon dioxide molecules were produced exerting the Forcite module and PCFF force fields. The simulation box is a super cell which is elected big sufficient to obey the minimum image contract with a potential cutoff 1.3 nm. For ZSM-5-type zeolite, the super cell includes of 8 unit cells (2 * 2 * 2, a = 2.007 nm, b = 1.992 nm and c = 1.342 nm). Intermittent border situation are practical in all orientation.

III. RESULTS AND DISCUSSION

The calculated results for carbon dioxide gas sorption was compared with the experimentally measured sorption isotherms. The conclusions are in fine assent with the empirical information. As Fig. 1 display increasing pressure causes an increase in the amount of gas sorption.

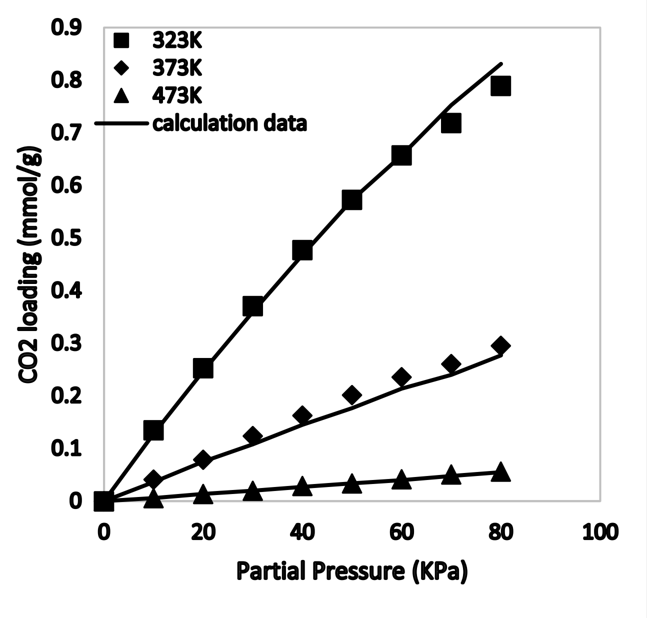

Fig.1: CO_2 sorption isotherms and experimental data [9].

Table1: %AARD for fig1

Pressure(kPa)	%*AARD* 323 K	%*AARD* 373 K	%*AARD* 473 K
10	4.47	10.0	0.0
20	1.98	3.84	0.0
30	2.7	12.19	0.0
40	1.88	10.49	3.57
50	0.0	11.94	0.0
60	0.0	8.93	4.53
70	-4.72	7.69	4.0
80	-5.06	6.2	1.78

Table2: The predicted amount of H_2 sorption(mmol/g)

Pressure(kPa)	323 K	373 K	473 K
10	0.001	0.001	0.0006
20	0.002	0.002	0.0012
30	0.004	0.003	0.0018
40	0.005	0.004	0.0020
50	0.007	0.005	0.0030
60	0.008	0.006	0.0036
70	0.010	0.007	0.0042
80	0.011	0.008	0.0049

Following this way, the sorption of hydrogen gas in ZSM-5 zeolite have been also estimated and shown in Table 2. In both cases, with increasing temperature, the amount of sorption decrease, so the maximum value of sorption for both carbon dioxide and hydrogen gas happens at 323 K.

IV. CONCLUSION

The sorption properties of ZSM-5 zeolite was studied by GCMC at various temperature. The conclusions display that ZSM-5 zeolite is a nice option for the sorption of carbon dioxide at low temperatures and large pressures but not a good option to absorb hydrogen.

REFERENCES

[1] M. Rahmati, H. Modarress, Applied Surface Science. vol. 255, pp. 4773–4778, **2009**.
[2] M. Rahmati, H. Modarress, Journal of Molecular Structure. vol. 901, pp. 110–116, **2009**.
[3] J. Liu, S. Keskin, D. Sholl, K. Johnson, The Journal of Physical Chemistry. vol. 115, pp. 12560–12566, **2011**.
[4] Y. Zeng, S. Separation and Purification Technology. vol. 67, pp. 71–78, **2009**.
[5] A.I. Skoulidas, D.S. Sholl, J.K. Johnson, The Journal of Chemical Physics. vol. 124, pp. 054708, **2006**.
[6] P.P. Ewald, Annalen der physik. vol. 64, pp. 253–287, **1921**.
[7] S. Agnihotri, P. Kim, Y. Zheng, J.P.B. Mota, L. Yang, Langmuir. vol. 24, pp. 5746–5754, **2008**.
[8] M.M. Biswas, T. Cagin, The Journal of Physical Chemistry. B vol. 114, pp. 13752–13763, **2010**.
[9] S.K. Wirawan, D.Creaser, Microporous and Mesoporous Materials. vol. 91, pp. 196-205, **2006**.

Comparison of the performance of chemical demulsifiers in the separation of water emulsions in Iranian heavy crude oils

N. Zamani Nejad[a], P. Parvasi[a]*, S. M. Jokar[a]
[a]Department of Chemical, Petroleum and Gas Engineering, Shiraz University of Technology, Shiraz, Iran
Email: parvasi@sutech.ac.ir

Abstract: Generally, one of the problems in the production, extraction, transportation and refining of crude oil, is the formation of a stable emulsion of water in crude oil. Water emulsions contain a variety of salts and other impurities. These salts damage the equipment for crude oil processing and transportation. Therefore, after extracting crude oil from the well, it is sent to desalting unit. Desalting operation is carried out at different stages and in different ways. One of the most important desalting steps (especially for heavy crude oil) is the chemical demulsifier injection. The chemical demulsifier material is capable of bonding with water emulsions. These materials have both hydrophobic and hydrophilic properties and can eliminate the stable emulsion and thus the water is separated from the crude oil. In Iran, a wide range of types of crude oil are being processed. Therefore, different chemical demulsifiers are used for demulsification. In this study, the performance of several chemical demulsifiers has been compared.

Keywords: Heavy crude oil, Chemical demulsifier, Emulsion;

I. INTRODUCTION

The complex nature of water-in-oil (W/O) emulsions is a principal obstacle to develop a satisfactory separation technique in the petroleum industry [1]. In spite of the recent attempts to develop a reliable demulsification technique, most of the water-in-crude oil emulsions cannot be broken in small timespans [1]. The stability of W/O emulsions originates from the creation of a rigid film at the water-oil interface [2]. The indigenous materials of crude oil such as asphaltenes and resins tend to accumulate at the interface, resulting in a film that performs as a structural barrier to the aggregation of the droplets [2]. The solidity of the film increases by time, as the accretion of the indigenous materials at the interface rises [3]. Chemical demulsification is known to be the most common method for the pretreatment of crude oil [1]. Due to the high interfacial activity of chemical demulsifiers, they tend to adsorb/displace the indigenous species present in crude oil, which results in weakening of the interfacial film [4]. Therefore, many studies have been done in this regard.

The effects of chemical demulsifiers on the properties of viscoelastic dilatants and the water-crude oil interface were measured [5]. The results clearly state that chemical demulsifiers can reduce dilatant of water at the water-crude oil interface [5-9]. To optimize the production and selection of chemical demulsifier formulation, the effect of parameters such as temperature, pH, hydrocarbon source, chemical demulsifier concentration, fresh water content and water salinity are important [10,11].

In this study, a comparison was made between several samples of chemical demulsifiers used in Iran for the separation of water from crude oil. Therefore, according to the results of this paper, it is possible to select the suitable chemical demulsifier for each crude oil faster in future studies.

II. METHOD

Bottle test procedure

Bottle test is a renowned technique in the chemical industry to evaluate the capability of chemical demulsifiers in the separation of water from crude oil. The procedure of bottle test is to place the treated samples in an oven at 60°C for 12 hours and measure the separation/segregation of aqueous and oil phases [4]. The difference between the amount of separation or segregation in the cases when the agent is added and not added shows the performance/influence of chemical demulsifier.

III. RESULTS AND DISCUSSION

In the first step, a list of crude oil from Iran's oil fields has been prepared. Table 1 shows the characteristics of selected crude oils. Then, mixing the chemical demulsifiers with the crude oil is prepared. In Table 2, a list of chemical demulsifiers for injection into crude oil has been prepared. Furthermore, the procedure for adding chemical demulsifier to crude oil is described in Table 2.

Figures and Tables

Table 1: Crude oils specifications

Crude oil	Parameters			
Physical Characterization	Density (°API)	Asphaltene (%W)	Resin (%W)	Number of Reference
Cheshmeh-khosh	8.73	6.8	13.5	[6]
Bangestan	73.8	3.4	4.6	[6]
Gachsaran	31.03	5	8	[2]
Persian Gulf	19	10	2.6	[7]
Cheshmeh-khosh	9.15	3.75	22.5	[8]
Omidieh	38	0.39	23.35	[9]
Ahwaz	38.2	0.5	20	[9]
Sarvestan	27.34	5	8	[10]
South of Iran	24.51	2.8		[11]

Table 2: The emulsion preparation in the demulsification tests

Emulsion preparation				
Temperature of mixer (°C)	Time of mixer (min)	Rate of mixer (rpm)	Time of prepare sample emulsion and demulsifier (min)	Number of reference
60	30	10,000	5	[11]
60	30	15000	5	[10]
70	15	15000	1	[9]

Table 3 shows the type of selected materials and their comparison as chemical synthesized demulsifiers. This materials are used in experiments to separate water emulsion from crude oil.

Table 3: Chemical demulsifier selection

First demulsifier	Type of demulsifier	Second demulsifier	Type of demulsifier	Ref
QAM[1]	polymer	DDBSA[2], NE13[3]	cationic surfactant	[6]
ARN63[4]	biodemulsifier			[8]
TOMAC, Basorol, PDB 9935,	ionic liquids	Urea, Triethanolamine,	polymer	[9]
Basorol E 2032,		Fattyalcohol, ethoxylate		
TOMAC[5]	ionic liquids	TOMAB[6], CTAB[7]	ionic liquids	[10]
1-decyl-3-methylimidazolium chloride, 1-dodecyl-3-methylimidazolium chloride 1-tetradecyl-3-methylimidazolium chloride ILs].[8]			ionic liquids copolymers	[11]

Table 4 shows the types of solvents that have been shown to be effective in chemical demulsifier. This solvent can increase the separation efficiency of chemical demulsifiers. Based on the articles in which these solvents have been studied, these solvents can be used in a variety of proportions.

Table 4: Types of solvents

Solvent	Reference
Methanol, xylene, toluene, isopropanol, ethylene glycol, propylene glycol	[6]
Chloroform, methanol,	[8]
Butanol, ethanol, Heavy aromatic, Mix xylene	[9]
Hydrochloric acid, sodium hydroxide, methanol, toluene, xylene,	[10]

Based on the results, it can be seen that organic solvents, along with polymer and ionic liquid compounds, can act as effective chemical demulsifiers to separate water from heavy crude oil.

IV. CONCLUSION

The optimum result of the process of separating water from heavy crude oil with a type of chemical demulsifier is determined by the design of experiment method. The results obtained from the field study showed that the reactivity of ionic liquid and polymeric materials are more likely to be selected. The results of the separation of water and oil with chemical demulsifier is 95%. In this study, in order to achieve the best results in separating water and oil emulsion, parameters such as type of materials and their concentration, pH, temperature and fresh water have been used as influential variables in experimental design. Therefore, one of the

[1] Didecyl dimethyl ammonium chloride ($C_{22}H_{48}ClN$)
[2] Dodecyl benzene sulfonic acid ($C_{12}H_{25}C_6H_4SO_3H$)
[3] Antisludge commercial from BJ Services Co
[4] The demulsifying performance of Paenibacillus alvei
[5] Trioctyl methylammonium chloride
[6] Trioctyl methylammonium bromide
[7] 1-Hexadecyltrimethylammonium bromide
[8] Imidazol iumionic liquids substituted with long alkyl chains (n=10, 12 and 14) were synthesized and used as surface-active demulsifiers which were coupled with Cl, *PF*6 and *NTf*2 anions.

parameters can be variables and the others are considered constant and the results are analyzed. At the end, it is possible to optimize the formulation of a suspending agent for the separation of water from heavy oil.

REFERENCES

[1] J.S. Eow, M. Ghadiri, A.O. Sharif, T.J. Williams, Chem. Eng. J. vol. 84, pp. 173–192, **2001**.
[2] J. Sjöblom, N. Aske, I.H. Auflem, Ø. Brandal, T.E. Havre, Ø. Sæther, A. Westvik, E.E. Johnsen, H. Kallevik, Adv. Colloid Interface Sci. vol. 100–102, pp. 399–473, **2003**.
[3] D. Langevin, S. Poteau, I. Hénaut, J.F. Argillier, Oil Gas Sci. Technol. vol. 59, pp. 511–521., **2004**.
[4] M. Razi, M.R. Rahimpour, A. Jahanmiri, F. Azad, J. Chem. Eng. Data. Vol. 56, pp. 2936–2945, **2011**.
[5] Y. Wang, L. Zhang, T. Sun, S. Zhao, J. Yu, Colloid and Interface Science, vol. 270,pp.163–170, **2004.**
[6] A. Mirvakili, M. R. Rahimpour, A. Jahanmiri, Chemical Engineering Data, vol. 57, pp. 1689−1699, **2012.**
[7] L. Vafajoo, K. Ganjian, M. Fattahi, Petrolum Science and Engineering, vol.90-91, pp. 107-111, **2012.**
[8] S. Sh. Amirabadia, A. Jahanmiria, M. R. Rahimpoura, B. Rafie niaa, P. Darvishib, A. Niazic, Colloids and Surfaces B: Biointerfaces,vol.109 ,pp. 244– 252, **2013**.
[9] P. Hajivand, and A. Vaziri, Brazilian Journal of Chemical Engineering, Vol. 32, pp. 107 - 118, **2015**.
[10] P. Biniaz, M. Farsi, M. R. Rahimpour, Fuel, vol. 184, pp.325–333, **2016**.
[11] N. Hazratia, A. A. Miran Beigib, M. Abdoussa, Fuel,vol 229, pp. 126–134, **2018.**

New Insight into Ice Growth and Inhibition by Antifreeze Protein: Atomistic Molecular Dynamics Simulation

M. Shahabi[a], K. Peyvandi[a]*, M. Maddah[a,b]
[a]*Faculty of Chemical, Petroleum and Gas Engineering, Semnan University, Semnan, Iran*
[b]*Department of Chemistry, K. N. Toosi University of Technology, Tehran, Iran*
Email: k_peyvandy@semnan.ac.ir

Abstract: Ice formation consisting of nucleation, growth, and recrystallization, is a ubiquitous process and crucial in the wide-ranging fields. Antifreeze proteins (AFPs) protect living organisms from freezing damage via controlling ice formation. AFPs are believed to prevent ice formation by shaping ice crystals, tuning ice nucleation, and inhibiting ice growth and recrystallization by binding to specific ice crystal planes. Despite active research, the mechanism of ice recognition by antifreeze protein has still been ambiguous. In this study, the process of ice growth and formation has investigated in the presence of antifreeze proteins through Molecular Dynamics (MD) simulation. We observe that the structure of ice has changed in the presence of AFP. Moreover, AFP binds on the ice surface through hydrophobic interaction which mediated between pendant groups of amino acids and ice cavity.

Keywords: Antifreeze protein, Hydrophobic interaction, Molecular Dynamic Simulation, Nucleation.

I. INTRODUCTION

Variety of organisms such as plants, insects, bacteria, and fishes produce antifreeze proteins (AFPs) to prevent ice formation and survive in subzero environments [1-4]. AFPs depress the freezing temperature without affecting the melting point and achieve a thermal difference which is termed as thermal hysteresis (TH) [5]. The extent of TH activities of different AFPs is various. Plant AFPs have been identified in species such as bittersweet nightshade, winter rye, carrot, and ryegrass [7]. They have a relatively weak TH activity about 0.1–0.5℃, which is less than that of fish AFPs and significantly less than that of insect AFPs. The mechanism behind the TH activity of AFPs is assumed to be due to the Gibbs−Thomson (Kelvin) effect [6]. AFPs bind to one or more ice crystal surfaces, and adsorption of protein on the ice surface causes micro curvatures and inhibits of further growth. AFPs also have a pronounced effect on ice recrystallization (IR), that is, the growth of large ice crystals at the expense of small ones. Plant AFPs have a greater effect on RI activity than on TH [8].

Two main hypotheses have been proposed for AFP activity on the inhibition of ice growth. Hydrogen bond matching hypothesis has been proposed which is primarily motivated by the fact that the ice-binding surface of many AFPs contains an array of repeating polar residues, and their repeat distances match with the oxygen atom repeat distances of that particular ice plane where it binds. Recent experiments, as well as simulation studies, reveal the role of hydrogen bond of IBS on ice inhibition [9-11]. Moreover, it has proposed that the binding of AFP to ice has driven by hydrophobic hydration, and hydrophobic moieties induce water order [12]. However, the ice-binding mechanism of AFPs, including a full interpretation, has not been understood yet.

In this paper, we study the ice crystals growth in the presence of antifreeze protein from DcAFP by atomistic molecular dynamics simulation. The effect of this protein and its binding on the ice crystal structure and the amount of deterioration and blockage of crystalline formation has considered.

II. METHODS

All of the molecular dynamics simulations were carried out using Gromacs 5.1.1 simulation software [13]. Amber99sb force field was used for the protein [14], and water molecules were modeled with the TIP4P-ice model. The initial structure of DcAFP protein was obtained from Protein Data Bank, PDB ID: 1OGQ. The starting ice slab was translated and replicated to create a simulation box with enough bulk water in both phases (liquid and solid). The final dimension of the boxes was 14×6×10 nm [15]. Protein was placed on the prism planes in the water to examine the growth of the ice as shown in Fig. 1. Moreover, we have simulated a system without AFP as a control. NPT ensemble was adopted for all simulations. Pressure was set to 1 atm and controlled by the Parrinello−Rahman barostat [16]. Temperature was controlled by the Nose−Hoover thermostat [17,18]. Cut-off radius for both Coulombic interactions (calculated using the PME method) and Lennard-Jones interactions was set to 10 Å. All bonds involving hydrogen atoms were treated by the LINCS algorithm. Time step was

2 fs for integrating the equation of motion. Final production simulations of 1 ns were performed in the NPT ensemble, and the trajectories were saved every 1 ps.

III. RESULTS AND DISCUSSION

In this study, root mean square deviation (RMSD), root mean square fluctuation (RMSF), hydrogen bond analysis and solvent accessible surface area (SASA) are calculated to elucidate the role of AFP on inhibition of ice growth. Different snapshots of simulation indicate that AFP leads to change in the pattern of ice growth compared to the control system.

To verify the stability of the protein structure during the simulation, the RMSD parameter is computed against the initial structure to represent the deviation of the simulated structure compared to the reference structure. RMSD is increased at first of the simulation, because adsorption of protein on the ice/water interface causes instability in the structure. When AFP completely binds on the ice surface, RMSD is converged to a distinct value.

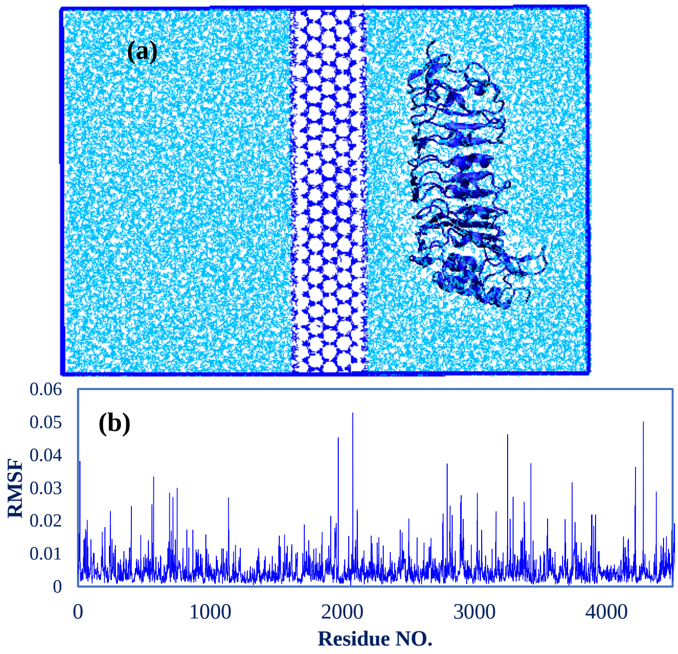

Fig.1: (a) The initial structure of the ice/AFP system. Secondary structure of DcAFP is shown in cartoon model. Ice slab is represented by blue colour. (b) RMSF.

To obtain which amino acids have an important role in the binding of AFP on the ice surface, the average RMSF has computed for all residues of the protein. As seen in Fig. 1b suggesting that ASN amino acids plays a crucial role in binding of AFP on ice surface and consequently inhibition of ice by AFP.

To investigate the ice formation from the water phase, the number of hydrogen bond which formed during simulation time has calculated in table 1. The amount of the HBs between water-water decreases in the presence of antifreeze protein compared to the control system, which indicates a decrease in the growth of ice in the presence of antifreeze proteins. The number of HBs between protein residues is on the contrary higher when the protein is at the interface. Comparing all these values it seems that when the protein is in bulk water, a portion of its internal hydrogen bonds are lost; at the same time the hydrophilic SAS grows, so water can now get in contact with hydrophilic residues and form new hydrogen bonds.

Table1: Hydrogen Bond Count and Solvent Accessible Surface of DcAFP in Water at Ice/Water Interface.

property	**Ice/water interface**
No. HBond (water-water)	4186
No. HBond (DcAFP - DcAFP)	50
No. HBond (DcAFP - water)	254
SAS hydrophobic (nm^2)	52.4
SAS hydrophilic (nm2)	95.06

IV. CONCLUSION

In this study, we performed MD simulation to consider the ice growth in the presence of antifreeze proteins found in the carrot (DcAFP) in the two-phase system of ice/water. The MD simulations of the DcAFP at the ice/water interface illustrate that AFP binds on the ice and because of this, it and displays instability behavior. Also, AFP changes the shape of ice crystals and prevents ice crystallization. Binding as a result of hydrophobic interaction and hydrogen bond formation causes reduces the freezing point. Finally, it could be concluded that DcAFP can trigger local melting of the ice slab and inhibiting the further growth of ice. The local melting of ice has been proposed as possible explanation for the controversial experimental results which show both quasi permanent and reversible binding of the AFPs onto the ice surface.

REFERENCES

[1] Z. He, K. Liu, and J. Wang, Acc. Chem. Res, vol. 51, pp. 1082−1091, **2018**.

[2] A.L. DeVries, D.E. Wohlschlag, Science vol. 163, pp. 1073−1075,**1969**.

[3] S.P. Graether, M. J. Kuiper, S. M. Gagne, V. K. Walker, Z. Jia, B. D. Sykes, P. L. Davies, Nature. Vol. 406, pp.325−328, **2000**.

[4] T. Sun, F. Lin, R. L. Campbell, J. S. Allingham, P. L. Davies, Science, vol. 343, pp.795−798, **2014**.

[5] J. A. Raymond, A. L. DeVries, Proc. Natl. Acad. Sci. U. S. A. , vol. 74, pp. 2589−2593, **1977**.

[6] Knight, C. A. Structural Biology: Nature, vol.406, pp. 249−251, **2000**.

[7] D. Worrall, L. Elias, D. Ashford, M. Smallwood, C. Sidebottom, P. Lillford, J. Telford, C. Holt, and D. Bowles, Science, vol. 282, pp.11–13, **1998**.

[8] C. A. Knight, A. L. DeVries, L. D. Oolman, Nature, vol. 308, pp.295−296, **1984**.

[9] Guido Todde, Sven Hovmöller, and Aatto Laaksonen, *J. Phys. Chem. B*, vol. 119, pp. 3407-3413, **2015**.

[10] K. Meister, S. Ebbinghaus, Y. Xu, J. G. Duman, A. DeVries, M. Gruebele, D. M. Leitner and M. Havenith, *Proceedings of the National Academy of Sciences*, vol. 110, pp. 1617- 1622, **2013**.

[11] S. Ebbinghaus, K. Meister, B. Born, A. L. DeVries, M. Gruebele and M. Havenith, *Journal of the American Chemical Society*, vol. 132, pp. 12210-12211, **2010**.

[12] K. Meister, S. Strazdaite, A. L. DeVries, S. Lotze, L. L. C. Olijve, I. K. Voets and H. J. Bakker, *Proceedings of the National Academy of Sciences*, vol. 111, pp. 17732-17736, **2014**.

[13] H. J. Berendsen, D. van der Spoel and R. van Drunen, Computer physics communications, vol.91, pp. 43-56, **1995**.

[14] Junmei Wang, Romain M. Wolf, James W. Caldwell, Peter A. Kollman, David A. Case, COMPUTATIONAL CHEMISTRY, vol. 25, pp 1157-1174, **2004**

[15] C. Yang and K. A. Sharp, *Proteins: Structure, Function, and Bioinformatics*, vol. 59, pp. 266-274, **2005**.

[16] Parrinello, M.; Rahman, A. Polymorphic Transitions in Single Crystals: a New Molecular Dynamics Method. J. Appl. Phys. vol. 52, pp.7182−7190, **1981**.

[17] Hoover, W. G. Canonical Dynamics: Equilibrium Phase-space Distributions. Phys. Rev. A vol. 31, pp.1695−1697,**1985**.

[18] Nose, S. A Molecular Dynamics Method for Simulations in The ´Canonical Ensemble. Mol. Phys. vol. 52, pp. 255−268, **1984**.

2-Acrylamido-2-Methyl-1-Propanesulfonic Acid hydrogel: thermal conductivity Improvement by carbon nanostructures

Mohammad Hassan Loghmani*, Erfan Zare
Department of Nanotechnology, University of Guilan, Rasht, Iran
Email: mhmdloghmani@guilan.ac.ir
Erfan_zare@msc.guilan.ac.ir

Abstract: Thermal conductive new materials offer new possibilities for replacing old materials in use or even invent new application. For example, in fuel cell membrane, corrosion inhibitory and etc. Heat exchange would expand material lifetime and performance. In this paper, 2-Acrylamido-2-Methyl-1-Propanesulfonic Acid (AMPS) polymerized and cross-linked with Ethylene glycol dimethacrylate (EGDMA) and several nanocomposites were synthesized with Graphene oxide (GO) and acid-treated multi-walled carbon nanotubes (AMWCNT). The thermal conductivity measured with P.A. Hilton Ltd Heat Conduction Unit, H940 and compared. AMWCNT composite has been shown best heat transfer among samples with 5.42 W/mK.

Keywords: AMPS, Hydrogel, Nanocomposite, Graphene, Thermal conductivity

I. INTRODUCTION

Thermal conductivity and interfacial thermal conductance play crucial roles in the design of engineering systems where temperature and thermal stress are of concerns. [1] This property in materials compare with their thermal conductivity coefficient that known as "k". Polymers, in essence, have low k because of that in some usage this factor doesn't allow to use polymer as a practical material. poly 2-Acrylamido-2-Methyl-1-Propanesulfonic Acid is an ionic polymer that used in many industrials such as renewable energies, oil industry, coating, water treatment, and etc. [2-4] that exchanging heat through the material could not only increase lifetime of material but also expand the variety of application for this particular material. One of the most common ways to improve thermal transfer is to composition polymer with additives that have high thermal conductivity for example in bulk materials metals shows high heat transfer. In order to improve this ability in polymer carbon-based Nanostructures have shown promising enhancement. [5-8]

II. METHODS

Materials that needed in order to synthesis the final samples purchased from different companies. 2-Acrylamido-2-Methyl-1-Propanesulfonic Acid (AMPS) (Merck, Germany), potassium persulfate (KPS) (Merck, Germany), ethylene glycol dimethacrylate (EGDMA) (Sigma-Aldrich, USA) and Graphene oxide colloid (GO) (GrapheneX, Iran) and acid-treated multi-walled carbon nanotubes (AMWCNT) were used as received.

In order to Homopolymerization as well as crosslinking reactions of AMPS was carried out in aqueous medium [10]. In this research set of reaction for polymerization, AMPS (4.0 g) and potassium persulfate (0.443 mM) were dissolved in 4.0 ml deionized water. The solution was stirred and heat to 50℃ for 30 min carried out under N_2 atmosphere. 0.505 mM EGDMA was added to that reaction mixture in order to form the network.

Furthermore, for composition 1%wt of additives were sonicated for 30 min in 4.0 ml deionized water then used as the solvent for the method mentioned above.

In order to thermal conductivity coefficient measurement, it is necessary to have 25 mm diameter and 8 mm thickness dimension samples. So a suitable template, considering the shrinkage hydrogel during losing water. fig 1

After the synthesis solution pours in the template and will dry in an oven for 24 hours.

fig 1: a: PAMPS/EGDMA b: AMWCNT 1%wt/ PAMPS/EGDMA c: GO 1%wt/ PAMPS/EGDMA

III. RESULTS AND DISCUSSION

A. *Polymerization of AMPS and network formation*

The polymerization initiated by a free radical initiator like ammonium persulfate. It is a clean and least energy-consuming process as it dissociates at the ambient temperature in the presence of water. To be sure poly AMPS (PAMPS) formed first of all it could notice with a change in melting point that observed it be an increase from 187℃ for AMPS monomer to 329℃ for PAMPS. Furthermore, the change of monomer to polymer and network forming could be seen in the FTIR spectrum fig 2.

The difference between monomer with other is obvious however to compare polymer with hydrogel It shows characteristic bands at 3435.9 cm^{-1} (-NH stretching of the secondary amide), 2360.3 cm^{-1} (-SO-H stretching strong and weak bands, respectively), 1647.3 cm^{-1} (C=O stretching of amide), 1555.5 (-N-H in-plane bending), 1450.9 cm^{-1} and 1395.0 cm^{-1} (-CH_3 group bending), 1042.7 cm^{-1} and 1210.1 cm^{-1} (-SO_3 symmetric as well as asymmetric stretching in –SO_3H), 626.9 cm^{-1} (-S-O stretching). In the spectrum of PAMPS/EGDMA the corresponding absorption peaks have been observed at 3431.5 cm^{-1}, 2928.3 cm^{-1} and 2366.5 cm^{-1}, 1654.8 cm^{-1} (C=O stretching in amide), 1042 cm-^{1} and 1222.6 cm^{-1} (SO_3 symmetric as well as asymmetric stretching in –SO_3H), 622.5 cm^{-1} (-S-O stretching). It also has one peak at 1742.5 cm^{-1} due to the stretching of –C=O of ester (of the cross-linker). [10]

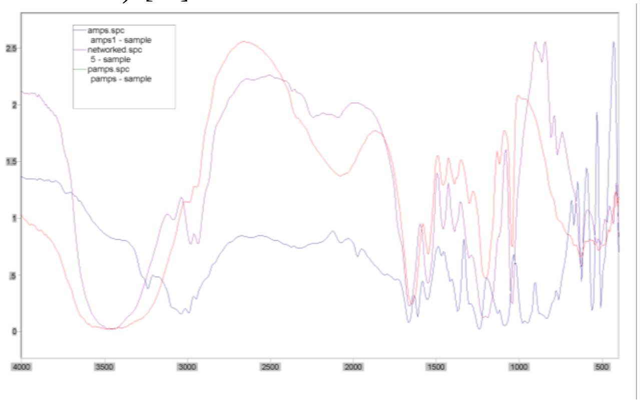

fig 2: FTIR spectrum of AMPS monomer (blue line) PAMPS (red line) and Networked PAMPS/EGDMA (Purple line)

Also, evidence for the presence of GO and AMWCNT could see in composite XRD Pattern that shown in fig 3 that shows the existence of carbon-based nanostructure. The noises in the pattern are because of polymer molecules complex structures and Nano-sized additive.

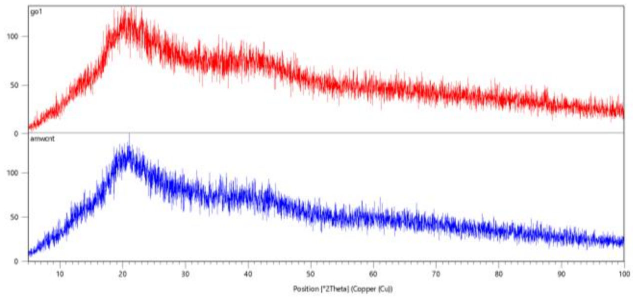

fig 3: Xrd pattern GO/PAMPS/EGDMA Composite (red) AMWCNT/PAMPS/EGDMA Composite (blue)

B. *Thermal conductivity coefficient*

Because of the lack of research about PAMPS, a sample of based polymer should observe first of all. In order to measure Thermal conductivity coefficient data that Heat Conduction Unit report should use in Fourier's law equation that shown in **Error! Reference source not found.**. Fourier's law equation where A is the cross-sectional surface area, ΔT is the temperature difference between the ends, Δx is the distance between the ends, Q is the amount of heat transferred per unit time an k is Thermal conductivity coefficient. The result of this experiment for PAMPS sample shown in

Table 1.

$$Q = -kA\frac{\Delta T}{\Delta x} \qquad (1)$$

Table 1: PAMPS/EGDMA

PAMPS/EGDMA	t1	t2	t3	t4
	22.25	23.62	55.69	61.75
	0.0015	0.0455	0.0555	0.101
	x1	x2	x3	x4
k	4.18			

In Table 2 and

Table 3 it can be seen adding carbon nanostructures can improve the heat transfer of PAMPS/EGDMA, this improvement for AMWCNT with k=5.42 W/mK is around 30 percent and for GO composite with k=5.01 W/mK near 20 percent.

Table 2: AMWCNT 1%wt/ PAMPS/EGDMA data

AMWCNT 1%wt/ PAMPS/EGDMA	t1	t2	t3	t4
	22.06	25	48.5	53.44
	0.0015	0.0455	0.0555	0.101
	x1	x2	x3	x4
k	5.42			

Table 3: GO 1%wt/ PAMPS/EGDMA data

GO 1%wt/ PAMPS/EGDMA	t1	t2	t3	t4
	22.19	29	55.75	62.25
	0.0015	0.0455	0.0555	0.101
	x1	x2	x3	x4
k	5.01			

As we can see AWMCNT not only improve the thermal conductivity of polymer but also heat traverse across the composite with AWMCNT easier than GO composite. That caused by its tube structure that allows heat to pass through and better bounding that it has with base polymer because of its functional surface.

IV. CONCLUSION

as a conclusion, it has been demonstrated that mixing PAMPS/EGDMA polymer base with a suitable additive will increase the thermal conductivity property of this polymer. And in the comparison between GO 1%wt and AMWCNT 1%wt composite, AMWCNT with k=5.42 W/mK has a better enhancement in the rate of 30 percentages.

REFERENCES

[1] Zhao, Dongliang, Xin Qian, Xiaokun Gu, Saad Ayub Jajja, and Ronggui Yang. *Journal of Electronic Packaging* 138, no. 4 (2016): 040802.

[2] Guo, Wenya, Canzhu Gao, Qimeng Li, Zhongfa Cheng, and Xiaojing Qi. *Environmental Progress & Sustainable Energy* 35, no. 3 (2016): 833-839.

[3] Qiao, Jinli, Takeo Hamaya, and Tatsuhiro Okada. *Chemistry of materials* 17, no. 9 (2005): 2413-2421.

[4] Büyükyağcı, Arzu, Gözde Tuzcu, and Leyla Aras. *Cement and Concrete Research* 39, no. 7 (2009): 629-635.

[5] Balandin, Alexander A., Suchismita Ghosh, Wenzhong Bao, Irene Calizo, Desalegne Teweldebrhan, Feng Miao, and Chun Ning Lau. *Nano letters* 8, no. 3 (2008): 902-907.

[6] Choi, S. U. S., Z. G. Zhang, WLockwoodFE Yu, F. E. Lockwood, and E. A. Grulke *Applied physics letters* 79, no. 14 (2001): 2252-2254.

[7] Nan, Ce-Wen, Gang Liu, Yuanhua Lin, and Ming Li. *Applied Physics Letters* 85, no. 16 (2004): 3549-3551.

[8] Eksik, Osman, Stephen F. Bartolucci, Tushar Gupta, Hafez Fard, Theodorian Borca-Tasciuc, and Nikhil Koratkar. *Carbon* 101 (2016): 239-244.

[9] Han, Zhidong, and Alberto Fina. *Progress in polymer science* 36, no. 7 (2011): 914-944.

[10] Chauhan, Ghanshyam S., and Godawari Garg. *Desalination* 239, no. 1-3 (2009): 1-9.

Numerical Investigation Effect of Geometry in Micro Droplet Generation

Elmira Ghazanfari jajin[a*], ***Farhad Sadegh Moghanlou***[a], ***Mohammad Vajdi***[a], ***Shapoor Jafargolinejad***[b]
[a]*Department of Mechanical Engineering, Mohaghegh Ardabili University, P.O. Box 179, Ardabil, Iran*
[b] *Department of Mechanical Engineering, Ardabil branch, Islamic Azad University, Ardabil, Iran*
Email: e.ghazanfari.j@student.uma.ac.ir

Abstract: Understanding the micro-scale physical phenomena is important because of their widespread use in industry, medical sciences, biological sciences and pharmaceuticals. As microfluidics technologies have developed into smaller dimensions, the application of droplets in the microfluidics system, with the possibility of precise and effective control over the generation of microparticles, has been extensively studied. In this research, the generation of droplets in three types of miniature microchannels with different geometries has been studied numerically by finite element method using water as dispersed fluid and oil as continuous fluid.The equations governing the fluid flow are discretized using the Galerkin method and solved using Comsol software.The effect of microchannel geometrical changes as a passive method on droplet size and frequency was investigated. The results shows that the droplet diameter decreased with changes in the primary geometry ,the frequency of droplet generation increases, by application two barrier geometries, Large volumes of droplets are produced.

Keywords: Microchannel, Droplet Generation, TwoPhase Flow, Newtonian Fluid, Geometry

I. INTRODUCTION

Droplet-based microfluidics has emerged as versatile platforms offering unique advantages with a wide span of applications in biology, chemistry and Industrial. Modern applications demand size-optimized droplets with various dimensions for encapsulation reagents within a (continuous- or dispersed phase) fluid. Size and frequency are important in the production of droplets and are essential requirements. In these systems, droplets of arbitrary dimensions can be produced in different geometries [1]. The formation of droplets depends on important factors such as fluid properties, channel dimensions, two-flow discharge (continuous phase and dispersed phase) that affect the diameter of the droplet and its frequency, change in either of these can have an effect on the output [2]. The droplet generation methods can be active or passive, the former being controlled by the external energy of the diameter and the frequency of the droplets formed, and the latter is controlled by the droplet's behavior without the use of external energy. Physical understanding of both active and passive droplet generation is essential for the production of droplets as required [3]. One of the passive methods of droplet generation is the application of microchannel geometrical changes. In this work, the effect of microchannel geometry on the diameter and frequency of droplet generation is studyed. The governing equations are solved using the finite element method in Comsol[1] software.

II. METHODS

In this study, three different geometries are designed for microchannel. The first geometry (Fig.1_a) is a simple T-shaped microchannel that has been used in several cases by previous research[4] similar to the geometry used to droplet generation.The second and third geometries were designed by modifying the first geometry and creating two different barriers (Fig.1_b,c). The boundary conditions governing the shape geometry are also given by the type of geometry in Fig.1. The angle of contact of each drop of liquid with its surface is effective in determining the wettability. As the contact angle tends to zero, the wettability is higher and the hydrophobicity increases. The walls all have a 20 degree wetting condition, which makes the angle between the wall and the joint surface when the joint surface contacts the microchannel wall. Water and oil have been used as dispersed and continuous fluids, The properties including density and dynamic viscosity shows in Table 1. The density of the selected oil is lower than that of water and the dynamic viscosity of the oil is higher than that of water. The fluid inlet has a specified discharge and in output, pressure is constant. wall and joint surface was non-slip.

As shown in Fig.1,continuous fluid enters the channel horizontally from the vertical and dispersed fluids. The continuous and dispersed fluid velocities at the inlet are (0.06 and0.09m/s).The fluid is laminar, incompressible and isothermal, with the exception of gravitational force and changes in physical properties such as viscosity, surface tension and density relative to temperature.

---

[1] *MultiPhysics Software*

III. RESULTS AND DISCUSSION

In the present work, numerical investigation of the droplet generation in three types of microchannels is investigated. Numerical simulation results showed that by modifying the geometry and impeding the microchannel geometry as a factor in the inactivation method in microparticles formation, microparticles production rates and dimensions changed dramatically. As can also be seen in Fig.2, two types of barriers can be observed in the microchannel geometry, taking into account the specific and constant velocity and discharge at the channel inlets (dispersed and stationary fluid) in all three from top to bottom, the diameter of the droplets has decreased, and this decrease has been accompanied by an increase in the number of droplet generation. The frequency of droplet generation also increase. The frequency and number of droplets produced in geometry (c) were higher than the other two geometries, while smaller droplets were also generated in this model. The results are consistent with the results of Zhang et al. [5] in predicting droplet diameter and frequency, while fine droplets have a higher importance in chemical and biological reactions and have a higher potential in applications. The scattered fluid in a barrier-like structure produces a smaller radius droplet, which is close to the results of research [6]. The barriers in the two geometries contribute to the rapid separation of the droplet from the fluid flow and the thawing phase by generating force against the dispersed fluid.

A. Figures and Tables

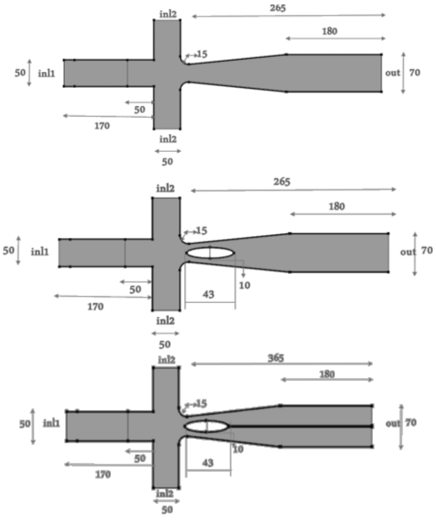

Fig.1: The geometries used in this work are top-down [a, b, c] (Micro_Scale)

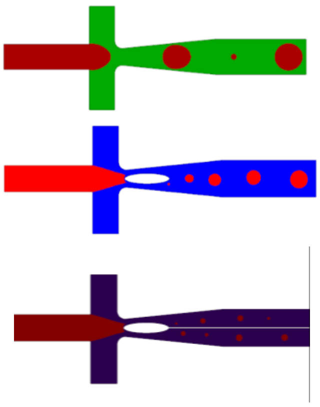

Fig.2: The results of numerical simulation of droplet generation in 3 type of geometries [a, b, c]

Table1: Properties of scattered and continuous fluids in the present study [4]

Fluid_Name	Density ($\frac{kg}{m^3}$)	Dynamic vicosity (Pa.s)
water	1000	0.001
Oil(FC-40)	800	0.003

B. Equations

The following equations are used to model droplet generation:

Mass survival equation:

$$\nabla . V = 0 \qquad (1)$$

Momentum survival:

$$\rho(u\frac{\partial u}{\partial x} + v\frac{\partial u}{\partial y}) = -\frac{\partial P}{\partial x} + \mu(\frac{\partial^2 u}{\partial x^2} + \frac{\partial^2 u}{\partial y^2}) \qquad (2)$$

Level set equation for analyzing two separate phase joint seasons

$$\frac{\partial \varphi}{\partial t} + \mathrm{V}.\nabla\varphi = \gamma\nabla.(\varepsilon_{ls}\nabla\varphi - \varphi(1-\varphi)\frac{\nabla\varphi}{|\nabla\varphi|}) \qquad (3)$$

In these relationships V represents the fluid velocity vector (m / s), ρ (kg/m^3)fluid density, u fluid velocity (m / s), P pressure, μ dynamic viscosity, φ characteristic distribution function (common boundary tracer). The two scattered and continuous fluids (γ), ε_ls are numerical stabilization parameters, the first of which represents the re-initialization parameter and the second parameter that determines the thickness of the joint surface, assuming the maximum lattice size under the domain adjacent to the joint surface.

IV. CONCLUSION

In the droplet formation process, the continuous formation of small droplets with equal spacing and the velocity of droplets generation are of great importance. In this study, the effect of geometry as a passive agent on droplet generation in miniature microchannels was investigated. The results of numerical simulation showed that by creating barrier, at discharge and constant velocity in the inlet channels and taking into account the constant mean pressure at the outlet, the diameter of the droplets produced decreases and the frequency of droplet production increases. Increasing frequency intensity and decreasing droplet diameter are more common in the third geometry than in the other two geometries. Barriers to geometries contribute to faster separation of dispersed fluids and to the formation of smaller droplets with higher volumes. The results of this numerical study can be used in the practical application stages of microparticles production in various industries.

REFERENCES

[1] phenomena Hua, B. Zhang, and J. Lou, Numerical Simulation of Microdroplet Formation in Coflowing Immiscible Liquids, American Institute of Chemical Engineers, Vol. 53, No. 10, pp 2534-2545, **2007**.

[2] H. Liu, Y. Zhang, Droplet formation in microfluidic cross junctions, Physics of Fluids, 23(8),pp 1-11, **2011**.

[3] Pingan Zhu, Liqiu Wang, Passive and active droplet generation with microfluidics: a review, Lab on a Chip Journal, www.rsc.org/loc, **2017**.

[4] A.Abrishamkar, A.S. Rane1, K.S. Elvira, R.C.R. Wootton, T. Sainio, A.J. deMello, A COMSOL Multiphysics® Model of Droplet Formation at a Flow Focusing Device, Comsol conferevcne Rotterdam, **2013**.

[5] Sh.Zhang,C.Guivier-Curien,S.Veesler,N.Candoni,Chemical EngineeringScience, 138(2015)128–139, **2015**.

[6] W.-C. Jeong, J.-M. Lim, J.-H. Choi, J.-H. Kim, Y.-J. Lee, S.-H. Kim, G. Lee, J.-D. Kim, G.-R. Yi and S.-M. Yang, Lab on Chip, 12, 1446–1453, **2012**.

The Effect of Core-Shell Magnetic Nano Catalyst on Oxidation of Alcohols

Z. Nikbakht[a], **F. Kabiri Esfahani**[a]*
Department of Chemistry, Faculty of Science, University of Zanjan, Zanjan, P.O. Box 45371-38791 Islamic Republic of Iran
Email: f.Kabiri@znu.ac.ir

Abstract: Keggin-type lacunary polyoxometalate supported silica coated magnetic nanoparticles ($Fe_3O_4@SiO_2@POM$), was prepared by using low cost precursors and a facile immobilization technique. The final catalyst, which was characterized by SEM and FT-IR techniques, was found to be an efficient and environmentally benign catalyst for the oxidation of alcohols leading to the carbonyl derivatives. After the reaction, the catalyst could be effortlessly separated by external magnet and reused for 8 consecutive runs, without any significant loss in catalytic efficiency. The catalytic system presented offers a reusable strategy for the efficient synthesis of carbonyl compound, simplicity in operation, and a green reaction profile by avoiding toxic conventional catalysts, oxidant and solvents.

Keywords: Heterogonous Catalyst, Magnetic Nanoparticles, Nano Catalyst, Polyoxometalate, Oxidation of Alcohols,

I. INTRODUCTION

The selective oxidation of alcohols to carbonyl compounds is one of the most fundamental and challenging processes from both a synthetic and industrial point of view, because the corresponding carbonyl compounds are versatile intermediates of valuable compounds such as pharmaceuticals, agricultural chemicals, and fine chemicals. Traditionally, the oxidation of alcohols has been achieved with stoichiometric inorganic oxidants, notably Cr(VI) and Mn(VII) based reagents. However these reagents are not only very expensive but there are serious toxicity problems associated with them. Consequently, due to the stringent environmental standards and economic pressures, much attention has been recently directed toward the use of new catalytic systems to achieve effective oxidation of alcohols with safer oxidant such as molecular oxygen or H_2O_2 as the terminal oxidant.

Therefore, due to the stringent environmental standards and economic pressures, the development of new reusable catalysts for the oxidation of alcohols under moderate conditions should attract a great deal of attention in both green chemistry and organic synthesis.

Polyoxometalates (POMs) are an exclusive class of molecular metal oxides with a tunable structure at the atomic level. They have established numerous potential applications in various fields. Especially, POMs have been extensively used as catalysts, because of their facilely modified acid–base properties and redox potential through molecular designing. Generally, POMs can be utilized as both heterogeneous and homogeneous catalysts, where the former favors facile separation of the catalysts, while the latter benefits high activity. Faced with the requirement for sustainable development, noteworthy effort has been made in the preparation of POM-based heterogeneous catalysts.

Recently, magnetic nanomaterials have emerged as alternatives to conventional materials as readily available, robust, high surface area heterogeneous catalyst supports. Notably, one of the interesting features of magnetically supported catalysts is that they can be easily recovered with an external magnet.

In this regard, we decided to stabilize POM on the magnetic nanoparticles and study its catalytic activity in the oxidation of alcohols at aqueous media (Scheme 3).

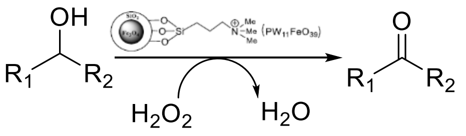

Scheme 1. Selective oxidation of various alcohols with Nanocatalyst Keggin-type of polyoxometalate in water.

II. METHODS

2.1. **Materials**. All of the chemicals used were of A. R. grade. Tetrabuthyl Ammonium bromide (Merck), Tetraethyl Orthosilicate (Merck), Sodium hydrogen phosphate (Merck), Sodium Tungstate (Merck), and Iron Nitrate (Merck). Acetic Acid, Toluen, benzyl alcohol were obtained from Merck and used as received.

2.2. **Synthesis of Nanoparticle Fe_3O_4.** First in a Round-bottom flask 5.4 g of ferric chloride (II) and 2 g of ferric chloride (III) were dissolved in 25 ml of 25% hydrochloric acid solution at room temperature. Next, 40 ml of 25%

ammonia was added slowly and dropwise to the reaction medium for 30 min. Subsequently, the mixture was stirred under argon for 30 minutes at room temperature. The magnetic nanoparticles were separated by an external magnet and washed with distilled water. Then the magnetic nanoparticles prepared inside the vacuum desiccator were completely dried.

3.2. **Synthesis of Core-shell magnetic nanoparticles Fe_3O_4 @ SiO_2.** The magnetic nanoparticles were added to a solution containing 6 ml of deionized water and 35 ml of ethanol and placed in an ultrasonic bath for 15 minutes to give a homogeneous and uniform solution. Next, 1.5 ml of tetraethyl Ortho Silicate was slowly added to the resulting mixture and then placed in the ultrasonic bath for 10 minutes. Then, 1.4 ml of 10% ammonia solution was added slowly for 10 minutes while stirring at room temperature. The resulting mixture was heated under argon atmosphere for 12 h at 40 °C. The Fe_3O_4 @ SiO_2 core-shell magnetic nanoparticles were separated by an external magnet and washed with deionized water and ethanol and dried in a desiccator under vacuum.

3.3. **Immobilization of Ammonium Propyl Trimethoxy Silane on the surface of the core-shell magnetic nanoparticles**. First in a Round-bottom flask One gram of Fe3O4 @ SiO2 magnetic nanoparticles and 15 ml of toluene were added and placed in an ultrasonic bath for 1 h to achieve a homogeneous, uniform solution. Then 0.8 ml of ammonium propyl Methoxy Silane was slowly added dropwise under severe stirring to a reaction medium. The resulting mixture was heated at 105 °C for 24 hours under reflux conditions. The material was separated by an external magnet and washed with deionized water and ethanol and dried for 10 h in an oven at 80 °C.

3.4. **Synthesis of Catalyst.**

First, 4.5 mmol (1.54 g) of sodium tungstate and 10 ml of distilled water were transferred to a 25 ml human. To the resulting solution was added 0.4 mmol (0.60 g) sodium hydrogen phosphate and 0.35 mmol (0.12 g) iron nitrate salt. The pH was adjusted to about 4.8 with the stirring of the solution by magnetic stirrer. It should be kept in mind that the pH of the solution should remain constant while mixing the solution. When the solution temperature reached about 80 to 85 °C, 0.4 g of magnetic substrate was added to the reaction medium. The precipitate was dried in the oven.

III. RESULTS AND DISCUSSION

The structure of prepared materials was characterized by various techniques including SEM and FT-IR, analysis. The morphology of the synthesized nanocatalysts was characterized through Scanning Electron Microscopy. It was found that the nanocatalysts had a spherical morphology and a relatively narrow particle size distribution (25-40 nm) (Fig. 1). FT-IR spectra of Fe_3O_4@SiO_2 magnetic nanoparticles showed characterization peaks for Fe–O–Fe, Si–O–Si and O–H groups (Fig. 2), which indicates the presence of iron oxide and silica phases. For polyoxometalate supported on Fe_3O_4@SiO_2 additional peaks were observed which confirms successful immobilization of POM on the surface of magnetic nanoparticles (Fig. 2).

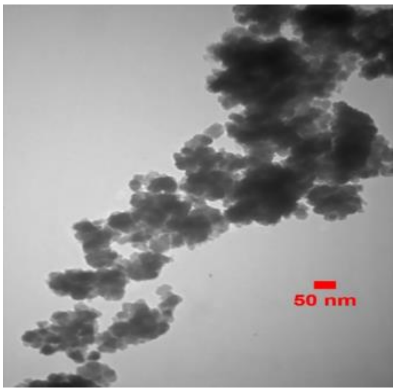

Fig.1: SEM Images of nanocatalyst Keggin-type of polyoxometalate

All of these observations confirmed the successful stabilization of POM onto the Fe_3O_4@SiO_2 nanoparticles. It is believed that the immobilization of POM on the surface of magnetic nanoparticles could provide a good distribution of catalytically active site on the support and stabilizes the POM during the chemical reaction, and also protects the polyoxometalate from aggregation.

Hence, we turned our attention to the catalytic activity of prepared catalysts in the oxidation of benzyl alcohol by emphasizing the possibility of employing water as a green solvent. Interestingly, it was found to be a significantly more efficient catalyst and the oxidation of benzyl alcohol proceeded at 90˚C within 4 h (Table 1, entry 1).

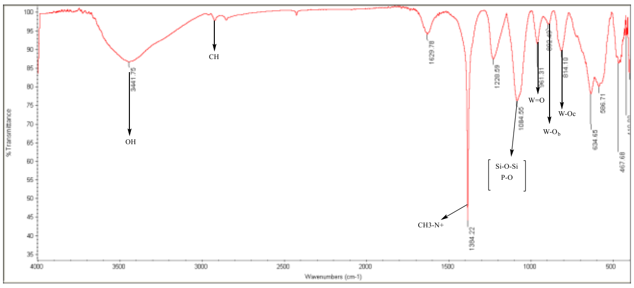

Fig. 2: FT-IR of Nanocatalyst Keggin-type of polyoxometalate

These promising observations encouraged us to examine the various primary alcohols bearing either electron-withdrawing or electron-donating groups or sensitive functional groups such as an allylic moiety were efficiently converted into the corresponding aldehyde in good to excellent yields and selectivity (Table 1). In particular, it is also found that the present protocol could be equally well with extremely challenging secondary benzylic alcohols and secondary aliphatic alcohols to give the corresponding ketones in good to excellent yields (Table 1).

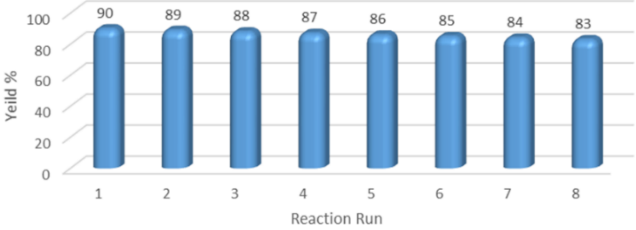

Fig. 3: Recyclability of the Nanocatalyst Keggin-type of polyoxometalate in the oxidation of benzyl alcohol with hydrogen peroxide in water.

In particular, the simple recycling and recovery of the supported catalysts from aqueous media are a very important issue from a sustainable chemistry point of view. In this regard, we investigated the recycling performance of the catalyst in the oxidation of benzyl alcohol. After the completion of the first run, catalyst was effortlessly separated from the reaction mixture with an external magnet, then washed with water and ethanol and finally dried before another reaction is performed. The recovered catalyst was then directly reused under the same conditions for at least 8 reaction cycles without significant loss of activity (Fig. 3), which clearly demonstrates the efficient immobilizing of POM on silica coated magnetic nanoparticles.

Table1: The oxidation reaction of various alcohols in the presence of POM catalyst

Entry	Substrate	Product	Time (h)	Efficiency (%)[a]
1	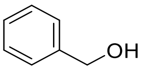	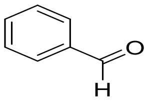	4	90
2	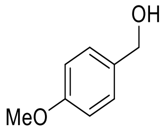	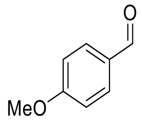	2	90
3	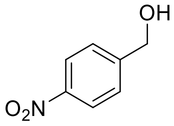	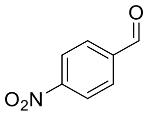	15	85
4	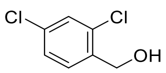	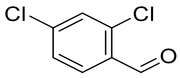	24	-
5	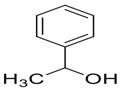	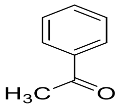	6	90
6	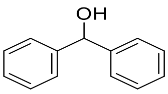	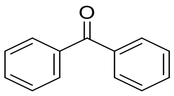	8	70
7	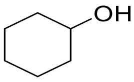	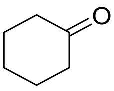	24	85
8	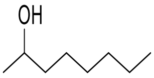	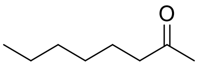	24	80
9	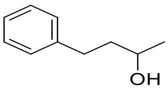	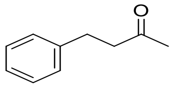	15	90
10	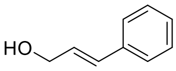	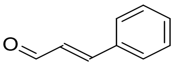	24	50
11	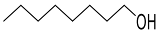	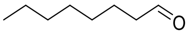	24	-

Reaction conditions: alcohol (0.5 mmol), catalyst (0.5mol %), water (1.5 mL), and 30% H_2O_2 (2.25 mmol) at 90°C.
a) Yields are quantitative and refer to GC yields.

IV. CONCLUSION

In conclusion, polyoxometalate core-shell magnetic nanoparticles was established as a simple and highly recyclable catalyst, which can be prepared by low cost precursors and facile immobilization technique. This catalyst was an effective for the oxidation of alcohols in water leading to the formation of excellent yields of carbonyl derivatives at 90˚C. The excellent catalytic capacity and outstanding recyclability of catalyst and the simple separation add to the versatility of this method.

REFERENCES

[1] D. J. Smith, ChemSusChem 10, 1, **2017**.

[2] V. Polshettiwar, and R. Varma, Green Chem. 12, 743, **2010**.

[3] G. Jessop, T. Ikariya, and R. Noyori, Chem. Rev. 99, 475, **1999**.

[4] Z. Lu, E. Lindner, and H. A. Mayer, Chem. Rev. 102, 3543, **2002**.

[5] C. Coperet, M. Chabanas, and J. M. Basset, Angew. Chem. Int. Ed. 42, 156, **2003**.

[6] P. S. Weiss, ACS Nano. 4, 1771, **2010**.

Effect of 1,3:2,4-Bis (3,4-dimethylobenzylideno) Sorbitol as a Nucleating Agent on Crystallization of Poly (3-hydroxybutyric acid)

Maede Zamani [a], ***Abdollah Omrani*** [b]*
Faculty of Chemistry, University of Mazandran, P. O. Box 453, Babolsar, Iran
Email:omrani@umz.ac.ir

Abstract: The behavior of isothermal crystallization and thermal properties of poly (3-hydroxybutyric acid) (PHB) with 1,3:2,4-Bis (3,4-dimethylobenzylideno) sorbitol (DMDBS) as a nucleating agent was studied using differential scanning calorimetry (DSC) and thermogravimetric analysis (TGA). The results showed that the addition of DMDBS increased the degree of crystallinity of PHB significantly. It was also observed that the used sorbitol derivative cannot improve the thermal stability of the polymeric films.

Keywords: Crystallization, DMDBS, Nucleating agent, Poly (3-hydroxybutyric acid)

I. INTRODUCTION

In recent years, environmental concerns have played a great impact in directing the extension of the next generation of materials, products and processes [1]. The inevitability of plastic in the environment, the reduction of oil resources and greenhouse gas emissions has been a source of concerns for human societies in the recent years. The production of biodegradable polymers from renewable sources is a promising alternative to replace raw materials with petrochemical resources. Reusable polymeric materials have excellent and flexible features and are used in a wide range of applications and play a vital role in our everyday lives [2]. Due to biodegradation, biocompatibility and adjustable mechanical properties, poly (3-hydroxybutyric acid) (PHB) is known as an appropriate candidate for the replacement of petroleum-based polymers. PHB is a thermoplastic polyester produced by a wide range of microorganisms and widely used in medical equipments such as surgical needles, repair tools, bone plates and stem cell growth [3-5]. This polymer can also be used in drug delivery because of its biocompatibility and biodegradation [6]. However, the application of PHB is limited by its low crystallization capacity, slow crystallization rate and the high melting temperature (176-180°C). In addition, during crystallization of PHB and owing to the very low concentration of nucleus some cracking of the polymer chains are expected [7].

So far, many strategies have been developed to overcome the fragility and increase the amount of PHB crystallization [8].

Adding some particles and nanoparticles to the polymer substrate can result in the rapid crystallization of semi-crystalline polymers such as polyethylene, polyamides and polyester. These chemicals act as nuclei when added to the polymers. Application of nuclear agents is critical for improving the physical and mechanical properties of crystalline and semi-crystalline polymers. A nucleus agent can change the degree of polymer crystallinity by two homogeneous and non-homogeneous nucleation mechanisms. In addition, a smaller size and higher crystallinity can be obtained, which in turn improves the mechanical, thermal and optical properties of the polymers [8]. The use of boron nitride (BN), talc, lignin, ureic acid, polyvinyl alcohol (PVA) as nuclear agents has been reported to improve the properties of biodegradable polymers [9]. But the use of talc and BN limits the use of biodegradable polymers in biomedical applications, so there is an urgent need to search for new nuclear agents [10].

Therefore, the main objective of this article is investigation of the effect of DMDBS on the crystallization of PHB.

II. METHODS

Materials: PHB sample powders with a Mw of 500000 were provided by Showa Denko Co (South Korea), 1,3:2,4-Bis(3,4-dimethylobenzylideno) sorbitol (DMDBS) was obtained from Sinopharm Chemical Reagent Co., Ltd (Shanghai, China).

Sample Preparation: Preparation of PHB samples with different amounts of DMDBS (0-5 wt %) was carried out by the solution-casting method. The blending components were dissolved in acetic acid as a solvent. Powdered poly (3-hydroxybutyric acid) and DMDBS were simultaneously dissolved in acetic acid above the solvent boiling point (118°C). The solution was subsequently poured onto a glass dish. Polymer films were prepared at a concentration of 0.05 g/mg and then dried at 120 °C for 3 minutes to evaporate the solvent.

Differential scanning calorimetry (DSC): Calorimetric analyses were carried out in a Mettler-Toledo (822^e, Switzerland) calorimeter at a heating rate of 20 ºC/min from 25 to 200 ºC and held in the molten state for 5 minutes to eliminate any influence of the thermal history. Then, the polymer was cooled to 20 ºC at 10 ºC/min. Crystallization temperature, T_c, was determined in the reversed scan.

Experiments were carried out under nitrogen atmosphere at a flow rate of 50 ml/min. Samples of 5-10 mg were used in the DSC experiments.

Thermo gravimetric analysis (TGA): TGA curves of the blend films were recorded using STA 504 Instrument (Germany) from 25 ℃ to 600 °C with a heating rate of 10 °C/min under argon atmosphere.

III. RESULTS AND DISCUSSION

Differential scanning calorimetry (DSC): Usually, the temperature of the crystallization peak is used to characterize the nucleating performance of a nucleating agent. Differential scanning thermometry curves for Poly (3-hydroxybutyric acid) and their blends films (1,3,5 wt%) are similar. There is only one clear crystallization curve. It was observed that with an increase in the percentage of DMDBS, enthalpy of melting and crystallization increases and the temperature of crystallization begins to be transferred to higher temperatures which showed in Table 1. Nuclear factor increases the percentage and speed of crystallization and decreases the size of crystals by increasing the number of effective nuclei at higher temperatures.

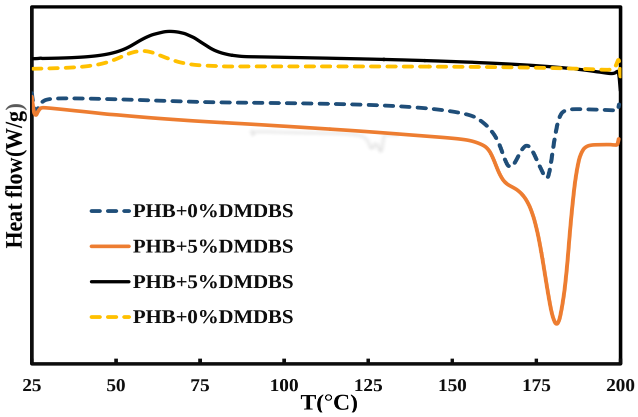

Fig.1: DSC thermograms of pure PHB and PHB+5%DMDBS

From the DSC thermograms, some important thermal parameters such as the melting temperature (T_m) and the melting enthalpy (ΔHm) as well as the degree of crystallinity (Xc) are obtained and results presented in Table 1.

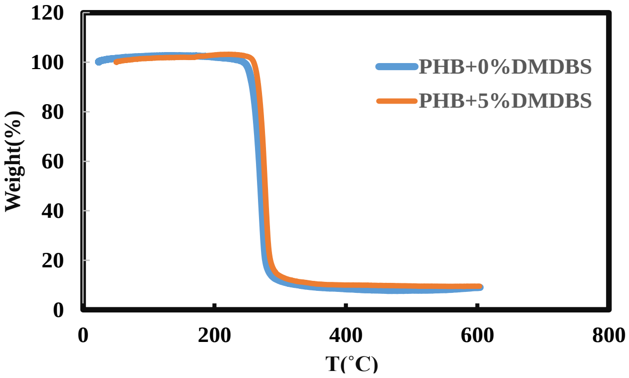

Fig.2: TGA curves of pure PHB and PHB+5%DMDBS

Table1: DSC thermal parameters of pure PHB and the respected composite films

Sample	T_m	T_c	ΔHm	ΔHc	Xc (%)
PHB+0%DMDBS	166.08	57.55	-16.74	40.53	11.46
PHB+1% DMDBS	174.3	56.58	-106.3	48.82	72.8
PHB+3% DMDBS	175.21	61.99	-100.15	57.04	68.59
PHB+5% DMDBS	180.91	65.93	-126.38	64.31	86.56

The crystallinity of PHB was determined by Eq. (1):

$$Xc(\%) = \frac{\Delta Hm}{\Delta H0} \times 100 \qquad (1)$$

Where ΔH_0 is melting enthalpy per unit weight of the100% crystalline PHB, which is assumed to be 146 J/g [11].

Thermogravimetric analysis (TGA): Thermgravimetric analysis was presented to investigate the changes in weight loss of polymeric films with the increase of temperature. All the sample films display a similar thermal degradation behavior which suffer an initial slight weight loss at approximately 270 ºC and then a sharp weight loss from 270 to 350 ºC. The disintegration temperature of the composite films was approximately constant with the change of the content of DMDBS. It was concluded that the thermal stability of the composite films did not decrease with an addition of DMDBS content.

IV. CONCLUSION

In this study, the effect of DMDBS addition on the isothermal crystallization behavior of PHB was investigated. As it has been observed, addition of 5 wt.% of DMDBS into the PHB matrix shifted the peak of crystallization exotherm to higher temperature about 8 °C confirming its role as a potential nucleating agent for PHB crystallization. In addition, the presence of DMDBS does not affect the thermal stability of polymeric polymers. Spectroscopy data with FT-IR demonstrated some interactions between DMDBS and PHB backbones which enhanced by the nucleating agent concentration.

REFERENCES

[1] F. Vilarinho, A. Sanches Silva, M. F. Vaz, and J. P. Farinha, Crit. Rev. Food. Sci, vol. *58*, pp. 1526-1537, **2018**.
[2] N. Jacquel, K. Tajima, N. Nakamura, H. Kawachi, P. Pan, and Y. Inoue, J. Appl. Polym. Sci, vol. 115, 709-715, **2010**.
[3] D. Jayanth, P. S. Kumar, G. C. Nayak, J. S. Kumar, S. K. Pal, and R. Rajasekar, J. Polym. Environ, vol. 26, pp. 838-865, **2018**.
[4] J. A. S. Puente, A. Esposito, F. hivrac, and E. Dargent, J. Appl. Polym. Sci. , vol. 128, pp. 2586-2594, **2013**.
[5] M. Koller, Appl. Food. Biotechnol, vol. 1, pp. 3-15, **2014**.
[6] R. P. Babu, K. O'connor, and R. Seeram, Prog. Biomater, vol. 2, pp. 8, **2013**.
[7] J. Xu, S. Zhang, and B. Guo, Chin. Chem. Lett., vol. 28, pp. 2092-2098, **2017**.
[8] J. C. C. Yeo, J. K. Muiruri, T. Warintorn, Z. Li, and C. He, Mater. Sci. Eng. C, vol. 92, pp. 1092-1116, **2017**.
[9] X. M. Che, H. M.Ye, and G. Q. Chen, Compos. Part A. Appl. Sci. Manuf, vol. 109, pp. 141-150, **2018**.
[10] H. Alata, B. Hexig, and Y. Inoue, J. Polym. Sci. Pol. Phys, vol. 44, pp. 1813-1820, **2006**.
[11] P. J. Barham, A. Keller, E. L. Otun, and P. A. Holmes, J. Mater. Sci., vol.*19*, pp. 2781-2794, **1984.**

Section:

Molecular Spectroscopy

The Effect of Urea on Aggregation Properties of Methylene Violet Dye

A.Ghary Haghighat[a], ***A.Ghanadzadeh Gilani*** [a]*
(Department of Chemistry, Faculty of Science, University of Guilan, Rasht, postal code: 4199613776, Iran)
Email: aggilani@guilan.ac.ir

Abstract: Methylene Violet Bernthsen (MV, Fig. 1) is a neutral synthetic member of phenothiazines family. Various biological and technological applications of it have been reported in scientific articles. It has photosensitizing properties and produces singlet oxygen ($^1O_2$) upon visible-light irradiation. Lots of examples of its potential use in photodynamic inactivation of microorganisms were reported. Because of diverse utilizations of MV, we experimentally studied it in urea solutions with different concentrations using spectral data.

Keywords: Aggregation, Methylene Violet, Thiazines, Urea, UV-Vis Absorption Spectra.

I. INTRODUCTION

Phenothiazines (PTZ) are an attractive class of molecules with appropriate properties for special usages [1]. Like other ionic dyes, phenothiazine molecules in solutions can exist as dimers and even higher-order aggregates [2-5]. Using the visible absorption spectra of the aggregates under different conditions is one of the most common ways of studying the characteristics and composition of them.

Methylene violet was studied during the last 15 years for potential applications as deactivator of viruses, bacteria and parasites in blood [6,7]. On the other hand, MV has been used for the amperometric detection of hydrogen peroxide [8] and as an effective inhibitor of steel corrosion in acidic media [9].

II. METHODS

Methylene violet (dye content > 65) purchased from Exciton and was used without further purification. The stock solution of MV (5×10^{-4} M) was prepared in 10 ml volumetric flasks by dissolving the dye in urea solutions between 0.2M and 1.6M. The sample solutions with different concentrations were made by using a micropipette. UV-visible absorption spectra were recorded with a Cary 100 spectrophotometer and the data were analyzed with Origin Software.

III. RESULTS AND DISCUSSION

MV typically possesses a doublet band, i.e. a maximum (λ_{max}) and a shoulder ($\lambda_{shoulder}$) in its optical absorption spectra. The shoulder at shorter wavelength represents the presence of the solute–solvent or solute–solute interactions (ion pairing and self-association of dye molecules). However, the dye usually aggregates at high concentrations (Fig. 2). The log K_d data for MV in different urea solutions listed in Table 1.

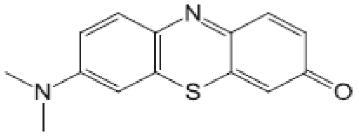

Fig.1. Chemical structure of methylene violet (**MV**)

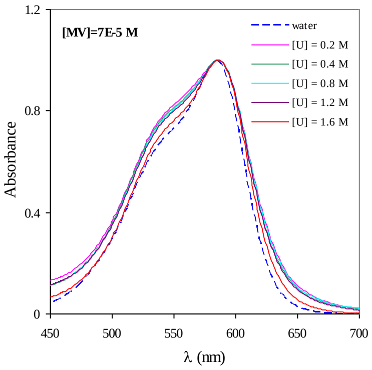

Fig.2. Absorbance spectra of methylene violet in different concentrations of urea

Table1: log K_d for methylene violet in different urea solutions

solution	log K_d
water	2.4
[Urea]=0.2M	3.9
[Urea]=0.4M	3.6
[Urea]=0.8M	3.3
[Urea]=1.2M	3.1
[Urea]=1.6M	2.8

Constant of Dimerization:

Presuming that we have only a single equilibrium between monomer (M) and dimer (D) in the solution, the constant of dimer association ($K_d=[D]/[M]^2$) can be given by the spectral data.

Linear Least Squares Fitting:

If we divide $A_t=\varepsilon_M[M]\cdot l+\varepsilon_D[D]\cdot l$ by $[C]\cdot l$ and $\alpha=[M]/[C]$ is the monomer fraction of dye molecules, then the constant of dimerization can be shown by these equations:

$$K_d = (1-\alpha)\left[c\right]/2\alpha^2\left[c\right]^2 \qquad (1)$$

$$\varepsilon_t = \varepsilon_M.\alpha + \varepsilon_D.(1-\alpha)/2 = (\varepsilon_M - \varepsilon_D/2).\alpha + \varepsilon_D/2 \qquad (2)$$

Non-linear Least Squares Fitting:

If we substituted $K_d=[D]/[M]^2$ and $[C]=[M]+2[D]$ into $A_t=\varepsilon_M[M]\cdot l+\varepsilon_D[D]\cdot l$, Eq.(3) can be obtained [10]:

$$\begin{aligned} A_t &= \varepsilon_M\left[-1+(1+8.K_d.[C]^{1/2})/8.K_d\right].l \\ &+\varepsilon_D\left\{[4.K_d[C]-[-1+(1+8K_d[C]^{1/2})]]/8.K_d\right\}.l \end{aligned} \qquad (3)$$

These formulas and the spectra (Fig.2) demonstrated that logK_d of MV decreased with the increase in concentration of urea solutions.

IV. CONCLUSION

It was obvious that the aggregation of MV in urea solutions decreases. The hetero-associations of MV with the urea molecules decrease the dimerization of it. The urea-urea interactions can lead to breaking of water structure at the higher urea concentrations, so the bond formation of MV-urea hydrogen is the important reason of spectral shift in MV- urea solutions.

V. REFERENCES

[1] F. Ronzani, A. Trivella, P. Bordat, S. Blanc, and S. Lacombe, Journal of Photochemistry and Photobiology A: Chemistry, vol. 284, pp. 8–17, **2014**.

[2] M. Havelcová, P. Kubát, and I. Němcová, Journal of Dyes and Pigments, vol. 44, pp. 49–54, **2000**.

[3] L. Antonov, G. Gergov, V. Petrov, M. Kubista, and J. Nygren, Journal of Talanta, vol. 49, pp. 99–106, **1999**.

[4] A. Chakraborty, R. Adhikari, and S.K. Saha, Journal of Molecular Liquids, vol. 143, pp. 81–88, **2008**.

[5] A. Ghanadzadeh, A. Zeini, A. Kashef, and M. Moghadam, Journal of Molecular Liquids, vol. 138, pp. 100–106, **2008**.

[6] A. Skripchenko, D. Robinette, and S. Wagner, Journal of Photochemistry and Photobiology, vol. 65, pp. 451-455, **1997**.

[7] M. Wainwright, and RM. Giddens, Journal of Dyes and Pigments, vol. 57, pp. 245-257, **2003**.

[8] M. Vreeke, R. Maidan, and A. Heller, Journal of Analytical Chemistry, vol. 64, pp. 3084-3090, **1992**.

[9] H. Ashassi-Sorkhabi, D. Seifzadeh, and MG. Hosseini, Journal of Corrosion Science, vol. 50, pp. 3363-3370, **2008**.

[10] A. Ghanadzadeh Gilani, Z. Poormohammadi-Ahandani, and R. Kian, Journal of Spectrochimica Acta Part A: Molecular and Biomolecular Spectroscopy, vol. 189, pp. 543–555, **2018**.

Multi-spectroscopy of the interaction behavior between calf thymus DNA and Rebeccamycin in binary and ternary approaches

***Zohreh Malek Esfandiyari*[a], *Mohammad reza Saberi*[a] *Jamshidkhan Chamani*[b] ***

a.Medical Chemistry Department, School of Pharmacy, Mashhad University of Medical Sciences, Mashhad, Iran
b.Department of Biology, Faculty of Sciences, Mashhad Branch, Islamic Azad University, Mashhad, Iran
E-mail: chamani.j@ut.ac.ir; z.malekesfandiyari@gmail.com

Abstract: DNA binding studies have remarkable relevance and implications in drug design aspect and cancer chemotherapy. In eukarute cells, histones play important roles of the biological function of DNA. The interaction between Rebeccamycin and calf thymus DNA (ct DNA), in the absence and presence of H1 was investigated by using multi-spectroscopic techniques. The fluorescence and circular dichroism spectroscopic indicated the Rebeccamycin interacted with ct DNA in the absence of H1 in an intercalator binding mode. In the presence of H1, ct DNA-Rebeccamycin complex revealed intercalator and groove binding modes with dominant of intercalator role.

Keywords: Rebeccamycin, Complex DNA-H1, Resonance light scattering, Circular dichroism, Intercalator.

I. INTRODUCTION

In the current study we also investigated of ct DNA-Rebeccamycin complex formation in ternary systems. Rebeccamycin Fig.1 is a natural product which inhibits DNA topoisomerase and has been studied as a potential anticancer agent because of the importance of DNA topoisomerase (I) in cell growth and proliferation [1].

The interaction between Rebeccamycin-DNA in binary and ternary systems with their mechanisms provide some instructions for the application of small molecular substances targeted to the DNA of cancer cells.

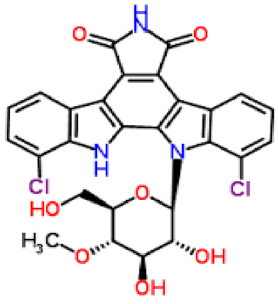

Fig.1 Chemical structure of Rebeccamycin

II. METHODS

Calf thymus DNA, Rebeccamycin, Histone H1 were prepared from Sigma Aldrich chemical Co (USA) 20mM Tris-HCL buffer solution and the PH was set to 6.8. The calf thymus DNA concentration was determind by uv absorption at 260nm using an extinction coefficient of 6600 mol-1cm-1[2].

Rebeccamycin stock solution was purchased in ethanol and kept in the dark. CD measurements have been performed on Jasco J-815 with 1.0 cm quartz cell (Japan spectroscopic company, Tokyo, Japan) in 25°C.

The RLS results have been recorded by a Hitachi model F-2500 spectrofluorometer (Japan).The excitation and emission wavelengths were observed to be 220 and 600 nm, respectively and $\Delta\lambda = 0\,nm$ at room temperature. In this method, various concentration of Rebeccamycin were enhanced to ct DNA and ct DNA -H1 complex

III. RESULTS AND DISCUTION

The results of RLS technique are shown in Fig 2(A,B) ,which determines the enhancement of Rebeccamycin concentrations can regularly increase the RLS spectra and illustrate the binding of Rebeccanycin to ct DNA in absence and presence of H1. However, the RLS values of Rebeccaingcin in ternary system was distinct from binary system.

As is evident, in both interactions there were two sets of positions for ct DNA- Rebeccamycin complex. Fig 2(C) displays the ΔI_{RLS} against Rebeccamycin concentration for binary and ternary systems. The results of this curve also confirm the difference behavior of these systems.

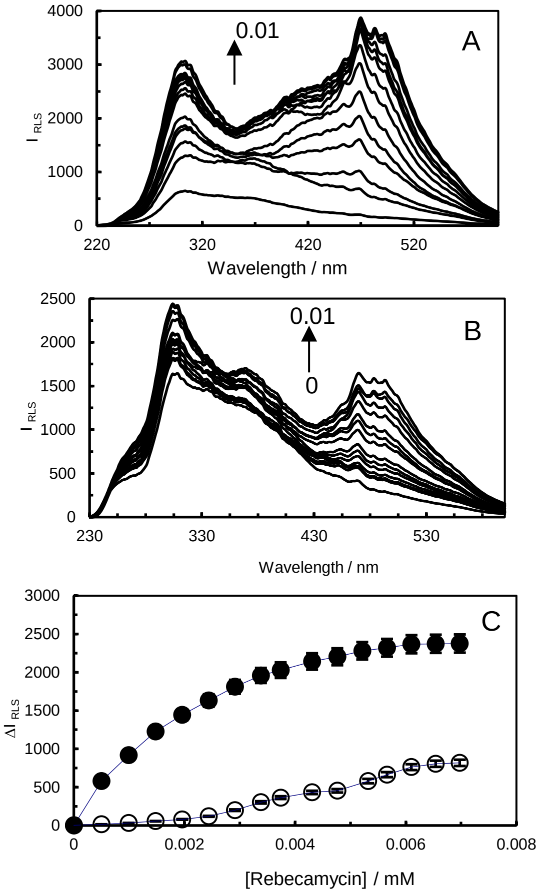

Figure 2. (A) RLS spectra of Rebeccamycin with ct DNA (B) The H1-ct DNA complex at PH 6.8 and 298k (C) Comparison of the ΔI_{RLS} curve against the concentration of Rebeccamycin. The close circles display Rebeccamycin–ct DNA and open circles demonstrate (ct DNA–H1) Rebeccamycin complex.

Fig 3. A shows a positive band at 275nm which represents stacking and 245mm, a negative band. Because of helicity, these are specific features of DNA in its right handed B form. Also by adding Rebeccamycin to ct DNA, a change in the conformational occurred.

As it turns out, Fig3 (B) illustrate changing structure and the intercalative mode of binding. Both results were assigned to the intercalative mode of binding of Rebeccamycin within the ct DNA molecule in the absence and presence of H1. The variations of circular dichorism in the presence of the drug evince stabilization of the right-handed B form of calf thymus DNA. [3].

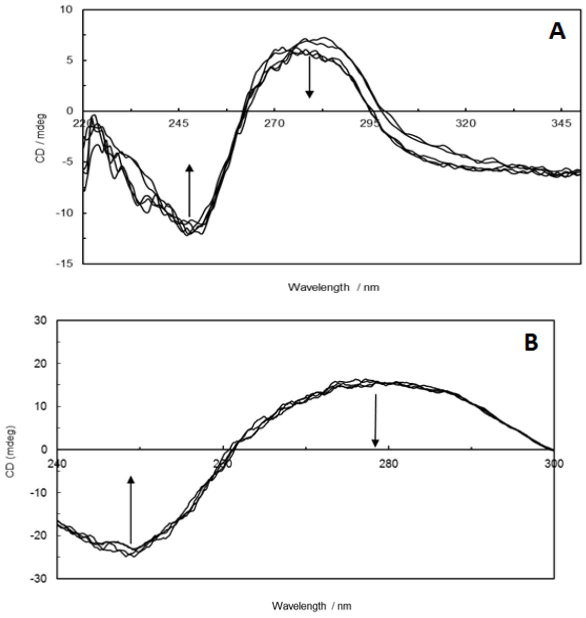

Figure 3. (A) Spectra of ct DNA. (B) H1-ct DNA in the presence of amounts of Rebeccamycin in pH 6.8 and in 0.01-M Tris–HCl buffer.

IV. CONCLUSION

The experiments conducted to the investigate the behavior of Rebeccamycin in binary and ternary systems help in understanding the mechanism of pharmacokinetics. To sketching anti-cancer drugs vander waals force and hydrogen bonding are the most interaction forces between Rebeccamycin and ct DNA in absence and presence of H1. All the results indicate that Rebeccamycin is more like to bind intercalative mode in binary system, However, in the presence of H1 it tends to be seen in the groove.

REFERENCE

[1] Production and biological activity of rebeccamycin, a novel antitumor agent: J.A. Bush, et al.; J. Antibiot. (Tokyo) 40, 668 (1987).
[2] Spectrosopic and molecular modeling methods to investigate the interaction between 5-Hydroxy methyl-2-furfural and calf DNA thymus.
[3] Y. Zhou, Y. Li, Colloids Surf. A: Physicochem. Eng. Aspects 233 (2004) 129–135.


بیست و دومین کنفرانس شیمی فیزیک انجمن شیمی ایران
22nd Iranian Physical Chemistry Conference
۲۹ الی ۳۱ مرداد ۱۳۹۸
گروه شیمی دانشگاه زنجان

Spectroscopic studies on the interaction of Rebeccamycin with calf thymus DNA in the absence and presence of Histone H1

Zohreh Malek Esfandiyari[a]***, Mohammad reza Saberi***[a] ***Jamshidkhan Chamani***[b] *
a.Medical Chemistry Department, School of Pharmacy, Mashhad University of Medical Sciences, Mashhad, Iran
b.Department of Biology, Faculty of Sciences, Mashhad Branch, Islamic Azad University, Mashhad, Iran
E-mail: chamani.j@ut.ac.ir; chamani_j@yahoo.com

Abstract: The interaction of Rebeccamycin with calf thymus DNA (ct DNA) in the absence and presence of Histone H1 was investigated by employing multi spectroscopic techniques. In the presence of H1, ct DNA-Rebeccamycin complex revealed intercalator and groove binding modes with dominant of intercalator role. The impression of ionic strength, such as Sodium Chloride and Potassium iodide on ct DNA-Rebeccamycin complex provided further evidence that their interaction modes were dependent on substituted groups.

One of the strong indication for the reciprocal of molecules into the helix is obtaining by DNA melting studies. In this experiment the melting curve of ct DNA –Rebeccamycin complex has revealed that the binding mode is intercalative, however in presence of H1, the results indicated that there were a few changes.

Keywords*:* Complex ct DNA-H1, Rebeccamycin, Melting temperature, Intercalative.

I. INTRODUCTION

It is interesting to note that, DNA is an inheritable molecule, which has the main role in living organism. It is severely profitable to perceive the drug-DNA binding mechanism in order to design the structure of new and efficient drug [1, 2].

Rebeccamycin (Fig.1) is a new kind of antibiotic, which inhibits DNA topoisomerase. Rebeccamycin analogues are being used in clinical trials for the treatment of neoplastic tumors, Renal cell cancer and Leukemia. In the present work, some methods have been used to identify the binding mode between Rebeccamycin and calf thymus DNA, also define the histone's connection position to drug.

II. Methods

Rebeccamycin, histone H1 and calf thymus DNA (ct DNA) were purchased from Sigma Chemical Co. The concentration of ct DNA solution per nucleotide was determined at 260 nm (Ɛ260=6600M-1cm-1, T=298 K), Moreover a Rebeccamycin stock solution (0.05 mM) was purchased in DMSO because of its low solubility in water. Sodium Chloride and Potassium iodide were exerted to control ionic strength of the solutions, by absorption spectra (Jasco V630). The melting temperatures of DNA, Rebeccamycin-DNA, DNA–H1 and (DNA–H1)-Rebeccamycin were given by inscription the absorbance at 260nm in various temperatures.

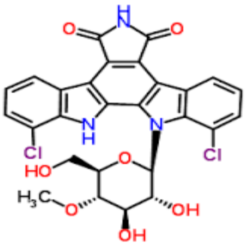

Fig.1 Chemical structure of Rebeccamycin

III. RESULTS AND DISCUTION

It is crystal clear from Fig.2 A and B that, the absorbance of a fixed concentration of the ct DNA- Rebeccamycin complex has an obvious increase, with the incremental addition of Nacl and K1. This fact indicates that a significant electrostatic binding interaction has been induced between ct DNA and Rebeccamycin. However, in ternary system Fig.3 (A,B), the absorbance of ct DNA-Rebeccamycin complex had a little change, which suggests that the hydrophobic forces seemed to be more powerful than the electrostatic interaction. This experiment has proved that the linker histone has a major role in the interaction behavior between ct DNA and Rebeccamycin.

Fig.4 A The supplied figure depicts, the melting temperature of ct DNA which has been demonstrated to increase by 50 °C as a result of binding to drug in the mode of intercalation.

Fig.4 B reveals that an improvement concentration of Rebeccamycin in the ct DNA–H1 solution has increased melting temperature of the complex. The data have proved that the mode of ct DNA–H1 complex connection to the Rebeccamycin, is an intercalation binding.

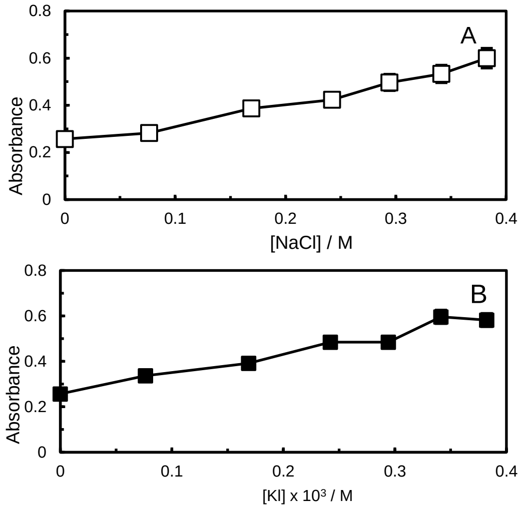

Figure 2. (A) The impression of ionic strength of NaCl (B) KI on the fluorescence intensity of Rebeccamycin–ct DNA complex

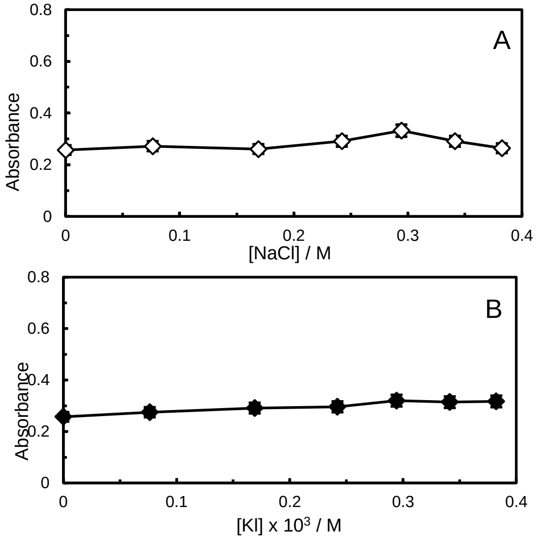

Figure 3 (A) The impression of ionic strength of NaCl (B) KI on the fluorescence intensity of (ct DNA-H1)-Rebeccamycin complex

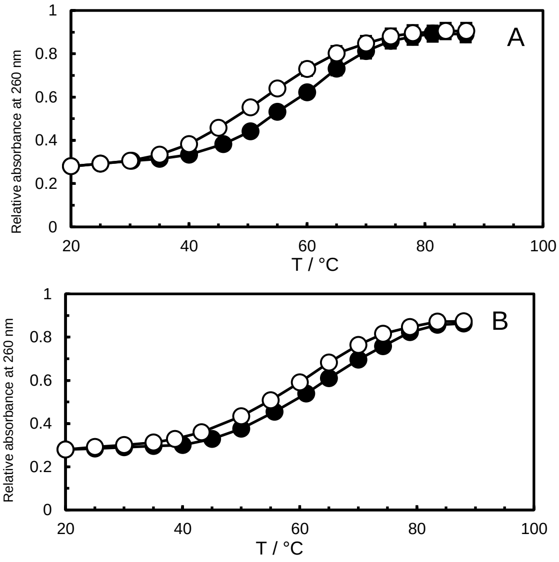

Figure 4. (A) The comprison of the ct DNA melting temprature in the absence of Rebeccamycin; open circles, and presence with close circles. (B) The comprison of the ct DNA-H1 melting temprature; open circles, with the presence of Rebeccamycin; close circles.

IV. CONCLUSION

The presented results expresses, how the type of Rebeccamycin interacted with ct DNA in binary and ternary systems, which proved that it is an intercalator drug with an inhibitors property of gene expression, moreover, the results of the salt competition acknowledged mode of binding, since in binary system, the drug competed with both Nacl and KI, which expresses how salt were bounded between the two strands of DNA. However, in ternary system the results were slightly different, ligand binding to the groove because there has not been any competition between Rebeccamycin and salts.

The melting temperature of all complexes were changed and up surged. Finally, the investigation proved the strongly role of histone in biological reactions and drug delivery.

REFERENCE

[1] E. Froehlich, J.S. Mandeville, C.M. Weinert, L. Kreplak, H.A. Tajmir-Riahi, Biomacromolecules 12 (2011) 511-517.

[2] E.R. Jamieson, S.J. Lippard, Chem. Rev. 99 (1999) 2467-2498.

Theoretical study of intramolecular hydrogen bond on 2-(2-Hydroxy phenyl)-5(4H)-Oxazolone halogenated derivatives in ground state

Peyman Mohammadzadeh Jahani[*1], *Hooshang Hamidian*[2], *Mohammad Ali Rostami Ravari*[3]

[1]*School of medicine, Bam university of medical sciences, Bam, Iran*

[2,3]*Department of chemistry,Payam Noor University(PNU), Kerman, Iran*

E-mail: mjpeyman@yahoo.com

Abstract: Intramolecular hydrogen bond (IHB) of 2-(2-Hydroxy phenyl)-5(4H)-Oxazolone(HPO) halogenated derivatives in the ground have been investigated by DFT method with the standard basis set 6-311 + +G (d,p). In this work, we evaluated and compared the substitution effects on the IHB strength by some of the IHB descriptors such as geometrical, topological and orbital charge transfer parameters. As with replacing of the halogen atoms at R_1 position the IHB energies increased while for the R_2, R_3 and R_4 decreased. Finally, the linear equations of the IHB energies versus the IHB descriptors parameters show that the open-close method (OPM) is inappropriate for calculation of the IHB energies in the HPO.

Keywords: 2-(2-Hydroxy phenyl)-5(4H)-Oxazolone, Intramolecular hydrogen bond,

I. INTRODUCTION

5-(4H)-Oxazolones are a group of heterocyclic compounds that biologically and pharmaceutically important and they are also important in the proration of amino acids [1]. In this research, we first calculated the IHB energies by potential energy density of Espinoza (PED) and open close methods [2,3] on the halogenated HPO (Fig.1). Then, the geometrical, topological and charge transfer energies are obtained and also the halogen effects on the structural properties of the HPO are explored. Ultimately, we investigated and compared the correlation between the IHB energies of HPO and the descriptor's IHB parameters to obtain the suitable linear equations.

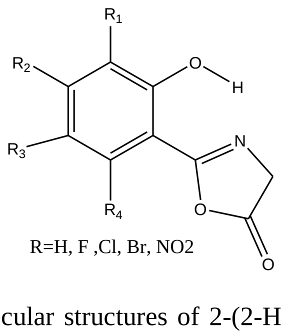

Fig.1: The molecular structures of 2-(2-Hydroxy phenyl)-5(4H)-Oxazolone(HPO) derivatives

II. COMPUTATIONAL DETAILS

In this work, in order to characterize the electronic properties of the systems, the density functional theory (DFT) calculations were performed by GAMESS software ab initio package [4]. The geometry of the single structures was fully optimized at B3LYP in conjunction with standard basis set 6-311 + +G (d,p .) The optimized structures were used to create input files for AIM and NBO analyses by mean of AIM200 software and NBO package included in Gaussian 03 suite of program [5].

III. Results and discussion

In this work, the IHB energies of HPO derivatives are calculated by PED and OPM and collected in Table1.Also, in order to evaluate the substituted effects, we can classify HPO derivatives in four categories R_1- substituted, R_2-substituted, R_3- substituted and R_4- substituted (R= H, F, Cl, Br , NO_2) (Fig1). A deeper looks at the data on the table1indicate that with replacement of halogen atoms in R_1, the IHB energies increased, while for others increased. However, within each category, the IHB energies are very close together. Moreover, geometrical parameters included $R_{O\ldots H}$, $R_{O\text{-}H}$ and $R_{O\text{-}O}$, Some of the most important AIM parameters including electron density (ρ), its Laplacian($\nabla^2\rho$), the kinetic G(r) and the potential electron energy V(r)densities, ratio of kinetic to potential electronic energy densities(G/V) and the total electron density or Hamiltonian H(r) on the bond and ring critical points and charge transfer parameters such as stabilization energies (E^2) (Lp $_{(O)}\rightarrow \sigma^*_{O-H}$) were obtained from output files of HPO molecule. Since that these results strongly support the IHB energies. Hence, the linear dependence between the mentioned parameters and IHB energies are studied.

The equations clearly show that the PED energies have good correlation while, for OPM the regression coefficient is unacceptable.

Table1:. IHB energy of 2-(2-Hydroxy phenyl)-5(4H)-Oxazolone(HPO) derivatives

R_1	PED	OPM
H	53.6	47.5
F	53.1	37.2
Cl	52.4	34.6
Br	51.6	33.1
NO_2	49.2	31.5

IV. CONCLUSIONS

The regression coefficients shown that geometrical, topological and charge transfer descriptors correlate the PED energies very well, while for the OPM the correlation is not acceptable. Hence, we can claim that the PED is a reliable method for calculation of the IHB energies of the heterocyclic RAHB systems

REFERENCES

[1] C. Cativiela, A. Jiménez, Study of the reaction of a chiral oxazolone with oxosulphonium methylides as cyclopropanating agents. *Tetrahedron*,vol. 51(10), pp3025-3032, 1995.
[2] P. Schuster, G. Zundel, The Hydrogen Bond Recent Development in Theory and Experiment, North-Holland.
[3] E. Espinosa, E. Molins, C. Lecomte, Chem. Phys. Lett, vol. 285, PP.170, 1998.
[4] M S. Gordon, pp M W Scmidt, C E Dykstra, G. Frenking, K S. Kim, G E. Scuseria Theory and Appilcations of Computational Chemistry: the first forty years and Advance in electronic structure theory: GAMESS a decade later , vol.1167,pp.1189, 2005.
[5] F. Biegler-Ko¨nig, J. Scho¨nbohm, D. Bayles AIM2000: a program to analyze and visualize atoms in molecules. J. Comp. Chem. Vol. 22, pp. 545, 2001.

بیست و دومین کنفرانس شیمی فیزیک انجمن شیمی ایران
22nd Iranian Physical Chemistry Conference
۲۹ الی ۳۱ مرداد ۱۳۹۸
گروه شیمی دانشگاه زنجان

Investigation of Gas Phase Protonation of 2-Mercaptobenzothiazole; An Ion Mobility Spectrometry and DFT Study

***Masoumeh Ghahremani*, Hamed Bahrami [*], Manijeh Tozihi**
Department of Chemistry, University of Zanjan, Zanjan, Iran, Fax: +98 24 33052477; Tel: +98 24 33052477;
E-mail: hbahrami@znu.ac.ir

Abstract*:* Proton transfer reaction between hydronium ions and 2-Mercatobenzothiazol was investigated in this study using corona discharge-ion mobility spectrometry. Two distinct product ion peaks were observed in the ion mobility spectra with clearly different intensities. Topical proton affinities for two tautomers of 2-Mercatobenzothiazol were theoretically calculated through protonation of all possible sites. Based on experimental and theoretical results, product ion peaks were assigned to the most probable ionization products.

Keywords: 2-Mercatobenzothiazol, Gas phase protonation, Ion mobility spectrometry, Proton affinity.

I. INTRODUCTION

2-Mercaptobenzothiazole (MBT) is an aromatic heterocyclic chemical compound consisted of 1,3-thiazole ring fused to a benzene ring [1]. As regards to structural aspects, MBT exists in two tautomeric forms, namely thiol and thione (Fig. 2). Therefore, the structure and properties of MBT have been a subject of interest for a long time. Today, it is accepted that the thione form of MBT is more stable than its thiol form [2]. Proton affinity (PA) is one of the most important thermodynamic properties. The PA of a molecule M is defined as -ΔH of its protonation reaction in the gas phase [3].

Ion mobility spectrometry (IMS) is basically a suitable technique for the identification and determination of chemical substances. However, IMS has been used to study ion-molecule reactions in the gas phase [4]. In short, the sample is ionized in reaction region of the IMS and product ions are collected after separation in a drift tube based on their mobility. Among different ionization sources employed in IMS, corona discharge ionization (CD) as an atmospheric pressure chemical ionization (APCI) method, has been highly accepted [3]. The known ionization mechanism in positive CD-IMS is the proton transfer from the reactant ions to sample molecules.

In the present study, positive ion mobility spectra of MBT had been obtained with a CD-IMS. The observed peaks in the ion mobility spectra were assigned to ions formed by proton transfer reaction. DFT/B3LYP calculation was conducted on the structure of neutral and all possible protonated isomers of MBT to support and extend the experimental conclusions.

II. MATERIAL AND METHODS

All experimental data were performed with a commercial ion mobility spectrometer (model: IMS-300) made by TOF Tech. Pars. Co., Isfahan, Iran. 2-Mercatobenzothiazol purchased from Sigma Aldrich and was injected to the IMS as a solid sample without further purification. The theoretical calculations were carried out using the GAUSSIAN 09 program. The theoretical results were based on density functional theory (DFT) calculations at the B3LYP/ 6-311++G** level.

III. RESULTS AND DISCUSSION

Fig.1 shows A typical IMS spectrum of the MBT at injection port and cell temperatures of 260 and 200 °C, respectively. From left to right, three first peaks correspond to NH4^{+}, NO^{+}, and H3O^{+} (reactant ions). Other peaks in the region from 6 to 8 ms are correlate with MBT.

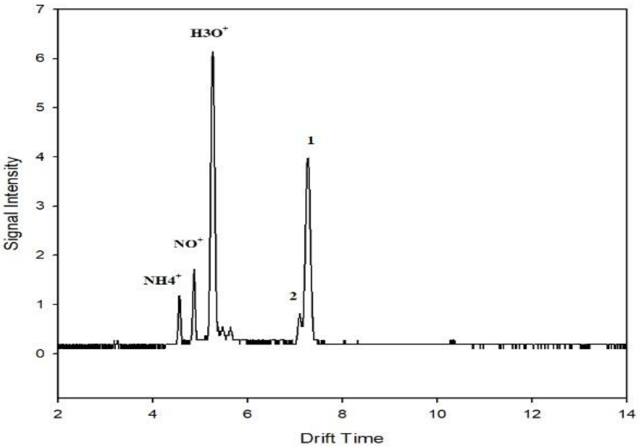

Fig. 1: Ion mobility spectrum of MBT in positive mode with corona discharge ionization source.

The values of the total energy for MBT thiol and thione form, obtained from the DFT method are -1120.924045 and -

1120.934305 Hartee, respectively. These values are indicating that the thione form is more stable than thiol form by about 27 kJ mol^{-1}. However, both tautomeric forms were considered for calculating the PA of the MBT.

There are ten possible sites for protonation in the MBT molecular structure; each will lead to a protonated isomer. To find the relative stability of the protonated isomers, a neutral molecule was protonated from all nitrogen, sulfur and carbon sites. The calculated enthalpies of the neutral and protonated isomers were given to obtain the topical proton affinities (TPAs) of MBT. Table 1 gives the calculated values for TPAs of MBT, protonated from ten individual sites at the B3LYP/6-311++G(d,p) level.

Table 1. The TPA of 2-MBT tautomers as well as water at 298K (kJ mol^{-1}). Atoms in parenthesis are the protonation sites.

Compound	TPA	
	Thiol	Thione
M (C1)	796.05	776.79
M (C2)	773.08	755.02
M (C3)	735.82	715.05
M(C4)	820.11	793.31
M(C5)	804.04	788.14
M(C6)	824.50	808.62
M(C13)	751.68	815.53
M(S12)	754.28	760.83
M(N11)	918.26	771.66
M(S14)	753.41	890.39
H_2O	687.79	-

The TPA values of MBT for protonation of all sites were greater than that of water; hence, all sites can attract a proton from the hydronium ion.

As indicated in table 1, the most probable protonation sites in the thione and thiol forms of MBT are sulfur (S14) and nitrogen (N11), respectively. The optimized structure of two tautomeric forms of MBT and its most stable protonated isomers are shown in Fig. 2.

.

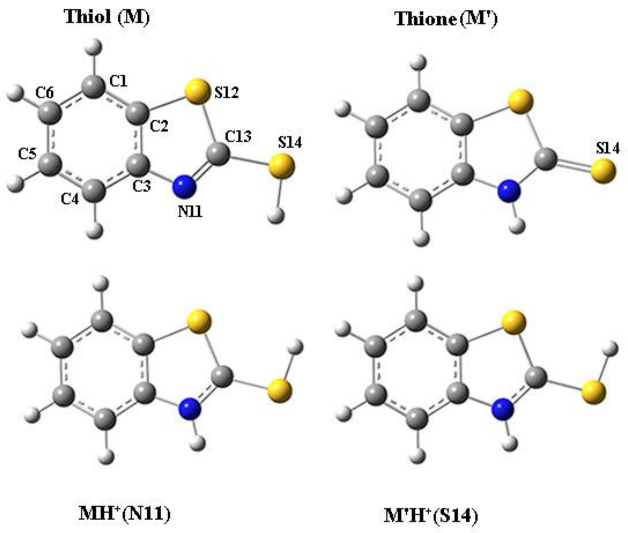

Figure 2. Optimized structures of Thiol and Thione tautomers of MBT, and their most stable protonated isomers obtained at the B3LYP/6-311+G(d,p) level of theory

Theoretical calculations indicated that the nitrogen protonated isomer of the thiol form (M(N)H$^+$) and the sulfur protonated isomer of the thione form (M′(S14)H$^+$), are the most probable product ions in the chemical ionization of the MBT. As shown in Fig. 2, these two isomers have the same molecular structure. For better comparison of the other protonation sites, "*Internal Proton Affinity*" (IPA) of protonated isomers were tabulated in table 2. The IPA is defined as the difference of TPAs with the more negative value, and thus, its value is zero for the most stable protonated isomer [5].

Table 2. Estimated IPAs of the MBT protonated isomers (kJ mol^{-1}). Atoms in parenthesis refer to the protonation site.

	Thiol	Thione
MH$^+$(C1)	-122.22	-113.60
MH$^+$ (C2)	-145.18	-135.36
MH$^+$(C3)	-182.44	-175.33
MH$^+$(C4)	-98.15	-97.083
MH+(C5)	-114.23	-102.24
MH+(C6)	-93.76	-81.77
MH+(C13)	-166.57	-74.86
MH+(S12)	-163.97	-129.55
MH+(N11)	0.00	-118.73
MH+(S14)	-164.85	0.00

Two product ion peaks were observed in IMS spectra of the MBT. The product ion peak 1, with higher intensity, can be assigned to the most probable protonated isomer of MBT. The peak 2 with lower drift time and lower intensity is probably originated from carbon protonated isomers of the MBT. The added proton to the carbon sites cannot migrate to the most probable protonation site due to the high energy barrier of this transfer.

CONCLUSION

The results obtained in this study indicated that the IMS technique could be used for studying the thermodynamic properties of chemicals with different tautomeric forms. Also, the interpretation of the IMS spectra along with the theoretical calculations can be used for identification of chemical ionization products.

REFERENCES

[1] H. Yekeler, M. Yekeler, J Mol Model, vol. 12, pp:763–768, **2006.**

[2] A. K Rai, R. Singh, K.N. Singh, V.B. Singh, Spectrochimica Acta Part A, vol. 3, pp. 483–490, **2006**.

[3] H. Bahrami, H. Salehabadi, Journal of Molecular Structure, vol. 1083, pp:330–335,**2015**.

[4] H. Bahrami, B. Farajmand, M. ShadmanLakmehsari, *Vol.* 430, pp. 110-116, **2018**.

[5] H. Bahrami, M, Tabrizchi, H, Farrokhpour, vol. 415, pp. 222-227, **2013**.

A Vehicle-Based Remote Methane Detector Using Absorption Molecular Spectroscopy

Mohammad Bakhtbidar*[a], *Atamalek Ghorbanzadeh*[b]* *Ali Tasnim
(*Laser Research Laboratory, Department of Physics, University of Tehran, Tehran, 1439955961, Iran)*
Email: ghorbanzadeham@ut.ac.ir*

Abstract*:* The design and manufacturing of a fast, high sensitivity and portable remote sensor for methane detection is reported. This system acts based on Tunable diode laser absorption spectroscopy (TDLAS) using the second harmonic spectroscopy (SHS), as a detection method. The emitter is a tunable distributed feedback laser (DFBL) centered at wavelength 1653 nm. The optical receiver subsystem collects the weak light backscattered from the ground (soil, sands, etc.) and introduces it into a Photodetector (PD). The electrical signal after PD is amplified and processed by a home-made lock-in amplifier (LIA) and then is sent to Lab.View software for extracting the methane concentration information on a PC. This system was able to detect minimum detectable concentration down to 80 ppm-m from 20 m away at 300 ms integration time. By using the more precise LIA (Stanford Instrum.) and unamplified PD, measurement of concentrations up to 20 ppm-m at a distance of 20 meters was possible. This minimum detectable concentration allows the application of the device in the regular pipeline inspection.

Keywords: Tunable diode laser absorption spectroscopy (TDLAS), second harmonic spectroscopy (SHS), CH4 detection, wavelength modulation spectroscopy (WMS), remote sensing

I. INTRODUCTION

Methane is an explosive and flammable gas and is a major part of the natural gas. The leak of this gas from high pressure pipelines leads to a considerable loss of the energy and also to the safety problems. It is also an important greenhouse gas which release of it in the atmosphere results in the global warming effect. Therefore, the detection of methane molecules is of particular importance. For safety in chemical plants, refineries, mines and gas factories, accurate methane remote detection is highly demanded. The remote detection is possible by the molecular spectroscopy in near and mid-IR region of electromagnetic waves. In this paper, we focus on the TDLAS technique and SHS by using distributed feedback laser (DFBL).

In the mentioned spectroscopy method, the amplitude and wavelength modulation on laser light are simultaneously performed using pure harmonic sinusoidal modulation. When light passes through methane cloud the amplitude of light decreases at a specific point in the sinusoidal wave as a result of absorption. The absorption produces a distortion in the sinusoidal wave. This distortion creates the higher harmonics in the wave. The intensity of the produced harmonics is proportional to the concentration of adsorbent molecules (methane). As a result, the concentration of methane can be determined by dividing the second harmonic to the principal harmonic.

II. METHODS

Theory:

According to the Beer-Lambert law, the intensity of light with frequency ν that emerges from a gas column of length L, is expressed by the relation [1]:

$$I_{out} = I_{in}\exp(-\sigma(\nu)nL) \tag{1}$$

where I_{in} is the incident light intensity, n is the absorbent molecular density, and $\sigma(\nu)$ the stimulated absorption cross section:

$$\sigma(\nu) = \frac{\lambda^2}{8\pi}A_{21}g(\nu)$$

In leak detection experiments one deal with the small concentrations ($^{n}/_{n_0} \ll 1, n_0$ being concentration at atmospheric pressure). Hence, the equation (1) may then be written as

$$I_{out} = I_{in}\exp(-\sigma(\nu)nL) \approx I_{in}(1-\sigma(\nu)nL) \tag{2}$$

In diode lasers, the wavelength is modulated by changing the feeding electrical current. By changing the electrical current, not only the wavelength but also the amplitude of the light is changed:

$$I_{in} = I(\nu_1) + \Delta I(\nu_1).\cos(\omega t) \tag{3}$$

$$\nu(t) = \nu_1 + \Delta\nu\cos(\omega t - \psi)$$

The line shape $g(\nu)$ is dominated by the collision broadening, having Lorentian shape:

$$g(\nu(t)) = \frac{^{\Delta\nu}/_{2\pi}}{(\nu(t)-\nu_0)^2 + (^{\Delta\nu}/_{2})^2}$$

Where, $\Delta\nu$ is the frequency broadening reaching several GHz in methane-air mixture at atmospheric condition. ν_0 is the central absorption frequency.

By inserting relations (3)-(5) into the relation (2), one obtains, after the Tailor expansion of exponential function [2]:

$$I_{out} = (I(\nu_1) + \Delta I(\nu_1).\cos(\omega t)) \times \left(1 - \alpha_0 CL \left\{a_0 + \sum_{n=1}^{\infty} a_n \cos(n\theta)\right\}\right), \quad (6)$$

$$\theta = \omega t - \psi.$$

As stated in equation (6), all harmonics, except for the principal harmonic, are directly proportional to the concentration. By dividing amplitudes of the harmonic 2 to harmonic1, the resulting expression would be proportional to the concentration of the target gas:

$$\frac{H_2}{H_1} \propto CL$$

In the above dividing fraction, all factors including the reflectance of the soil, etc., geometrical, collection efficiency of optical receiver, and the gain of the electronics are cancelled out.

Experiment:

The structure and photo of the CH4 remote detection device is depicted in Fig. 1. It consists of an electrical part and an optical part. The optical part involves a laser (DFBL:DL-BF12), purchased from Dense Light Semiconductors Co. with an emitting wavelength around 1.650 μm and 0.5 nm tunability, a single mode optical fiber (SMOF), optical collimator, Spherical lens with anti-reflective coating (Ø=20 cm, f≈25 cm), bandpass filter (BF) (1650nm, Thorlabs Co.), InGaAs free space amplified PD (PDA20CS, Thorlabs) or mounted InGaAs photodiode (SM05PD4A, Thorlabs). The electrical part contains all the laser control panel electronics plus the lock-in amplifier, LIA (SR830m, Stanford), analog-to-digital converter (ADC) (ADS1248, TEXAS INSTRUMENT), amplifiers and filters, main control unit (MCU), etc.

Methane has a wide absorption band around 1650 nm with multiple absorption lines. Two important lines, 1650.9 nm and 1653.7 nm, are well-known. The second absorption line is often used and we also used the latter. These lines do not overlap with the lines of different molecules present in the air, such as water vapor, making them suitable for the leak detection.

The laser light was modulated by a sine-wave 4 kHz in frequency. The modulated light was directed towards the target at 15-20 m distance, by the collimating optics. The back scattered light is collected by a lens (30 cm in diameter), focusing on the filter optics at the front of PD. The electrical signal emerging from PD is first pre-amplified with a gain of almost 10^3 and then is passed through an electronic filter (40 kHz bandwidth). The signal is then fed to the Lock-in where two harmonics amplitudes are derived. In the last step the analog signal is converted to the digital one and is delivered to a PC and lab. view software for the more mathematical procedure including the division of harmonics.

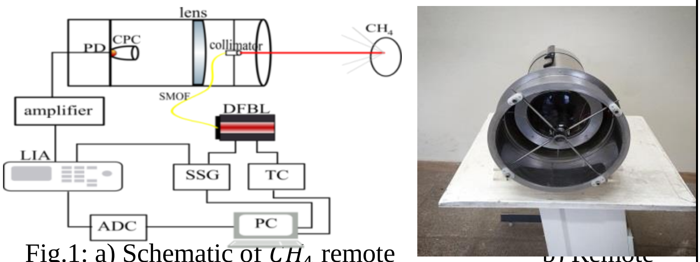

Fig.1: a) Schematic of CH_4 remote CH_4 detector system based on TDLAS b) Remote detector system

Two sets of experiments were accomplished with the domestic electronics (#1) and the amplified PD, and while the lock-in and amplification electronics were replaced by the Stanford LIA (#2) plus the conventional unamplified PD.

III. RESULTS AND DISCUSSION

The best results obtained in #1 experiment revealed the minimum detectable concentration of almost 80 ppm-m from 15 m distance with 300 ms integration time. In other words, it is able to detect a cloud of 80 ppm concentration of methane while the diameter of the cloud is 10 m. The signal level from 15 m distance with a time constant of 300 ms when methane detector system moves, presented in FIG. 2.

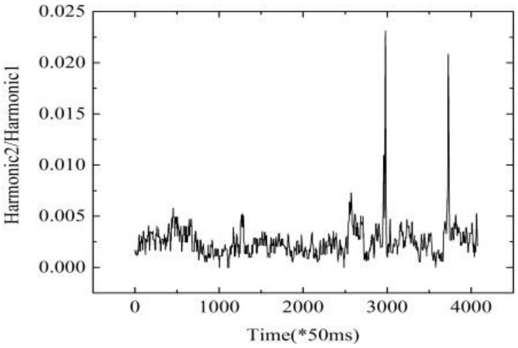

Fig.2 : Signal level from 15 m distance with a time constant of 300 ms when methane detector system moves

By increasing the detection velocity (changing the time constant to 100 ms), the noise level is increased, as observed in Fig. 3. The setup #2 revealed a minimum detectable concentration of about 20 ppm-m, improving 3-fold the results of setup #1. More studies showed that the origin of the excess noise in set up #1 is the amplification process in both PD and the electronic part. We are working on the improvement of the noise level in set up #1 by replacing the electronics.

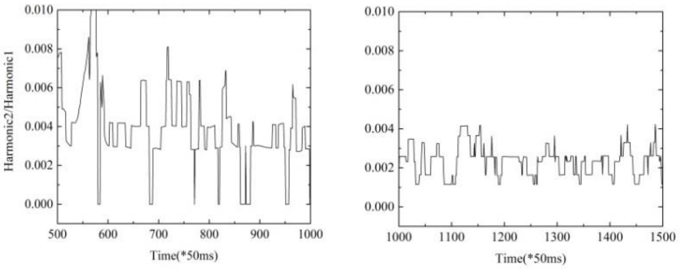

a) 300 ms time constant

b) 100 ms time constant

Fig.3: the noise level at different time constants

IV. CONCLUSION

A domestic standoff laser sensor of methane was developed that is able to detect a minimum methane concentration of about 80 ppm-m from a distance of 15-20 m. The time constant of the detection is 300 ms, corresponding to about 10 km/hr of speed of the vehicle on roof of which such remote sensor is to be installed to inspect the pipelines. More studies are under way to improve both the minimum detectable concentration and the velocity of the detection (towards 50 ms).

ACKNOWLEDGMENTS

This work was by part supported by the Directorate of Research, Development and Technology affairs of Iranian National Gas Company (NIGC) and also by the Vice Chancellor of Research of University of Tehran.

REFERENCES

[1] H. T. Chang, J. Chang, P. P. Wang, C. G. Zhu, Opt and Quantum Electronics, 2016, vol.48, No13, 1-13

[2] J. Huang, Ch. Zheng , Z. Gao, W. Ye & Y. Wang, Spectroscopy Letters, vol 47, 197–205, 2014

[3] G. Stewart,W. Johnstone, J. R. P. Bain, K. Ruxton and K. Duffin, Lightwave Technology, vol.29, March 15, 2011, 811-821

Experimental and Theoretical Investigation of 5-aminoindole Chemical Ionization

M. Yousefian, M. Vahedpour* and H. Bahrami
Department of Chemistry, University of Zanjan, P. O. Box: 38791-45371, Zanjan, Iran
Email: vahed@znu.ac.ir

Abstract*:* Ion mobility spectrometry was used for studying chemical ionization of 5-aminoindole. The ionization source was corona discharge in positive mode. Two product ion peaks were observed in the ion mobility spectrum obtained at cell and injection port temperatures of 200 and 260 °C, respectively. Product ion peaks were assigned to the protonated isomers of 5-aminoindole. Density functional theory calculations were carried out to confirm the experimental results. Topical proton affinities of 5-aminoindole and dipole moments of its protonated isomers were calculated to identify the chemical structures of ions which have contributed in the creation of product ion peaks. It was shown that the combination of DFT calculations and ion mobility experiments leads to a reliable prediction of reactive protonation sites of the studied compound.

Keywords: 5-aminoindole, Chemical ionization, Ion mobility spectrometry, Density functional theory, Protonation site.

I. INTRODUCTION

Indole and substituted indoles have been extensively investigated both experimentally and theoretically [1-3]. The 5-aminoindole molecule can be found in various biological systems. It occurs in coal tar, jasmine flower, and orange blossoms. It melts in the range of 133–136 ˚C. The structural and dynamic studies of proteins in biological investigations chiefly involve the tryptophan, which is a derivative of indole [4].

In atmospheric pressure chemical ionization (APCI) methods, sample ions are produced by ion-molecule reactions with the primary reactant ions. Ionization of an analyte is carried out mainly by proton-transfer reactions from the reactant ions. Therefore, Proton affinity (PA) is an important property of molecules that shows the tendency of a molecule to grab a proton. The PA of molecule M is defined as the negative of the enthalpy change of the protonation reaction:

$$M(g) + H^+ (g) \rightarrow MH^+ (g) \qquad -\Delta H=PA(M) \qquad (1)$$

In the case of multifunctional molecules that have several potential sites for protonation, the concept of topical proton affinity (TPA) arises. If the conditions are met, proton transfer can be occurred between a neutral (M), and a protonated molecule (MH^+) led to the formation of a more stable protonated isomer. In this competition, the quantity of internal proton affinity (IPA) will be decisive. The IPA is defined as the difference of TPAs, and its value is zero for the most stable protonated isomer [5].

In the present study, positive ion mobility spectra of 5-aminoindole have been obtained with a CD-IMS. The observed peaks in the ion mobility spectra were assigned to ions formed by proton transfer to the sample. DFT calculation was conducted on the structure of the neutral and all possible protonated isomers of 5-aminoindole to support and extend the experimental conclusions.

II. MATERIAL AND METHODS

All experiments were performed with a commercial ion mobility spectrometer (IMS-300) made by TOF Tech. Pars Co. (Iran). The cell and injection port temperatures were set to be 200 and 260 °C, respectively. Purified air was used as drift and carrier gas. Drift field was set at 500 $V.cm^{-1}$. 5-aminoindole purchased from Sigma Aldrich was injected to the IMS as a solid sample without further purification.

The theoretical calculations were carried out using the quantum computational Gaussian09 package [7] based on density functional theory B3LYP level [6] in connection with the 6-311++G(d,p) basis set. The frequency calculations were performed at the same level of theory on optimized structures to search for the imaginary frequency and obtain the enthalpy of the species involved in protonation reaction.

III. RESULTS AND DISCUSSION

Fig.1 shows a typical IMS spectrum of the 5-aminoindole obtained at injection port and cell temperatures of 260 and 200 °C, respectively. From left to right, three first peaks are corresponding to $NH4^+$, NO^+, and $H3O^+$ (reactant ions). Two peaks in the region from 6 to 8 ms correlate with 5-aminoindole.

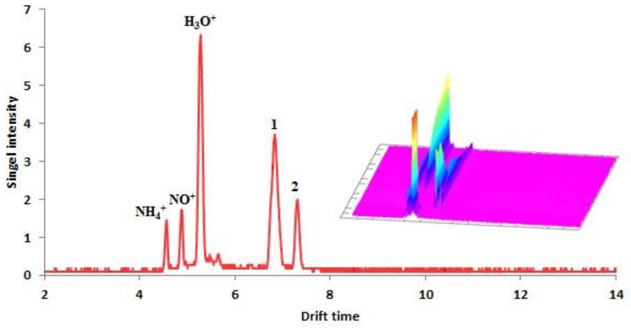

Fig.1. Ion mobility spectrum of 5-AI in positive mode with corona discharge ionization source.

There are ten possible sites for protonation in the 5-aminoindole molecular structure, including eight carbon and two nitrogen atoms; each will lead to a protonated isomer. To find the relative stability of the protonated isomers, the neutral molecule was protonated from all nitrogen and carbon sites. The structures of protonated isomers were then optimized. The calculated TPAs of 5-aminoindole and IPAs of protonated 5-aminoindole isomers are given in Table 1.

Table1: Topical proton affinities of 5-aminoindole and internal proton affinities at 273K (in kcal/mol), and dipole moments (in Debye) of protonated 5-aminoindole isomers. Atoms in parenthesis are the protonation sites.

Compound	TPA	IPA	µ
MH$^+$(C1)	209.97	-15.61	1.194
MH$^+$(C2)	195.86	-29.72	1.811
MH$^+$(C3)	225.58	0.00	2.296
MH$^+$(C4)	195.47	-30.11	2.048
MH$^+$(C5)	221.24	-4.35	1.984
MH$^+$(C6)	206.81	-18.78	1.818
MH$^+$(C7)	216.19	-9.40	1.969
MH$^+$(C8)	222.62	-2.97	3.322
MH$^+$(N9)	219.42	-6.16	7.893
MH$^+$(N10)	206.54	-19.05	4.196

The theoretical calculations show that the protonated structure from the C3 site MH$^+$(C3) was the most stable isomer among the protonated forms. The next most stable isomers were MH$^+$(C8), MH$^+$(C5) and MH$^+$(N9), respectively. The optimized structures of the most stable protonated isomers are shown in Fig. 2.

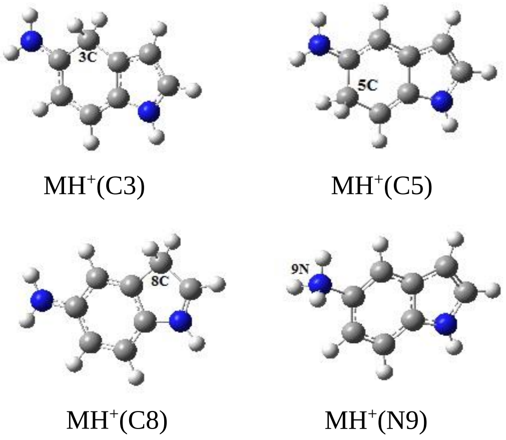

MH$^+$(C3) MH$^+$(C5)

MH$^+$(C8) MH$^+$(N9)

Fig. 2. Optimized structure of the four most stable 5-aminoindole protonated isomers.

As shown in Fig. 1, the two product ion peaks (PIPs) in the ion mobility spectrum of 5-aminoindole are denoted as peaks 1 and 2. The drift times of the PIPs were considerably different. The drift time of an ion in IMS is depending on its interactions with neutral molecules in the drift tube, especially with the water molecules. The more polar the ion, the stronger the interactions with neutral molecules and the lesser the drift velocity, and thus the corresponding peak will appear at a higher drift time. The dipole moments of the protonated isomers are listed in table 1. The calculated dipole moments for nitrogen protonated isomer (MH$^+$(N9)) is significantly more than carbon protonated isomers. Therefore it can be concluded that the peak corresponding to the nitrogen protonated isomer must appear at a higher drift times relative to the carbon protonated isomers.

Based on the experimental evidence and theoretical calculations, the PIP1 with lower drift time and higher intensity can be attributed to the carbon protonated isomers, especially C3, C8, and C5 protonated isomers. The PIP2 with higher drift time and lower relative intensity was assigned to the MH$^+$(N9) protonated isomer.

CONCLUSION

The results obtained in this study indicated that the IMS technique could distinguish between different protonated isomers of a chemical compound. Also, the interpretation of the IMS spectra along with the theoretical calculations can be used for exact identification of chemical structures of ionization products.

REFERENCES

[1] T. Vondrak, S. Sato, K. Kimura, J. Phys. Chem, vol. 101, pp. 2384, **1997**.

[2] W. Caminati, S.D. Bernardo, J. Mol. Struct, vol. 240, pp. 253, **1990**.

[3] P.R. Callio, J.T. Vivian, L.S. Slater, J. Chem. Phys. Lett, vol, 244, pp. 53, **1995**.

[4] G. Moretti, G. Quartarone, A. Tassan, A. Zingales, J. Electrochim. Acta. Vol. 41, pp. 1971, **1996**.

[5] Bahrami, H. Salehabadi, J. Mol. Struct., vol. 1083, pp:330–335**,2015**.

[6] G.W.T.M.J. Frisch, H.B. Schlegel, G.E. Scuseria, M.A. Robb, J.R. Cheeseman, G. Scalmani, V. Barone, B. Mennucci, G.A. Petersson, H. Nakatsuji, M. Caricato, X. Li, H.P. Hratchian, A.F. Izmaylov, J. Bloino, G. Zheng, J.L. Sonnenberg, M. Hada, M. Ehara, K. Toyota, R. Fukuda, J. Hasegawa, M. Ishida, T. Nakajima, Y. Honda, O. Kitao, H. Nakai, T. Vreven, J.A. Montgomery Jr., J.E. Peralta, F. Ogliaro, M. Bearpark, J.J. Heyd, E. Brothers, K.N. Kudin, V.N. Staroverov, T. Keith, R. Kobayashi, J. Normand, K. Raghavachari, A. Rendell, J.C. Burant, S.S. Iyengar, J.Tomasi, M. Cossi, N. Rega, J.M. Millam, M. Klene, J.E. Knox, J.B. Cross, V. Bakken, C. Adamo, J. Jaramillo, R. Gomperts, R.E. Stratmann, O. Yazyev, A.J. Austin, R. Cammi, C. Pomelli, J.W. Ochterski, R.L. Martin, K. Morokuma, V.G. Zakrzewski, G.A. Voth, P. Salvador, J.J. Dannenberg, S. Dapprich, A.D. Daniels, O. Farkas, J.B. Foresman, J.V. Ortiz, J. Cioslowski, D.J. Fox, Gaussian 09, Revision B.01, Gaussian Inc., Wallingford, CT, **2010**.

[7] A.D. Becke, Density-functional thermochemistry. III. The role of exact exchange, J. Chem. Phys. 98, pp. 5648–5652. **1993**.

Chemical Ionization of Thiosemicarbazide; Ion Mobility Spectrometry and Theoretical Calculations

***F. Khouini*, M. Vahedpour*, and H. Bahrami**
Department of Chemistry, University of Zanjan, P. O. Box: 38791-45371, Zanjan, Iran
Email: vahed@zun.ac.ir

Abstract: Chemical ionization of thiosemicarbazide in corona discharge environment was investigated using ion mobility spectrometry. Two peaks were observed in the ion mobility spectrum in the positive ion mode. The mean peak was assigned to the protonated thiosemicarbazide, and the other one was assigned to a fragment ion produced by thermal decomposition of the sample. The experimental results were confirmed with the use of theoretical calculations. The most probable protonated structure of thiosemicarbazide was found to be sulfur protonated isomer.

Keywords: Thiosemicarbazide, Chemical ionization, Protonation site, Ion mobility spectrometry, Theoretical calculations.

I. INTRODUCTION

Thiosemicarbazides and their derivatives have continued to be the subject of extensive investigation in chemistry and biology [1,2]. In this study, the ionization of thiosemicarbazide in the gas phase has been investigated.

The experimental data have been obtained from ion mobility spectrometry (IMS). The IMS is a suitable technique for the identification and determination of chemical substances. However, IMS has been used to study the thermal decomposition and ionization of chemical compounds in the gas phase [3]. In short, the sample is ionized in the reaction region of the IMS and product ions are collected after separation in a drift tube based on their mobility. Among different ionization sources employed in IMS, corona discharge ionization (CD) as an atmospheric pressure chemical ionization (APCI) method, has been highly accepted [4]. The known ionization mechanism in positive CD-IMS is the proton transfer from the reactant ions to sample molecules. The sample molecules should have PA values greater than those of the reactant ions to be ionized in CD-IMS. The PA of molecule M is defined as the negative of the enthalpy change of the protonation reaction:

$$M(g) + H^+(g) \rightarrow MH^+(g) \qquad PA(M) = -\Delta H \qquad (1)$$

If there are more than one protonation sites in a molecule, the concepts of topical proton affinity (TPA) and internal proton affinity (IPA) arise [5].

In the present study, positive ion mobility spectra of thiosemicarbazide have been obtained with a CD-IMS. The observed peaks in the ion mobility spectra were assigned to ions formed by thermal decomposition and chemical ionization of the sample. Quantum calculation was conducted on the structure of neutral and all possible protonated isomers of thiosemicarbazide to support and extend the experimental conclusions.

II. METHODS

All experiments were performed with a commercial ion mobility spectrometer (IMS-300) made by TOF Tech. Pars Co. (Iran). The cell and injection port temperatures were set to be 200 and 260 °C, respectively. Purified air was used as drift and carrier gas. Drift field was set at 500 $V.cm^{-1}$. Thiosemicarbazide purchased from Sigma Aldrich and was injected to the IMS as a solid sample without further purification.

The theoretical calculations were carried out using quantum computational Gaussian09 software based on density functional theory B3LYP, and MP2 approaches in connection with the 6-311++G (d, p) basis set.

III. RESULTS AND DISCUSSION

Fig. 1 shows the CD-IMS spectrum of thiosemicarbazide. Three peaks were observed in the background spectrum (Fig. 1a), which are originated from NH_4^+, NO^+, and H_3O^+ reactant ions. As seen in Fig. 1b, two product ion peaks were observed for thiosemicarbazide at drift time of 5.39, and 5.92 ms denoted as PIP2 and PIP1, respectively.

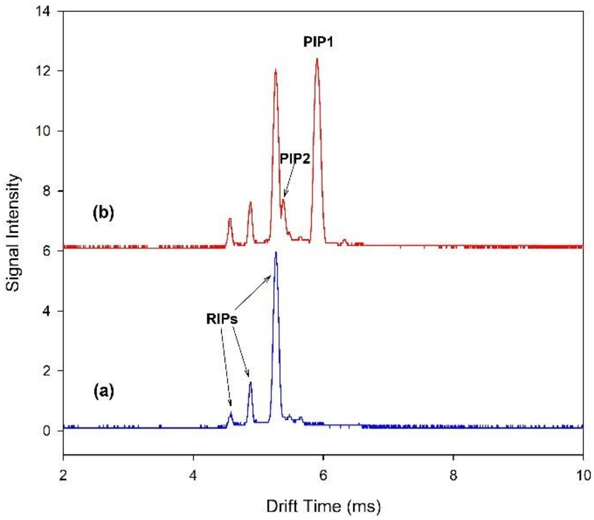

Fig. 1. (a) Background CD-IMS spectrum, (b) the CD-IMS spectrum of thiosemicarbazide.

The known ionization mechanism in positive CD-IMS is the proton transfer from the reactant ions to sample molecules. Therefore, the PIP1, with the largest drift time can be assigned to the protonated thiosemicarbazide. The PIP2 is probably originated from a fragment ion produced by the decomposition of the neutral or protonated sample molecules. This issue can be clarified by investigating the variation of the peak intensities over time. In IMS, the peak intensities change over time after the introduction of the sample into the ionization region (Fig. 2).

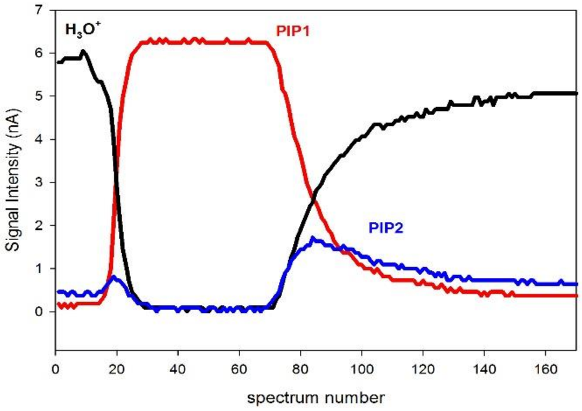

Fig. 2. The time evolution of the peaks appeared in the IMS spectra of Fig 1b.

As shown in Fig. 2, with the introduction of the analyte to the spectrometer, the intensity of RIP decreases while the intensities of PIP1 and PIP2 increases. However, unlike PIP1, the intensity of PIP2 decreases immediately and finally grows concurrent with a decrease in intensity of PIP1. These behaviors relate that the fragmentation happens through thermal decomposition of the sample at the injection port of IMS. Then the fragment molecules ionize after introduction to the reaction region of the IMS and appear as PIP2 in the spectrum. The failure of the fragment molecule to receive proton in competition with the parent molecule decreases the intensity of the PIP2.

To predict the structure of protonated isomer, which has the most contribution in the production of PIP1, TPAs were calculated for thiosemicarbazide. Fig. 3 shows the optimized molecular structure of thiosemicarbazide. There are five suitable sites for protonation of thiosemicarbazide including sulfur, carbon, and three nitrogen atoms. To find the most stable protonated isomer, the optimized structure of the neutral molecule was protonated from all possible sites. The geometry of the protonated isomers was then optimized. Frequency calculations were performed on protonated thiosemicarbazide isomers at 473K, the temperature at which the ion mobility spectra were recorded.

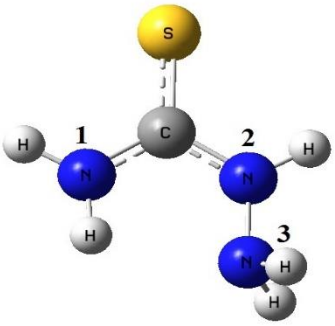

Fig. 3. The optimized structure of Thiosemicarbazide at B3LYP/6-311++G (d, p) level of theory.

The calculated enthalpies of the components contributing to reaction (1) were used to obtain the topical PA of thiosemicarbazide. Table 1 gives the calculated values for TPA and IPA of thiosemicarbazide. It can be seen that protonation tended toward the sulfur site. On the contrary, the carbon atom was the must unstable protonation site.

Table 1. The TPAs and IPAs (kcal mol^{-1}) of thiosemicarbazide obtained with MP2 and B3LYP methods and 6-311++G (d, p) basis set.

Ref.	TPA		IPA	
Compound	B3LYP	MP2	B3LYP	MP2
M(S)	216.268	217.164	0	0
M(N1)	198.375	201.905	-17.893	-15.259
M(N2)	193.026	196.274	-23.242	-20.890
M(N3)	191.251	195.039	-25.017	-22.125
M(C)	168.281	172.290	-47.987	-44.874

Based on the experimental evidence and theoretical PA calculations, the PIP2 can be attributed to the M(S)H$^+$ protonated isomer. The PIP2 was assigned to the thermal decomposition product of thiosemicarbazide.

IV. CONCLUSION

The results obtained in this study indicated that the IMS technique along with the theoretical calculations can be used for studying the chemical ionization of thiosemicarbazide. Also, investigating the variation in the relative IMS peak intensities assists the identification of the final decomposition and ionization products.

REFERENCES

[1].E.O Offiong, O.E Martelli, Transit, Met. Chem, vol 22, pp. 263-269, **1997**.
[2]. U.J Ekpe, U.J Ibok U, B.I Ita , E.O Offiong , E.E Ebenso , Chem. Phys, , vol 40, pp.87-93, **1995**.
[3]. H. Bahrami, B. farajmand, M.S. Lakmehsari, International journal of Mass Spectrometry, vol 430, pp110-116, **2018**.

[4]. H. Bahrami, H. Salehabadi, Journal of Molecular Structure, vol. 1083, pp:330–335, **2015**.
[5]. H. Bahramai, M. Tabrizchi, H. Farrokhpour, Chemical Physics, vol 415, pp. 222-227, **2013.**

Chemical Ionization of Barbituric acid in Corona discharge

***Masoumeh Ghahremani**, **Hamed Bahrami** [*]*
Department of Chemistry, University of Zanjan, Zanjan, Iran, Fax: +98 24 33052477; Tel: +98 24 33052477;
E-mail: hbahrami@znu.ac.ir

Abstract: Ion mobility spectrometry was used for studying the chemical ionization of Barbituric acid. The ionization source was corona discharge in positive mode. Four product ion peaks were observed in the ion mobility spectrum obtained at the cell and injection port temperatures of 170 and 260 °C, respectively. Product ion peaks were assigned to the protonated isomers of Barbituric acid as fragment ions. Density functional theory calculations were carried out to confirm the experimental results. Topical proton affinities of Barbituric acid and dipole moments of its protonated isomers were calculated to identify the chemical structures of ions which have contributed to the creation of product ion peaks. It was shown that the combination of DFT calculations and ion mobility experiments leads to a reliable prediction of probable protonation sites of the studied compound.

Keywords: Barbituric acid, Chemical ionization, Ion mobility spectrometry, Density functional theory, Protonation site.

I. INTRODUCTION

Barbituric acid (BA) is a well-known organic compound based on a pyrimidine heterocyclic skeleton (Fig. 1). BA itself is not pharmacologically active, but it is the parent compound of a large class of barbiturates that act as central nervous system depressants. They are used in medicine as sedatives, hypnotics, and soporifics [1].

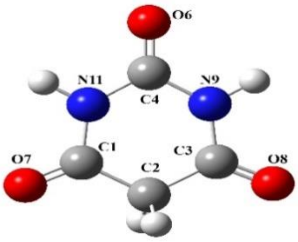

Fig. 1. The optimized structure of BA at B3LYP/6-311++G (d, p) level of theory.

The ion mobility spectrometry (IMS) is a suitable technique for the identification and determination of chemical substances. However, IMS has been used to study the ionization of chemical compounds in the gas phase [3]. Among different ionization sources employed in IMS, corona discharge ionization (CD) as an atmospheric pressure chemical ionization (APCI) method, has been highly accepted [4]. The known ionization mechanism in positive CD-IMS is the proton transfer from the reactant ions to sample molecules. The sample molecules should have PA values greater than those of the reactant ions to be ionized in CD-IMS. The PA of molecule M is defined as the negative of the enthalpy change of the protonation reaction:

$$M(g) + H^+(g) \rightarrow MH^+(g) \qquad PA(M) = -\Delta H \qquad (1)$$

If there are more than one protonation sites in a molecule, the concepts of topical proton affinity (TPA) and internal proton affinity (IPA) arise [5].

In the present study, positive ion mobility spectra of BA have been obtained with a CD-IMS. The observed peaks in the ion mobility spectra were assigned to ions formed by thermal decomposition and chemical ionization of the sample. Quantum calculation was conducted on the structure of neutral and all possible protonated isomers of BA to support and extend the experimental conclusions.

II. METHODS

All experiments were performed with a commercial ion mobility spectrometer (IMS-300) made by TOF Tech. Pars Co. (Iran). The cell and injection port temperatures were set to be 170 and 260 °C, respectively. Purified nitrogen was used as drift and carrier gas. Drift field was set at 500 V.cm^{-1}. BA purchased from Sigma Aldrich and was injected to the IMS as a solid sample without further purification.

The theoretical results were based on density functional theory (DFT) calculations at the B3LYP/ 6-311++G** level.

III. RESULTS AND DISCUSSION

Fig. 2 shows a typical IMS spectrum of the BA. From left to right, three first peaks are corresponding to reactant ions. Four peaks in the region from 6 to 8 ms are correlated with BA.

The known ionization mechanism in positive CD-IMS is the proton transfer from the reactant ions to sample molecules. Therefore, peak 1, with the largest drift time, can be assigned to the protonated BA.

As shown in Fig. 1, there are three suitable protonation sites in BA molecular structure named O6, O8, and N9. To find the topical PA of BA, the neutral molecule was protonated from nitrogen and two oxygen atoms. The structures of protonated isomers were then optimized, and frequency calculations were performed. The calculated TPAs of BA and IPAs of protonated BA isomers were calculated based on eq. 1 and 2 and are listed in Table 1.

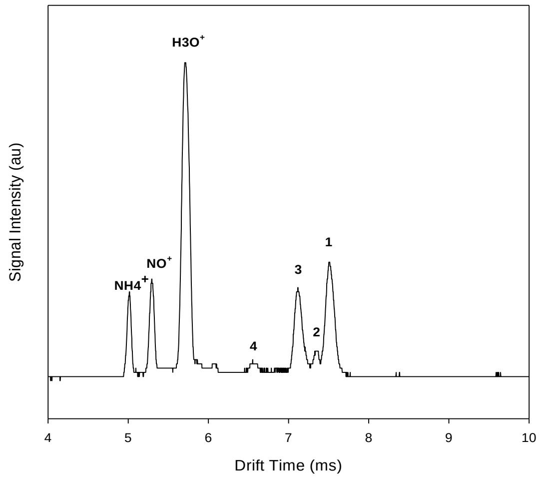

Fig. 2: Ion mobility spectrum of BA in positive mode with corona discharge ionization source.

Table1: Topical proton affinities of BA at 298 K, internal proton affinities (in kJ mol^{-1}), and dipole moments (in Debye) of protonated BA isomers. Atoms in parenthesis are the protonation sites.

Compound	TPA	IPA	μ
MH^+(O8)	781.32	0	6.34
MH^+(O6)	779.63	-1.69	5.56
MH^+(N9)	694.90	-86.42	4.03

The theoretical calculations show that the protonated structures from the oxygen sites were more stable than nitrogen protonated isomer. Therefore, peak 1 can be assigned to the oxygen protonated isomers.

The ion mobility spectrum of BA was converted to a mass spectrum based on the regression equation of the mass-to-drift time correlation via two standard mass method. To this end, the masses of 54 amu and 129 amu corresponding to the hydrated ammonium reactant ion ($NH_4^+(H_2O)_2$) and protonated BA were considered as the standards. The obtained mass spectrum is shown in Fig. 3.

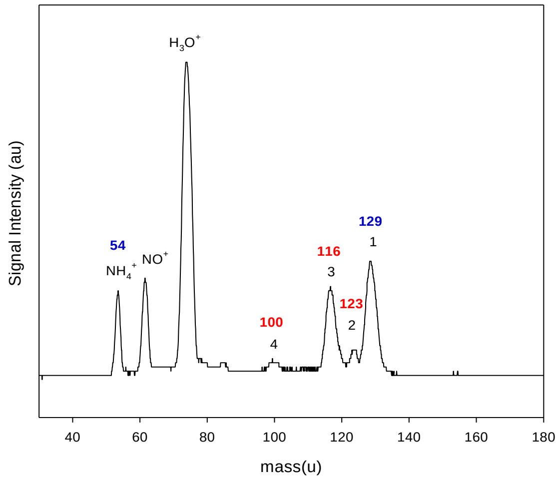

Fig. 3. Mass converted spectrum of BA obtained at injection port temperature of 260 ºC and cell temperature of 170 ºC based on two standard masses.

A mass of 123 amu was predicted for peak 2. Given the closeness of the mass associated with peak 2 to that of peak 1, it can be concluded that the origin of this peak is an isomer of the protonated BA with less topical proton affinity since such mass value cannot be created by any neutral loss from the protonated or parent BA molecule. In this regards, peak 2 can be assigned to nitrogen protonated isomer of BA. This assignment is confirmed with calculated dipole moments for protonated isomers of BA (table 1). The calculated dipole moments for nitrogen protonated isomer (MH^+(N9)) is lower than oxygen protonated isomers. The more polar the ion, the stronger the interactions with neutral molecules and the lesser the drift velocity, and thus the corresponding peak will appear at a higher drift time.

The peak 3 and 4 are probably originated from a fragment ion produced by the decomposition of the neutral or protonated BA molecules.

The peak 3 can be assigned to a fragment produced by losing neutral CO molecule from protonated BA. There are two candidates for the small peak 4, including MH^+-CH_2CO and MH^+-HNCO.

IV. CONCLUSION

The results obtained in this study indicated that the IMS technique, along with the theoretical calculations, could be used for studying the chemical ionization of BA. A chemical sample may be decomposed during ionization by corona discharge.

REFERENCES

[1] M.V Roux, M. Temprado, R. Notario, et al, J. Phys. Chem. A, vol. 112, pp. 7455-7465, **2008**.

[2] H. Bahrami, B. farajmand, M.S. Lakmehsari, International Journal of Mass Spectrometry, vol 430, pp.110-116, **2018**.

[3] H. Bahrami, H. Salehabadi, Journal of Molecular Structure, vol. 1083, pp. 330-335, **2015**.

[4] H. Bahrami, M. Tabrizchi, H. Farrokhpour, Chemical Physics, vol 415, pp. 222-227, **2013**.

Section:

Nano Computation

Electronic and structural properties of Sc decorated graphdiyne toward hydrogen adsorption

***Mona Akbari**, Adel Reisi-Vanani**[*]

Department of Physical Chemistry, Faculty of Chemistry, University of Kashan, Kashan, Iran

(areisi@kashanu.ac.ir)

Abstract: Today, graphdiyne (GDY), as a two-dimensional carbon surface, is used in various fields such as gas storage, catalysis, water purification, etc. Interaction of H_2 molecules with pristine carbon structures is very weak and it is essential that modifies. Transition metal decoration is a method for this purpose. Here, we studied the best site for putting Sc atom on GDY sheet, and then we put several H_2 molecules on it. Results show that modification with Sc decoration can improve hydrogen adsorption of GDY, extremely.

Keywords: Hydrogen storage, Graphdiyne, Decoration, DFT, Adsorption.

I. INTRODUCTION

GDY is a new carbon nano-sheet with unique π-conjugated carbon frame contains expanded pore size and sp- and sp^2-hybridized carbon atoms [1]. In two-dimensional materials, transition metals may be considered as very active centers for molecular adsorption such as H_2, CO, CO_2, etc. Hydrogen can be an alternative and renewable source of clean energy that has been center of attention and has been considered in the last decades for solving its difficulties that can be applied as a safe source of energy. Abundant, environment friendly and high ratio of energy to weight are some of vital properties of hydrogen as an energy carrier [2]. In this work, modification of GDY carbon nano-sheet using Sc atom has been done to promote its adsorption behavior.

II. METHODS

For this study, spin-polarized DFT calculations were performed using $DMol^3$ package. The generalized gradient approximation (GGA) with the Perdew-Burke-Ernzerh of (PBE) exchange-correlation with the double numerical plus polarization (DNP) was applied. Here, the empirical correction scheme proposed by Grimme (DFT-D3) was used to account the effect of van der Waals interactions. This method has successfully been applied to address intermolecular dispersion correction in various cases such as the interaction of different small gas molecules with 2D carbon sheets such as GDY. GDY unit cell contains 18 carbon atoms. In calculations, we used a 2 × 2 super cell and we selected a vacuum of 20 Å along the non-periodic z direction (perpendicular to the plane of GDY) to avoid the interactions between neighboring periodic structures [2]. For integration in Brillouin zone, a 7 × 7 × 1 k-point mesh by the Monkhorst−Pack scheme was used for the systems.

III. RESULTS AND DISCUSSION

For investigation of the binding energy of Sc single atom on 2 × 2 GDY supercell, we examined three possible binding sites that were presented in Fig.1 and are contain the corner of the acetylenic ring (C), above the center of hexagonal ring (H1) and the hollow site in the center of the acetylenic ring (H2) [3]

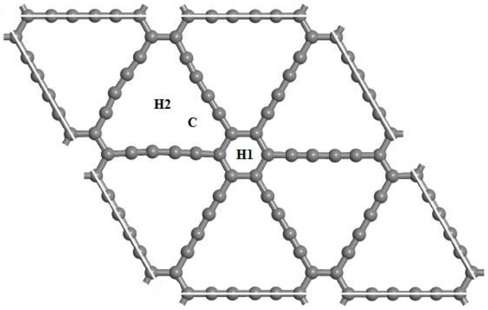

Fig.1. Atomic configuration of free-standing graphdiyne sheet. C, H1 and H2 are the considered adsorption sites for Sc adatom.

All three sites are stable for lying of Sc atom, but results show that with respect to E_{ads}, C site is the best and has the highest E_{ads}. So in the following of the work, we study adsorption of H_2 molecules on the Sc-decorated GDY that there is an adatom in its C site.

Next, we increased number of H_2 molecules onto Sc-decorated GDY, step by step in both sides and optimized the structures. Results showed that for the first H_2 molecule, adsorption energy is about 0.417 eV, and after that with increasing of H_2 molecule number, adsorption energy per H_2 molecule gradually decease to 0.191 eV for 20th molecule. Desirable adsorption energy for practical applications is in the range of –0.2 to –0.4 eV, so can be say that Sc-decorated GDY is a suitable material for hydrogen storage systems. The calculated hydrogen storage capacity for twenty H_2 molecules per a unit cell of Sc-decorated GDY is about 13.29 wt.% that is very good on the basis of DOE targets in 2020. Optimized structures of the Sc-decorated GDY contain twenty H_2 molecules is seen in Fig.2.

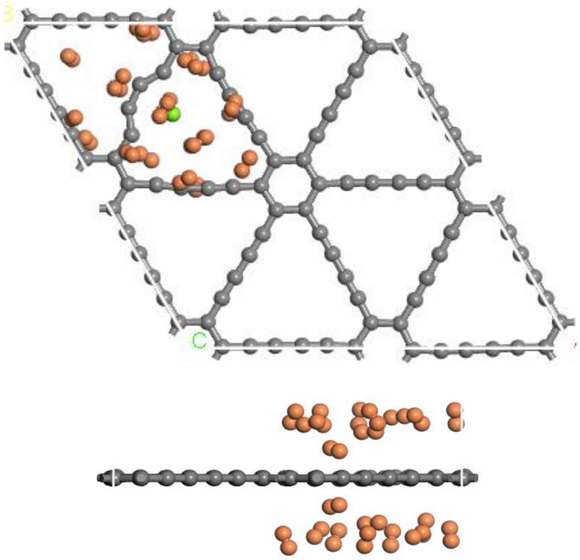

Fig.2. Top and side views for optimized structure of the system contains twenty H_2 adsorbed on Sc-GDY sheet.

IV. CONCLUSION

In this study, adsorption energy of Sc onto three sites of GDY was calculated and the best site was determined. Then, adsorption energies of H_2 molecules on this structure were studied by DFT calculations. Results showed that Sc-decorated GDY can trap up to twenty H_2 molecules in both sides of himself that is equivalent to a hydrogen storage capacity of 13.29 wt.%.

REFERENCES

[1] N. Wang, J. He, Z. Tu, Z. Yang, F. Zhao, X. Li, C. Huang, K. Wang, T. Jiu, Y. Yi, and Y. Li, Ang. Chem. Int, 56, 10740-10745, **2017**.

[2] P. Panigrahi, A.K. Dhinakaran, S.R. Naqvi, S.R. Gollu, R. Ahuja, and T. Hussain, Nanotechnology, 29, 355401-410, **2018**.

[3] Z. Z. Lin, Carbon, 108, 343-350, **2016**.

Modification of graphdiyne by vanadium single atom to promote hydrogen adsorption

Mona Akbari, *Adel Reisi-Vanani*[*], *Soha Shamae*
Department of Physical Chemistry, Faculty of Chemistry, University of Kashan, Kashan, Iran
Email:areisi@kashanu.ac.ir

Abstract*:* Hydrogen storage, like wind power as a reproducible energy is used to supply grid energy storage and fuel for transportation, especially for ships and airplanes. Graphdiyne (GDY), a new two-dimensional (2D) carbon allotrope, has been receiving increased attention. we have theoretically investigated the electronic structures and stabilities of the transition-metal adsorbed GDY (namely TM-GDY (TM = V)) single atom by means of spin polarized density functional theory calculations. Results show that V-decoration can improve hydrogen adsorption onto GDY.

***Keywords*:** Hydrogen, Graphdiyne, Decoration, DFT, Adsorption.

I. INTRODUCTION

Hydrogen, similar to wind, is one of the reproducible energy sources and it is used to supply grid energy storage and fuel for transportation. GDY in pristine form such as other carbon structure has weak interactions with H_2 molecules. In order to provide a suitable energy source by GDY-based materials, GDY must be improved and one of the best methods is decoration. Its unique sp–sp^2 hybridized carbon atoms, uniform pores, and highly π-conjugated structure introduce promising potential in practical usages, such as gas separation, catalysis, water remediation, humidity sensor, and energy-related aspects [1,2]. Recently, noticeable efforts toward the development of well-defined GDY have been consumed. According to previous surveys, considering the basic physicochemical properties, and achievement of promising applications, GDY could store hydrogen efficiently [1,2]. In this study, we have theoretically investigated the electronic structure and stability of the vanadium decorated GDY by means of spin polarized density functional theory calculations. We probed the best site for V atom onto GDY sheet and then its H_2 adsorption behavior was investigated. Density of states and band structure diagrams were used to help better understanding adsorption phenomena.

II. METHODS

Spin polarized DFT-D3 calculations were performed using $DMol^3$ module in Materials Studio software. The generalized gradient approximation (GGA) of Perdew–Burke–Ernzerhof (PBE) was employed. Grimme's DFT-D3 correction to DFT was used to evaluate dispersion interactions. Single-layer GDY was simulated using a slab model of 2 × 2 supercell [3]. The replicas of GDY layers were separated by a vacuum layer of 20 Å. The Brillouin zone was sampled by using 7 × 7 × 1 Monkhorst–Pack grid for geometry optimization.

III. RESULTS AND DISCUSSION

The primitive cell of GDY contains 18 C atoms, including 6 C atoms in the hexagonal ring with sp^2 hybridization and 12 C atoms in the linear acetylenic chains with sp hybridization. To investigate the binding energy of V adatom on 2 × 2 GDY supercell, we considered three thinkable adsorption sites [4]. These three sites contain: (*i*) the corner of the 12-membered ring and in GDY plane (C), (*ii*) the center of 12-membered ring and in GDY plane (H) and (*iii*) the center of hexagonal ring and above GDY plane (X) (Fig.1). Geometry relaxation showed that the C and X sites are stable adsorption sites, while the H site is not stable because the V adatom on the H site will travel to C site during the optimization [5]. The best site for V decoration is C site with adsorption energy of – 2.544 eV.

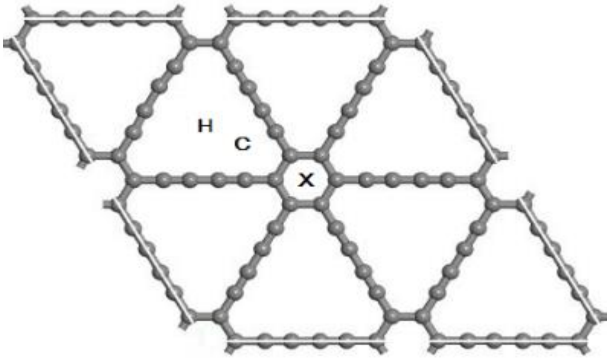

Fig.1: Three considered adsorption sites on GDY plate C, H and X sites.

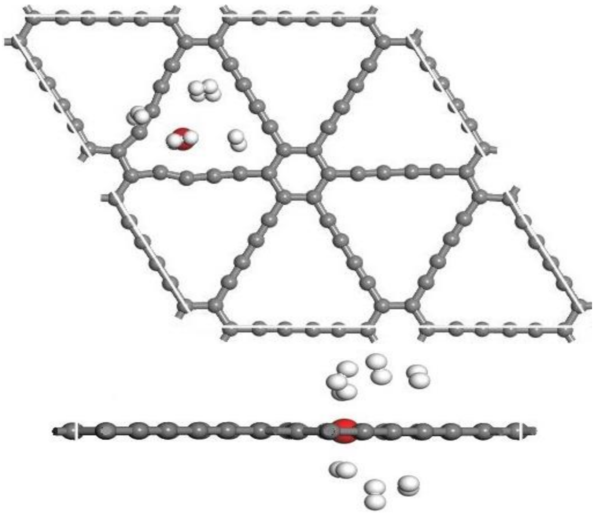

Fig.2: Top and side views for optimized structure of the system contains seven H_2 adsorbed on V-decorated GDY sheet.

Then, we start to put H_2 molecules onto V-decorated GDY, one by one in both sides and optimize the structures. The results show that for the first H_2 molecule, adsorption energy is about –0.840 eV. After that, with increasing the number of H_2 molecules, adsorption energy of the H_2 molecule decreases to –0.326 eV for seventh molecule. The calculated hydrogen adsorption capacity for seven H_2 molecules per a unit cell of V-decorated GDY is about 5 wt.%. Optimized structure of the V-decorated GDY contains seven H_2 molecules is depicted in Fig.2.

Evaluation of the band structure diagrams shows that pristine GDY is a semiconductor with band gap of 0.463 eV. When V atom lies in C positions, it changes band structure of GDY and Fermi level crosses some of the conduction bands and shows semi-metal characters.

IV. CONCLUSION

In summary, for adsorption of V onto GDY, corner of 18-membered ring is the best site. Putting of H_2 molecules on V-decorated GDY shows that with increasing hydrogen molecules, adsorption energy decreases. For seven H_2 molecules per a unit cell of V-decorated GDY, hydrogen adsorption capacity is about 5 wt.%. Introduction of V atom changes the character of GDY from semiconductor to semi-metal.

REFERENCES

[1] X. Gao, H. Liu, D. Wang, and J. Zhang, Chem. Soc. Rev., 48(3), 908-936, **2019**

[2] M. Ebadi, A. Reisi-Vanani, F. Houshmand, P. Amani, Int. J. Hydrogen Energy, 43(52), 23346-23356, **2018**.

[3] X. Li, D. Xing, J. Phys. Chem. C 123(14), 8843-8850, **2019**.

[4] Z. Z. Lin, Carbon, 108, 343-350, **2016**.

[5] X. Chen, P. Gao, L. Guo, Y. Wen, D. Fang, B. Gong, Y. Zhang, S. Zhang, Phys. Lett. A, 381(9), 879-885, **2017** .

Titanium decorated graphdiyne as a hydrogen storage medium

***Soha Shamae*, *Adel Reisi-Vanani*[*]**

Department of Physical Chemistry, Faculty of Chemistry, University of Kashan, Kashan, Iran
Email: *areisi@kashanu.ac.ir*

Abstract: Hydrogen, a reproducible clean energy, has been accepted that could replace fossil fuels. Due to special structural features of graphdiyne (GDY) with *sp*- and *sp*^{2}-hybridized carbon atoms, it is more attractive for future applications. We probed the best site for decoration of GDY by Ti single atom. Next, we put, one by one, H_2 molecule on this modified carbon nano sheet to obtain its hydrogen storage capacity. The results show that Ti-decorated GDY is a good option for hydrogen storage applications.

Keywords: Hydrogen storage, Graphdiyne, Decoration, DFT, Adsorption.

I. INTRODUCTION

Hydrogen, a renewable clean energy source, has been accepted as a suitable alternative for fossil fuels. Designing a safe, compact and efficient storage system is the major challenge in hydrogen application [1]. GDY is consist of self-assembly 18-member ring hexagon unit, which is from the benzene ring and diacetylenic linkages (−C≡C−C≡C−), forming a largely delocalized π-conjugated architecture in comparison with graphene. GDY demonstrates the fascinating physicochemical electronic conductivity and mobility extreme thermal resistance. Due to special structural features of GDY with *sp*- and *sp*^{2}-hybridized carbon atoms, it is more attractive for future applications [2]. In previous works, density functional theory (DFT) calculations were employed to evaluate the molecular adsorption and detection by TM-atom-decorated graphdiyne. It was seen that Ti adatom on GDY have large adsorption energy [3] and adsorption energy is higher than the Ti cohesive energy, so it hinders clustering of Ti on the GDY surface.

II. METHODS

DFT calculations were performed within the spin-polarized density functional method as implemented in the DMol^3 module in Materials Studio software. The generalized gradient approximation (GGA) with the Perdew-Burke-Ernzerh (PBE) of exchange correlation functional was used in combination with the double numerical basis pluspolarization (DNP) basis set [4]. To measure scattering interactions, Grimme's DFT-D3 method was used. To hamper the interlayer interaction between neighboring layers, a vacuum space of 20 Å was applied along the direction perpendicular to the graphdiyne sheet. For coalition of the Brillouin-zone, we used a 7 × 7 × 1 gamma-centered Monkhorste-pack set of k-points.

III. RESULTS AND DISCUSSION

We considered three possible adsorption sites for adsorption of Ti on the GDY surface. These sites are the corner site (**C**), the center site of 18-membered ring (**H**) and center site of the hexagonal rings (**X**) (Fig.1). We put single Ti atom in these three sites and optimized them. Results show that **C** and **X** sites are stable adsorption sites, while the **H** site is not stable, because the Ti adatom on the **H** site travels to **C** site during the optimization. Also, the best distance between Ti and GDY plate is 0 Å that is consistent with other works [3]. Adsorption energy of Ti to GDY is about –5.064 eV. In the next step, we put the first H_2 molecule on the Ti-decorated GDY. For this molecule, adsorption energy is about 0.765 eV. We put one by one H_2 molecule to Ti-decorated GDY and optimized them. The results show that with increasing of H_2 molecule number, adsorption energy per H_2 molecule gently deceases, so that for 18th hydrogen molecule, adsorption energy is about 0.230 eV. Favorable adsorption energy for practical applications is in the range of –0.2 to –0.6 eV. So, can be said that Ti-decorated GDY is a appropriate material for hydrogen storage systems. The calculated hydrogen storage capacity for eighteen H_2 molecules per a unit cell of Ti-decorated GDY is about 12.03 wt.% that is very good on the basis of DOE targets in 2020. Optimized structure of the Ti-decorated GDY contains eighteen H_2 molecules is seen in Fig.2 from two views.

Band structure diagrams show that pristine GDY is semiconductor with band gap of 0.463 eV. Decorating with Ti atom causes that its band structure changes and Fermi level crosses conduction bands, so Ti-GDY shows semi-metalic character.

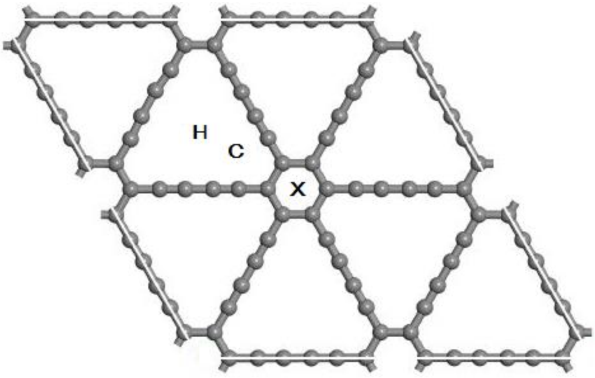

Fig.1 . Three considered adsorption sites on GDY plate (C, H and X).

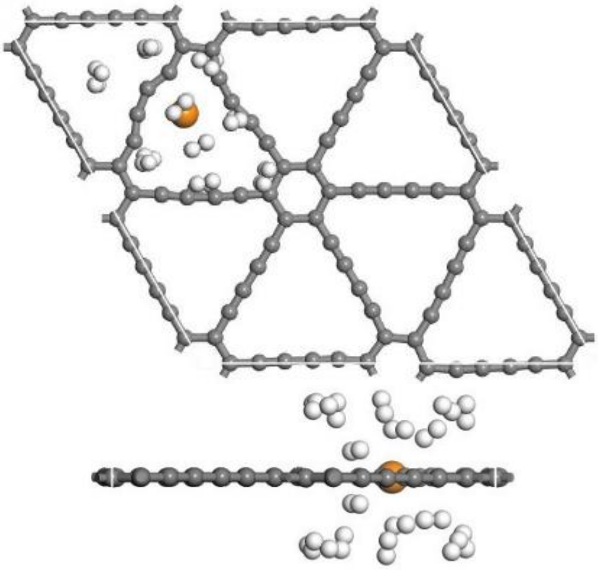

Fig.2. The optimized structure of the eighteen H_2 molecules adsorbed on the GDY plate.

IV. CONCLUSION

Probe of the best site for Ti decoration in GDY nanosheet shows that corner of the 18-membered ring is the best site with the highest adsorption energy. Also, introduction of Ti in GDY causes that its semiconductor character changes to semi-metallic due to change in the band structure of GDY. The calculated hydrogen storage capacity for eighteen H_2 molecules per a unit cell of Ti-decorated GDY is about 12.03 wt.% that shows Ti-GDY based materials are good substrates for hydrogen storage application.

REFERENCES

[1] M. Ebadi, A. Reisi-Vanani, F. Houshmand, and P. Amani, Int. J. Hydrogen Energy, 43(52), 23346-23356, **2018**.

[2] X. Li, D. Xing, J. Phys. Chem. C, 123(14), 8843-8850, **2019**.

[3] X. Chen, P. Gao, L. Guo, Y. Wen, D. Fang, B. Gong, Y. Zhang, and S. Zhang, Physics Letters A, 381(9), 879-885, **2017**.

[4] M. Shams, A. Reisi-Vanani, Int. J. Hydrogen Energy, 44(10), 4907-4918, **2019**.

N and Al doped Graphene as nano catalyst for Hydrogen Production

Milad Ghanbari, Sadegh Afshari S. Ahmad Nabavi Amri*

School of Chemistry, Damghan University, Damghan, Iran

s.afshari@du.ac.ir

Abstract: In this study, we have used the Aluminum and Nitrogen doped graphene as a nano catalyst to produce hydrogen from water. We used Gaussian 09 package by density functional theory (m062x/6-311G) to optimize the structures energetically. The interaction of water with the Al and N atoms of doped graphene have been studied. After adsorption, decomposition of the water has been studied, too.

Keywords*:* graphene, nanocatalysis, decomposition, water

I. INTRODUCTION

With the advent of human societies, people's need for transportation has increased, and fossil fuelconsumption such as gasoline and diesel hasincreased dramatically. The energy crisis has forcedthe developed countries to reviewthe use of fossil fuels and find the best alternativefor them. Increasing prices, pollution and non-renewable fossil fuels have made it a substitute forcheap, clean and renewable fuels. Hydrogen fuel is the most important source of alternative fossil fuels. More than 90% of the world's compounds consist of hydrogen and is the most abundant substance in the world. Hydrogen is the main source of energy in the fuel cells and can have a special place in global energy supplies in the future. There is no contamination in the combustion of hydrogen. Hydrogen fuel is derived from renewable and non-renewable materials. Scientists have studied about hydrogen production from many materials on different catalysts, experimentally and theoretically [1-3]. One of the most applicable method of hydrogen production is production by the water [4, 5]. Most of the catalysts used for H_2O decomposition are based on transition metals. the high costs and toxicity of the transition metal-based catalysts might greatly limit their applications for H_2O decomposition. Nanomaterials has been widely used in the development of catalysts. Many of the important reactions are made by the nanoscale catalyst. Graphene is one of the most important nano catalysts [6]. Scientists have discovered the unique properties of graphene and its derivatives [7]. The chemical and physical properties of the graphene could be adjusted by doping [2, 8]. It is highly desirable to develop inexpensive, active and stable non-toxicity catalysts for the H_2O decomposition. So, in this study, we have used the Aluminum and Nitrogen doped graphene as a nano catalyst to produce hydrogen from water.

II. CALCULATION METHOD

In this work the all of the structures have been optimized energetically by the Gaussian 09 package by density functional theory (m062x/6-311G). For more study about the results, we have used GaussView and GaussSum software. Bond length, bond angle, HOMO&LUMO gape adsorption energy and free Gibbs energy were the most important results that we have studied about the reactions. Also, the electrostatic surface potential (ESP) and partial atomic charge have been studied in this work.

III. RESULT AND DISCUSSION

To study about the adsorption and decomposition of the water on Al and N-doped graphene, first the geometric structures of the Al and N-doped graphene have been optimized. The interaction of H_2O molecule by the several orientations have been studied. There was not any interaction between H_2O and carbon atoms of graphene surface. So, for adjusting the electronic properties of graphene the graphene has been doped by Al and N atom. The interaction of H_2O molecule with the mentioned doped graphene have been studied, too. For this, we closed two H_2O molecule to Al and N atoms. H_2O molecule could be adsorbed on Al atom only from O atom site. There was not any adsorption on the N atom the configuration that one C atom replaced by N atom. We investigate the absorption and decomposition of the H_2O molecule on Al atom. For this, transition state (TS) energy, the free Gibbs energy and adsorption energy of the reaction and production materials have been calculated and reported in table 1. As can be seen from table 1, the adsorption process was spontaneously at room temperature. It is for the negative amount of adsorption energy. The negative amount of free Gibbs energy says the same thing, too.

Table1: Thermodynamic parameters for adsorption and decomposition process

	ΔE (kcal.mol^{-1})	ΔG (kcal.mol^{-1})
Adsorption	-577.822	-75.997
Decomposition	-462.594	-24.974

Also, ESP of the one of the configurations have been shown in figure1, for briefness. As can be seen from figure 1, hydrogen atoms of water have positive potential and the oxygen atom has negative potential. On the other hand, Al atom on the doped graphene has a little positive potential. So, we see an adsorption interaction between O atom of water and Al atom of doped graphene. We have also calculated the mean path way for one of the hydrogen decompositions of water on doped graphene and DOS diagrams and partial atomic charges, but for briefness they have not shown here.

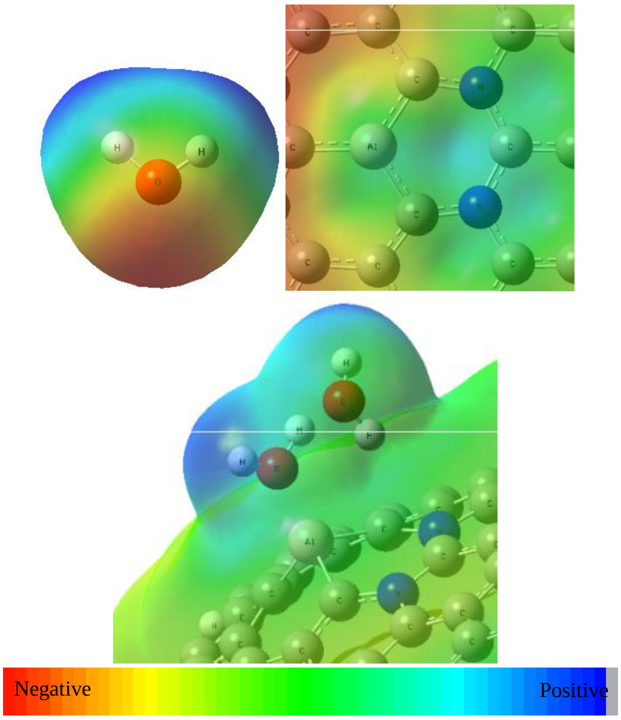

Fig.1: ESP of the H_2O and Al, 2N- doped graphene before and after water adsorption.

IV. CONCLUSION

The water molecule was adsorbed from the oxygen atom on aluminum and there was no adsorption on nitrogen atom. The calculated free Gibbs energy and adsorption energy for adsorption process of water on Al atom have shown that it was the spontaneously process at room temperature. Also, the calculated free Gibss energy for the decomposition of the H_2O on the Al and N-doped graphene have shown this process was spontaneously, too. The second H atom of water have not decomposed on the mentioned graphene sheet.

REFRENCES

[1] Myint, M., Yan, Y., Chen, J.G. Reaction Pathways of Propanal and 1-Propanol on Fe/Ni(111) and Cu/Ni(111) Bimetallic Surfaces. The Journal of Physical Chemistry C. 2014, 118, 11340-9.

[2] Mukherji, A., Seger, B., Lu, G.Q., Wang, L. Nitrogen Doped Sr2Ta2O7 Coupled with Graphene Sheets as Photocatalysts for Increased Photocatalytic Hydrogen Production. ACS Nano. 2011, 5, 3483-92.

[3] Ge, Y., Shah, Z.H., Lin, X.-J., Lu, R., Liao, Z., Zhang, S. Highly Efficient Pt Decorated CoCu Bimetallic Nanoparticles Protected in Silica for Hydrogen Production from Ammonia–Borane. ACS Sustainable Chemistry & Engineering. 2017, 5, 1675-84.

[4] Wang, Z., Yang, X., Yang, T., Zhao, Y., Wang, F., Chen, Y., et al. Dibenzothiophene Dioxide Based Conjugated Microporous Polymers for Visible-Light-Driven Hydrogen Production. ACS Catalysis. 2018, 8, 8590-6.

[5] Wang, L., Ertem, M.Z., Kanega, R., Murata, K., Szalda, D.J., Muckerman, J.T., et al. Additive-Free Ruthenium-Catalyzed Hydrogen Production from Aqueous Formaldehyde with High Efficiency and Selectivity. ACS Catalysis. 2018, 8, 8600-5.

[6] Kataev, E.Y., Itkis, D.M., Fedorov, A.V., Senkovsky, B.V., Usachov, D.Y., Verbitskiy, N.I., et al. Oxygen Reduction by Lithiated Graphene and Graphene-Based Materials. ACS Nano. 2015, 9, 320-6.

[7] Wang, Y., Jaiswal, M., Lin, M., Saha, S., Özyilmaz, B., Loh, K.P. Electronic Properties of Nanodiamond Decorated Graphene. ACS Nano. 2012, 6, 1018-25.

[8] Wang, Y., Shao, Y., Matson, D.W., Li, J., Lin, Y. Nitrogen-Doped Graphene and Its Application in Electrochemical Biosensing. ACS Nano. 2010, 4, 1790-8.

Computational Study of Electric Dipole Moment and HOMO–LUMO Gap Energy of Some Isovalent functionalized (5, 0) Zigzag carbon nanotube

Hossein Mostaanzadeh*
Department of Chemistry, University of Qom, Qom, Iran.,
Email: h.mostaan@qom.ac.ir

Abstract: Functionalization is an important method to change electrical and thermodynamic properties of carbon nanotube. In this study, the effect of isovalent electron functionalization of a single-walled carbon nanotube (SWCNT) was studied with density functional theory. For this case, a (5, 0) zigzag SWCNT model containing 60 C atoms with 10 hydrogen atoms added to the dangling bonds of the perimeter carbons was used. To model functionalized CNT one terminal H atoms were replaced by –F, –OH, -Cl and -SH groups. All the functionalized CNTs have higher dipole moment with respect to the pristine CNT. The Gibbs free energy calculations demonstrate that except SH-CNT the other structures are more stable than pristine CNT. The optimized structure and molecular properties such as the HOMO-LUMO gaps, the dipole moments, and the density of state were calculated. Our results indicate that the HOMO–LUMO gap and electric dipole moment strongly respectively depends on the valence and electronegativity of the functional group on the nanotubes.

Keywords: Electric dipole moment, Deformation, Carbon nanotube, Functionalization, HOMO–LUMO Gap.

I. INTRODUCTION

Carbon nanotubes have significant potential for application in molecular electronics [1, 2], nanomechanics [3], optics [4], and catalysis [5]. Single-wall carbon nanotubes (SWCNT) are frequently referred to as one-dimensional structures because of their nanoscale dimensions and quantum properties. The functionalization of pristine SWCNTs dramatically changes their chemical, electronic and transport properties [6]. Molecular modeling of structure and energetic, in particular at the density functional theory (DFT) level, provides in material sciences a fairly efficient and inexpensive way of support for future laboratory studies.

The present work is a theoretical study of end-substituted zigzag SWCNTs with some isovalent groups. Full-geometry optimizations are performed on the (5, 0) pristine and properties of the resulting isomers have been studied.

II. METHODS

In this study, we used a (5, 0) zigzag carbon nanotube with 60 C atoms as SWCN model. 10 H atoms saturated the dangling bonds of both sides in the pristine CNT. The functionalized models were obtained by replacing one H atom by –F, –OH, -Cl and -SH groups to get five structural isomers as shown in Fig 1. In order to obtain the lowest energy level (true ground state), the ground state geometries of the single-walled carbon nanotubes (SWCNTs) and the functionalized-SWCNTs (f-SWCNTs) were optimized without symmetry restriction on the initial structures.

HO-CNT	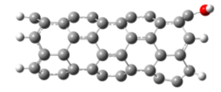	**F-CNT**	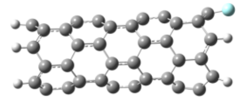
HS-CNT	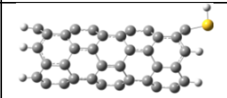	**Cl-CNT**	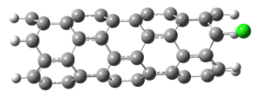

Fig. 1. Model of functionalized (5, 0) zigzag CNTs with 60 C atoms which is used in this study.

All the calculations were performed using density functional theory (DFT). The basis set used is 6-31G(d), as implemented in the Gaussian 03 software package [7]. The vibrational mode descriptions were made on the basis of the calculated nuclear displacements using visual inspection of the animated normal modes using the GaussView03 software [8].

III. RESULTS AND DISCUSSION

3.1. Thermodynamic aspects

All structures, including non-functionalized CNT are fully optimized using B3LYP/6-31G(d) level of theory. Supposing the functionalized CNTs are produced from the following reactions.

$$C_{60}H_{10} + X_2 \rightarrow C_{60}H_9X + HX \quad X= Cl, F$$

$$C_{60}H_{10} + 1/2\ O_2 \rightarrow C_{60}H_9OH$$

$$C_{60}H_{10} + 1/8\ S_8 \rightarrow C_{60}H_9SH$$

The reaction Gibbs free energy in the standard condition (ΔG^0) were obtained from above reactions. The last column of table 1 represents the reaction Gibbs free energies of functionalized CNTs.

Table1. Orbital energies for HOMO, LUMO, HOMO-LUMO gaps (ΔE), dipole moments (μ), Gibbs Free Energies (G°) of CNTs and reaction Gibbs free energies.

Comp.	E_{HOMO} (ev)	E_{LUMO} (ev)	ΔE (ev)	μ (D)	G° (kj/mol)	ΔG° (kj/mol)
C60H9Cl	-3.904	-3.089	0.815	7.523	-7222323	-113
C60H9F	-4.387	-3.095	1.292	7.588	-6276190	-357
C60H9OH	-4.252	-2.940	1.312	4.612	-6213118	-222
C60H9SH	-3.822	-3.065	0.757	5.773	-7061077	4
CNT	-3.761	-2.979	0.782	0.364	-6409957	-

The data in table 1 show that all molecular properties such as frontier orbital energies, gapes between E_{HOMO} and E_{LUMO} (ΔE) and the electrical dipole moments (μ) strongly depend to the kind of substituted group. From the thermodynamic point of view, the lowest value of ΔG (-357.2 $kJmol^{-1}$) for the reaction of CNT with F_2 shows the high percent of production. However, SH-CNT shows the positive value for ΔG (3.6 $kJmol^{-1}$), therefore, it is thermodynamically less stable with the lowest percent of production.

3.2. Geometries, dipole moments and frontier orbital energies

The cross sections of CNTs have elliptical shapes and are not circular. The ellipses major and minor axis of both inlets and the difference between them (δ) which are reported in table 2 reveal the degree of deformation in one of inlets that contain a functional group.

Table 2. Geometrical parameters of CNTs major and minor axis of the cross section of the CNT inlets. X represents the inlet where containing substituent groups. δ is the distance between the minor and the major axis. All data are reported in Å.

Comp.	Min	Max	δ_1	Min	Max	δ_2
	X			-		
C60H9Cl	3.46	4.19	0.73	3.70	3.83	0.13
C60H9F	3.24	4.09	0.85	3.71	3.82	0.11
C60H9OH	3.18	4.14	0.96	3.70	3.83	0.13
C60H9SH	3.55	4.12	0.56	3.66	3.89	0.23
CNT	-	-	-	3.58	3.99	0.41

When hydroxyl group was added, CNT perform highest deformation with respect to the original CNT and other functionalized CNTs. Interestingly in all functionalized CNTs the inlet without substituent has a more circular shape than the pristine CNT.

The shapes of HOMO and LUMO orbitals which are shown in Figure 2 are related to similarity of valence electron of substituted group. This object nicely can be seen in the structures contain -F and –OH or –Cl and -SH groups.

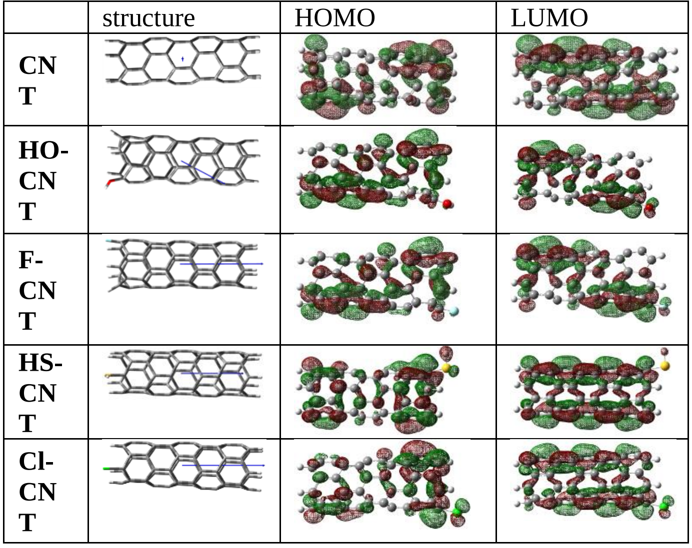

Fig 2. Optimized geometries and the shapes of HOMO and LUMO molecular orbitals. Arrows represent the dipole moments.

The direction and the relative magnitude of the electric dipole moments also are shown in Figure 2. Dipole moments are strongly depending on the electronegativity of functionalized group. From the higher electronegativity of O, F, S and Cl atoms with respect to C atoms, we expect that the magnitude of μ in the structures that F atom is in one side would be higher than other structures. We also are able to predict the direction of the dipole moments vectors from the positions of functionalized groups. In the structure HO-CNT, the direction of the dipole moment vector has the greatest angle with respect to the direction of the nanotube.

3.3. IR spectra of functionalized CNTs

The calculated IR-spectra of all structures including pristine CNT are shown in Figure 3. The strongest vibrational modes reveal that the IR vibrational frequencies depend to the kind of functional group on the CNT. The isovalent electron functionalized CNTs containing HS- & Cl- or HO- & F- groups have similar IR spectra. For instance, the global breathing modes (which appear in fingerprint area) in the pristine CNT, HS-CNT and Cl-CNT do not see in HO-CNT and F-CNT. Moreover, the stretching vibrational frequency of O-H group is about 1000 cm^{-1} greater than vibrational frequency of S-H group.

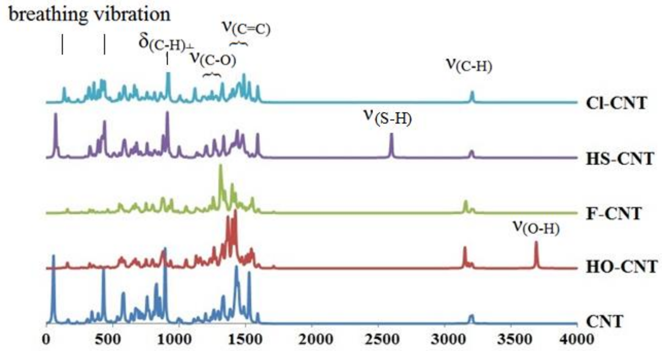

Fig 3. IR spectra of all structures obtained using UB3LYP/6-31G(d) theory level.

CONCLUSION

In this study the structure of different structures of isovalent functionalized (5,0) zigzag CNT have been studied using DFT calculations. For this purpose -OH, -F, -SH and -Cl groups substituted in the end of CNT contain 60 C atoms have been used. One functional group was replaced by the one of terminal hydrogens that were used to saturate dangling bonds. All the four structures of $C_{60}H_9X$ were optimized and analyzed in detail. These calculations show all the molecular properties such as geometry, stability, vibrational frequencies, and electrical properties strongly depend on the kind of functional group. $C_{60}H_9F$ has higher dipole moments and band gap. The IR spectra of isovalent functinalized CNTs are similar.

REFERENCES

[1] N. Ferrer-Anglada, V. Gomis, Z. El-Hachemi, U. D. Weglikovska, M. Kaempgen, and S. Roth, Carbon nanotube based composites for electronic applications: CNT conducting polymers, CNT-Cu, Physica Status Solidi. 203 (2006) 1082–1087.

[2] Z. Chen, J. Appenzeller, Y. M. Lin et al., An integrated logic circuit assembled on a single carbon nanotube, Science. 311 (2006) 1735.

[3] D. A. Britz and A. N. Khlobystov, Noncovalent interactions of molecules with single walled carbon nanotubes, Chemical Society Reviews. 35 (2006) 637–659.

[4] Y. Sakakibara, A. G. Rozhin, H. Kataura, Y. Achiba, and M. Tokumoto, Carbon nanotube-poly(vinylalcohol) nanocomposite film devices: applications for femtosecond fiber laser mode lockers and optical amplifier noise suppressors, Japanese Journal of Applied Physics. 44(2005) 1621– 1625.

[5] P. Serp, M. Corrias, and P. Kalck, Carbon nanotubes and nanofibers in catalysis, Applied Catalysis A. 253(2003) 337–358.

[6] J. Zhao, J. P. Lu, J. Han, and C. K. Yang, Noncovalent functionalization of carbon nanotubes by aromatic organic molecules, Appl. Phys. Lett. 82 (2003) 3746.

[7] M.J. Frisch et al., Gaussian 03, Revision E.01, Gaussian, Inc., Wallingford CT, 2004.

[8] Gaussview 03, Gaussian, Inc., Wallingford, CT, 2003.

Electronic transport of molecular nanowires

M. Roohi[a], ***S.Jalili[b]***, ***A.Pakzadiyan[c]****

[a]Department of Chemistry, Faculty of Chemistry, Islamic Azad University Of Central Tehran Branch, Tehran, Iran;
mahnazroohi90@gmail.com
[b]Department of Chemistry, Faculty of chemistry, K.N. Toosi University of Technology, Tehran, Iran;
Fax: +98 21 22853650; Tel: +98 21 22853649; sjalili@kntu.ac.ir
*[c]*Department of Chemistry, Faculty of chemistry, K.N. Toosi University of Technology, Tehran, Iran;*
a.pakzadiyan@email.kntu.ac.ir

Abstract*:* Methods based on quantum mechanics are used to obtain the characteristic curves belonging to the density of states (DOS) of a molecular nanowire and to bridge two metallic electrodes. The impact of the electronic structure of molecules and the coupling mechanism of the metallic contacts on these curves are presented for conjugated compounds based on sulfur, also known as oligothiophene. The molecular nanowire is attached to a couple of gold clusters that represent the electrodes. The molecular electronic structure in the wire was modeled via the Atomistic Tool Kit- Virtual Nano Laboratory (ATK-VNL). The density functional theory and the extended Hückel methods were employed to extract the Hamiltonian matrix elements corresponding to these molecules. Moreover, the impact of the number of Au contact atoms on the DOS was investigated through the use of two models, namely two-atom contact at each electrode and three-atom contact at each electrode via the hollow sites of the gold (111) plane. Furthermore, the impact of the number of thiophene rings present in the wire on the conductance characteristics was determined.

Keywords*:* Virtual Nano Laboratory, Nanowire, thiophene, extended Hückel theory (EHT), density of states (DOS).

I. INTRODUCTION

Owing to their advantages compared to bulky materials, considerable attention has been recently drawn to semiconductor nanowires. For example, vertical nanowires that are grown on substrates are capable of being essentially dislocation-free because of their large surface-to-volume ratio permitting efficient strain relief. This fact is especially important in the nitrides in which a high density of dislocations can be normally found in thin films. This harms the performance of the device. On the other hand, the high crystalline quality of nitride nanowires can be high, up to microns in length. These superior crystalline properties, found in many nanowire materials, are a sign that nanowires can have superior photonic and electronic characteristics. In fact, numerous experiments conducted on different semiconductor nanowires have revealed potentially useful properties for electronics [1, 2], optoelectronics [3, 4], and sensing [5]. A scanning tunneling microscope (sSTMd) with its tip acting as a counter-electrode was used to study electronic transport via one or a few molecules fixed to an Au surface [3-7]. Oligothiophenes were selected in this work because of their several promising practical applications [8-14]. Oligothiophenes possess fewer than ten thiophene thiol (TT) ring molecules. Numerous innovative optical or electrical tools make use of oligothiophenes [15-17]. They are also utilized in electronic components that are based on thiophenes and in various instruments, such as energy storage tools [17], ICs and transistors [18], photovoltaic cells [19], electroluminescent devices [19], and electrochromic devices [16]. Molecular electronics is where these types of materials are most commonly employed.

In this research, the MES and the density of states (DOS) of the nanowire and the electrodes were computed.

II. METHODS

In order to demonstrate the behavior of the Au reservoirs (leads), an all-atom central cluster was proposed [34–36]. Furthermore, according to the first principle approach, DFT and NEGF were utilized to present the analytical model. The Atomistic Tool Kit- Virtual Nano Laboratory (ATK-VNL) software package version 13.8.0 was used to illustrate and study the semi-empirical model to the 2TT. Furthermore, a simple and basic technique is the Extended Hückel theory (EHT) technique that utilizes as basis functions all the atomic valence orbitals. Making a TT substituted molecule is the most conventional manner of connecting conjugated molecules and an electron drain/source. An S atom has substituted a TT molecule whose end group has a hydrogen atom, and a sulfur-gold (S-Au) binding has been used to attach it to an Au electrode. The main objective of computational modeling of molecular nanowires is to provide an insight into the electronic coupling between the molecule and the metal and the geometry of the metal contacts that influences how the current flows through the wire.

III. RESULTS AND DISCUSSION

In this work, first-principles-based computation of the MES characteristic curves belonging to a molecular nanowire made up of several TT molecules (rings), the schematic of which is displayed in Figure. 3, is proposed. In addition, the transmission function and the density of states (DOS) of the electrodes and the nanowire and the properties of the molecules have been computed. Furthermore, the DOS calculation for 2TT and 3TT molecules acting as bridges between two Au electrodes was performed. Figure 2 shows the graph of the energy levels of the molecule relative to the Fermi levels of the Au contacts. In this figure, the Fermi levels were aligned via the total DOS corresponding to the extended molecule (the molecule in addition to a number of Au atoms). The Fermi energy can be set near to the appropriate number of electrons in the molecule using the electron energy-number graph (Figures 3 and 5). In order to comprehend the effect of the attached atoms on conduction characteristics, these two techniques are studied. Since the narrowest section of the bridge mainly determines the conductance, merely the central cluster details were examined. The molecule was assumed to stand normal to the metal surfaces in each technique.

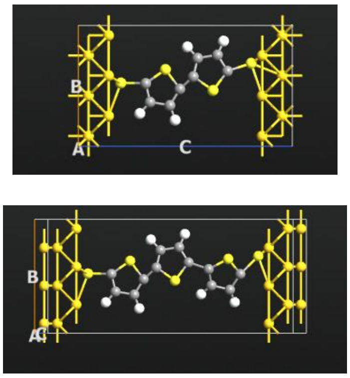

Figure 1. Schematic of a molecular nanobridge, made up of conjugated molecules (2TT) and (3TT) chemisorbed onto Au electrodes using the thiol terminal group. The figure displays the central cluster and the electrodes.

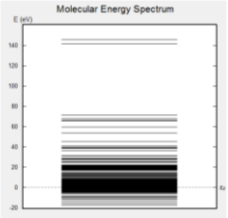

Figure 2. Diagram of the 2TT molecule energy levels and the relative positions of the Au contacts Fermi levels.

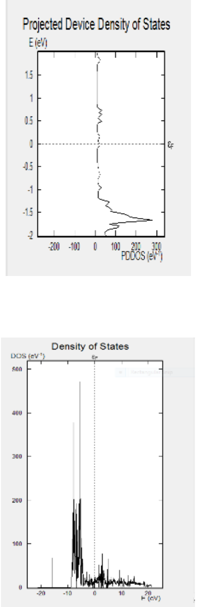

Figure 3. Computed 2TT density of states (DOS) and DDOS function.

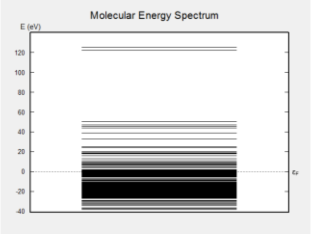

Figure 4. Diagram of the 3TT molecule energy levels and the relative positions of the Au contacts Fermi levels.

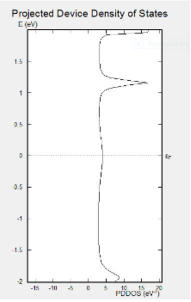

Figure 5. Computed 3TT DDOS function.

IV. CONCLUSION

The Molecular Energy Spectrum and the Density of State for 2TT placed between two gold (111) surfaces were obtained via a combination of the DFT technique and the

NEGF method. During all the procedures, the oligothiophenes were assumed to be attached to the Au (111) surface by a contact made up of a single atom. From an experimental perspective, the transmission through all these systems is similar to their DOS. This similarity is more striking for the 2TT molecule. In case the connection of the 2TT molecule with one of the Au contacts is stronger than that with the other, there should be wider peaks in the DOS diagram and the asymmetric transmission wave functions corresponding to the 2TT and 3TT. However, this trend is not observed in the transmission and DOS diagrams, implying that there is a strong connection between the 2TT molecule and both Au contacts. This strong connectivity to both contacts is studied also for other oligothiophenes. The size of the flat part of the DOS diagrams, which represents the HOMO-LUMO band gap, gradually reduces from the 2TT to the 3TT oligothiophene with an increase in the length of the system. This behavior expected for these systems and leads to improved overlap of the *p* orbitals, resulting in the π orbitals. Therefore, peaks should be narrow, which should be the case since the length of the molecular wire was determined to be a major factor influencing the conductance properties. Further research can be carried out in order to determine the impact on the rings of the electron-withdrawing and electron-donating groups.

REFERENCES

[1] D. Wang et al., J. Am. Chem. Soc. 126, 11 602 (2004).
[2] J. Goldberger et al., Nano Lett. 6, 973 (2006).
[3] X. Duan et al., Nature (London) 409, 66 (2001).
[4] H. Pettersson et al., Nano Lett. 6, 229 (2006).
[5] G. Zheng et al., Nat. Biotechnol. 23, 1294 (2005).
[6] M. Law et al., Annu. Rev. Mater. Res. 34, 83 (2004).
[7] A. A. Talin et al., Phy. Rev. Lett., 101, 076802 (2008).
[8] F. Léonard et al., Phys. Rev. Lett., 102, 106805 (2009).
[9] J.W. Dailey et al., J. Appl. Phys. 96, 7556 (2004).
[10] D. E. Perea et al., J. Solid State Chem. 181, 1642 (2008).
[11] E. Tutuc et al., Appl. Phys. Lett. 89, 263101 (2006).
[12] T. Nishimura et al., App. Phys. Lett., 91, 123123 (2007).
[13] J.E. Allen et al., Nat. Nanotech. 3, 168 (2008).

بیست و دومین کنفرانس شیمی فیزیک انجمن شیمی ایران

22nd Iranian Physical Chemistry Conference

۲۹ الی ۳۱ مرداد ۱۳۹۸

گروه شیمی دانشگاه زنجان

A theoretical investigation on interaction of deposited B_{38} borofullerene on bowl-shaped B_{36} cluster

M. Keyhanian[a], **D. Farmanzadeh**[a]*

Department of Physical Chemistry, Faculty of Chemistry, University of Mazandaran, Babolsar, 47416-95447, Iran

Email: d.farmanzad@umz.ac.ir

Abstract: Density functional theory (DFT) calculations were implemented to investigate the interaction of the bowl-shaped B_{36} cluster with B_{38} borofullerene. The binding energies, charge transfer, the shortest interaction distance and HOMO–LUMO gap energies of B_{36}-B_{38} complex were obtained. In the most stable configuration of the mentioned system, it is observed that borofullerene prefers to interact from its hexagonal hole with the quasi-planar cluster via its concave side of central vacancy. This result is verified by the greater absolute values for binding energy and charge transfer. Furthermore, the sensing ability of optimal B_{36}-B_{38} complex is confirmed due to its high energy gap variation respect to the isolated molecules.

Keywords: Borofullerene, Bowl-shaped, Concave, Density functional theory, Sensing, Vacancy

I. INTRODUCTION

Boron materials, including zero-dimensional (0D) borospherenes, one-dimensional (1D) boron nanotubes (BNTs), two-dimensional (2D) single-atomic layer borophenes, have attracted researchers due to their superior properties [1-3]. These materials have many different applications due to their dimensional [4, 5]. It seems utilizing advantage of each member with its particular characteristic, their hybrid materials such as borophenes-borospherenes, BNTs-borospherenes and borophenes-BNTs can generate some exciting mechanical, electronic and optical properties in comparison with the isolated materials.

Recently, a quasi-planar boron structure with a central hexagonal hole has been synthesized [6]. This structure with 36 boron atoms and C_{6V} symmetry has slightly bowl-shaped and highly stability. Some theoretical studies have investigated B_{36} applications. One of them is related to remarkable adsorption of Fluorouracil, a chemotherapy drug, at the edge of B_{36} cluster [7]. Closely following the discovery of bowl-shaped B_{36}, B_{38} as a stable all-boron fullerene was proposed through first-principles swarm structure searching calculations [8]. The B_{38} borofullerene are composed of four hexagonal holes. In this work, we want to answer the question to whether B_{36} cluster and B_{38} borofullerene can create a stable hybrid system. For this aim, we perform DFT calculations in order to obtain the most stable structure of B_{36}-B_{38} system and the strength of interaction between the considered molecules.

II. METHODS

DMol^3 package in Materials Studio software was employed to investigation the geometrical structures, energetic analyses and electronic properties of the quasi-planar B_{36} cluster, B_{38} borofullerene and B_{36}-B_{38} system [9]. In all calculations, the electronic exchange-correlation effects were considered using generalized gradient approximation (GGA) with the Perdew–Burke–Ernzerhof (PBE) functional [10]. Grimme's method was also utilized for description of the noncovalent interactions [11].

In order to evaluation the stability of the system, the binding energy (E_{bind}) are calculated by:

$$E_{bind} = E_{tot} - E_{cluster} - E_{cage} \qquad (1)$$

where E_{tot}, $E_{cluster}$ and E_{cage} denotes the total energy of B_{36}-B_{38} complex, the isolated B_{36} cluster, and B_{38} cage, respectively.

III. RESULTS AND DISCUSSION

At the first step, the structures of B_{36} cluster and B_{38} borofullerene were optimized. After geometrical optimization, it is observed that the bond lengths of B-B in the corresponding boron nanostructures were in agreement with previous studies. All active sites of B_{38} borofullerene for interaction with B_{36} cluster were investigated at the next step. Fig. 1 presents the most stable configurations of B_{36}-B_{38} system, which have been determined by the binding energy values. The HOMO and LUMO distributions for these complexes are also shown in this figure.

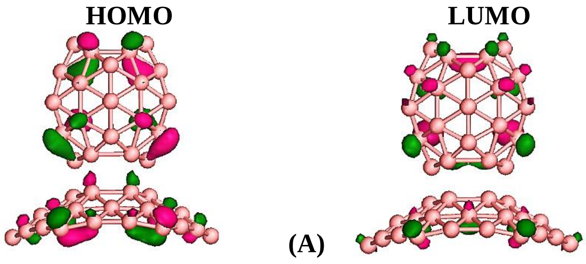

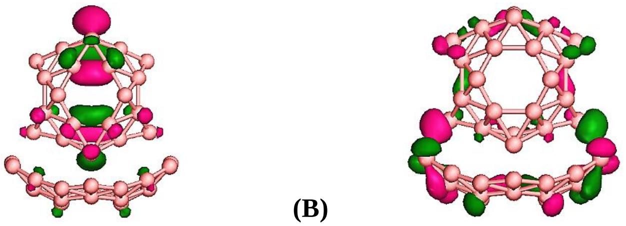

(B)

Fig. 1 The optimized configurations as well as HOMO and LUMO distributions of A) B_{36}-B_{38} system at the convex side of B_{36} B) B_{36}-B_{38} system at the concave side of B_{36}.

According to Fig. 1, in both (A) and (B) complexes, the convex and concave sides of the hexagonal hole of B36 cluster are clearly preferred for interaction with B38 borofullerene. Furthermore, as it is visualized in this figure, the LUMO orbital of B36-B38 system at the concave side of B36 has been expanded at the interaction region. Therefore, it can be expected that the mentioned system shows stronger interaction. The binding energy (Ebind), the Hirshfeld charge transfer from B38 borofullerene to B36 cluster (Qcluster), the interaction distance (R), and HOMO–LUMO gap (Eg) energies for the corresponding systems are reported in Table 1. The binding energy values from this Table reveal that B36 cluster strongly interacts with B38 borofullerene. Moreover, the stronger interaction between B38 and the concave side of B36 is emphasized by the higher absolute values of binding energy and charge transfer in B system. To clarify the effect of interaction between B36 and B38 on the electron conduction, the energy gaps of these nanostructures before and after interaction were evaluated. The energy gap values, which are defined as the subtraction of the lowest unoccupied molecular orbital (LUMO) energy from the highest occupied molecular orbital (HOMO) energy, are obtained 0.39 and 0.31 eV for A and B complexes. These results show that after interaction between B36 cluster and B38 borofullerene, the electronic conductivity significantly increases due to decrease of Eg.

Table1. The obtained binding energy (E_{bind}), charge transfer (Q), the shortest interaction distance (R) and energy gap (E_g) values for the considered systems.

System	E_{bind} (kJ mol^{-1})	$Q_{cluster}$ (e)	R (Å)	E_g (eV)
B_{36}	-	-	-	0.91
B_{38}	-	-	-	0.98
A	-289.90	-0.07	1.71	0.39
B	-306.59	-0.32	1.76	0.31

IV. CONCLUSION

In this work, we have performed DFT calculations to investigate the interaction between B_{36} cluster and B_{38} borofullerene for the formation of B_{36}-B_{38} composite. The electronic sensitivity of these molecules was also predicted before and after interaction. It is found that B_{38} borofullerene considerably tends to interact via its hexagonal hole with the concave sides of the hexagonal vacancy of B_{36} cluster. Investigation of the energy gap variation in the corresponding systems revealed that this hybrid materials has sensitivity ability for drug delivery applications.

REFERENCES

[1] H. J. Zhai, Y. F. Zhao, W. L. Li, Q. Chen, H. Bai, H. S. Hu, Z. A. Piazza, W. J. Tian, H. G. Lu, Y. B. Wu, and Y. W. Mu, Observation of an all-boron fullerene, Nature chemistry, vol. 6, p.727, **2014**.

[2] D. Ciuparu, R. F. Klie, Y. Zhu, and L. Pfefferle, The Journal of Physical Chemistry B, vol. 108, pp. 3967-3969, **2004**.

[3] A. J. Mannix, X. F. Zhou, B. Kiraly, J. D. Wood, D. Alducin, B. D. Myers, X. Liu, B. L. Fisher, U. Santiago, J. R. Guest, and M. J. Yacaman, Science, vol. 350, pp. 1513-1516, **2015**.

[4] S. Pan, M. Ghara, S. Kar, X. Zarate, G. Merino, and P. K. Chattaraj, Physical Chemistry Chemical Physics, vol. 20, pp. 1953-1963, **2018**.

[5] A. J. Mannix, Z. Zhang, N. P. Guisinger, B. I. Yakobson, and M. C. Hersam, Nature nanotechnology, vol. 13, p. 444, **2018**.

[6] Z. A. Piazza, H. S. Hu, W. L. Li, Y. F. Zhao, J. Li, and L. S. Wang, Nature communications, vol. 5, p. 3113, **2014**.

[7] E. Shakerzadeh, Journal of Molecular Liquids, vol. 240, pp. 682-693, **2017**.

[8] J. Lv, Y. Wang, L. Zhu, and Y. Ma, Nanoscale, vol. 6, pp. 11692-11696 2014.

[9] B Delley, Theoretical and computational chemistry, vol. 2 pp. 221–254, **1995**.

[10] J. P. Perdew, K. Burke, and M. Ernzerhof, Physical review letters, vol. 77, p. 3865, **1996**.

[11] S. Grimme, Journal of computational chemistry, vol. 27, pp. 1787–1799, **2006**.

The adsorption behaviors of phenol on the surfaces of pristine and M-encapsulated B_{38} borofullerene

M. Keyhanian[a]***, D. Farmanzadeh***[a]*****

Department of Physical Chemistry, Faculty of Chemistry, University of Mazandaran, Babolsar, 47416-95447, Iran
Email: d.farmanzad@umz.ac.ir

Abstract: Density functional theory (DFT) calculations using PBE functional have been carried out to investigate the adsorption behaviors of phenol on the surfaces of pristine and M-encapsulated (M= Co and Ni) B_{38} borofullerene. According to the obtained results, phenol molecule can be adsorbed on pristine B_{38} with the adsorption energy -48.96 kJ mol^{-1}. On the other hand, encapsulation of Co and Ni considerably increases the absolute adsorption energy values. Further investigations show that dissociation of hydrogen atom bonded to oxygen atom in OH group of phenol molecule can be the main reason of significant adsorption energy in encapsulated cages.

Keywords: Adsorption, Borofullerene, Density functional theory, Dissociation, Encapsulation.

I. INTRODUCTION

The first borofullerene was synthesized seven years after the theoretical proposition of the stability of B_{80} boron-based fullerene structure [1, 2]. Whereas, subsequent studies on B_{80} indicate that its core-shell type counterparts are thermodynamically much more stable than the proposed cage-like structure [3, 4]. To date, experimental and theoretical effort were used to discover new borofullerenes [5, 6]. One of them is the theoretical prediction of B_{38} cage, which is highly symmetric [7]. This fullerene analogue was proposed through first-principles swarm structure searching calculations. The cage-like structure consists of 56 triangles and four hexagonal holes.

One of the common contaminants in wastewaters are phenolic compounds which can be cause high priority concerns. This hazardous organic molecule can be generated from pharmaceuticals, petroleum and petrochemical, paint, and plastic industries [8]. Because of carcinogenicity effects, strict regulations have been enforced to reduce phenol concentration in wastewater [9]. Adsorption process is one of several methods used for the effective treatment of wastewaters containing phenol before their discharge into environment [10].

The purpose of this work is to investigate the adsorption of phenol on the surface of B_{38} cage. Then, in order to the improvement of adsorption, one of Co or Ni atoms is encapsulated into B_{38} borofullerene. The adsorption behaviors of phenol are clarified on the mentioned metalloborofullerenes.

II. METHODS

All DFT calculations were performed with the use of DMol^3 package in Accelrys Material Studio software [11]. For description of the electron exchange-correlation effects, the generalized gradient approximation (GGA) with the Perdew–Burke–Ernzerhof (PBE) functional correction has been utilized [12]. Dispersion corrections were considered by Grimme's method [13]. Furthermore, vibrational frequencies are calculated to verify the nature of local minima of the species The adsorption energy (E_{ad}) of phenol molecule on the surface of cages is obtained by the subtraction of the total energy of adsorbent-adsorbate system from sum of its isolated parts.

III. RESULTS AND DISCUSSION

Firstly, all the studied structures were optimized using the double numerical plus polarization function (DNP) basis set. In the case of encapsulated cages, the considered metals (Co, Ni) were incorporated into B_{38} borofullerene. After optimization, among all the configurations, the structure with positive frequencies and the lowest total energy value was introduced as the most stable structure. The optimized structures of individual molecules have been depicted in Fig. 1.

After obtaining the geometric structures, we investigate the adsorption of phenol on the surface of mentioned cages. Several initial orientations of phenol molecules on various active sites of cages have been considered. The structures with the lowest adsorption energy are selected as the most stable systems. Fig. 2 presents the most favorable adsorption configurations.

Table 1 reports the adsorption energy (E_{ad}), HOMO-LUMO energy gap (E_g) and Mayer bond orders (BO) of the corresponding systems. These values are related to the most stable structures. According to this Table, the obtained adsorption energy values are -48.96, -263.43 and -229.13 kJ mol^{-1} for B_{38}-phenol, Co@B_{38}-phenol and Ni@B_{38}-phenol systems, respectively, which refer to appreciable adsorption of phenol on the encapsulated cages. Moreover, compared to

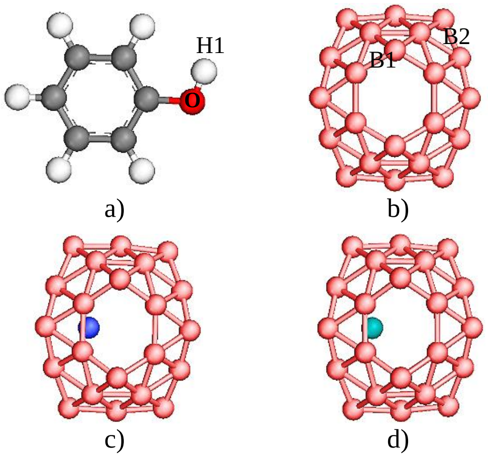

Fig. 1 The optimized structures of a) phenol b) B_{38} c) Co@B_{38}, and d) Ni@B_{38}.

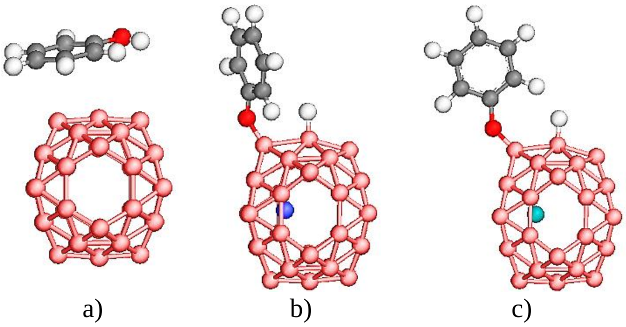

Fig. 2 The most stable optimized structures of a) B_{38}-phenol Co@B_{38}-phenol, and d) Ni@B_{38}-phenol systems.

Table1. The obtained binding energy (E_{bind}), charge transfer (Q), the shortest interaction distance (R) and energy gap (E_g) values for the considered systems.

System	E_{ad}	E_g	$BO_{O\text{-}H1}$	$BO_{O\text{-}B1}$	$BO_{B2\text{-}H1}$
Phenol	-	4.33	0.94	-	-
B_{38}	-	0.98	-	-	-
B_{38}-phenol	-48.96	0.92	0.92	-	-
Co@B_{38}	-	0.45	-	-	-
Co@B_{38}-phenol	-263.43	0.36	-	1.10	0.92
Ni@B_{38}	-	0.66	-	-	-
Ni@B_{38}-phenol	-229.13	0.41	-	1.08	0.90

B_{38} cage, it is obvious that HOMO-LUMO energy gap (E_g) of M@B_{38}-phenol (M= Co, Ni) systems has been considerably decreased relative to free cages. This result show that encapsulation process with Co and Ni atoms leads to increase their electronic conductance toward phenol molecule. Further information about the nature of adsorption in the corresponding systems, have been obtained by Mayer bond order values. From Fig. 2 and Table 1, it is clearly revealed that after encapsulation of B_{38}, one phenol molecule can dissociate to $–OC_6H_5$ and –H fragments. Therefore, Co@B_{38} and Ni@B_{38} can be the catalysts for –OH cleavage in phenol.

II. CONCLUSION

In this letter, DFT calculations have been performed in order to study the adsorption of phenol on the pristine and M-encapsulated (M= Co and Ni) B_{38} borofullerene. The results show that the adsorption energy of B_{38}-phenol is -48.96 kJ mol^{-1}, while it is -263.43 and -229.13 kJ mol^{-1} for Co@B_{38}-phenol and Ni@B_{38}-phenol systems, respectively. It was found that the main reason for substantial adsorption on encapsulated cages is related to the dissociative adsorption of phenol molecule onto these surfaces. Therefore, the present observation can provide new insight in the design of effective catalysts.

REFERENCES

[1] N. G. Szwacki, A. Sadrzadeh, and B. I. Yakobson, Physical review letters, vol. 98, p. 166804, **2007**.

[2] H. J. Zhai, Y. F. Zhao, W. L. Li, Q. Chen, H. Bai, H. S. Hu, Z. A. Piazza, W. J. Tian, H. G. Lu, Y. B. Wu, and Y. W. Mu, Nature chemistry, vol. 6, p.727, **2014**.

[3] H. Li, N. Shao, B. Shang, L. F. Yuan, J. Yang, and X. C. Zeng, Chemical Communications, vol. 46, pp. 3878–3880, **2010**.

[4] J. Zhao, L. Wang, F. Li, and Z. Chen, The Journal of Physical Chemistry A, vol. 114, pp. 9969-9972 **2010**.

[5] Y. J. Wang, Y. F. Zhao, W. L. Li, T. Jian, Q. Chen, X. R.You, ... and J. Li, The Journal of chemical physics, vol. 144, p. 064307, **2016**.

[6] H. Liu, Q. Chen, H. R. Li, X. Y. Zhao, X. X. Tian, Y. W. Mu, … and S. D. Li, Physical Chemistry Chemical Physics, vol. 20, pp. 15344-15349 **2018**.

[7] J. Lv, Y. Wang, L. Zhu, and Y. Ma, Nanoscale, vol. 6, pp. 11692-11696, **2014**.

[8] F. A. Banat, B. Al-Bashir, S. Al-Asheh, and O. Hayajneh, Environmentasl pollution, vol. 107, pp. 391-398, **2000**.

[9] P. Hadi, K. Y. Yeung, J. Barford, K. J. An, and G. McKay, Chemical Engineering Journal, vol. 269, pp. 20-26, **2015**.

[10] Y. Pan, Z. Li, Z. Zhang, X. S. Tong, H. Li, C. Z. Jia, ... and D. Y. Ma, Adsorptive removal of phenol from aqueous solution with zeolitic imidazolate framework-

67. Journal of environmental management, vol. 169, pp. 167-173 **2016**.

[11] B Delley, Theoretical and computational chemistry, vol. 2 pp. 221–254, **1995**.

[12] J. P. Perdew, K. Burke, and M. Ernzerhof, Physical review letters, vol. 77, p. 3865, **1996**.

[13] S. Grimme, Journal of computational chemistry, vol. 27, pp. 1787–1799, **2006**.

Endohedral and Exohedral adsorption of helium on $X_{12}N_{12}$ (X = B, Al) nano-cluster: A DFT study

Sanaz Kaveian[a]**, *Morteza Moradi***[a]*****
[a]*Materials and Energy Research Center, Department of Semiconductors, P.O. Box 31787-316, Karaj, Iran*
Email: m.moradialborzi@merc.ac.ir

Abstract*:* The behavior of noble gas (such as helium) adsorption inside and outside the $B_{12}N_{12}$ and $Al_{12}N_{12}$ was investigated within density functional theory calculations. In the case of inside encapsulation, both clusters have endothermic reactivity with helium which shows from standpoint of stability, helium encapsulation in these cages is not favorable. But, for exohedral functionalization of clusters with He, $B_{12}N_{12}$ was good candidate. The most stable adsorption site found to be atop the boron atom of the cluster surface with adsorption energy of -1.29 eV. We predict that in outside of cluster each boron atom in a $B_{12}N_{12}$ can adsorb one He molecules.

Keywords: DFT, Nano-cluster, Adsortion, Noble gas, Band gap

I. INTRODUCTION

Noble gases are an important class of industrial chemicals essential to numerous applications, including lighting, insulation, cryogenic refrigerants, carrier gases, anesthetics, and excimer lasers. Most high-purity, industrial quantities of noble gases are obtained by separating the gas of interest from air. However, due to their filled valence shell, noble gases exhibit low chemical reactivity [1-4]. Currently, most noble gases are obtained via cryogenic distillation -an extremely energy intensive and therefore costly process. Consequently, large scale isolation of noble gases via selective adsorption near room temperature is highly desirable [5-7].

One of the promising approaches for low-cost noble gas separation is physisorption onto microporous materials, such as activated carbons (ACs), zeolites and metal organic frameworks (MOFs); however, achieving distinguishable equilibrium adsorption abilities among the noble gases for separation is still challenging. Recently, fullerene-based materials with have shown excellent performance on He separation due to strong interactions between the He molecule and inside of cage. In the current work, the interaction of He with $B_{12}N_{12}$ and $Al_{12}N_{12}$ will theoretically be investigated based on analyses of structure, energies, electronic properties, stability, etc [8, 9].

II. METHODS

Geometry optimizations, energy calculations, and density of states (DOS) analysis were performed on the $X_{12}N_{12}$ and different He/$X_{12}N_{12}$ complexes using B3LYP functional with 6–31G (d) basis set as implemented in GAMESS suite of program]. We define adsorption energy in the usual way as:

$E_{ad} = E\,(He/X_{12}N_{12}) - E\,(X_{12}N_{12}) - E\,(He)$

where E (He/$X_{12}N_{12}$) corresponds to the energy of the $X_{12}N_{12}$ in which the single or multiple He has been adsorbed on the cluster, E ($X_{12}N_{12}$) is the energy of the isolated cluster and E (He) is the energy of a single He molecule. The negative value of E_{ad} indicates the exothermic character of the adsorption process.

III. RESULTS AND DISCUSSION

A. *Endohedral adsorption of He in $B_{12}N_{12}$ and $Al_{12}N_{12}$*

Optimized structure of $X_{12}N_{12}$ is built from six squares and eight hexagons (Fig. 1a). Structurally, there are two individual X–N bond types among the 36 X–N bonds in the $X_{12}N_{12}$; one is shared by two six-membered rings (*B66*), and another by a four- and a six-membered ring (B_{64}). In order to find minimum energy for encapsulated configurations of He@$X_{12}N_{12}$, the computational procedures start from different initial positions for He atom inside the cluster including on the center of cluster, on the top of a hexagon or a tetragon. Full geometry optimization has been performed without any symmetry constraint. The most stable structure of He@$X_{12}N_{12}$ has the He atom situated on the center of cage (Fig. 1). Although, helium adsorption inside of both studied clusters are endothermic with positive E_{ad}, but $Al_{12}N_{12}$ due to bigger cage is twice more stable for He encapsulation.

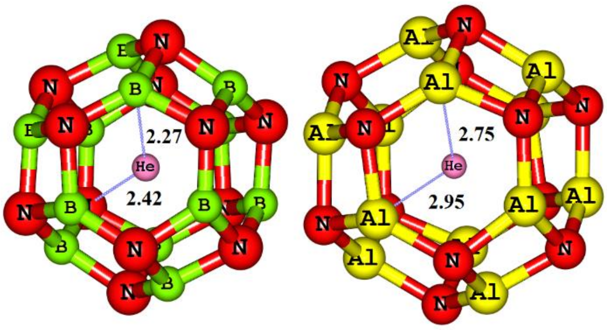

Fig.1: Optimized configuration of He@$X_{12}N_{12}$.

B. Exohedral adsorption of He on $B_{12}N_{12}$ and $Al_{12}N_{12}$

Subsequently, we investigated the adsorption of He in the outside of both clusters. In order to find minimum adsorption configurations of He/$X_{12}N_{12}$, the He atom was initially placed at different positions above cage. Interestedly, after geometrical full optimization without any constraints, we found that two cage show different adsorption behavior. In the case of AlN cluster only a weak physisorption of He top of six membered rings has been occurred in which the length of gas and substrate is more than 3 angstrom. helium atom strongly adsorp atop of boron atom with distance of 2.03 Å, and a high E_{ad} of -1.29 eV. A local structural deformation at the adsorption site of cluster can be observed upon the NH_3 molecule adsorption. The bond length of B_{66} and B_{64} of cluster is increased from 1.79 and 1.85 Å in the pristine $Al_{12}N_{12}$ to 1.82 and 1.89 Å in the adsorbed form (Fig. 2a), respectively.

Why is the reaction of He with $B_{12}N_{12}$ more favorable than that of the $Al_{12}N_{12}$ one? To answer this question we have investigated FMO analysis of both clusters. As shown in Fig. 2, the FMO analysis indicates that, in both cluster, the LUMO located in X atoms (B and Al). This site which can accept electrons is referred to as ‘‘Lewis acid sites” (and conversely, N atom of molecule is termed as ‘‘Lewis base”). Therefore, He gas can donate an electron pair to both of B and Al atoms. It seems that the different adsorption behavior of clusters toward helium is not related to HOMO/LUMO energies and another factor affected to reactivity.

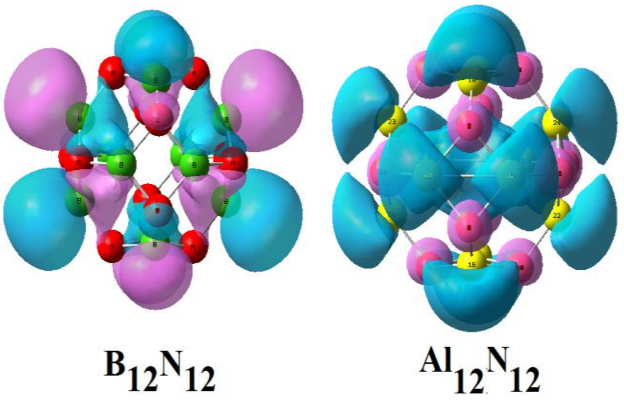

Fig.2: LUMO orbital of $X_{12}N_{12}$.

This observation may be explained based on the Pearson’s hard-soft acid-base theory (HSAB), states that the soft acids react strongly with the soft bases and in contrary, the hard acids react strongly with the hard bases, when all other factors being equal. As a result, mercury (a soft acid) prefers to bind with sulfur (a soft base) through covalent attachment, and can be immobilized strongly in the adsorbent. In this work, He atom with very small atomic radius is hard base which can strongly react with hard acid. Here, boron atom with smaller atomic radius is a harder acid than Al one. Furthermore, for investigating the change of electronic structures in cluster caused by the adsorption of He atom, the net charge transfer (Q_T) from the atom to the cluster is calculated by NBO analysis. Q = 0.082 e in the He/$B_{12}N_{12}$ complex is larger than that Q = 0.015 e in the He/$Al_{12}N_{12}$ complex.

The nature of the cluster’s DOS (density of state) near the Fermi level is critical to the understanding of electrical transport through this material. Calculated DOS plot of pristine $B_{12}N_{12}$ and exohedral complex (Fig. 3) shows that the endohedral adsorption has no sensible effect on the electronic properties of the cluster so that the E_g of the He@$B_{12}N_{12}$ has a slight reduction from 6.03 to 5.91 eV.

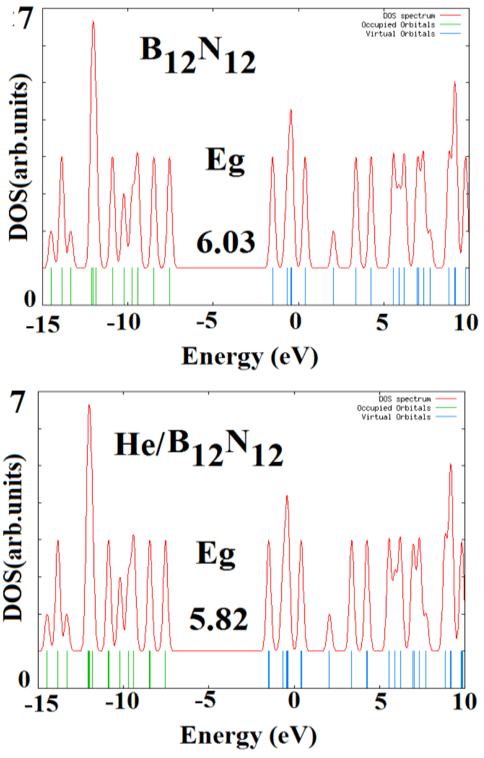

Fig.3: DOS plots of $B_{12}N_{12}$ before and after adsorption of He.

IV. CONCLUSION

The adsorption of He atom inside and outside of $X_{12}N_{12}$ (X = B, Al) is investigated by using DFT calculations. It is found that He atom is only weakly adsorbed on the $Al_{12}N_{12}$ with less negative adsorption energy and large separation. In contrast, the helium shows strong interactions with the $B_{12}N_{12}$ due to hard-soft acid-base theory.

REFERENCES

[1] Belbruno, J. J. (1999). The structure of Al_nN_n (n=2–4) clusters: a DFT study. *Chem. Phys. Lett*. Vol. 313, pp. 795-804.

[2] Guo L., Wu, H. & Jin, Z. (2005). Magic behavior and bonding nature in hydrogenated aluminum nitride clusters. *Appl. Surf. Sci*. Vol. 242, pp. 88-96.

[3] Guo, L., Wu, H. & Jin, Z. (2004). First principles study of the structure, electronic state and stability of $Al_nN_m^-$ anions. *THEOCHEM,* Vol. 677, pp. 105-111.

[4] Collins, P. G., Bradley, K., Ishigami, M.. & Zettl, A. (2000). Extreme Oxygen Sensitivity of Electronic Properties of Carbon Nanotubes. *Science,* Vol. 287, pp. 1801-1804.

[5] Peng, S. & Cho, K. (2003). Ab Initio Study of Doped Carbon Nanotube Sensors. *Nano Lett*. Vol. 3, pp. 513-517.

[6] Beheshtian, J., Bagheri, Z., Kamfiroozi, M. & Ahmadi, A. (2012). A comparative study on the B12N12, Al12N12, B12P12 and Al12P12 fullerene-like cages. J. Mol. Model, Vol. 18, pp. 2653-2658.

[7] Belbruno, J. J. (1999). The structure of AlnNn (n=2–4) clusters: a DFT study. Chem. Phys. Lett. Vol. 313, pp. 795-804.

[8] Guo L., Wu, H. & Jin, Z. (2005). Magic behavior and bonding nature in hydrogenated aluminum nitride clusters. Appl. Surf. Sci. Vol. 242, pp. 88-96.

Theoretical Study On Solubility Of Vitamin C-adsorbed Carbon Nanotube And Graphene In Some Organic Solvents

Sanaz Kaveian[a]***, Morteza Moradi***[a]*******
Materials and Energy Research Center, Department of Semiconductors, P.O. Box 31787-316, Karaj, Iran
Email: m.moradialborzi@merc.ac.ir

Abstract*:* Vitamin C (ascorbic acid, AsA) with the chemical formula $C_6H_8O_6$, whose L-enantiomer is popularly known as vitamin C, it is an organic acid with antioxidant properties. In this work, solubility of the AsA/CNT and AsA/graphene were studied in different solvents such as acetone, acetonitrile, methanol, benzene and toluene with corresponding dielectric constants of 20.493, 35.688, 32.613, 2.270 and 2.374 respectively. Polar solvents have high dielectric constants and maybe are good solvents for dissolution of AsA-functionalized CNT and graphene.

Keywords: DFT, CNT, Graphene, Vitamin C

I. INTRODUCTION

The discovery of carbon nanotubes (CNTs) and graphene has attracted considerable attention because they have a wide range of applications in electronic devices such as gas sensors, field emission displays, and metal-free catalysts . Following the CNT and graphene discovery, it was soon acknowledged that its poor solubility in polar solvents (which has implications in the formation of aggregates in aqueous solutions) is detrimental for biological applications. Functionalized CNT and graphene are typically easy to disperse in organic solvents and water. Therefore, functionalization procedure can improve the dispersion and homogeneity of these compounds in the desired solvents. Numerous methods for chemical functionalization of CNT and graphene, have already been reported [1-3].

The functionalization of nanostructures is achieved through covalent bonding or physical interaction of foreign species. It has been demonstrated that the covalent bonding of amino acids, hydroxyl and carboxyl groups, and so forth through the replacement of C-C bonds improves the CNT and graphene ability to interact with the biological environment. An alternative nondestructive method for solubilization is based on noncovalent binding, as observed for CNT and graphene solubilization in organic compounds for which the weaker binding ability is described in terms of van der Waals interactions [4-6].

II. METHODS

We have selected a zigzag (8, 0) CNT (consisting 128 carbon atoms) and a graphene sheet (consisting 132 carbon atoms) in which open ends have been saturated with hydrogen atoms in order to avoid boundary effects. The full geometry optimizations and property calculations on the CNT and graphene in the presence and absence of an AsA molecule were performed using three parameter hybrid generalized gradient approximation with the B3LYP functional and the 6-31G basis set including the d-polarization function (denoted as 6-31G (d)) as implemented in the GAMESS suite of program [7]. We have defined the adsorption energy (E_{ad}) as follows:

$$E_{ad} = E\ (AsA/adsorbate) - E\ (adsorbate) - E\ (AsA) \qquad (1)$$

where E (AsA/adsorbate) is the total energy of the adsorbed AsA molecule on the tube or graphene surface, and E(adsorbate) and E(AsA) are the total energies of the pristine CNT or graphene, and AsA molecule, respectively. Solvation effects were included through the use of the polarized continuum model (PCM).

III. RESULTS AND DISCUSSION

In order to obtain the most stable configuration of single AsA adsorbed on the CNT, various possible initial adsorption geometries including single (hydrogen, oxygen or carbon) and double (C-O, C-H, O-H) bonded atoms to C atoms on different adsorption sites are considered. However, only one stable structure was obtained upon the relaxation process. More detailed information from the simulation of the AsA/CNT system, including values of E_{ad}, electronic properties and the charge transfer (QT) for this configuration is listed in Table 1. This configuration indicated that a net charge of about 0.031 electrons transfers from tube to the molecule and its corresponding calculated E_{ad} value (Table 1) is about -15.85 kcal/mol. The low E_{ad} of AsA on CNT and transferred charge between them reveal the non-covalent nature of the interaction.

Table 1. Calculated adsorption energy (E_{ad}, kcal/mol), the HOMO, LUMO and gap (E_g) in between energies (eV) for the pristine and functionalized-CNT and graphene in vacuum medium.

System	E_{ad}	Q_T	E_{HOMO}	E_{LUMO}	E_g
CNT	-	-	-3.647	-3.467	0.180
Vitamin C/CNT	-15.85	-0.031	-3.781	-3.606	0.175
Graphene	-	-	-3.697	-3.551	0.146
Vitamin C/graphene	-14.25	-0.067	-3.706	-3.560	0.146

Further, we have studied the interaction of graphene with an AsA molecule. To find stable AsA-adsorbed configurations, several distinct starting structures were used for optimization including H, C or O atoms located on top of the sheet. Interestingly, after full relaxation with no constraints, all of the initial configurations moved to one stable configuration with an exothermic adsorption energy of -14.25 kcal/mol which is almost close to E_{ad} of vitamin C-CNT complex. The two hydrogen atoms bound to the O19 and O8 atoms have the smallest distances to the tube, 2.15 and 2.66 Å respectively. The adsorption of vitamin C on the graphene from O7 and O8 can be rationalized by NBO and molecular electrostatic potential (MEP) analysis. Based on the NBO population analysis, the point charge of O7 and O8 in the free AsA is -0.453 and -0.643 e, which is in agreement with our calculated MEP. As shown by the mapped-MEP of AsA in Fig. 1, O7 and O8 atoms are negatively charged (red colors) while other atoms are positively charged (blue colors). As a result, AsA is adsorbed on electron-rich graphene from its O7 and O8 due to their stronger electronegativity in comparison with other atoms. As expected in this configuration 0.067 e was transferred from graphene to AsA molecule.

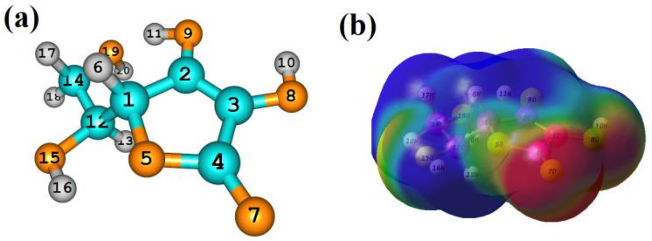

Fig 1. (a) Optimized structure of free AsA and (b) computed electrostatic potential on the molecular surface of a single AsA molecule.

From inspection of the DOS plot it is revealed that band gap of graphene is unchanged after adsorption but in the case of CNT, the HOMO and LUMO energies shift down from -3.647 and -3.467 eV in bare tube to -3.781 and -3.606 eV, respectively, in functionalized CNT. On the other word, the E_g value of the tube is decreased from 0.180 to 0.175 eV after AsA adsorption (Fig 2).

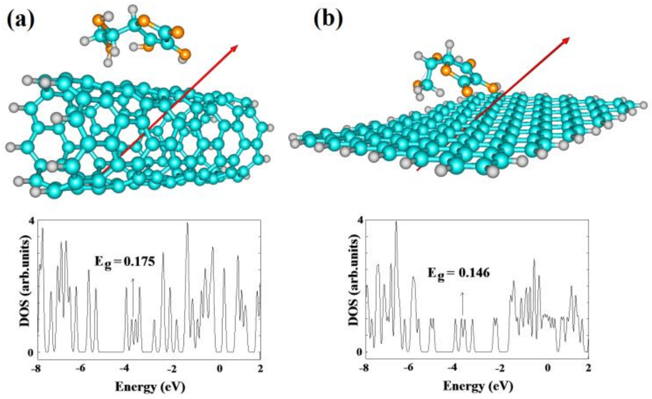

Fig 2. Optimized structures of (a) vitamin C/CNT, (B) vitamin C /graphene and their density of states (DOSs). Distances are in Å.

As the electric dipole moment is one of the properties traditionally used to discuss and rationalize the structure and reactivity of many chemical systems, it is of high importance to obtain information of the electronic distribution in a molecule. From Fig. 2 it is seen that the dipole moment vector is directed toward the high charge zone, where the adsorption process occur. The dipole moment of the CNT and graphene are 0.00 D. This parameter increases when adsorbates and vitamin C interact, taking the value 6.34 and 1.74 D for the AsA/CNT and AsA/graphene, respectively; High values on the polarity suggest a possible solubilization on hydrophilic nanomaterials. The solubilization of nanostructures (such as CNT and graphene) had been a research goal for the past few years. These compounds could be solubilized in different solvents to promote their potential applications in the form of polymers, copolymers, ceramics, and gasoline, etc. In this work, solubility of the AsA/CNT and AsA/graphene were studied in different solvents such as acetone, acetonitrile, methanol, benzene and toluene with corresponding dielectric constants of 20.493, 35.688, 32.613, 2.270 and 2.374 respectively. Polar solvents have high dielectric constants and maybe are good solvents for dissolution of vitamin C adsorbed CNT and graphene. Solvation energies (E_{solv}) of the pristine and functionalized C_{60} have been obtained by optimizing the structures in the vacuum and water. The difference between these optimization energies equals to E_{solv}. The solvation energies have been calculated with the aid of the 'Conductor-like Screening Model' for solvation. More negative Esolv will result in a higher degree of solubility.

Table 2. Calculated solvent energies (E_{solv}, kcal/mol) for the pristine and functionalized-CNT and graphene in different solvent.

System	Acetone	Acetonitrile	Methanol	Benzene	Toluene
CNT	-6.31	-6.51	-6.48	-3.32	-3.45
AsA/CNT	-15.80	-16.23	-16.18	-8.50	-8.82
Graphene	-11.46	-11.78	-11.73	-6.13	-6.36
AsA/graphene	-18.28	-18.78	-18.71	-9.86	-10.24

Functionalized CNT and graphene are more soluble than the pristine one (Table 2) and these compounds have negative Esolv, being for compounds in five mentioned solvents are in the range of -8.50 to -16.23 kcal/mol (for AsA/CNT) and -9.86 to -18.78 kcal/mol (for AsA/graphene). Also it demonstrates that the AsA/CNT and AsA/graphene in acetonitrile with E_{solv} of -16.23 and -18.78 kcal/mol, respectively, should be more soluble than other studies solvents, while in benzene (with E_{solv} of -8.50 and -9.86 kcal/mol, respectively) have lower solubility.

IV. CONCLUSION

In the present work, non-covalent functionalization of a CNT and graphene with ascorbic acid (AsA) has been theoretically investigated in terms of geometric, energetic, solubility and electronic properties through density. Our results may be useful for further studies in density functional theory (DFT).

REFERENCES

[1] Katsnelson MI, Novoselov KS, Geim AK (2006) Nat Phys 2:620-625.
[2] Guinea F, Katsnelson MI, Geim AK (2010) Nat Phys 6:30-33.
[3] Meyer JC, Girit CO, Crommie MF, Zettl A (2008) Appl Phys Lett 92:123110-123113.
[4] Son YW, Cohen ML, Louie SG (2006) Phys Rev Lett 97:216803-216806.
[5] Novoselov KS, Geim AK, Morozov SV, Jiang D, Zhang Y, Dubonos SV, Grigorieva IV, Firsov AA (2004) Science 306:666-669.
[6] Contreras CN, Cocoletzi HH, Anota EC (2011) J Mol Model 17:2093-2097
[7] Schmidt MW, Baldridge KK, Boatz JA, Elbert ST, Gordon MS, Jensen JH, Koseki S, Matsunaga N, Nguyen KA, Su S, Windus TL, Dupuis M, Montgomery JA (1993) J Comput Chem 14:1347-1363.

Section:

Nano Physical Chemistry

Sono-synthesis of AuNPs@PMo$_{12}$ nanohybrids as a smart nanoprobe

Abolphazl Ghaedi[a], ***Tahereh Rohani Bastami****[a], ***Scott G. Mitchell***[b]
a) Department of Chemical Engineering, Quchan University of Technology, Quchan 94771-67335, Iran.
b) Instituto de Ciencia de Materiales de Aragón (ICMA), Consejo Superior de Investigaciones Científicas (CSIC)-Universidad de Zaragoza and CIBER-BBN, C/ Pedro Cerbuna 12, 50009 Zaragoza, Spain.
Email: t.rohani@qiet.ac.ir

Abstract*:* We report a facile eco-friendly sonochemical synthesis of polyoxometalate-stabilized gold nanoparticles that can be used as colorimetric nanosensors to detect acetaminophen. Low frequency ultrasound sonication (20 kHz) under ambient condition in the presence of phosphomolybdic acid ($H_3PMo_{12}O_{40}$, PMo$_{12}$) was used to reduce Au^{3+} to Au^0 and stabilize the resulting Au^0 nanoparticles (Au NPs). The polyoxometalate self-assembly on the Au NP surface gives rise to a nanoprobe that undergoes a red-shift in its absorption spectrum (color change from red to purple) as the result of the aggregation of the Au NPs upon the addition of acetaminophen. The aggregation of the Au NPs induced by the acetaminophen was confirmed by electron microscopy and spectroscopic methods and the method was validated in the concentration range of 1–30 mg/L, where it demonstrated good linearity with a limit of detection of 0.42 mg/L.

Keywords: Ultrasound, Polyoxometalate, Gold nanoparticle, Colorimetric, Acetaminophen, Probe

I. INTRODUCTION

Acetaminophen (paracetamol, N-acetyl-p-aminophenol) (APAP) is extensively prescribed as an antipyretic and analgesic drug which relieves moderate pain in the head, back and arthritis [1]. The rapid detection of acetaminophen has attracted attention from the analytical chemistry field. Colorimetric methods could be the most practical way of fast detection in analysis and point-of-care diagnosis since the color changes can be recognized qualitatively by the naked eye [2] and even quantitatively using colour reference guides akin to pH indicator strips. Noble metal nanoparticles (NPs), and especially gold NPs (Au NPs), are excellent candidates for colorimetric detection of various chemicals [3]. In this study, we report the first eco-friendly and practical synthesis of polyoxometalate-stabilized gold nanoparticles (AuNPs@POM) using ultrasonication. Furthermore, the sono-synthesized AuNPs@POM were used to detect of acetaminophen with a LOD of 0.42 mg/L.

II. METHODS

Ultrasonic synthesis (US method) of AuNPs@PMo$_{12}$ carried out with an ultrasonic equipment at various temperature for 15, 30 and 60 min with different ratio of Au: POM (1:2, 1:1, 2:1). In this experiment, the effect of intensity, Au: POM ratio, and reaction temperature on colorimetric detection of acetaminophen has been investigated.

III. RESULTS AND DISCUSSION

After reduction of Au^{3+} ions with POM as a reducing and stabilizing agent, prepared AuNPs@PMo$_{12}$ nanohybrids were characterized by UV–visible, FT-IR, HAADF-STEM, EDS, zeta potential and DLS, respectively.

XRD pattern of the AuNPs@PMo$_{12}$ nanohybrid reveals the face centered cubic (fcc) structure of the Au crystals. FTIR spectroscopy was performed to verify the formation of AuNPs@PMo$_{12}$ nanohybrids. Table 1 shows the spectra and infrared transmission frequencies the phosphomolybdic acid POM and AuNPs@PMo$_{12}$.

Table 1: The most important IR vibrations for POM and AuNPs@PMo$_{12}$ nanohybrid.

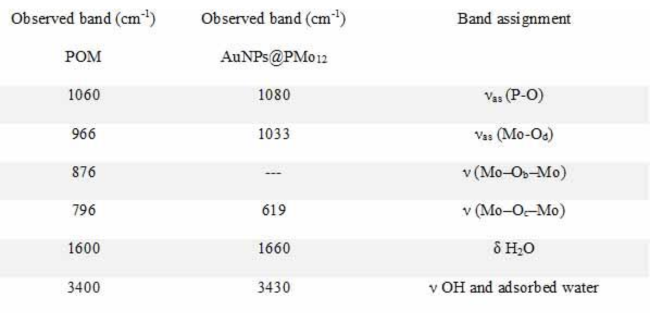

Observed band (cm^{-1}) POM	Observed band (cm^{-1}) AuNPs@PMo$_{12}$	Band assignment
1060	1080	ν_{as} (P-O)
966	1033	ν_{as} (Mo-O$_d$)
876	---	ν (Mo–O$_b$–Mo)
796	619	ν (Mo–O$_c$–Mo)
1600	1660	δ H_2O
3400	3430	ν OH and adsorbed water

Scanning electron microscopy (SEM) and high angle annular dark field scanning transmission electron microscopy (HAADF-STEM) images were effectively applied to investigate the morphology of AuNPs@PMo$_{12}$. All figures show truncated tetrahedral and hexagonal shapes.

Furthermore, the rode-like structure was observed by increasing of acoustic power. The analysis of chemical composition of the nanoparticles has been performed using EDS analysis. A cross-sectional EDS line scan profiles extracted from the HAADF-STEM image clearly confirms the coverage of Mo elements in the immediate area surrounding the AuNPs, suggesting they are from PMo_{12} structure. It should be mentioned that the EDS spectra was adjusted to determine only Au and Mo elements. The Cu peaks are the signal detected from the SEM grid.

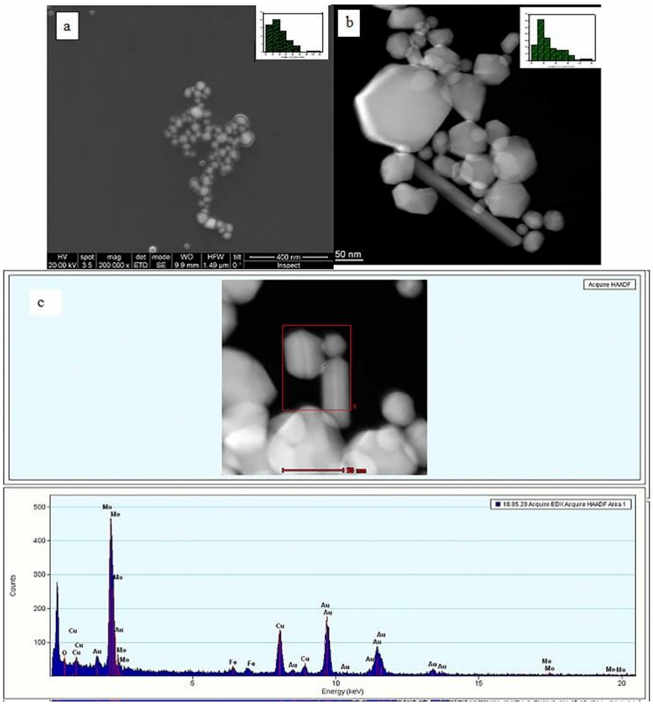

Fig. 1. HAADF-STEM images for AuNPs@PMo_{12} synthesized by a) 21 Wcm^{-2}, b) 26 Wcm^{-2}, and c) EDS analysis and corresponding HAADF-STEM image of nanohybrid synthesized by 21 Wcm^{-2}.

To optimize the ability of AuNP@PMo_{12} for sensing of acetaminophen, some parameters like temperature of reaction, intensity, Au: POM ratio, and pH effect were investigated.

To test the analytical performance of AuNP@PMo_{12}, various concentrations of acetaminophen were added into individual AuNP@PMo_{12} solutions (AuNP@PMo_{12}) at pH 3.0 ± 0.5. The changes of AuNP@PMo_{12} dispersions both in terms of the color and the absorbance spectra are recorded and shown in Fig. 2. These results indicate that linear correlation existed between intensity ratio ($A_{560/540}$) versus concentration of acetaminophen, over the range of 1 mg/L and 30 mg/L with regression equations of $y = 0.0242x + 0.4798$ (0.989) and $y = 0.014x + 0.2093$ (0.9944).

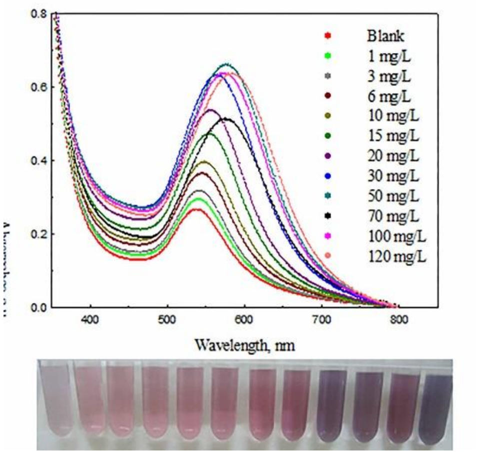

Fig.2. UV–visible spectra of AuNP@PMo_{12} solutions with different concentrations of acetaminophen and Photographic images of AuNP@PMo_{12} in concentration range of 1 mg/L to 120 mg/L (Concentrations of all acetaminophen solution were (from left to right) 0, 1, 3, 6, 10, 15, 20, 30, 50, 70, 100 and 120 mg/L, respectively).

IV. CONCLUSION

In conclusion, we present a rapid, facile and eco-friendly sonochemical synthesis of polyoxometalate-stabilised nanoparticles. The AuNP@PMo_{12} nanohybrid we report can be used as a nanoprobe for colorimetric detection of acetaminophen. The A_{600}/A_{540nm} values of AuNP@PMo_{12} nanohybrid indicated a linear relationship with concentration range of acetaminophen (1–120 mg/L) used in our study. Importantly, both the qualitative and quantitative determination of acetaminophen were investigated, and our method demonstrated limits of detection as low as 0.42 mg/L. These results showed that this biosensing set-up could potentially be used in the real world medical setting for the real-time point-of-care detection of acetaminophen with accuracy, convenience, and efficiency, even in the presence of other pharmaceuticals, in this instance methadone, methylphenidate and tramadol. Future work will involve practical application of this set-up by integrating mobile phone devices and the appropriate applications to detect a range of pharmaceuticals in more complex media, e.g. other buffers, cell culture media, blood serum, and so forth.

REFERENCES

[1] B.G. Mahmoud, M. Khairy, F.A. Rashwan, C.E. Banks, Anal. Chem, **2017.**
[2] T.Rohani. Bastami, M.H. Entezari, Ultrason. Sonochem. 19 830–840, **2012.**
[3] T.Rohani. Bastami, M.H. Entezari, Ultrason. Sonochem. 19 560–569, **2012.**

Sono-synthesis of $Cu_xO/Fe_2O_3/MoC$ nano-hybrid: evaluation of digital camera as portable colorimetric device for low cost detection of organic dyes in water media

Sina Khaknahad[a], ***Tahereh Rohani Bastami****[a],
a) Department of Chemical Engineering, Quchan University of Technology, Quchan 94771-67335, Iran.
Email: t.rohani@qiet.ac.ir

Abstract: In this study, $Cu_xO/Fe_2O_3/MoC$ nano-hybrid was synthesized by sono-assisted reverse-precipitation method using bath sonicator and compared with prepared sample using magnetically stirred rout. It was used for the removal of reactive dyes. The synthesized nano-hybrids were characterized by X-ray diffraction (XRD) analysis, field emission scanning electron microscopy (FESEM), Fourier-transform infrared spectroscopy (FTIR). The removal data showed that the ultrasonically synthesized nano-hybrids are more effective than stirrer synthesized nano-hybrids and also it has a meaningful influence on removal of RY84 and RR198. The kinetic and adsorption isotherm studies have shown that the best models are Ho's pseudo-second order and Langmuir model, respectively. A colorimetric method according to RGB value was used for determination of dye concentration in water media. The image was taken by a smartphone and the pictures were analyzed by Image j software. The accuracy of RGB results was confirmed by a UV–vis spectrophotometer.

Keywords: Compact digital camera, Colorimetry, Ultrasonic irradiation, Reactive dye, Adsorption

I. INTRODUCTION

Dyes are usually synthetic organic compounds that are used to clarify different substances for various destinations in various industries as tissue, tire, paper, leather, plastics, cosmetic, printing industries and etc.[1]. Different types of adsorbents have been used since the past as active carbon, clays, metal oxides and etc. [2]. Various new adsorbents especially nano-sorbents have solved these problems; but the main problems of these types of adsorbents are their separation and recycle. Magnetic material overcomes these deficiencies by applying externally magnetic field [3].

The performance of magnetic nanostructure materials is strongly dependent on size, surface chemistry, state of aggregation and synthesis methods [4]. Different methods such as co-precipitation, ball mill, hydrothermal techniques, and sonochemistry are employed to prepare these kinds of materials [5]. Sonochemistry has emerged as one of the promising and scalable methods to obtain metal nanoparticles, [6,7] where the chemical effects of ultrasound irradiation can be exploited due to the acoustic cavitation process. When a liquid is subject to ultrasonic irradiation, some air bubbles emerge initially, but then they collapse, leading to the release of the accumulated ultrasonic energy over a short period of time. The extremely high local temperature (> 5000 K), pressure (> 20 MPa) and high cooling rates (> 10^{10} Ks^{-1}) provide suitable conditions for metal ions reduction and chemical reaction [8].

In this research a new nano-hybrid adsorbent was synthesized by conventional precipitation and ultrasonically assisted precipitation and was used for adsorption of two reactive dyes, namely reactive yellow 84 (RY84) and reactive red 198 (RR195). RGB method was used for color detection and assuming the performance of adsorbents.

II. METHODS

The $Cu_xO/Fe_2O_3/MoC$ nano-hybrid was prepared by a sono-assisted reverse-precipitation method. Briefly, solution A was prepared by dissolving iron (II) sulfate in ultrapure water; solution B was prepared by dissolving copper (II) acetate in ultrapure water, and solution C was prepared by dissolving sodium hydroxide and PMo_{12} in ultrapure water. Solution A and B were fed to solution C dropwise over a period of 160 min in the presence of ultrasonic irradiation (Parsonic 2600s, ultrasonic cleaner, 40 kHz).

Prepared sample was used for the removal of reactive dyes, reactive yellow 84 (RY84) and reactive red 198 (RR198) in the presence and absence of ultrasonic irradiation.

III. RESULTS AND DISCUSSION

The synthesized nano-hybrids were characterized by X-ray diffraction (XRD) analysis, field emission scanning electron microscopy (FESEM), and Fourier-transform infrared spectroscopy (FTIR).

The X-ray diffraction patterns of nanosorbent prepared in the presence and absence of ultrasonic irradiation. The position of peaks and the phases for each nano-hybrid was investigated using JCPDS reference data. The results demonstrated that the successive synthesis of $CuO/Cu_2O/MoC/Fe_2O_3$ phase in the presence of ultrasonic irradiation (US method). The morphological properties of the nano-hybrids synthesized with US and MS methods were investigated using FESEM analysis (Fig.1).

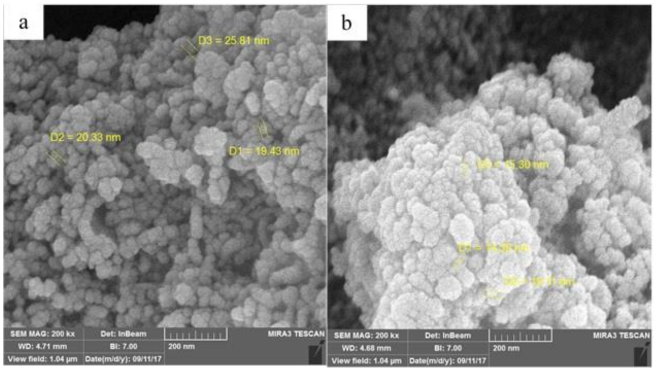

Fig.1. FESEM images of nano-hybrids a) US method, and b) MS method (Scale: 200 nm).

The FTIR spectroscopy analysis was applied to obtain information about the characteristics of sorbent and sorbent–sorbate interactions.

Table 1. The most important IR vibrations for as-synthesized nanohybrids.

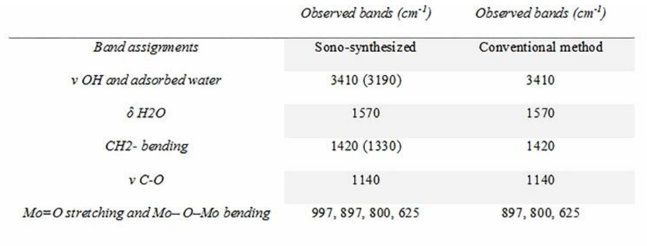

	Observed bands (cm^{-1})	Observed bands (cm^{-1})
Band assignments	Sono-synthesized	Conventional method
ν OH and adsorbed water	3410 (3190)	3410
δ H2O	1570	1570
CH2- bending	1420 (1330)	1420
ν C-O	1140	1140
Mo=O stretching and Mo– O–Mo bending	997, 897, 800, 625	897, 800, 625

The empirical studies of dye adsorption on synthesized adsorbents have been accomplished by different strategies. RGB method was applied to determine the concentration of dyes in the solution before and after sorption process. This colorimetric measurement was made by taking pictures of different concentrations of dye samples and obtaining an average of RGB (red, green, and blue) measure by the Image J software. In this method first the average of RGB of a blank solution was obtained in the same way, and then the difference of the RGB value of the intended sample and the blank was obtained. Finally, quantitative information could be obtained by transforming the RGB value to dyes concentration. To verify the reliability of the smartphone as a chemical detector, some results were compared with the results of UV-vis spectrophotometer (Fig.2). In this experiment sono-synthesized nano-hybrid was used for the removal of RY84 by stirrer (MS) method (US-MS method). As can be seen in this figure, the obtained results by RGB method are in good agreement with the spectroscopy obtained results. Hence the rest of results we analyzed by RGB.

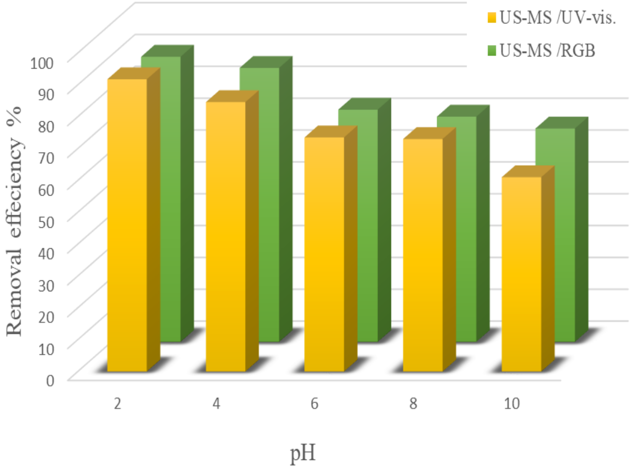

Fig. 2. The comparison of accuracy of RGB and UV-vis spectrophotometer in detection of RY84 concentration (US-MS).

To specifying the adsorption isotherm a set of experiments was carried out. In these experiments the time (20 min), adsorbent dosage (0.01 gr of $CuO/Cu_2O/MoC/Fe_2O_3$ nano-hybrid), pH = 2.5 ± 0.5 and temperature (26±1°C) of 50 mL of solution were set constant and just the initial concentration of RR195 and RY84 were variable between 10-60 mgL^{-1}. The results of both models are given in the table 2.

Table 2. Isotherm parameters of Langmuir and Freundlich model.

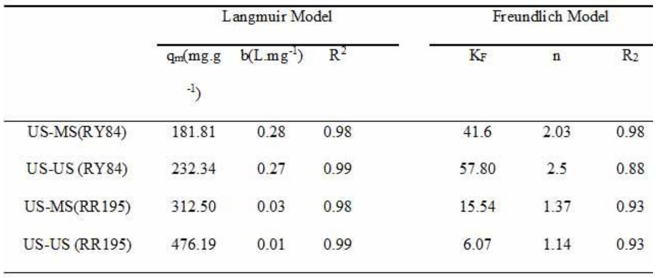

	Langmuir Model			Freundlich Model		
	q_m(mg.g^{-1})	b(L.mg^{-1})	R^2	K_F	n	R_2
US-MS(RY84)	181.81	0.28	0.98	41.6	2.03	0.98
US-US (RY84)	232.34	0.27	0.99	57.80	2.5	0.88
US-MS(RR195)	312.50	0.03	0.98	15.54	1.37	0.93
US-US (RR195)	476.19	0.01	0.99	6.07	1.14	0.93

IV. CONCLUSION

This study has reported synthesis of $Cu_xO/Fe_2O_3/MoC$ nano-hybrid by sono-assisted reverse-precipitation method using bath sonicator and compared with prepared sample using magnetically stirred rout. It was used for the removal of RR195 and RY84 as a model of wastewater pollutants. According to the results, sono-sorbent was more efficient for RR195 and RY84 removal in comparison with those obtained with conventional method. The other important point of this investigation was about using a cheap method, RGB, instead of spectrophotometer for color detection in solutions. The maximum removal of RR195 on $CuO/Cu_2O/MoC/Fe_2O_3$ nano-hybrid is around 80% in pH=2.0 and its equilibrium time is achieved after 20 min. The best pH for RY84 is also pH=2.0 with 89.5% removal on $CuO/Cu_2O/MoC/Fe_2O_3$ nano-hybrid, but its equilibrium time is about 10 min. The adsorption kinetics of both colors on $CuO/Cu_2O/MoC/Fe_2O_3$ nano-hybrid followed pseudo-second order model with $R_2 > 0.99$ at the different temperatures in US adsorption process. The adsorption isotherm models of both dyes onto $CuO/Cu_2O/MoC/Fe_2O_3$ nano-hybrid followed Langmuir model, with $R_2 > 0.98$ at the different temperatures in US adsorption process. A colorimetric method according to RGB value was used for determination of dye concentration in water media. The image was taken by a smartphone and the pictures were analyzed by Image j software. The accuracy of RGB results was confirmed by a UV–vis spectrophotometer.

REFERENCES

[1] M.A. Hassaan, A. El Nemr, To cite this article: Mohamed A. Hassaan, Ahmed El Nemr. Am. J. Environ. Sci. Eng. 1 (2017) 64–67.
[2] T.Rohani, Bastami, M.H. Entezari, Ultrason. Sonochem. 19 (2012) 830–840.
[3] T. Rohani, Bastami, M.H. Entezari, Chem. Eng. J. 210 (2012) 510–519.
[4] M. Aliofkhazraei, Handbook of nanoparticles, 2015.
[5] T.R. Bastami, M.H. Entezari, Chem. Eng. J. 164, 261–266,2010.
[6] H. Liu, X. Zhang, X. Wu, L. Jiang, C. Burda, J.J. Zhu, Chem. Commun. 47, 4237–4239, 2011.
[7] A. Sánchez-Iglesias, I. Pastoriza-Santos, J. Pérez-Juste, B. Rodríguez-González, F.J. García De Abajo, L.M. Liz-Marzán, Adv. Mater. 18,2529–2534,2006.
[8] T. Rohani, Bastami, M.H. Entezari, Ultrason. Sonochem. 19, 830–840, 2012.

Electrophilic and Nucleophilic Activities of $C_{40}N_{20}$ and $C_{42}N_{18}$, a DFT Study

A.R. Nekoei, S. Haghgoo
Department of Chemistry, Shiraz University of Technology, Shiraz 71557-313, Iran
Email: nekoei@sutech.ac.ir

Abstract: C_{60} fullerene participates easily in nucleophilic addition reactions, while it has low affinity to interact with electrophiles. Substitution of carbon atoms in the fullerene cage by heteroatoms, could improve its nucleophilic and especially electrophilic activities. In this study, electrophilic and nucleophilic activities of $C_{40}N_{20}$ and $C_{42}N_{18}$ azafullerenes have been investigated, in comparison with the C_{60}, by using DFT methods. Adsorptions of several electrophiles and nucleophiles on the most active sites of different separated-nitrogen (SN) and nitrogen-belt (NB) isomers of the both azafullerenes have been studied by analyzing several parameters and by comparison with the C_{60}. It is concluded that the SN-isomers of the both azafullerenes have stronger nucleophilic nature than the C_{60} (and NB-isomers). In the case of electrophilic activity, the results show that the NB-isomers of the both target azafullerenes are stronger than the C_{60} (and SN-isomers).

Keywords: Azafullerene, Electrophile, Nucleophile, Active site, Complexation.

I. INTRODUCTION

C_{60} fullerene behaves like an electron-deficient olefinic unit. This electron acceptor characteristic of C_{60} is theoretically attributed to a triply degenerated LUMO (lowest unoccupied molecular orbital) surface with low energy, and its small gap between HOMO (highest occupied molecular orbital) and LUMO [1]. Accordingly, the C_{60} participates easily in various nucleophilic addition reactions [2-4].

The C_{60} is hardly oxidized. C_{60}^{2+} is very unstable, and the third process (C_{60}^{3+}) is studied only at low temperatures. Addition of proton [5], nitronium ion (NO_2^+) [6], and also adding some carbocation species to the C_{60} [7] are some examples that have been done in this field.

Nitrogen-belt (NB) isomers of $C_{42}N_{18}$ and $C_{40}N_{20}$ [8] have somewhat distorted from the spherical form. Their electronic properties are significantly different from their separated-nitrogen (SN) isomers (with electron donor features), also from the C_{60} [8]. Moreover, presence of many nitrogens with many lone pair electrons in their structures influences the electrophilic and nucleophilic activities of them. Since, relatively high electron acceptor properties have been reported for these isomers [8], it is expected that they could more effectively interact with nucleophiles in compared to the C_{60}. Studying their reactivities may be useful to achieve more suitable sensors than the C_{60}.

The aim of this study is investigation of electrophilic and nucleophilic properties of the $C_{42}N_{18}$ and $C_{40}N_{20}$, and comparing them with the C_{60}. For this purpose, the ionic and neutral electrophiles H^+, CH_3^+, $COCH_3^+$, NO_2^+ and SO_3, and nucleophiles OH^-, NH_2^-, NO_2^-, CN^-, NH_3 and H_2O have been selected, and placed at different sites of both SN and NB isomers of the target azafullerenes. Various parameters related to the interactions in the resulting complexes have been analyzed, and compared with each other, and also with the corresponding complexes with the C_{60} (as a reference).

II. METHODS

All DFT calculations have been carried out using Gaussian 09 program package [9]. The geometries of all free structures and complexes have been fully optimized at the B3LYP/6-31G(d) level [10,11], following by harmonic vibrational frequency calculations. Enthalpy changes for complexation reactions have been also analyzed. Using GENNBO 5.0 software, natural bond orbital (NBO) analyses has been performed in order to obtain the natural atomic charges [12]. GaussView 5.0 program has been employed for visualization of the structures and calculated parameters [13].

III. RESULTS AND DISCUSSION

The studied electrophiles and nucleophiles have been placed in all different sites of both SN and NB isomers of the $C_{42}N_{18}$ and $C_{40}N_{20}$, and after full optimization and comparison with the Fukui functions, the most active sites for complexation were determined. Optimized structures for the complexes of the SN-$C_{40}N_{20}$ and NB-$C_{40}N_{20}$ with the CH_3^+ have been shown in Fig. 1, as an example of many optimized structures.

The binding energies (E_b) for the interactions of all studied electrophiles and nucleophiles with the most active sites of the SN- and NB-isomers of the target azafullerenes have been calculated and the results, together with the corresponding calculated results for the C_{60}, have been given in Table 1.

According to the E_b results, all interactions of studied electrophiles and nucleophiles with the both isomers of the target azafullerenes (except for the electrophiles with NB-$C_{40}N_{20}$), are stronger than those corresponding interactions with the C_{60}. In the case of electrophiles according to the calculated E_bs, they have stronger adsorption on the SN-isomers (with electron donor property) than on the NB-isomers (with electron acceptor property) of both $C_{42}N_{18}$ and $C_{40}N_{20}$. This result is consistent with the previous study [8], which shows that in both azafullerenes, the SN-isomers have higher HOMO levels and lower ionization potentials in comparison with the NB-isomers and C_{60}, (in which the HOMO of the SN-$C_{42}N_{18}$ is higher than the SN-$C_{40}N_{20}$). Therefore, the SN-isomers display stronger interactions with the electrophiles LUMO surfaces.

Table1: Binding energies (E_b) and enthalpy changes (ΔH) for complexes between studied electrophiles and nucleophiles with the most active sites of the azafullerenes $C_{42}N_{18}$, $C_{40}N_{20}$ and C_{60}, calculated at B3LYP/6-31G(d) level (in kcal/mol)

Electrophiles and Nucleophiles	**$C_{42}N_{18}$**				**$C_{40}N_{20}$**				**C_{60}**	
	SN		**NB**		**SN**		**NB**			
	E_b	**ΔH**	**E_b**	**ΔH**	**E_b**	**ΔH**	**E_b**	**ΔH**	**E_b**	**ΔH**
H^+	-257.94	-250.85	-248.54	-240.60	-255.96	-249.03	-205.71	-199.47	-218.32	-212.63
CH_3^+	-159.83	-155.41	-149.78	-145.18	-158.31	-154.04	-110.31	-106.27	-115.24	-111.62
$COCH_3^+$	-78.62	-75.99	-76.30	-72.83	-76.80	-74.30	-35.01	-33.35	-37.82	-36.25
SO_3	-26.75	-24.79	-12.91	-10.99	-26.56	-24.71	-7.75	-6.33	-3.35	-2.16
NO_2^+	-113.54	-111.42	-98.48	-96.20	-111.00	-109.08	-46.55	-45.69	-69.27	-68.30
OH^-	-114.44	-112.46	-172.36	-168.99	-104.48	-102.83	-123.51	-121.02	-103.52	-101.58
NH_2^-	-117.61	-116.44	-181.45	-176.38	-108.68	-105.29	-130.98	-126.81	-110.56	-106.84
CN^-	-54.75	-54.28	-131.20	-128.80	-46.14	-45.96	-75.68	-74.10	-55.73	-55.03
NO_2^-	-40.40	-39.14	-107.07	-104.17	-32.47	-31.52	-52.15	-49.92	-37.96	-36.61
H_2O	-3.82	-2.36	-23.17	-21.89	-4.11	-2.68	-7.28	-5.68	-1.89	-0.64
NH_3	-3.12	-1.79	-28.02	-27.23	-2.82	-1.54	-5.40	-3.95	-1.24	0.02

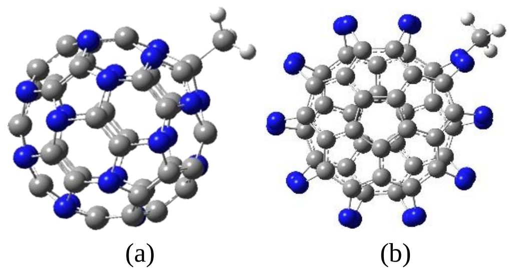
(a) (b)

Fig.1: Optimized complex structures of (a) SN-$C_{40}N_{20}$, and (b) NB-$C_{40}N_{20}$ with CH_3^+

This is while that in the case of nucleophiles, they exhibit more effective interactions with the NB-isomers than with the SN-isomers. This is also in agreement with the previously reported results [8], which show that the LUMO levels of the NB-isomers are lower than those of the SN-isomers and C_{60}, and therefore display stronger interactions with the nucleophiles HOMO surfaces. All nucleophiles have stronger interactions with the NB-$C_{42}N_{18}$ than the NB-$C_{40}N_{20}$, because the former's structure exhibit higher electron acceptor due to its higher electron affinity and lower LUMO level, in comparison with the latter. Thus, NB-$C_{42}N_{18}$ has more potential for stronger interaction with the HOMO surfaces of the nucleophiles with electron donor features.

The values of enthalpy changes (ΔH) for all studied interactions have been also calculated and given in Table 1. In addition to the high E_bs for adsorption of the electrophiles on the SN-isomers and nucleophiles on the NB-isomers, high negative values of the corresponding ΔHs are additional confirmation for the strength of these exothermic interactions.

IV. CONCLUSION

The C_{60} easily participates in various nucleophilic addition reactions, and effectively adsorbs most of the nucleophile anions, such as OH^- and NH_2^-. Our calculations show that these nucleophiles have stronger adsorptions on the NB-isomers of the target azafullerenes (having more electron acceptor character than the C_{60}), and even on their SN-isomers. This is while that the anions such as CN^- and nitrite ion (NO_2^-) have much more significant interactions with the

NB-isomers of both azafullerenes, in comparison with the C_{60}. In the case of H_2O and NH_3 nucleophiles, it could be said that they do not interact with the C_{60}, but display relatively effective adsorptions on the NB-isomers. Therefore, doping of fullerenes with the connected nitrogens could be introduced as one of the ways to improve their solubility in polar solvents such as H_2O and NH_3.

It is expected that the SN and NB-isomers of the studied azafullerenes, perform various electrophilic and nucleophilic addition reactions, respectively, better than C_{60}. In addition, some of these structures might be used as suitable electronic sensors or proper compounds for removal and filtering of toxic and pollutant species, such as NO_2^-, CN^-, NH_3, and SO_3.

REFERENCES

[1] T. Tadesse, J. Phys. Chem. Biophys., vol. 8, pp. 1000263-1-1000263-6, **2018**.

[2] Y. Murata, K. Komatsu, and T. S. Wan, Tetrahedron Lett., vol. 37, pp. 7061-7064, **1996**.

[3] H. Nagashima, M. Saito, Y. Kato, H. Goto, E. Osawa, M. Haga, and K. Itoh, Tetrahedron, vol. 52, pp. 5053-5064, **1996**.

[4] H. Nagashima, H. Terasaki, Y. Saito, K. Jinno, and K. Itoh, J. Org. Chem., vol. 60, pp. 4966-4967, **1995**.

[5] G. A. Olah, I. Bucsi, D. S. Ha, R. Aniszfeld, C. S. Lee, and G. S. Prakash, Fuller. Nanotub. Car. N, vol. 5, pp. 389-405, **1997**.

[6] L. Y. Chiang, R. B. Upasani, and J. W. Swirczewski, J. Am. Chem. Soc., vol. 114, pp. 10154-10157, **1992**.

[7] T. Kitagawa, H. Sakamoto, and K. I. Takeuchi, J. Am. Chem. Soc., vol. 121, pp. 4298-4299, **1999**.

[8] A. R. Nekoei, and S. Haghgoo, Comput. Theor. Chem., vol. 1067, pp. 148-157, **2015**.

[9] M. J. Frisch, et al. Gaussian 09, Revision A.02, Gaussian, Inc., Wallingford CT, **2009**.

[10] A. D. Becke, J. Chem. Phys., vol. 98, pp. 5648-5652, **1993**.

[11] C. Lee, W. Yang, and R.G. Parr Phys. Rev. B, vol. 37, pp. 785-789, **1988**.

[12] E. D. Glendening, J. K. Badenhoop, A. E. Reed, J. E. Carpenter, J. A. Bohmann, C. M. Morales, and F. Weinhold, NBO 5.0; Theoretical Chemistry Institute, University of Wisconsin, Madison, WI, **2001**.

[13] R. Dennington, T. Keith, and J. Millam GaussView, Version 5. Semichem Inc., Shawnee Mission KS, **2009**.

Theoretical Study on the Absorption of some Metal Oxides on Fullerene C_{60} as Potential Detectors for NO_2

A.R. Nekoei, S. Haghgoo

Department of Chemistry, Shiraz University of Technology, Shiraz 71557-313, Iran

Email: nekoei@sutech.ac.ir

Abstract: Combination of fullerene and metal oxides (MOx) are interesting, not only because they display the individual properties of fullerene and of MOx nanoparticles, but they may also exhibit synergetic properties that are advantageous for gas sensing applications. In the present work, the adsorption of some different MOxs on fullerene C_{60}, and NO_2 sensing properties of these complexes, have been theoretically studied. All quantum mechanical computations have been carried out using Gaussian G09, employing DFT method at B3LYP/6-31G(d) level. NBO theory have been used for analysis of the charge transfers during NO_2 adsorption. The results show that MOx/C_{60} complexes are much stronger adsorbent for the NO_2 than the C_{60} is. It is also expected that these complexes have more optical and electrical sensitivity in the selectivity of gases, including NO_2.

Keywords: Fullerene, Metal oxide, NO_2 gas, Adsorption, Gas sensor.

I. INTRODUCTION

Metal oxide (MOx) nanoparticles have a high ability in photocatalytic activity. However, quick charge carriers' recombination is a major limitation of most MOxs and reduces their quantum efficiency [1]. The photocatalytic activity of MOxs is improved by modifications such as coupling to other semiconductors [2,3]. Fullerenes C_{60} with spherical closed-shell configuration consisting of 30 bonding molecular orbitals with 60 π-electrons, is suitable for conjugation with the MOxs, and improves electron transfer [4].

MOxs are widely used as sensors for various gases, including toxic and polluting gases (such as CO and NO_x) [5,6]. However, these sensors hold an obvious disadvantage of high operating temperature, resulting in high power consumption, which in turn adversely affects the integration and long-term stability. Moreover, high working temperatures may threaten safety issues for measurements in environment where explosive gases may also exist [7]. The combination of fullerene and MOxs, to form combined nanostructures, could show unique features in addition to the individual components advantages, which increases their efficiency in variety fields, including gas adsorption.

The goal of this study is investigation on the adsorption of ZnO, TiO_2 (n-type semiconductors), NiO and Cu_2O (p-type) MOxs on the fullerene C_{60} surface, and effect of this adsorption on electronic structures of the resulting complexes and their behavior for the adsorption or sensing of NO_2 gas that may be helpful in reaching sensors with higher sensitivity and capability. For this purpose, the adsorption energies, geometric structure changes, intermolecular distances in the MOx/C_{60} complex structures, energy of HOMO-LUMO surfaces and their gap, ionization potentials, NBO charges analysis, and some reactivity indices in these interactions have been analyzed and compared with each other.

II. METHODS

All calculations of optimization and harmonic vibration frequencies for the free structures (fullerene, NO_2, and MOxs) and the studied complexes have been carried out using Gaussian 09 package [8], by density functional theory (DFT) at the B3LYP/6-31G(d) level [9,10]. Using GENNBO 5.0 software, natural bond orbital (NBO) analyses has been performed in order to obtain the natural atomic charges [11]. Also, GaussView 5.0 program has been employed for visualization of the structures and calculated parameters [12].

III. RESULTS AND DISCUSSION

The optimized MOxs have been placed in different sites of the optimized fullerene C_{60}, and the most stable structures of all MOx/C_{60} complexes have been identified, after full optimization. Binding energies, changes of NBO charges in metal MOxs after interacting with C_{60}, the energy of HOMO-LUMO levels and their gap for the most stable C_{60}-MOx complexes and their components have been calculated and the results have been presented in Table 1.

Table1: Binding energies (E_b, in kcal/mol), Changes of NBO charges for the MOxs after complexation (Δq, in a.u.), Ionization potential (IP), E_{HOMO}, E_{LUMO} and their gap for C_{60}, MOxs and MOx/C_{60} complexes, calculated at B3LYP/6-31G(d) level (in eV)

Structure	**E_b**	**Δq**	**IP**	**E_{HOMO}**	**E_{LUMO}**	**gap**
Cu_2O/C_{60}	-85.77	0.701	6.497	-5.689	-3.461	2.228
ZnO/C_{60}	-52.93	0.172	6.718	-5.605	-3.620	1.985
NiO/C_{60}	-79.86	0.141	6.363	-5.588	-3.172	2.417
TiO_2/C_{60}	-19.96	-0.062	6.982	-5.665	-3.916	1.748
C_{60}			7.184	-5.986	-3.225	2.760
Cu_2O			7.478	-5.261	-2.487	2.774
ZnO			8.769	-6.634	-4.094	2.540
NiO			8.674	-6.176	-3.998	2.179
TiO_2			9.284	-6.501	-3.006	3.495

As the calculated binding energies in Table 1 show, the order of stability for the MOx/C_{60} complexes is Cu_2O/C_{60} > NiO/C_{60} > ZnO/C_{60} > TiO_2/C_{60}. This sequence is in the best agreement with the values of ionization potential (IP) of the MOxs. According to the calculated values of IPs, and NBO charges analyses, Cu_2O, NiO, and ZnO, during the interactions with the fullerene C_{60} transfer some electrons to the C_{60}, and their total charges have been significantly positive compared to their initial neutral forms. The TiO_2 (n-type) with the highest value of IP have even gained very small amount of electrons from the C_{60} and has the lowest binding energy in complex with the C_{60}. The Cu_2O, having the lowest value of IP and the highest level of HOMO orbital, show the most strong interaction with the LUMO surface of the C_{60} molecule, relative to the other MOxs.

Binding energies, changes of NBO charges on the NO_2 after adsorption on different studied adsorbents, the energy levels of HOMO-LUMO and their gap for the most stable structures have been calculated, and the results have been summarized in Table 2.

Optimized structures for the resulting complexes of $NO_2/Cu_2O/C_{60}$ and $NO_2/ZnO/C_{60}$ have been shown in Fig. 1, as an example of many optimized structures in this study.

Table2: Binding energies (E_b, in kcal/mol), Changes of NBO charges for the MOxs after complexation (Δq, in a.u.), E_{HOMO}, E_{LUMO} and their gap for adsorption of NO_2 on the C_{60}, MOxs and MOx/C_{60} complexes, calculated at B3LYP/6-31G(d) level (in eV)

Structure	**E_b**	**Δq**	**E_{HOMO}**	**E_{LUMO}**	**gap**
$NO_2/Cu_2O/C_{60}$	-35.32	-0.53	-6.150	-3.543	2.607
$NO_2/ZnO/C_{60}$	-62.68	-0.58	-5.741	-3.460	2.280
$NO_2/NiO/C_{60}$	-64.64	-0.49	-6.003	-3.860	2.143
$NO_2/TiO_2/C_{60}$	-38.24	-0.04	-5.088	-3.693	1.395
NO_2/C_{60}	-1.10	0.00	-5.975	-3.220	2.755
NO_2/Cu_2O	-85.52	-0.62	-6.582	-2.603	3.979
NO_2/ZnO	-74.95	-0.59	-8.681	-2.891	5.790
NO_2/NiO	-98.97	-0.48	-8.155	-4.526	3.629
NO_2/TiO_2	-52.56	-0.51	-9.007	-3.565	5.443

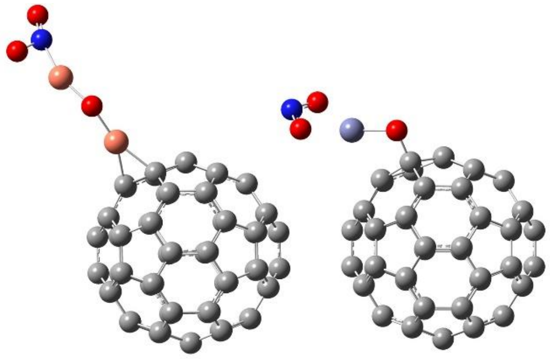

(a) (b)

Fig.1: Complex structures of (a)$NO_2/Cu_2O/C_{60}$, and (b)$NO_2/ZnO/C_{60}$

According to the analyses of the NBO charge transfers, a significant charge transfer proceeds from the MOxs to the NO_2 during the strong interactions of the NO_2 and MOxs. Interaction of the NO_2 with the fullerene C_{60} is very weak and there are almost no charge transfer between them. As the data in Table 2 show, NO_2 adsorption on the MOx/C_{60} complexes is significantly stronger than C_{60}, and the high charge transfers from these complexes to the NO_2, in comparison with those from C_{60}, the confirm the strength of these connections. According to the obtained data from this study, it can be said that NO_2 adsorption sequence on the MOx/C_{60} complexes is perfectly according to the energy sequence of HOMO levels for the MOx/C_{60} complexes, in Table 1. Accordingly the NiO/C_{60} with the highest HOMO orbital surface, has strongest interaction with the LUMO of the NO_2 molecule (-2.456 eV).

According to the tables, it could be clearly seen that before and after NO_2 adsorption, all complexes containing the C_{60} have smaller gaps compared to the corresponding structures without C_{60}. Considering the correlation of chemical hardness by gap/2, the complexes containing fullerene C_{60} have higher softness, and it is predicted that they exhibit higher reactivity and conductivity.

IV. CONCLUSION

MOx/C_{60} complexes are much stronger in the NO_2 adsorption process than the C_{60}, but they are weaker adsorbent in comparison with the studied MOxs. The C_{60} in all studied complexes decreases the HOMO-LUMO gap and the chemical hardness, and it is expected that the MOx/C_{60} complexes have more optical and electrical sensitivity in the selectivity of gases, including NO_2. In addition, organic compounds (such as fullerenes) are more readily modified than inorganic materials (including MOxs); hence, the MOx/C_{60} complexes have more potential for selectivity of gases, such as NO_2, and they require lower operating temperatures than the MOxs.

REFERENCES

[1] H. S. Yun, K. Miyazawa, I. Honma, H. S. Zhou, and M. Kuwabara, Mater. Sci. Eng. C, vol. 23, pp. 487-494, **2003**.

[2] N. Todorova, T. Giannakopoulou, and T. Vaimakis, Mater. Sci. Eng. B, vol. 152, pp. 50-54, **2008**.

[3] G. P. Lepore, C. H. Langford, J. Vichova, and A. Vlcek, J. Photochem. Photobiol. A: Chem., vol. 75, pp. 67-75, **1993**.

[4] S. Fukuzumi, and D. M. Guldi, Electron Transfer in Chemistry, Wiley-VCH, Weinheim, pp. 270-337, **2001**.

[5] H. Meixner, and U. Lampe, Sens. Actuators B: Chem., vol. 33, pp. 198-202, **1996**.

[6] P. T. Moseley, Meas. Sci. Technol. vol. 8, pp. 223-237, **1997**.

[7] S. G. Chatterjee, S. Chatterjee, A. K. Ray, and A. K. Chakraborty, Sens. Actuators B: Chem., vol. 221, pp. 1170-1181, **2015**.

[8] M. J. Frisch, et al. Gaussian 09, Revision A.02, Gaussian, Inc., Wallingford CT, **2009**.

[9] A. D. Becke, J. Chem. Phys., vol. 98, pp. 5648-5652, **1993**.

[10] C. Lee, W. Yang, and R.G. Parr Phys. Rev. B, vol. 37, pp. 785-789, **1988**.

[11] E. D. Glendening, J. K. Badenhoop, A. E. Reed, J. E. Carpenter, J. A. Bohmann, C. M. Morales, and F. Weinhold, NBO 5.0; Theoretical Chemistry Institute, University of Wisconsin, Madison, WI, **2001**.

[12] R. Dennington, T. Keith, and J. Millam GaussView, Version 5. Semichem Inc., Shawnee Mission KS, **2009**.

Urea And Green Tea Like Precursors For The Preparation Of g-C_3N_4 Based Carbon Nanomaterials (CNMs) Composite: Used As Photocatalyst For Photodegradation of Pollutants Under UV-Light Irradiation

Simon Yves DJOKO T.[a,b]***, Hadis BASHIRI****[b]***, Estella T. NJOYIM***[a]***, Arab AMIRI M.***[b]***, Serges DJEPANG***[c,d]***, Arnaud Kamdem T.***[e]***, Samuel LAMINSI***[c]***, Reinhard Schomäcker****[f]

[a] *Department of Chemistry, Faculty of Sciences, University of Dschang, P.O. Box 67, Dschang, Cameroon*
[b] *Department of Physical Chemistry, Faculty of Chemistry, University of Kashan, Kashan, Islamic Republic of Iran*
[c] *Department of Inorganic Chemistry, Faculty of Science, University of Yaounde I, P.O. Box 812, Yaounde, Cameroon*
[d] *Institute of Geological and Mining Research, Nuclear Technology Section, P.O. Box 4110, Yaounde, Cameroon*
[e] *Laboratory for Sensors, Institute of Microsystems Engineering-IMTEK, University of Freiburg, Georges-Koelher-Allee 103, 79110 Freiburg, Germany*
[f] *Department of Chemistry, Technische Universitat Berlin Straße des 17. Juni 124, 10623 Berlin, Germany*

Email:djokoyves@yahoo.fr/ hbashiri@kashanu.ac.ir

Abstract*:* Graphitic carbon nitride (g-C_3N_4) has proven to be a benchmark metal-free catalyst because of its photocatalytic applications for hydrogen generation and pollutants remediation. However, its photogenarated charge carriers (electron and hole pairs) exhibit a fast recombination and insufficient light absorption during photocatalytic process. Making g-C_3N_4-based nanocomposite is one way to overcome its drawbacks. Therefore, this review focuses on a novel route by which we can now insert materials like carbon nanomaterials (CNMs) in the structure of g-C_3N_4 to form hybrids nanocomposites which possess great surface area and high photocatalytic properties. Then, a novel kind of nanosheets g-C_3N_4/CNT composites with high UV-light photoactivity were developed via one-pot preparation using urea and green tea leaves wastes as precursors (starting materials) and as a cheap and natural sources of carbon and nitrogen. As results, we finally obtained CNTs nanoparticles-hybridized g-C_3N_4 and denoted as g-C_3N_4/CNT^{BGt} which possess a great surface area (128,26 m2.g-1) with more mesoporous active sites leading to a strong adsorption capability and efficient photocatalytic activity for Methylene Blue photodegradation related to its low recombination of photogenerated charge carriers as it was predicted by PL analysis. The subscript B stands for Biochar and subscript Gt stands for green tea. According to the characterization analysis results we believed that green tea leaves acted as a template agent that controls the morphology, the growing and the final structure leading to the in situ incorporation of CNTs in the structure of g-C_3N_4. g-C_3N_4/CNT^{BGt} exhibited a perfect Reusability and its stability was also improved as compared to g-C_3N_4. This study provides new insights for the preparation of g-C_3N_4-based carbon nanomaterials and facilitates their potential application in the synergistic removal of harmful organic pollutants.

Keywords: graphitic carbon nitride, CNTs, CNMs, degradation, natural precursors, heterogeneous photocatalysis, organic pollutants

I. INTRODUCTION

Heterogeneous catalysis has been largely developed and occupies today an important place in most of chemical engineering processes, particularly because of its multiple applications such as contaminant removal[1] and hydrogen generation from water[2]. So far, researchers have developed many free-metal materials that have the potential to act as photocatalysts for a wide range of applications including energy generation in form of hydrogen and environmental protection. Among them, carbon nitride[3] (CNs) has proven to be a benchmark catalyst because it is the most stable form, non-toxic, earth-abundant nature and it is an emerging material as an organic semiconductor photocatalyst active for various kinds of reactions such as water splitting, CO_2 reduction, and degradation of harmful organic compounds[5]. This polymeric material is usually synthesized form nitrogen-rich precursors compounds (cyanamide, dicyanamide, melamine, thiourea and urea…) by thermal condensation at very high temperature (450-650°C)[4]. It has a band gap energy of ca. 2.7 eV, originating from the sp^2 hybridization of carbon and nitrogen atoms. This appropriate band gap allows him to absorb light energy in the visible range of 450-460 nm. However, it has been observed from previous works that it still has the drawbacks of insufficient light absorption and as a result it showed little completion of mineralization of organic contaminants mainly due to its low specific surface area, poor optical absorption and fast recombination process of photogenerated electron and holes pairs[4]. As a result, many researchers and scientists tried to enhance its photoactive properties by various methods such as providing large surface area, making nanomaterial composites of $g\text{-}C_3N_4$, utilizing various catalysts and creating hybrids with other materials[3,4].

This review focuses on a novel approach by which we can now insert materials like CNTs in the structure of $g\text{-}C_3N_4$ to form hybrids nanocomposites. This final material has been used as catalyst for testing the photodegradation of an organic contaminant in water under UV-light irradiation. Methylene blue dye has been used as pollutant for this purpose. The aim of this work is to provide and highlight the scientific idea by which we can now achieve the synthesis of a mesoporous nanocomposite made of graphitic carbon nitrite and carbon nanotubes by using natural precursors from waste materials for the future perspective. The fascinating aspect of this research work is that green tea leaves is a natural material (biomass) which contains several families of hydrocarbon and N-rich species (proteins, Alkaloids, glucides…), therefore, some of these species may serve as additional source of carbon and nitrogen while the others may serve as hard templates for controlling the morphology, the growing and the structure of the hybrid composite and then as a result, improving its stability, its activity and its optical absorption capacity suitable for various applications such as photocatalytic degradation of organic pollutants. The advantages of using green tea as a carbon feedstock combined with urea for making $g\text{-}C_3N_4/CNT^{BGt}$ is that, green tea provides in situ chemical materials for templating the synthesis process which may lead to the creation of mesoporous material helpful to its optical absorption capacity. Green tea leaves are already available in abundance on earth, therefore they are inexpensive and have no chance of shortage in the near future. This work fits well with the principle of green chemistry which state that the feedstock of any industrial process must be renewable, rather than depleting a natural resource.

II. METHODS

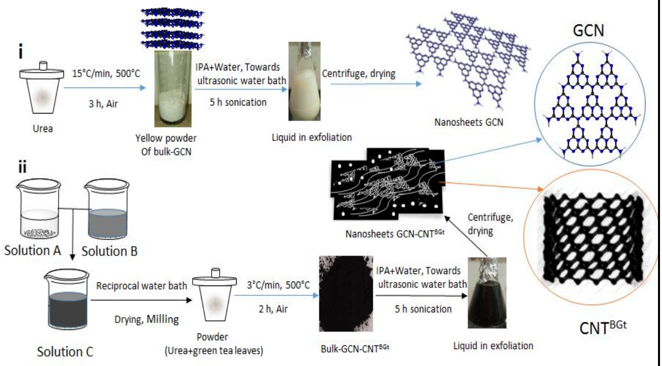

Fig 1: Schematic illustration routes for the synthesis process of i) nanosheets GCN and ii) nanoporous composites of GCN-CNT^{BGt}

III. RESULTS AND DISCUSSION

the recombination rate of photo-excited electrons and holes pairs is greatly inhibited and bring out higher photoactivity for $g\text{-}C_3N_4/CNT^{BGt}$.

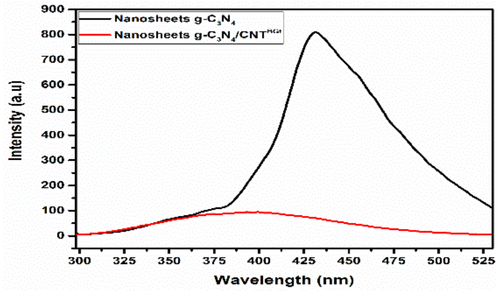

Fig 2: The Photolumiscence (PL) emission spectra of nanosheets $g\text{-}C_3N_4$ and $g\text{-}C3N4/CNT^{BGt}$

The important aspect to underline is that, the $g\text{-}C_3N_4/CNT^{BGt}$ composite has great light adsorption ability as compared to single g-C3N4 which is consistent to BET/BJH results.

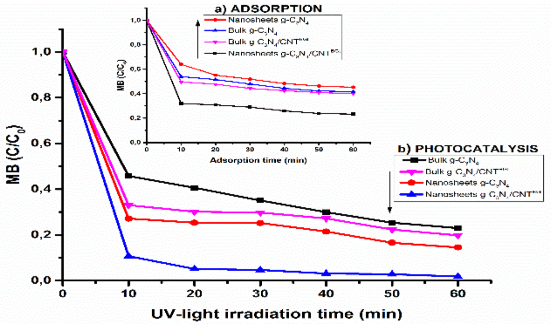

Fig 3: (a): The adsorption and (b): the photocatalytic degradation of MB dye

$g\text{-}C_3N_4/CNT^{BGt}$ material has not only high photocatalytic ability but also excellent stability and an admirable repeatability, both of which enable the composite to be a promising light driven catalyst for contaminant removal.

The $g\text{-}C_3N_4/CNT^{BGt}$ composite allows to a fast generation of reactive species such as hydroxyl radicals (OH) and oxy-radicals (O), both of which quickly react and effectively degrade the organic species.

Table 1 : Chemical elementary analysis, BET coupled BJH analysis and band energy

Sample Name	**EC[a] (Wt%)**				**S_{BET}[b] ($m^2\ g^{-1}$)**	**P_{SR}[c] (nm)**	**P_V[d] ($cm^3\ g^{-1}$)**	**E_g[e] (eV)**	
	C	N	H	N/C				Direct	Indirect
nanosheets $g\text{-}C_3N_4$	33,934	59,825	2,037	1,76	60,053	1,9378	0,1592	2.98	2.79
nanosheets $g\text{-}C_3N_4/CNT^{BGt}$	54,855	26,301	2,008	0,48	128,26	2,0276	0,2163	3.55	3.55
Bulk $g\text{-}C_3N_4$	-	-	-	-	52,065	1,935	0,173	3.04	2.77
Bulk $g\text{-}C_3N_4/CNT^{BGt}$	-	-	-	-	78,352	1,9223	0,2499	-	-
calcined green tea (gt)	72,651	4,913	2,138	0,07	22,717	1,9174	0,0065	-	-

[a] : Elementary composition ; [b] : Specific surface area ; [c] : Pore size radius; [d]: Pore volume; [e]: band gap energy

IV. CONCLUSION

In this study, a new synthetic route through a facile one-pot procedure that produces highly photocatalytically active mesoporous $g\text{-}C_3N_4$ based carbon nanomaterials (CNMs) composites has been developed using urea and green tea leaves wastes as precursors (starting materials) and as a cheap and natural sources of carbon and nitrogen. Of course, we finally obtained CNTs nanoparticles-hybridized g-C3N4 and denoted as $g\text{-}C_3N_4/CNT^{BGt}$ which possess a great surface area (128,26 m^2.g-1) with more mesoporous active sites leading to a strong adsorption capability and efficient photocatalytic activity for MB photodegradation related to its low recombination of photogenerated charge carriers. Therefore the inhibition of recombination process of photogenerated charges carriers play an important role in the production of OH radicals. As a result, we obtained a $g\text{-}C_3N_4$-hybridized CNT that exhibited a perfect Reusability and its stability was also improved as compared to $g\text{-}C_3N_4$.

REFERENCES

[1] V. Píšťková, M. Tasbihi, M. Vávrová and U. L. Štangar, J. Photochem and Photobio A: Chemistry, 2015, 305, 19–28

[2] R. Luque and J. Garcia Martinez, ChemCatChem, 2013, 5, 827–829.

[3] Z. Pu, S. Wei, Z. Chen and S. Mu, Applied Catalysis B: Environmental, 2016, 196, 193–198.

[4] G. Zhang, Z.-A. Lan and X. Wang, Chemical Science, 2017, 8, 5261–5274.

The effect of mole ratio variation of poly vinyl alcohol as capping agent on size and shape of $KTiOPO_4$(KTP) nano particles synthesized by co-precipitation method

E. Gharibshahian[a*]
[a] *Narjes Vocational college, Technical and Vocational University, Semnan, Iran*
Email:e.gharibshahian.physic@gmail.com

Abstract: $KTiOPO_4$(KTP) nanoparticles were synthesized by co-precipitation method using poly vinyl alcohol (PVA) as capping agent. Different mole ratios of PVA (1:3,1:2 and 1:1) with respect to titanium ion were used. XRD patterns confirmed the formation of KTP structure. By change of capping agent mole ratio Spherical-form and polyhedral – form of KTP nanoparticles were observed. Biggest and smallest grain size and particle size was obtained by 1:3 and 1:1 mole ratios.

Keywords: Co-precipitation method, nanoparticles, potassium titanyl phosphate, size control, shape control.

I. INTRODUCTION

Potassium titanyl phosphate ($KTiOPO_4$ or KTP) single crystals are excellent nonlinear optical materials. Also they have important technological applications in laser frequency mixing and in wave guides. They are a good ionic conductor and a piezoelectric material. Many valuable properties of this crystal have made it a standard material in many industrial, medical and other applications [1-3]. Study on the growth conditions of KTP single crystals to improve in their properties for different applications especially for SHG was started from late nineteenth century and now these crystals are industrialized, but there are very little reports on the same studies for KTP nano crystalline powders. In recent years, nanoscience and technology have potential applications in the field of science and technology. Because of it, attention of scientists, have been focused to produce the KTP nanostructures for different applications such as second harmonic generation [4] and charged nano filtration membranes [5]. The size and shape of nano crystals act as critical parameters for determining materials properties therefore precise control of size and shape of nanocrystals, results in desired chemical and physical properties. Pechini [1], Sol-gel [6], Mechanochemical mixing [7], Combustion [8] and Chemical methods [5] have been used to prepare nanostructures of KTP. Mechano chemical, Sol-gel and Pechini are primitive methods for synthesis of KTP nanoparticles. Among these methods, there are problems such as expensive raw materials, presence of OH^- ions and lack of control of particle morphology. Co-precipitation method is known as appropriate, cheap and simple method for size and shape control of nanoparticles. In this method size, size distribution and shape of obtained nanoparticles can be controlled by controlling the relative rates of nucleation and growth during the synthesis process [9]. For nano crystals prepared by solution based chemical methods, a capping agent, generally is added both to control the size of nano crystals and to prevent agglomeration of synthesized nano crystals. Capping agent with selective adsorption to specific crystal faces, could be used to kinetically control of the growth of single crystalline and it plays an important role on morphology of nanocrystals. When we use from polymers as capping agents, length of their polyol's hydrocarbon chain can be determined solution viscosity, therefore polymers as capping agent can greatly control diffusion, growth process and morphology of obtained nano particles. In this paper we report a low temperature aqueous solution based co precipitation method for the synthesis of KTP nano particles and selected poly vinyl alcohol (PVA) as capping agents. PVA generally acts as a holding matrix and is expected to control the size of nanoparticles and their distribution. Average grain size, particle size and morphology of obtained nanoparticles were studied by XRD patterns and scanning electron microscopy (SEM) analysis.

II. METHODS

In this method, the aqueous titanyl chloride solution, high purity of potassium dihydrogen phosphate (KH_2PO_4), potassium carbonate (K_2CO_3) and PVA as capping agent in different mole ratios (1:3,1:2 and 1:1) with respect to titanium ion were used for the synthesis of KTP nanoparticles. Capping agent-mixed titanyl chloride solution was reacted with aqueous solution of KH_2PO_4 with solution concentration equal to 0.5M and K_2CO_3 to obtain white precipitate at $pH \approx 6$. The precipitate was washed with distilled water several times to remove chloride ion from the solid and finally dried at 100˚C under ambient condition. Initial amorphous phase, after precipitation, was calcined at 700 ˚C for 2h.

III. RESULTS AND DISCUSSION

A. X-Ray diffraction studies

Fig.1 shows the XRD patterns of KTP nanoparticles synthesized without using capping agent and with different mole ratios of PVA as capping agent after their calcination at

700˚C. For all the samples, diffraction peaks were well assigned to orthorhombic structure of KTP with lattice constants a= 10.58A˚, b= 12.81 A˚ and c=6.40 A˚ which are in consistent with the values in the standard card of ASTM (35-0802). The average crystallite size of produced samples was calculated by measuring the broadening of the XRD peaks using the Scherrer equation.

$$D = \frac{k\lambda}{\beta \cos\theta} \qquad (1)$$

Where D is the crystallite size, λ is the wavelength of the CuKα radiation (1.542Å), K is a constant (0.9), β is the full-width at half-maximum and θ is the Bragg angle. The crystallite size of obtained KTP nanoparticles under different conditions is given in Table 1.

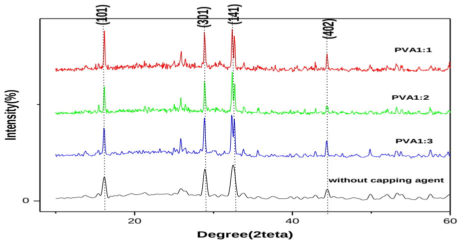

Fig.1**:** XRD patterns of synthesized KTP nanoparticles without and with different mole ratios of PVA as capping agent.

Table 1: Crystallite size, particle size and PDI for KTP nanoparticles obtained under different conditions.

sample	***Type of capping agent***	***Mole ratio of capping agent***	***Graine size(nm)***	***Particle size(nm)***	***PDI***
S	Without capping agent	-	39/49	100	1/26
PVA1:3	PVA	1:3	56/36	115	2/25
PVA1:2	PVA	1:2	42/50	110	2/23
PVA1:1	PVA	1:1	39/42	90	1/53

B. Scanning electron microscopy (SEM) studies

The FE-SEM images of KTP nanoparticles synthesized without and with different mole ratios of capping agent are shown in figure 2. Poly dispersity index (PDI) was calculated via Image-J software. PDI and particle size of obtained samples with different mole ratios are given in table1. It is observed that size, size distribution and shape of obtained nanoparticles have been changed by using variant mole ratios of PVA. Particle size of obtained KTP nanoparticles increased with decrease the mole ratio of PVA. Only for sample PVA1:1, particle size of synthesized KTP nanoparticles was decreased using PVA as capping agent rather than sample S. Morphology of KTP nanoparticles for sample S was dumbly-form but by using PVA as capping agent for samples PVA1:3 and PVA 1:2 changed to spherical-form and for sample PVA1:1 changed to polyhedral-form. For obtained KTP nanoparticles, PDI decreased by increasing the PVA mole ratios. PVA generally has the role of the holding matrix and OH functional group of PVA may temporarily bind with the metal ions through Vander Waals forces [10]. Amount of PVA as capping agent plays a definite role in determining the growth habit of the various crystal faces and thus morphology of KTP nanocrystals. The selective adsorption of capping agent on the crystal surface results in formation of nanoparticles with certain morphology. From another perspective, solution viscosity is increased by increasing the concentration of PVA.

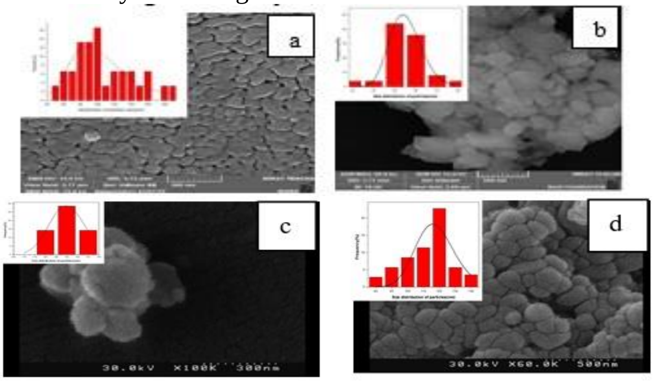

Fig.2: FE-SEM images of KTP nanoparticles synthesized (a) without capping agent, with PVA as capping agent with mole ratio, (b)1:1, (c) 1:2, (d) 1:3, accompanied by size distributions curve of obtained samples with different mole ratio

Viscosity increasing results in diffusion and migration of ions in solution become more difficult. Also nucleation process become more difficult by increasing the amount of capping agent. Decreasing the nucleation alongside used stirring rate can provide required conditions to steady growth at appropriate PVA concentration. In this work increasing the amount of capping agent and a used relatively high speed stirring lead to decrease the grain and particle size and increase the structural quality of obtained nanocrystals. In the absence of capping agent, we will usually have spherical-form nanoparticle. In the process of crystal growth, the capping agent effectively reduce the grain surface energy. Which can effectively reduce the grain adhesion and as a result agglomeration decreased and KTP nanoparticles with certain crystal faces are obtained at 1:1 mole ratio. On the

other hand, shape of nanoparticles is very sensitive to the stirring rate. Low amount of capping agent in addition to relatively high stirring rate result in spherical form of KTP nanoparticles at 1:3 and 1:2 mole ratios of PVA.

IV. CONCLUSION

Amount of PVA as capping agent and stirring speed were used as control parameters in this work. Solution viscosity was increased by increasing amount of PVA and PVA may temporarily bind with the metal ions through Vander Waals forces. Both of these parameters could be used to kinetically control the growth of KTP nanocrystals and result in change of grain and particle size and nanocrystal morphology. For constant stirring rate at 1:1 mole ratio of PVA, growth condition was more stable to development of crystal faces. This mole ratio results in smallest grain and particle size.

REFERENCES

[1] S. Dahaoui, N. K. Hansen, J. Protas, H.-G. Krane, K. Fischer and G. Marnier; J. Appl. Cryst. 32(1999), 1-10
[2] E. Gharibshahian, M. JafarTafreshi, M.Fazli , J. Pure. Ap. Phy 47(2009)356-361.
[3] E. Gharibshahian and M. Jafar Tafreshi , Cryst. Res. Technol. 50(2015) 603–612.
[4] L.L. Xuan, C. Zhou, A. Slablab, D. Chauvat, C.Tard, S.Perruchas, T.Gacoin, P.Villeval, J.F. Roch, Journal of Small 4[9] (2008)1332–1336.
[5] S.K.Biswas, A.Pathak, P.Pramanik , J.Am.Ceram.Soc 90 (2007)1071-1076.
[6] C.J. Barbi, M.A.Harmer, G.W.Schere, Journal of Sol-Gel Science and Technology 9(1997) 183-199.
[7] Y. Kanno, Journal of Alloys and Compounds 210 (1994) 45-5.
[8]N. Arul Dhas, K.C.Patil , Journal of Alloys and Compounds 202(1993) 137-141.
[9] M. Houshiar, F.Zebhi , Z.JafariRazi, A.Alidoust, Z.Askari, Journal of Magnetism and Magnetic Materials 371(2014) 43-48.
[10] B. Sadeghi, M. A. S. Sadjadi, A. Pourahmad IJNN,Vol.4, No.1, 20084,3-12


بیست و دومین کنفرانس شیمی فیزیک انجمن شیمی ایران
22nd Iranian Physical Chemistry Conference
۲۹ الی ۳۱ مرداد ۱۳۹۸
گروه شیمی دانشگاه زنجان

Unexpected Electronic and Conductive Properties of Aniline/$CONH_2$-SWCNT Binary Nano-combination for Use as Counter Electrode

Sara Naseh*
Department of Physical Chemistry, Faculty of Chemistry, University of Kashan, Kashan, I.R. Iran
Email: sara_nasseh@yahoo.com

Abstract*:* In current paper, the structural and conductive properties of aniline/functionalized zigzag single wall carbon nanotubes (SWCNTs) binary Nano-combinations have been calculated via density functional theory (DFT). It was found that functionalization of carbon nanotubes increments the sorption of aniline on the wall of nanotube, significantly. Novel density of states (DOSs) and band structures for modified SWCNTs have been reported, as well. The result originated from computed electronic properties especially gaining the value of 5.25 1/eV for DOS and creating new state nearby Fermi level powerfully suggest that aniline/$CONH_2$-SWCNT can be efficiently applied as counter electrode in dye-sensitized solar cells. Certainly, employing this Nano-composite in electronic devices will improve charge transfer and capability of them, considerably.

Keywords: Solar cells, counter electrode, carbon nanotube, electronic properties, aniline

I. INTRODUCTION

In the last decade, a growing attention has dedicated to the combination of benzene and its derivatives especially aniline with carbon nanotubes (CNTs). Joining aniline to carbon nanotubes creates amazing and extraordinary features which causes its highlighted applying in numerous applications particularly in solar cells .Firstly in 2008, Li and his scholars substituted platinum with a low-cost polyaniline (PANI) to construct the counter electrode (CE) in dye-sensitized solar cells (DSSCs). The accomplished replacement brought overall energy conversion efficiency of DSSC to 7.15% and higher than DSSC with Pt counter electrode [1]. Also, a noteworthy power conversion efficiency of 7.81% and a high charge-transfer has been reported for PANI–4% SWCNT complex CE [2]. The complexes of polyaniline-graphene and polyaniline-SWCNT synthesized via reflux method by Wang et al. These complexes mixed with graphene oxide through layer-by-layer self-assembly technique. The conversion efficiency of DSSC using (PANi-G/GO)n and (PANi − SWCNT/GO)n multilayer counter electrodes reached to 7.88% and 6.88%, respectively [3]. Recently, the quasi-solid-state DSSCs have yield a maximized efficiency of 8.23% because of using polyaniline (polypyrrole)-carbon nanotube complexes [4].

To the best of our knowledge, no theoretical analysis is accessible for aniline/functionalized CNT binary combined systems. In this paper, I scrutinize the structural and electronic properties of aniline/functionalized SWCNT composite with the aim of using it as counter electrode in solar cells. Meanwhile, the remarkable electronic conductivity behavior of both aniline/COOH-SWCNT and aniline/$CONH_2$-SWCNT was compared calculating density of states (DOSs) and band structures.

II. METHODS

Calculations were performed basing on density functional theory (DFT) using pseudo potential method as implemented in plane-wave self-consistent field package Quantum-Espresso [5]. Norm-conserving pseudo potentials were chosen for C, N, O and H atoms. Nanotube modeling was carried out by a semiconductor (10, 0) zigzag SWCNT. A kinetic energy cut-off of 50 Ry and a well converged value of 1×1×7 *k*-point mesh over The Brillouin zone were considered. Initially, optimizing of four super cells of COOH-SWCNT, $CONH_2$-SWCNT, aniline/COOH-SWCNT and aniline/$CONH_2$-SWCNT was executed by fully relax calculations. Then, the electronic properties of them were extracted and compared. The optimized super-lattices after relax computations are depicted in Fig. 1.

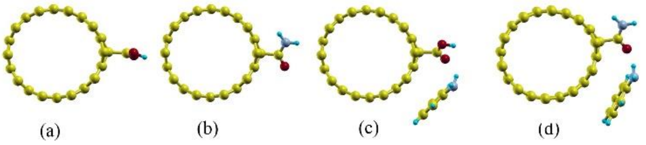

Fig. 1: Optimized structures for (a) COOH-SWCNT, (b) $CONH_2$-SWCNT, (c) aniline/COOH-SWCNT, (d) aniline/ $CONH_2$-SWCNT.

III. RESULTS AND DISCUSSION

According Fig. 1, deviation is illustrated in the carbon atom of nanotube in derivative site and also carbon atom situated under this place because of adding COOH and $CONH_2$

functional groups. The adsorption energies exhibited in Table 1 have achieved from two following equation:

$$E_{ads} = E(\text{functionalized SWCNT}) - E(\text{pure SWCNT}) - E(\text{functional group}) \tag{1}$$

$$E_{ads} = E(\text{aniline/functionalized SWCNT}) - E(\text{functionalized SWCNT}) - E(\text{aniline}) \tag{2}$$

The former equation for adsorption energy is related to COOH-SWCNT and $CONH_2$-SWCNT, the latter is belongs to two other systems of aniline/COOH-SWCNT and aniline/$CONH_2$-SWCNT.

The negative values of all adsorption energies described stable sorption progress. It is obvious from the value of adsorption energies that functionalization of SWCNT by acid or amide groups is a chemical process whereas adsorption of aniline on the outer surface of functionalized SWCNT is a physical progression. A comparison of the results achieved in this paper and another work (adsorption energies of -0.302 eV has been reported for aniline/pristine SWCNT) revealed that treating SWCNT with acid and amide functional moieties remarkably improves the adsorption of aniline on carbon nanotube. It is to be noted that decorating SWCNT with COOH enhances the interaction between aniline and nanotube more than $CONH_2$. This fact demonstrates that the new created π-π interactions between benzene ring of aniline and functional groups augment the reactivity of aniline molecule into SWCNT. In four modified systems, the bond length of C-C is higher than 1.43 in pure SWCNT. The angle of three carbon atom at functionalized site is lower than 117 degree in pristine (10,0) SWCNT approving sp^3 defect on the wall of nanotube.

Table 1: Adsorption energies, C-C bond length between carbon nanotube and functional group, angle of three carbon atoms of SWCNT at functionalized site, density of states and Fermi energy

system	**Eads (eV)**	**CCNT-CF (Å)**	**<C-C-C (degree)**	**DOS (1/eV)**	**E_{Fermi} (eV)**
a	-1.5611	1.5474	106.90	2.4516	-1.8228
b	-1.4322	1.5796	107.71	2.4496	-1.7924
c	-0.4774	1.5412	107.16	3.5112	-1.5294
d	-0.4686	1.5734	108.10	5.2500	-0.2186

Calculating and plotting the density of states (DOSs) (Fig. 2), we determined the electronic properties of four considered systems. DOSs curves relating modified SWCNTs are different at the Fermi level. All mentioned super cells displayed a metallic property at the Fermi level whereas DOS of pristine around Fermi level is equal to zero. It is well known that adding aniline to both functionalized SWCNT increases the value of DOSs. DOSs of aniline/$CONH_2$-SWCNT (5.2500 1/eV) is significantly higher than aniline/COOH-SWCNT (3.5112 1/eV). Hence, it is expected that aniline/$CONH_2$-SWCNT possesses the highest charge transfer and electrical conductivity. Consequently, it seems that aniline/$CONH_2$-SWCNT composite with great conductive properties is a worthy choice to apply in electronic device especially solar cells. The Fermi energy for pure SWCNT is about -3.55 eV. Comparison this value with the calculated Fermi energies in current study is obviously indicative of shifting all values to more positive ones, better electronic charge movement and finally higher conductive properties.

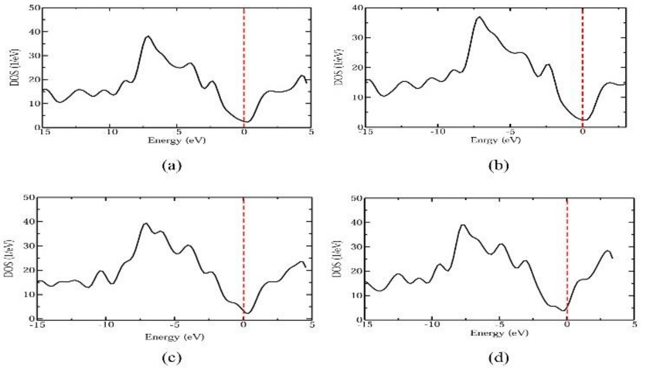

(a) (b) (c) (d)

Fig. 2: The density of states (DOSs) for (a) COOH-SWCNT, (b) $CONH_2$-SWCNT, (c) aniline/COOH-SWCNT, (d) aniline/ $CONH_2$-SWCNT.

Further describing of electronic properties has been performed by calculating the band structures and plotted in Fig. 3.

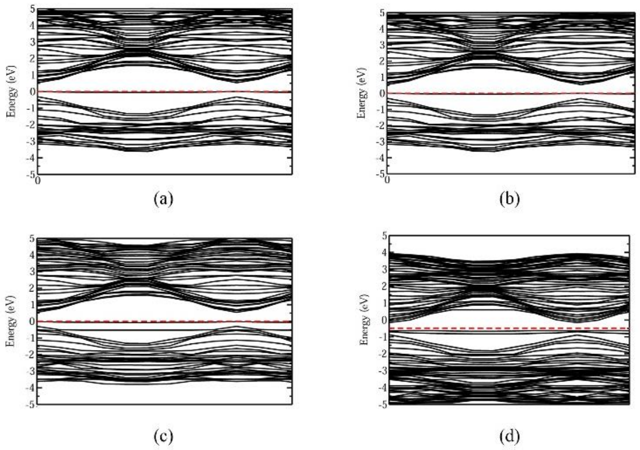

(a) (b) (c) (d)

Fig. 3: The band structure for (a) COOH-SWCNT, (b) $CONH_2$-SWCNT, (c) aniline/COOH-SWCNT, (d) aniline/ $CONH_2$-SWCNT.

Pristine (10, 0) SWCNT is a semiconductor with a band gap of 0.81 eV. By functionalizing SWCNTs, the electronic properties change at the Fermi level and π–π* band overlap was disturbed by a half-occupied impurity state. This is a result of forming a sp^3 deficiency on the sidewall of nanotube. Entering aniline to composites, more amendments were made in the band structure of these systems. Novel states which are responsible for electronic and conductive features were apparent under the Fermi level. In aniline/$CONH_2$-SWCNT the created states is closer to Fermi level and more effective in charge transfer from valance band to conduction band. A consensus is that aniline/$CONH_2$-SWCNT combined system possesses better electronic properties than aniline/COOH-SWCNT. Undoubtedly, mentioned binary composite can apply in counter electrode and improve the capability of solar cells.

IV. CONCLUSION

This paper investigates the structural and electronic properties of aniline/functionalized SWCNT super cells. The result specified that aniline molecule shows higher intention to absorb on SWCNT with oxygen-containing functional groups than pristine. Although, acidified zigzag SWCNTs is better sorbent for aniline but SWCNT with amide functional group possesses stronger conductive properties. It was revealed that noticeable novel changes in DOSs and band structures of SWCNTs were occur after adding aniline to functionalized SWCNTs. Taking the cue from computational findings, aniline/$CONH_2$-SWCNTs can apply in solar cells due to its superconductivity properties.

REFERENCES

[1] Z. Li, B. Ye, X. Hu, X. Ma, X. Zhang, Y. Deng, Electrochemistry Communications, vol. 11, pp. 1768–1771, **2009**.
[2] M. Wang, Q. Tang, P. Xu, B. He, L. Lin, H. Chen, Electrochimica Acta, vol. 137, pp. 175-182, **2014**.
[3] M. Wang, Q. Tang, H. Chen, B. He, Electrochimica Acta, vol. 125, pp. 510-515, **2014**.
[4] X. Jin, L. You, Z. Chen, Q. Li, Q. Electrochimica Acta, vol. *260*, pp. 905-911, **2018**.
[5] S. Baroni, A. Dal Corso, A., S. De Gironcoli, P. Giannozzi, P., **2007**. https://www.quantum espresso.org.

Fabrication and Investigation of an Easy-to-Prepare Highly Sensitive Temperature Sensor Based on Epoxy Resin/Copper (II) Oxide Nanoparticles/ MWCNTs Nanocomposite

Iraj Ahadzadeh*[1], Amin Norouzi[2], Samira Nematdoust[3], Mahtab Khattat Khiyabani[4], Niloufar Farhang Benam[5]
**Corresponding Author, Email: irajahadzadeh@gmail.com, Ahadzadeh@tabrizu.ac.ir*
1-Assistant Professor, Department of Physical Chemistry, Faculty of Chemistry, University of Tabriz, Tabriz, Iran
2- M.Sc. Student of Nano Chemistry, Faculty of Chemistry, University of Tabriz, Tabriz, Iran
3- Ph. D Candidate, Department of Organic Chemistry, Faculty of Chemistry, University of Tabriz, Tabriz, Iran
4- M.Sc. Student of Nano Chemistry, Faculty of Chemistry, University of Tabriz, Tabriz, Iran
5- M.Sc. Student of Organic Chemistry, Faculty of Chemistry, University of Tabriz, Tabriz, Iran

Abstract*:* An easy-to-prepare highly sensitive temperature sensor based on epoxy resin/multiwalled carbon nanotubes (MWCNTs) /copper (II) oxide nanoparticles nanocomposite was fabricated and studied.

Keywords: MWCNTs, Copper (II) Oxide Nanoparticles, Epoxy Resin, Temperature Sensor, Nanocomposite

I. INTRODUCTION

Copper (II) oxide nanoparticles with a diameter range of about 80-200 nm were synthesized by a sol/gel followed by thermal decomposition process[1]. These nanoparticles were the core p-type semiconducting material acting as temperature sensing constituent due to its sharp resistance temperature-dependence[2].

The electrical resistivity of the composite has shown temperature dependence consistent with the fluctuation-induced tunneling model. This model assumes that the electrical resistance of the nanotube network is dominated by the interconnections between the individual nanotubes and CuO nanoparticles rather than by the nanotube resistance itself[3].

II. METHODS

The MWCNTs were obtained from Neutrino Co (Iran), synthesized by catalytic carbon vapor deposition (CCVD) process. As reported by the producer, the nanotubes are purified to produce a carbon purity >95 wt% and an ash content of <1.5 wt%. The specific surface area (SSA) determined with the BET method is around 200 m2 /g. An average diameter of about 10-20 nm and a true density of 2.1 g/cm3 characterize the MWCNTs morphology. The MWCNTs were employed at 1 wt% as the highly conductive matrix to tune the electrical resistance properties of the basic epoxy/CuO nanoparticles matrix. An amount of 0.5 g of epoxy diglycidil-ether bisphenol-A (DGEBA) resin, 0.49 g of CuO nanoparticles and 0.01 g of the MWCNT were sonicated in an ultrasound bath for 45 min[4,5]. The nanocomposite paste material had excellent stability under normal ambient temperature (from -3 oC to +120 oC) and humidity (from 0% RH to even condensation 100% RH). The resulting paste was manually applied by Doctor Blade method as a thin layer on the copper conductive surface of interdigitated electrode arrays and subsequently cured on a hot plate at 100 oC for 24 h. Interdigitated electrode arrays with dimensions of about 2×1 cm2 were prepared by common printed circuit board (PCB) fabrication process comprised of laser printing and subsequent chemical etching in FeCl3 solution. Resistivity of the electrode array sensor as a function of temperature was measures in a closed thermostat heating chamber equipped with a precision (±0.01 oC) NTC based temperature control and monitoring system. For resistivity measurements, each electrode array sensor was connected in series with a DC power supply of 30.00V and a digital voltmeter with an internal DC resistance of 985 KΩ. Voltage drop on the digital voltmeter was used to calculate the resistance of the sensor.

III. RESULTS AND DISCUSSION

Results showed that the developed temperature sensor exhibits exponentially decreasing resistance-dependence on the temperature with a rather steep decrease in the resistance from about 28 MΩ at 25 °C to about 150 kΩ at 110 °C, i.e. a relative variation of about 99.46 %. Also the fabricated sensor showed very fast characteristics and long term stability as the times of response and recovery obtained for the sensor are in the order of a few ten seconds (typically less than one minutes).

IV. CONCLUSION

Due to ease of preparation, good reproducibility, satisfactory long term stability and high sensitivity, this temperature sensor based on epoxy resin/multiwalled carbon nanotubes/copper (II) oxide nanocomposite, can be practically applied for routine ambient temperature sensing and monitoring.

REFERENCES

[1] Biercuk M. J., Llaguno, M. C., Radosavljevic, M., Hyun, J. K., Johnson, A. T. and Fischer, J. E., Carbon nanotube composites for thermal management, Appl. Phys. Lett., 80 (2002) 2767-2769.

[2] H. C. Neitzert, A. Sorrentino, and L. Vertuccio, “Epoxy/MWCNT composite based temperature sensor with linear characteristics,” in Sensors and Microsystems: Lecture Notes in Electrical Engineering, vol. 54, P. Malcovati, A. D’Amico, and C. Di Natale, Eds. New York: Springer-Verlag, 2010, pp. 241–245.

[3] Fung, C. K. M. and Li, W. J. Ultra-low-power Polymer Thin Film Encapsulated Carbon Nanotube Thermal Sensors, Proc. of the 4th IEEE Conf. on Nanotechnology (2004) 156-160.

[4] L. Guadagno, C. Naddeo, V. Vittoria, A. Sorrentino, L. Vertuccio, M. Raimondo, V. Tucci, B. De Vivo, P. Lamberti, G. Iannuzzo, E. Calvi, and S. Russo, “Cure behavior and physical properties of epoxy resin— Filled with multiwalled carbon nanotubes,” J. Nanosci. Nanotechnol., vol. 10, pp. 2686–2693, 2010.

[5] H. C. Neitzert, A. Sorrentino, L. Vertuccio, and V. Vittoria, “Curing monitoring of an epoxy/carbon nanotube composite using DC conductivity measurements,” presented at the 26th Polym. Process. Soc. Meet. (PPS26), Banff, Canada, 2010.

Fabrication and Investigation of an Easy-to-Prepare Extremely Sensitive Resistive-Type Humidity Sensor Based on Epoxy Resin/MWCNTs Nanocomposite

Iraj Ahadzadeh*[1], Amin Norouzi[2], Samira Nematdoust[3], Mahtab Khattat Khiyabani[4], Niloufar Farhang Benam[5]
**Corresponding Author, Email: irajahadzadeh@gmail.com, Ahadzadeh@tabrizu.ac.ir*
1-Assistant Professor, Department of Physical Chemistry, Faculty of Chemistry, University of Tabriz, Tabriz, Iran
2- M.Sc. Student of Nano Chemistry, Faculty of Chemistry, University of Tabriz, Tabriz, Iran
3- Ph. D Candidate, Department of Organic Chemistry, Faculty of Chemistry, University of Tabriz, Tabriz, Iran
4- M.Sc. Student of Nano Chemistry, Faculty of Chemistry, University of Tabriz, Tabriz, Iran
5- M.Sc. Student of Organic Chemistry, Faculty of Chemistry, University of Tabriz, Tabriz, Iran

Abstract: In resistive humidity sensors, the change in electrical resistance of a material due to humidity is measured. Typical materials are salts and conductive polymers. In this research, an easy-to-prepare extremely sensitive resistive-type humidity sensor based on nanocomposite of epoxy resin/multiwall carbon nanotubes (MWCNTs) was fabricated and investigated.

Keywords: MWCNTs, Epoxy Resin, Humidity Sensor, Nanocomposite

I. INTRODUCTION

The humidity sensor is a differential capacitance type that consists of a layer sensitive to water vapor[1,2].

Also the fabricated sensor showed very fast characteristics and long term stability as the times of response and recovery obtained for the sensor were in the order of a few seconds (typically less than 10 s).

II. METHODS

The MWCNTs were obtained from Neutrino Co (Iran), synthesized by catalytic carbon vapor deposition (CCVD) process. As reported by the producer, the nanotubes are purified to produce a carbon purity >95 wt% and an ash content of <1.5 wt%. The specific surface area (SSA) determined with the BET method was around 200 m^2 /g. An average diameter of about 10-20 nm and a true density of 2.1 g/cm^3 characterize the MWCNTs morphology. The multiwalled carbon nanotubes (MWCNTs) were employed at about 0.5 wt% as the highly conductive matrix to finely adjust and also to reach a uniformly distributed electrical resistance properties of the epoxy basic matrix[3]. An amount of 1 g of epoxy diglycidil-ether bisphenol-A (DGEBA) resin and 0.01 g of the MWCNT were sonicated in an ultrasound bath for 120 min[4]. The nanocomposite paste material had excellent stability under normal ambient temperature (from 0 ^{o}C to +80 ^{o}C) and humidity (from 0% RH to even condensation 100% RH) without any damage and/or decrease in its cohesion. The resulting paste was manually applied by Doctor Blade method as a thin layer on the copper conductive surface of interdigitated electrode arrays and subsequently cured on a hot plate at 100 ^{o}C for 48 h[5]. Interdigitated electrode arrays with dimensions of about 2×1 cm^2 were prepared by common printed circuit board (PCB) fabrication process comprised of laser printing and subsequent chemical etching in $FeCl_3$ solution. Resistivity of the electrode arrays as a function of relative humidity was measures in a closed thermostat chamber equipped with a precision (±0.01 ^{o}C) NTC based temperature control and monitoring system. Various relative humidity (RH) levels in the closed chamber were developed by placing a 50 ml of distilled water in a beaker on an electric heater inside the chamber. Relative humidity inside the chamber was monitored by a commercial hygrometer with a resolution of ±5% RH. Also, for confirmation purposes, a series of saturated salt calibration tests were performed with sodium chloride saturated solution bath for higher end calibration point of approximately 75% RH and lithium chloride saturated solution bath for lower end of about 11% RH. For resistivity measurements, each electrode array sensor was connected in series with a DC power supply of 30.00 V and a digital voltmeter with an internal DC resistance of 985 KΩ. Voltage drop on the digital voltmeter was used to calculate the resistance of the sensor.

III. RESULTS AND DISCUSSION

Results showed that the developed sensor exhibits extremely high resistance-dependence on the relative humidity with a very sharp decrease in the resistance from about 30000 MΩ at 4% RH to just about 0.005 MΩ at 85% RH, i.e. a relative variation of practically equal to 100%.

IV. CONCLUSION

Due to ease of preparation, good reproducibility, satisfactory long term stability and extreme sensitivity, this resistive-type humidity sensor based on epoxy resin/multiwall carbon nanotubes nanocomposite, can be practically applied for routine humidity sensing and monitoring purposes.

REFERENCES

[1] H. Yu, T. Cao, L. Zhou, E. Gu, D. Yu, D. Jiang, Layer-by-Layer assembly and humidity sensitive behavior of poly(ethyleneimine)/multiwall carbon nanotube composite films, Sens. Actuators B: Chem. 119 (2006) 512–515.
[2] J.F. Feller, H. Guézénoc, H. Bellégou, Y. Grohens, Smart poly(styrene)/carbon black conductive polymer composites films for styrene vapour sensing, Macromol. Symp. 222 (2005) 273–280.
[3] M. Castro, J. Lu, S. Bruzaud, B. Kumar, J.F. Feller, Carbon nanotubes/poly(e-caprolactone) composite vapour sensors, Carbon 47 (2009) 1930–1942.
[4] L. Liu, J.C. Grunlan, Clay assisted dispersion of carbon nanotubes in conductive epoxy nanocomposites, Adv. Funct. Mater. 17 (2007) 2343–2348.
[5] Chena H W, Wua R J, Chana K H, et al. The application of CNT/Nafion composite material to low humidity sensing measurement. Sensors and Actuators B, 2005, 104: 80.

Propranolol removal from aqueous solution using ionic liquid-LDH nanocomposite

***Fateme Noorni*[1], *Bahram Ghalami- Choobar*[1*], *Mohammad Hossein Ahmadi Azqhandi*[2]**

[1]*Department of Chemistry, Faculty of Science, University of Guilan, P.O. Box: 19141, Rasht, Iran*
[2] *Applied Chemistry Department, Faculty of Gas and Petroleum (Gachsaran), Yasouj University, Gachsaran, 75813-56001, Iran*
Email:B-Ghalami@guilan.ac.ir

Abstract*:* Propranolol is very significant drug but causes some problems and side effects for public and animals while enter to the surface water. In this work, for propranolol removal from water ionic liquid- layered double hydroxides nanocomposite were synthesized, characterized and exploited as adsorbent in aqueous medium. The propranolol in water was monitored by spectrophotometer at wavelength of 290 nm. The maximum removal of propranolol was 95% through preliminary concentration 60ppm; sonication time: 15 min., pH: 8.0, adsorbent dose: 15mg and 35 °C temperature. The sorption data modeled by Langmuir, Freundlich, and Temkin models. The thermodynamic properties; ΔG°, ΔH° and ΔS° in optimal condition and different temperature was calculated. Kinetics modeling demonstrated that the removal of propranolol followed by pseudo first order.

Keywords: LDH; ionic liquid; propranolol, removal; nanocomposite.

I. INTRODUCTION

Recently the pollution of water because of drug residues is rising continuously [1]. Among them, β-blockers are being consumed worldwide due to maximum patients of the cardiovascular diseases globally [2]. Amongst, propranolol (PPL) is the most recommend β-blocker owing to its wide range of using. Since, the PPL frequent prescribe as β-blocker it is possible to be observed in many water resources as pollutant.

On the other hand, PPL exist in the water creates several problems, include infantile haemangiomas, feasibility reduction, insomnia, vivid dreams and nightmares, diabetes, cold extremities, nausea, glucose alteration and lipid metabolism [3]. Hence, it is valuable to use water without propranolol contaminated. Thus, the efforts were made to expand economic, effective, fast, and reproducible sorption method for PPL removal. In this work, Ionic liquid-LDH nanocomposite was prepared, characterized and used for the purpose. The residual drug was determined by UV-Visible spectroscopy.

II. METHODS

Ethanolamine, acetic acid, phosphoric acid, ethanol, $Al(NO_3)_3$. $Mg(NO_3)_2.6H_2O$, NaOH and Na_2CO_3 were bought from Merck. All reagents were used without further purification.

Hydroxyl ammonium ionic liquids were prepared by neutralization of ethanolamine in ethanol with phosphoric acid: 0.3 mole of 2-aminoethanol was dissolved in 50 mL of ethanol to form a liquid mixture. The obtained mixture was placed in a water bath at T=298.2K. A mixture of 0.3 mole of phosphoric acid dissolved in 50 mL of ethanol was added dropwise to the 2-aminoethanol mixture in about 60 min. The reaction lasted for 2 h. The solvent was removed by evaporation under vacuum. The resulting crude residue was filtered and dried under vacuum at 323.2 K for 48 h.

The preparation of ILs/LDHs intercalation composites were made by using co-precipitation technique. The reaction was carried out in a 250 mL four neck round bottom flask with a magnetic stirrer. 0.5 mole ionic liquid and 30 mL water were mixed up uniformly and put into the flask. The mixture was heated to 90 °C in a water bath. A solution was prepared by mixing $Mg(NO_3)_2.6H_2O$ and $Al(NO_3)_3.9H_2O$ ($Mg^{2+}/_{Al^{3+}}$ molar ratio of 2 and Mg^{2+}+ concentration is 0.5 M) in 100 mL of deionized water. This solution and the aqueous solution of 1.0 M NaOH were simultaneously added dropwise into a flask under vigorous stirring. Meanwhile, the pH value of the mixed suspension liquid should be controlled at about 10 during the dropping process. Afterwards, the samples should be acutely stirred for 5 h at 90 °C and then aged at 100 °C for 24 h. The precipitate was filtrated and then washed with deionized water and dried in an oven at 80 C for 12 h.

III. RESULTS AND DISCUSSION

The XRD patterns of LDHs indicate the sharp and symmetric peaks which provide perfect sign the sample are well crystallized. In the ILs/ LDHs, the position of diffraction of some peaks of LDHs moved to small angle integrally corresponding to the increase of interlayer spacing. To further verify the above deduction, the made samples were characterized by FTIR. For LDHs, the broad peak was observed at 3500 cm^{-1} (vibration of hydroxyl group stretching), originated by the interlayer water molecules and hydroxyl groups in the brucite-like layers. The weak band around 1640 cm^{-1} region (HOH) is due to the H_2O from the interlay water. The 1385 cm^{-1} peak corresponds to the carbonate group. Following the ionic exchange of carbonate by ILs, several characteristic bands are observed at 1550 cm^{-1} (antisymmetric vibrations of -COOH groups) 1403 cm^{-1} (symmetric vibrations of -COO groups) and 1159 cm^{-1} (C-N stretching vibration). These results show that the anion radical of ILs has efficaciously intercalated into the gallery of LDHs and substitute part of the carbonate group.

Also, the specific surface area of LDH and ILs/LDH, as derived from the adsorption data using a BET equation, are 98.6 and 105.6 m^2 /g, respectively. Clearly, a large specific surface area can be an important factor in the adsorption of organic species by the sorbents.

Adsorption characteristics: The fixing of the intake of PPL was determined by various adsorption parameters. Optimized parameters were initial PPL concentration, sonication time, pH, dosage and temperature. Optimized values were found at 0.015 g, 15 min, 8.0, 60 ppm and 35°C, respectively and lead to achievement 95% removal percentage which strongly confirmed by five replicates at these conditions.

The adsorption isotherms: The equilibrium adsorption isotherms are fundamental in describing the interactive behavior between adsorbates and adsorbent and are essential in giving an idea of the adsorption capacity of the adsorbent. The sorption isotherms were established using ILs/ LDHs suspension in PPL solutions at different concentrations (10–70ppm). The mixtures were stirred in a thermostatic bath at 35 °C through equilibrium times and then centrifuged. The PPL equilibrium concentration in the supernatants was made the same above. The obtained data modeled by Langmuir, Freundlich, and Temkin models. The isotherm results are summarized in table 1.

Kinetics of adsorption: The pseudo-second-order model was found to explain the adsorption kinetics most effectively and the theoretical qe values were closer to the experimental qe values. As a result, the adsorption fits to the pseudo-second order better than the pseudo-first-order kinetic model.

Thermodynamics of Adsorption

The study of the temperature effect on PPL adsorption on ILs/LDHs allowd us to get the thermodynamic parameters (Gibbs free energy ΔG°, enthalpy ΔH° and entropy ΔS°). The positive ΔH° values (20.59 kJ/mole) reveal that the adsorptions on ILs/LDHs are endothermic and physical in nature. The positive values of ΔS° (95.98 J mole^{-1} K^{-1}), which indicate an increase of randomness at the interface adsorbent/adsorbate during adsorption process. Furthermore, the negative values of ΔG° indicate that the adsorptions onto ILs/LDHs is spontaneous. The ΔG° for 25, 35 and 45°C was -8.01, -8.98 and -9.93 respectively.

Table1: Obtained parameters for Langmuir, Freundlich and Temkin Isotherms

Isotherm	**parameters**	
Langmuir	q_{max} K_L R^2	301.20 19.18 0.9699
Freundlich	K_f 1/n R^2	259.96 0.06 0.9978
Temkin	B_1 K_T R^2	250.98 17.98 0.8978

IV. CONCLUSION

The ionic liquid-LDH nanocomposite was made with green technology with good yield. The developed sorption technology for the removal of propranolol drug residue indicated removal up to 95%. The adsorption method was effectual and choosy for propranolol. The kinetics modeling indicated pseudo-second-order mechanisms accurately described the PPL adsorption. The experimental factors such as adsorbent dosage and pH to affect the adsorption were measured. The adsorption isotherm data are in agreement with the Freundlich model. Thermodynamic data indicated PPL adsorptions were spontaneous and endothermic nature.

REFERENCES

[1] M.H.A. Azqhandi, M. Foroughi, E. Yazdankish, Journal of colloid and interface science, (**2019**).

[2] M.H.A. Azqhandi, B.V. Farahani, N. Dehghani, Materials Science and Engineering: C, 79 **(2017)** 841-847.

[3] S. Rossi, Australian medicines handbook, Adelaide: Australian Medicines Handbook, **(2006)** 2-3.

Naproxen removal from aqueous solution using Fe_3O_4-PEI-GO nanocomposite

Seyedeh Fateme Noorni*[1], *Bahram Ghalami- Choobar*[1]*, *Mohammad Hossein Ahmadi Azqhandi*[2], *Mohammad Hassan Omidi*[1]
[1]*Department of Chemistry, Faculty of Science, University of Guilan, P.O. Box: 19141, Rasht, Iran*
[2] *Applied Chemistry Department, Faculty of Gas and Petroleum (Gachsaran), Yasouj University, Gachsaran, 75813-56001, Iran*
Email:B-Ghalami@guilan.ac.ir

Abstract*:* Naproxen (NPE) is one of the mostly consumed drugs worldwide and is most abundant in wastewater. In this paper, a novel magnetic polyethyleneimine - graphene oxide ($\boldsymbol{Fe_3O_4}$-PEI-GO) was synthesized, characterized and used as adsorbent for removal of NPE residue in aqueous medium. The corresponded variables influencing the removal efficiency were adjusted. A suitable performance was made under the optimal conditions. The pseudo-first-order kinetic model, pseudo-second-order kinetic model, Weber–Morris intra-particle diffusion model, and Bangham model were used for determination of adsorption mechanisms. Also, the isotherm and thermodynamic properties (i.e. ΔG°, ΔH° and ΔS°) were calculated for this process.

Keywords: Naproxen; polyethyleneimine; graphene oxide, removal; nanocomposite.

I. INTRODUCTION

Drugs are harmful pollutants due to they are possibly bioactive chemicals in environment [1]. These materials enter to the water in different way such as industrial or people residue (e.g. urine and improper disposal). The most used pharmaceuticals are analgesics, anti-inflammatory drugs, antipyretic, and antibiotics [2]. Especially, the analgesics and antipyretic drugs are mostly used in daily life. NPE is one of the most used drugs in the world. NPE can be found in environment

There are different elimination methods for removal of drug residuals from water, for example; Adsorption, ozonation, nanofiltration, and advanced oxidation processes [3].

In the past decade, the more efforts were made to prepare the economic, effective, fast, and reproducible adsorbent for removal. In this work, a novel magnetic polyethyleneimine - graphene oxide was prepared, characterized and used for the purpose. The residual drug was estimated by UV-Visible spectroscopy.

II. METHODS

The chemicals used were of analytical in this work. Polyethyleneimine (PEI, M.W. 70000, 99%) was purchased from Merck.

Synthesis of Fe_3O_4@PEI:

The magnetic polyethyleneimine composite (Fe_3O_4@PEI) was synthesized via a green method [4, 5]. Briefly, $FeCl_3 \cdot 6H_2O$ (5g) and $FeCl_2 \cdot 4H_2O$ (3.7g) was homogeneously dispersed in 100 mL of water, by ultrasonication. Then, 10 mL of ammonia (25%) was slowly added and the solution was continuously stirred for 10 min at 80°C. After this time, 10 mL of PEI 10% was added to the above mixture and the solution was sonicated for another 10 min to obtain a transparent solution. This solution was then refluxed for 5 h. The precipitate was filtrated and then washed with deionized water, ethanol and dried in an oven at 80 C for 12 h.

Synthesis of Fe_3O_4-PEI-GO

In the first graphene oxide was prepared based on the previous report [6, 7].

The synthesized GO (15 mg) was sonicated in 50 mL of water. The prepared Fe_3O_4@PEI (200 mg) and the GO mixtures were sonicated for 20 minutes [4, 8]. The reaction was performed at 90°C for 3 h. Then, the obtained product (Fe_3O_4-PEI-GO) was thoroughly rinsed with water, and finally dried in vacuum at 50°C overnight.

III. RESULTS AND DISCUSSION

The morphologies of $\boldsymbol{Fe_3O_4}$-PEI and $\boldsymbol{Fe_3O_4}$-PEI-GO were investigated by TEM. The TEM of $\boldsymbol{Fe_3O_4}$-PEI nanocomposite showed a spherical shape with slightly aggregation. After loading $\boldsymbol{Fe_3O_4}$-PEI on the GO, the obtain TEM image show that nanomagnetic-PEI had grown and well distributed on the surface of GO.

It well known that the FT-IR spectrometry can be applied to recognize the chemical structures of the polymer nanocomposite. Therefore, the $\boldsymbol{Fe_3O_4}$-PEI and $\boldsymbol{Fe_3O_4}$-PEI-GO were examined by FTIR (the figure is not shown). In the spectrum of magnetic-polyethylene imine, the peaks at 2950, 2928, 2850, 1550, 1465 and 1050 cm^{-1} was observed that they can be assigned to C-H stretching of the alkyl chain, the bending vibration of N-H, and the stretching vibration of C-N in the polyethylene imine structure. The FTIR peaks of $\boldsymbol{Fe_3O_4}$-PEI-GO proved that the oxygen-containing in the

$\boldsymbol{Fe_3O_4}$-PEI was successfully modified with GO. Moreover, the broad peaks at 1570 cm^{-1} assigned to the stretching vibrations of C=C in the GO was appeared.

The XRD analysis was used to recognize the crystalline phase and structure of $\boldsymbol{Fe_3O_4}$-PEI and $\boldsymbol{Fe_3O_4}$-PEI-GO. According to the XRD patterns (Fig. 1), both $\boldsymbol{Fe_3O_4}$-PEI and $\boldsymbol{Fe_3O_4}$-PEI-GO indicated characteristic diffraction peaks of $\boldsymbol{Fe_3O_4}$ matching well with JCPDS card, file No. 19-0629. The obtained results indicated that the crystal structure of magnetic would not be damaged in the preparation of nanocomposite.

Adsorption characteristics: The tests were made in batch mode by mixing a specific amount of adsorbent and 50 mL of NPE solution. The effects of contact time, amount of adsorbent, initial NPE concentration, pH, and temperature of the naproxen solutions were studied. The equilibrium time of adsorption was between 0–50 min.

The adsorption isotherms: The equilibrium adsorption isotherms are fundamental in describing the interactive behavior between adsorbates and adsorbent and are essential in giving an idea of the adsorption capacity of the adsorbent. The sorption isotherms were established using Fe_3O_4-PEI-GO suspension in NPE solutions at different concentrations (5-35 ppm). The suspensions were stirred in a thermostatic reciprocating shaker bath at 40 °C during equilibrium times and then centrifuged. The NPE equilibrium concentration in the supernatants was determined as above. The sorption data modeled by Langmuir, Freundlich, and Temkin models. The isotherm results are summarized in table 1.

Kinetics of adsorption: The pseudo-first-order kinetic model, pseudo-second-order kinetic model, Weber–Morris intra-particle diffusion model, and Bangham model were applied to the kinetic data. The obtained result show that the pseudo-second-order model was better to explain the adsorption kinetics. Also, the theoretical qe values were closer to the experimental qe values.

Thermodynamics of Adsorption: The study of the temperature effect on NPE adsorption on Fe_3O_4-PEI-GO enabled us to determine the thermodynamic properties (Gibbs free energy ΔG°, enthalpy ΔH° and entropy ΔS°).
The adsorption of naproxen on Fe_3O_4-PEI-GO is spontaneous because the obtained ΔG° values are negative. The ΔG° values vary between -4.75 and -7.09 kJ/mol. The increasing temperature caused decrease in ΔG° value. The both ΔS° and ΔH° values are positive. According to ΔH° values, adsorption processes are endothermic. This result shows that while NPE adsorbed on the adsorbents, randomness was increased on the surface.

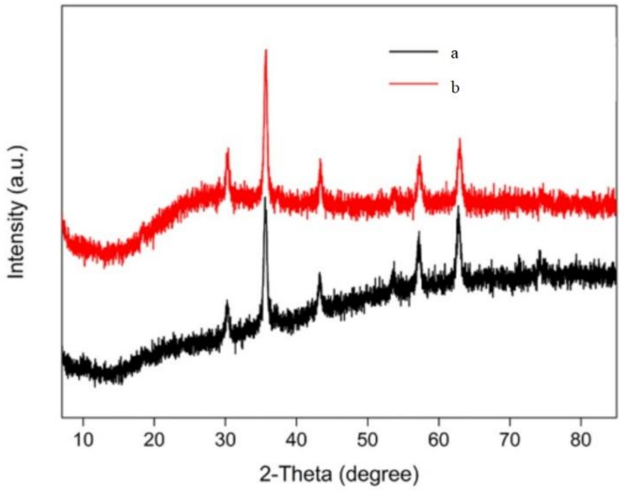

Fig. 1: XRD spectra of Fe_3O_4-PEI (a) and Fe_3O_4-PEI-GO (b).

Table 1: Obtained parameters for Langmuir, Freundlich and Temkin Isotherms

Isotherm	parameters	
Langmuir	q_{max}	200.98
	K_L	12.57
	R^2	0.999
Frendlich	K_f	180.95
	1/n	0.32
	R^2	0.978
Temkin	B_1	157.98
	K_T	18.25
	R^2	0.0.968

IV. CONCLUSION

The Fe_3O_4-PEI-GO nanocomposite were synthesized, characterized and used as adsorbent for naproxen removal. The adsorption efficiency of NPE reached 94.89 % at 40 °C, and pH 6.2 on the 15mg adsorbent. The kinetics modeling indicated pseudo-second-order mechanisms accurately described the NPE adsorption. The adsorption isotherm data are in agreement with the Langmuir model. Thermodynamic data indicated NPE adsorptions were spontaneous and endothermic nature.

REFERENCES

1. K. Kümmerer, *Chemosphere*, 2001, **45**, 957-969.
2. J. Rivera-Utrilla, M. Sánchez-Polo, M. Á. Ferro-García, G. Prados-Joya and R. Ocampo-Pérez, *Chemosphere*, 2013, **93**, 1268-1287.
3. M. H. A. Azqhandi, M. Foroughi and E. Yazdankish, *Journal of colloid and interface science*, 2019.
4. J. Geng, Y. Yin, Q. Liang, Z. Zhu and H. Luo, *Chemical Engineering Journal*, 2019, **361**, 1497-1510.
5. W. Lu, M. Ling, M. Jia, P. Huang, C. Li and B. Yan, *Molecular medicine reports*, 2014, **9**, 1080-1084.
6. Y. He, Y. Xia, J. Zhao, Y. Song, L. Yi and L. Zhao, *Applied Physics A*, 2019, **125**, 160.
7. J. W. S. Hummers, *Journal*, 1957.
8. J.-W. Liu, T. Yang, L.-Y. Ma, X.-W. Chen and J.-H. Wang, *Nanotechnology*, 2013, **24**, 505704.

Electrophoretic Deposition of Graphen-Cobalt-Phosphor Based Nanocomposite for Hydrogen Evolution Reaction

Ganji Lisar. Samaneh*, ***Ahmadi Daryakenari. Ahmad***
Department of Nanomaterials, University of Guilan, Rasht, Iran
Email: Samane.lisar@gmail.com

Abstract*:* A higly active electrocatalyst for hydrogen evolution reaction is developed based on cobalt phosphor on graphene. The different temperature for the phosphating process could be show different catalytic activity. The electrode which was phosphidated in 450°C exhibit the best of result for HER by a small onset potential -157 mV v.s RHE and a small over-potential value of -210 mV at 10 mA cm^{-2}.

Keywords: HER, Electrocatalyst, Electrophoretic, Graphene cobalt phosphide.

I. INTRODUCTION

Hydrogen as one of the most clean and renewable energy carrier can be a suitable alternative for fossil fuels. Recently, electrochemical water splitting has attracted growing attention [1]. The electrochemical hydrogen evolution reaction needs catalysts with a high current density at a low overpotential. Platinum group noble metals are the most efficient catalysts for the hydrogen evolution reaction (HER), but suffer from scarcity and high cost. Therefore, the development of new advanced HER electrocatalysts, especially those composed of inexpensive and abundant material is very important. One of this promising HER electrocatalysts is cobalt phosphor composite. In this paper a type of non-noble metal composite, composed of cobalt phosphor and graphene have been studied as an economical material for HER. Previously studies have been described that phosphide compositions performed excellent properties for hydrodesulphurization (HDS), having a similar operation mechanism with HER mechanism. Hence, we could consider Co phosphides as a new candidate for HER catalysts [2]. Further the use of Graphene as a support material can modify the conductivity of the composite and also increase the dispersion of the active sites and stop the rapid decrease of activity sites [3]. In order to enhance electrochemical result of the fabricated nanocomposites, the different temperatures for the phosphating process was carried out. X-ray diffraction (XRD) and scanning electron microscopy (SEM) for analyzing the structures, morphologies and compositions of the fabricated catalysts were implemented. Moreover HER activities were studies by using linear sweep voltammetry (LSV) techniques.

II. METHODS

Materials: graphene, ethylene glycol, cobalt acetate tetrahydrate, sodium hypophosphite monohydrate, acetone, I_2, nickel foam are purchased from Merck

Synthesis of the Gr-Co_3O_4 nanostructures: The Gr-Co_3O_4 nanostructures were fabricated by a hydrothermal method. In this approach, graphene (33 mg) and cobalt acetate tetrahydrate (168 mg) were added in 50 ml of ethylene glycol and then were stirred for 30 min. The prepared solution was transferred in Teflon-lined steel and heated in a silicon oil bath at 180 °C for 18 h. Next, the solution was sonicated for 30 min at room temperature. The autoclave was then allowed to cool naturally to ambient temperature. The final products were washed with redistilled water several times to remove unreacted ingredients, and dried at 80 °C for 4 h was

Synthesis of the Gr-CoP Nanocomposites: 50 mg of the Gr-Co_3O_4 were phosphidated at different temperatures of 300, 350, 400, 450 and 500 °C for 2 h with a heating rate of 10 °C min^{-1} under atomosphere with 250 mg of NaH_2PO_2 to prepare the Gr-CoP Nanocomposites.

Preparation of working electrodes: To obtain a stable suspension for the EPD process, the as-prepared Gr-CoP nanocomposites (25 mg) were dispersed in 25 mL of acetone for 1 h using an ultrasonic. To obtain positively charged the Gr-CoP nanocomposites; I_2 was added during the EPD process. When I_2 is mixed with acetone, H^+ ions are produced in the EPD solution. The H^+ ions attached on the

Gr-CoP nanocomposites thus producing the positive nanocomposites. The deposition EPD cathode electrode was a nickle foam plate with the dimensions of 0.5 cm*0.5 cm and the anode electrode was made of a stainless steel with the same shape as the anode electrode. The distance between the two electrodes in the EPD solution was 1.5 cm. The EPD technique was operated using a DC voltage of 50 V.

Electrochemical measurements: Electrochemical measurements were performed in a standard three-electrode system at room temperature. Prepared electrodes were used as the working electrode, and Pt wire and Ag/AgCl (in saturated KCl solution) electrodes were applied as the counter and reference electrodes, respectively. The electrolyte used was 1.0 M NaOH solution. The linear sweep voltammetry (LSV) tests were measured by using a SAMA electrochemical analyzer. All potentials showed in this work are converted to the reversible hydrogen electrode (by using the formula $E_{RHE} = E_{Ag/AgCl} + 0.059pH + 0.197$ V, where PH is PH value of the electrolyte).

Current densities are the ratios of currents and geometric areas of working electrodes.

III. RESULTS AND DISCUSSION

The LSV experiments were carried out to indicate the HER electrochemical performance of the Gr-CoP electrodes which were phosphidated at 300, 350, 400, 450 and 500°C. As shown in Fig. 1c), the curves were obtained in 0.5 M NaOH solution with a scan rate of 2 mV s^{-1}. The commercial Pt catalyst was studied for comparison. It can be seen that the Pt catalyst illustrates a small onset potential (E_{onset}) of -22 V, giving a current density (j) of 10 mA cm^{-2} just at a small over-potential of -60 mV.. However,the Gr- CoP were calcinated on 300, 350, 400, 450 and 500°C show E_{onset} values of -187, -181, -170, -157 and -207 mV, respectively. These results exhibit the electrode which was phosphidatedat 450°C demostrate the best of result for HER was obtained by a small onset potential -157 mV and a small over-potential value of -210 mV at 10 mA cm^{-2}.

The SEM image of sample which was calcinated at 450°C was shown in fig. 1.a).It can be observed that cobalt species nanoparticles with a size of smaller than 50 nm were deposited on tthe planar morphology of nanographitic flakes (Fig. 1.b)) Moreover, the obtained XRD pattern belongs the structures of CoP and Co_2P nanocomposites as shown in Fig. 1.d).

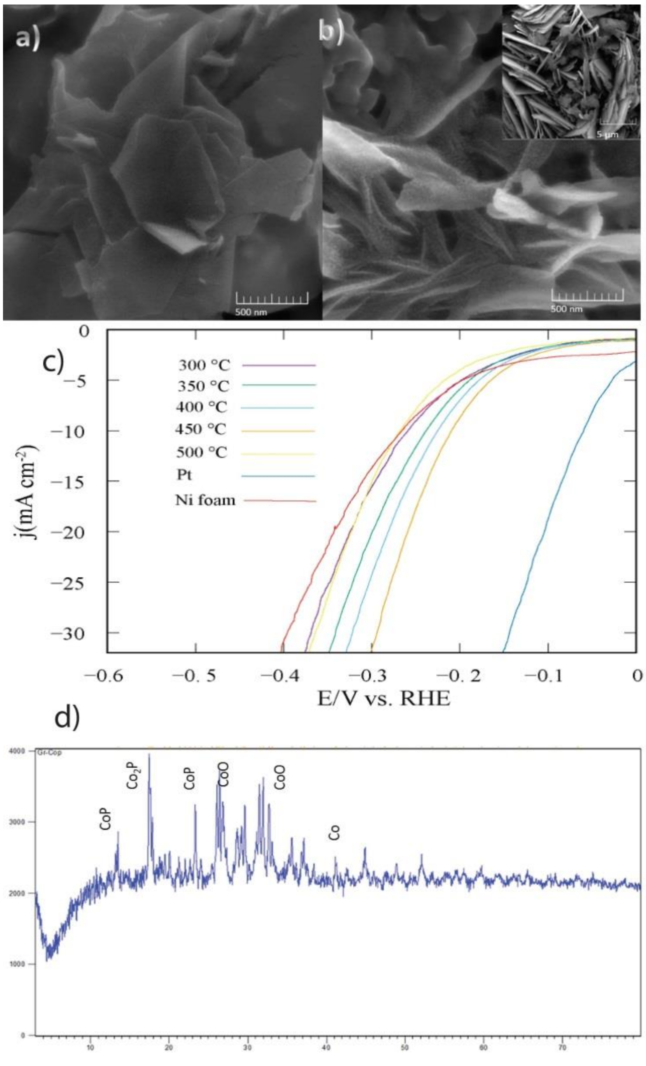

Fig.1: SEM of a) Gr- CoP nanocomposite, b) Gr- CoP electrode, c) HER performances of Gr-CoP at different temperature in 1.0 M NaOH with scan rate of 2 mVs^{-1} and d) XRD pattern of CoP based material.

IV. CONCLUSION

Gr-CoP nanostructured were synthesized by a combination methods of hydrothermal and electrophoretic deposition. The best temperature for phosphating process were determined at 450°C by a small onset potential -157 mV and a small over-potential value of -210 mV at 10 mA cm^{-2}.

REFERENCES

[1] Fulin Yang, Yongting Chen, Gongzhen Cheng, Shengli Chen, and Wei Luo; An Ultrathin Nitrogen-Doped Carbon Coated with CoP for Efficient Hydrogen Evolution; ACS Catal., Just Accepted Manuscript • Publication Date (Web): 24 Apr 2017.

[2] Jiahai Wang, Wei Cui, Qian Liu, Zhicai Xing, Abdullah M. Asiri and Xuping Sun; Recent Progress in Cobalt-Based Heterogeneous Catalysts for Electrochemical Water Splitting; Adv. Mater. 2016, 28, 215–230.

[3] Mian Li, Xiaotian Liu, Yueping Xiong, Xiangjie Bo, Yufan Zhang, Ce Hana and Liping Guo; Facile synthesis of various highly dispersive CoP nanocrystal embedded carbon matrices as efficient electrocatalysts for the hydrogen evolution reaction; J. Mater. Chem. A, 2015, 3, 4255–4265.

A Novel ZnO/BiFeO₃ Photocatalyst for Highly Efficient Visible Photocatalytic Performance

N. Foghahazade[a], ***M. Hamzehloo***[a *], ***H.Behnejad***[a], ***M. Mousavi***[a]
[a] *Department of Physical Chemistry, School of Chemistry,College of Science, University of Tehran, Tehran, Iran*
Email: majhamzehlo@ut.ac.ir

Abstract*:* Nowadays, a major issue about natural water resources protection is the removal of organic pollutants from different industrial sources. In this research, $ZnO/BiFeO_3$ heterojanction nanocomposites have been successfully synthesized and studied by FESEM analysis. The photocatalytic activity of as-prepared samples was evaluated by degradation of RhB as pollutant target under visible light. The pseudo-first-order constants for RhB degradation reaction on the samples reveal that the $ZnO/BiFeO_3$ (30%) heterostructure has excellent photocatalytic ability, which was about 15.3 times as high as the pure ZnO. The enhanced photocatalytic activity could be assigned to the formation of heterojunction at the interface of ZnO and $BiFeO_3$.

Keywords: $ZnO/BiFeO_3$, Heterojunction photocatalyst, Photocatalytic mechanism, Visible-light-driven, Electron–hole separation, Wastewater treatment.

I. INTRODUCTION

In recent decades, Environmental pollution, global warming and energy shortages are three major challenges facing modern society. Environment treatment via advanced oxidation processes (AOPs) by energetic oxidizing agents such as $^{\bullet}O_2^-$, $OH^{\bullet}$, and h^+ leads to the complete degradation and mineralization of contaminants [1-3]. Heterogeneous photocatalysis as one of the most appealing AOPs has attracted more attention [4-7]. Zinc oxide (ZnO) is a well-known semiconductor due to its amazing properties like low-cost, high chemical stability, biocompatibility, favorable excellent electrical, mechanical and optical properties, which has been widely used in various energy conversion and photocatalytic fields [8-10]. Some shortcoming such as wide band gap and rapid recombination of charge carriers restrict the photoability of ZnO. Numerous methods such as morphology control, doping with metal and non-metals, and construction of heterojunction semiconductors have been employed to overcome these drawbacks. Among all the methods forming heterojunction with a visible-light-driven semiconductor is an ideal strategy to collaboration the absorption of visible light and separation of charge carriers, and then increases the photocatalytic activity [11-13]. The perovskite-type $BiFeO_3$ is known as a high chemical stable with good carrier transport properties and one of the visible-light-induced photocatalysts with a band gap of ~2.2 eV [14, 15]. In this research we prepared $ZnO/BiFeO_3$ nanocomposites and studied their photoactivity for eliminating RhB dye in an aqueous solution under visible-light irradiation.

II. METHODS

The ZnO was prepared by ultrasonic method with $Zn(NO_3)_2.4H_2O$ as precursor [16]. For preparation of $ZnO/BiFeO_3$, $Bi(NO_3)_3.5H_2O$ and $Fe(NO_3)_3.H_2O$ were dispersed in 20 ml deionized water and added into the ZnO solution. Then the mixture was stirred for 30 min. afterwards 10ml Ethylene glycol (EG) as gelling agent was added. The solution was stirred for 1 h. After centrifuging, washing and drying, finally the mixture was calcined at 400 ^{0}C for 3 h in air to obtain $ZnO/BiFeO_3$ powder [17].

III. RESULTS AND DISCUSSION

To study the surface morphologies of as-prepared ZnO and $ZnO/BiFeO_3$ (30%) photocatalysts, FESEM analyses were done and the results are shown in Fig. 1 (a, b). It is clear that the ZnO sample consist of mainly flat-like particles with different sizes (Fig. 1a). For the $ZnO/BiFeO_3$ (30 %) nanocomposite, particles of the $BiFeO_3$ are seen on the ZnO particles (Fig. 1b).

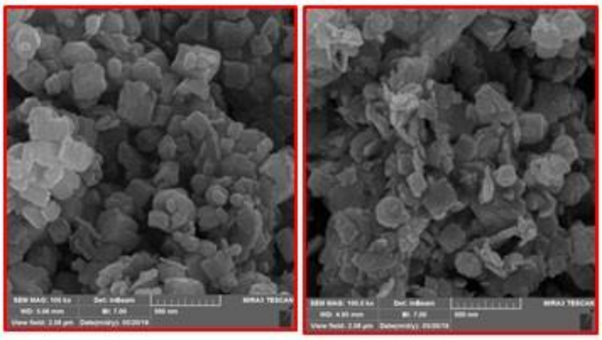

Fig.1: FESEM images of (a) ZnO and (b) $ZnO/BiFeO_3$ (30%) samples.

The reaction kinetics of as-synthesized photocatalysts for degradation of RhB were investigated via the pseudo-first-order kinetics model: $\ln(C/C_0) = -kt$, where C_0 and C is the primary and moment concentration at time 0 and t, and k is the reaction rate constant [18]. From Fig. 2, the $ZnO/BiFeO_3$ (30 %) nanocomposite displays the highest rate constant, which is olmost 15.3 folds as high as that of bare ZnO. Kinetic results proved that the construction of binary $ZnO/BiFeO_3$ heterojunction could obviously increase the photocatalytic ability of pristine ZnO.

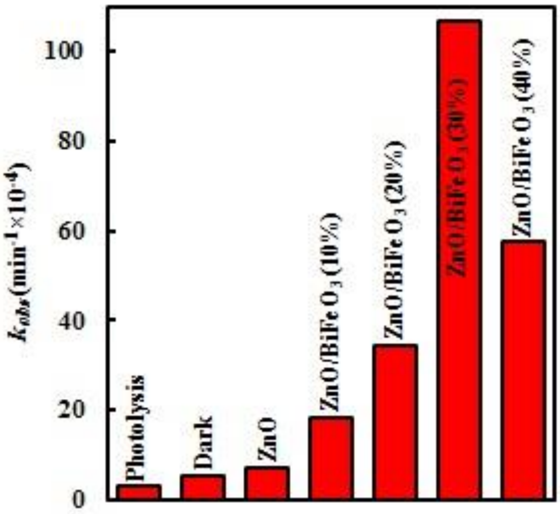

Fig.2: The degradation rate constants of RhB over different photocatalysts.

IV. CONCLUSION

ZnO and $ZnO/BiFeO_3$ photocatalysts were successfully synthesized. As-fabricated samples were studied by FESEM images. The detailed photocatalytic investigations confirmed that between binary nanocomposites, the $ZnO/BiFeO_3$ (30%) samples showed the highest photocatalytic activity. The degradation reactions followed the pseudo-first-order kinetic model, and the reaction rate constant of RhB over the $ZnO/BiFeO_3$ (30%) composite was approximately 15.3 folds as high as ZnO. This study confirmed that $ZnO/BiFeO_3$ composites has universal potential applications in organic pollutant degradation, and may attain the long-range development of environment.

REFERENCES

[1] B.Srikanth, R. Goutham, R. B. Narayan, A. Ramprasath, K. P. Gopinath, and A. R. Sankaranarayanan, Journal of environmental management, vol. 200, pp. 60-78, **2017**.

[2] L. V. Bora, and R. K. Mewada, Renewable and Sustainable Energy Reviews, vol. 76, pp. 1393-1421, **2017**.

[3] M. Mousavi, A. Habibi-Yangjeh, and S. R. Pouran, Journal of Materials Science: Materials in Electronics, vol. 29, pp. 1719-1747, **2018**.

[4] S. Giannakis, S. Rtimi, and C. Pulgarin, Molecules, vol. 22, pp. 1070–1091, **2017**.

[5] N.A. Ab Aziz, P. Palaniandy, H. Abdul Aziz, and I. Dahlan, Journal of Chemical Research, vol. 40, pp. 704–712, **2016**.

[6] A. Haghighat Mamaghani, F. Haghighat, and C.-S. Lee, Applied Catalysis B: Environmental, vol. 203, pp. 247–269, **2017**.

[7] M. Rani, U. Shanker, and V. Jassal, Journal of Environmental Management, vol. 190, pp. 208–222, **2017**.

[8] M. Pirhashemi, A. Habibi-Yangjeh, and S. Rahim-Pouran, Journal of Industrial and Engineering Chemistry, vol. 29 pp. 1719–1747, **2018**.

[9] M. Shekofteh-Gohari, A. Habibi-Yangjeh, M. Abitorabi, and A. Rouhi, Critical Reviews in Environmental Science and Technology, vol. 48, pp. 806-857, **2018**.

[10] M.A.M. Adnan, N.M. Julkapli, and S.B.A. Hamid, Reviews in Inorganic Chemistry, vol. 36, pp. 77–104, **2016**.

[11] R. Vittal, and K.C. Ho, Renewable and Sustainable Energy Reviews, vol. 70, pp. 920–935, **2017**.

[12] A. Mirzaei, Z. Chen, F. Haghighat, and L. Yerushalmi, Sustainable Cities and Society, vol. 27, pp. 407–418, **2016**.

[13] S.B.A. Hamid, S.J. Teh, and C.W. Lai, Catalysts, vol. 7, pp. 93–107, **2017**.

[14] E. Karamian, and S. Sharifnia, Materials Science and Engineering: B, vol. 238, pp. 142-148, **2018**.

[15] Q.Duan, F. Kong, X. Han, Y. Jiang, T. Liu, Y. Chang, and X. Zhang, Materials Research Bulletin, vol. 112, pp. 104-108, **2019**.

[16] M. Pirhashemi, and A. Habibi-Yangjeh, Journal of Materials Science & Technology, vol. 34, pp. 1891–1901, **2018**.

[17] T. Liu, Y. Xu, S. Feng, and J. Zhao, Journal of the American Ceramic Society, vol. 94, pp. 3060-3063, **2011**.

[18] M. Mousavi, and A. Habibi-Yangjeh, Journal of colloid and interface science, vol. 465, pp. 83-92, **2016**.

Improvement of electrocatalytic performance of graphene with Germanium (Ge) heteroatom for oxygen reduction reaction

Nafiseh mohammadirad[a], *,Dr. Jaber jahanbin*[b], *Dr.Mehdi esrafili*[c*]
a)Department of Chemistry, University of Azarbaijan Shahid Madani, Tabriz, Iran, nafisehmohammadird68@gmail.com
b) Department of Chemistry, University of Azarbaijan Shahid Madani, Tabriz, Iran, jsardroodi@azaruniv.edu
c) Department of Chemistry, University of Maragheh, Maragheh, Iran, md.esrafili@gmail.com

Abstract*:*As one of the potential candidates for electrocatalysis, metal free and nitrogen co-doped graphene has attracted extensive attention in recent years. In this work, the structural stability and ORR mechanism of GeN_3 embedded graphene have been Studied theoretically. The kinetically most favorable reaction pathway for ORR is a four-electron process. The kinetically main favorable pathway is O_2 dissociation, in witch rate-determining step is the O atom hydrogenation into OH with an energy barrier of 1.41 eV.

Keywords: oxygen reduction reaction (ORR), metal-free catalysts,GeN_3-graphene, Reaction mechanism, DFT

I. INTRODUCTION

The oxygen reduction reactions (ORR) play a important role in the electrochemical energy storage devices, such as fuel cells[1-3].The slow kinetics of the oxygen reduction reaction (ORR) at the cathode electrode [4] is one of the key feature that interdicts the high efficiency of FCs. Up to now, Pt and Pt-based alloys are found to have high activity for ORR and considered to be the most effectual catalysts[5].nonetheless, the scarce and high price of Pt-based materials[6] limit their wider usage. Since the Germanium (Ge) has a carbon element in one group, we observed as one of the best candidates in carbon-based materials, mostly due to Ge engrossed similarly the outmost electron distribution com-pared with C atom.She et al.[7] synthesized Ge and N co-doped graphene materials and evidenced their higher ORR performances experimentally and theoretically. Therefore, the model Ge-N_3-doped graphene might also be a qualifie candidate as a promising metal-free catalyst for ORR.

II. METHODS

All calculations in this work were performed using in Dmol3code [8]embedded in Materials Studio (Accelrys, San Diego, CA).The exchange and correlation effects are described employing the generalized gradient approximation (GGA) within the Perdew-Burke-Ernzerh of (PBE)[9].A double numerical plus polarization (DNP) is used as the basis set. The convergence tolerance of energy of 1.0×10-5Ha.A 4*4 hexagonal supercell graphene unit cell containing 32 atoms with lattice parameters a=b=9.84 Å, c=15 Å. The adsorption energy (ΔE_{ads}) is calculated as:

$$\Delta E_{ads}=E_{adsorbate/\ Ge\text{-}N3\text{-}Gra}-(E_{adsorbate}+E_{Ge\text{-}N3\text{-}Gra})$$

III. RESULTS AND DISCUSSION

a)Adsorption of involved species on Ge-N_3-graphene:

Firstly, we optimized ORR intermediates on active sites surface catalyst. For each ORR intermediate (including O_2, O+O, H, O, OH, OOH and H_2O) and these are located on the upper site of Ge atom. After the optimization of the ORR intermediates on these possible sites, all of the obtained stable adsorption configuration and adsorption energy is summarized in Fig.1 and table1. For O_2 adsorption specie, we earned side-on most stable configuration and the calculated adsorption energy for side-on is -0.27 eV.

b) The ORR pathway on Ge-N_3-graphene:

In the first step, we studied chemisorption of the O2 molecule on the surface, after there are two possible reaction pathways :I) O_2 dissociation II) O_2 hydrogenation. In this work O_2 dissociation pathway occurred. The O_2 molecule adsorbs on Ge-N_3-Gra surface with O-O bond distance of 1.63 Å and Ge-O bond distance of 1.81 Å in the initial state. The $O_2 \rightarrow O + O$ is exothermic with an energy of 0.69 eV and the energy barrier is 0.10 eV. So the separation O_2 molecule can occur easily on the surface. Following the O_2 dissociation, the one of the oxygen atoms are hydrogenated with an energy reaction -3.69 eV and an energy barrier 0.29 eV . The product is O+OH. Then, another O atom and OH, hydrogenated and the O+H_2O are generated. It is an exothermic reaction by -1.06 eV and with an energy barrier 0.35 eV . So, the first H_2O molecule is desorbed from the surface, the remaining O atom should form the second H_2O through two sequential hydrogenation reaction. For $O+H \rightarrow OH$ process, the reaction energy is -0.42 eV and energy barrier is by 1.41eV. After the first H_2O molecule is desorbed from the Ge-N_3-Gra surface, the remaining O atom will proceed with two sequential hydrogenation processes to form the second H_2O.

$O_2 \rightarrow {}^*O + {}^*O$ $\Delta E_{barrier}$,ΔH=0.10,-0.69 eV
$O^* + {}^*O + H \rightarrow {}^*O + {}^*OH$ $\Delta E_{barrier}$,ΔH=0.29,-3.67eV
${}^*O + {}^*OH + H \rightarrow {}^*O + H_2O$ $\Delta E_{barrier}$,ΔH=0.35,-1.06eV
${}^*O + H \rightarrow {}^*OH$ $\Delta E_{barrier}$,ΔH=1.41,-0.42eV
${}^*OH + H \rightarrow H_2O$ $\Delta E_{barrier}$,ΔH=0.12,-1.93eV

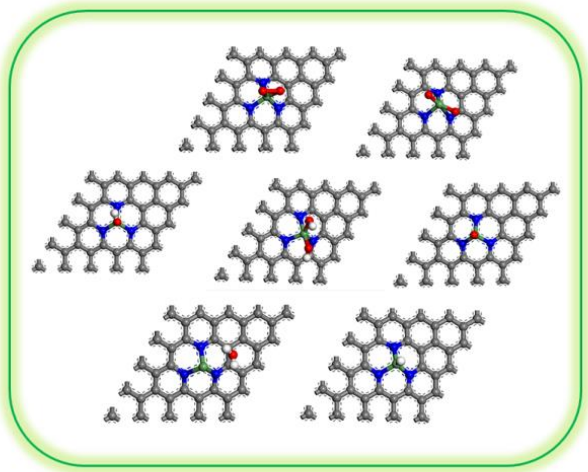

Fig.1: The most stable adsorption structures of the ORR involved species on the Ge–N_3-Gra

Table1: The Ge–O and O–O bond distance (˚ A) in GeN_3-Gra and charges of absorbed species and adsorption energy(eV)

	E(ads)	d_{Ge-O}	Q(ads)
O_2	-0.27	1.81	-0.48
2O	-7.22	1.72	-0.74
O	-4.21	1.67	-0.41
OH	-1.61	1.79	-0.10
H	-0.80	-	-0.007
2OH	-6.24	1.82	-0.35
H_2O	-0.19	2.93	0.05

IV. CONCLUSION

In summary, Ge-N_3 embeded graphene as ORR catalyst has been researched by the density functional method. The calculated results also reveal that O_2 dissociation is the mainly favorable pathways energetically and kinetically. The rate-determining step is the O atom hydrogenation into OH with an energy barrier of 1.41 eV. We look for that GeN_3-doped graphene could be helpful for modelling new high efficiency metal-free catalysts for fuel cells.

REFERENCES

[1]Y. Jia, L .Zhang, A.Du, et al. Adv Mater,vol.28,pp.9532–9538,**2016.**
[2]R.Cao, JS.Lee, M.Liu , et al. Adv Energy Mater,vol.2, pp.816–829,**2012**.
[3]S.Wang x, S .Jiang. Natl Sci Rev,vol.4, pp.163–166, **2017**.
[4]J. Snyder, T. Fujita, M. W. Chen, and J. Erlebacher,Nat. Mater., vol.9,pp. 904 ,**2010**.
[5]K. Li, Y. Li, Y. Wang, F. He, M. Jiao, H. Tang, and Z. Wu,J. Mater. Chem. A, vol.3,pp.11444 ,**2015**.
[6]W.Zhao, P .Yuan, X .She, et al. ,J Mater Chem A,vol.3,pp.14188–14194, **2015**.
[7]X .She, Q .Li, N .Ma, et al. ACS Appl Mater Interfaces, vol.8,pp.10383–10391, **2016**.
[8]B. Delley, J. Chem. Phys. Vol.92,pp. 508-517, **1990**.
[9]J.P. Perdew, K. Burke, M. Ernzerhof, Phys. Rev. Lett.,vol. 77 ,pp.3865, **1996**.

Self-assembly and DNA Binding of Cationic Gemini Amphiphiles: A Biophysical Study

S. Davoodi[a], **P. S. Pourhosseini**[a*], **N. Ghorbanmehr**[a], **A. A. Saboury**[b], **F. Najafi**[c], **Z. Landarani**[a]
[a]*Department of Biophysics, Faculty of Biological Sciences, Alzahra university, Tehran, 1993893973, Iran*
[b]*Institute of Biochemistry and Biophysics, Tehran University, Tehran, 1417614411, Iran*
[c]*Department of Resin and Additives, Institute for Color Science and Technology, Tehran, 1668836471, Iran*
Email: p.pourhosseini@alzahra.ac.ir

Abstract: In this research, the interaction of cationic gemini surfactants, having a 6 methylene group (C_6) as a spacer and urethane bonds in their chains, with plasmid DNA (pDNA) is investigated by conductometry. Results confirm the formation of surfactant-DNA complex. The thermodynamic parameters of binding, such as changes in the standard Gibbs free energy of micellization (ΔG^o_{mic}) and that of complex formation (ΔG^o_{agg}) are reported. Besides, the critical aggregation concentration (cac), the polymer saturation point (psp), the ionization degree of complexes (α_1) and that of micelles (α), are determined.

Keywords: conductivity, critical micelle concentration, degree of ionization, gemini surfactant, polymer saturation point (psp).

I. INTRODUCTION

Gemini or dimeric surfactants are an attractive class of amphiphiles that are composed of two surfactant monomers covalently linked at or near the head groups by a spacer [1-3]. They are categorized into different sub-classes depending on the variation of their chains, head groups and spacer. Among them, cationic gemini surfactants have attracted considerable attention [3, 4]. Here, a kind of cationic gemini surfactants having a 6 methylene group (C_6) as a spacer and urethane bonds in chains is investigated. The conductivity of surfactant dispersion in Tris-HCl buffer (10 mM, pH 8.0) in the absence and presence of DNA is measured. The thermodynamic parameters are determined.

II. METHODS

Materials: Cationic gemini surfactants having a 6 methylene group (C6) as a spacer, Tris-Hcl buffer (10 mM, pH 8.0), Plasmid DNA (pUC19).

Preparation of Surfactant dispersion: A dispersion of gemini surfactants in 10 mM Tris-Hcl buffer was prepared. It was sonicated for 22 min at RT to obtain a homogenous sample and then used for conductometry experiments.

Conductivity Measurements: Conductivity measurements were performed by an LCR meter instrument equipped with a conductivity cell (cell constant = 0.6 cm^{-1}). The measurement was performed at a frequency of 1 kHz, and the voltage of 0.1 V.

First, the conductivity of a given volume of Tris-HCl buffer was measured. Then small aliquots of the surfactant dispersion were added to the buffer and the conductivity of the solution was measured at each step after 1.30-2 min.

Conductivity Measurements of DNA – Surfactant solution: The experiment was carried out in a solution of DNA in Tris-HCl buffer in the same way as mentioned in the previous section.

III. RESULTS AND DISCUSSION

Results of conductivity measurements in the presence of DNA is shown in Fig. 1.

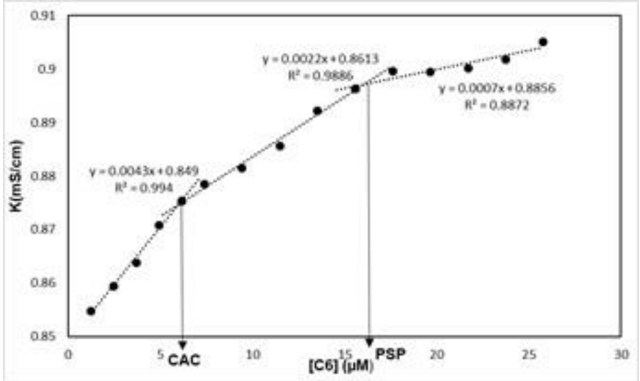

Fig1. Specific conductivity of DNA solution in Tris-Hcl buffer (pH=8, 10 mM) versus gemini surfactant concentration, at 298 K.

There are two breakpoints in this plot. The first breakpoint is cac and the second one is psp. The CAC is the concentration at which the surfactant begins to interact with DNA. The interaction continues to PSP. At PSP, the DNA molecule is saturated by the surfactant. At higher concentrations of surfactant, free micelles are formed. Therefore, the PSP could be considered as the CMC of surfactant in the presence of bio-macromolecule. The ionization degree of DNA-surfactant complexes (α_1), is obtained from the ratio of the slopes of the linear regions above and below the cac. The ionization degree of free micelles (α_2) is also calculated from the ratio of the slopes above the psp and below the cac.

Results of the experiment in the absence of DNA was thoroughly analyzed and the corresponding parameters were determined. In this case, two linear regions with different slopes are distinguished. The intersection of these two lines is defined as the critical micelle concentration (CMC = 8.5 µM). Here too, the degree of micellar ionization (α), is the ratio of slopes above and below the cmc.

Furthermore, the standard Gibbs energy of the micellization are calculated as follows:

$$\Delta G^{o}_{mic} = RT(1/2+\beta)\ \ln \mathrm{cmc} - RT/2\ \ln 2 \qquad (1)$$

where, R is the gas constant, T is the absolute temperature, and β is the degree of counter-ion binding to micelles,

$$\beta = 1 - \alpha \qquad (2)$$

The thermodynamic parameters of DNA interaction with gemini surfactants are summarized in Table 1.

Table 1. Micellar Parameters for surfactant solution in Tris-HCl buffer, 10 mM, pH 8, in the presence of DNA

parameter	**Gemini surfactant (C6)**
CAC (µM)	5.86
PSP (µM)	16.2
α_1 (%)	51
α_2 (%)	16
ΔG^{o}_{agg} (kJ/mol)	-30.4
CAC/CMC	0.69
ΔG^{o}_{PS} (kJ/mol)	+3.4

The standard Gibbs energy for the formation of the DNA-surfactant aggregation (ΔG^{o}_{agg}) is obtained using Eq. (1), with corresponding parameters for complex associations.

ΔG^{o}_{ps} is the standard Gibbs energy for the transfer of 1 mole of surfactant molecules from the micelles (in the absence of DNA) to the complex. It is calculated by Eq. (3):

$$\Delta G^{o}_{ps} = \Delta G^{o}_{agg} - \Delta G^{o}_{mic} \qquad (3)$$

The comparison of CMC in the presence and absence of DNA shows that the formation of free micelles in the presence of DNA occurs at higher concentrations. The negative values of both ΔG^{o}_{mic} (-33.8 kJ/mol) and ΔG^{o}_{agg} indicate that these processes ocurr spontaneously.

Table 1 also display that CAC is smaller than CMC, indicating that the surfactant molecules in the monomeric form interact with the DNA.

In the studies of polymer- surfactant complex formation, results show that the CAC/CMC molar ratio represents the affinity of binding of surfactant to polymer (here, the DNA molecules). The smaller the ratio, the higher the affinity is [3]. Moreover, the positive value of ΔG^{o}_{ps} indicates that the formation of micelles in the absence of DNA is more favorable than the association of surfactant with DNA molecules.

IV. CONCLUSION

Conductivity measurements of gemini surfactant solution in the absence and presence of DNA confirms the formation of DNA-surfactant complex. Results show that both the formation of micelles and the association of surfactant- DNA occur spontaneously.

The value of CMC in the absence and presence of DNA shows that the formation of micelles in the presence of DNA take place at concentrations higher than the CMC in the absence of the bio-macromolecule. It is also found out that the interaction between surfactant and DNA happens in the monomeric form of the surfactant.

Moreover, the formation of micelles in the buffer is more favorable than the association of surfactant with DNA.

REFERENCES

[1] N. Kumar, R. Tyagi, J. Dispersion Sci. Technol., vol. 35, pp. 205-214, 2014.
[2] V. Chauhan, S. Singh, R. Kamboj, R. Mishra, G. Kaur, J. Colloid Interface Sci., vol. 417, pp. 385–395, 2014.
[3] C. M. C. Faustino, A. R. T. Calado, L. Garcia-Rio, Biomacromolecules, vol. 10, pp. 2508–2514, 2009.
[4] T. Yin, M. Qin, W. Shen, Colloids and Surfaces A: Physicochem. Eng. Aspects, vol. 461, pp. 22–29, 2014.

Production of Carbon Nanotubes by Chemical Vapor Deposition Method

M. Janbazi[a]*, A.M. Beigzadeh[a], M. Sadeghi[b], M. Shadman[c]
[a]*Radiation Application Research School, NSTR Institute, P.O. Box 11365-3486, Tehran, Iran*
[b]*Physics Department Shiraz University, Shiraz, , P.O. Box 71555-313, Shiraz Iran*
[c]*Department of Chemistry, Faculty of Science, University of Zanjan, P.O.Box 45195-313, Zanjan, Iran*
Email:mjanbazi@aeoi.org.ir

Abstract: Duo to their unique properties, the (Carbon Nanotubes) CNTs have the potential for many applications, including electronic devices, fuel cells, nano-composites, and Though there are several methods for producing nanotubes, but over the past years, catalytic growth has been considered by the chemical vapor deposition to produce of nanotubes, in this study by means of CVD method the carbon nanotube is constructed.

Keywords: Nanotubes, CVD method, nanoparticles, alumina, Pyrex.

I. INTRODUCTION

Duo to their unique properties, the **(**Carbon Nanotubes**)** CNTs have the potential for many applications, including electronic devices, fuel cells, nano-composites, and …. Though there are several methods for producing nanotubes, but over the past years, catalytic growth has been considered by the chemical vapor contact layer for the production of nanotubes. Since with this method, we can produce nanotubes that have a desirable quality, in addition this method has high efficiency.

Using CVD method to produce nanotubes, we will be able to produce multi-branch Y, T, and K shaped nanotubes, which are widely used in electronics. Most of the used catalysts in manufacturing of the nanotubes by CVD are iron, copper, cobalt, yttrium, nickel and gold. In this study the CVD method used to produce of carbon nanotubes.

II. METHODS

First, for production of carbon nanotubes, silicon samples were coated with alumina and then one nanometer gold layered on it [1], finally CVD method was used to generate carbon nanotubes. The method of nanotubes production was: first thin gold layer by the furnace's heat shaped as spherical and elliptical nanoparticles.

Then the carbon produced from acetylene decomposition located in the vicinity of these nanoparticles and form the nanotubes in two ways of growing from the tip and the root.

The used furnace in the experiment for heating, decomposition of the acetylene gas and the formation of nanotubes is shown in Figure 1.

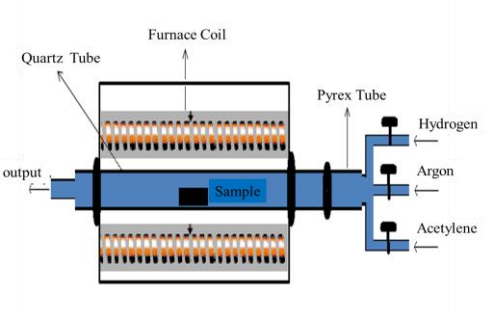

Fig1: A simple view of the furnace designed to produce carbon nanotubes

Since in producing nanotubes by chemical vapor deposition method may the temperature rise up to 1000 degrees Celsius, It is necessary to use a placed pipe in the furnace with high temperatures resistance.

Considering that quartz has a high temperature tolerance up to 2800 Celsius so it is a good choice for use in experiments. Considering quartz has a high temperature tolerance up to 2800 Celsius so it is a good choice for use in experiments. We can also choose a thin quartz tube to make the better heat transfer from the furnace to the tube and the carbon dioxide decomposition.

Due to the fact that the thickness of the quartz tube was selected small, so it is very sensitive to the impact. To solve this problem a Pyrex tube was used. In this way, the inlet valves of the three different gases connected to the relatively large Pyrex pipe with good resistance were connected, then the Pyrex tube was connected to the quartz tube.

During the experiment, it was necessary to enter gases at different times and flows. For this purpose, three separate valves were used that were spaced approximately 7 centimeters apart.

To produce of a gold nanotubes, it is necessary that a uniform plate of gold dissolves into separate nanoparticles [2].

To investigate the production of gold nanoparticles, the sample was placed at a temperature of 800 ° C for one hour in the furnace. The SEM images of this sample is shown in Fig. 2 after being placed in the furnace.

III. RESULTS AND DISCUSSION

In the form above the islands are well separated and the conditions for the formation of gold nanoparticles and subsequent production of carbon nanotubes are favorable.

The diagram of the diameter distribution of the nanotubes at 800 is shown in Fig. 3. The graph shows that, the diameter distribution is gaussian and at 800 ° C the diameter of the nanotubes is between 20 and 60 nm and the most frequent is near the diameter of 40 nm.

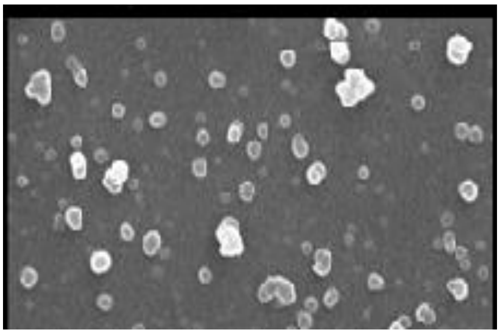

Fig.**2**: Gold nanoparticles produced at 800 ° C

Fig3: Nanotubes produced at 800 ° C

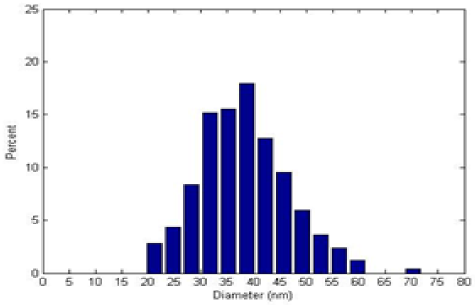

Fig.3: the diameter distribution of the nanotubes at 800 ° C

IV. CONCLUSION

In this study, the nanotubes are formed on a 1 nm gold layer. The furnace in the experiment for heating, decomposition of the acetylene gas and the formation of nanotubes. In this experiment, the nanotube was deposited at 800 ºC on a substrate layer. The results shows that, the diameter distribution is Gaussian and at 800 ° C the diameter of the nanotubes is between 20 and 60 nm and the most frequent is near the diameter of 40 nm.

REFERENCES

[1] S. Iijima, Nature, 354, 56 (1991).
[2] K. Uchiyama, H. Miaki, S. Terada, and Masahiro Hoso., Science, 47, 722 (2009).

Proposed use of cobalt-zinc ferrite nanoparticle ($CoZnFe_2O_4$) to improve the quality of MRI images: Non-clinical approach

Hadi Hamid**, **Safari Reza, **Ehsani Ali***
Faculty of Science, Department of Chemistry, Physical Chemistry Group, University of Qom, Iran.
Email: hamid7.new@gmail.com and r.safari@qom.ac.ir

Abstract: Magnetic nanoparticles are useful as factors for improving the quality of images in magnetic resonance imaging (MRI). The unique properties and advantages of magnetic nanoparticles lead to the superiority of these particles as image boosters in the MRI. The basis of MRI work is based on the interaction between the magnetic field and the tissue protons. The use of magnetic nanoparticles in MRI provides better contrast of images (andallows for imaging on cellular and molecular levels).In this work, the cobalt-zinc ferrite nanoparticles ($CoZnFe_2O_4$) are proposed to improve the quality of MRI images. Non-clinical predictions have shown that the use of these nanoparticles can help improve the images received from MRI.In this regard, some properties of these magnetic nanoparticles are studied.

Keywords: Magnetic nanoparticles, Magnetic resonance imaging (MRI), Zinc Cobalt Ferrite Nanoparticles

I. INTRODUCTION

Nanoscience and nanotechnology have had a great influence on biology, chemistry, physics and chemistry in the last few decades. One of the uses of these nanoparticles is the increase in the ability to detect magnetic resonance imaging or the development of new imaging techniques [1].

Nanosized materials have been extensivelystudied by researchers worldwide because of theirunique physical properties, such as electrical conductivity, optical bandgap, refractive index and magnetic properties, and superior mechanical properties such as hardnessof nanomaterials and chemical properties compared withtheir counterpart bulk materials[2]. In this regard, spinel nanoparticles, cobalt-zinc ferrite ($CoZnFe_2O_4$) due to their magnetic and electrical properties have been considered. Fig. 1 [3].

Magnetic resonance imaging (MRI) is a medical imaging technique used in radiology to form pictures of theanatomyand the physiological processes of the body. Magnetic resonance imaging (MRI) is a noninvasive technique which can acquire important quantitative and anatomical information from an individual in any plane or volume at comparatively high resolution.

Over the past several years, developments in scanner hardware and software have enabled the acquisition of fast MRI imaging, proving extremely useful in various clinical and research applications such as in brain mapping or functional MRI (FMRI), perfusion weighted imaging (PWI), and diffusion-weighted imaging (DWI). These techniques have revolutionized the use of MRI in the clinics, providing great insight into physiologic mechanisms and pathologic conditions [4-5].

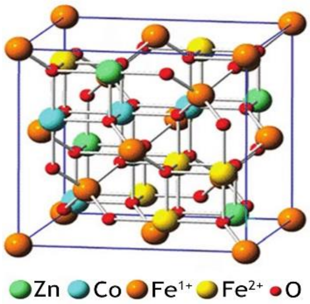

Fig. 1. Ball & stick model depicting Co cations as blue spheres, Zn cations as green spheres and Fe^{1+} cations as orange, Fe^{2+} cations as gold and Oanions in red.

In this work, the ($CoZnFe_2O_4$) nanoparticles are proposed to improve the quality of MRI images. Thus, some properties (such as size, spin and magnetic properties) of these magnetic nanoparticles are non-clinical studied.

II. METHOD

A- Cobalt-Zinc Ferrite Nanoparticle:

So far, various methods for the production and study of cobalt nanoparticles have been proposed [1-3,6-10]. For example, cobalt zinc mixed ferrite $Co_xZn_{1-x}Fe_2O_4$ (where x = 0, 0.2, 0.4 and 0.6) were synthesized by chemical solution [2]. Also, cobalt zinc mixed ferrite $Co_xZn_{1-x}Fe_2O_4$ where x = 0, 0.2, 0.4 and 0.6 synthesized by chemical solution technique, using metallo-organic precursors [6]. In order to appreciate the contrast mechanisms in MRI, it is necessary to understand how the magnetization of the multitude of spins in the object combines to produce the NMR signal.The most important site of this resonance relevant to MRI is the nucleus of the hydrogen atom in water. While other proton occurs within biological molecules, water represents the most important site for MRI due to the concentration of protons inwater and the dynamical properties of water [5-6].

B- Spin and SizeEffects

Cobalt-zinc ferrite nanoparticle ($CoZnFe_2O_4$)is a well-known hard magnetic material with high coercively and moderate magnetization[7-10]. In this work, the nanoparticles $CoZnFe_2O_4$ are proposed to improve the quality of MRI images. Non-clinical predictions have shown that the use of these nanoparticles can help improve the images received from MRI.Among various ferrites, $ZnFe_2O_4$ and $CoFe_2O_4$ have been most extensively studied systems, because they exhibit the typically *normal* and *inverse spinel* ferrites respectively.

Generally, the contrast of MRI in soft metabolism is due to the difference in proton at the time of the spin-Lattice relaxation, T_1, and the spin-spin relaxation time, T_2. In addition, contrast factors commonly used in MRI have a number of disadvantages, including high toxicity, low half-lives, and the impossibility of multi-function (compared to magnetic nanoparticles that have low toxicity, high half-life and multiple functions, they are suitable).Also, the diameter of the magnetic nanoparticles is effective on the amount of signal amplification and half-life of the particles in the body. This dependence can be considered as the following [10]:

$$\frac{1}{T_2} = \left(\frac{256\pi^2\gamma^2}{405}\right) V^{*\mu_s^2} d^2 / D(1+\frac{L}{d}) \qquad (1)$$

where T_2 is spin-spin relaxation time, Also, γ, V^*, d, D, and L are the proton gyromagnetic ratio, volume fraction, saturation magnetization, core radius of magnetic nanoparticles, diffusivity of water molecules, and thickness of the impermeable surface.

III. RESULTS AND DISCUSSION

Based on the Eq. (1), it can be seen that with increasing particle size, the T_2 value is reduced and, as a result, decreases the intensity of the MRI signals, Fig. 2. It should also be noted here that the signal strength is inversely related to T_2 (because the comfort velocity is related to $1/T_2$).

Based on theoretical/non-clinical research, it can be predicted that the $CoZnFe_3O_4$ nanoparticels play role as a superparamagnetic particles. Also, in cobalt ferrite nanoparticles, dipoles tend to be in a particular direction (this property has caused the cobalt ferrite to have anomalous magnetic anisotropy with normal spinel).

On the other hand, zinc ferrite with reverse spinel has anti-ferromagnetic properties (at low temperature).Also, when ferrite particles are reduced to a nanoscale, they find ferromagnetic or superparamagnetic properties. In summary, these spin/size effectscan be reduced the T_2 time (spin-spin relaxation time) for **$CoZnFe_2O_4$**nanoparticels, and consequently increases the received-MRI-image quality.

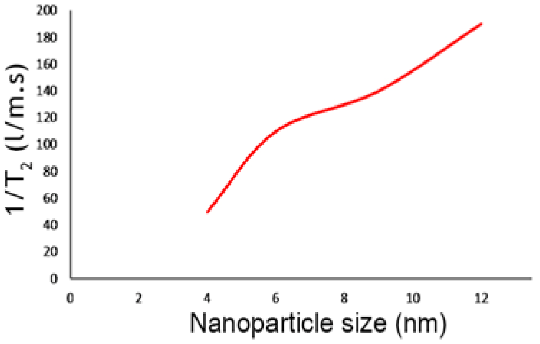

Fig. 2. Graph of $1/T_2$ values versus nanoparticle size.

IV. CONCLUSION

In this work, zinc-cobalt ferrite nanoparticles ($CoZnFe_2O_4$) has been proposed to improve the quality of the images received from the MRI (non-clinical method), which increases the interactions of protons with an external magnetic field (due to high saturation magnetization), and thus increases the signal received from the MRI.

This study results show that when spin-spin relaxation time (T_2) of $CoZnFe_2O_4$ decreased (or when the concentration of cobalt increased, as superparamagnetic nanoparticles), it is expected that the quality of the images received from the MRI increased.

Moreover, analysis of these study results show that the reducing the size of the $CoZnFe_2O_4$ has a significant effect on the zinc magnetic spin-spin relaxation time.

REFERENCES

[1] B. Gleich, J. Weizenecker and *Tomographic imaging using thenonlinear response of magnetic particles*, Nature, vol. 435, pp. 1214-1217, **2005**.

[2] M. G. Naseri, E. B. Saion, H. A. Ahangar and A. Halim, *Synthesis and characterization of zinc ferrite nanoparticles by a thermal treatment method*, Sol. Stat. Commun. vol. 151, pp. 1031-1035, **2011**.

[3] E. Girgis, M. M. S. Wahsh, A. G. M. Othman, L. Bandhu, and K.V. Rao, *Synthesis, magnetic and optical properties of core/shell*$Co_{1-x}Zn_xFe_2O_4$*/SiO2nanoparticles*, Nanoscal. Res. Lett., vol. 6, pp. 460, **2011**.

[4] . E. M Haacke and R. W Brown, *Magnetic resonance imaging. physical principles and sequence design*., Wiley-Liss. ***1999***.

[5] T. Callaghan, *Principles of nuclear magnetic resonance micropscopy*, Oxford Science Publications, **1991**.

[6] . A. Sharma, K. Parmar1, R. K. Kotnala and N. S. Negi, *Magnetic and dielectric properties of coxzn1-xfe2o4 synthesized by metallo-organic decomposition technique*, Inter. J. Advan. Engin. Techn., **2012**.

[7] T. K. Jain, J. Richey, M .Strand, D. L. Leslie-Pelecky, C. A. Flask, V. Labhasetwar, *Magnetic nanoparticles with dual functional properties: drug delivery and magnetic resonance imaging*. Biomater. Vol. 29, pp.4012-4021, **2008**.

[8] G. Baldi, D. Bonacchi, C. Innocenti, G. Lorenzi, and C. Sangregorio, *Cobalt ferrite nanoparticles: thecontrol of the particle size and surface state and their effects on magnetic properties*, Magnetism. Magnetic Mater. vol. 311, pp. 10–16, **2007**.

[9] T. Tatarchuk, M. Bououdina, W. Macyk, O. Shyichuk, N. Paliychuk, I. Yaremiy, B. Al-Najar and M. Pacia, *Structural, Optical, and Magnetic Properties of Zn-Doped CoFe2O4 Nanoparticles*, Nanoscale Res. Lett., vol. 12, pp. 141, **2017**.

[10] W. Zhang, L. Liu, H. Chen, K. Hu, I. Delahunty, S. Gao, and J. Xie, *Surface impact on nanoparticle-based magnetic resonance imaging contrast agents*, Theranostics., vol. 9, pp. 2521-2548, **2018**.

Green synthesis of silver nanoparticles using Garlic extract and evaluation of antibacterial activity

Zaman nasrnia[a] ***, Ali Bahari[b]****
Department of Solid State Physics, University of Mazandaran, Babolsar 4741695447, Iran
Email: a.bahari@umz.ac.ir.

Abstract: simple, environmentally friendly and cost-effective method has been developed to synthesize silver. nanoparticles (AgNPs) using Garlic extract. We synthesized The AgNPs by using silver nitrate and garlic extract, and the reaction was carried out for 24 h at room temperature. Antibacterial activities of synthesized silver nanoparticles were evaluated against four bacteria, E.coli, S. aureus, B. subtilis and P. aeruginosa. The results revealed tha silver nanoparticles show good antibacterial activities. Also, we characterize the synthesized nanoparticles with X-ray diffraction (XRD), Scanning electron microscopy (SEM) and UV-Vis absorption spectrophotometry. The absorption peak was found in the region of 422 nm. These nanoparticles would contain an average mean diameter of 24.42 nm by Scherrer equation.

Keywords: Green synthesis, silver nanoparticles, Garlic extract, antibacterial

I. INTRODUCTION

In recent years, silver nanoparticles (AgNPs) have been widely used in many consumer goods, such as medical devices, cleaning agents, and clothing, due to its unique antimicrobial properties. Generally, the method for the AgNP preparation involves the reduction of silver ions in the solution or in high temperature in gaseous environments[1]. Natural sources have the potential to reduce metal ion into metal nanoparticles [2]. The size, shape and surface morphology of nanoparticles plays a vital role in controlling the physical and chemical properties. The synthesis of metal nanoparticles by chemical reduction method was often performed in the presence of stabilizing agent to prevent the unwanted agglomeration of colloids. Furthermore, the chemically synthesized metal nanoparticles are expensive, hazardous to environment and require high energy consumption. Biological approaches using plant extracts for metal nanoparticles synthesis have been suggested as valuable alternative tool towards chemical methods [3].

Green nanotechnology is gaining importance due to the elimination of harmful reagents and provides effective synthesis of expected products in an economical manner. The conventional methods for the production of nanoparticles are expensive, toxic and non- environmentally friendly [2]. To overcome these problems researchers have found the precise green routes. In this method, extracts of plants, algae and sometimes microorganisms are used as stabilizing and reducing agents. Silver nanoparticles due to the release of silver ion, exhibit such an effect against aerobic and anaerobic bacteria. The important thing is that the bacteria don't resist these particles, so it will be possible to influence a wide range of bacteria [3]. The main feature of silver nanoparticles is the antibacterial properties of these particles, so this feature is used in wound dressing, distinction and medical instrument coatings[4]. In this study, we first synthesized silver nanoparticles using garlic extract and then examined their antibacterial properties.

II. METHODS

The raw materials used to make Silver nanoparticles
1. Ag (No3)(99% W/W Merck)
2. garlic
3. de-ionized water
4. Whatman No. 1 paper

To prepare garlic extract, the fresh garlic were first washed with de-ionized water Then it was placed at room temperature for one day to dry. 200 g of dried garlic, grated and then taken its extract with a clean cloth. The extract was then filtered by Whatman No. 1 paper. To prepare the silver nanoparticles, first 50 ml of a 1 Mm solution of silver nitrate in de-ionized water was prepared and placed on magnetic stirrer for 10 minutes until completely homogeneous solution was obtained. Then the 10 ml Garlic extract, was added drop wise and added to the silver nitrate solution .By gradually adding the Garlic extract, a change of color from transparent (primary solution) to dark brown was observed in the solution. Then the precipitate was collected by centrifugation and washed with 5000 rpm and 10 minutes 3 times with de-ionized water and 3 times with ethanol.

III. RESULTS AND DISCUSSION

Silver nanoparticles are usually indicated by the presence of a plasmon resonance resonator of a peak absorption spectrum in the field of the electromagnetic spectrum.

The absorption peak was found in the region of 422 nm (Figure. 1). Due to the size of the silver nanoparticle, as expected, the absorption length has progressed to shorter wavelengths and the results of the experiments are very consistent with the theoretical conclusions that the high quality of nanoparticles produced from approves the view of the properties. The silver nanoparticles spectrum shows wavelength at 450 nm. The average crystallite size for the samples has been estimated using the scherrer equation:

$$D = \frac{K\lambda}{\beta_{hkl}\cos\theta_{hkl}} \qquad (1)$$

Where K is the shape factor, λ is the X-ray wavelength (Figure 2), β_{hkl} is the full width at half maximum (FWHM) and θ is the Bragg angle. Using the Scherrer equation, the size of Ag nanoparticles was 24.42 nm.

The Scanning electron microscopy shows the shape Of nanoparticles, spherical (Figure 3).

Due to excessive intake of antibiotics, resistance to them is one of the problems in bacterium elimination. Nanomaterials, cause them to exhibit the lowest level of toxicity in ecosystems to fight bacterial infections. The difference between the negative charge of microorganism and the positive charge of nanoparticles tend to act as an electromagnetic absorber leading to the oxidation of molecules. In this investigation, antibacterial activities of synthesized Ag nanoparticles were evaluated against four bacteria, i.e. E.coli, S.aureus, B.subtilis and P.aeruginosa. Table 1 show the results of the bacterial and numerical measures of their diameters after 24 hours. As shown in Table 1, Ag nanoparticles proved even more effective than antibiotics against the bacteria P.aeruginosa. The results indicated that the synthesized nanoparticles would show noteworthy antimicrobial behavior. Based on these results, it is expected that these nanoparticles could be successfully used against disease-causing microbes and prevent the advent of new diseases.

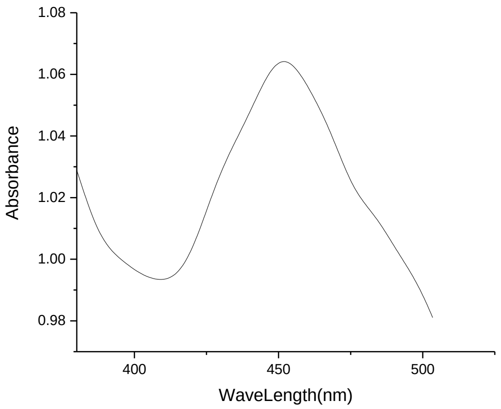

Figure 1. UV absorption spectrum of Ag nanoparticles

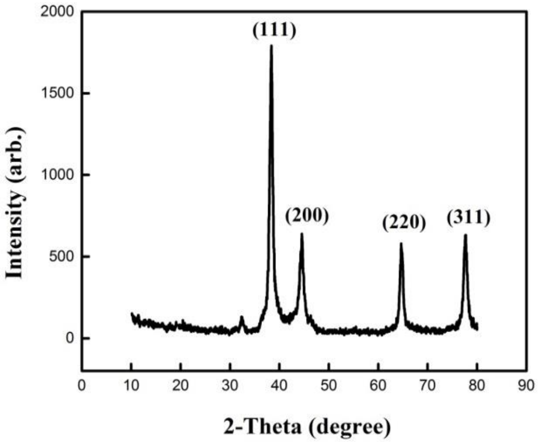

Figure 2. Powder X-ray diffraction (XRD) pattern of Ag nanoparticles

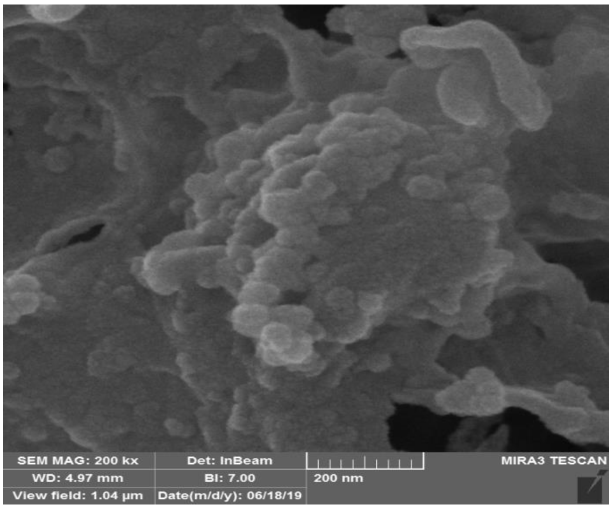

Figure 3. Scanning electron microscopy (SEM) of Ag nanoparticles

Table1. Antibacterial activity of the Ag nanopticles

Test strain	**Ag nanoparticles**	**Gentamicin (10μg/disc)**	**Cloramphenicol (30μg/disc)**
E.coli	12 mm	20.5 mm	21 mm
S.aureus	12 mm	17.5 mm	34.5
B.subtilis	10.5 mm	23mm	34.5
P.aeruginosa	13	7.5	

IV. CONCLUSION

Silver nanoparticles were prepared by green synthesis. The results of the XRD pattern confirmed the fcc structure. The absorption spectrum of silver nanoparticles was 422 nm. Antibacterial tests showed that silver nanoparticles affect bacteria *P.aeruginosa* more than Gentamicin and Cloramphenicol antibiotics.

REFERENCES

[1] B. Ulug, M. H. Turkdemir, A. Cicek, and A. Mete, “Role of irradiation in the green synthesis of silver nanoparticles mediated by fig (Ficus carica) leaf extract,” *Spectrochim. Acta Part A Mol. Biomol. Spectrosc.*, vol. 135, pp. 153–161, **2015.**

[2] D. Kumarasamyraja and N. S. Jeganathan, “Green synthesis of silver nanoparticles using aqueous extract of acalypha indica and its antimicrobial activity,” 2013.

[3] P. Mohanpuria, N. K. Rana, and S. K. Yadav, “Biosynthesis of nanoparticles: technological concepts and future applications,” *J. nanoparticle Res.*, vol. 10, no. 3, pp. 507–517, **2008**.

[4] S. Kaviya, J. Santhanalakshmi, and B. Viswanathan, “Green synthesis of silver nanoparticles using Polyalthia longifolia leaf extract along with D-sorbitol: study of antibacterial activity,” *J. Nanotechnol.*, vol. **2011**.

Novel Cu_2O/Cu-MOF/rGO is reported as Highly Efficient Catalyst for Reduction of 4-Nitrophenol

*E. Akbarzadeh[a], F. Mirzaee[a], H. Zare Soheili[a], M. R. Gholami[a]**
Affiliation: *Department of chemistry, Sharif University of Technology, Tehran, 11365-11155, Iran.*
Email:gholami@sharif.ir

Abstract*:* Cu-MOF/rGO nanocomposite was synthesized by a one step hydrothermal method and used as proper support for Cu_2O particles. Divers microscopic and spectroscopic methods were applied to characterize morphology and structure of Cu_2O/Cu-MOF/rGO nanocatalyst. Catalytic results of 4-nitrophenol reduction in the presence of $NaBH_4$ ascertained that as-synthesized nanocomposite shown remarkable improved activity compared with pure Cu_2O particles. Enhanced catalytic performance of nanocomposite can be ascribed to the high adsorption ability of Cu-MOF and effective electron transfer due to the presence of rGO. A possible mechanism for catalytic reduction of 4-nitrophenol was proposed based on synergistic effects between Cu_2O and Cu-MOF/rGO in nanocomposite.

Keywords: 4-NP reduction, Cu-based Metal organic frameworks, Cu_2O, Reduced graphene oxide.

I. INTRODUCTION

Catalytic reduction of nitro group in the presence of a reducing agent is a beneficial approach to decline 4-NP toxicity because its reduction product (4-aminophenol) is a valuable intermediate for manufacturing of dyes, corrosion inhibitors, cosmetics and pharmaceuticals [1-3]. Cu_2O has attracted much interest as a promising substituent for expensive noble metal to reduce nitro-substituted arenes [4-6]. However, due to the narrow band gap value of this semiconductor (about 2.0 eV), electrons can quickly reduce Cu_2O to Cu particles instead of reduction of 4-NP [7]. Accordingly, coupling with other materials to transfer active electrons to the other active sites can be an acceptable method to improve the catalytic performance of Cu_2O particles. Metal organic Frameworks (MOFs) as a new category of materials have attracted huge attention due to their remarkable properties in catalysis field [8, 9]. In the present work, Cu-MOF/rGO nanocomposite was prepared by one step hydrothermal method and employed as efficient support for Cu_2O particles. Catalytic performance of the as-prepared Cu_2O/Cu-MOF/rGO nanocomposite was explored in the 4-NP reduction reaction. A plausible mechanism for catalytic reduction of 4-nitrophenol was suggested based on synergistic effects between Cu_2O and Cu-MOF/rGO in nanocomposite.

II. METHODS

To prepare Cu_2O/Cu-MOF/rGO nanocomposite, 118 mg of $Cu(CH_3COO)_2$. H_2O, 432 mg of NaOH and 368 mg of glucose were added into 80 mL mixed solution of water and ethanol (the volume ratio 1:1) and kept at 70 ℃ under reflux conditions. After 1h, a certain amount of Cu-MOF/rGO was introduced to the above solution and the reaction continued for 5h more. The as obtained Cu_2O/Cu-MOF/rGO particles were separated and washed with deionized water several times, and dried at 60 ℃.

The as-synthesized In order to determine the activity of Cu_2O/Cu-MOF/rGO nanocomposite reduction of 4-NP in the presence of $NaBH_4$ was investigated. As the first step, 3 mL of 4-NP aqueous solution (0.1 mM) was introduced to a quartz cell (1.0 cm path length and 4 mL volume). Adding of reducing agent (1.5 mL of 0.01 M $NaBH_4$ aqueous solution) to the above solution changed the color of the solution as result of formation of 4-nitrophenolate ions. By adding 1 mg of the catalyst into the reaction cell the reduction of 4-NP was started which followed by its UV-vis absorption spectra (at 400 nm) at determined time intervals.

III. RESULTS AND DISCUSSION

X-ray diffraction peaks of Cu-MOF/rGO and Cu_2O/ Cu-MOF/rGO are demonstrated in Figure 1. All of the characteristic diffraction patterns in Cu-MOF/rGO are according to the pure Cu-MOF and due to the low intensity of GO compare to MOF, there is not any remarkable peaks related to GO. Diffraction peaks in XRD patterns of Cu_2O/Cu-MOF/rGO composite at $2\theta = 29.6, 36.5, 42.4, 52.5, 61.5, 69.6, 73.6$ and 77.5 are related to the cubic phase of Cu_2O (JCPDS no. 05-0667) . There is not any obvious peaks accordance to Cu-MOF/rGO patterns due to the high intensity of Cu_2O peaks and relatively low amount of Cu-MOF/rGO in composite.

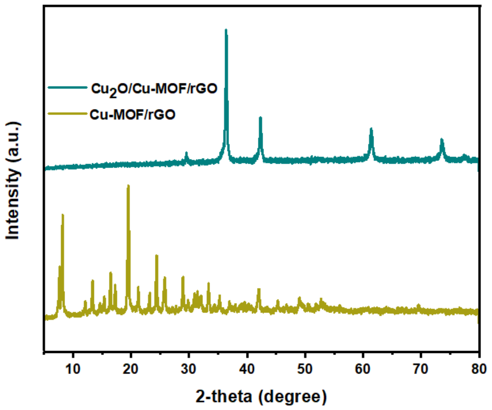

Fig 1. XRD patterns of Cu-MOF/rGO and Cu_2O/Cu-MOF/rGO.

Field emission scanning electron microscopy was applied to characterize microstructures of the as-synthesized samples. Figure 2 shows that spherical Cu2O particles were successfully introduced to GO (Figure 2a) and Cu-MOF/rGO (Figure 2b). The SEM image of Cu2O/Cu-MOF/rGO indicates presence of cubic Cu-MOF particles with the size less than 100 nm which formed without agglomeration. The EDX spectrum in Figure 2c obviously demonstrates the coexistence of O, Cu and C elements in the Cu2O/Cu-MOF/rGO nanocomposite.

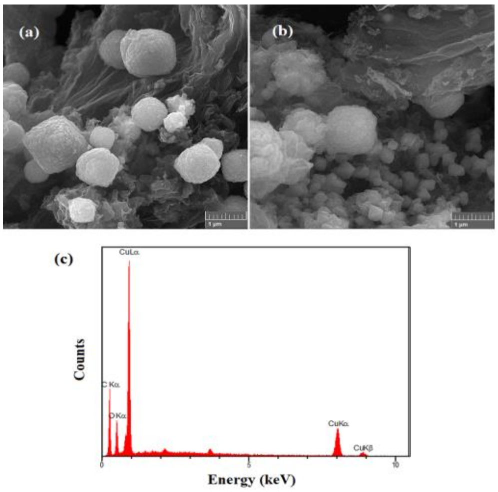

Figure 2. FESEM images of as-synthesized Cu_2O/GO (a) Cu_2O/Cu-MOF/rGO (b) EDX spectrum of Cu_2O/Cu-MOF/rGO (c).

Catalytic activity

The catalytic activity of Cu_2O/Cu-MOF/rGO was explored in catalytic reduction of 4-NP to its correspond aminophenol. A neutral aqueous solution of 4-NP indicates an intensive absorption peak at 317 nm. In alkaline condition (after addition of $NaBH_4$), 4-nitrophenolate ions are produced and the maximum of this peak shift to 400 nm. When Cu-MOF/rGO was added into the 4-NP/$NaBH_4$ solution, the absorption peak at 400 nm rapidly decreased without any signs of 4-aminophenol production (a new peak at 300 nm). It can be deduced that Cu-MOF/rGO nanoparticles quickly adsorb 4-nitrophenolate ions (Figure 3a). When Cu_2O/Cu-MOF/rGO particles were introduced to the reaction cell, 4-aminophenol peak slightly increased as the reduction reaction proceeds (Figure 3c).

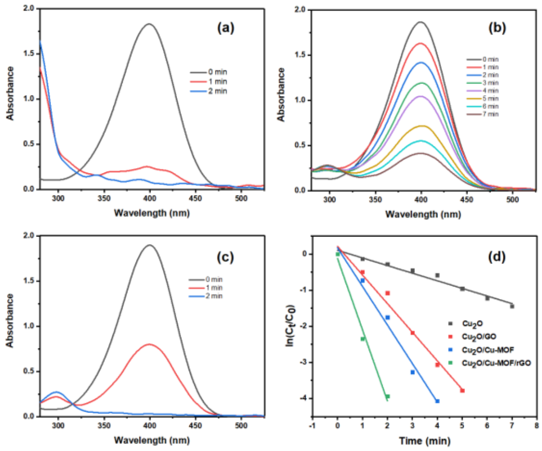

Figure 3. UV-vis absorption spectra of catalytic reduction of 4-NP by Cu-MOF/rGO (a), Cu_2O (b), Cu_2O/Cu-MOF/rGO and plot of $\ln(C_t/C_0)$ against of reaction time.

Scheme 1. briefly demonstrates the most possible process of 4-NP catalytic reduction over Cu_2O/Cu-MOF/rGO nanocomposite. Based on this proposed mechanism, Cu_2O particles react with BH_4^- and produce active Hydrogen species and electrons for reduction reaction. These electrons rapidly migrate from Cu_2O to the adsorbed 4-nitrophenolate ions on the surface of Cu-MOF particles to produce 4-AP.

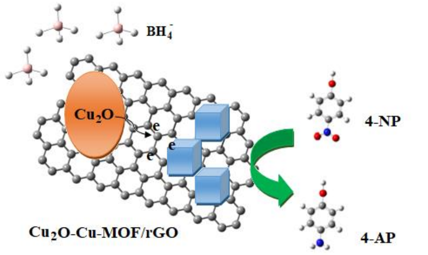

Scheme 1. Possible catalytic reduction process over Cu_2O/Cu-MOF/rGO nanocomposite.

IV. CONCLUSION

In summary, Cu-MOF/rGO nanocomposite was employed as an appropriate support for Cu_2O particles to prepare a high active catalyst for reduction of 4-NP in the presence of $NaBH_4$. Catalytic results revealed that introduction of Cu-MOF considerably improved catalytic performance of Cu_2O. Cu-MOF significantly enhanced 4-nitrophenolate ions adsorption on the surface of catalyst and notably affect catalytic activity. On the other hand, graphene was served as a great charge carrier to transfer electrons from Cu_2O to the adsorbed 4-nitrophenolate ions on the surface of Cu-MOF particles.

REFERENCES

[1] C. Gong, Z. Zhou, J. Li, H. Zhou, R. Liu, Journal of the Taiwan Institute of Chemical Engineers 84 (2018) 229-235.
[2] R. Begum, Z.H. Farooqi, E. Ahmed, K. Naseem, S. Ashraf, A. Sharif, R. Rehan, Applied Organometallic Chemistry 31 (2017) e3563.
[3] T.K. Das, S. Ganguly, P. Bhawal, S. Mondal, N.C. Das, Research on Chemical Intermediates 44 (2018) 1189-1208.
[4] P.C. Rath, D. Saikia, M. Mishra, H.-M. Kao, Applied Surface Science 427 (2018) 1217-1226.
[5] T. Aditya, J. Jana, N.K. Singh, A. Pal, T. Pal, Acs Omega 2 (2017) 1968-1984.
[6] E. Akbarzadeh, S.R. Setayesh, M.R. Gholami, New Journal of Chemistry 41 (2017) 7998-8005.
[7] A.K. Sasmal, S. Dutta, T. Pal, Dalton Transactions 45 (2016) 3139-3150.
[8] Y.-B. Huang, J. Liang, X.-S. Wang, R. Cao, Chemical Society Reviews 46 (2017) 126-157.
[9] H.-Y. Zhang, X.-P. Hao, L.-P. Mo, S.-S. Liu, W.-B. Zhang, Z.-H. Zhang, New Journal of Chemistry 41 (2017) 7108-7115.

Noble Metal Nanoparticles Supported on Ni Promoted MoS_2 as an Efficient Catalyst for p-Nitrophenol Reduction

E. Akbarzadeh, F. Mirzaee[a], F. Bahrami[a], M. R. Gholami[a]*

Affiliation: Department of chemistry, Sharif University of Technology, Tehran, 11365-11155, Iran.
Email:gholami@sharif.ir

Abstract*:* In present study, a facile method was used to synthesis noble metal nanoparticles on Ni modified MoS_2 (MNi/MoS_2 (M = Au and Pt). The morphology and structure of prepared products were detected using different microscopic and spectroscopic methods. The as-synthesized MNi/MoS_2 nanocomposites were applied for catalytic reduction of p-nitrophenol in the presence of $NaBH_4$. The obtained catalytic results indicate that noble metal nanoparticles significantly affect catalytic performance of MoS_2. Synergistic effect between metal NPs and MoS_2 was introduced as the origin of this improved catalytic activity of metals decorated MoS_2 particles. The enhanced catalytic activity of Ni modified MoS_2 particles in comparison to that of unmodified MoS_2 nanocomposites emphasis on the role of Ni in catalytic efficiency.

Keywords: P-nitrophenol, catalytic reduction, Ni promoted MoS_2, noble metal nanoparticles

I. INTRODUCTION

Nitroaromatic compounds as one of the most prevalent contaminants in industrial and agricultural effluent are hazardous and resistant to natural degradation in the environment. Removing of nitro groups through the catalytic reduction of these compounds in the presence of a reducing agent is an effective solution to decrease their toxicity. On the other hand, the reduction products, aromatic amines, are used as precious intermediate for manufacturing of dyes, fungicides, cosmetics and pharmaceuticals [1-3]. Recently, molybdenum disulfide (MoS_2) has been widely investigated as a promising material in electrocatalysis [4, 5], supercapacitors [6, 7], lithium-ion batteries [8] and photocatalysis [9-11] due to its appealing properties. It has been reported that addition of Ni atoms to the MoS_2 matrix elevates structural stability and exposed more reaction site for catalysis of reactions. In this work, we proposed a facile method to synthesis noble metal NPs on Ni modified MoS_2 particles (MNi/MoS_2 (M = Au and Pt). The as-synthesized MNi/MoS_2 nanocomposites were applied for catalytic reduction of p-NP with $NaBH_4$. Efficient catalytic activities were achieved in the presence of Ni promoted MoS_2 catalysts in comparison to that of unmodified MoS_2 nanocomposites.

II. METHODS

For the preparation of M50Ni50/MoS_2 nanocomposite, a certain amount of $Ni(NO_3).6H_2O$ and a specified amount of aqueous solution of noble metals ($HAuCl_4$•$3H_2O$ and H_2PtCl_6•$6H_2O$) were added to the as prepared MoS_2 mixture (40 mg MoS_2 into 20 mL water and ethanol mixed solution) and the resulted suspension was stirred for 24 h. Subsequently, 30 mg of $NaBH_4$ was poured to the above suspension and kept under intense magnetic stirring for another 30 min. Finally, resulted powders were separated, washed and dried to obtain MNi/MoS_2 nanocomposite.

Catalytic reduction reactions

The MNi/MoS_2 nanocomposites were applied for the catalytic hydrogenation of p-NP to its correspond aminophenol. As the first step, 3 mL of p-NP aqueous solution (0.1 mM) was added to a quartz cell (1.0 cm path length and 4 mL volume). Introduction of $NaBH_4$ solution (0.15 mL, 0.1 M) to the reaction cell caused formation of p-nitrophenolate ions which change the color of the solution immediately. Catalytic reactions was started by adding 1 mg of MoS_2 nanocomposites into the above solution and reduction reaction was monitored by UV-vis absorption spectra of p-NP (at 400 nm) at specified time intervals.

III. RESULTS AND DISCUSSION

Characterization

Scanning electron microscopy (SEM) and transmission electron microscopy (TEM) were used to investigate morphology and structure of MoS_2 nanocomposites. Figure 2 indicate FE-SEM images of flower-like MoS_2 decorated with AuNi (Figure 2a) and PtNi (Figure 2c). The elemental mapping images of AuNi/MoS_2 (Figure 2b) and PtNi/MoS_2 (Figure 2d) demonstrate that Ni and noble metal NPs were uniformly distributed on the MoS_2 surface.

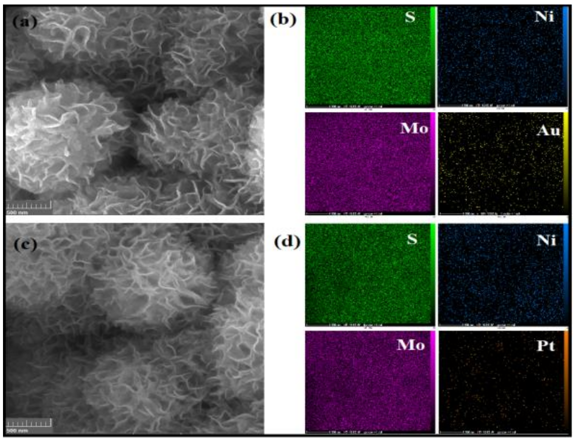

Fig. 1: FE-SEM images of AuNi/MoS_2 (a), PtNi/MoS_2 (c) FE-SEM mapping of AuNi/MoS_2 (b), PtNi/MoS_2.

XRD analysis was used to evaluate phase structure of the MoS_2 nanocomposites (Figure 1). XRD patterns of MoS_2 demonstrate diffraction peaks at around 13°, 32.2°, 34.8° and 57.2° which belong to the (002), (100), (103) and (110) crystal planes of MoS_2. For noble metals modified MoS_2 materials, XRD patterns demonstrate new characteristic peaks at 38.2° , and 39.8° which implied to the (111) planes of cubic Au(JCPDS no. 89-3697) and Pt(JCPDS no. 87-0642).

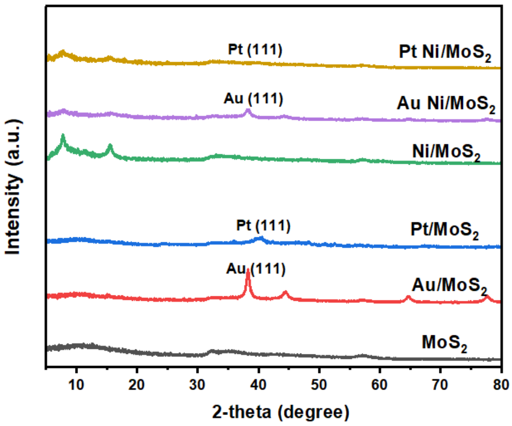

Fig.2: XRD patterns of different Ni modified MoS_2 nanocomposites.

Due to the high initial concentration of $NaBH_4$, the concentration of BH_4^- is nearly stable within the reaction time and the reduction reaction could be supposed to follow a pseudo-first-order kinetics. The kinetics of the catalytic reactions were studied by the plot of $\ln(C_t/C_0)$ against reaction time where C_0 and C_t are the p-NP concentrations at initial time and t min after that, respectively.

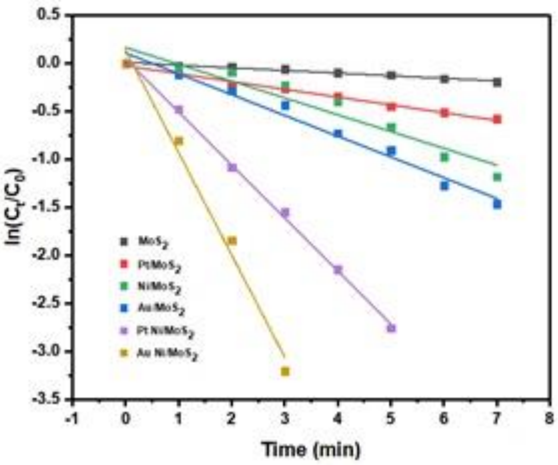

Fig 3: of $\ln(C_t/C_0)$ against reaction time for different MNi/MoS_2 nanocomposite.

The origin of the excellent catalytic activity of the noble metals decorated MoS_2 can be resulted from synergistic effects between metal NPs and MoS_2. Proposed electron transformation process of p-NP reduction over MNi/MoS_2 composites is shown by Scheme 1.

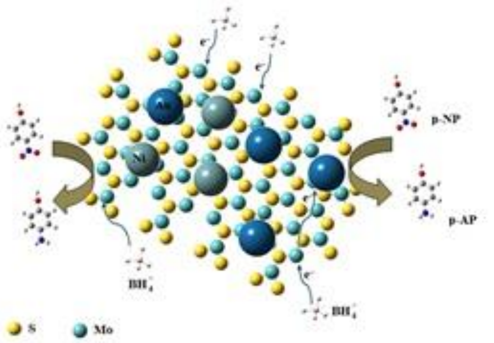

Scheme1. Proposed electron transformation process of p-NP reduction over Au(Pt)Ni/MoS_2 composite.

IV. CONCLUSION

A In this study, Ni promoted MoS_2 particles were applied as proper support for noble metal NPs to prepare efficient catalysts for catalytic reduction of p-NP with $NaBH_4$. Catalytic results asserted that as synthesized Ni modified MoS_2 particles demonstrated remarkably enhanced catalytic activity in comparison to that of unmodified MoS_2 particles. Synergistic effect between metal NPs and MoS_2 was introduced as the origin of excellent catalytic activity of metals decorated MoS_2 particles. On the other hand, Ni atoms on the MoS_2 surface exposed more reaction sites for reduction reaction and play and effective role in electron transformation on MoS_2.

REFERENCES

[1] Q. Zhang, X. Jin, Z. Xu, J. Zhang, U.F. Rendon, L. Razzari, M. Chaker, D. Ma, The journal of physical chemistry letters, (2018).

[2] S. Lu, J. Yu, Y. Cheng, Q. Wang, A. Barras, W. Xu, S. Szunerits, D. Cornu, R. Boukherroub Applied Surface Science, 411 (2017) 163-169.

[3] E. Akbarzadeh, M.R. Gholami, Research on Chemical Intermediates, 43 (2017) 5829-5839.

[4] R. Li, L. Yang, T. Xiong, Y. Wu, L. Cao, D. Yuan, W. Zhou, Journal of Power Sources, 356 (2017) 133-139.

[5] X. Li, T. Li, Y. Ma, Q. Wei, W. Qiu, H. Guo, X. Shi, P. Zhang, A.M. Asiri, L. Chen, Advanced Energy Materials, (2018) 1801357.

[6] S.A. Ansari, H. Fouad, S. Ansari, M.P. Sk, M.H. Cho, Journal of colloid and interface science, 504 (2017) 276-282.

[7] L. Fang, Y. Qiu, T. Zhai, F. Wang, M. Lan, K. Huang, Q. Jing, Colloids and Surfaces A: Physicochemical and Engineering Aspects, 535 (2017) 41-48.

[8] Q. Pan, F. Zheng, X. Ou, C. Yang, X. Xiong, M. Liu, Chemical Engineering Journal, 316 (2017) 393-400.

[9] D. Lang, T. Shen, Q. Xiang, ChemCatChem, 7 (2015) 943-951.

[10] W.-K. Jo, J.Y. Lee, N.C.S. Selvam, Chemical Engineering Journal, 289 (2016) 306-318.

[11] E. Akbarzadeh, S.R. Setayesh, M.R. Gholami, New Journal of Chemistry, 41 (2017) 7998-8005.

Application of Taguchi Method for Investigation the Removal Ability of Oil Pollution by Zeolite/Copper Oxide Nanocomposite

<u>M. Kamani</u>[a], R. Fazaeli[a]*, M. Arjmand[a], M. H. Ghorbani[a]
[a]Department of Chemistry, South Tehran Branch, Islamic Azad University, Tehran, 11365-4435, Iran
Email: R_Fazaeli@azad.ac.ir

Abstract*:* In this study, zeolite/copper oxide (Z/CuO) nanocomposite, as a nanocatalyst, was successfully synthesized to the removal of oil pollutions by advanced oxidation. The synthetic nanocomposite was characterized by X-ray diffraction (XRD), field emission scanning electron microscopy (FESEM) and energy-dispersive X-ray spectroscopy (EDS) analyses. The efficiency of quinoline removal as an oil model was determined by Taguchi design of experiment (DOE), in which, there are three variable factors consist of pollutant density (ppm), light, and oxidant concentration (mM), and two constant factors consist of solution pH and composite (gr). The results showed that the zeolite/copper oxide adsorption capacity was higher than that of copper oxide nanoparticles.

Keywords: Advanced oxidation, Nanocomposite, Quinoline, Taguchi, Zeolite.

I. INTRODUCTION

Increasing the number of oil pollutions during the process of extraction to purification and use, due to disordering the ecosystem and having the environmental losses, the life of the organisms have fallen in trouble. Therefore, removing these pollutants is very important. Oil cuts containing nitrogenous aromatic hydrocarbons such as quinoline are considered as environmental pollutants. In recent years, researchers have been looking for ways to eliminate these pollutants; In this regard, researchers have investigated nanocatalysts for the oxidation of contaminants, or absorption, and then removing them. Zeolites have used as catalytic adsorbents in a wide range of applications, because of their unique physical properties (pore size, crystallite size, ion exchange capacity, and absorption capacity), and chemical composition. In this study, the elimination of quinoline with the help of the synthetic nanocomposite was studied by the DOE [1].

II. METHODS

To synthesize nanoparticles of zeolite MCM-41, it has been used from Nikoorazm, and his colleagues [2]. Briefly: To a CTAB solution (0.2% by weight), 3.5ml of NaOH solution was added and the resulting mixture was stirred at 80°C for half an hour to prepare a homogeneous mixture. Then TEOS was gradually added and the solution was refluxed for 2h. The final product was filtered and washed with deionized water, dried in an oven, and calcined for 5.5h at 550°C.

To prepare zeolite/copper oxide nanocomposite, a certain amount of synthetic zeolite MCM-41 was dispersed in 100ml of Cu^{2+} 0.2M solution, and the suspension was stirring for 24 h. After that the suspension was washed centrifugally and dried at 100°C for 3h, then it reached 450°C and calcined for 12h.

Nanocomposite characterization was performed by FESEM (ZEISS), XRD (X'PERT PRO-Panalytical), and EDS (OXFORD). The removal studies have also been designed and tested by the Minitab16.0 software by the Taguchi Method. Table1 shows the variable and constant factors for Taguchi Method.

Table1: Levels and factors used in DOE.

Number of levels	H_2O_2 (mM)	Pollutant Concentration (ppm)	Light
1	0	8	UV-C
2	10	16	Visible
3	100	32	Darkness

III. RESULTS AND DISCUSSION

Fig.1 shows the XRD of the Z/CuO composite compared to primary zeolite. The initial structure of zeolite has changed since the addition of copper oxide. This change can be seen after the disappearance of the zeolite Bragg reflections in the low angle region (2θ=4-10), which is commonly used to identify the zeolite structure from this region (0241-038-1870,00 ° A). The structure of CuO crystal was observed at the angle of 2θ=32.5°. Other strips may have interfered with those of zeolite. The reports are seen in this research is also confirmed by other authors.

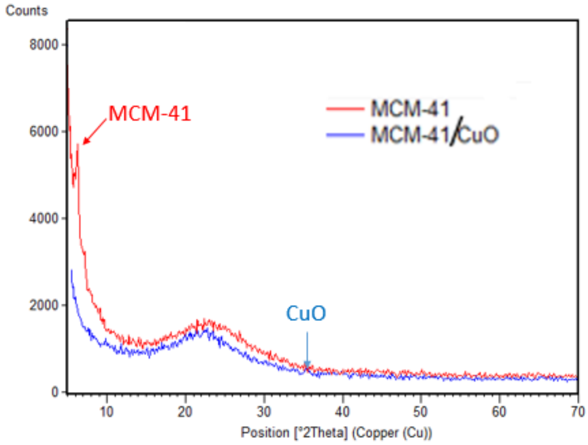

Fig.1: XRD Pattern of Z/CuO Composite Compared to MCM-41 Zeolite

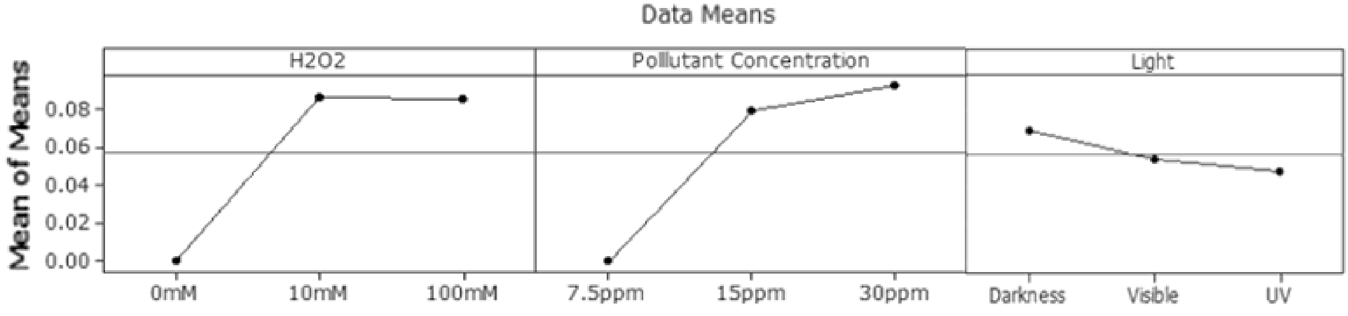

Fig.2: Main Effects Plot for Means

Fig.2 shows the brief results of DOE. By using DOE, it is predicted that the best state of reaction related to the darkness.

Fig.3, (A and B) shows, FESEM of zeolite and Z/CuO nanocomposite, respectively. In the Nikoorazm et al. research, it is stated that the pore size of the MCM-41 zeolite is 2.45nm [2] and, in general, the minimum particle size of CuO that can be synthesized by the sol-gel method is about 30nm [3]. Therefore, CuO particles cannot form inside zeolite pores, and these particles are deposited on zeolite by reaction with hydroxyl groups.

Fig.4 shows EDS of the nanocomposite. The peak of the main elements of zeolite is visible in the form and after CuO loading, to all the characteristic peaks of zeolite, copper peaks have also been added which represent the successful synthesis of CuO. As the Fig.4 shows, the percentage of Cu is 2.6 Wt.%.

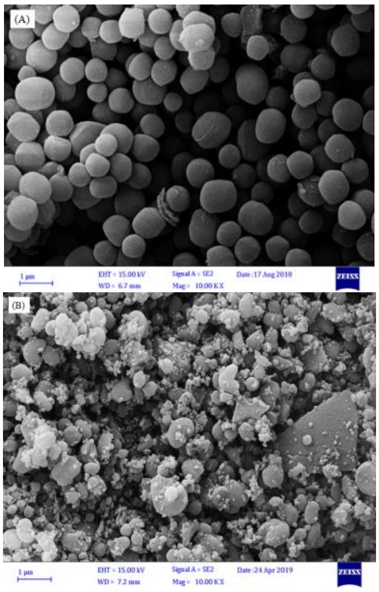

Fig.3: A) MCM-41, B) MCM-41/CuO nanocomposite

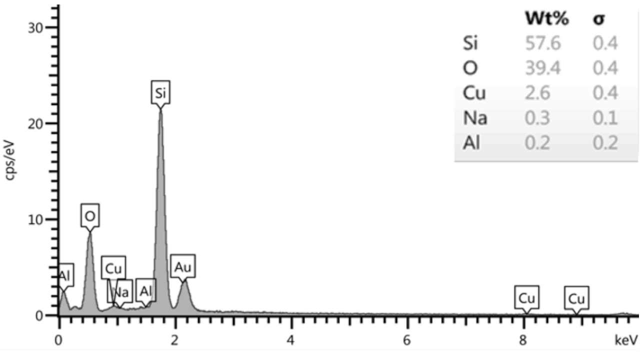

Fig.4 EDS of nanocomposite

IV. CONCLUSION

The zeolite/copper oxide (Z/CuO) nanocomposite, as a nanocatalyst, were successfully synthesized for removal oil contaminants by advanced oxidation. After characterizing the nanocomposite by XRD, FESEM, and EDS analyses, the results of the efficiency of quinoline removal as an oil model by Taguchi DOE, showed that the Z/CuO adsorption capacity was higher than that of CuO nanoparticles.

REFERENCES

[1] H. Zollinger, VCH Publishers, 1987.
[2] M. Khanmoradi, M. Nikoorazm, and A. Ghorbani- Choghamarani, Synthesis and Characterization of Pd Schiff Base Complex Immobilized onto Functionalized Nanoporous MCM-41 and its Catalytic Efficacy in the Suzuki, Heck and Stille Coupling Reactions, Catalysis Letters, vol. 147, pp. 1114–1126, 2017.
[3] M. Nikazar, Kh. Gholivand, and K. Mahanpoor, Journal of the Chinese Chemical Society, vol. 54, pp. 1261-1268, 2007

Application of MCM-41/CuO for Oil Pollutions Treatment: Optimization Process Based on Taguchi Design Method

M. S. Rahmati[a], *R. Fazaeli*[a]*, *M. Giahi Saravani*[a], *R. Ghiasi*[b]

[a]*Department of Chemistry, South Tehran Branch, Islamic Azad University, Tehran, 11365-4435, Iran*

[b]*Department of Chemistry, East Tehran Branch, Islamic Azad University, Qiam Dasht, Tehran, 18735-136, Iran*

Email: R_Fazaeli@azad.ac.ir

Abstract: In this study, the immobilized copper oxide onto MCM-41 nanostructure was prepared and characterized using X-ray diffraction (XRD), field emission scanning electron microscopy (FESEM) and energy-dispersive X-ray spectroscopy (EDS) analysis. This synthesized nanocomposite was used as photo catalyst for removing N-compounds from cut oil by H_2O_2 as oxidant. Effect of operating parameters on the Efficiency of Carbazole removal (model oil) under the Taguchi design of experiment was investigated. The results indicated that the complete elimination of carbazole was done under the mild condition. In order To design the experiments with optimize operating conditions to achieve higher removal of carbazole (model oil) as pollutants, Taguchi experimental model has been used

Keywords*:* Advanced Oxidation, Carbazole, MCM-41, Photocatalyst.

I. INTRODUCTION

The removal of N-compounds in fuel due to the Environmental contamination by NO_x compounds emission has been a challenge for many years. This can be achieved by the development of processes to upgrade heavy oil to environmentally friendly products [1]. Recently, the removal of S-compounds and N-compounds from fuel has been reported by different methods [1-3]. In this regard, the use of nanoporous material with cavities in the nanoscale which make up much of their structure as free space can be considered as an appropriate option. Among the nanopore materials, MCM-41 is of interest due to some of its special properties such as its high thermal stability, high surface area, high pore volume, structural simplicity, narrow pore size distribution and ease of preparation with negligible pore networking and pore blocking [2-3]. Hence, in order to develop the nanoporous material MCM-41, in this study, MCM-41/CuO was prepared. The aim of the study was to determine a simple and highly efficient protocol for advanced oxidation by TAguchi (DOE).

II. METHODS

The pure mesoporous MCM-41 was synthesized using the procedure given by Nikoorazm etc. [4]: To synthesis MCM-41 mesoporous material, CTAB (1 g) was added into an aqueous solution containing 3.5 mL of NaOH solution (2 M) and stirred at 80 °C. After the mixture was uninformed, 5 mL of TEOS was gradually added and the mixture was refluxed for 2 h at the same temperature. The obtained white solid was washed with deionized water and calcined at 550 C for 5 h at a rate of 2°C per min. to remove the residual surfactant.

Preparation of MCM-41/CuO**:** The certain amount of synthesized mesoporous MCM-41 was dispersed in 100mL aqueous solution containing copper acetate monohydrate 2M and stirred for 24 h at the room temperature. Then the achieved suspension is centrifuged at 12,000 rpm for 10 min. The obtained solid was washed with deionized water and allowed to dry at 100°C for 3h, then it was calcined at 450° C for 12h.

The photo catalyst characterization was performed by FESEM (ZEISS), XRD (X'PERT PRO-PAnalytical), and EDS (OXFORD) techniques.

In order to study the effect of this catalyst on removal of pollution from cut oil, the desired model have been designed and tested by the Minitab16.0 software using the Taguchi method (Table1).

Table1: Levels and factors used in DOE.

Number of levels	H_2O_2 (mM)	Pollutant Concentration (ppm)	Catalyst Volume (gr)
1	0	8	0.1
2	10	16	0.01

Number of levels	H_2O_2 (mM)	Pollutant Concentration (ppm)	Catalyst Volume (gr)
3	100	32	0.001

III. RESULTS AND DISCUSSION

The X-ray diffraction pattern of MCM-41 presented in Fig.1. Appearance of the MCMs Bragg reflections in the low angle region (2θ=4-10) confirm regular hexagonal array [4], compared to the parent MCM-41, it can be seen that the intensity of these characteristic peaks in the XRD pattern of the MCM-41/CuO sample becomes weaker and shifts to higher angles when CuO nanoparticle is loaded on MCM-41. The structure of copper oxide crystal was observed at the angle of 2θ=36.5°. Other strips may have interfered with those of zeolite.

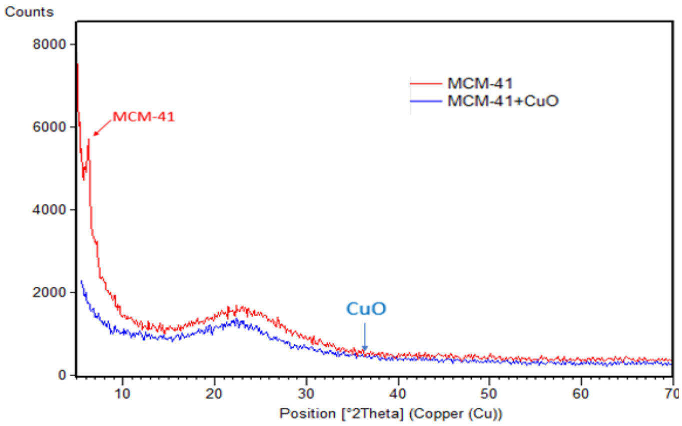

Fig.1: XRD Pattern of MCM-41/CuO nanocomposite compared to MCM-41 mesoporous.

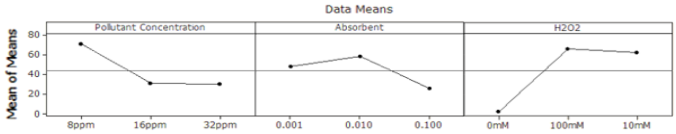

Fig.4: Main effects plot for means.

The FESEM images of MCM-41 mesoporous and MCM-41/CuO nanocomposite are shown in Fig.2. The FESEM images confirm that MCM-41 and MCM-41/CuO have a regular and spherical morphology and average pore sizes (2.0 nm and 11.0 nm) has been reported for pore size of the MCM-41 [4,5]. It is expected that CuO nanoparticles are deposited on MCM-41 by reaction with hydroxyl groups

Elimination of carbazole from cut oil in the presence of nanocatalyst using the Taguchi (DOE) method was studied. Under this method the best result was obtained with pollutant concentration of 8ppm, 0.01gr of absorbent, and 100mM of H_2O_2. The results indicated that the elimination of carbazole was done with 100% efficiency under mild reaction conditions (Fig.4).

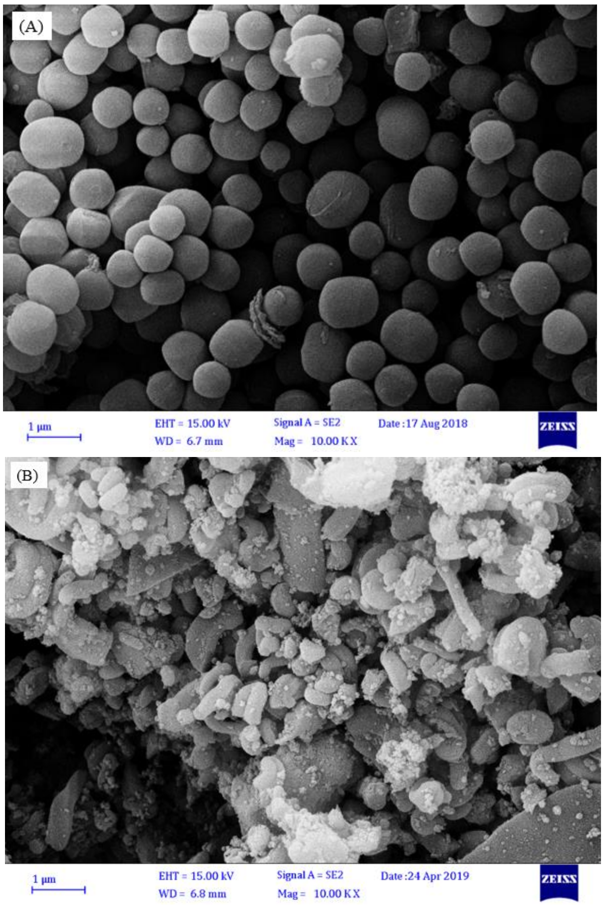

Fig.2: A) MCM-41, B) MCM-41/CuO nanocomposite

In order to check the percentage of stabilized CuO on the catalyst, EDS analysis was performed (Fig.3)

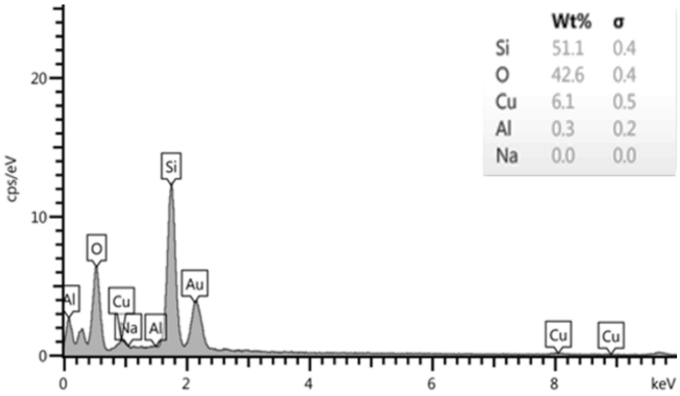

Fig.3 EDS of nanocomposite

IV. CONCLUSION

After characterization of the nanocomposite of MCM-41/CuO by XRD, FESEM, and EDS analyses, the catalytic activity of this nanocatalyst was investigated for removal oil contaminants by H_2O_2. Results obtained revealed that carbazole (oil model) removal was done with 100% efficiency using the mild conditions suggested by Taguchi.

REFERENCES

[1] H.S. Ahmed, S.A. Shaban, M.F. Menoufy, F.Y. El Kady, Effect of catalyst

[2] D. Rath, S. Rana, K. M. Parida, RSC Adv. 2014, 4, 57111.

[3] M. Nikoorazm, A. Ghorbani-Choghamarani, M. Khanmoradi, Appl. Organomet. Chem. 2016, 30, 236.

[4] M. Khanmoradi, M. Nikoorazm, and A. Ghorbani-Choghamarani, Synthesis and Characterization of Pd Schiff Base Complex Immobilized onto Functionalized Nanoporous MCM-41 and its Catalytic Efficacy in the Suzuki, Heck and Stille Coupling Reactions, Catalysis Letters, vol. 147, pp. 1114–1126, 2017.

[5] M. Nikazar, Kh. Gholivand, and K. Mahanpoor, Journal of the Chinese Chemical Society, vol. 54, pp. 1261-1268, 2007

Study and investigation TCTA as a hole transport layer in the organic light-emitting diode

Saleh fallah samakosh[a*], ***Ali. Bahari***[a], ***Vaheed fallah***[b]
Department of Solid State Physics, Faculty of Science, University of Mazandaran, Babolsar
sallehfallah1995@gmail.com

Abstract*:* In this study, An Organic Light Emitting Diode (OLED) is fabricated by ITO/TCTA/Alq_3/LiF/Al structure. TCTA as a hole transport layer in various thickness deposited by thermal evaporation method on the ITO. The thermal evaporation method was also used for deposition Alq_3 as the emission layer and the LiF/Al layer as a cathode. The effect of TCTA hole-transporting layer thickness on the electrical and optical properties of OLED devices are studied; such as light intensity, threshold voltage. The current-voltage density characteristic and electroluminescent were investigated. The best thickness for the hole transport layer according to maximum electroluminescent and minimum threshold voltage is 20nm. In order to achieve the high efficiency in OLEDs, a Quantum well as a hole transport layer is being introduced,
The best device turns on in 3(V) and the highest luminescence of the device is 1700 cd/m^2.

Keywords: Transport layer; Electron block layer; OLED; Nanostructure

I. INTRODUCTION

Recently, people are faced with a serious shortage of energy sources due to the excessive consumption of energy and the excessive use of ineligible resources. This issue is one of the main concerns of researchers and manufacturers of various components that have a close relationship with energy consumption[1]. One of the most important types of energy using in these days is electrical energy, most of them are used in the lighting industry. The use of low-power optical devices with proper operational stability is one of the most effective ways of reducing electric energy consumption in the lighting industry and reducing costs. For this reason, many efforts have been made to expand the technology of producing optical springs such as gas lamps, fluorescents, neon lights, and so on[2].

Generally, an OLED includes a variety of layers anode, hole injection layer (HIL), hole transport layer (HTL), an emission layer (EML), hole blocker layer (HBL), electron transport layer (ETL) and the cathode. In this study physical for all layer physical thermal evaporation method is used[3].

In this work, first, we change the thickness of our hole transport layer (TCTA) to finding the optimum thickness. Hole transport layer thickness is very important because this layer is balanced the hole and the electron in the emission layer. TCTA shows good hole transport properties due to the efficacy of the OLED device's performance.

Second, a double Quantum well(QW) was introduced for the hole transporting and balancing exition annihilation in EML. Our QW structure is NPB/TCTA/NPB/TCTA, this QW reduce the hole injection barrier and help hole to inject in EML, the result shows the huge improvement in device performance.

II. METHODS

Deposition of all materials was prepared in a nitrogen-filled glove box, where also the corresponding organic thin-films were spin-coated and annealed. Prior to deposition. Optical absorption spectra were collected in transmission mode using an optical fiber system by Avantes.

The pre-patterned indium tin oxide (ITO) glass substrates were purchased from Naranjo Substrates. The substrates were subsequently cleaned with soap, deionized water, and isopropanol in an ultrasonic bath for 10 minutes each, followed by 20 minutes of UV-ozone treatment[5].

Our OLED structure is ITO / TCTA / Alq_3 / LIF / AL
the ITO was used as an Anode and TCTA as a hole transport layer with 20nm thickness, lAlq_3 as the electron transport layer and organic light emission layer coated 50nm The devices were finished with a low work function cathode (1 nm thick LiF capped with 100 nm thick Al). The thicknesses of all films were determined using an Ambios XP1 profilometer. Devices were not encapsulated and were characterized in a glove box. Current density and luminance versus voltage were collected using a Keithley 2400 source meter and a

photodiode coupled to a Keithley 6485, using a Minolta LS100 to calibrate the photocurrent.

III. RESULTS AND DISCUSSION

I. *DEVICE FABRICATION*

On the clean pre-pattern ITO, different thickness TCTA layer was deposited (10nm -100nm), then 50 nm of Alq_3 as emission layer and LiF/Al deposited subsequently on TCTA. For QW device, we deposited 5nm of NPB/TCTA layer for two times, then the $Alq_3$and LiF/Al layer deposited like last device (Figure 1)

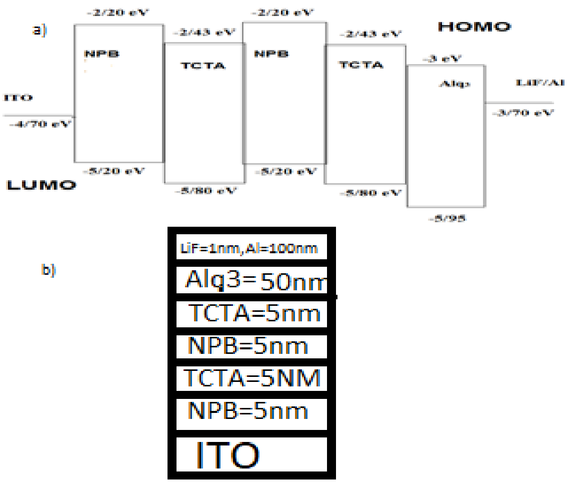

Figure 1 a) Energy band diagram of QW OLED b) OLED device structure

II. *DEVICE CHARICTARIZATION*

Figure 2 shows the luminance vs voltage for three different thickness TCTA layer device. It shows that the luminance intensity increase due the voltage and it start 15V for first device which the TCTA thickness s 70nm and it decrease to 8V for the device which the TCTA thickness is 20nm the results indicate that by decreasing the TCTA thickness the exciton can create more and the annihilation of exciton in the EML layer and created 1600 cd/m2 light and the best device efficacy is 1 Cd/A

Figure 3 shows the performance of the OLEDs which use QW for transporting hole. QW decrease the injection barrier for hole and by changing mechanism to quantum effect the hole can inject to EML layer more better and more exciton created in EML and the threshold voltage decrease to 4V and for best device the highest luminance is 1700 Cd/m2 and efficiency of the luminesce increased two time and archived 2 Cd/A.

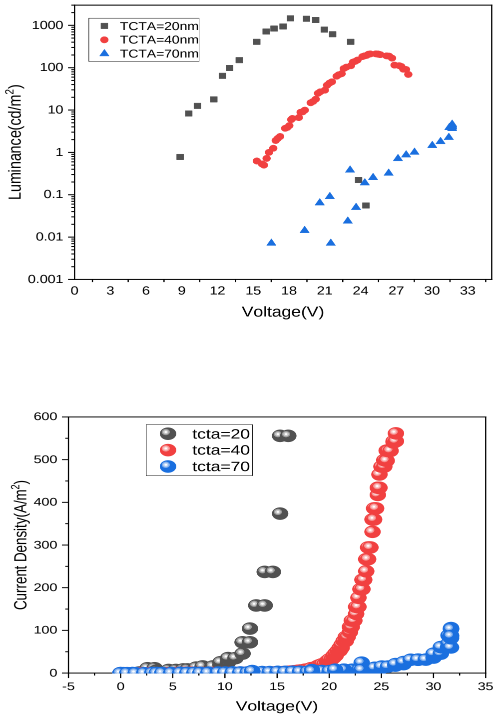

a

b

Figure 2: a) Luminance (cd/m^2)-Voltage (V)

b) Current Density (A/m^2)-Voltage (V)

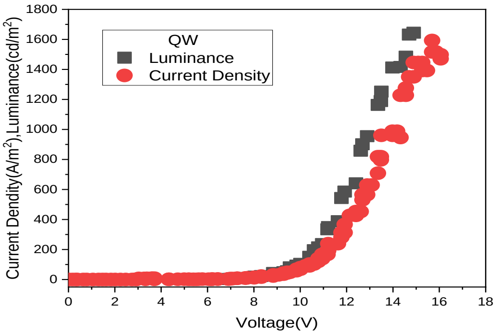

Figure3: Luminance (cd/m^2)-Voltage (V) AND Current Density (A/m^2)-Voltage (V) QW OLED

IV. CONCLUSION

We present a new transport layer TCTA due to the high Lumo for electron blocking and deep Homo for hole transporting layer. The results shows that by using TCTA as HTL the turn on voltage of OLED decrease to 8 volt and The light intensity reaching a maximum of 1600 cd/m^2, and we present A multi QW for injecting hole to EML and by using this method the turn on voltage decrease to 4V and the maximum light intensity reaching 1700cd/m2and in best device the efficacy reach 1Cd/A As a proof of concept a multi-layer Green light emitting OLED was prepared showing excellent rectification and promising current efficiency.

REFERENCES

[1] "A decade of perovskite photovoltaics," *Nat. Energy*, vol. 4, no. 1, p. 1, 2019.

[2] A. Babaei, K. Rakstys, S. Guelen, V. Fallah Hamidabadi, M.-G. La-Placa, L. Martínez-Sarti, M. Sessolo, H. A. Joel, O. P. M. Gaudin, V. Schanen, M. K. Nazeeruddin, and H. J. Bolink, "Solution processed organic light-emitting diodes using a triazatruxene crosslinkable hole transporting material," *RSC Adv.*, vol. 8, no. 62, 2018.

[3] R. K. Hallani, V. Fallah Hamidabadi, A. J. Huckaba, G. Galliani, A. Babaei, M.-G. La-Placa, A. Bahari, I. McCulloch, M. K. Nazeeruddin, M. Sessolo, and H. J. Bolink, "A new cross-linkable 9,10-diphenylanthracene derivative as a wide bandgap host for solution-processed organic light-emitting diodes," *J. Mater. Chem. C*, vol. 6, no. 47, 2018.

[4] H. J. Bolink, E. Coronado, J. Orozco, and M. Sessolo, "Efficient polymer light-emitting diode using air-stable metal oxides as electrodes," *Adv. Mater.*, 2009.

[5] M. Eslamian, "Inorganic and organic solution-processed thin film devices," *Nano-micro Lett.*, vol. 9, no. 1, p. 3, 2017.

Green Synthesis of Copper Oxide Nanoparticles Using *Gundelia tournefortii* and *Aloe Vera* Extract and Removal of Lead ions from Wastewater

Hananeh Zaferanlou [a], ***Masoumeh Rahmati*** [b], ***Ghazaleh Chizari Fard*** [c]
[a] *Student in Kahrizak, Tehran, Iran*
[b] *Chemistry expert, Kavosh research center, Kahrizak, Tehran, Iran*
[c] *Assistant Professor, Textile Chemistry & Fiber Science, Department of Textile and Polymer Engineering, Islamic Azad University, Tehran, Iran*
Email: HanaZaferanlou@gmail.com

Abstract*:* Since the industrial revolution, Water pollution, including wastewater has attracted researchers' attention. An efficient and environmentally-friendly technique has been developed for the green synthesis of CuO nanoparticles (NPs) by aqueous extract of Aloe Vera and Gundelia tournefortii as a lead-off heavy metal Sorbent. CuO NPs were characterized by XRD, FESEM and FT-IR spectroscopy. Absorption experiments were performed on aqueous solutions at different concentrations and pH. The removal rate of Pb^{2+} was investigated by Atomic absorption system. According to the results, different conditions for removal of lead ions were considered and the green synthesized CuO NPs presented excellent Photocatalytic activity for removing Pb^{2+} from wastewater.

Keywords*:* Gundelia tournefortii, Aloe Vera Pb^{2+}, CuO NPs

I. INTRODUCTION

Human life is dependent on the environment, while environmental pollution, especially water, has long been considered in public health. Recent advances in the field of technology, particularly nanotechnology, have led to the development a new concept of synthesizing NPs of desired shape and size [1]. Therefore, the need for the development of an eco-friendly, clean and low cost process to synthesis NPs forced many researchers to develop "green" chemistry [5]. Among various nanoparticles, metal oxide NPs are more widely used [2]. CuO is a semiconductor material with narrow band gap of 1.7 e.V [2]. Therefore, CuO NPs synthesized by plant extract can be used for eliminating contaminations due to their easy synthesis method, environment-friendly and Photocatalytic properties [4].

II. METHODS

To prepare the extract of *G. tournefortii* the aerial parts of it was separated and thoroughly washed then dried at room temperature for one week. 14.5 g of dried aerial parts including leaves were powdered and refluxed at 80°C with 145.3 ml of sterile distilled water for 120 min at 120 RPM. The mixture cooled down to room temperature and after filtration the aqueous extract was obtained. In green synthesis of CuO NPs, 50 ml of the *G. tournefortii* extract was added to 50 mL of a 0.003 M aqueous solution of $CuCl_2$ with stirring for 2 h at 60 °C. The color of the solution was changed from yellow to dark brown after 20 min, then the deposition was collected in a glass. For preparing the extract of *A. Vera*, leaves (250 g) were completely washed for 3 times to eliminate dust, then dried and chopped. The chopped material boiled at 120 °C for 50 min with 1000 ml of de-ionized water then 20 ml of 2 M solution of potassium chloride was added to the extract until the pH increased to 8.5 and cooled down to room temperature. For green synthesis of CuO NPs 500 ml of a 100 mM aqueous solution of copper nitrate was added to 50 ml *A. Vera* extract and it stirred on a magnetic stirrer at 100-120 °C. The solution's color changed from blue to colorless and then to brick and dark red during 24 h stirring. The solution was centrifuged at 10000 RPM at room temperature for 10 min and deposition was collected in a glass. Therefore, the obtained materials characterized by Fourier Transform Infrared Spectroscopy (FT-IR), X-ray Diffraction (XRD) and Scanning Electron Microscopy (SEM) in Tehran University.

III. RESULTS AND DISCUSSION

Fig.1 shows the powder XRD pattern of CuO NPs.The green synthesized of CuO NPs examined by XRD indicates high crystallinity. The diffraction peaks at (110), (111), (220), (202), (020), (113), (311) and (440) shows CuO NPs [6].

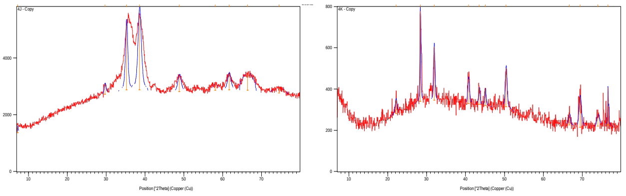

NPs synthesized by *G. tournefortii* extract   NPs synthesized by *A. Vera* extract

Fig.1: XRD pattern of green synthesized CuO NPs.

The FTIR pattern in Fig.2 shows the available peak in 2800-4000 cm^{-1} indicates the presence of $OH^-$and carbonyl (C=O). The presence of peaks in 500-700 cm^{-1} (618, 622) confirms the presence of synthesized CuO NPs [6].

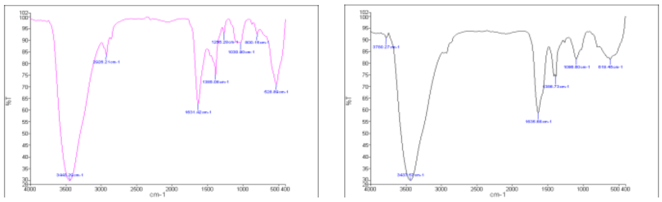

NPs synthesized by *G. tournefortii* extract NPs synthesized by *A. Vera* extract

Fig.2: FT-IR spectrum of green synthesized CuO NPs.

The SEM image (Fig.3) shows the well dispersion of CuO NPs and the size of synthesized NPs by *A. Vera* extract is approximately 10-60 nm. The size of synthesized NPs by *G. tournefortii* is 10- 40 nm with polygon morphology.

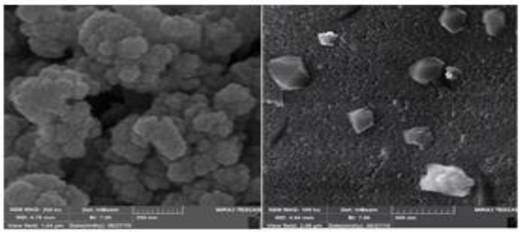

NPs synthesized by *A. Vera* extract NPs synthesized by *G. tournefortii* extract

Fig.3. SEM image of CuO NPs.

To investigate the Photocatalytic effect of synthesized NPs, there were separately placed in beakers containing 75 ml of Pb^{2+} solution at room temperature and at pH=7.5 and the amount of heavy metal removal was studied using Atomic absorption device (Unicam 939) then the impact of NPs doses on the removal of heavy metal ions (0.002- 0.1g), the effect of pH in different pH (2.5, 4, 6, 7.5, 8.5) and the effect of the concentration of primary metals (100, 200, 300, 400 mg/L) were investigated. The amount of absorbed metal per unit mass of NPs (q) and the percentage removal of heavy metals (R) were calculated according to equations (1) and (2).

$$q = \frac{(C_0 - C_e) \times V}{M} \qquad (1)$$

$$\mathrm{R} = \frac{\mathrm{C_0 - C}}{\mathrm{C_0}} \times 100 \qquad (2)$$

C_0 shows the initial concentration, C_e is the equilibrium concentration of metal ions in solution (mg/L), V is the volume of the solution (L), C indicates the concentration of metal ions and M is the absorbing mass. By increasing the amount of NPs, the removal percentage of heavy metals has increased due to the high available absorption sites with the fixed metal ion content. Also, increasing the amount of NPs reduced the maximum heavy metal ion absorption capacity, which could be due to the number of unsaturated absorption sites during the process Fig.4[3]. According to Fig.4, 0.008g of NPs were selected as optimal.

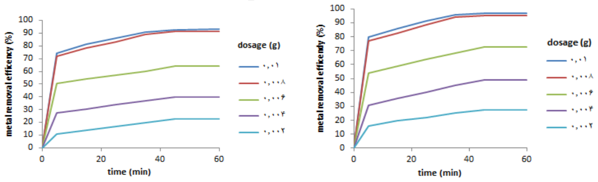

Fig.4.The effect of absorbent amount in removing heavy metal ions.

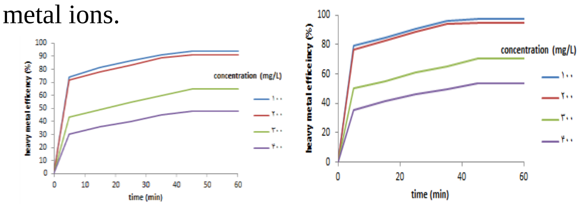

Fig.5.The effect of concentration in removing (Pb^{2+}) percentage.

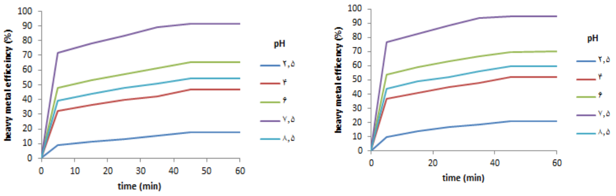

Fig.6.The effect of pH

Increasing the initial concentration of metal ions reduced the removal percentage which was related to the presence of a fixed number of absorption sites against the increase in the number of metal ions. However, the absorption capacity increased with rising the initial concentration of heavy metal ions. The absorption of Pb^{2+} was very fast in the early minutes Fig.5. The rapid absorption of ions at this stage might be due to uncoated surfaces and active sites on the absorber surface. Afterward, the absorption was slowed down because of the decrease in the number of absorption equilibrium[4]. Fig.6, shows that the absorption percentage increased by raising the pH. The least amount of absorption in the acidic pH was due to the high concentration of H^+ in comparison with the metal ion during the absorption process[5]. In strong base condition, metal ion was precipitated because of the high concentration of OH^-, in this solution, negative oxygen atoms were suitable for absorbing Pb^{2+}. In this case, electrostatic absorption could occur between metal ions and oxygen atoms with different loads. The maximum metal absorption in pH=7.5 has occurred.

III. CONCLUSION

In conclusion, CuO NPs with high scale-up were synthesized at room temperature. The green synthesis of CuO NPs was carried out by using *G. tournefortii* and *A. Vera* extract. The CuO NPs presented Photocatalytic activity as a heavy metal (Pb^{2+}) remover. According to experiments, by increasing the amount of NPs, the percentage of removal of Lead ions has increased due to high available absorption sites against the fixed amount of metal ions. Furthermore, due to the presence of a constant number of absorption sites by raising number of Pb^{2+}, in fact, increasing the initial concentration of Lead ions reduced the removal percentage. However, the absorption capacity increases with increasing concentration of heavy metal ions.

REFERENCES

[1] Kumar, P. V., Shameem, U., Kollu, P., Kalyani, R. L., & Pammi, S. V. N. (2015). Green synthesis of copper oxide nanoparticles using Aloe Vera leaf extract and its antibacterial activity against fish bacterial pathogens. *BioNanoScience*, *5* (3), 135-139.

[2] Arash Almasian, Niyaz Mohammad Mahmoodi, Mohammad Ebrahim Olya, 2015, Tectomer grafted nanofiber: Synthesis, characterization and dye removal ability from multicomponent system, Journal of Industrial and Engineering Chemistry 32, 85–98.

[3] Parvin Karimi Neghlani, Mehdi Rafizadeh, Faramarz Afshar Taromi, 2011, Preparation of aminated-polyacrylonitrile nanofiber membranes for the adsorption of metal ions: Comparison with microfibers, Journal of Hazardous Materials, 186, 182–189.

[4] M. Ghasemi, M. Naushad, N. Ghasemi, Y. Khosravi-fard, 2014, Adsorption of Pb (II) from aqueous solution using new adsorbents prepared from agricultural waste: Adsorption isotherm and kinetic studies, Journal of Industrial and Engineering Chemistry, 20, 2193–2199.

[5] Nasrollahzadeh, M., Maham, M., & Sajadi, S. M. (2015). Green synthesis of CuO nanoparticles by aqueous extract of Gundelia tournefortii and evaluation of their catalytic activity for the synthesis of N-monosubstituted ureas and reduction of 4-nitro-
Phenol. Journal of colloid and interface science, 455, 245-253.

[6] Ghidan, A. Y., Al-Antary, T. M., & Awwad, A. M. (2016). Green synthesis of copper oxide nanoparticles using Punica granatum peels extract: effect on green peach Aphid. Environmental Nanotechnology, Monitoring & Management, 6, 95-98.

Synthesis Palladium Nanoparticles by Laser Ablation and Deposition on Carbon Cloth

Shohreh karami[a], Babak Jaleh[a]*, Bahareh Feizi Mohazzab[a], Saeid Azizian[b]

[a] Department of Physics, Bu-Ali Sina University, Hamedan, 65178-38695, Iran
[b] Department of Physical Chemistry Faculty of Chemistry, Bu-Ali Sina University
Hamedan,65178-38695, Iran
Email :jaleh@basu.ac.ir

Abstract: Recently green chemistry has attracted a lot of attention due to the eco-friendly properties. Palladium nanoparticles'(Pd NPs) specific properties turn it to a good choice to utilize in different fields. In this paper, Pd NPs was fabricated by means of Laser ablation in liquid (LAL) technique. Carbon cloths (CC) was used as a substrate for deposition Pd NPs in a simple stirring method. The morphology of CC was studied by SEM analysis, and presence of Pd NPs on the surface of CC was investigated by EDX and XRD.

Keywords: laser ablation in liquids (LAL), palladium nanoparticles (Pd NPs), carbon cloth(CC).

I. INTRODUCTION

Carbon cloth (CC) has been known for its unique properties, such as crystalline structure adjustment and porosity [1,2]. The CC deposition by many nanoparticles [3-5] like Platinum (Pt) and graphene oxide (GO)[6], titanium oxide (TiO_2)[7], manganese oxide (MnO_2) [8].

Some of methods has been deployed to attach nanoparticles on CC's surface include the laser ablation and chemical reduction methods. In the past decade, different technique have been used to produce palladium nanoparticles (Pd NPs). In recent years, laser ablation of solid sample in liquids is one of the accepted methods and it has appeared as an adaptable method to fabricate nanoparticles. Several advantages of LAL with respect to the chemical methods are presented as follows: eliminating contamination and chemical reagents. There are some studies describing the fabrication of Pd NPs by LAL with and without surfactant for diverse applications such as catalyst and hydrogen storage.[9,10]

II. METHODS

Carbon cloth CH-700(CC) was purchased from Kuraray Chemical Co. Ltd., Japan and and for the ablation process a fiber laser (RFL-P30Q) was used. To generate palladium nanoparticles palladium target (99.9%, Aldrich) was used. The Surface morphology of samples were studied by scanning electron microscope (SEM, Cam scan MV2300). To ensuring Pd NPs deposition on the surface of CC Energy-dispersive X-ray spectrometry microprobe (EDX) and X-ray diffraction (XRD) was used.

Pd NPs deposition on CC:

The Pd NPs were deposited on CC using the LAL and was carried out as follows: The CC (2.5*1.5 cm^2) was immersed in cell filled with deionized water to hang the specimens. At the same time, the palladium target (99.9%, Aldrich) is placed at the bottom of cell and to reduce the absorption of laser wavelength, about 2 mm of water covers the whole target surface. For ablation process a fiber laser (RFL-P30Q) is exploited at 1064 nm with 100 ns duration, 1.5 mJ pulse energy, about 59.68 J cm^2 laser pulse fluence and 20 KHz repetition rate. Then, irradiation beam was focused through a quartz lens to 40 µm spot size. LAL process was performed on palladium target over a rectangular area of 4mm×4 mm horizontally with step of 10 µm in y-direction.The cell was kept under constant stirring using a stir plate, in a way that the magnet did not collide with the specimens and palladium target. As LAL process was being performed, formation of Pd NPs in DI water and deposition of Pd NPs on CC was observed, simultaneously. In typical LAL as the ablation time increases the ablation rate decreases due to the absorption of laser beam by colloidal NPs.

Consequently, the preparation Pd NPs and their deposition on the surface of samples in one-step is advantageous; during laser ablation a portion of ensuing Pd NPs deposited on CC surface. LAL was applied for different time (10, 15 and 20 min) when the laser ablation process was finished, stirring was continued for 5 min. The specimens were labeled CC/Pdx, where x represented LAL's time. Figure 1 illustrates the experimental setup for Pd NPs deposition on CC.

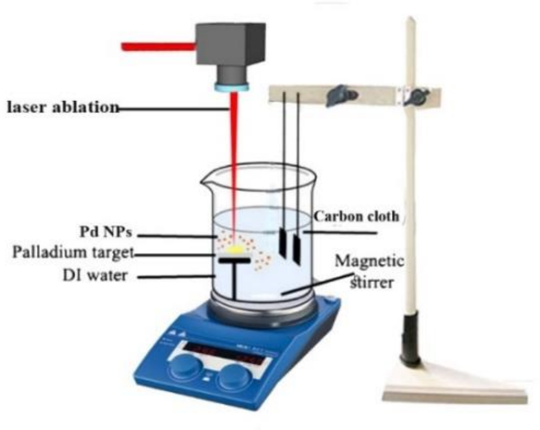

Fig.1schematic of Pd NP deposition on CC

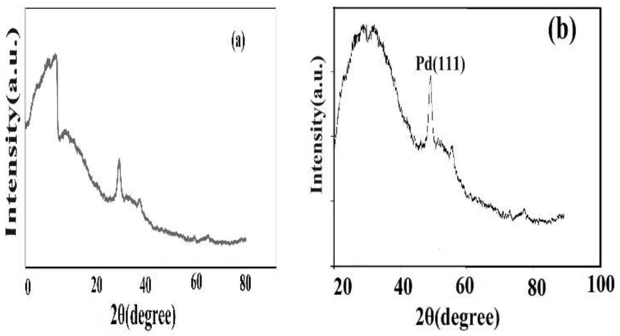

Fig2.XRD patterns of (a) virgin sample and (b) deposited sample

III. RESULTS AND DISCUSSION

The Figure2 shows XRD curves of carbon cloth before and after deposition Pd NPs. The Figure2-b confirmed Pd NPs were deposited on the surface of samples. The wide peak was related to carbon clothe .There is one sharp reflection peak at 49.119° derived from the regular adjustment of (111) plane of the Pd (JCPDS 46-1043) [11,12].

To assess morphology of cc and cc/Pdx SEM analyses was deployed. Figure 3-a shows the surface of the cc and its fiber before deposition. As can be seen CC’s porosity provides a good space for Pd NPs deposition. Comparison SEM image of CC/Pdx (x=10, 15 and 20) shows presence of Pd NPs on the surface of CC, demonstrated LAL was succeeded in fabrication Pd NPs.

The morphology of the surface of the CC/Pd10 demonstrate that the Pd NPs was loaded uniformly onto the carbon cloth surface. The surface morphology of CC/Pd15 and CC/Pd20 are shown in Figure3-c and d, respectively. Throughout the pictures, Pd NPs were aggregated in some regions attributed to increasing LAL’s time.

The EDX analysis was performed to study presence of Pd NPs. The results shows in Figure 4, demonstrated presence of Pd NPs on the surface of samples.

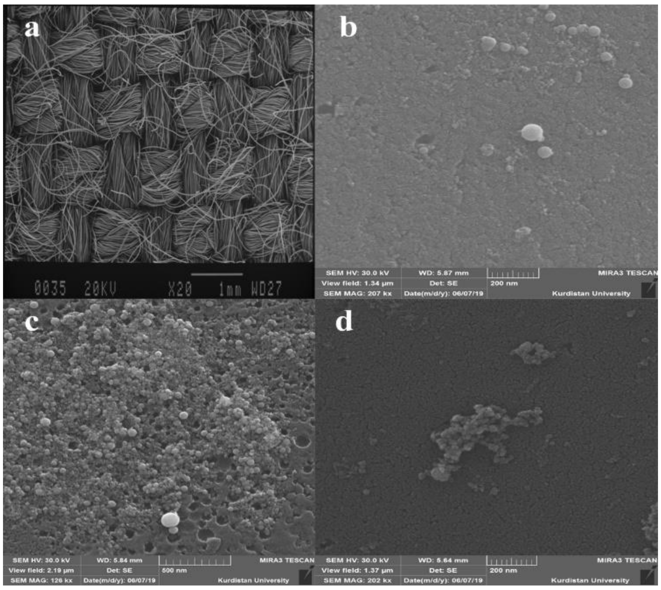

Fig 3. SEM images of CC(a), CC/Pd10 (b) CC/Pd15 (c), CC/Pd20 (d).

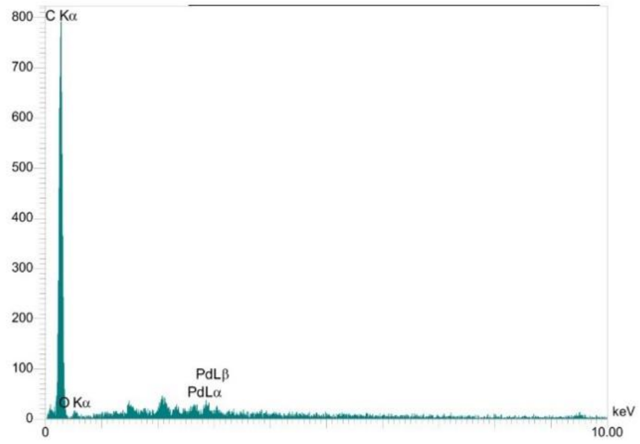

Fig4 EDX analyses of CC/Pd15

IV. CONCLUSION

In this paper, Pd NPs was fabricated by laser ablation in liquid technique. CC was utilized as substrate for nanoparticles deposition. Pd NPs was deposited on the surface of CC in different time. The results of deployed analysis leads to conclusion that Pd NPs were deposited on the surface of carbon cloth down to the it's surface porosity. In respect of deposited degree comparison morphology of samples suggest that nanoparticles were almost uniformly deposited on the surface of CC/Pd15 related to agglomeration of fabricated Pd NPs.

REFERENCES

[1] Choi, D., Kil, H.-S. and Lee, S.J.C.142,carbon ,2018.
[2] Al Aiti, M., et al, Progress in Materials Science. 98: p. 477-551, 2018.
[3] Yang, H., B. Shi, and S.J.C. Wang, Catalyst, 8(5): p. 207. 2018

[4] Teng, C., Zhang, N., Gao, X., Li, X., Wu, Z., Wang, W., Zhi, M. and Hong, Z.J.M.t.e,11, 192-198.et al catalysts, 11: p. 192-198, 2019.
[5] Ouyang, Y., Huang, R., Xia, X., Ye, H., Jiao, X., Wang, L., Lei, W. and Hao, Q.J.C.E.J, Chemical Engineering Journal,. 355: p. 416-427, 2019.
[6] Yao, Z., Zhu, M., Jiang, F., Du, Y., Wang, C. and Yang, P.J.J.o.M.C Journal of Materials Chemistry, 22(27), p. 13707-13713,2012.
[7] Zhu, Y., Y. Fu, and Q.-Q.J.A.S.S. Applied Surface Science 257(6): p. 2275-2280.2011.

[8] Chen, Y.-C., Hsu, Y.-K., Lin, Y.-G., Lin, Y.-K., Horng, Y.-Y., Chen, L.-C. and Chen ,K.-H.J.E.A, Electro chemical Acta56(20): p. 7124-7130.2011.
[9] Cristoforetti, G., Pitzalis, E., Spiniello, R., Ishak, R., Giammanco, F., Muniz-Miranda, M. and Caporali, S.J.A.S.S, Applied Surface Science. 258(7), 3289-3297. (7): p. 3289-3297. 2012.

[10] Feizi Mohazzab, B.F., Jaleh, B., Issaabadi, Z., Nasrollahzadeh, M. and Varma, R.S.J.G.C, Green Chemistry,12,(2011) 9810-9812,2019.
[11] Pernites, R., Vergara, A., Yago, A., Cui, K. and Advincula, R.J.C.C., Chemical Communications , 47(35), 9810-9812,2011.
[12] Feizi Mohazzab, B.F., Jaleh, B., Nasrollahzadeh, M. and Issaabadi, Z.J.C.L, Green Chemistry**,** 149(1): p. 169-179, 2019.
[13]

Synthesize of Carbon Nanoparticles by Fiber Laser Ablation of Activated Carbon in Water

Hamed Ghanbari Gol [a], **Babak Jaleh** [a*], **Behnaz Feizi Mohazzab** [a], **Saeid Azizian** [b]
[a] Department of Physics, Bu-Ali Sina University, Hamedan, 65178-38695, Iran
[b] Department of Physical Chemistry Faculty of Chemistry, Bu-Ali Sina University
Hamedan,65178-38695, Iran
Email: jaleh@basu.ac.ir

Abstract: In general, carbon nanoparticles (CNPs) have different applications in the environment [1], energy [2], biomedical [3], and the other fields of science. There are quite an extensive diversity of techniques which could be applied to produce nanoparticles. In this work, carbon nanoparticles were produced using laser ablation in liquid (LAL) medium in one-step producer. In this method first, the activated carbon (AC) was dispersed into deionized water and irradiated via a Fiber laser with a wavelength of 1064 nm. The UV-visible spectroscopy was done to investigate the optical properties of the product. Also, SEM and EDAX were used to examine the morphology and atomic percentage of elements, respectively.

Keywords*:* Activated carbon (AC), Carbon nanoparticles (CNPs), Deionized water, Laser ablation in liquid (LAL).

I. INTRODUCTION

Carbon nanoparticles due to their special properties such as nontoxicity [3] and large surface area [1] have potential applications in biomedical as drug delivery [4] and in the environment as adequate filters to remove industrial pollution [1]. Laser ablation in liquid medium is a safe and cost-effective method to produce nanomaterials [5]. In this method, a plasma plume is made in the liquid-target interface precisely at the point of the laser irradiation. High-pressure and high-temperature of plasma plume provides the necessary condition to generate particles with new properties [6]. Due to the use of water as liquid medium, the broken molecules of water and carbon into the plasma plume combine together and make carboxyl and hydroxyl groups [7].

II. METHODS

In this work, the activated carbon with a mean size of 1 µm was used. 5 mg of activated carbon was dispersed ultrasonically into the 10 ml of deionized water to obtain a homogeneous suspension. The obtained suspension was exposed to fiber laser irradiation with a power of 27 W, wavelength of 1064 nm, pulse width of 100 ns, scan speed of 2000 mm/s, and irradiation time of 60 min. In order to have a homogeneous collide and prevent the deposition of activated carbon particles during irradiation process, the suspension was stirred magnetically. During the irradiation process, the color of suspension changed from black to brilliant yellow, and its color became thicker yellow over time. After the laser ablation process, in order to separation of nanoparticles from the larger particles, the colloidal product was filtered in two steps. Firstly, the colloidal product was filtered using a filter paper. After that, the nanoparticles were gathered from the filtered colloid using a centrifuge (rotational speed of 15000 RPM). The UV-VIS, EDX and SEM analysis were applied to study the product and the results were investigated.

III. RESULTS AND DISCUSSION

Fig. 1a shows activated carbon dispersed into deionized water and Fig. 1b shows the obtained carbon nanoparticles in colloidal form after laser ablation process.

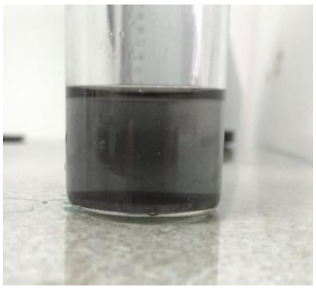

Fig. 1a: Activated carbon in deionized water (before LAL).

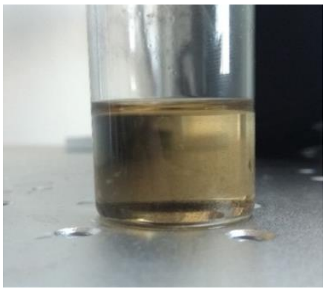

Fig. 1b: Synthesized CNPs in deionized water (after LAL).

A. *Optical characterization*

Fig. 2 represents the absorbance spectrum of the carbon nanoparticles in the range of 190-500 nm. The shoulder-like peak at 263 nm is an evidence of the formation of CNPs which corresponds to π-π* transition of C=C [8] or C=O [9] bond of nanoparticles.

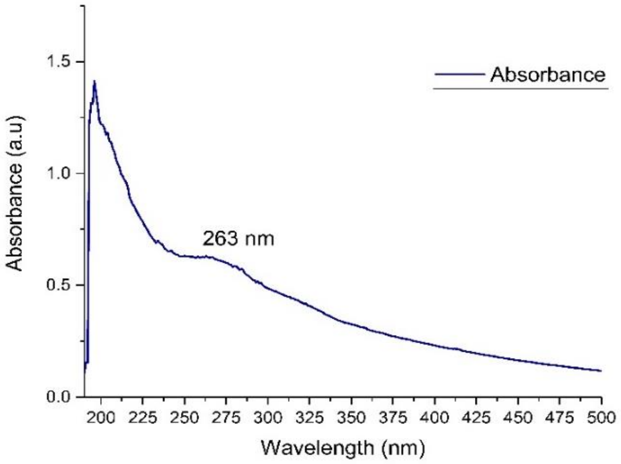

Fig. 2: UV-VIS spectrum of synthesized carbon nanoparticles in deionized water.

B. *Morphological analysis*

The SEM image of the product is shown in Fig. 3 (scale of 200 nm). By calculating the size of the particles, the average diameter of particles is obtained 10-50 nm. On top of that, it is obvious that nanoparticles have approximately spherical shape.

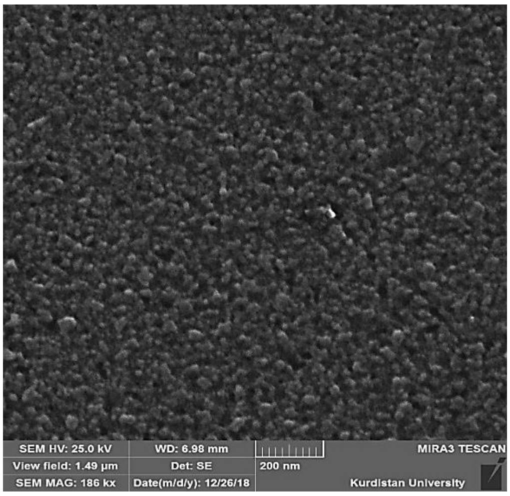

Fig. 3: SEM image of carbon nanoparticles.

C. *EDAX analysis*

For doing the EDAX analysis several drops of colloidal product were dried on a glass slide. So, the EDAX results not only include the product's elements, but also the slide's elements (Table 1).

Table 1: Quantitative results of the dried product on a glass slide.

Elements	Atomic %
C (k)	10.38
O (k)	58.35
Na (k)	5.58
Mg (k)	1.35
Si (k)	19.44
Ca (k)	4.91

According to Table 1, it can be seen that the atomic concentration of Oxygen is significantly more than the rest of elements. This might be due to presence of oxygen functional groups in the obtained CNPs. In addition, the usage of the glass slide is the other reason for adjusting the high value of Oxygen in EDAX results.

IV. CONCLUSION

The carbon nanoparticles were synthesized using laser ablation method by activated carbon as the only regent. The SEM results verified that the obtained carbon nanoparticles are in the size range of 10-50 nm. Synthesized CNPs have very good stability. Also, given that carbon nanoparticles are synthesized in water and carbon is a non-toxic material, it is expected these nanomaterials to be usable in biomedicine.

REFERENCES

[1] Russo. R, D'Urso. L, Hu. A, Zhou. N, Compagnini. G. Applied Surface Science. 348: P. 85-91, 2015.

[2] Yang. D, Bock. C. Journal of Power Sources. 337: P. 73-81, 2017.

[3] Dudek. M, Rosowski. A, Koperkiewicz. A, Grobelny. J, Wach. R, Sharp. M, French. P, Janasz. L, Kozanecki. M. physica status solidi (a). 214.2: P. 1600318, 2017.

[4] Oh. W-K, H. Yoon, J. Jang. Biomaterials. 31.6: P. 1342-1348, 2010.

[5] Karatutlu. A, Barhoum. A, Sapelkin. A. Emerging Applications of Nanoparticles and Architecture Nanostructures. Elsevier: P. 1-28, 2018.

[6] Yang, G.W. Progress in Materials Science. 52.4: P. 648-698, 2007.

[7] Calabro. R, Yang. D, Kim. D. Journal of colloid and interface science. 527: P. 132-140, 2018.

[8] Yogesh. G, Shuaib. E.p, Sastikumar. D. Materials Research Bulletin. 91: P. 220-226, 2017.

[9] Bagga. K, McCann. R, Wang. M, Stalcup. A, Vazquez. M, Brabazon. D. Journal of colloid and interface science. 447: P. 263-268, 2015.

Donor-Acceptor group effects on structure and NLO properties of some small Fullerenes

H.R. Shamlouei
Department of Chemistry,Lorestan University, Khorram Abad, Iran,
Email: Shamlouei.ha@lu.ac.ir

Abstract: In this study the influence of donor and acceptor groups on structures, electrical and optical properties of some small fullerene, C_{20}, C_{24} and C_{26}, were explored. It was displayed that the donor and acceptor groups presence have drastic effects on their structures. Additionally it was demonstrated that the electrical properties of those fullerenes were considerably influenced by the donor and acceptors groups' existence. In final part it is illustrated that the linear and non-linear optical properties of these nanoclusters is remarkably enhanced in presence of the donor and acceptor groups.

Keywords: NLO, Small Fullerene, Donor- Acceptor group

I. INTRODUCTION

The C60 fullerene was discovered in 1985 [1] and was synthesized in large scale [2]. They have novel and unusual physical and chemical properties [3–5]. The structure of normal fullerenes is composed of 12 pentagons and different number of hexagons. For instance the C60 contain 12 five-membered rings and 20 six-membered rings. The investigation and use of the expected properties of smaller fullerenes await their macroscopic scale syntheses, but the bulk synthesis of them has been proved extremely difficult due to the strained pentagon–pentagon fusions. The smallest possible fullerene cage C_{20}, which consists of only 12 pentagons, had been produced in the gas phase and characterized by anion photoelectron spectroscopy [6]. These fullerenes are molecular allotropes of carbon, exhibiting a wealth of interesting phenomena due to their π-electron nature that can be easily manipulated by chemical means. The large curvature of the conjugated π-electron systems of these hollow spheres has facilitated a rich chemical behavior allowing the synthesis of many different derivatives thereby making the fullerene family a versatile building block of materials of importance in physics, chemistry, and biology. In this research, the structure of some small fullerene as C_{20}, C_{24}, and C_{26} were studied and the donor-acceptor group effect on their structure and optical properties (NLO) was explored.

II. METHODS

All structures of considered molecules were optimized using B3LYP method and exchange and correlation functional with 6-311g(d,p) basis set. Vibrational frequencies were implemented at the same level of theory to confirm all structural are in global minimal. All calculation employed using Gaussian09 package [7]. Gap energy (E_g) was calculated based on following equation:

$$E_g = E_{LUMO} - E_{HOMO}$$

where E_{HOMO} is the energy of highest occupied molecular orbital (HOMO) and E_{LUMO} is the energy of lowest unoccupied molecular orbital (LUMO). The non-linear optical (NLO) properties of nanocages were calculated by polar method. The –NO group was selected as electron acceptor group and –NH_2 group was selected as electron donor group.

III. RESULTS AND DISCUSSION

In the first step of this research, the optimized structures of pristine and substituted fullerene were calculated. For instance the structure of C_{26} in pristine and substituted forms is illustrated in Fig 1.

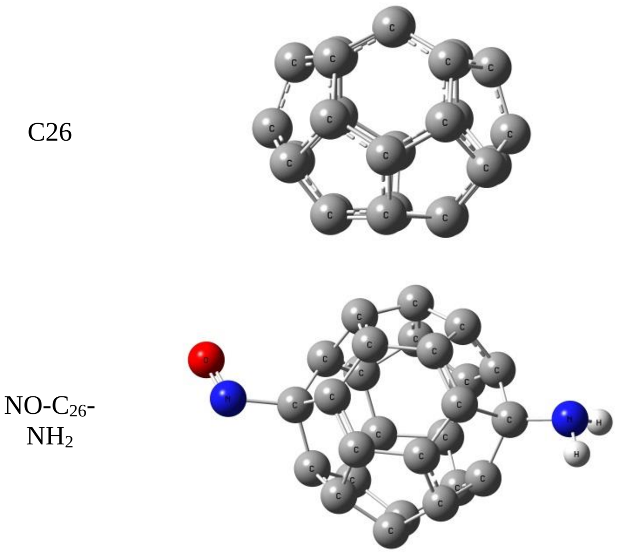

Fig 1: the optimized structure of pristine and substituted C26 fullerene

Then the electronic properties of all clusters were calculated which the density of states for pristine and substituted fullerene is illustrated in Fig. 2.

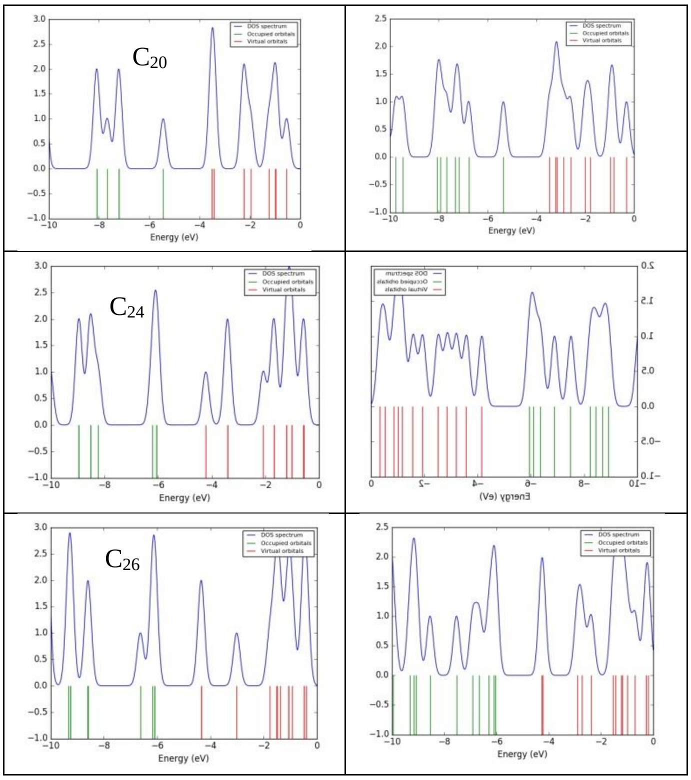

Fig 2: the DOS spectrum of considered fullerenes in pristine and substituted forms

The values of gap energy for all considered nanoclusters were calculated which the results are gathered in Table 1.

Table 1: the values of Eg considered fullerenes in pristine and substituted forms

Nanocage	E_g
Pristine C_{20}	1.94
Substituted C_{20}	1.88
Pristine C_{24}	1.83
Substituted C_{24}	1.79
Pristine C_{26}	1.74
Substituted C_{26}	1.77

As shown in Table 1, the value of E_g for C_{20} and C_{24} fullerenes decrease in donor and acceptor groups presence. However the donor and acceptor group slightly decrease the E_g of C_{26} fullerene.

The polarizability and first hyperpolarizability which is corresponding to optical properties were calculated. In Table 2, the result of calculated values of dipole moments, polarizability and first hyperpolarizability of pristine and substitutes forms of these fullerenes was compared.

Table 2: the results of calculated μ, α and β for pristine and substituted form of fullerene.

NanoCage	μ(Debye)	α(a.u.)	β(a.u.)
Pristine C_{20}	0	166.73	30.75
Substituted C_{20}	1.43	182.103	289.49
Pristine C_{24}	0.002	188.28	5.89
Substituted C_{24}	1.48	220.57	303.73
Pristine C_{26}	0.001	219.52	26.65
Substituted C_{26}	1.36	240.76	220.98

As illustrated in Table 2, the dipole moment of nanocage is drastically improved by donor and acceptor groups existence. Other results illustrated in Table2, is that the optical properties of the fullerene are substantially improved in donor and acceptor substituents presence.

IV. CONCLUSION

In this research the effect of donor and acceptor groups on structures, electrical and optical properties of small fullerene were studied. It was shown that the structures of them were drastically affected by donor and acceptor presence. In continue, the electrical properties of them were calculated and sowed that the donor and acceptors groups have substantial effects on their electrical properties. Finally the linear and non-linear optical properties of them were calculated and it was illustrated that the optical properties of them is noticeably improved by donor and acceptor groups.

The results of this research may be used to design new material with high NLO response.

REFERENCES

[1] Kroto HW, Heath JR, O'Brien SC, et al. C60: Buckminsterfullerene. Nature 1985;318:162

[2] Kratschmer W, Lamb LD, Fostiropoulos K, et al. Solid C60: a new form of carbon. Nature 1990;347:354

[3] Koma A. Van der Waals epitaxy e a new epitaxial growth method for a highly lattice-mismatched system. Thin Solid Films 1992;216:72

[4] Sakurai T, Wang XD, Xue QK, et al. Scanning tunneling microscopy study of fullerenes. Prog Surf Sci 1996;51:263

[5] Yoneda Y, Sakaue K, Terauchi H. Epitaxial growth of single-crystal C60 films on GaAs(111) substrates. J Phys Soc Jpn 1994; 63:3560

[6] Yao JH, Zou YJ, Zhang XW, et al. The (111) oriented growth of C60 films on GaAs(100) substrates. Thin Solid Films 1997;305:22

[7] M.J. Frisch, et al., Gaussian 09, Revision A.1, Gaussian, Inc, Wallingford, CT, 2009.

Synthesis of two-component TiO_2-ZnO nanoparticles

F. Nasirzadeh, R. Rasuli*
Department of Physics, University of Zanjan, Zanjan, Iran
Email:fatemeh_nasirzadeh@znu.ac.ir

Abstract: In this study, two-component TiO_2-ZnO nanoparticles were synthesized in two steps by the arc-discharge method. Titanium and zinc electrodes were used to produce these nanostructures. The optical and the crystalline properties of nanoparticales were investigated using UV–Vis spectroscopy and X-ray diffraction. The results show that the nanoparticles were mostly crystallized with hexagonal structure and rutile.

Keywords: TiO_2, ZnO, nanoparticles, arc-discharge

I. INTRODUCTION

The hybrid nanocomposites are generally considered to produce new functionalized materials. In a two-component system, the created electron-hole pairs can easily separate from each other. Among these systems the TiO_2-ZnO system has been studied previously [1]. In a such system, the electron transfers from the conduction band of TiO_2 to the conduction band of the ZnO while hole can transfer from the valence band of ZnO to the valence band of TiO_2. Consequently, the recombination of electron-hole pairs decreases and the accumulation of electrons increase at the surface of composite [1].

There are many methods for synthesizing two-component systems such as sol–gel technique [2], spray pyrolysis [3], metal/organic chemical vapor deposition [4], chemical vapor synthesis [5], electric arc discharge. As reported arc-discharge in liquid environment is powerful method to synthesis the two-component nanoparticles [6]. This method requires a DC power supply, liquid environment, and two electrodes. In this paper, we synthesis the two-component system by two-step. Results show better efficiency in comparison with the previous results.

II. METHODS

The arc-discharge method was used to synthesis TiO_2-ZnO nanocomposites. In this method, titanium electrodes were placed in the deionized water and 10A current was established between two titanium electrodes. In next step, zinc electrodes were placed in an aqueous solution of TiO_2 nanoparticles. The obtained solution was dried at 80 ° C subsequently. Finally, the powder was annealed in a furnace at 450ºC. X-ray analysis was performed by D8 Advance X-Ray diffractometer from Bruker and UV-Vis spectroscopy was done with a V900 apparatus from OPTC Company.

III. RESULTS AND DISCUSSION

The UV–Vis spectroscopy of the ZnO and TiO_2-ZnO nanostructure were presented in Fig. 1 and 2, respectively. As shown in Fig. 1 there is intensive absorption in the ultraviolet band at 236 nm while the absorption wavelength of ZnO is about 369 nm. The UV-Vis results in Fig. 2 show that the prepared nanocomposite has a stronger absorption than bare ZnO and TiO_2 nanoparticles. This suggest that enhancing its electron-hole creation increases as well [7].

X-ray diffraction patterns were used to investigate the crystallographic structure. As seen in the Fig. 3, the peaks at the Bragg angles 41.00, 27.30 are due to (110) and (111) planes of Rutile TiO_2 according to JCPDS 01-077-0446. Peaks at the angles of 31.77, 34.43, 47.55 are related to the (010), (002), (012) plane of ZnO (JCPDS 01-079-0206) showing a hexagonal crystalline structure with the space group of P63mc. Therefore, the prepared nanostructure is a two-component TiO_2-ZnO material.

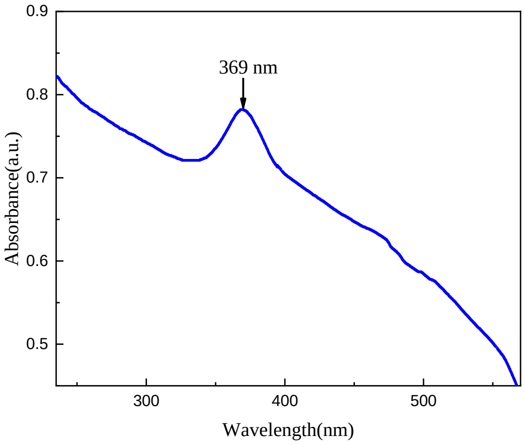

Fig. 1: Typical UV-Vis spectrum of ZnO nanoparticles synthesized by arc-discharge method.

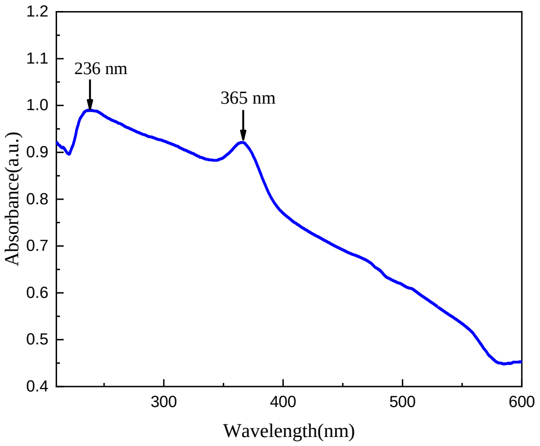

Fig. 2: Typical UV-Vis spectrum of TiO_2-ZnO nanoparticles synthesized by arc-discharge method.

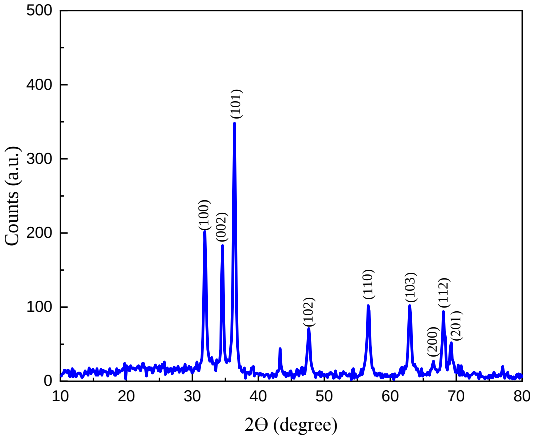

Fig. 3: X-ray diffraction pattern of ZnO nanoparticles synthesized by arc-discharge method.

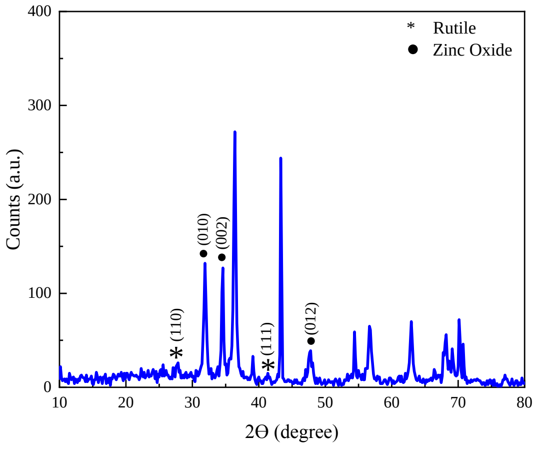

Fig. 4: X-ray diffraction pattern of TiO_2-ZnO nanoparticles synthesized by arc-discharge method.

IV. CONCLUSION

Two-component TiO_2-ZnO nanoparticles were produced in two steps by the two-step arc-discharge method. Titanium and zinc electrodes were used to produce these nanoparticles. The morphological and crystalline properties of nanoparticles were studied using UV-Vis spectroscopy and X-ray diffraction. The results show that two-component TiO_2-ZnO nanomaterial was produced as well with improved light absorption compare to the bare TiO_2 and ZnO nanoparticles.

REFERENCES

1. Avcı, A., et al., *ZnO–TiO 2 nanocomposites formed under submerged DC arc discharge: preparation, characterization and photocatalytic properties.* Applied Physics A, 2014. **116**(3): p. 1119-1125.
2. Hoyer, P. and H. Weller, *Size-dependent redox potentials of quantized zinc oxide measured with an optically transparent thin layer electrode.* Chemical physics letters, 1994. **221**(5-6): p. 379-384.
3. De Merchant, J. and M. Cocivera, *Preparation and doping of zinc oxide using spray pyrolysis.* Chemistry of Materials, 1995. **7**(9): p. 1742-1749.
4. Maruyama, T. and J. Shionoya, *Zinc oxide thin films prepared by chemical vapour deposition from zinc acetate.* Journal of materials science letters, 1992. **11**(3): p. 170-172.
5. Brehm, J.U., M. Winterer, and H. Hahn, *Synthesis and local structure of doped nanocrystalline zinc oxides.* Journal of applied physics, 2006. **100**(6): p. 064311.
6. Wang, H., et al., *Large-scale synthesis of single-walled carbon nanohorns by submerged arc.* Nanotechnology, 2004. **15**(5): p. 546.
7. Li, D., et al., *Preparation of a ZnO/TiO 2 vertical-nanoneedle-on-film heterojunction and its photocatalytic properties.* RSC Advances, 2014. **4**(35): p. 18186-18192.

Synthesize, Characterization and Band Gap Calculation of Zinc Ferrite Nanostructures

M. Shaterian*, M. Youlchikhani, S. Esmkhani, M. Balaei
Department of Chemistry, Faculty of Science, University of Zanjan, 451561319, Zanjan, Iran
Email: shaterian@znu.ac.ir

Abstract*:* The work reports a new method for synthesize of zinc ferrite nanostructures. The method is based on sol-gel route. The nanostructures are characterized by X-ray diffraction (XRD) and ultraviolet-visible diffuse reflectance spectroscopy (UV-DRS). Using the techniques the crystalline phase and band gap of samples are studied. The XRD results confirm the formation of cubic zinc ferrite nanostructures. Also, zinc ferrite nanoparticles show an optical band gap value of 1.93 eV.

Keywords: Zinc ferrite, Nanostructures**,** Sol-gel method, Optical applications

I. INTRODUCTION

Nanotechnology is an area of nanoscience deals with the synthesis methods and applications of nanostructures in many interdisciplinary fields such as medicine, biology, chemistry, physics and agriculture. In the last decade, nanosized materials have been used usually in many industrial due to their excellent characteristics such as optical, magnetic, electronic, chemical, thermal and mechanical properties [1]. One of the most main nanomaterials is magnetic compounds due to the properties depending on their morphology and size [2]. Various methods such hydrothermal [3], co-precipitation [4], ultrasonic [5] and etc. have been reported for synthesis of various magnetic nanostructures. The methods have some disadvantages, such as, too long duration and energy consuming. The sol-gel method has performed as a versatile technique for preparation of chemical compounds and inorganic materials. This method possesses advantages of chemical homogeneity, easy components adjustment and low cost.

Herein, a new method based on sol-gel was used for synthesize of zinc ferrite nanostructures. Also, structural and optical properties of the as-synthesized samples were studied using X-ray diffraction (XRD) and ultraviolet-visible diffuse reflectance spectroscopy (UV-DRS).

II. METHODS

All chemicals for the synthesis of zinc ferrite nanostructures containing iron (III) nitrate, zinc nitrate and other materials were obtained from Merck Company and applied without any purification.

Deionized water was used for preparation of all solutions. The sol-gel route was used for synthesize of the nanostructures.

The XRD patterns of the nanopowders were obtained by a Model PI TS 3003 of SEIFERT diffractometer using Cu Kα radiation (k = 1.5418 Å) to examine the crystallization and structural properties of the as-synthesized samples. The UV-DRS were obtained from UV-Vis Scincom 4100 spectrometer.

III. RESULTS AND DISCUSSION

XRD result of the nanostructures is presented in Fig. 1. The crystallite size of the nanopowders can be achieved by the Scherrer's equation [6]. Using the data, the crystallite size of the nanoparticles was obtained 35.1 nm.

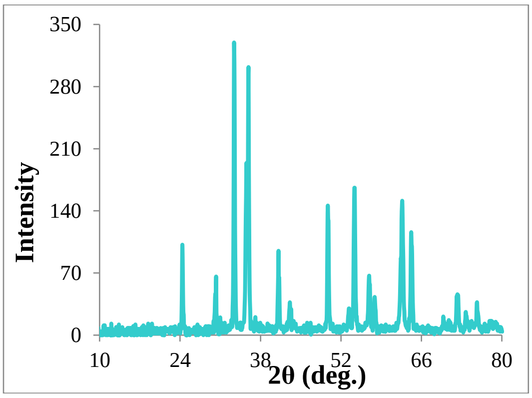

Fig. 1: XRD pattern of zinc ferrite nanostructures.

Also, UV-DRS was used for study of optical band gap

(E_g). Then, the E_g has been calculated using Tuac's equation (Eq. 1) [7]:

$(\alpha h\upsilon)^n = A\,(h\upsilon - E_g)$ (1)

where hυ describes photon energy, α is defined as absorption coefficient, A is a constant relative to the material and n is 2 or 1/2 for a direct or an indirect transition, respectively.

The graph of $(\alpha h\upsilon)^2$ *vs.* hυ was plotted by extrapolating the linear portion of the curve to horizontal axis in which $(\alpha h\upsilon)^2 = 0$ (Fig. 2). The curve indicates that the value of the direct band gap (E_g) is about 1.93 eV. The obtained value of band gap provides the energy required to disassociate water as well as makes harvesting solar energy possible by these nanostructures.

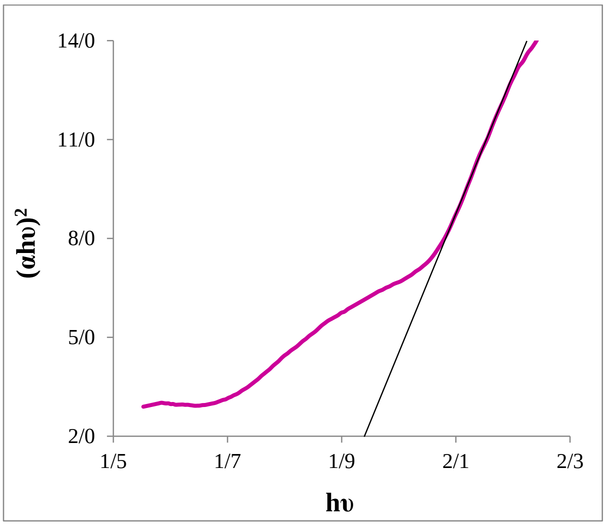

Fig. 2: Tauc plot exhibiting $(\alpha h\upsilon)^2$ *vs.* photon energy (hυ) for the direct band gap calculation of zinc ferrite nanostructures.

IV. CONCLUSION

Zinc ferrite nanostructures were synthesized via sol-gel method. Characterization techniques confirmed that the nanostructures were actually formed without any impurity. Also, UV-DRS was used for calculation of the direct band gap of zinc ferrite nanostructures. Using the Tauc model, it has been concluded that the product has a direct band gap value of 1.93 eV which is in the range of effective photo-catalysts behaviors in hydrogen production processes from decomposition of water.

REFERENCES

[1] J. Saxena, P.K. Sharma, M.M. Sharma, A. Singh, Springerplus, 5, 861-871, **2016**.

[2] V. Patsula, M. Moskvin, S. Dutz, D. Horák, J. Phys. Chem. Solids, 88, 24-30, **2016**.

[3] X. Zhou, F. Cao, J. Li, F. Chen, J. Liu, W. Shen, Mater. Lett. 182, 269-272, **2016**.

[4] K. Rana, P. Thakur, M. Tomar, V. Gupta, A. Thakur, Ceramics International, 44, 6370-6375, **2018**.

[5] A. Asfaram, M. Ghaedi, S. Hajati, A. Goudarzi, Ultrason. Sonochem. 32, 418-431, **2016**.

[6] H.P. Klug, L.E. Alexander, X-ray Diffraction Procedures for Polycrystalline and Amorphous Materials, Second ed., John Wiley, New York, **1974**.

[7] J. Tauc, R. Grigorovici, A.Vancu, Phys. Status Solidi B, 15, 627-637, **1966**.

[8]

Investigation on the Mutual Interplay between the Physicochemical Properties of 1-octyl-3-Methylimidazolium Bromide, [C$_8$mim][Br], and CuO Nanofluids by Measuring the Electrical Conductivity, Surface Tension ,and Static Contact Angle.

R. Sadeghi; M. Ziaee*
Department of Chemistry, University of Kurdistan, Sanandaj, Iran
Email: ziaee_mehdi@yahoo.com

Abstract*:* The present study was undertaken to investigate the effect of temperature on the micelle characteristics and synergy of [C$_8$mim][Br] in the presence and absence of CuO NPs into the bulk and interfacial of air/water using the data obtained from measuring the electrical conductivity. The specific conductance was measured as a function of the [C$_8$mim][Br]concentration at pure water and with 0.01 wt%, 0.005 wt%, 0.00066 wt% of CuO nanofluids as the solvent at; 288.15, 293.15, 298.15, and 303.15 K. In order to clarify whether the residence of CuO at different concentration can affect on Thermodynamic of Micellization, the specific conductance (κ) versus the concentration dependence of ionic liquid, m, was measured at different temperatures. the experimental conductivity for the aqueous solutions of [C$_8$mim][Br] measured at (288.15, 293.15, 298.15 and 303.15) K are given.

Keywords: CuO nanoparticle, Electrical conductivity, Ionic liquid

I. INTRODUCTION

Copper oxide nanoparticles (CuO NPs) have attracted particular attention because they are the simplest member of the family of copper compounds and exhibits a range of potentially useful physical characteristics [1]. CuO is cheaper than silver, easily mixed with polymers and relatively stable in terms of both chemical and physical assets [2].

II. METHODS

1-bromooctane (≥ 99%), 1-methylimidazole (≥ 99%) and ethyl acetate (≥ 99%) were purchased from Merck Co. and used without any further purification. Double distilled and deionized water was used for the preparation of the solutions. 1-octyl-3-methylimidazolium bromide ([C$_8$mim]Br) were prepared according to the procedure reported by Dupont and Naderi [3,4]. Copper oxide nanopowder (APS: 40 nm, purity > 99 %) was purchased from Iranian Nanomaterial's Pioneers Company, NANOSANY (Mashhad, Iran) were used in this work. The CuO NPs were characterized using several techniques including scanning electron microscopy (SEM, Leo 440i, Carl Zeiss, Germany), transmission electron microscopy (TEM, EM 208, Philips), X-ray diffraction (XRD, EQUINOX 3000, INEL, France). Conductivities were performed with a Metrohm 712 digital conductivity meter with automatic range switching and measuring frequency selection (300 Hz or 2.4 kHz). Firstly, the conductivity bridge was calibrated by the determination of the cell constant, Kcell, using different standard potassium chloride solutions, of known concentration (0.1-300 mmol.L^{-1}) and known specific conductance, κ, at 298.15 K. The cell constant of the cell was 0.855 cm^{-1}.

The sample solutions were thermostatted in the glass cell with a double-walled jacket containing circulated water with an uncertainty of ±0.02 K and the temperature range examinations were from 288.15 K to 308.15 K at interval of 5 K. Incremental amounts of aqueous [C$_8$mim][Br] solution with a known concentration ~ 30–35 times the cmc was added to the conductivity cell having a sample of 10 mL of solvents. After each SAIL solution addition, the solution in the cell stirred magnetically and allowed to ensure homogeneous mixing, for at least 20 min at working temperature and then its stabilized conductance value was recorded.

III. RESULTS AND DISCUSSION

The specific conductance was measured as a function of the [C$_8$mim][Br]concentration at pure water and with 0.01 wt%, 0.005 wt%, 0.00066 wt% of CuO nanofluids as the solvent at; 288.15, 293.15, 298.15, and 303.15 K. In order to clarify whether the residence of CuO at different concentration can effect on Thermodynamic of Micellization, the specific conductance (κ) versus the concentration dependence of ionic liquid, m, was measured at different temperatures.

According to the pseudo phase model of micellization, The standard enthalpy (ΔH_m°), the entropy (ΔS_m°) and the free energy of micellization (ΔG_m°) of [C$_8$mim][Br] in various nanofluid of CuO NPs is calculated by follow the ing equations:

$$\Delta G_m^{\circ} = RT(2-\beta)[\ln(X_{cmc})] \quad (1)$$

$$\Delta H_m^{\circ} = -T^2 \left[\frac{d\left(\frac{\Delta G_m^{\circ}}{T}\right)}{dT} \right] \quad (2)$$

$$\Delta S_m^{\circ} = \frac{(\Delta H_m^{\circ} - \Delta G_m^{\circ})}{T} \quad (3)$$

Where, the ionization degree (β) of micelles estimated from the ratio of slopes above and below cmc.

$$\beta = \frac{S_2}{S_1} \quad (٤)$$

cmc is in mol.kg^{-1}, X_{cmc} = cmc/55.4 is the cmc in terms of the molar fraction (55.4 comes from 1 L of water corresponding to 55.4 moles of water at 298.15 K). Thermodynamic properties for the binary water + [C_8mim][Br] systems and the ternary water + CuO NPs + [C_8mim][Br] obtain from electrical conductivity.

The electrical conductivity of nanofluids may be higher than of pure water, As the thermal conductivity of nanofluid is bigger than their base fluid. The two critical requisites that surpass the thermal conductivity of nanofluids include dispersion and consistency which are the key criteria to assess final individualities of nanofluids. For many materials, their thermal and electrical conductivities behave in similar manners. Therefore, it is expected that just as the thermal conductivity of nanofluid is higher than their base fluid, similarly the electrical conductivity of nanofluids may be larger than those of their base fluids.1)

IV. CONCLUSION

The electrical conductivity of nanofluids may be higher than that of pure water, as the thermal conductivity of nanofluid is larger than that of their base fluid. The two critical requisites that surpass the thermal conductivity of nanofluids include dispersion and consistency which are the key criteria to assess final individualities of nanofluids. For many materials, their thermal and electrical conductivities behave similarly. Therefore, it is expected that similar to the higher thermal conductivity of nanofluid compared to their base fluid, the electrical conductivity of nanofluids may also be larger than that of their base fluids.

REFERENCES

[1] S. Chen, B. Mulgrew, and P. M. Grant, Journal, vol. 4, pp. 570-578, **1993**.
[2] J. U. Duncombe, Journal, vol. 10, pp. 34-39, **1995**.
[3] C. Y. Lin, M. Wu, J. A. Bloom, I. J. Cox, and M. Miller, Journal, vol. 10, pp. 767-782, **2001**.

بیست و دومین کنفرانس شیمی فیزیک انجمن شیمی ایران
22nd Iranian Physical Chemistry Conference
۲۹ الی ۳۱ مرداد ۱۳۹۸
گروه شیمی دانشگاه زنجان
دانشگاه زنجان

The role of polypropylene monofilament and effective parameters in the design and size of Nanoscale surgical mesh pile fabrics

Morteza Ebrahimnezhad
Faculty Member Department of Textile and Chemistry, Faculty of Engineering, Imam Mohammad Bagher Sari, Mazandaran Technical University,
Email: ebi450@yahoo.com

Abstract*:* Surgical mesh is a porous cloth that is usually produced using blu-ring knitting and using different types of monofilament yarns, especially polypropylene. The use of these fabrics is used to treat hernia and pelvic organ damage. A cloth that is implanted as an implant in the body should have the biological and functional properties of the medicine. Among the structural properties of the surgical meshes, pore size and relative porosity of the surgical mesh are of particular importance and have a special effect on the properties of surgical meshes, especially the probability of infection in the body after the surgical mesh graft; therefore, accurate measurement of the surface porosity and relative porosity at the surface The piercing blotter fabrics used in the surgical mesh are important and should be controlled and standardized in terms of the physico-chemical biochemistry process. In this study, four types of conventional puncture bladed cloth were produced in the manufacture of surgical meshes using polypropylene monofilament and after image stabilization, images were provided on the surface of the mesh. In the following, the image processing method using nanotechnology and MATLAB software has been measured to measure the area and diameter of the equivalent surface pores and relative porosity at the surface of the piercing blade. Based on the results, relative porosity percentage, mean porosity and mean pore diameter, fabric with pseudo-marcosite texture and sandwich texture are the best textures of the textures.

Keywords: Polypropylene, Surgical Mesh, Image Processing, Porosity Size

I. INTRODUCTION

Surgical mesh (Fig. 1) is a porous cloth that is usually produced by a blunt ring method using diffused monofilament melts of different sexes, in particular polypropylene, which is used in the treatment of cases such as hernia, pelvic organs and etc. [1, 2 and 3].

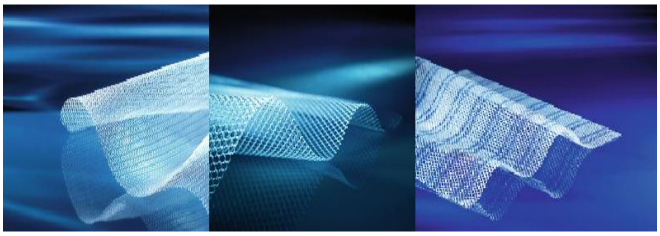

Figure 1: Examples of commercial surgical masts [7].

II. METHODS

In this research, four types of perforated blunt cloth (with different tissue designs including needle puncture, tricho, syndhalfa, pseudomarcositis) are commonly used in the production of surgical meshes using polypropylene monofilament and after image stabilization, images have been obtained from the surface of the mesh. . In the following, suitable images of fabrics with suitable lighting conditions are provided in the form of lighting and using black backgrounds which are most closely examined with the color of the surgical mask, which is visible in Fig. 2.

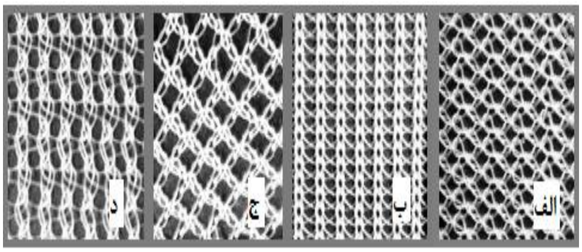

Figure 2: Images prepared from the examined surgical mask, a) Needle puncture, b) Tricho, c) Sandeflia, d) Pseudomarcosis

In the following, using the method of image processing using programming in MATLAB software, the size of the

area and the diameter of the equivalent porosity and relative porosity at the surface of the perforated blade are measured. The structure of the program used to measure relative porosity and pore size is summarized in the following sections:

1 - Read the image in a suitable format by MATLAB software

2 - Carrying out simulation and image enhancement to eliminate potential noise in all parts of the image

3 -Transform the image into a gray image to determine a brightness threshold for converting an image into a black-and-white image (binary) in such a way that the points where the brightness is greater than this value are whitened and the points with less brightness are black (Fig. 3a).)

4 - Transform gray image to binary image (black spots) with determined brightness threshold (Fig. 3b)

5. Removing the noise in the background of the binary image (Fig. 3c)

6 - In this image, the black pores and fabric threads of the fabric are white; with a proper code, the porcelain cloth and the threads that make up the black fabric (Fig. 3d).

7 - Removing the noise in the monofilament yarns in the resulting image (Fig. 3e)

8. The count must be the sum of the white points (white pixels) and the total number of points of the image (total image pixels) and the ratio of the number of white points to the total image points to calculate the relative porosity of the perforated fabric. It should be noted that in Binary mode The dark (black) points are marked with a number zero and bright spots (white) with a number one.

9 - Measure the average pore area of the perforated cloth in square meters by random selection of 5 pores from the pores of the fabric and finding the mean area of these points and using the appropriate conversion coefficient of the pixel in length (in millimeters)

10 -Measure the equivalent diameter for the perforated hollow core porosities (the equivalent diameter is the circle diameter of the area with the pore area considered, which does not have a definite shape).

III. RESULTS AND DISCUSSION

The results of the above steps on the image of the piercing blotter fabric are examined by performing the above steps using the image processing section of the MATLAB software, and the relative porosity, area size, and diameter equivalent of the pores in the perforated blade ring fabric are examined. The results are presented in

The relative porosity is among the studied materials. Two other texture designs, ie, sandwiches and needles, are considered relative porosity between the two texture designs. In terms of the average pore size, the texture with the largest textured area of texture and the texture of the knit texture with the least average size of the pore space between the perforated blotting fabrics is examined. Two other tissue designs, namely pseudo-marsocosite and needle puncture, are located between the two syndeflia and tricho tissues in terms of the average size of the pore pores, respectively. In terms of the average size of the diameter of the equivalent pore, the cloth with the design of the texture of sandwiches has the largest diameter equivalent to the pores and the fabric with the design of the knit texture having the smallest diameter of the equivalent pore diameter between the piercing blotter fabrics. Two other tissue designs, namely pseudo-marsocytes and needle punches, are in terms of the mean size of the diameter of the equivalent pores of the fabric, respectively, between the two syndeflia and tricho texture designs.

Table 1: Results of measurement of relative porosity percentage, mean area size and diameter equivalent to surgical mesh vents

Average pore diameter equivalent)mm(	Average pore space)mm^2(	Relative porosity percentage (%)	Texture Design Name
1/42	1/57	43/24	Tricho
2/41	4/56	47/38	Sandfelay
2/16	3/66	47/18	Needle hole
2/30	4/17	50/17	Pseudomarcosis

Conclusion and Results

By examining the results of measuring the relative porosity, the mean pore area and the mean pore diameter of the perforated blunt ring porcelain were examined in this study and considering that both the size of the large pores and relative porosity are the most important surgical masts. Also, with careful attention to the fact that the values obtained for fabrics with pseudomarcosite and syndfella texture are slightly different (less than 10%), thus, perforated blotting fabrics with two pseudomarcosite texture patterns and sandwiches of the best design Tissues were evaluated for relative porosity percentage, mean pore area and mean pore diameter, among four The textures examined are in this study.

REFERENCES

[1] Mirjavan, M, Asayesh, A, Asgharian Jeddi, A, 2017. " The effect of fabric structure on the mechanical properties of warp knitted surgical mesh for hernia repair", *Journal of the Mechanical Behavior of Biomedical Materials*, 66, February, pp 77-86

[2] Zhu, LM., Schuster, P., Klinge, U., 2015. “Mesh implants: An overview of crucial mesh parameters”, *Word Journal of Gastrointestinal Surgery*, vol.7, 226–236, 27 Oct.

[3] Prashanth, K., Ayyathurai, R., Gomez, C., 2012. "Evaluation of Current Synthetic Mesh Materials in Pelvic Organ Prolapse Repair"; *Current Urology Reports*, 13, June, pp 240–246**.**

The production of protein absorbing suture from casein(milk) by means of nanotechnology

Morteza Ebrahimnezhad
Faculty Member Department of Textile and Chemistry, Faculty of Engineering, Imam Mohammad Bagher Sari, Mazandaran Technical University.
Email: ebi450@yahoo.com

Abstract*:* The technology of suture yarn production is very novel and diverse, and the trend of specialists has grown to absorb stitches. Because body tissue structure is protein, and if you want the suture to be easily absorbed into the body, then it should be a protein chase, so for the first time in this article, a protein extracted from milk called casein has been used. We found that casein is a protein that is present in milk at a high level. We know that the more stable the protein is, the more it is able to become more polymeric fibers, we also know that protein is actually the same amino acid that is produced by the addition of polypeptides or proteins together. . The most important amino acids in the milk are: Cysteine, Glycine, Trinin. First, we need to isolate casein as a stable protein in milk. This part of the project is, in fact, a complex biochemical process, which is needed on the basis of the process. Electric induction and in the next stage the casein coagulation process, which, by introducing formaldehyde and acidifying the environment, causes the protein to coagulate and produce stitches.

Keywords: Polymer, Milk, Cain, Suture, Fiber, Protein, Nanotechnology

I. INTRODUCTION

First, we need to become familiar with the history of the production of yarn in the world and examine a variety of manufacturing methods. Surgical suture sutures are single or multiple sterile filaments that play a role in keeping the wounded tissues together until they are recovered. These threads are usually used with a needle for suturing or surgical incisions, or as an articulation strap without using the needle to tie the ends of the veins or other arches to prevent bleeding and Or other fluid leaks. Suture sutures may contain fluorocarbons and silicones, these coatings are used to reduce the varnish properties and improve other properties.

Multi-filament suture sutures may be used smoothly or woven (threaded). The braid type is easier to work with and makes the knot more stable. The smooth sutures are easier to handle than the fabric, and are also easy to pull out of the fabric. This type does not have a stitch fabric.

Suture sutures may be classified into two absorbable and non-absorbable groups. The absorbable type is able to absorb and dissolve in body tissues and usually disappears after two to six months. An inert form is resistant to biological degradation and remains in place as an external object, The place is turned away or sent out by tissue. The stiffness of the suture and the stiffness of the knot at the site of the tissue is one of the most important mechanical properties of these particular threads, which, depending on the types, can be grown to over 1,700. The stiffness of the knot at the site of the tissue is therefore important, which usually connects the surgeon after stitching the injuries or draining the vessel and duct. The low node strength, slip, and open the node. Suture stitch stiffness is affected by factors such as coefficient of strength, dimensions, structure, stiffness, knot type and number, and moisture absorption. Using very delicate filaments and low number of nodes creates the ideal condition for stitching. . For the production of yarns, it may use metal fibers and natural fibers such as linen, silk and cotton, and collagen and animal intestines, as well as synthetic fibers. The stitches are the strongest metal strands and the most common types of natural yarns. Suture sutures from the animal intestines and collagen recovered

The small intestine of animals such as lambs and cows, which is essentially made out of collagen protein, is used to prepare stitches. After the mechanical or chemical separation of the impurities, the intestine is cut in the longitudinal direction and the direction Increased strength is placed in materials such as chromium or aldehyde salts, then, depending on the thickness, a number of strips are drawn together, this type of suture that is rarely used to suture the skin The absorption rate depends on the type of tissue. The stitches produced from

the animal intestines up to the appearance of polygluconic acid threads was the only absorbent suture.

II. METHODS

We know that there are many amino acids in the milk, the most important of which are in Table 1

Table 1: Important Puteines in Milk

Amino acid formula	Name amino acid	Row
NH3CH2COOH	Glycine	1
HOOCCHNH2CH2SSCH2CHNH2COOH	Cysteine	2
CH2CHOHCHNH2COOH	Trinin	3

Regarding the organic structure of proteins, due to the electrical induction capability of proteins, it is necessary that, among the isolated proteins, casein is the most suitable amino acid that has a positive inductive effect and can be used in nanosilver processes and spectra The light can be made of fibers similar to silk and wool fibers, casein is a protein that is present in milk at a high rate.

III. RESULTS AND CONCLUSION

On the other hand, milk is a source of plenty and relatively inexpensive, which is almost universally available. On the other hand, because of the high cost of silk fibers, it is necessary to choose a suitable and relatively cheap, silk place alternative, which in this paper, while analyzing The exact protein in the milk, the most suitable protein, which has a good degree of stability to become fibers, is the casein that is produced by the biochemical process, thereby eliminating the presence of casein in the milk and its degree of stability Measured and induced by the induction effect, casein can be filtered into mass and The development of the degree of stability of compounds such as formaldehyde and sulfuric acid, and the ability to achieve it in different tables, and finally, "by spinning the casings, we can thread yarns in a yarn that, due to its structural similarity, based on protein as a protein absorption yarn It can be used and compared with silk, indicating the high stability of the protein in casein. Although this article is a positive step for the production of absorbent suture for the first time in the country, it can be described as one The manufacturing process in the country is expanding.

IV. CONCLUSION

In conclusion, we present a rapid, facile and eco-friendly sonochemical synthesis of polyoxometalate-stabilised nanoparticles. The AuNP@PMo_{12} nanohybrid we report can be used as a nanoprobe for colorimetric detection of acetaminophen. The A_{600}/A_{540nm} values of AuNP@PMo_{12} nanohybrid indicated a linear relationship with concentration range of acetaminophen (1–120 mg/L) used in our study. Importantly, both the qualitative and quantitative determination of acetaminophen were investigated, and our method demonstrated limits of detection as low as 0.42 mg/L. These results showed that this biosensing set-up could potentially be used in the real world medical setting for the real-time point-of-care detection of acetaminophen with accuracy, convenience, and efficiency, even in the presence of other pharmaceuticals, in this instance methadone, methylphenidate and tramadol. Future work will involve practical application of this set-up by integrating mobile phone devices and the appropriate applications to detect a range of pharmaceuticals in more complex media, e.g. other buffers, cell culture media, blood serum, and so forth.

REFERENCES

can be made of fibers similar to silk and wool fibers, casein is a protein that is present in milk at a high rate.

V. RESULTS AND CONCLUSION

On the other hand, milk is a source of plenty and relatively inexpensive, which is almost universally available. On the other hand, because of the high cost of silk fibers, it is necessary to choose a suitable and relatively cheap, silk place alternative, which in this paper, while analyzing The exact protein in the milk, the most suitable protein, which has a good degree of stability to become fibers, is the casein that is produced by the biochemical process, thereby eliminating the presence of casein in the milk and its degree of stability Measured and induced by the induction effect, casein can be filtered into mass and The development of the degree of

stability of compounds such as formaldehyde and sulfuric acid, and the ability to achieve it in different tables, and finally, "by spinning the casings, we can thread yarns in a yarn that, due to its structural similarity, based on protein as a protein absorption yarn It can be used and compared with silk, indicating the high stability of the protein in casein. Although this article is a positive step for the production of absorbent suture for the first time in the country, it can be described as one The manufacturing process in the country is expanding.

Reference sources

[1] Booth,J,E,principles of Testing
[2] Goodman,The Royal Institute of Chemistry
[3] ساسان شریفی نشر دانشگاهی شیمی علوم الیاف،
[4] فیزیک الیاف، دکتر توانایی نشر اصفهان
[5] Allan, S.E., B.W. Smith, and K.A. Anderson, *Impact of the Deepwater Horizon Oil Spill on Bioavailable Polycyclic Aromatic Hydrocarbons in Gulf of Mexico Coastal Waters.* Environmental Science & Technology, 2012. 46(4): p. 2033-2039.
[6] Srinivasan, A. and T. Viraraghavan, *Removal of oil by walnut shell media.* Bioresource Technology, 2008. 99(17): p. 8217-8220.
[7] Vandermeulen, J.H. and C.W. Ross, *Oil spill response in freshwater: Assessment of the impact of cleanup as a management tool.* Journal of Environmental Management, 1995. 44(4): p. 297-308.

The application of isotactic polypropylene fibers in the production of fiber reinforced concrete with the help of nanotechnology and the effect of electrical induction compared to carbon fiber and polypropylene fibers, cynodeoctatic and otactic

Morteza Ebrahimnezhad
Faculty Member Department of Textile and Chemistry, Faculty of Engineering, Imam Mohammad Bagher Sari, Mazandaran Technical University,
Email: ebi450@yahoo.com

Abstract*:* We know that ordinary concrete is a material composed of aggregate and mortar. Concrete against compressive strength has acceptable resistance, however, it works against weak tensile strength. On the other hand, steel has an acceptable tensile strength. Consequently, by arming the concrete into steel bars, concrete is obtained, which has both compressive strength and acceptable tensile strength, this type of concrete, reinforced concrete, is referred to. Since the coefficient of thermal expansion of the steel is identical with the concrete, the rebar is used. But because of weight and weight, fiber can also be used. Usually, carbon fiber or glass or steel is used, each with its own advantages and disadvantages. In this paper, we first used nano technology and the electrical effect of composite or composite polypropylene isotactic fibers and tested the advantages of this type of reinforced concrete with flexural, tensile and strain tests. The fibers are commonly used to control the cracks caused by dental contractions and cracking cracks resulting from the drying of concrete. Concrete fibers produce directional strength in concrete.
Concrete fibers also increase the impact resistance, abrasion resistance and concrete breakage resistance.

Keywords: isotactic, Nanofibre, polypropylene, Polymer, electrical, Cement, Fiber, Reinforced Concrete.

I. INTRODUCTION

First we need to get acquainted with cement making methods . Basically there are four methods for producing cement : 1. More method – 2-Neutral method -3-Semi-dry method - 4. Dry method Conventional concrete is a material composed of aggregate and mortar. Concrete aggregates include gravel (sand) and gravel aggregate (sand), and concrete mortar, which causes aggregate adherence to each other, is a mixture of cement and water. Concrete against compressive strength has acceptable resistance, however, it works against weak tensile strength. On the other hand, steel has an acceptable tensile strength. Therefore, by arming the concrete into steel bars, concrete is obtained, which has both compressive strength and tensile strength, this type of concrete, reinforced concrete or reinforced concrete is referred to. The reason for using steel to arrange concrete is the same coefficient of thermal expansion of concrete and steel. This means that due to the similarity of the coefficient of thermal expansion with concrete, the steel does not crack concrete if it expands. In other words, steel does not impose tension on concrete due to temperature change. Another reason is the adhesion and non-slipping of steel into concrete.

II. METHODS

On the other hand, the combination of steel and concrete has other advantages, which are discussed below. Steel has a high tensile strength as one of the most vulnerable materials in the building. Because steel is corroded against chemicals. Also, in contrast to the high resistance of concrete to fire, steel has high resistance to high temperatures. By mixing steel and concrete and creating reinforced concrete or reinforced concrete, a robust combination has been created in the building, which eliminates all the disadvantages of using concrete and steel alone.

In the following, we need to answer this question:

What is pre-bonded concrete and concrete so tied?

What are the disadvantages of pre-tensioned concrete and retardant concrete?

Pretensioned concrete

Although the reinforced concrete is more resistant than ordinary concrete, it is still not completely resistant to cracking and may not fully resist the tensile force. Also, if water enters the concrete, there is a risk of rotting steel. The solution to these problems is to put the reinforced concrete under constant stress, which is called pre-tensionPre-tension enters internal tensions in opposition to external forces on the body (dead and live loads imposed on the structure) to thwart them. Pre-tension increases concrete bearing strength. So instead of placing steel in a concrete that is still wet, it first pulls the cables into concrete molding, then performs concrete work. By starting the concrete action, the cables are placed inside the concrete and permanently pressurize the concrete.With the help of nanotechnology, the Iso-Tactics fibers are first deposited and embedded in the polymer structure, and the stress and strain of the fiber are stronger against the forces that are made and more resistant to carbon fibers..

III. RESULTS AND DISCUSSION

post tensioned concrete : In the retreated concrete, put the cables in pods and then put them in the form of concrete. After completing the clamping of the concrete, they pull the cables from both ends. After the cable pulling is done, if the cement slurry is injected inside the pods, then this kind of concrete is said to be a sticky retardant concrete

The effect of electrical induction on isotactic fibers by photovoltaic spectra causes a lot of changes in the fiber structure.The most important benefits include:
The fibers are commonly used to control cracking caused by dentin contraction and cracking cracks resulting from concrete drying.
Concrete fibers produce directional strength in concrete
Some types of concrete fibers increase the impact resistance, abrasion resistance, and concrete breakage resistance
Studies have shown that microfiber fibers have a greater impact on concrete impact resistance than tall fibers.
Concrete fibers improve durability and hardness of concrete
The fibers reduce permeability and penetration, and thus reduce concrete sweating

If the coefficient of elasticity of concrete fibers is more than concrete and mortar, the fibers increase the tensile strength.

Concrete fibers reduce air bubbles and water bubbles The direction, volume and type of fiber used in concrete have a significant effect on the performance of concrete against creep. Graphite fibers and glass fibers have good creep resistance (Figure 3)If the length of the lips is too large, they will bullet them and thus reduce their effectiveness(Figure 1) Increased flexural strength of concrete is limited by fiber and concrete fibers can not replace the bending metal frames.

Figure 1: A View of Nano isoactics

The most important effects of steel fibers are increased shear strength, flexural strength and tensile strength of concrete. Steel fibers reduce the amount of small cracks caused by external loading, which increases concrete tensile strength (Figure 2). If you use steel fibers, you can exclude the crumb from the shear reinforcement because the steel fibers increase the shear strength of the concrete. Concrete steel fibers increase the thermal conductivity of concrete and increase the strength of concrete against sudden changes in temperature and high temperatures..

Figure 2: View of an electric induction polypropylene fiber

Polypropylene fibers :Polypropylene is one of the cheapest and affordable polymers. This polymer is resistant to most chemicals. The melting point of the polypropylene polymer is high, so working at high temperatures will not damage concrete fibers. Polypropylene prevents cracking and shrinkage in concrete during the early hours of concrete. Concrete reinforced with polypropylene fibers has a high ductility and is not easily crushed.One thing to keep in mind is that the percentage of water absorption of polypropylene is close to zero and no additional water should be added to increase the fluidity of the concrete.

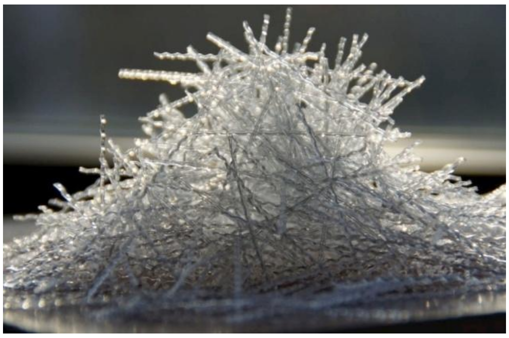

Figure 3: View of Carbon Fiber Induced by Polypropylene after Nanotechnology

These fibers increase the impact strength, bending, shear and tensile strength of concrete. Carbon fiber does not absorb water (Figure 4) resistant and is to corrosion, acids and alkaline materials. These fibers prevent cracking in concrete and increase durability

Figure 4: Reinforced concrete with polypropylene fibers

Fiber glass ::A. The glass fiber consists of 200 to 400 distinct strands, which slowly blend together and create a single page. These pages can be split or integrated in various dimensions.

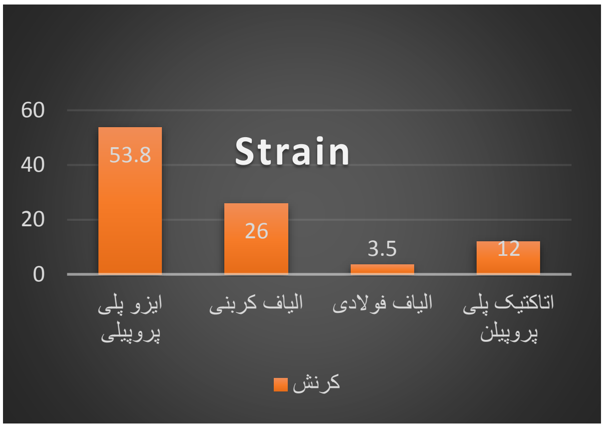

Diagram 1: Comparison of the strain force of isotactic fiber with other fibers in the reinforced concrete

BThe most used glass fiber reinforced mortar used on narrow plates (such as the facade of the building). The glass fibers are strongly inclined to stick together and be bullet-wrapped in new concrete; it is true that, in the event of bulleting of the fiber, the distribution of the other fibers is not uniform and the concrete does not have the desired performance.

Figure 5: A view of nano-fiber-reinforced polypropylene fiber

IV. CONCLUSION

In this paper, we found that with the help of nanotechnology and electrical induction, we can increase the polypropylene fiber in the isotonic state for tensile and tensile forces.

In the isotactic state, monomers are very important As a result of electrical induction, monomers fall into one

Monomers are pregnant and find an induction

Consequently, by introducing this type of fiber, tensile forces are controlled

While in the cine-oceanic and ottactic state, the amount of monomer loading is greatly reduced

In order to be able to find reinforced concrete more resistance in terms of tensile forces, the comparison is made in the following diagram. In this chart, the polypropylene fibers are evaluated before and after using electronically induced load with nanoscale technology.

Thanking :

In the end, we would like to thank the head of the faculty and director of the Civil Engineering Department of Sari Mazandaran University.

REFERENCES

[1] S. Chen, B. Mulgrew, and P. M. Grant, Journal, vol. 4, pp. 570-578, **1993**.
[2] J. U. Duncombe, Journal, vol. 10, pp. 34-39, **1995**.
[3] C. Y. Lin, M. Wu, J. A. Bloom, I. J. Cox, and M. Miller, Journal, vol. 10, pp. 767-782, **2001**.
[4] - DYEING AND CHEMICAL TECHNOLOGY OF TEXTILE FIBERS , SIXTH EDITION , E.R.Trotman
[5] تاب فناوری پلاستیسیته در بتن مسلح ، و.ف.چن ، مک گروهیله ۱۹۸۲ ، صفحه۲۰۲ –
[6] – جونز و ریچارت ، مجموعه مقالات ای.سی.آی به نقل از اچ . روش ، ۲۰۱۲ فصل ۸ و۱۱ و ۱۲
[7] مجله بخش سازه ، جلد ۹۵ ، شماره ۱۲ ، اقتباس از پ،کارسون و ج.آ.جیرسا سال انتشار ۲۰۱۵
[8] ، مقاله ٦۹۳٥، ۲۰۱۸ ، انتشارات شیمی فایبر ST
شیمی الیاف ، دکتر ساسان شریفی ، نشر دانشگاهی ، صفحه ۱۰ تا
[9] فیزیک الیاف، دکتر توانایی، نشر اندیشه اصفهان٦۲۲
[10] ۰
– و.اچ.پرایس ، مجموعه مقالات فناوری نانو شیمی ، جلد ٤۷ ، صفحه ٤۲۹

، ۲۰۰۹

Section:

Quantum Chemistry

Density Functional Theory to Calculate Redox Potential of 3-Phenylthiophen Derivatives

F. Kordnezhad*[a]*, H. Nikoofard*[b]*
Faculty of Chemistry, Shahrood University of Technology, Shahrood, 36199-95161, Iran
*Email:**nikomahdieh@yahoo.com***

Abstract: In this work, the electro-oxidation reaction of the 3-(p-X-phenyl) thiophene monomers (X= H, CH_3, OCH_3, F, Cl) was studied to predict their redox potential (E^o) by DFT technique. Geometric structure of titled monomers optimized in both gas-phase and solution via the B3LYP/6-311G(d,p) level of theory. The values of redox potential were calculated relative to the Ag/AgCl reference electrode. In the case of un-substituted monomer, a good agreement was observed between the theoretical value (1.482 V) and experiment (1.771 V). The effect of substitution on the predicted E^o was discussed for that substituted ones. Results obtained showed that the theoretical level is adequate and the CPCM solvation model is valid for calculating the solvation energies of the studied molecule.

Keywords: Density functional theory, Redox potential, Conductive polymer, Phenylthiophenes, Gibbs energy.

I. INTRODUCTION

Polymers are compounds with very high molecular weight, that are made up of interconnected small repeating units called monomers [1]. There is a bunch of polymers that has a conjugated structure consisting of single and dual interconnect bonds in their chains, called conductive polymers, that emerge from an unsaturated monomer. Conjugated polymers with enhanced or doped action by oxidizing or reducing agents acquire electrical conductivity [2]. Among conductive polymers, ones composed of 3-phenylthiophene monomers due to chemical and environmental stability; good electrical conductivity in doping mode; easy and cost-effective preparation are very much considered. Conductive polymers are prepared by chemical and electrochemical methods. It is found that monomeric constituents of these compounds have a significant effect on the polymerization process and the properties of the final polymers. The electrochemical experiments resulting from the effect of substitution in the position of para-phenylthiophene showed that the redox potential of polymer is affected by the redox potential of monomer concerned which itself depends on the inductive and the resonance effects of the monomer substrate [3]. In this regard, the production of conductive polymers with a good stability and more electrical conductivity is interested by academic and industrial researchers. It is very important to study the effect of the subordinate on the properties of the monomers that make up these compounds. Therefore, the use of theoretical studies helps to design new materials and reduce the cost of experimental and experimental methods. In the current work, the electro-oxidation reaction of the 3-(p-X-phenyl) thiophene monomers (X= H, CH_3, OCH_3, F, Cl), PTs, was investigated using the functional density theory. First, molecular structure of titled monomers optimized in both gas phase and solution via the B3LYP/6-311G(d,p) level of theory. The values of redox potential (E^o) were calculated relative to Ag/AgCl. The substitution effect on the predicted E^o was carried out.

II. METHODS

Both the ground-state and singly ionized geometries for each molecule studied were fully optimized using the gradient procedures at the hybrid density functional B3LYP techniques, together with the 6-311G(d,p) basis set, as implemented in the Gaussian 09 program package. The optimized structures were confirmed to be real minima through the construction and diagonalization of the corresponding hessian matrices. The most stable structures of reductive (PT) and oxidized ($PT^{\bullet+}$) species in solution are shown in Scheme. 1. The last procedures also served to obtain the set of harmonic vibrational frequencies which, after being property scaled by the zero-point energy (ZPE), provided the thermal corrections required to obtain the energies at any temperature above the absolute zero. The absolute Gibbs free energies at 298.15 K and 1.0 atmosphere were then obtained by considering the corresponding thermal calculations obtained from the calculated harmonic vibrational frequencies.

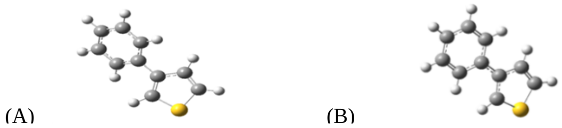

Scheme 1. The optimized structures of PT (A), and $PT^{\bullet +}$ (B) species in acetonitrile at the B3LYP/6-311G(d,p) level.

III. RESULTS AND DISCUSSION

To calculate the redox potential, it is necessary to calculate the standard free energy change (ΔG^o) for reaction (1) as:

$$\text{Red(sol)} \rightarrow \text{Ox(sol)} + \text{e} \tag{1}$$

ΔG^o is related to the absolute redox potential through the following thermodynamic relation:

$$E^o = - \Delta G^o / nF \tag{2}$$

where n is the number of transferred electrons in the reaction which is equal to 1 for reaction (1) and F is the Faraday constant (23.061 kcal mol^{-1} V^{-1}). To calculate ΔG^o, it is necessary to use the following thermodynamic cycle (Scheme 2) which is used for transferring all of the species involved in the reaction (1) from the gas to solution phase.

$$\begin{tikzcd}
\text{Red (sol)} \arrow[r, "\Delta\text{G (sol)}"] & \text{Ox (sol) + e} \\
\text{Red (g)} \arrow[u, "\Delta\text{G(solv,Red)}"'] \arrow[r, "\Delta\text{G (g)}"] & \text{Ox (g) + e} \arrow[u, "\Delta\text{G(solv,Ox)}"']
\end{tikzcd}$$

Scheme 2. Thermodynamic cycle for obtaining the $\Delta G^o(sol)$ of reaction in solution from the $\Delta G^o(g)$ of reaction in gas phase.

Based on the above thermodynamic cycle, ΔG^o (total) can be written as:

$$\Delta G^o(total) = \Delta G^o(g) + \Delta G^o(solv,Ox) - \Delta G^o(solv,Red) \tag{3}$$

where $\Delta G^o(g)$ is the change of the standard free energy of reaction (1) in the gas phase. $\Delta G^o(solv,Ox)$, $\Delta G^o(solv,Red)$ are the standard free energy solvation of Ox. and Red. species, respectively. To obtain the standard free energy of electron, we used its energy (3.720 kJ.mol^{-1}) and entropy (0.022734 $\text{J.mol}^{-1}\text{K}^{-1}$) at 298 K [4]. In order to calculate the solvation energy for Red. and Ox. species, the Polarized Continuum Model (PCM) which defines the cavity as the union of a series of interlocking atomic sphere [5], was used for ab initio calculations. Similar to gas phase calculations, the molecular structure of Red. and Ox. species were re-optimized in acetonitrile solvent using PCM model at the same level of theory and basis set. Then, the vibrational frequency calculations were performed to obtain the Gibbs free energy of Red. and Ox. in solution. $\Delta G^o(solv,Ox)$ and $\Delta G^o(solv,Red)$ is obtained from the subtraction the standard Gibbs free energy of each compound in solution from the corresponding value in gas phase. Using the value of ΔG (total) and Eq. (2), the standard reduction potential of P is equal to 6.144 V. The standard reduction potential of PT relative to Ag/AgCl reference electrode (4.6624 V) is about 1.482 V. The experimental value is 1.771V.

The calculated values of gas-phase Gibbs energies $G°(g)$, and solvation energies $\Delta G(solv)$ in CPCM model of solvation for each component obtained at B3LYP/6-311G(d,p) level of theory. In the case of un-subtituted PT, the total changes of Gibbs free energy for oxidation reaction (1), $\Delta G°(total)$, is calculated via Eq. (3) and tabulated in Table 1. The redox potential, E_{cal}, is derived via Eq. (2) in which was compared with its experimental value E_{exp} in Table 1. According to this table, a good agreement was observed between the theoretical value (1.482 V) and experiment (1.771 V). This consistency certifies that the theoretical level is adequate and the CPCM solvation model is valid for calculating the solvation energies of the studied molecule.

Table 1. The values of Gibbs free energy in gas-phase, and acetonitrile for un-substituted PT with both calculated and experimental values of *E*.

1	ΔG^o (solv,Red) /kcal.mol^{-1}	-3.17896566
2	ΔG^o (solv,Ox) /kcal.mol^{-1}	-36.7971864
3	ΔG^o (g)/kcal. mol^{-1}	175.3165758
4	ΔG^o (total)/kcal. mol^{-1}	141.6983551
5	E_{cal} /V	1.771
6	E_{exp} /V	1.482

In a similar method, the results obtained for substituted PT are given in Table 2.

Table 2. The predicted values of redox potential for PT derivatives at the B3LYP/6-311G(d,p) level of theory.

PT species	PT-CH_3	PT-OCH_3	PT-F	PT-Cl
E / V	1.104	0.852	1.227	1.288

IV. CONCLUSION

In this work, by means of quantum mechanics calculations, the geometry structure and thermodynamic properties of phenylthiophene and its derivatives were studied to predict their potential of redox. Initially, the molecular structure, vibrational frequencies and thermodynamic functions of the compounds with electron receiver and receptor substitutions were investigated and compared using DFTcomputations at the level of theory B3LYP/6-311G(d,p) in the presence of the acetonitrile solvent**.** Then, by using the thermodynamic properties of the PT monomer and its other analogs (X= H, CH_3, OCH_3, F, Cl), their redox potential were calculated and compared with each other. Results obtained showed that the values of redox potential are affected by the relevant monomer subunit groups. This substitution effect is referred to induction and resonance effects of phenylthiophene substitution. In this way, monomers with the electron - donating groups showed lower oxidation potential, but electron-receiver groups showed more oxidation potential.

REFERENCES

[1] M. L. Liu, S. J. Visco and L. C. Dejonghe, J. Electrochem. Soc., vol. 138, pp. 896-901, **1991**.
[2] I. Stassen and G. Hambitzer, J. Electroanal. Chem., vol. 440, pp. 219-228, **1997**.
[3] R. Holze and W. Alahalasah, ECS Trans., vol. 2, pp. 45-62, **2007**.
[4] J. E. Bartmess, J. Phys. Chem., vol. 98, pp. 6420-6424, **1994**.
[5] C. J. Cramer, Essentials of Computational Chemistry: Theories and Models, 2nd ed., Wiley, Chichester, **2004**

The Influence of Li Atoms on Electronic and Structural Properties of Silicon Carbide Nano sheets.

H.Roohi and T. Lotfi*
Department of Chemistry, Faculty of Science, University of Guilan, P.O. Box 98135-674 Rasht, Iran
Email:lotfichemist@yahoo.com

Abstract*:* In this work, influence of Li atoms on electronic and structural properties of SiC nanosheets was investigated by means of M06-2X and B3LYP functionals and 6-31+G(d) basis set. The optimized structures, binding energies, band gap energies, dipole moments, DOS (density of states) of complexes were calculated.

Keywords: DFT, dipole moment, band gap, basis set, DOS

I. INTRODUCTION:

In recent years, two-dimensional (2D) materials such as graphene, boron nitride, silicon carbide and aluminum nitride monolayer sheets have obtained increasing attentions universal [1–6]. Among these, SiC nanosheets due to its outstanding properties such as larger ratio of surface area to volume, the thermal conductivity, thermal stability, saturated carrier mobility, mechanical strength properties have attracted much notice in recent years [7,8] . SiCNSs are extensively attended to be useful in electronic devices. Today there is increasing worldwide demand for advanced Li ion batteries (LIBs) with higher energy capacity and longer cycle lifetime for applications in mobile communication devices, portable electronic devices, electrical/hybrid vehicles, and miscellaneous power devices. Hence, improving the anode compositions, which is economical, and having advanced electrochemical properties, are needed to continuously research. In present paper, we employed density functional theory to examine the electronic and structural properties of a series of SiCNSs and Li-SiCNSs.

II. METHODS

In percent work , in the first section all structures of pristine SiC nanosheets and Li-SiC nanosheets were fully optimized using M06-2X method and 6-31+G(d) basis set as implemented in the computer program packages. The binding energies were calculated using Highly parameterized empirical M06-2X. The binding energy were calculated with this formula: $E_b = (E_{Sic\text{-}Li}) - (E_{Li} + E_{Sic\text{-}rings})$, where $E_{SiCNS/Li}$, E_{Li} and E_{SiCNS} indicate the energy of Li-SiCNSs complexes, Li atom and SiCNS, respectively. Furthermore, single-point energies have been calculated at the B3LYP hybrid functional and 6-31+G(d) basis set to obtain the energy of molecular orbitals. The E_{gap} is obtained from the difference between the energies of the LUMO and HOMO at B3LYP/6-31+G(d) level. To plot the density of states (DOS), we used the MultiWfn Software. Besides, some of the global molecular desiptors such as chemical hardness, chemical potential (negative of the electronegativity), chemical softness and electrophilicity index were estimated. The relation of chemical potential (μ) and the electronegativity (χ) is: $\mu = -\chi = -(I + A)/2$. The chemical hardness (η) is given by $\eta = (I - A)/2$, where I and A are the first ionization energy and electron affinity, sequentially. The chemical softness can be written as following equation: $S = 1/\eta$. Conceptually electrophilicity index can be defined according to the following equation: $\omega = \mu^2/2\eta$

III. RESULTS AND DISCUSSION

The structures of pristine $Si_5C_5H_8$ (E), $Si_7C_7H_{10}$ (F), $Si_8C_8H_{10}$ (G) and Li-SiCNSs complexes $Si_5C_5H_8Li_2$ (E_{12}) , $Si_7C_7H_{10}Li_2$ (F_{13},F_{23}), $Si_8C_8H_{10}Li_2$ (G_{12},G_{24}), $Si_7C_7H_{10}Li_3$ (F_{123}) , $Si_8C_8H_{10}Li_3$ (G_{134}) are given in Fig. 1. The density of states (DOS) for pristine and Li-SiCNSs complexes for two models E and E_{12} are shown in Fig. 2. The calculated global descriptors including (μ, η, S, ω) and electric dipole moments are listed in Table 1. The electronic energies including binding energy, HOMO and LUMO and the energy gap of the pristine and Li-SiC nanosheets are given in Table 2. The computed average value of Si-C bond length for pure structures E, F and G is 1.779, 1.779 and 1.78 Å, respectively which is in good agreement with previous results 1.78A^0 [9] . In Li-SiCNSs structures, the calculated average value of Si-C in E_{12} , F_{13}, F_{23}, G_{12}, G_{24}, F_{123} and G_{134} is 1.828, 1.848, 1.957, 1.828, 1.904, 1.9 and 1.869 Å that are greater than those of corresponding pristine structures by 0.049, 0.069, 0.178, 0.048, 0.124, 0.121 and 0.089 Å. This can be related to the electrostatic repulsion between electron density of Li and SiC ring. The binding energy of Li to SiC nanosheets is 0.15, 4.93, 3.99, 4.81, 4.91, 6.78 and 8.11ev for E_{12}, F_{13}, F_{23}, G_{12}, G_{24}, F_{123} and G_{134} respectively. The binding energies increase by increasing the size of sheet and number of Li atom. The energy difference between HOMO and LUMO makes the pristine models an insulator with a wide band gap. The DOS curve is changed by adding Li atoms in SiCNSs. Our calculations indicated that the band gap of investigated Li-SiC nanosheets decreases and in turn, the electrical conductivity increases.

Table1: Values of μ, η, S, ω, Q, for studied models calculated at B3LYP / 6-31+G (d) level

SiCNSs	μ (eV)	η(eV)	S(eV)$^{-1}$	ω(eV)	Q/debye
E	-3.767	1.89	0.529	3.753	1.067
E_{12}	-3.84	1.581	0.632	4.664	2.541
F	-3.774	1.551	0.645	4.592	2.322
F_{13}	-2.415	0.601	1.664	4.852	0.345
F_{23}	-2.457	0.57	1.753	5.293	4.935
F_{123}	-2.622	0.668	1.496	5.143	0.632
G	-3.761	1.53	0.654	4.624	4.184
G_{24}	-2.643	0.343	2.918	1.0194	5.862
G_{12}	-2.719	0.586	1.706	6.311	0.722
G_{134}	-2.556	0.153	6.527	21.321	1.0213

Table2: HOMO, LUMO, band gap energies for studied models. Calculated at B3LYP/6-31+g (d) level.

SiCNSs	E_b(ev)	E_{HOMO}(eV)	E_{HOMO}(eV)	E_{L-H}(eV)
E	-	-5.657	-1.876	3.781
E_{12}	0.151	-5.421	-2.259	3.162
F	-	-5.326	-2.223	3.103
F_{13}	4.913	-3.016	-1.814	1.202
F_{23}	3.991	-3.028	-1.887	1.141
F_{123}	6.786	-3.29	-1.953	1.337
G	-	-5.29	-2.231	3.058
G_{24}	4.910	-2.986	-2.301	0.685
G_{12}	4.813	-3.306	-2.134	1.172
G_{134}	8.11	-2.709	-2.404	0.306

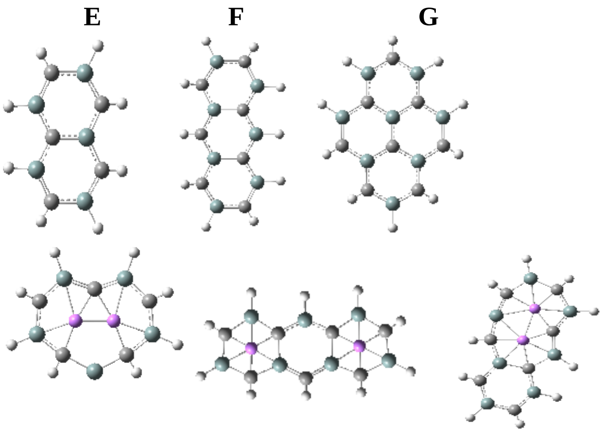

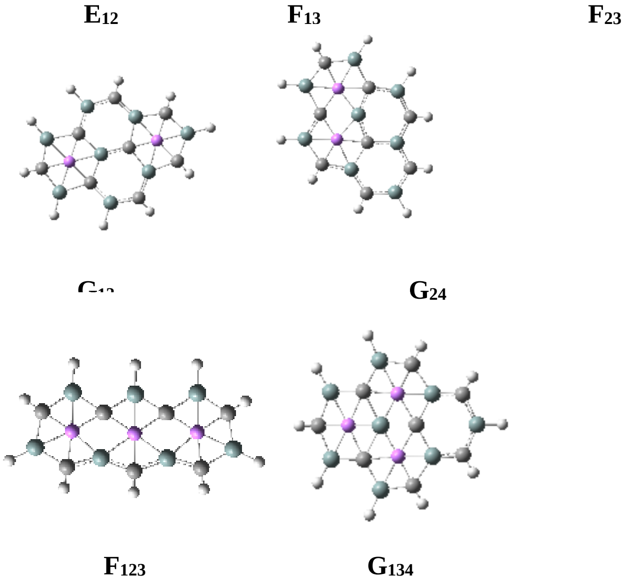

Fig.1.The optimized structures. The Gray, turquoise blue and violet spheres represent C, Si and Li atoms, respectively.

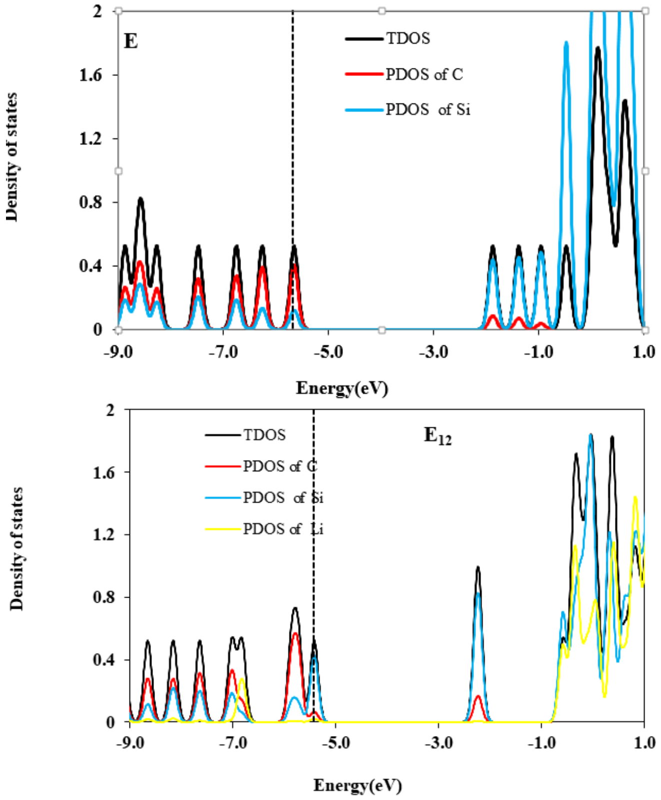

Fig. 2. Total and projected density of states (DOS) of E and E_{12}.

IV. CONCLUSION

By means of DFT methods, the effects of Li atom on the structural and electronic properties of the SiCNSs were explored. It is predicted that the conductivity of SiCNSs is increased by adding Li atoms. Increase in the size of sheet and number of Li atoms leads to increase in binding energy.

REFERENCES

[1] Q. H. Wang, K. Kalantar-zadeh, A. Kis, J. N. Coleman, and M. S. Strano, NANO TECHNOLOGY,vol. 7, pp. 699–712, **2012**.
[2] S. Z. Butler *et al.*, ACS NANO, vol.7, pp. 2898–2926, **2013**.
[3] R. Ansari, S. Rouhi, M. Mirnezhad, and M. Aryayi, *Phys. E* vol. 53, pp. 22–28, **2013**.
[4] S. S. Lin, PHYSICAL CHEMISTRY,vol.116,pp.3951-39 55,**2012**
[5] J. N. Coleman *et al.*, *Science* , vol. 331, , pp. 568–571, **2011**.
[6] C. W. Zhang, *J. Appl. Phys.*, vol. 111, **2012**.
[7] A. A. Kuzubov, N. S. Eliseeva, P. O. Krasnov, F. N. Tomilin, A. S. Fedorov, and A. V. Tolstaya, *Russ. J. Phys. Chem. A*, vol. 87 , pp. 1332–1335, **2013**.
[8] H. Şahin *et al.*, *Phys. Rev. B - Condens. Matter Mater. Phys.*, vol. 80, pp. 1–12, **2009**.
[9] B. Baumeier, P. Krüger, and J. Pollmann, PHYSICAL REVIEW.vol.76 pp. 1–10, **2007.**

The Investigation of Thermal Conversion of Spiropyran to Merocyanine and its Derivatives

H.Roohi, T.Rostami*
Department of Chemistry, Faculty of Science, University of Guilan, P.O. Box 98135-674, Rasht, Iran
Email: trostami97@gmail.com

Abstract*:* The thermal conversion of spiropyran derivatives (R-SP, R = H, OH, and CF_3) to merocyanine (MC) were investigated theoretically in the ground state. In S_0, the most stable isomer is SP. In the SP to MC switching, the C_{spiro}–O bond of SP is broken and ring-opening occurs. Since the cis-isomer is energetically unstable, it tends to reach a stable form with lower energy level. The rotation around the central torsion dihedral angle in cis-isomer ultimately yields trans-isomer. The trans-isomer is energetically stable and the cis-isomer is an intermediate in the conversion of ring-closed form to trans-isomer.

Keywords*:* Merocyanine, Photoswitching, Spiropyran

I. INTRODUCTION

In molecular switching, a molecule can be reversibly transformed between two or more stable states by external stimuli. It can occur in different ways such as photodissociation, rotating around the bond, proton transfer, electron transfer, etc under the influence of different stimuli such as light, temperature, electric current and mechanical stress [1]. The process of switching can also occur in a thermal way in the S_0 state. So far, there have been a number of switchable molecules such as azobenzenes, stilbenes, diarylethenes, spiropyran [2,3], etc. which extensively studied but among them, SP has shown unique properties. The SP isomers which have different properties cause to distinguish it from other switching molecules. The isomers of SP are different from each other in terms of optical properties, absorption spectra and geometrical structures [4]. Using molecular switching can bring useful applications such as optical data storage, smart windows, fluorescence probes [5] and so on. Until now a considerable number of studies have been devoted to the molecular switches both theoretically and experimentally [6–8]. In the present study, the process of the thermal conversion of SP derivatives (H, OH, and CF_3) to MC was investigated theoretically in the S_0 state.

II. METHODS

In the present study, electronic structure calculations and energies are reported by applying the density-functional theory (DFT) method. The calculations were performed using the Gaussian 09 program packages. The SP and its derivatives in all cases of isomer structures were optimized using CAM-B3LYP method in conjunction with 6-31G(d) basis set. The absorption wavelengths and oscillator strengths of all systems were calculated.

III. RESULTS AND DISCUSSION

In this study, we were interested in understanding the switching behaviour conversion of SP to MC theoretically. Scheme1. Shows the structure of closed form and trans isomer with SP derivatives.

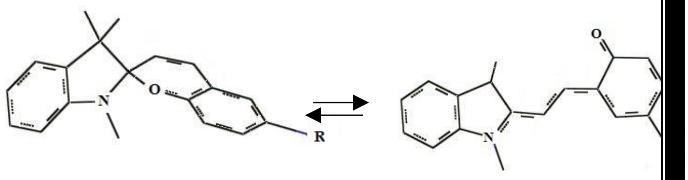

Scheme.1: Structure of conversion of SP to MC. R= H, CF_3, OH.

The SP derivatives were designed by replacing of a hydrogen atom at the position 6 of the benzopyran part by CF_3 and OH. The CAM-B3LYP/6-31G(d) optimized structures of the SP and MC derivatives at S_0 state is shown in Fig. 1

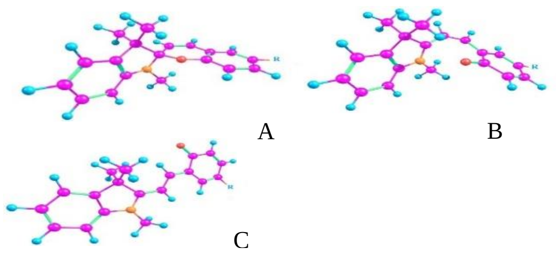

Fig.1: Optimized structures of the SP derivatives at S_0 state. (A=Closed, B=Cis, and C= Trans)

According to these calculations, in the S_0 state, the structure is stable in the ring-closed form. In a thermal reaction, the C_{spiro}–O bond is broken and ring-opening occurs. In this process, the ring-closed form switches to cis-open isomer as an intermediate. The relative energies of cis (trans) isomers for H, CF_3, and OH is 23.1(19.4), 21.1(17.7), 23.9(20.0) kcal mol^{-1}, respectively indicating that trans isomer is more stable than cis one. Since the cis-isomer is energetically unstable, it tends to reach a stable form with lower energy level. It should be added that the rotation around the central torsion dihedral angle (C_{spiro}–C=C–C) in cis-isomer yields trans-isomer. The absorption wavelengths (λ) and oscillator strengths (f) for SP derivatives at CAM-B3LYP/6-31G(d) level of theory are exhibited in Table 1. As reported, the oscillator strengths for H, CF_3 and OH is 0.059, 0.039, 0.072, respectively. Comparing these data shows that the intensity of the oscillator strengths of molecules changes as: OH> H> CF_3. The calculated absorption λ_1 values in the closed form of H, CF3, and OH is 272.8, 273.1, and 319.1nm, respectively.

Table.2: Absorption wavelengths (nm) and oscillator strengths at CAM-B3LYP /6-31G(d) level of theory.

		λ_1	λ_2	λ_3	f_1	f_2	f_3
H	closed	272.8	253.2	245.3	0.059	0.1546	0.040
	cis	458.6	374.0	311.9	0.163	0.1969	0.221
	trans	418.7	393.9	306.1	0.758	0.000	0.210
CF_3	closed	273.1	257.9	244.8	0.039	0.148	0.039
	cis	455.9	367.5	302.8	0.182	0.222	0.200
	trans	421.0	391.6	302.1	0.827	0.000	0.169
OH	closed	319.1	275.6	252.1	0.072	0.164	0.026
	cis	480.2	381.2	316.7	0.205	0.132	0.235
	trans	449.8	389.6	311.6	0.684	0.000	0.233

IV. CONCLUSION

In this work, we have theoretically investigated the conversion of SP to MC and its derivatives (H, CF_3, and OH) in the S_0 state. In the S_0 state, the structure is stable in ring-closed form. In the SP to MC switching, the C_{spiro}–O bond can be broken and converted to cis and trans ring-open form isomers. The trans-isomer is energetically stable and the cis-isomer is an intermediate in the conversion of ring-closed form to trans form. Our results show that increasing energy is observed for switching the closed form to cis and trans isomers, therefore cis and trans isomers are less stable than the closed form in the S_0 state. The process of switching in SP is energetic.

REFERENCES

[1] R. Klajn, Chem Soc Rev, vol. 43, pp. 148-184, **2014**.

[2] S. Frolova, V. Gorbunov, N. Shubina, A. Perepukhov, S. Romanova, and K. Agladze, Biosci. Rep, pp. 1–14, **2019**.

[3] A. Tavassoli, A. D. Hamilton, D. R. Spring, A. A. Beharry, and G. A. Woolley, Chem Soc Rev, no. 8, pp. 4422–4437, **2011.**

[4] M. Irie, T. Fukaminato, K. Matsuda, and S. Kobatake, Chem. Rev., vol. 114, no. 24, pp. 12174–12277, **2014**.

[5] V. A. Online *et al.*, pp. 3716–3721, **2013**.

[6] K. Kinashi, S. Nakamura, M. Imamura, K. Ishida, and Y. Ueda, J. Phys. Org. Chem., vol. 25, no. 6, pp. 462–466, **2012**.

[7] S. Kumar, K. Velasco, and A. Mccurdy, J. Mol. Struct., vol. 968, no. 1–3, pp. 13–18, **2010**.

[8] Y. Shiraishi, M. Itoh, and T. Hirai, pp. 13737–13745, **2010**.

Investigation of Thermodynamic Stability of para-Phenylthiophen Derivatives Using G4 Theory

Hossein Nikoofard
Faculty of Chemistry, Shahrood University of Technology, Shahrood, 36199-95161, Iran
*Email:**nikomahdieh@yahoo.com***

Abstract: In the current work, the standard molar enthalpies of formation , ΔH_f° , of para-position substituted phenylthiophene (PT) derivatives are computed using the quantum chemistry composite method (G4) at 298.15 K. The results obtained are carried out based on the substituent effect on the electronic, structural, and energetic properties of the studied molecules in gas-phase and acetonitrile media. In the atomization reaction route, the calculated values of ΔH_f° for these compounds can be successfully associated with the substituent characteristics. The electron-withdrawing substituents increase the both ΔH_f° and ionization potential (IP), while electron-donating ones cause a vice versa effect. In comparison with gas-phase, acetonitrile solvent satisfies the substituent effect on all calculated results. Moreover, both the calculated ΔH_f° and IP values for substituted PT indicate a linear dependency on the energy of the highest occupied molecular orbital (HOMO) of studied molecules in two different environments.

Keywords: G4 theory, Enthalpies of formation, Ionization potential, Substituted phenylthiophene.

I. INTRODUCTION

in the last decade, the compounds based on thiophene have been extensively applied in biochemistry, modern drug design, electrically conductive polymers, and opto-electronic devices [1,2]. Application of these materials have received a great deal of consideration from both the industrial research and academic centers. The facility in the chemical modification of their structures can potentially allow one to fine-tune optical and electronic properties of these materials. On the other hand, the characteristics of these monomers intensely be contingent upon the effective conjugated length, degree of the electronic delocalization, and introduction of substituents at specific positions present in such monomers [3,4]. Though, an important disadvantage of thiophene-based compounds is their poor stability and low fluorescence with respect to ones consisting of substituted derivatives [3-5].

A knowledge of the structure-energetic relationships of thiophene derivatives is vital not only in the development and identification the thermo-chemical properties but also in the streamlining of their new applications. It is known that the study of substituent effect on the characteristics of the thiophene-based molecules is one of the most broadly studied subjects in physical chemistry. The development in understanding of geometry structure on the thermodynamic stabilities of titled molecules is reflected in their standard molar enthalpies of formation.

Theoretical surveys on a series of substituted PTs are desirable intensively for designing novel functional materials, thereby, this is the main purpose of the presented work. The atomization energy route was used as the selected approach. The Gaussian-4 theory, G4 theory, for the calculation of energies was used to estimate the ΔH_f° values of PTs. It was focused mainly on the energetic differences between the PT compounds having various substituted-phenyls (*X*: -CH_3, -OCH_3, -Cl, -F), and the substituent effect in PTs relative to phenylthiophene as a reference molecule (Scheme 1).

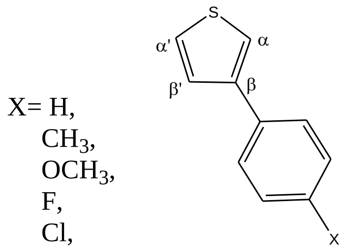

Scheme 1. Molecular structures of PT derivatives.

II. METHODS

The G4 method is a compound technique in spirit of the other Gaussian theories which make an effort to take the accuracy achieved with G3 theory as one small step further. The introduction of an extrapolation scheme for finding basis set limit Hartree-Fock energies, a highest-level single point calculation at CCSD(T) instead of QCISD(T) level, the use of geometries and thermochemical corrections obtained at B3LYP/6-31G(2df,p) level with supplement of extra polarization functions in the largest-basis set MP2 calculations are involved in this version. Both the ground-state and singly ionized geometries for each molecule studied were fully optimized using G4 technique, as implemented in the Gaussian 09 software. By performing the frequency calculations, the optimized structures were examined to be the real minima. With aim of the corresponding thermal calculations obtained via the calculated harmonic vibrational frequencies, the absolute thermos-chemical properties were obtained at 298.15 K and 1.0 atm.

III. RESULTS AND DISCUSSION

Several important structural characteristics of PTs obtained via the G4 calculations are illustrated in Table 1. The molecular planarity, as one of these parameters, related to the extent of the aromaticity of the thiophene derivatives can be revealed by the torsional angle, D_{mnop}, where m, n, o, and p are the atom numbers (scheme 1). As it can be seen in this table, the dihedral angles defining the torsion between the phenyl (Ph) and adjacent thiophene (Th) rings indicate that all PTs have a lower deviation from planar structure ($< 30^{o}$). It is found that the influence of phenyl substituted on the structure of PTs does not affect substantially their torsion angles relative to the parent phenylthiophene molecule (29.04^{o}).

Table 1. Torsion angle $D_{\text{Ph-Th}}$ (in degree) and bond lengths R (in angstrom) for PTs at G4 theory.

PTs	$D_{\text{Ph-Th}}$	$R_{\text{Ph-Th}}$	$R_{\text{Ph-X}}$
PT-CH_3	28.66	1.4754	1.5084
PT-OCH_3	28.35	1.4748	1.3588
PT-Cl	29.18	1.4755	1.3414
PT-F	28.55	1.4747	1.7575

Moreover, compared to the parent phenylthiophene monomer, the attendance of substituted groups could develop the electron delocalization over the molecular structure. In this regard, delocalization of the π-electrons onto the molecular structure leads to suitable resonance systems and improved stabilization of the PT derivatives. It is known that an extended aromatic system may be correspond to the narrow gap between the HOMO and LUMO. Since the relative ordering of the occupied and virtual orbitals provides a reasonable qualitative indication of the excitation properties and of the ability of electron or hole transport, it is useful to examine HOMO and the lowest virtual orbitals for the studied molecules. As the first dipole-allowed electron transitions along with the strongest electron transitions correspond almost exclusively to the promotion of an electron from the HOMO level to the LUMO one, we computed the IP and HOMO-LUMO gaps (HLGs) values for all the PT derivatives, the results of which were collected in Table 2.

Table 2. IP and HOMO-LUMO gaps values for PT derivatives.

PTs	IP/eV	HLG^{a}/eV	HLG^{b}/eV
PT-CH_3	5.68	0.187	0.061
PT-OCH_3	5.44	0.181	0.059
PT-Cl	5.81	0.189	0.062
PT-F	5.87	0.185	0.060

a: in neutral state; *b*: in radical cation form

According to Table 2, the values of HLG for the PT derivatives at grand state are less than that for their radical ions (doped state). The results obtained show that closing the para-position of the phenyl ring by different groups destabilizes both the HOMO and LUMO levels. Our results show favorably an increase in the HOMO level and a decrease in the LUMO level after linking the para-position of the phenyl ring by substitutions, which offer reductions in the HOMO-LUMO gaps.

The values of the gas-phase standard molar enthalpies of formation at 298 K, for PTs were calculated through the atomization energy method. The calculation route and detailed description of the procedure have been reported in the literature [6]. The calculated values of ΔH_f° for PTs at G4 theory are given in Table 3.

Table 3. Predicted values for gas-phase standard molar enthalpies of formation (kJ mol^{-1}) for PTs at 298 K via G4 theory.

PTs	PT-CH_3	PT-OCH_3	PT-Cl	PT-F
	-31.25	-30.92	-29.50	-28.11

According to Table 3, one can be see that attachment of substituted-phenyls to the thiophene ring leads to an evident reduction in the standard molar enthalpies of formation, which corresponding to an increase in their thermodynamic stability. Generally, one may be concluded that the relationships found between the standard molar enthalpies of formation and the characteristics of the substitution supports us to estimate the relative thermodynamic stability of new PT derivatives, for which the respective experimental data was not reported.

IV. CONCLUSION

In this work, the influence of phenyl-substituted groups on the structure-energetics of para-position phenylthiophene was investigated through the Gaussian-4 theory. The results obtained showed that the electron donating substituents in the phenyl ring play a fine-tune effect on the electronics, structures, and thermodynamic stabilities of PT derivatives. The calculated results carried out on the PTs showed that substituted phenyl may create more satisfactory characteristics for corresponding polymers. The substitution effect is referred to both induction and resonance effects of phenyl-substituted groups. Furthermore, The calculated values of ΔH_f° for PTs in the condensed phase, confirmed that G4 level of theory is capable to predict the relative thermodynamic stabilization of PTs.

REFERENCES

[1] G. Gustafson, Y. Cao, G. M. Tracy, F. Klavetter, N. Colaneri and A. J. Heeger, Nature, vol. 357, pp. 477-479, **1991**.

[2] A. Kraft, A. C. Grimsdale and A.B. Holmes, Angew. Chem., vol. 110, pp. 416-443.**1998**.

[3] D. Fichou (Ed.), Handbook of Oligo- and Polythiophenes, Wiley, New York, **1999**.

[4] 11808-11813, **1988**.

[5] S. Suramitr, A. piriyagagoon, P. Wolschann and S. Hannongbua, Theor. Chem. Acc., vol. 131, pp. 1209-1217, **2012**.

[6] J.W. Ochterski, Gaussian white paper, Thermochemistry in Gaussian 2000, http://www.gaussian.com/g_whitepap/thermo. htm.

Spin-Orbit Coupling Matrix Elements in Electronic States of PdH

A. Shayesteh*, F. A. Nabi
School of Chemistry, College of Science, University of Tehran, Tehran, 14176, Iran
Email: ashayesteh@ut.ac.ir

Abstract: Potential energy curves for several electronic states of PdH were calculated using the multi-reference configuration interaction method, including relativistic and spin-orbit corrections. Diagonal and off-diagonal elements of the spin-orbit Hamiltonian matrix were computed for vibrational levels of the five lowest electronic states. The eigenvectors of the matrix indicate significant mixing for vibrational wavefunctions in the $\Omega = 3/2$ states.

Keywords: Multi-reference configuration interaction, Palladium monohydride, Relativistic corrections, Spin-orbit Hamiltonian, Matrix diagonalization.

I. INTRODUCTION

The group 10 metals (Ni, Pd and Pt) are important in heterogeneous catalytic reactions such as addition of hydrogen to carbon monoxide for production of methanol [1,2]. Relativistic effects and electron correlation in nickel, palladium, platinum, and their diatomic hydrides have been a challenge for ab initio methods. There has not been a comprehensive theoretical study on excited electronic states of PdH and PdD that have been detected in spectroscopic measurements, although some low-lying states of PdH have been studied previously by ab initio methods [3]. In the present study, we have calculated several electronic states of PdH using the multi-reference configuration interaction method including relativistic and spin-orbit corrections.

II. METHODS

The program ORCA 2.9.0 was used to carry out all electronic structure calculations [4]. The initial state-averaged CASSCF calculations were performed at 42 Pd - H distances using the 11 valence electrons of Pd ($4d^{10}$) and H ($1s^1$) as in 12 active orbitals: Pd (4d 5s 4d′) and H (1s); CAS(11,12). The 4d′ orbital represents a set of diffuse d functions with radial expectation value of $\langle r \rangle_{4d'} = 2.11$ Å while the radial expectation value for the 4d orbital is $\langle r \rangle_{4d} = 1.45$ Å. In the next step, MRCI calculations were performed taking relativistic and spin-orbit corrections into account. The DKH-QZVPP basis sets of Pantazis et al. [5] were used for both atoms. Using the potential energy points calculated at 42 Pd - H distances, the one dimensional radial Schrödinger equation was solved by the LEVEL program [6], and vibrational energies were computed.

III. RESULTS AND DISCUSSION

The diagonal and off-diagonal elements of the spin-orbit Hamiltonian matrix for the $X^2\Sigma^+$ ground state and the $1^2\Delta$, $1^2\Pi$, $2^2\Sigma^+$ and $3^2\Sigma^+$ excited states are plotted as a function of Pd - H distance (r) in Fig. 1. Vibrational energy levels of the seven lowest-lying Ω states, i.e., Ω = 1/2(I), 5/2(I), 3/2(I), 3/2(II), 1/2(II), 1/2(III) and 1/2(IV) were computed precisely by diagonalizing a Hamiltonian matrix that contains diagonal and off-diagonal spin-orbit terms between vibrational levels of the $X^2\Sigma^+$, $1^2\Delta$ and $1^2\Pi$, $2^2\Sigma^+$ and $3^2\Sigma^+$ electronic states.

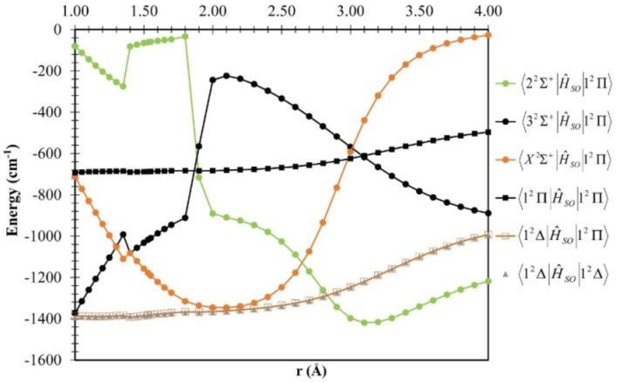

Fig. 1. Spin-orbit matrix elements for the $X^2\Sigma^+$, $1^2\Delta$, $1^2\Pi$, $2^2\Sigma^+$ and $3^2\Sigma^+$ states of PdH.

The spin-orbit matrix elements are calculated using the following Hamiltonian:

$$H_{ij,kl} = \left\langle \psi_{el,i} \psi_{vib,k} \left| \hat{H}^{(0)} + \hat{H}_{SOC} \right| \psi_{el,j} \psi_{vib,l} \right\rangle$$

$$= T_v + \left\langle \psi_{vib,k} \left| \left\langle \psi_{el,i} \left| \hat{H}_{SOC} \right| \psi_{el,j} \right\rangle \right| \psi_{vib,l} \right\rangle$$

in which T_v is the vibronic energy calculated at the MRCI level. The spin-orbit matrix elements (Fig. 1) have variations with Pd - H distance (r). They were inserted between vibrational wavefunctions ($\psi_{\mathrm{vib},k}$ and $\psi_{\mathrm{vib},l}$) of the same or different electronic states, and the LEVEL program was used for calculation of integrals. The spin-orbit Hamiltonian matrix was diagonalized to obtain eigenvalues and eigenvectors. The eigenvectors for Ω = 3/2 states ($^2\Delta_{3/2}$ and $^2\Pi_{3/2}$) indicate significant mixing between vibronic states.

The obtained eigenvalues (vibrational energy levels) were compared with those from individual spin-orbit corrected potential energy curves. For all Ω values, there are small differences between vibronic energies obtained from the two methods. However, the differences for the two Ω = 3/2 states, i.e., $^2\Delta_{3/2}$ and $^2\Pi_{3/2}$, are significant, because when vibrational levels of the $^2\Delta_{3/2}$ and $^2\Pi_{3/2}$ states become nearly degenerate, they are shifted in opposite directions. The actual energy levels have positive and negative shifts with respect to E_{SOC} which is based on separation of nuclear motion from electronic energy. The vibronic energies for the low-lying states and their differences are presented in Tables 1 and 2, for PdH and PdD, respectively. For both isotopologues, the discrepancies in Ω = 3/2 states are relatively large, although near-degeneracies are less severe for PdD, and the resulting shifts are smaller for PdD, compared to the PdH isotopologue.

Table 1. Vibronic energies of PdH (in cm^{-1}) obtained from matrix diagonalization and comparison with direct SOC calculations.

Ω State	E(SOC)	E(Matrix)	Difference
1/2 (I) v	1012.5	1025.9	13.4
1/2(I) v	2977.3	2989.9	12.7
1/2(I) v	4879.9	4892.4	12.6
1/2(I) v	6705.5	6718.4	12.9
5/2(I) v	7186.5	7193.5	7.0
1/2(I) v	8418.3	8432.0	13.7
3/2(I) v	8487.7	8507.5	19.9
5/2(I) v	8925.7	8932.4	6.7
1/2(I) v	10048.6	10063.4	14.8
3/2(I) v	10102.2	10087.4	-14.8
5/2(I) v	10618.1	10624.8	6.7
1/2(II) v	11244.1	11255.3	11.1
3/2(II) v	11309.8	11336.4	26.6
1/2(I) v	11604.2	11621.6	17.4
3/2(I) v	11670.3	11667.3	-3.1
5/2(I) v	12225.0	12231.9	6.9
1/2(II) v	12882.1	12917.0	34.9
3/2(II) v	13047.1	12975.7	-71.4
1/2(I) v	13073.2	13095.0	21.8
3/2(I) v	13166.3	13268.3	102.0
5/2(I) v	13768.0	13774.8	6.8
1/2(II) v	14444.7	14491.3	46.5
1/2(I) v	14449.5	14476.4	26.9
3/2(I) v	14621.3	14475.9	-145.4
3/2(II) v	14723.5	14898.4	174.9
5/2(I) v	15239.0	15245.8	6.8

Table 2. Vibronic energies of PdD (in cm^{-1}) obtained from matrix diagonalization and comparison with direct SOC calculations.

Ω State	E(SOC)	E(Matrix)	Difference
1/2(I) v =	720.2	733.3	13.2
1/2(I) v =	2130.8	2143.5	12.6
1/2(I) v =	3511.0	3523.5	12.5
1/2(I) v =	4862.0	4874.6	12.6
1/2(I) v =	6168.0	6180.9	12.9
5/2(I) v =	6929.0	6936.1	7.1
1/2(I) v =	7409.8	7423.1	13.2
5/2(I) v =	8172.9	8179.7	6.8
3/2(I) v =	8249.5	8264.4	14.9
1/2(I) v =	8607.6	8621.5	13.9
5/2(I) v =	9400.4	9407.1	6.7
3/2(I) v =	9402.4	9405.0	2.6
1/2(I) v =	9774.5	9789.4	14.9
3/2(I) v =	10545.1	10535.1	-10.1
5/2(I) v =	10597.9	10604.6	6.7
1/2(I) v =	10901.1	10918.0	16.9
1/2(II) v	11002.0	11009.5	7.5
3/2(II) v	11052.9	11084.2	31.3
3/2(I) v =	11645.3	11626.0	-19.3
5/2(I) v =	11745.6	11752.4	6.8
1/2(I) v =	11983.6	12003.8	20.1
1/2(II) v	12176.9	12199.0	22.0
3/2(II) v	12296.2	12338.3	42.1
3/2(I) v =	12717.5	12692.4	-25.2
5/2(I) v =	12866.4	12873.3	6.9
1/2(I) v =	13020.5	13044.5	23.9
1/2(II) v	13325.2	13362.8	37.6
3/2(II) v	13522.3	13567.5	45.1
3/2(I) v =	13771.1	13745.6	-25.5

IV. CONCLUSION

Potential energy curves for the low-lying electronic states of PdH were calculated at the MRCI level of theory with scalar relativistic and spin-orbit corrections. To calculate accurate vibronic energies for PdH and PdD in their low-lying electronic states, diagonal and off-diagonal elements of the spin-orbit Hamiltonian matrix were calculated for all vibrational levels of the $X^2\Sigma^+$, $1^2\Delta$, $1^2\Pi$, $2^2\Sigma^+$ and $3^2\Sigma^+$ states, and the matrix was diagonalized to obtain eigenvalues and eigenvectors. The results were compared with those obtained from potential energy curves of the individual Ω states. Eigenvectors of the Hamiltonian matrix for Ω = 3/2 indicate significant mixing between vibrational levels of the $^2\Delta_{3/2}$ and $^2\Pi_{3/2}$ states.

REFERENCES

[1] K. Christmann, G. Ertl, T. Pignet, Surf. Sci., 54, 365, **1976**.
[2] J. Sauer, Chem. Rev., 89, 199, **1989**.
[3] K. Balasubramanian, P. Y. Feng, M. Z. Liao, J. Chem. Phys., 87, 3981, **1987**.
[4] F. Neese, WIREs Comput. Mol. Sci., 2, 73, **2012**.
[5] D. A. Pantazis, X.-Y. Chen, C. R. Landis, F. Neese, J. Chem. Theory Comput., 4, 908, **2008**.
[6] R. J. Le Roy, J. Quant. Spectrosc. Radiat. Transfer, 186, 167, **2017**.

A Quantum Study on the Fe-Containing Ionic Liquids

A. Daneshvar[a*], S. Hajiyan[a], and M. Moosavi[a]
[a] *Department of Chemistry, University of Isfahan, Isfahan, 81746-73441, Iran*
Email:a.daneshvar88@yahoo.com

Abstract: The aim of this study is to obtain the better understanding of the intermolecular interaction and the bond characterization in imidazolium- and cholinium-based Fe-containing ionic liquids namely [hmim][$FeCl_4$] and [Chol][$FeCl_4$]. In this regards, the atom in molecule (AIM) analysis has been performed for each studied ILs. The results showed that the anion-cation interactions of [Chol][$FeCl_4$] is stronger than [hmim][$FeCl_4$] . Also, the strongest interactions in each IL is related to Fe-imidazolium ring and Cl-H(hydroxyl) in imidazolium and cholinium-based ILs, respectively. The laplacian electron density shows that in contrast of [hmim][$FeCl_4$], the [Chol][$FeCl_4$] has two different type of interactions.

Keywords: AIM, Quantum mechanics, Laplacian of electron density, Ionic liquid, intermolecular interaction.

I. INTRODUCTION

Ionic liquids (ILs) are new environmentally benign chemicals which have been synthesized to replace those chemicals that are harmful for the environment. [1] There are many experimental studies on the properties of different ionic liquids in pure and mixture states [2-4]. Since, the synthesis of these unique liquids are expensive, the computational studies can be a good way to reduce costs and times. As were as the authors are aware, there is a few computational studies on the properties of the Fe-containing ILs. Molecular dynamics simulation and quantum mechanical studies are two attended computational methods for IL systems. Quantum mechanical methods such as density functional theory (DFT) and atom in molecule (AIM) can help us to obtain a fundamental understanding of intermolecular interactions.

In this paper, the AIM analysis of 1-hexyl-3-methylimidazolium tetracholoroferrate [hmim][$FeCl_4$] and N-hexyl-N-2-hydroxyethyl-N,N-dimethyl ammonium tetracholoroferrate [Chol][$FeCl_4$] have been down to obtain a better insight of the interionic interactions.

II. METHODS

The B3LYP density functional with the 6-311++G** basis set have been employed to optimize the structures of the studied ILs using Gaussian 09 package [5]. The NBO and the CHELPG methods have been chosen for charge transfer of imidazolium-based and cholinium-based ionic liquids, respectively, due to their lower percentage error between simulated density data and their experimental values in the literature. The AIM2000 program has been used to performed atoms in molecule (AIM) analysis [6]. The electron density of bonds and their laplacians have been calculated using Multiwfn 3.6 program.

III. RESULTS AND DISCUSSION

The topological graphics of the lowest energy of ionic pairs obtained from AIM analysis shows the bond critical point (BCP) which are defined by the points localized between pairs of atoms bonded or interacting. Each bond critical point is characterized by two parameters, namely, electron density (ρ_{BCP}) which shows the strength of bond and its laplacian ($\nabla^2\rho_{BCP}$) which describes the characteristic of bond. The ρ_{BCP} is used to describe the strength of a bond, with stronger bond associated with larger ρ_{BCP} value. The $\nabla^2\rho_{BCP}$ describes the characteristic of the bond. If $\nabla^2\rho_{BCP} < 0$, it is named as the covalent bond and if $\nabla^2\rho_{BCP} > 0$, it refers to a closed-shell interaction [7, 8] and characteristics of ionic bond, H-bond, or vdW interaction.

The topological graphics obtained from AIM analysis of each ILs have been given in Fig. 1. Also, the values of ρ_{BCP} and $\nabla^2\rho_{BCP}$ of each bond critical points have been tabulated in Table 1. The results showed that the electron density of Fe-H(CR) bond critical point in [hmim][$FeCl_4$] has the highest value which may reveal that the anion prefers to interact with the imidazolium ring of cation more than the alkyl chain residue. The positive values of $\nabla^2\rho_{BCP}$ for all of the bond critical points show that they are covalent type. It is interesting that Cl2-----H(C-methyl) and Cl2-----H(C-hydroxyl) interactions in [Chol][$FeCl_4$] have different bond type. It is due to its negative laplacian electron density which refers to the closed shell bond. Also, the strongest bond is related to Cl2 atom, which has the largest value of electron density in Cl2-----H(C-methyl) bond. Accordingly, the probability of the presence of anion around the nitrogen atom in cation is more than the alkyl chain residue.

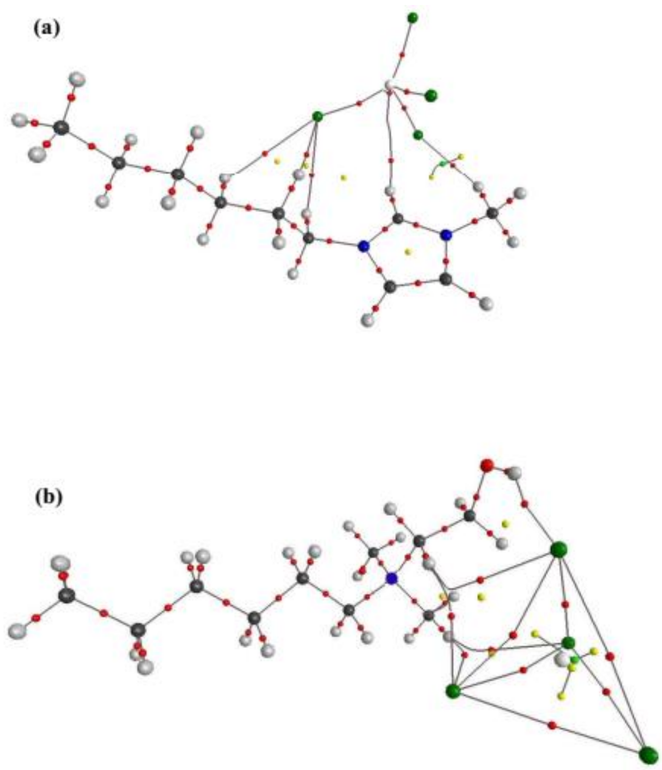

Fig. 1. Topological graphics of the lowest energy of ionic paires obtained from the AIM analysis of the (a) [hmim][$FeCl_4$], and (b) [Chol][$FeCl_4$] showing bond critical points (BCP, red circles), ring critical points (yellow circles), and cage critical points (pale green circles).

Table 1. Electron density (ρ_{BCP}) and laplacian of the electron density ($\nabla^2\rho_{BCP}$) in the BCPs (Bond Critical Points) for the studied ILs.

Structure	bond	ρ_{BCP}	$\nabla^2\rho_{BCP}$
[hmim][$FeCl_4$]	Fe-----HA(CR)	0.0135	0.0440
	Cl-----H(C-methyl)	0.0072	0.0292
	Cl-----H(C-chain)	0.0065	0.0221
	Cl-----H-C2	0.0041	0.0152
	Cl-----H-Cs-C2	0.0033	0.0100
[Chol][$FeCl_4$]	Cl1-----H(hydroxyl)	0.0160	0.0589
	Cl1-----H(C- hydroxyl)	0.0288	0.0110
	Cl2-----H(C- hydroxyl)	0.0361	-0.0079
	Cl2-----H(C-methyl)	0.273	-0.782
	Cl3-----H(C-methyl)	0.030	0.0011

IV. CONCLUSION

In this work, the AIM analysis has been used to obtain a better insight of interionic interactions in two ionic liquids with different cation type namely [hmim][$FeCl_4$] and [Chol][$FeCl_4$]. The results indicated that the anion has the strongest interaction with imidazolium ring in [hmim][$FeCl_4$] and the atoms around nitrogen in [Chol][$FeCl_4$]. From the laplacian electron density values it is found that there are two different bond type in [Chol][$FeCl_4$]. The electron density of bond critical points of the studied ILs showed that the strength of the anion-cation interaction in cholinium-based IL is more than the imidazolium-based one with the same alkyl chain length.

REFERENCES

[1] M. Moosavi, and A. Daneshvar, J. Mol. Liq., vol. 225, pp. 810-821, **2017**.

[2] M. Deetlefs, and K.R. Seddon, Chim. Oggi., vol. 24, pp. 16–18, **2006.**

[3] M. S. Calado, et al., Fluid Phase Equilib., vol. 344, pp. 6-12, **2013.**

[4] P. Wasserscheid, T. Welton (Eds.), Ionic Liquids in Synthesis, Wiley-VCH, Weinheim, **2007.**

[5] M. Frisch, et al., Gaussian 09, Revision D01, Gaussian. Inc., Wallingford CT **2009**.

[6] F. Biegler-Konig, et al., Software News and Updates AIM 2000, J. Comput. Chem., vol. 22, pp. 545-559, **2001.**

[7] M. Solimannejad, et al. Chem. Phys. Lett., vol. 449, pp. 23–27, **2007.**

[8] M. Torkzadeh, and M. Moosavi, J. Phys. Chem. *B*, vol. 121, pp. 7946-7962, **2017.**

Rotational and Spin-Orbit Hamiltonian Matrices for Low-Lying States of NiH

A. Shayesteh*, F.A. Nabi
School of Chemistry, College of Science, University of Tehran, Tehran, 14176, Iran
Email: ashayesteh@ut.ac.ir

Abstract: Potential energy curves for several electronic states of nickel hydride were calculated using the MRCI method with relativistic and spin-orbit corrections. Diagonal and off-diagonal matrix elements of the rotational and spin-orbit Hamiltonians were calculated for the six lowest vibrational levels of the $X^2\Delta$, $1^2\Sigma^+$ and $1^2\Pi$ electronic states. The eigenvectors indicate significant mixing between vibrational wavefunctions of the Ω=3/2 and Ω=1/2 states.

Keywords: MRCI, Nickel hydride, Spin-orbit coupling, Rotational Hamiltonian, Matrix diagonalization.

I. INTRODUCTION

Nickel is an important metal in heterogeneous catalytic reactions such as formation of methanol from carbon monoxide and hydrogen [1,2]. Relativistic effects and electron correlation in this metal and its hydride have been a challenge for theoretical methods. Moreover, NiH has been found in the atmosphere of cold stars and solar spots and thus is of astrophysical interest [3]. In the present study, the low-lying electronic states of NiH have been calculated using the multi-reference configuration interaction method including scalar relativistic and spin-orbit corrections. The effect of rotational Hamiltonian in mixing near-degenerate states has been investigated computationally.

II. METHODS

The program ORCA 2.9.0 was used to carry out the calculations [4]. The initial state-averaged CASSCF calculations were performed using the 11 valence electrons of Ni ($3d^9 4s^1$) and H ($1s^1$) in 12 active orbitals: Ni (3d 4s 3d′) and H (1s); CAS(11,12). The 3d′orbital represents a new set of diffuse d functions that have radial expectation value of $<r>_{3d'}$ = 1.608 Å while the corresponding value for the 3d orbital is $<r>_{3d}$ = 0.986 Å. In the next step, MRCI calculations were performed taking relativistic and spin-orbit corrections into account. The aug-cc-pVQZ basis sets [5] were fully decontracted for both Ni and H atoms, and used for all calculations. After obtaining the potential energy curves, the one dimensional radial Schrödinger equation was solved by the LEVEL program [6] to obtain vibrational energies. Matrix elements of the spin-orbit Hamiltonian between various vibrational levels were also calculated using the LEVEL program.

III. RESULTS AND DISCUSSION

The diagonal and off-diagonal elements of the spin-orbit Hamiltonian matrix for the $X^2\Delta$ ground state and the $1^2\Sigma^+$ and $1^2\Pi$ excited states were obtained as a function of Ni-H distance (r). These matrix elements were used to obtain vibrational energy levels of the five lowest-lying **Ω** states, i.e., **Ω** = 5/2(I), 3/2(I), 3/2(II), 1/2(I) and 1/2(II) precisely by diagonalizing a Hamiltonian matrix that contains diagonal and off-diagonal spin-orbit terms between vibrational levels of the $X^2\Delta$, $1^2\Sigma^+$ and $1^2\Pi$ states. The related elements of the matrix are calculated according to the following Hamiltonian:

$$\begin{aligned} H_{ij,kl} &= \left\langle \psi_{el,i}\psi_{vib,k} \left| \hat{H}^{(0)} + \hat{H}_{SOC} \right| \psi_{el,j}\psi_{vib,l} \right\rangle \\ &= T_v + \left\langle \psi_{vib,k} \left| \left\langle \psi_{el,i} \left| \hat{H}_{SOC} \right| \psi_{el,j} \right\rangle \right| \psi_{vib,l} \right\rangle \end{aligned}$$

in which T_v is the vibronic energy calculated at the MRCI level. The electronic spin-orbit matrix elements were inserted between vibrational wavefunctions ($\psi_{\mathrm{vib},k}$ and $\psi_{\mathrm{vib},l}$) of the same or different electronic states, and integrations were done using the LEVEL program. The spin-orbit Hamiltonian matrix was diagonalized to obtain eigenvalues and eigenvectors. The obtained eigenvectors for Ω = 3/2 states ($^2\Delta_{3/2}$ and $^2\Pi_{3/2}$) and Ω = 1/2 states ($^2\Pi_{1/2}$ and $^2\Sigma^+_{1/2}$) indicate significant mixing between vibronic states.

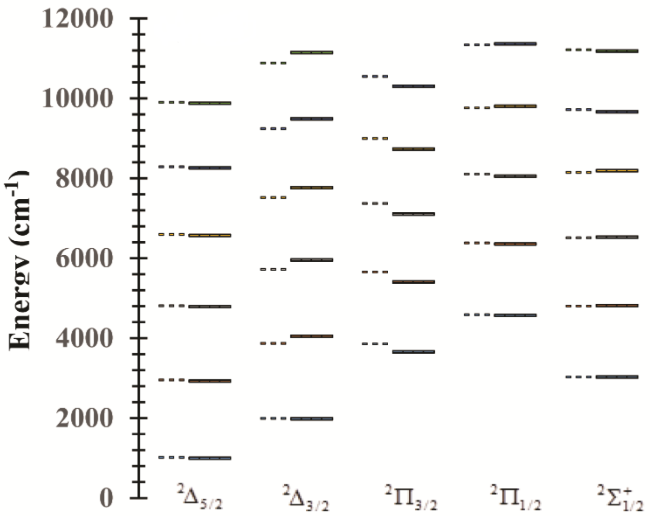

Fig. 1. Eigenvalues (vibronic energies) of the spin-orbit Hamiltonian matrix (solid lines) versus the corresponding values obtained from individual spin-orbit corrected potential energy curves (dashed lines) for NiH.

The obtained eigenvalues (vibronic energy levels) were compared with those from individual spin-orbit corrected potential energy curves (Fig. 1). The vibronic energies obtained from the two methods are slightly different for all Ω values. The differences for the two Ω = 3/2 states ($^2\Delta_{3/2}$ and $^2\Pi_{3/2}$) and Ω = 1/2 states ($^2\Sigma^+_{1/2}$ and $^2\Pi_{1/2}$) are significant. When vibrational levels of the $^2\Delta_{3/2}$ and $^2\Pi_{3/2}$ states become nearly degenerate, they are shifted in opposite directions, resulting in positive and negative shifts with respect to E_{SOC} which is based on the Born-Oppenheimer approximation. The vibronic energies for the low-lying states of NiH and their differences are presented in Table 1. For NiH, the discrepancies in Ω=3/2 are relatively large and have oscillating behavior; near-degeneracies are less severe for the Ω=1/2 states, and the resulting shifts are smaller for these states, compared to the Ω = 3/2 states.

Table 1.Vibronic energies of NiH (in cm^{-1}) obtained from matrix diagonalization and comparison with direct spin-orbit calculations.

Ω State	E(SOC)	E(Matrix)	Difference
5/2(I) v = 0	1015.25	996.39	-18.9
3/2(I) v = 0	1995.52	1981.66	-13.9
5/2(I) v = 1	2953.03	2927.54	-25.5
1/2(I) v = 0	3030.28	3028.56	-1.7
3/2(II) v = 0	3852.17	3655.85	-196.3
3/2(I) v = 1	3870.57	4046.25	175.7
1/2(II) v = 0	4582.55	4567.67	-14.9
1/2(I) v = 1	4805.72	4812.59	6.9
5/2(I) v = 2	4809.69	4785.68	-24.0
3/2(I) v = 2	5657.17	5407.99	-249.2
3/2(II) v = 1	5722.4	5953.53	231.1
1/2(II) v = 1	6381.52	6354.66	-26.9
1/2(I) v = 2	6507.62	6527.97	20.4
5/2(I) v = 3	6593.39	6566.41	-27.0
3/2(I) v = 3	7367.87	7099.95	-267.9
3/2(II) v = 2	7517.51	7764.18	246.7
1/2(II) v = 2	8103.34	8053.63	-49.7
1/2(I) v = 3	8145.27	8188.65	43.4
5/2(I) v = 4	8285.51	8258.68	-26.8
3/2(I) v = 4	8994.96	8728.5	-266.5
3/2(II) v = 3	9237.65	9484.99	247.3
1/2(I) v = 4	9714.44	9663.36	-51.1
1/2(II) v = 3	9755.47	9800.82	45.4
5/2(I) v = 5	9902.32	9875.57	-26.8
3/2(I) v = 5	10546.35	10301.77	-244.6
3/2(II) v = 4	10883.83	11145.00	261.2
1/2(I) v = 5	11212.73	11183.10	-29.6
1/2(II) v = 4	11336.77	11363.50	26.7

Since the available experimental data have been reported for rovibronic levels of e/f parities, the rotational Hamiltonian was also added to the matrix, and eigenvalues were obtained for both e and f parities at J = 2.5 (the lowest total angular momentum quantum number in the $^2\Delta_{5/2}$ ground state). The rotational Hamiltonian is:

$$\hat{\mathbf{H}}_{rot} = B(r)\mathbf{R}^2 = \left(\hbar^2/2\mu r^2\right)\left(\mathbf{J}-\mathbf{L}-\mathbf{S}\right)^2$$

$$H^{rot}_{ikm,jln} = \left\langle \psi_{el,i}\,\psi_{vib,k}\,\psi_{rot,m} \middle| \hat{\mathbf{H}}_{rot} \middle| \psi_{el,j}\,\psi_{vib,l}\,\psi_{rot,n} \right\rangle$$

in which **R**, **L** and **S** are rotational, orbital and spin angular momenta, respectively. The $B(r)$ in rotational Hamiltonian is integrated between vibrational wavefunctions, and the $\mathbf{R}^2$ term gives diagonal and off-diagonal matrix elements between electronic and rotational wavefunctions. The diagonal terms result from the following elements:

$$\left\langle \psi_{el,i}\psi_{rot,m} \middle| (\hat{J}^2 + \hat{L}^2 + \hat{S}^2 - 2\hat{J}_z\hat{L}_z - 2\hat{J}_z\hat{S}_z + 2\hat{L}_z\hat{S}_z) \middle| \psi_{el,j}\psi_{rot,n} \right\rangle$$

and the off-diagonal terms result from:

$$\left\langle \psi_{el,i}\psi_{rot,m} \middle| -(\hat{J}^+\hat{L}^- + \hat{J}^-\hat{L}^+) - (\hat{J}^+\hat{S}^- + \hat{J}^-\hat{S}^+) + (\hat{L}^+\hat{S}^- + \hat{L}^-\hat{S}^+) \middle| \psi_{el,j}\psi_{rot,n} \right\rangle$$

Two separate matrices were generated for the e and f parities, and diagonalized to obtain eigenvalues (rovibronic energies). The ab initio rovibronic energies were compared with the experimental data of Abbasi et al [7], and the disagreements were in the range −40 to +100 cm^{-1} for NiH. A portion of this disagreement is due to the difference in the calculated and experimental excitation energies for the $1^2\Sigma^+$ and $1^2\Pi$ states. When these electronic energy shifts are corrected manually, the agreement with experimental data improves significantly.

IV. CONCLUSION

Potential energy curves for the low-lying electronic states of NiH were calculated at the MRCI level of theory with scalar relativistic and spin-orbit corrections. Potential energy curves for various Ω states were obtained. To calculate more accurate vibronic energies for NiH in the lowest-lying electronic states, diagonal and off-diagonal matrix elements of the spin-orbit Hamiltonian were calculated for the six lowest vibrational levels of the $X^2\Delta$, $1^2\Sigma^+$ and $1^2\Pi$ electronic states. Rotational Hamiltonian was then added to calculate rovibronic energies for the lowest electronic states and to compare with the available experimental data. Eigenvectors of the Hamiltonian matrix indicate significant mixing between vibrational levels of the $\Omega = 3/2$ ($^2\Delta_{3/2}$ and $^2\Pi_{3/2}$) and $\Omega = 1/2$ ($^2\Pi_{1/2}$ and $^2\Sigma^+_{1/2}$) states.

REFERENCES

[1] K. Christmann, G. Ertl, T. Pignet, Surf. Sci., 54, 365, **1976**.
[2] J. Sauer, Chem. Rev., 89, 199, **1989**.
[3] H. Wohl, Solar Phys., 16, 362, **1971**.
[4] F. Neese, WIREs Comput. Mol. Sci., 2, 73, **2012**.
[5] N. B. Balabanov, K. A. Peterson, J. Chem. Phys., 123, 64107, **2005**.
[6] R. J. Le Roy, J. Quant. Spectrosc. Radiat. Transfer, 186, 167, **2017**.
[7] M. Abbasi, A. Shayesteh, P. Crozet, A. J. Roos, J. Mol. Spectrosc., 349, 49, **2018**.

بیست و دومین کنفرانس شیمی فیزیک انجمن شیمی ایران
22nd Iranian Physical Chemistry Conference
۲۹ الی ۳۱ مرداد ۱۳۹۸
گروه شیمی دانشگاه زنجان

QTAIM study of a single molecular wire: Quantum atomic-scale study

Safari Reza*[*],*Hadi Hamid*, Ehsani Ali
Faculty of Science, Department of Chemistry, Physical Chemistry Group, University of Qom, Iran.
Email: safari_physicalchemistry@yahoo.com & r.safari@Qom.ac.ir

Abstract: The current study investigated the external electric field (EF) effects on electronic, at atomic scale, characteristics of a single molecular wire (as isolated, M, and electrode-molecule-electrode, E-M-E, systems) are studied, using density functional theory (DFT) at the theoretical level UB3LYP/6-311G+. To this end, the quantum theory of atom in molecules (QTAIM) is used. In addition, using the Landauer formula, the electrical conductivity of this molecular wire is investigated.

Keywords*:* QTAIM, Quantum methodology, Atomic scale, Molecular wire, Field-effect device.

I. INTRODUCTION

Generally, function of the most molecular electronic devices (such as molecular wires) is based on the molecular or intra-molecular charge/energy transfer mechanism in these molecular devices [1-5]. Therefore, in this work, external electric field effects (EF) on some electronic characteristics, at atomic scale, of a single molecular wire (as isolated, M, and electrode-molecule-electrode, E-M-E, wire systems, shown in Fig.1), are studied, using quantum theory of atoms-in-molecules (QTAIM)[6].

Based on the QTAIM, the atomic/local electronic kinetic (K_{elec}), potential (V_{elec}) and thus total atomic electronic energies (E_{elec}) can be obtained by summing the corresponding quantities of all N_Ω atomic basins (Ω) of the molecule as,

$$K_{elec} = \sum_{\Omega}^{N_\Omega} K_{elec}(\Omega);\ V_{elec} = \sum_{\Omega}^{N_\Omega} V_{elec}(\Omega) \qquad (1)$$

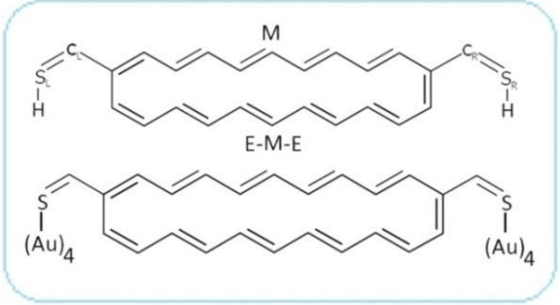

Fig. 1. The molecular wire studied in this work (as isolated, M, and electrode-molecule-electrode, E-M-E, wire systems).

Moreover, the temperature-independence direct-tunneling electric conduction (G) of a single molecule nanoelectronic system can be evaluated using the Landauer formula, as

$$G \equiv \frac{1}{R} = \left(\frac{2e^2\tau_{elec}(\varepsilon)}{h}\right) \qquad (2)$$

where $\frac{h}{2e^2} = 12.91\,\mathrm{k\Omega}$, and $\tau_{elec}(\varepsilon)$ being the electronic transition function [7].

In the most field-effect nanoelectronic molecular systems, the transmission function, $\tau_{elec}(\varepsilon)$, is the charge transport (electron transmission) through the molecular system, induced by the applied external field. This transmission function, which describes the probability of electron transfer from one contact point to another, can be calculated using Green's function (GF) method based on molecular density of states. Generally, in the real molecular nanoelectronic circuits, $\tau_{elec}(\varepsilon)$ and thus molecular electronic conductance dependent on electrode-molecule-electrode coupling constant Γ which is dependent on external bias voltage regime and molecular contact/junction properties (for a symmetric junction, such as $\mathrm{Au-S-(Ph)_n-S-Au}$, we have $\Gamma \approx 0.5\mathrm{eV}$).

In this study, the EF effects on electronic, at atomic scale, characteristics of a single molecular wire system are studied, using density functional theory (DFT) at the theoretical level UB3LYP/LANL2DZ/6-311G+. In this regard, the quantum theory of atom in molecules (QTAIM) is used. Moreover, based on Landaur formula, Eq. (2), the electric conduction, and thus I–V characteristic curve, of the molecular wire (E-M-E) are calculated.

II. RESULTS AND DISCUSSION

Most investigations of molecular-level systems capable of playing functions that mimic those performed by the components of macroscopic electronic devices involve photo-induced/field-induced charge and energy transfer processes in nanoelectronic molecular species. Therefore, atomic-scale electric field effects on electronic structure of molecular wires studied in this work (Fig. 1), are studied, and sample of results plotted in Fig. 2.

In addition, starting from the electronic wave functions obtained, at each EF intensity, the atomic basins are determined using density gradient method. Also, based on the QTAIM, the average value of the some atomic electronic properties (such as atomic electron density and energy) of the molecular wires shown in Fig. 1, are calculated. Sample of these results reported in Table 1.

Moreover, based on Landaur formula, Eq. (2), the I–V characteristic curve of the molecular wire (E-M-E) are calculated, and plotted in Fig.3.This figure shows that the currentincreases non-linearly with increasing the bias voltage.

Table1: The average value (all in a.u.) of the electron density, $\rho(r)$, Laplacian of the electron density, $\nabla^2\rho(r)$, and atomic electronic kinetic energy, $K(\Omega)$, for some atomic basins (Ω), of the molecular wire studied in this work (Fig. 1., E-M-E system), are calculated, using QTAIM.

Ω	$\rho(r)$	$\nabla^2\rho(r)$	$K(\Omega)$
C$_{\text{Right}}$	6.3114	2.4265×10^{-3}	3.7937×10^{2}
C$_{\text{Left}}$	6.2478	3.1488×10^{-3}	3.7935×10^{2}
S$_{\text{Right}}$	16.076	2.6723×10^{-3}	3.9750×10^{2}
S$_{\text{Left}}$	15.862	2.6274×10^{-3}	3.9749×10^{2}

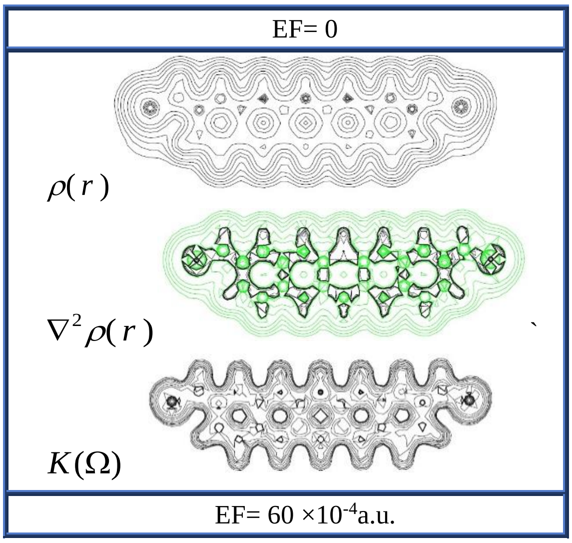

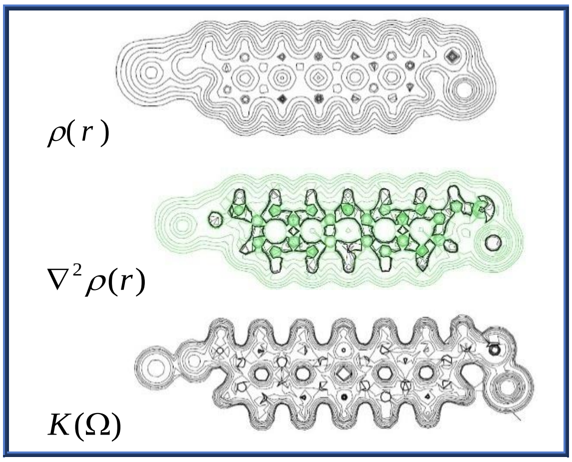

Fig. 2. The contour maps of the electron density, $\rho(r)$, Laplacian of the electron density,$\nabla^2\rho(r)$, and electronic kinetic energy $K(\Omega)$ of the molecular wire shown in Fig. 1. (E-M-E), in the absence (up) and presence (down) of the EF with 60 $\times 10^{-4}$a.u. intensity.

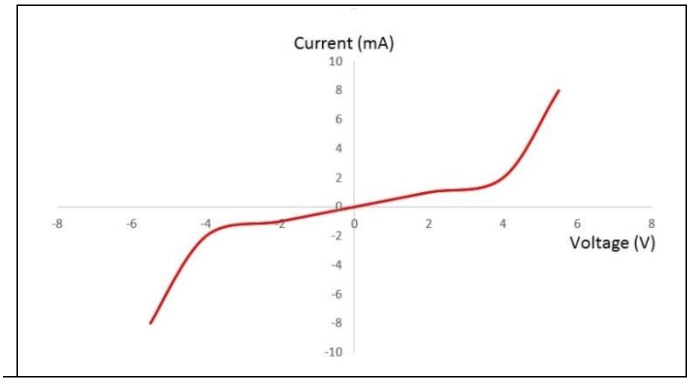

Fig. 3. The I–V characteristic curve, at various electric field intensities, ofthe molecular wire studied in this work (E-M-E system, Fig. 1.).

III. CONCLUSION

In this work, based on the QTAIM, atomic electronic properties and intra-molecular charge and thus local charge and energy transfer in the candidate field-effect molecular wire are studied. In this regard, starting from the electronic wave functions, obtained at each EF intensity, the atomic basins are determined using density gradient method, and their electronic energies and their changes are calculated. This study show that even similar atoms (such as end Sulfur atoms, S_{Left} and S_{Right}) response differently to the external EF.

In addition, the calculated I-V characteristic curve for the proposed molecular wire shows that this molecule can be used as an acceptable molecular wire. Also, these results show that I-V characteristic curve of this wire depends almost non-linearly on the EF strength.

REFERENCES

[1] S. E. Lyshevski, *Nano and Molecular Electronics Handbook*, CRC Press, Boca Raton, **2007**.
[2] M. A. Reed and T. Lee, *Molecular Nanoelectronics*, American Scientific, USA, **2003**.
[3] J. M. Tour, Acc. Chem. Res., vol. 33, pp. 791-804, **2000**.
[4] R. Safari, H. Sabzyan, J. Iran. Chem. Soc.vol. 11, pp. 1513-1532, **2014**.
[5] H. Sabzyan, R. Safari, Europhys. Lett. vol. 99, pp. 67005 -67009, **2012**.
[6] P. Popelier, *Atoms in Molecules*, Prentice Hall, London, **2000**.
[7] A. Salomon, D. Cahen, S. Lindsay, J. Tomfohr, V. B. Engelkes, C. D. Frisbie, Advan. Mater., vol. 15, pp.1881-1890, **2003**.

What is quantum clock?

J.Tariverdi*. F.Ghasemi .A.shafiee
Department of Sharif University of Technology, Tehran, IRAN
Email:shafiee@sharif.edu

Abstract: Various investigations have been done to study the time transitions at the molecular level, to see that if time passes at microscopic level is equal to time passes in macroscopic level. Scientists have done a variety of activities for these kinds of questions, one of which is the design of quantum clocks, which examines time passage in quantum mechanics. In this paper, at first, the mathematical relations and the formalism of quantum clocks are introduced describe. In addition, we two types of quantum clocks. The first one is Peres quantum clock, and the second is quantum clock of Faraday.

Keywords: Quantum mechanics, Quantum clocks, Time passages, Peres quantum clock, Faraday quantum clock.

I. INTRODUCTION

In quantum mechanics, there are variables for which we consider the operators, such as energy and position. In some cases, we need to look at changes over time, such as decaying a particular radioactive element. In these cases, we need to introduce a time operator within the framework of the theory in order to relate empirical results to the formalism.

We must consider the fact that the measured time is not errorless. In addition to the inherent quantum error to measure time, if time measurement comes with some errors, for any classic or quantum reason, a strange effect on the evolution of the quantum system will be appeared that should be studied. Studies in this field have led to the introduction of the concept of "quantum clocks".

According to Perez “A clock is a dynamical system which passes through a succession of states at constant time intervals”, the construction of such a device, using quantum systems with various interactions, allows the clock to start or stop and enables to use it as a chronometer to measure the time of a process. The first ideas on this subject were presented by Slacker and Wagner in 1985, which utilizes a clock for analyzing the nature of quantum limitations of microscopic systems to measure space-time events. In [1,2,3] he proposed to use the Lamour rotation in the presence of a weak magnetic field, as a clock to measure the time of occurrence of quantum events, Rubikator implemented this method. In next section, the mathematical relations and the formalism of the quantum clocks is introduced, which is essential to study of the quantum clocks. In addition, we introduce two types of quantum clocks which the first one is Peres quantum clock, and the second is quantum clock of Faraday.

II. METHODS

1-Mathematical Description of a Quantum Clock

As is well known, in the Quantum Mechanics time is a parameter, not a dynamical variable. However, it is possible to find dynamical variables which depend linearly on t, so we can determine the value of t by looking at them. For example, the position of the hand of a clock is not a time parameter but depends on it in a very simple manner: the angle θ swept out by the hand of the clock is a simple function of t, i.e., θ = ωt (mod 2π) [4,5].

The canonical conjugate variable to this angle is the so-called “operator” $\hat{J}$, which always has dimension of angular momentum.

$$\left[\hat{\Theta},\hat{J}\right]=i\hbar \tag{1.1}$$

The eigenvalue equation of the angle operator $\hat{\Theta}$ and eigenvalue equation for $\hat{J}$ the angular momentum operator J is

$$\hat{\Theta}\left|\theta\right\rangle=\theta\left|\theta\right\rangle$$

$$\hat{J}\left|m\right\rangle=m\hbar\left|m\right\rangle$$

where the eigenstates $\{|\theta\rangle\}$ form a continuous orthonormal basis satisfying also for $\{|m\rangle\}$ with m = 0, ±1, ±2. with $\langle m|m'\rangle=\delta_{m',m}$. We define

$$u_m(\theta)=\left\langle\theta\middle|m\right\rangle=(2\pi)^{-1/2}e^{im\theta} \tag{1.2}$$

Using the closure relation in $|m\rangle$ we

$$\left|\theta\right\rangle=(2\pi)^{-1/2}\sum_{m=-\infty}^{\infty}e^{im\theta}\left|m\right\rangle \tag{1.3}$$

The dynamics of the clock is determined by the Hamiltonian $\hat{H}_C=\omega\hat{J}$, where ω is a constant frequency. Clearly, we have

$$\hat{H}_c u_m(\theta) = i\hbar\omega\frac{\partial}{\partial\theta}u_m(\theta) = m\hbar\omega u_m(\theta) \qquad (1.4)$$

$\hat{H}_C$ is the generator of translations in time defined by the unitary operator $\hat{U}(t) = e^{-i\hat{H}_C t/\hbar}$. Now we have

$$\hat{U}(t)|\theta\rangle = e^{-i\hat{H}_c t/\hbar}|\theta\rangle$$
$$= (2\pi)^{-1/2}\sum_{m=-\infty}^{\infty} e^{-im\theta - im\omega t}|m\rangle$$
$$= |\theta + \omega t\rangle$$
(1.4)

As is obvious see, θ has moved as far as the ωt, so that we could show the change of time to a change in the angle that is directly related to the time.

In wave function, we have

$$\langle\theta|\hat{U}(t)|\psi\rangle = \psi(\theta,t) = \psi(\theta - \omega t, 0) \qquad (1.5)$$

2-The Quantum Clock of Peres

Peres [3,4] paid attention to this subject with a more realistic view He restricted the sum in (1.3) to values of m satisfying -j ≤ m ≤ j, where j is a positive integer. Now considere the set of orthonormal states

$$|k\rangle = N^{1/2}\sum_{m=-j}^{j} e^{-i2\pi km/N}|m\rangle \qquad (2.1)$$

where k = 0, 1, ..., N - 1 and N = 2j + 1 is the total number of states of our clock. Then, the wave function is obtained as

$$u_k(\theta) = \langle\theta|k\rangle = N^{1/2}\sum_{m=-j}^{j} e^{-i2\pi km/N}u_m(\theta) \qquad (2.2)$$

The time evolution of these states satisfies

$$\hat{U}(t = \tau = 2\pi/N\omega)u_k(\theta) = u_{k+1(\mathrm{mod}\,N)}(\theta)$$
(2.3)

or, in a slightly different notation, $u_k(\theta,\tau) = u_{k+1(modN)}(\theta,0)$. These are eigenfunctions of the clock time operator

$$\hat{T}_c \equiv \tau\sum_{k'=0}^{N-1} k'\hat{P}_{k'} \qquad (2.4)$$

with eigenvalues kτ. The projection operators P_k satisfy $\hat{P}_{k'}u_k(\theta) = \delta_{k',k}u_k(\theta)$. At time $\tau = {}^{2\pi}/_{N\omega}$ and according to the time accuracy, we can find the point *k*th of the clock with uncertainty ${}^{2\pi}/_{N\omega}$. For large values of j energy is given with energy uncertainty $\Delta\hat{H}_C = (2\pi/\sqrt{3}\tau)$.

Peres compares this quantity with the maximum value of the energy, $\pi\hbar/\tau$, and infers that this clock is basically a nonclassical object. As is expected, the uncertainty product relation remains true. $\tau\Delta\hat{H}_C \ge \hbar/2$.

3-Faraday Clock

Several people have exploited the analogies between tunneling electrons and evanescent electromagnetic waves to construct an optical clock [1,2,8]. The first proposal was presented by Gasparian et al. [1]. They used Faraday polarization rotation to measure the traversal and reflection times of an evanescent electromagnetic wave in a slab and in a magnetorefractive layered structure.

In physics, the Faraday effect or Faraday rotation is a magneto-optical phenomenon, that is an interaction between light and a magnetic field in a medium. The Faraday effect causes a rotation of the plane of polarization which is linearly proportional to the component of the magnetic field in the direction of propagation (of length L, Faraday constant g and refractive index n_0). The electric field E in this incident wave is orientated along the z-axis and a weak magnetic field B is applied along the x-direction across the slab. Gasparian et al. [8] quantified both effects through the complex angle θ given by

$$\theta = \theta_1 - i\theta_2 \qquad (3.1)$$

where the real part of the angle is

$$\theta_1 = \frac{\psi_+ - \psi_-}{2} \qquad (3.2)$$

which corresponds to Faraday rotation. Here the + and - signs correspond to the outgoing right and left polarized light, respectively. The imaginary part is defined as

$$\theta_2 = \frac{1}{4}\ln\frac{T_+}{T_-} \qquad (3.4)$$

which corresponds to the ellipticity ratio. Then, following Buttiker's analysis for electrons, Gasparian et al. [1] defined the characteristic time

$$\tau = \tau_1 - i\tau_2 \qquad (3.5)$$

where

$$\tau_1 = \frac{\theta_1}{\Omega} = \frac{n_0}{\omega}\frac{\delta\psi}{\delta n_0} \qquad (3.6)$$

and

$$\tau_2 = \frac{\theta_2}{\Omega} = \frac{n_0}{2\omega}\frac{\delta\ln T}{\delta n_0} \qquad (3.7)$$

These results and those obtained for a quantum particle are very similar: the real component of this time, τ_1 , is analogous to the time associated with the Larmor precession in the electronic case. Also, the imaginary part, τ_2, is analogous to the rotation time associated with Zeeman splitting in the electronic case.

III. CONCLUSION

In this short article, we have introduced the notion of Quantum Clocks using the quantum formalism. Similar to classical designs, some proper parameters are defined here, satisfying quantum commutation relations, to show how an angle θ corresponding to a hypothetical arm of clock is changed, as time passes. Accordingly, two kinds of time passages have been discussed, regarding different definitions of θ. Such investigations help us to grasp more clearly the similarities and differences of time passage in Classical physics and Quantum theory.

REFERENCES

[1] Y. Japha, G. Kurizki, Phys. Rev. A 60, 1811 (1999)
[2] M. Deutsch, J.E. Golub, Phys. Rev. A 53, 434 (1996)
[3] J.Y. Lee, H.W. Lee, J.W. Hahn, J. Opt. Soc. Am. B, 17, 401 (2000)
[4] P. Carruthers, M.M. Nieto, Rev. Mod. Phys. 40, 441 (1968).
[5] P. Busch, M. Grabowski, P.J. Lahti: Phys. Lett. A, 191, 357 (1994)
[6] A. Peres, Am. J. Phys. 48, 552 (1980)
[7] A. Peres, Quantum Theory: Concepts and Methods, Kluwer, Dordrecht, (1993)
[8] V. Gasparian, M. Ortuno, J. Ruiz, E. Cuevas, Phys. Rev. Lett. 75, 2312, (1995)
[9] J.G. Muga, R. Sala Mayato and I.L. Egusquiza (Eds.), Lect. Notes Phys. 734, (2008)

Pterostilbene: a Theoretical Elucidation on Its Antioxidant Activity

L. H. Saremi[a], **A. Ebrahimi**[a*]
a: Department of Chemistry, Computational Quantum Chemistry Laboratory, University of Sistan and Baluchestan, Zahedan, Iran
Email: heidarpoorleily@yahoo.com
a: Department of Chemistry, Computational Quantum Chemistry Laboratory, University of Sistan and Baluchestan, Zahedan, Iran*
Email: ebrahimi@chem.usb.ac.ir

Abstract*:* Pterostilbene is a natural dietary Resveratrol (RES) analog, having less hydroxyl groups than RES, has a more favorable pharmacokinetic profile than RES.
Bond dissociation enthalpies (BDEs) for the Pterostilbene and its derived compounds have been calculated using density functional theory (DFT) methods. It was found that the favorable antioxidant mechanism of Pterostilbene was an H-atom abstraction from the phenolic group in the 4´ position i.e. the natural species, not from the 3 and 5 position as related derivatives of this compound.

Keywords: Antioxidant activity, Bond dissociation enthalpy (BDE), Density functional theory (DFT), Pterostilbene, Resveratrol.

I. INTRODUCTION

Pterostilbene (trans-3,5-dimethoxy-4´-hydroxystilbene, PTS) is an natural dietary Resveratrol (RES) analog of blueberries, having less hydroxyl groups than RES, has a more favorable pharmacokinetic profile than RES (much slower clearance, longer mean transition time and a more abundant plasma exposure) consequently, increasing its bioavailability [1,2]. The therapeutic characteristics of PTS in human disease have been attributed to its antioxidant, anti-inflammatory, and anticarcinogenic properties [3].

The structure–activity relationship has been used to study the determination of antioxidant activity for natural compounds using quantum chemistry calculations by the density functional theory (DFT) method. A hydrogen atom transfer defined in Eq. 1 is pathway to evaluate the profiles of antioxidant activities of polyphenolic compounds [4].

$$\mathrm{ArOH} + \mathrm{R}^{\bullet} \rightarrow \mathrm{ArO}^{\bullet} + \mathrm{RH} \qquad (1)$$

In the present study we aim to explore the PTS structure and its derivatives for the antioxidant identification. In Fig. 1, the new compounds included PTS derivatives constructed by molecular simplification (PTS-3 and PTS-5) and by hydroxyl replacement on occupied position by methoxy group in primary structure of PTS. We are interested in investigating the role of OH position on the corresponding antioxidant properties of studied compounds.

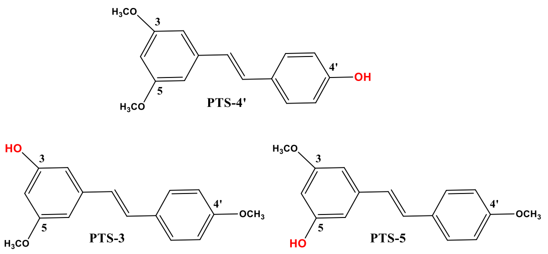

Fig.1: The natural chemical structure of Pterostilbene (PTS-4´) and its derivatives PTS-3: OH in 3, and PTS-5: OH in 5 position, respectively.

II. METHODS

The geometries of structures investigated in this study, were fully optimized using the Gaussian 09-D1 software package [5] at the DFT-B3LYP/6-311++G** level of theory in gas phase. Frequency analysis have been performed here at the same level as optimizations to confirm that the structures optimized correspond to energetic minima. The bond dissociation energies were calculated as the energy differences between a neutral molecule and the respective radical species (semi-quinone) plus hydrogen radical (equivalent to Eq. 1).

III. RESULTS AND DISCUSSION

To compare the derivative analogs with natural PTS i.e. PTS-4′, we also calculated the O-H BDE of the OH group for two its constructed molecules (PTS-3 and PTS-5) which this group is exist in 3 and 5 position labeled in Fig. 1, respectively. The relative energies of all radical species are presented in Table 1. As observed, the OH-4´ radical of Pterostilbene is the most stable, probably due to resonance effects around the radical center with semiquinone free radical production.

Table 1. Pterostilbene (PTS) and its constructed analogs radical relative energies (kcal/mol)

Compounds	**OH-3**	**OH-5**	**OH-4′**
PTS-3	4.42	-	-
PTS-5	-	7.12	-
PTS-4′	-	-	0.00

The results indicate that the H-atom abstraction from the O-H bond is not very difficult, because the O-H BDE (76.79 kcal/mol) is in the middle range of energy. The O-H BDE of the phenolic group for PTS-3 and PTS-5 are 4.59 and 7.1 kcal/mol higher than that of PTS-4′, respectively (see Table.2).

Table 2. Bond Dissociation Energies (BDE) of Pterostilbene (PTS) and its constructed analogs radical in the Gas Phase in kcal/mol.

Compounds	**OH-3**	**OH-5**	**OH-4′**
PTS-3	81.38	-	-
PTS-5	-	83.89	-
PTS-4′	-	-	76.79

IV. CONCLUSION

Our results manifest that 4′-hydroxyl-Pterostilbene is a potential antioxidant than its derivatives because its corresponded free radicals have more stabilization energy and less BDE-OH value than the Pterostilbene hydroxylated derivatives in 3 and 5 positions.

REFERENCES

[1] D. McCormack, and D. McFadden, Oxid Med Cell Longev, vol. 2013, pp. 1-15, **2013**.
[2] Perečko T, Drábiková K, Račková L, Číž M, Podborská M, Lojek A, et al, Neuro Endocrinol Lett, vol. 31, pp. 84, **2010**.
[3] A. M. Rimando, M. Cuendet, C. Desmarchelier, R. G. Mehta, J. M. Pezzuto, and S. O. Duke, Journal of Agricultural and Food Chemistry, vol. 50, pp. 3453–3457, **2002**.
[4] M. Leopoldini, T. Marino, N. Russo, and M. Toscano, J. Phys. Chem. A, vol. 108, pp. 4916-22, **2004**.
[5] M.J. Frisch, G.W. Trucks, H.B. Schlegel, et al. Gaussian 09 Revision D. 01. Wallingford (CT). See the Supporting Information for full reference Google Scholar. **2013**.

Electron-holes Asymmetry behavior of single wall carbon nanotube (5, 0) as semiconductor exposed to external electric field

S.Amini[a], S. Amini[a], M. Azami[b]*

Affiliation Department of chemistry, yasuj University, yasuj, *74934-75918*, Iran,

Email: azami.smz@gmail.com

Abstract*:* The term "ADOcon/depl" known as asymmetry deformation orbitals concentration/depletion is a concept used for examination of transient symmetry behavior of carriers in the Single Wall Carbon Nanotubes exposed to electric field. We found Increasing lengths and electric fields yield to promotion of electron –hole asymmetry in SWCNTs (5, 0) exposed to longitudinal electric field.

Keywords*:* ADOcon/depl, SWCNTS, electron-hole asymmetry, external-exposed electric field

I. INTRODUCTION

Nanotechnology has been brought a tremendous evolution together with experimental and theoretical researches, in which molecular electronic as a subfield of nanotechnology attracted much attention in last decade[1]. Among various π-conjugated structures, graphene and Carbon Nanotubes (CNTs) have excellent promise for fabrication of organic components in molecular electronics because of inherent fabricating of macromolecular blueprint and its interfacing with metal electrodes[2]. In this way, Because of switching off effect, as an important role in electronic circuits, many theoretical researches have been assigned to investigate mechanical, structural, optical and electrical properties of CNTs since1991, as Subset of molecular electronics [3-5].

Single Wall Carbon Nanotubes (SWCNTs) as one of types of CNTs possess electronic properties that are distinguished by chirality, diameter and length. Because of having a nano-ranged diameter, they have quantum effects[6, 7].

Depending on their chirality, Single-wall Carbon Nanotubes (n,m), are metallic (n=m), semi-metallic(n-m is a multiple of 3, n≠ m and nm ≠0), and semiconductors (otherwise)[4, 8, 9]. As solids with different range conductivity, they adhere to the rules governing solid state physics [4, 10, 11].

Combining the ideas of CNTs as effective molecular electronics conductor, also inspiration from Manado et al. (analyzing the electric response of molecular conducting), we have analyzed the asymmetric electronic response of different rings of zigzag SWCNT semiconductor (5.0) exposed to External electric field.

II. METHODS

In this work, we have selected Zigzag carbon nanotubes (5, 0), as molecular semiconductor, with different lengths ranged from one to eight rings. The internal coordinates of CNTs tubes were centralized by several Dummy atoms to impose perfect cylindrical symmetry, and partially optimized at B3LYPP/6-31G (d, p) theoretical level. To saturate the CNTs, dangling hydrogens are used to terminate the two ends of CNTs

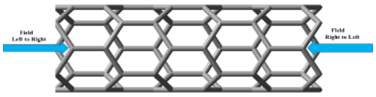

Fig.1. illustration of SWCNTs exposed to the electric field

Adding Electron Density Orbitals (EDOs) from the Right app lied electric Field (L) to EDOs of opposite direction(r), subtracting from density charge of unexposed field structure, F0, have been yield to ADOcons in SWCNTs(5, 0) by Densitizer program.

III. RESULTS AND DISCUSSION

In the exposed field, energies of tubes are functions against fields as downward curves with different gradients. Energies of each tube has been promoted by increasing the lengths of tubes and approximately, at 2[-2] a.u. field energies reduced with increasing of field. The results indicate extremely decreasing of the energy by increasing of the field. Images in Fig.2 have generally illustrated qualify asymmetry behavior of semiconductor SWCNT (5, 0). Although in the first -three images apparently no traces has been emerged, we have observed increasing of the intensity of concentration-depletions asymmetry through the rings with gaining the field concentrations and depletions are appeared from
5 [-3] a.u, as an asymmetry behavior of CNTs. At 1[-2] a.u. electron-holes (blue-yellow colors) are visible all over the tube. From this point onwards, the field increase by order of hundred and intensity of the paints increase and expand through the ring. In other words, concentrations and

depletions possess more appearance and as mentioned before, this are illustrating asymmetry in the SWCNT. It seems that the fields ^[-2] to 1[-1] a.u. have the exactly same intensity in concentrations/depletions ADOs so that it comes to mind that it could be result in same asymmetry behavior and information in SWCNT, but this is not true, detailed and described in our work.

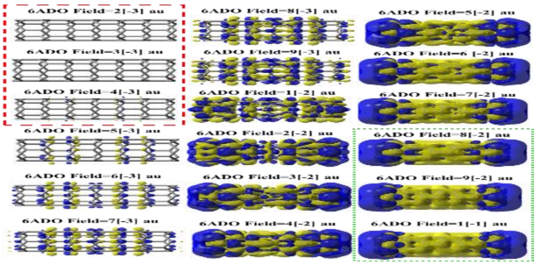

Fig.2: Representation of six- fold SWCNT (5, 0)'s electron-holes -transient asymmetry behavior semiconductor exposed to external electric field ordered from 1[-3] to 1[-1] a.u. invisible electric field effect at 1[-3] a.u. is abandoned in this picture. Red and green-dashed boxes are ambiguous shapes in the picture which is result from lack of resolution of isovalue density (.02)

Fig.3 has expressed single point electronic energies of SWCNTs by external exposed electric field ranged from order of 1[-3] to 1[-1] a.u. We have scaled energies with respect to number of electrons of Carbons of each tubes as energies /number of electrons of carbons of CNTs.

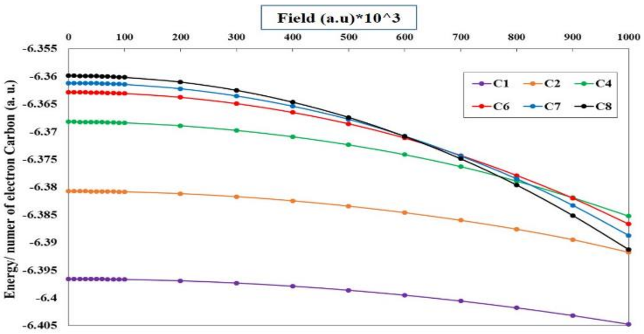

Fig.3 representation of Energies of tubes exposed to electric field, purple (C1). orange(C2), green(C4), red(C6), blue(C7), and black color lines are energies of singe, two, four, six, seven, and eight rings vs electric field.

IV. CONCLUSION

The electron-hole asymmetry performance of SWCNT (5, 0) as semiconductor with cylindrical symmetry with the smallest nanoscale diameter among single wall carbon nanotubes (n, 0) has been surveyed using "asymmetry deformation orbitals" (ADOcon)'s response, exposed to external electric field. Subtracting of the sums of the charges density of exposed electric field from left to right and right to left from the charge densities (electron and holes) of the tubes without the action of the electric field has been yields to values known as asymmetry deformation orbitals which are used for determination/ characterization of symmetry –transient behavior of electric carriers (electrons and holes) of our systems. Electric fields ordered 1[-3] to 1[-1] a.u. for typical lengths 1, 2 4, 6, 7, 8 rings of SWCNT (5.0) were examined. The results of this manuscript disclosed the following findings. Electronic energies of electric field- exposed SWCNT (5, 0) possess curvature with different maximums for each ring and has the maximum for eight ring. Dipole moments have linear relations with respect to increasing of field and lengths of SWCNT (5, 0). The most purpose of this work is to examine electron-holes asymmetry behavior of SWCNT (5, 0) exposed by external electric field that is done by expression ADOcons/depl. Generally, SWCNT (5, 0) possess asymmetry behavior in the electric field. Different rings of SWCNT have similar asymmetry behavior by exposed external field. By increasing lengths, and fields, ADOcon increases and yield to increase of asymmetry in our SWCNT. Eight ring SWCNT (5, 0) possess the maximum of asymmetry in variety of electric field and 7, 6… are in the next ranks. In spite of linear increasing of induced dipole moment by electric field, the electric field effect -induced asymmetry behavior of SWCNT (5, 0) was very different.

REFERENCES

[1. Tao, N., *Electron transport in molecular junctions*, in *Nanoscience And Technology: A Collection of Reviews from Nature Journals*. 2010, World Scientific. p. 185-193.

2. Javey, A., et al., *Ballistic carbon nanotube field-effect transistors.* 2003. **424**(6949): p. 654.

3. Marquina, J., et al., *Ab Initio Study of the Electronic and Vibrational Properties of 1-nm-Diameter Single-Walled Nanotubes.* 2013. **3**(02): p. 178.

4. Tetik, E., et al., *The Electronic Properties of the Graphene and Carbon Nanotubes: Ab Initio Density Functional Theory Investigation.* 2012. **2012**.

5. Vasylenko, A., et al., *Encapsulated nanowires: Boosting electronic transport in carbon nanotubes.* 2017. **95**(12): p. 121408.

6. McEuen, P.L., M.S. Fuhrer, and H.J.I.t.o.n. Park, *Single-walled carbon nanotube electronics.* 2002. **99**(1): p. 78-85.

7. Mandado, M. and N.J.J.o.c.c. Ramos-Berdullas, *Analyzing the electric response of molecular*

conductors using “electron deformation” orbitals and occupied-virtual electron transfer. 2014. **35**(17): p. 1261-1269.

8. Li, T.-S. and M.-F.J.P.R.B. Lin, *Electronic properties of carbon nanotubes under external fields.* 2006. **73**(7): p. 075432.
9. Janas, D.J.M.C.F., *Towards monochiral carbon nanotubes: a review of progress in the sorting of single-walled carbon nanotubes.* 2018. **2**(1): p. 36-63.
10. Sharma, H. and Z. Xiao. *Single-walled carbon nanotube-based field-effect transistors (non-reviewed)*. in *IEEE SoutheastCon 2008*. 2008. IEEE.
11. Pinzon, J.R., A. Villalta-Cerdas, and L. Echegoyen, *Fullerenes, carbon nanotubes, and graphene for molecular electronics*, in *Unimolecular and Supramolecular Electronics I*. 2011, Springer. p. 127-174.

The Role of Internuclear Distances in the Minima Structure of HHG of H_2^+

***G. Gharajeh Marand*, N. Hadipour, S. Taghipour, M. Vafaee**[*]*
Department of Chemistry, Tarbiat Modares University, Tehran 14115-175, Iran
Email:m.vafaee@modares.ac.ir

Abstract: We numerically solve the full-dimensional electronic time-dependent Schrödinger equation for H_2^+ under different $\sin^2$-shaped laser pulses at 1400 nm wavelength, with 6×10^{13} Wcm^{-2} intensity at 3.5, 4.73, 5.5 a.u internuclear distances applying Born-Oppenheimer approximation. Some structures such as minima and oscillatory patterns appearing in the high-order harmonic generation (HHG) spectra are investigated.

Keywords: High-order harmonic generation, Minimum, Time-dependent Schrödinger equation.

I. INTRODUCTION

The interaction between intense laser pulses and atoms or molecules has received considerable attention recently. Observation of the electron dynamics requires ultrashort lasers around the attosecond time scale (~10^{-18} s). True understanding of the phenomena in attosecond and strong-field physics often needs the quantum evolution of an involved atomic system driven by a strong laser pulse [1]. High-order harmonic generation (HHG) caused by the interactions of the intense pulses with the atoms and the molecules attracts lots of attentions in ultrafast optics and strong-field physics. Generally, the harmonic emission process from atoms and molecules can be described by the ‘ionization-acceleration-recombination’ model [2]. That is to say, the electrons tunnel through the barrier and then accelerate in the laser field; finally, when the laser field reverses its direction, the electron may return and recombine with the parent ion, and emit a harmonic photon simultaneously [3]. Signatures of interference in terms of minima in high-order harmonic generation (HHG) spectra from small linear molecules have raised a lot of interest both theoretically and experimentally since structural and dynamical information may be retrieved from the position of these minima. The position of the minimum is dependent on the internuclear distance and orientation angle of the molecule [4].

II. METHODS

Time-depended Schrödinger equation (TDSE) for a fixed-nuclei model of H_2^+ exposed to an external linearly polarized electric field can be expressed (in atomic units; $e = \hbar = m_e = 1$) as [5,6]

$$i\frac{\partial\psi(Z,\rho;t,R)}{\partial t} = H(z,\rho;\ t\,,R)\,\psi$$

(1)

with electron cylindrical coordinate (z,ρ) which are measured with respect to the center of mass of the two nuclei (after a separation of the center-of-mass motion and ignoring molecular vibration and rotation) and R is the internuclear distance of the molecular ion. H is the total electronic Hamiltonian for H_2^+

$$\begin{aligned} &H(z,\rho;\ t\,,R) \\ &= -\frac{2m_n+m_e}{4m_n m_e}\left[\frac{\partial^2}{\partial\rho^2}+\frac{1}{\rho}\frac{\partial}{\partial\rho}+\frac{\partial^2}{\partial z^2}\right] \\ &+ V(z,\rho;\ t\,,R), \qquad (2) \end{aligned}$$

$m_e = 1$ and m_n are the masses of electron and a single nuclei, respectively, with

$$\begin{aligned} V(z,\rho;\ t\,,R) = &-\frac{1}{\sqrt{\left(z+\frac{R}{2}\right)^2+\rho^2}}-\frac{1}{\sqrt{\left(z-\frac{R}{2}\right)^2+\rho^2}} \\ &+\frac{1}{R}+\left(\frac{2m_n+2m_e}{2m_n+m_e}\right)zE_0f(t)\cos(\omega t \\ &+\ \varphi)\,. \qquad (3) \end{aligned}$$

The high-order harmonic generation spectrum is formed by the signal from a single molecule

$$\begin{aligned} S_{tot}(\omega) &= \left|\int <\ddot{d}\,(t)> e^{i\omega t}dt\right|^2 \\ &= \left|\int\{<\psi_{tot}(r,t)|\nabla V(r)|\psi_{tot}(r,t)\right. \qquad (4) \\ &\qquad \left. > +F(t)e^{i\omega t}dt\right|^2 \end{aligned}$$

In the exact phrase for ground and excited states, $\Psi_{tot}(r,t)$ can be written as follows

$$\begin{aligned} \psi_{tot}(r,t) = k_g(t)\psi_g(r) + k_u(t)\psi_u(r) \qquad (5) \\ + \psi_{res}(r,t) \end{aligned}$$

where $\psi_g(r)$ and $\psi_u(r)$ show the orbitals of the σ_g ground state and the σ_u first excited state, respectively. The wave packet $\psi_{res}(r,t)$ represents the residual part of $\psi_{tot}(r,t)$, containing other excited states and continuum state and with the above conditions, the equations are as follows

$$\begin{aligned} &S_{tot}(\omega) \simeq S_g(\omega) + S_u(\omega) + 2\left[A_g^*(\omega)A_u(\omega)\right] \qquad (6) \\ &with\ \ S_g(\omega) = \left|A_g(\omega)\right|^2, S_u(\omega) = |A_u(\omega)|^2 \end{aligned}$$

The equation above shows that the HHG function consists of the share of the ground state (σ_g) recombination and the contribution of the recombination of the first excited state (σ_u). The last point in the equation $(2[A_g^*(\omega)A_u(\omega)]$) is the interference between the two components. In the following, the two-centers interference and the orbital interference model in the different HHG spectra are investigated [7].

III. RESULTS AND DISCUSSION

The high-order harmonic spectra for the H_2^+ system, under 20 cycles $\sin^2$-shaped laser pulses at 1400 nm wavelength and 6×10^{13} Wcm^{-2} intensity for internuclear distances 3.5, 4.73, 5.5 a.u. has an interesting and special structure (shown in Fig. 1). The right panel of Fig. 1 corresponds to smoothed spectra of HHG (related to left panel) [8]. Fig. 1(d) shows the smoothed spectrum of HHG for the internuclear distance 3.5 a.u.. At the minima specified in the spectrum, it is clearly seen that $S_u(\omega)$ has not played a role and the reason is that, in relatively short internuclear distances, the low population of electrons exist in the first excited state. Minima in orders 21, 43 and 57 are depicted in fig .1(e) (smoothed spectrum at R=4.7 a.u.). According to Han's report in Ref. [7], the inconsistency of the $S_{tot}(\omega)$ and $S_g(\omega) + S_u(\omega)$ in the minimal region in Fig. 1(e) can be related to $2[A_g^*(\omega)A_u(\omega)]$ term in Eq. (6). As a result, the minimum of the orders of 21 and 43 are due to orbital interference [7].

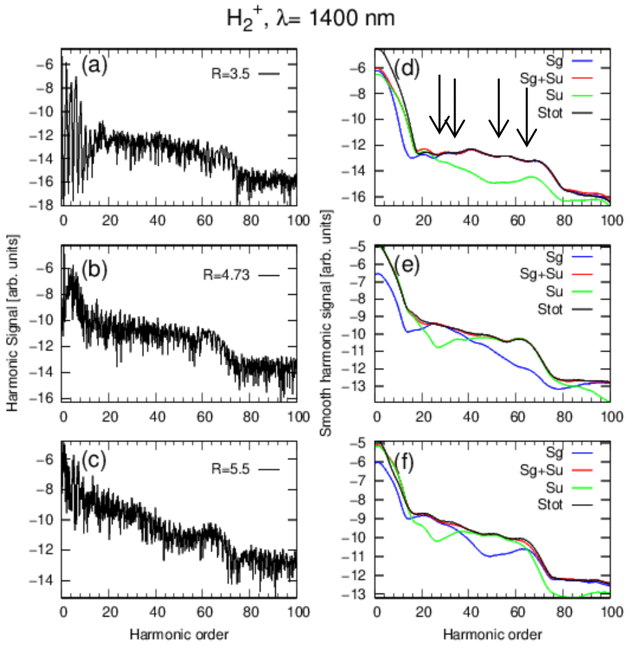

FIG. 1. (left panel) the HHG spectrum of H_2^+. (right panel) the smoothed spectrum of HHg of H_2^+ for internuclear distances 3.5 a.u. (d), 4.7 a.u. (e) and 5.5 a.u. (f). The peak intensity of the 20 cycle laser pulse is 6×10^{13} Wcm^{-2}, and the wavelength is 1400nm.

By increasing the harmonic orders in Fig. 1(e), the role of $S_u(\omega)$ enhances gradually in contrast with $S_g(\omega)$. Minima in orders 29, 47 and 57 are depicted in fig .1(f) (smoothed spectrum at R=5.5 a.u.). It can be observed in these minima, $S_u(\omega)$ has a main role and this can be justified in considerable internuclear distances. A slight difference between $S_g(\omega) + S_u(\omega)$ and $S_{tot}(\omega)$ in these minima due to the small contribution toward the higher excited states and one can ignore the orbital interference term in Eq. (6). The minima we examined in 57th order (Fig. 1(e)) and 47th, 57th orders (Fig. 1(f)) are not due to the two-centers interference, or orbital interference. These minima originated from $S_g(\omega)$ or $S_u(\omega)$ and this can be attributed to non-adiabatic electron behavior.

Fig. 2 shows the time-dependent electron population in electron states (σ_g and σ_u) for a H_2^+ molecule under 20 cycle laser radiation of 1400 nm wavelengths and 6×10^{13} Wcm^{-2} intensity at internuclear distances of 3.5, 4.7 and 5.5 a.u.. Fig 2(a). The population correspond to R=3.5 a.u. This figure shows that most of the electron population is in the ground state. The reason is that in relatively short internuclear distances, the electron states are away from each other, which causes most of the electrons to remain in the ground state. In Fig. 2(b) and 2(c), it is obvious that with increasing internuclear distances from 3.5 to 4.7 and 5.5 a.u., the electron population in the first excited state grows. The electron exchange has raised with increasing internuclear distance in Fig. 2(c). It can be observed, the oscillating behavior between the population of σ_g and σ_u, so, the minima are observed in $S_g(\omega)$ and $S_u(\omega)$ are due to these oscillation in $S_g(\omega)$ and $S_u(\omega)$.

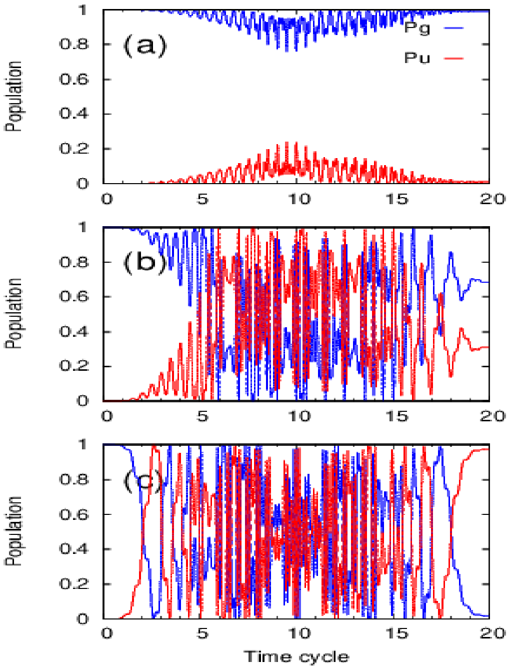

FIG. 2. Electron populations in the σ_g and σ_u for R=3.5 a.u.(a), R=4.7 a.u.(b) and R=5.5 a.u.(c).

IV. CONCLUSION

In this work, we solved numerically the full-dimensional electronic time-dependent Schrödinger equation for H_2^+ with Born-Oppenheimer approximation under different $\sin^2$-shaped laser with 6×10^{13} Wcm^{-2} intensity at 3.5, 4.73, 5.5 a.u internuclear distances and obtained HHG spectra. The minima and oscillatory patterns appeared in the HHG spectra were investigated in this report. We have shown that the oscillatory patterns of the HHG spectra are originated from the oscillatory patterns of the $S_g(\omega)$ and $S_u(\omega)$spectra.

REFERENCES

[1] F. Krausz, M. Ivanov, Attosecond physics, Reviews of Modern Physics, 81 (2009) 163.

[2] P. Corkum, Plasma perspective on strong multiphoton ionization, Phys. Rev. Lett, 71 (1994) 1993.

[3] X.-Y. Miao, H.-N. Du, Theoretical study of high-order-harmonic generation from asymmetric diatomic molecules, Physical Review A, 87 (2013) 053403.

[4] Y.-C. Han, L.B. Madsen, Minimum in the high-order harmonic generation spectrum from molecules: role of excited states, Journal of Physics B: Atomic, Molecular and Optical Physics, 43 (2010) 225601.

[5] Vafaee, M., Nuclear kinetic energy spectra of D 2+ in an intense laser field: Beyond the Born-Oppenheimer approximation. Physical Review A, 2008. 78(2): p. 023410

[6] Hiskes, J.R., Dissociation of molecular ions by electric and magnetic fields. Physical Review, 1961. 122(4): p. 1207.

[7] Y.-C. Han, L.B. Madsen, Internuclear-distance dependence of the role of excited states in high-order-harmonic generation of H 2+, Physical Review A, 87 (2013) 043404.

[8] M. Lein, N. Hay, R. Velotta, J. Marangos, P. Knight, Interference effects in high-order harmonic generation with molecules, Physical Review A, 66 (2002) 023805.

Photophysical Properties of Thermally Activated Delayed Fluorescence Emitters From Optimally Tuned Range-Separated Functionals

Mojtaba Alipour and Zahra Safari*
Department of Chemistry, College of Sciences, Shiraz University, Shiraz 71946-84795, Iran
E-mail: malipour@shirazu.ac.ir

Abstract: Over the last years, the interests toward the molecules exhibiting thermally activated delayed fluorescence (TADF) have been increased. In this work, we propose novel optimally tuned range-separated hybrid density functionals (OT-RSHs) for reliable description of the photophysical properties such as absorption and emission energies as well as singlet-triplet gaps for the TADF emitters. Taking the BLYP, PBE, and TPSS density functional approximations as the exchange and correlation terms with various options for the short- and long-range exact-like exchange admixtures and the range-separation parameter, several OT-RSHs are proposed for predictions of the photophysical properties for a set of TADF emitters prone to be used in organic light emitting diodes (OLEDs). It is shown that the presented models not only have superior performance with respect to the standard counterparts but also outperform the earlier developed hybrids with both fixed and interelectronic distance-dependent exact-like exchange.

Keywords: OLED, TADF, DFT, Optimally tuning

I. INTRODUCTION

The first observation of the thermally activated delayed fluorescence (TADF) mechanism can be referred to the pioneering work by Perrin.[1] In 2012, Uoyama *et al*.[2] pointed out the important role of this phenomena as a promising mechanism for harvesting triplet excited states in organic light emitting diodes (OLEDs). To having an efficient OLED in which the TADF mechanism can ascertainably be occurred, the condition of a small singlet-triplet gap has to be satisfied. Herein, we present a detailed time-dependent density functional theory (TD-DFT) study based on optimally tuned range-separated hybrid density functionals (OT-RSHs)[3] for reliable prediction of not only singlet-triplet energy gaps but also other photophysical properties like absorption and emission energies for TADF-based OLEDs. More specifically, our work is not limited to assessing the existing density functionals through a benchmarking study but we propose novel OT-RSHs without any empirical parameter for the purpose.

II. METHODS

The RSHs represent an approach which can be used for a balanced description of Hartree-Fock (HF) exchange and DFT for the exchange and correlation terms. In practice, short-range (SR) density functional exchange is mixed with long-range (LR) HF exchange through separating the electron repulsion operator into SR and LR parts,

$$r_{12}^{-1} = r_{12}^{-1}\{1-[\alpha+\beta\ \mathrm{erf}\,(\mu r_{12})]\} + r_{12}^{-1}[\alpha+\beta\ \mathrm{erf}\,(\mu r_{12})] \qquad (1)$$

where r_{12} is the interelectronic distance, μ is the range-separation parameter controlling how HF and DFT exchanges are mixed as a function of r_{12}, $\Theta(\mu r_{12})$ is a smooth range-separation function, and α and β are the adjustable parameters. In this work, we have considered the RSHs with LR correction based on various density functional approximations with the full exchange at asymptotic distance and several choices for the parameters to propose new models for photophysical properties of TADF-based OLEDs. To this end, instead of using empirical parameterization against standard benchmark datasets, we have considered the optimally tuning scheme based on the minimization of the following function to obtain optimal μ

$$J^2 = \sum_{i=0}^{1}\left[\varepsilon_{\mathrm{HOMO}}^{\mu}(N+i) + \mathrm{IP}^{\mu}(N+i)\right]^2 \qquad (2)$$

where HOMO and IP refer to the highest occupied molecular orbital and ionization potential, respectively, and N is the number of electron of the systems of concern. Our calculations were carried out on a series of TADF emitters with a wide variety of singlet-triplet gaps (As illustrative examples, three of them are shown in Figure 1).

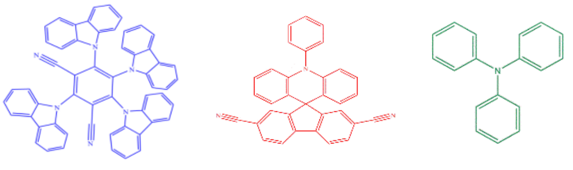

4CzIP ACRLFCN NPh_3

Figure 1. Geometrical structures of three molecules with the small (blue), medium (red), and large (green) singlet-triplet energy gaps.

To compute the photophysical properties in both gas phase and solvent for these molecules using the developed OT-RSHs, we first performed the range-separation parameter tuning based on minimization of Eq. (2). We have included different admixtures of HF exchange at SR, ranging from 0% to 25% with the intervals of 5%. For each choice of parameter SR HF exchange different values for the range-separation parameter, varying from 0.1 Bohr^{-1} to 0.3 Bohr^{-1} in increments of 0.05, were employed. As the exchange and correlation terms we utilized the widely used density functional approximations BLYP, PBE, and TPSS. Based on the literature data and our analyses, we utilized the 6-31G(d) basis set throughout. From the methodological viewpoint, the Tamm-Dancoff approximation (TDA) of TD-DFT has been used. All the runs were implemented in the GAUSSIAN09 suite of codes.

III. RESULTS AND DISCUSSION

At first, we carried out the optimally tuning of the range-separation parameter for the RSHs under study (see, for instance, Figure 2). We can see that although the minima do not exactly coincide, the minimization curves behave almost similar. The quadratic fittings were applied for all the resulting curves and the optimally tuned values of μ were subsequently determined by minimizing the derived second order polynomials. Overall, the obtained optimally tuned values of μ are in the range of 0.11 to 0.23 Bohr^{-1}.

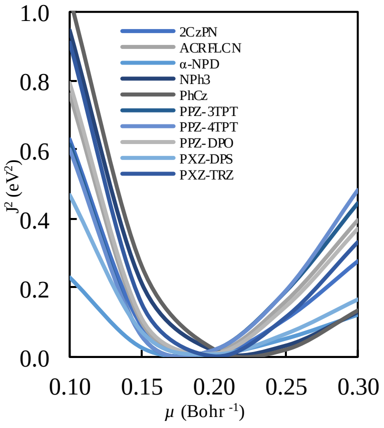

Figure 2. Plot for the rang-separation parameter tuning for the benchmarked set of molecules for the case of $\alpha = 0.0, \beta = 1.0$ using the BLYP density functional approximation. Name of the molecules are also given.

Having optimally tuned the values of the range-separation parameter, they were used for all the subsequent calculations of the photophysical properties. As a representative example, the results for the case of singlet-triplet gaps are reported in Table 1. Our data show that the values of mean signed deviations (MSDs) are positive and have a tendency of overestimating all the photophysical properties using the OT-RSHs. On the other hand, the values of mean absolute deviations (MADs) and root mean square deviations (RMSDs) reveal that for all the combinations of α and β parameters the OT-RSHs based on BLYP and PBE density functional approximations with nearly equivalent performances are the winners. Almost similar findings were found for other properties in both gas and solution phases. We also assessed the performance of the proposed OT-RSHs for predicting the photophysical properties of another set of emitters for which the range-separation parameter tuning has not been performed. The MADs as 0.30, 0.27, and 0.10 eV were found for absorption, emission, and singlet-triplet energies, respectively. The obtained accuracy is remarkable where we find that for all the considered molecules the reasonable statistical data are obtained from the OT-RSHs. Putting all the findings together, one can say that the optimally tuning procedure of the RSHs predicts the options of $\alpha = 0.0, \beta = 1.0$, and $\mu = 0.21\,\mathrm{Bohr}^{-1}$ along with the considered exchange and correlation terms as the inexpensive promising candidates for our purpose, yielding a reliable description for photophysics of TADF-based OLEDs with a good compromise between accuracy and computational cost.

Table 1. Statistical descriptors on the performance of the proposed OT-RSHs in the calculations of singlet-triplet energy gaps for the benchmarked set of molecules.

Functionals	MSD	MAD	RMSD
OT-RSHs			
$\alpha = 0.0, \beta = 1.0$			
BLYP	0.08	0.10	0.13
PBE	0.09	0.10	0.13
TPSS	0.14	0.14	0.17
$\alpha = 0.05, \beta = 0.95$			
BLYP	0.12	0.13	0.16
PBE	0.12	0.13	0.17
TPSS	0.17	0.17	0.21
$\alpha = 0.10, \beta = 0.90$			
BLYP	0.14	0.14	0.18
PBE	0.14	0.15	0.19
TPSS	0.19	0.19	0.23
$\alpha = 0.15, \beta = 0.85$			
BLYP	0.15	0.16	0.20
PBE	0.15	0.16	0.21
TPSS	0.20	0.20	0.25

$\alpha = 0.20,\ \beta = 0.80$			
BLYP	0.13	0.15	0.20
PBE	0.14	0.16	0.22
TPSS	0.19	0.19	0.25
$\alpha = 0.25,\ \beta = 0.75$			
BLYP	0.10	0.16	0.21
PBE	0.11	0.16	0.23
TPSS	0.15	0.19	0.25

IV. CONCLUSION

In short, within this work we have unveil the applicability of optimally tuned range-separated density functionals for the description of photophysical properties of TADF-based OLEDs. It was shown that the developed optimally tuned range-separated hybrids with right asymptotic exchange-correlation potential behavior give the reliable estimates of the TADF photophysics. Comparing the results with the literatures data revealed that the proposed models not only outperform their conventional counterparts but also perform better than the earlier proposed hybrids. Summing up, the presented models can be employed as promising tools to theoretical design of the specific molecules with small singlet-triplet energy gap in OLEDs applications.

REFERENCES

[1] F. Perrin, Ann. Phys, vol.10, pp. 169–275, **1929**.
[2] H. Uoyama, K. Goushi, K. Shizu, H. Nomura, and C. Adachi, Nature, vol.492, pp.234–238, **2012**.
[3] T. Stein, L.Kronik, R. Baer, J. Am. Chem. Soc. vol.131, pp. 2818-2820, **2009**.
[4] M. Alipour, Z. Safari, J. Phys. Chem. C, vol.123, pp. 746-761, **2019**.

First Principles Calculation to Investigate of Temperature and Environmental Effect on the EPR Properties of α-Aminoisobutyric acid Radicals in Aqueous Solution at Different pH Values

M. Janbazi *[a]**, *Y.T. Azar* [b]*, F.Ziaie* [a]*, M. Shadman* [c]
[a]*Radiation Application Research School, NSTRI, P.O. Box 11365-3486, Tehran, Iran*
[b]*Physics and Accelerator Research School, Nuclear Science and Technology Research Institute, Tehran, Iran*
[c]*Department of Chemistry, Faculty of Science, University of Zanjan, P.O.Box 45195-313, Zanjan, Iran*
Email: mjanbazi@aeoi.org.ir

Abstract: In this study, hydrogen bonds and temperature effects on EPR parameters of the α-Aminoisobutyric radicals in acidic and alkali solutions investigated by means of density function theory. The formation of hydrogen bonds between the water molecules with the hydrogen atoms of the amino group and the oxygen atoms of the carboxylic group have a significant effect on the EPR parameters. A good agreement was obtained between the simulation results obtained from the calculations and the experimental results.

Keywords: Ionization Radiation, Dosimetry, Radical α-Aminoisobutyric, EPR, ab-initio calculation, Solution.

I. INTRODUCTION

Ionizing radiation has long been used to sterilize of the materials. Biological molecules, such as proteins and DNA are very sensitive to ionizing radiation. Amino acids, which are building blocks of protein, are among the simplest organic molecules therefore it used as an appropriate model system for radiation damage studies.

The study of the amino acids irradiation has double importance: Primarily due to their role in biological processes and, secondly, use of some amino acids as dosimetric systems. EPR is used as a method for measuring radiation doses in the irradiation industry. α-Aminoisobutyric is one of the amino acids with $C_4H_9NO_2$ chemical formula (Fig. 1) that plays a role in the human body metabolism [1]. In this study, the EPR parameters of various α-Aminoisobutyric radicals will be investigated.

So far, theoretical calculations have been done to calculate the EPR parameters of different radicals in soluble phase using cluster and periodic methods [2]. However, no theoretical studies have been performed to calculate the EPR parameters of α-Aminoisobutyric radicals in the solution phase. Based on experimental studies, affecting radicals on the EPR spectrum at low and high pHs are $H_3^+NCH_3(C^\bullet H_2)COO^-$)$R^{ZW}$ and $H_2NCH_3(C^\bullet H_2)COO^-$) R^{neg} , respectively (Fig. 1).

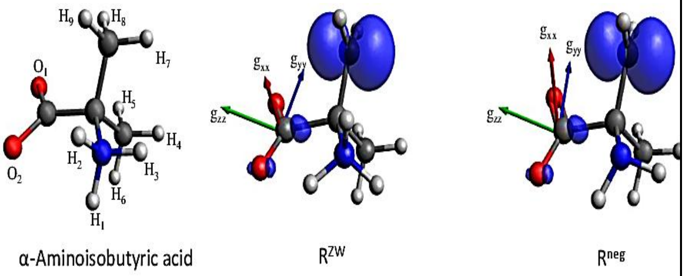

α-Aminoisobutyric acid R^{ZW} R^{neg}

Fig1: α-Aminoisobutyric Structure and its Radicals in Acid and alkali Solution

The main objective of this study is determining the effect of environmental factors (temperature and hydrogen bonds) on the magnetic properties of α-Aminoisobutyric radicals in acidic and alkali solutions using the density functional theory. This paper is organized as follows. First the ab-initio molecular dynamics performed in order to investigate the hydrogen bonds of water molecules and temperature-induced changes in solution on the EPR parameter of the radicals and then cluster calculation was used to investigate of the influence the short-range hydrogen bond and the polarized effects of the solution using a hybrid function on the EPR parameters of the radicals.

II. THEORY

Details of our density-functional theory (DFT) method for the calculation of EPR parameters have been given in ref [3]. Here we only summarize the salient features. Considering the second-order perturbation theory, the g-tensor can be expressed as:

$$g_{ij} = g_e\delta_{ij} + \Delta g_{ij}^{RM} + \Delta g_{ij}^{CG} + \Delta g_{ij}^{oz/soc} \quad (1)$$

Where g_e is value of the free-electron (g_e = 2.0023193). Δg^{RM} and Δg^{CG} are introduced as relativistic mass and gauge corrections respectively which have weak contributions to the g-tensor so that their contributions can be ignored. The main cause of the $\Delta g^{oz/soc}$ term in Eq. 1 arises from the coupling of

the orbital Zeeman (OZ) and the spin-orbit coupling (SOC) operator which is given by

$$\Delta g_{SO/OZ,\mu\nu} = \frac{2g_e\beta_e^3}{4\pi\epsilon_0\hbar c^2}\frac{1}{\langle S_z\rangle}\sum_N Z_N \times\sum_N\left\{\frac{\langle\psi_0^{(0)}|\sum_i \frac{1}{r_{iN}^3}\times(I_{iN})_\mu S_{jz}|\psi_n^{(0)}\rangle\langle\psi_n^{(0)}|\sum_j (I_{jN})_\nu|\psi_0^{(0)}\rangle}{E_0^{(0)}-E_n^{(0)}}+C.C.\right\}, \quad (2)$$

where β_e is Bohr magneton; I_N is spin angular momentum of nucleus N; r_{iN} define the position of electron *i* with respect to the position of nucleus n ($r_{iN}=r_i-r_N$; Z_N) is the proton number of nuclear; S_j is the spin angular momentum vector of electron *j*; $\psi_0^{(0)}$ and $\psi_n^{(0)}$ are the unperturbed wave-function of the ground state and the *n-th* excited state associated with the energies $E_0^{(0)}$ and $E_n^{(0)}$ and C.C. indicates addition of the complex conjugate of the preceding term.

The hyperfine coupling tensor, describing the interaction between unpaired electron and with neighboring nuclear-dipole moments can be divided into two main Categories: the isotropic Fermi contact interaction and the anisotropic dipole-dipole interaction. Since, anisotropic part of the hyperfine tensor in the solution does not affect the EPR hyperfine coupling, only the isotropic components term was considered. The contribution from the Fermi-contact hyperfine operator H_{FC}^N is given by

$$A_{FC}^N = \frac{8\pi}{3}\frac{g_e g_N\beta_e\beta_N}{4\pi\epsilon_o c^2}\frac{1}{\langle S_z\rangle}\langle\psi_0^{(0)}|\sum_i\delta(r_{iN})S_{iZ}|\psi_0^{(0)}\rangle, \quad (3)$$

Where the quantities g_N and β_N describe g factor and magneton of the nucleus, respectively.

III. METHODS

Periodic calculations: Initial formulation for system consisting of 65 molecules of water and α-Aminoisobutyric in a single-cell unit with size of $12\times12\times12A^0$ (Fig. 2). The R^{ZW} and R^{neg} radicals in acidic and alkali solutions were made in this formulation. Then, molecular dynamics simulation, which included 2,000 snapshots (one femtosecond for each snapshot), was constructed for the periodic structure of each radical using the CP2K software package. EPR parameters of radicals at high and low pH were calculated in the QE software package based on the density function theory.

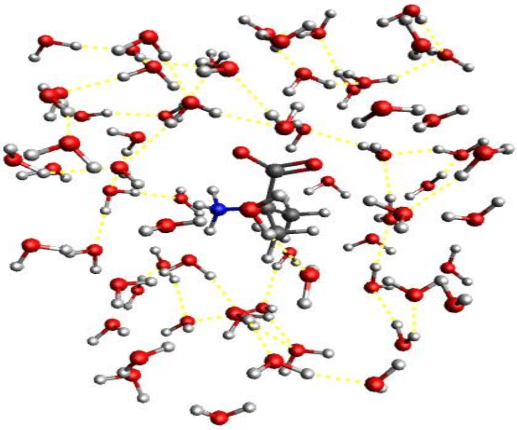

Figure 2: α-Aminoisobutyric structure and 65 molecules of water in molecular dynamics simulation

Cluster Analysis: A cluster model was used to investigate the effect of short-range hydrogen bonds. In this method, α-Aminoisobutyric radicals were surrounded by a number of water molecules in the first shell. The number of water molecules in the first shell for R^{ZW} and R^{neg} radicals contains 7 and 6 respectively. Then, for the resulted cluster structure, the continuous polarized model (COSMO) was applied to investigate the polarized effects of the solution. The structure of all clusters were optimized using the NWChem software package. EPR property was calculated using this program.

IV. RESULTS AND DISCUSSION

The formation of soluble around radicals due to the presence of hydrogen bonding with NH_3, CO_2 groups with change in the geometric structure and distribution of spin atomic atoms causes a change in the EPR properties of radicals. The results of the experimental spectrum show that the spectrum is dependent to g-tensor and the hyperfine coupling constant of hydrogen atoms (8 and 9) and the nitrogen atom. In Table 1, the calculated results of EPR parameters for molecular and cluster dynamical calculations R^{ZW} and R^{neg} radicals were compared with experimental data. It is found from Table 1 that the obtained results from both molecular and cluster dynamics are in good agreement with experimental data.

Table 1: Comparison of g-the tensor (in ppm) and the hyperfine coupling constants of the atoms (Gauss) for the radicals R^{ZW} and R^{neg} obtained from the simulation of molecular and cluster dynamics with experimental results [4].

	g_{iso}	$H_{avg(8,9)}$	N
R^{ZW}			
MD	2/00273	-21/11	3/73
Cluster	2/00269	-21/93	1/29
Exp ($pH \approx 2.5-5$)	2/00255	-22/24	3/51
R^{neg}			
MD	2/00270	-21/80	1/55
Cluster	2/00269	-20/31	1/16
Exp ($pH \approx 11-13.5$)	2/00249	-21/94	2/97

It is found from Eq. 2 that the main contribution of g-tensor components is spin-orbit coupling. Considering direction of g-tensor components (Fig. 1) and the spin iso-surface we can find significant contribution of g_{xx} and g_{yy} but that the contribution in g_{zz} component is negligible, and in the following order: $g_{xx} > g_{yy} > g_{zz}$. It should be noted that Oxygen O_1 and O_2 atoms have the highest share in g-tensor components due to the highest spin-orbital coupling. The change in *g* tensor components is due to changes in the density distribution of the O_1 and O_2 oxygen atoms.

According to the Eq. 3, hyperfine coupling constant is due to the interaction between the nucleon spin and the atomic momentum of the atom. Therefore, the hyperfine coupling constant change of the each atom depends on the change in the spin density of the atom itself.

V. CONCLUSION

In this study, ab-initio molecular dynamics and clustered calculations were used to elucidate the structure and EPR parameters of the α-Aminoisobutyric radicals in acidic and alkali solutions. The ab-initio molecular dynamics calculations due to the simultaneous effect of temperature and hydrogen bonding and the cluster computations due to the use of hybrid function are in good agreement with experimental results. The results indicated that from the experimental standpoint, the hydrogen bonds of water molecules with the oxygen atoms of carboxyl groups and N atoms and hydrogen atoms of amino group (7 and 6 water molecules for R^{ZW} and R^{neg} radicals respectively) exceed all other factors in importance.

REFERENCES

[1] Neacsu, Ana, et al. REVISTA DE CHIMIE 65.3 (2014): 306-310.

[2] G. Brancato, N. Rega, V. Barone, J. Am. Chem. Soc. 129 (2007) 15380–15390.

[3] I. Ciofini, C. Adamo, V. Barone, J. Chem. Phys. 121 (2004) 6710–6718.

[4] P. Neta and R. W. Fessenden, The Journal of physical chemistry 74, 2263 (1970).

Spin-Orbit Coupling Effect on the Electronic Properties of Neutral Gold Clusters

*Mahnaz Jabbarzadeh Sani**
Chemistry Department, College of Science, Shiraz University, 7146713565 Shiraz Iran
E-mail: mjsani@shirazu.ac.ir

Abstract*:* At the Douglas-Kroll-Hess level, the spin-orbit coupling (SOC) effect on the electronic properties of small neutral gold clusters are evaluated applying all-electron relativistic double-ζ-level basis set. Spin-orbit correction to the chemical potential, hardness, softness and electrophilicity index are calculated. It is revealed that spin-orbit coupling has important effect on Au_3 and greatly increases the vertical electrophilicity index of this cluster.

Keywords: Density functional theory, Douglas-Kroll-Hess, Electronic properties, Gold clusters, Spin-orbit coupling.

I. INTRODUCTION

As a kind of promising nanomaterials, metal nanoclusters (NCs) have sparked wide-spread attention. In recent years, gold nanoparticles (AuNPs) have been applied to biomedicine and biological sensing [1] due to their biocompatibility and unique physical properties. AuNPs are one of the most promising catalysts, in spite of bulk Au as an inactive material [2]. Most of the computations on small neutral gold clusters have been performed using spin-free (scalar-relativistic) methods [3]. However, the spin-orbit coupling is expected to be important. There exist theoretical studies regarding spin-orbit coupling effect using effective core potentials or plane-wave basis sets [4,5]. In the present work, spin-orbit coupling (SOC) effect on the electronic properties of small neutral gold clusters are investigated applying the Douglas-Kroll-Hess Hamiltonian and all-electron relativistic basis set of valence double-ζ quality plus polarization functions (DZP-DKH). The spin-orbit coupling effect on the electronic chemical potential, absolute hardness, softness and electrophilicity index are examined.

II. METHODS

All calculations are performed using the Gaussian 09 suite of program. The B3P86 functional is used in conjunction with the valence double-ζ quality plus polarization functions (DZP-DKH) basis set. The B3P86 functional has already proven to perform well for ionization potential computations of small neutral gold clusters [6]. The second-order Douglas-Kroll-Hess Hamiltonian [7] is used instead of the Schrödinger operator. Using the second-order Douglas-Kroll-Hess Hamiltonian, all geometries are fully optimized at the DKH2-B3P86/DZP-DKH level of theory followed by harmonic vibrational frequency analysis. Then, from these optimized geometries, the spin-orbit coupling (SOC) energies are calculated using the fourth-order Douglas-Kroll-Hess Hamiltonian and the generalized Hartree-Fock method.

The electronic energy including spin-orbit coupling, E_{SO}, is calculated using Eq. (1). Here, E_{SC} is the electronic energy obtained from spin-orbit free (scalar-relativistic) optimizations at the DKH2-B3P86/DZP-DKH level, and $\Delta_{SO}E$ is the spin-orbit coupling energy calculated by the DKH2-B3P86/DZP-DKH //DKHSO- GHF/DZP-DKH level of theory. In order to determine the spin-orbit coupling (SOC) effect on the electronic properties of neutral gold clusters, the spin-orbit correction to the chemical hardness, softness, chemical potential and electrophilicity index [8] of the gold clusters are computed. In the following, the spin-orbit correction to a particular property, $\Delta_{SO}P$, is defined using Eq. (2), where P_{SO} and P_{SC} are the calculated properties with considering the spin orbit coupling energy E_{SO}, and without considering the spin-orbit coupling energy E_{SC}, respectively. Within the valence state parabola model [8], the chemical potential, chemical hardness, softness and electrophilicity index are introduced by Eq. (3). 'N' and 'v' are the number of electrons and the potential due to the nuclei plus any external potential, respectively. The spin-orbit correction to these properties are calculated from Eq. (4).

III. RESULTS AND DISCUSSION

The calculated spin-orbit coupling (SOC) corrections to the chemical potential, hardness, softness and electrophilicity index are given in the Table 1. Chemical hardness has been used to characterize the relative stability of clusters. The principle of maximum hardness (PMH) states that systems at equilibrium present the highest value of hardness [9]. As Fig. 1a shows, the spin-orbit correction to the vertical chemical hardness has important effect on Au_3 and Au_6. The $\Delta_{so}\eta$ value for Au_3 and Au_6 is negative (-0.037 eV) and positive (0.045 eV), respectively, i.e. spin-orbit coupling decreases (increases) the hardness of gold trimer (hexamer). The variation of the spin-orbit correction to the softness of neutral gold clusters as a function of cluster size is plotted in Fig. 1b. The spin-orbit correction to the softness shows an even-odd alternation behavior. Moreover, the inclusion of spin-orbit coupling increases (decreases) the softness of Au_3 (Au_6) and thus destabilizes (stabilizes) it, $\Delta_{so}\sigma_v = +\ 0.005$ eV ($\Delta_{so}\sigma_v = -0.006$ eV).

Chemical potential, μ, is related to the charge transfer from a system to another having a lower value of μ. Fig. 1c shows the spin-orbit correction to the chemical potential of neutral gold clusters versus the cluster size. Spin-orbit coupling increases the vertical chemical potential of Au_2 by 0.021 eV, while decreases that of Au_3 and Au_6 by 0.038 and 0.037 eV, respectively. Hence, spin-orbit coupling has more important effect on the chemical potential of Au_3. Electrophilicity has been a measure of the energy stabilization of a cluster due to acquiring additional electronic charge from its surroundings [8]. To better understand the spin-orbit coupling effect on the electrophilicity index of small neutral gold clusters, the variation of spin-orbit correction to the ω as a function of cluster size has been presented in Fig. 1d. An odd-even alternation behavior is obvious. Moreover, the spin-orbit correction to the vertical and adiabatic electrophilicity values of Au_3 ($\Delta_{so}\omega_v = 0.115$ eV and $\Delta_{so}\omega_a = 0.046$ eV) and Au_5 ($\Delta_{so}\omega_v = 0.011$ eV and $\Delta_{so}\omega_a = 0.013$ eV) are positive, indicating that spin-orbit coupling increases the electrophilicity index of these clusters. It is evident that spin-orbit coupling has significant effect on the vertical electrophilicity index of gold trimer.

A. *Figures and Tables*

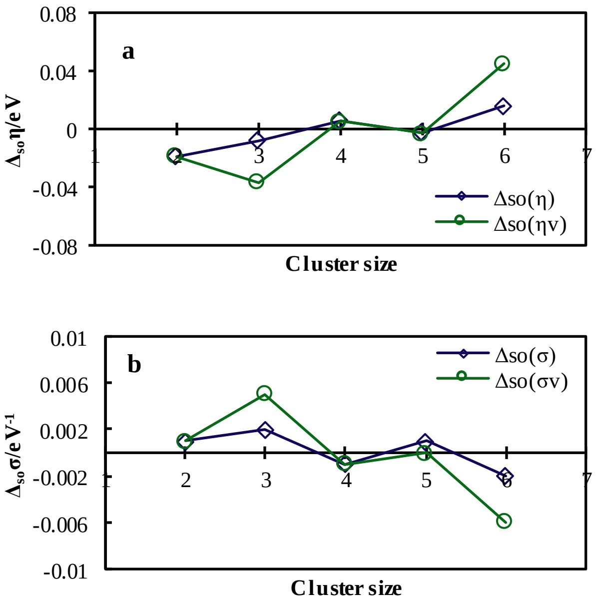

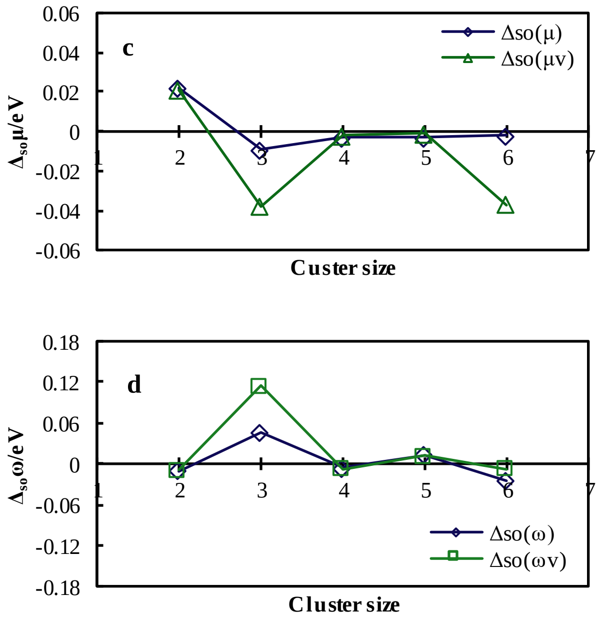

Fig.1: Spin-orbit corrections to the (a) chemical hardness, (b) softness, (c) chemical potential and (d) electrophilicity index. Subscripts 'so' and 'v' indicate 'spin-orbit' and 'vertical', respectively.

Table 1: Spin-orbit coupling (SOC) corrections to the vertical and adiabatic chemical potential ($\Delta_{so}\mu$/eV), hardness ($\Delta_{so}\eta$/eV), softness ($\Delta_{so}\sigma$/eV^{-1}) and electrophilicity index ($\Delta_{so}\omega$/eV).

n	$\Delta_{so}\mu_v$/eV	$\Delta_{so}\eta_v$/eV	$\Delta_{so}\sigma_v$/eV^{-1}	$\Delta_{so}\omega_v$/eV
2	0.021	-0.019	0.001	-0.009
3	-0.038	-0.037	0.005	0.115
4	-0.002	0.005	-0.001	-0.007
5	-0.001	-0.003	0.000	0.011
6	-0.037	0.045	-0.006	-0.008
n	$\Delta_{so}\mu_a$/eV	$\Delta_{so}\eta_a$/eV	$\Delta_{so}\sigma_a$/eV^{-1}	$\Delta_{so}\omega_a$/eV
2	0.022	-0.019	0.001	-0.011
3	-0.009	-0.008	0.002	0.046
4	-0.003	0.006	-0.001	-0.006
5	-0.003	-0.002	0.001	0.013
6	-0.002	0.016	-0.002	-0.025

Subscripts 'v', 'a' and 'so' indicate 'vertical', 'adiabatic' and 'spin-orbit', respectively.

B. Equations

$$E_{SO} = E_{SC} + \Delta_{SO}E \qquad (1)$$

$$\Delta_{SO}P = P_{SO} - P_{SC} \qquad (2)$$

$$\mu = \left(\frac{\partial E}{\partial N}\right)_v = -\frac{IP+EA}{2} \quad , \quad \eta = \left(\frac{\partial^2 E}{\partial N^2}\right)_v = \frac{IP-EA}{2}$$

$$\sigma = \frac{1}{\eta} \quad , \quad \omega = \frac{\mu^2}{2\eta} \qquad (3)$$

$$\Delta_{SO}\mu = \mu_{SO} - \mu_{SC} \quad , \quad \Delta_{SO}\eta = \eta_{SO} - \eta_{SC}$$

$$\Delta_{SO}\omega = \omega_{SO} - \omega_{SC} \quad , \quad \Delta_{SO}\sigma = \sigma_{SO} - \sigma_{SC} \qquad (4)$$

IV. CONCLUSION

The spin-orbit coupling (SOC) effect on the electronic properties of small neutral gold clusters has been evaluated using Douglas-Kroll-Hess Hamiltonian and all-electron relativistic double-ζ quality basis set. It is found that spin-orbit coupling has a significant effect on the calculation of vertical electrophilicity index of Au_3 and increases its value by 0.115 eV. Spin-orbit correction is also relatively important in the calculation of vertical chemical potential, vertical hardness and vertical softness of this cluster.

REFERENCES

[1] W. Liu, Z. Zhang, Z. M. Zhang, P. Hao, K. Ding and Z. Li, Chem. Commun., vol. 55, pp. 1596-1599, **2019**.

[2] Y. Han, H. Xu, Y. Su, Z. L. Xu, K. Wang and W. Wang, J. Catal., vol. 370, pp. 70-78, **2019**.

[3] F. E. Jorge and A. S. Santos, J. Braz. Chem. Soc., vol. 29, pp. 838-844, **2018**.

[4] L. Xiao and L. Wang, Chem. Phys. Lett., vol. 392, 452-455, **2004**.

[5] M. A. Flores and E. Menéndez-Proupin, J. Phys. Conf. Ser., vol. 720, 012034, **2016**.

[6] H. Baek, J. Moon and J. Kim, J. Phys. Chem. A, vol. 121, 2410-2419, **2017**.

[7] M. Reiher and A. Wolf, second ed., WILEY-VCH, Germany, pp. 469-501, **2015**.

[8] R. G. Parr, L. V. Szentpály and S. Liu, J. Am. Chem. Soc., vol. 121, 1922-1924, **1999**.

[9] F. E. Jorge, I. B. Ferreira, D. D. Soprani and T. Gomes, J. Braz. Chem. Soc., vol. 27, 127-135, **2016**.

Theoretical study of adsorption of trichloroethylene on the surface of beryllium oxide nanotubes

Nasibeh Tavakoli [a], ***Davood Farmanzadeh*** [b]*
Department of Physical Chemistry, Faculty of Chemistry, University of Mazandaran, Babolsar 47416-95447, Iran
Email:d.farmanzad@umz.ac.ir

Abstract: The adsorption of trichloroethylene (C_2HCl_3) molecule on the surfaces of the beryllium oxide (BeO) nanotube was investigated by means of density functional theory. The results show that the adsorption of trichloroethylene on both (4,4) and (8,0) nanotubes are inn chemical adsorption range, and changes energy gap in the (4,4) nanotube are more significant.

Keywords: Adsorption, Beryllium oxide, Density functional theory, Nanotube, Trichloroethylene.

I. INTRODUCTION

BeO compound often has different properties from the counterparts of C, BN, and SiC due to the large iconicity of Be–O bond. For example, wurtzite BeO is an insulator with wide band gap, high melting point, high thermal conductivity, and large elastic constants [1]. In addition, compared with CNTs, it was found that the BeONTs have larger band gaps which are less dependent on the chirality and diameter of tubes [2]. Moreover, the BeONTs adopt interesting mechanical properties, namely, their Young's modulus are comparable to those for carbon nanotubes [3-4]. Trichloroethylene, known as TCE, is commonly used as an industrial solvent. This organic compound appears colorless and non-flammable. The most widely used solvent for trichloroethylene is an industrial solvent for removing grease from the surface of metals, anesthetic agent, color cleaner and disinfectant. Of course, for reasons of safety and environment, applications of that are getting smaller [5-6]. In this work we're going to investigate the adsorption of trichloroethylene over zigzag and armchair beryllium oxide nanotubes. The sensitivity of these two nanotubes toward gas molecule is compared.

II. METHODS

In this study, all structures were designed with the $Dmol^3$ of software and then optimized for geometric structure. All calculations are performed electronically of the generalized gradient approximation (GGA) framework with functional PBE for the correlation-exchange energy estimation.

III. RESULTS AND DISCUSSION

The most stable optimized structures of trichloroethylene complex with (4,4) and (8,0) BeO nanotubes are displayed in Fig. 1.

Different configurations of C_2HCl_3 molecule on top of the each atoms (Be and O) of BeO nanotube are scrutinized for finding the stable configuration.

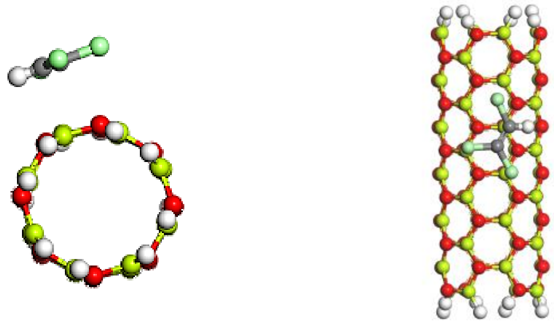

(4,4) BeO Nanotube-C_2HCl_3

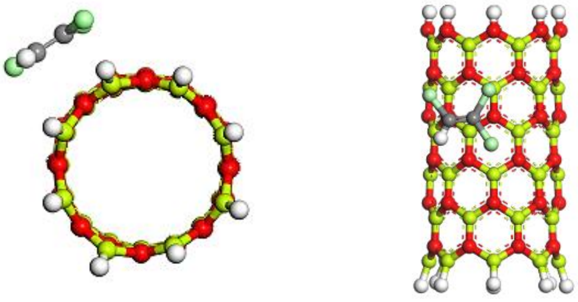

(8,0) BeO Nanotube-C_2HCl_3

Fig. 1 The most stable structures of BeO nanotube compared with trichloroethylene.

The calculated adsorption energy, charge transfer (Q), the HOMO energy, LUMO energy and E_{gap} (HLG) energy are reported in table 1.

The results in this table show that the adsorption energy of (8,0) zigzag nanotube is -66.49 kJ/mol and (4,4) armchair nanotube is -58.53 kJ/mol. In both nanotubes, charge from the trichloroethylene has been transferred to the nanotube.

The calculated HOMO- LUMO gap (E_g) in table 1 show that variation of E_g in (4,4) BeO nanotube is significant relative to (8,0) BeO nanotube.

Table 1: The adsorption energy, the charge transfer, the HOMO energy, the LUMO energy, and the energy gap of the considered systems.

structure	E_{ads}	Q	E_{HOMO}	E_{LUMO}	E_g
(4,4) BeO	-	-	-6.85	-1.49	5.35
(4,4)BeO-C_2HCL_3	-58.53	0.23	-6.73	-2.48	4.25
(8,0) BeO	-	-	-4.25	-3.62	0.63
(8,0)BeO-C_2HCL_3	-66.49	0.19	-4.23	-3.58	0.65

IV. CONCLUSION

The results show that the adsorption of trichloroethylene on both (4,4) and (8,0) nanotubes is in the chemical adsorption range. Furthermore, the energy gap change in the (4,4) nanotube are more significant.

REFERENCES

[1] S . Duman, A. Sutlu, S. Bagcl, H. M. Tutuncu, and G. P. Srivastava. Journal of Applied Physics, vol. 105, p. 033719, **2009**.
[2] B . Baumeier, P. Kruger, and J. Pollmann. Physical Review B, vol. 76, p. 085407, **2007**.
[3] P B . Sorokin, A S . Fedorov, and L A . Chernozatonskii. Physics of the solid state, vol. 48, p. 398, **2006**.
[4] B. I. Yakobson, and P. Avouris. Carbon Nanotubes , Springer, Berlin, Heidelberg, pp. 287-327, **2001**.
[5] G. D. Hopkins, and McCarty, P. L. Field. Environmental Science & Technology, vol. 29, pp. 1628-1637. **1995**.
[6] B. Schrick, , J. BloughL, A. D. Jones, and T. E. Mallouk. Chemistry of Materials, vol. 14, pp. 5140-5147, **2002**.

Generation of Attosecond Pulses Using Polarization Gating of High-order Harmonic Emission from H_2^+

***H. Alinejad*[a], *M. Vafaee*[a]**, *B. Naghdi*[a], *M. Eidi*[b]**

[a] *Department of Chemistry, Tarbiat Modares University, Tehran 14115-175, Iran*

[b] *Max Planck Institute for the Physics of Complex Systems, 01187 Dresden, Germany*

Email: m.vafaee@modare.ac.ir

Abstract: The Quantum-mechanical investigation is presented to study single attosecond pulse generation by gating high-order harmonic emission from H_2^+ in intense laser pulses with time-dependent ellipticity. Numerical solution of the time-dependent Schrödinger equation employing static coherent states (SCS) method for H_2^+ has been investigated. The SCS has been performed aiming generation of the attosecond pulse.

Keywords: Generation of attosecond pulse, Short intense attosecond pulse, Time-dependent Schrödinger equation (TDSE)

I. INTRODUCTION

High-order harmonic generation (HHG) from atoms and molecules in intense laser fields has been proved to be an important technique for producing coherent high-energy attosecond pulses [1-3]. The HHG process is explained by the three-step semiclassical model [4]. In the first step, under an intense laser field, the potential well of the atom where the electron is trapped is turning to a potential barrier, so the electron could tunnel (ionize) through it (quantum step), then the freed electron accelerates in the external laser field which could be treated classically (classical step). Finally, electron recombines with the parent ion and emits a photon (quantum step) (fig. 1). Generally, these steps lead to an attosecond pulse trains which is due to the interference of these attosecond pulses there is a frequency comb with an interval of twice the driving field photon energy. In recent years, the generation of single isolated attosecond pulse has gained enormous interest and have its the applications, for example, pump-probe experiments. Such pulses can be generated by suppressing all the pulses in the train except one.

Generation and characterization of single isolated attosecond pulses are achieved using variety of techniques including spectral selection of half-cycle cutoffs [5] as in amplitude gating [6] and ionization gating [7], temporal gating techniques such as polarization gating [8] and double optical gating (DOG) [9], and spatiotemporal gating with the attosecond lighthouse effect [10].

Safaei [11] conducted a calculation to solve the two-dimensional time-dependent Schrödinger equation. In this work, three-dimensional time-dependent Schrödinger is solved. For the last two decades, different methods based on coherent states have been developed in order to address high dimensional quantum problems solving time-dependent Schrödinger equation [12-17].

II. METHODS

Interaction between H_2^+ and laser field with time-dependent polarization is described by the three-dimensional time-dependent Schrödinger equation solution via SCS method (atomic units (a.u.) are used throughout the paper unless stated otherwise.). The wavefunction of a single-electron system like H_2^+ could be represented as

$$|\psi\rangle = \sum_{k=1}^{N} D_k |Z_k\rangle. \tag{1}$$

Then TDSE could be read as [18]

$$\langle Z_j| \frac{d|\psi\rangle}{dt} = -\frac{i}{\hbar}\sum_{k,l}^{N} \langle Z_j|H|Z_k\rangle (\Omega^{-1})_{k,l} \langle Z_l|\psi\rangle \tag{2}$$

where Ω^{-1} is the inverse of the overlap matrix. So, we obtain

$$\frac{dC_j}{dt} = \frac{-i}{\hbar}\sum_{k=1}^{N} \langle Z_k|H|Z_l\rangle D_k \tag{3}$$

where H is the Hamiltonian of the system which is (assuming no dynamics for nuclei)

$$H = \frac{|p_e|^2}{2} - \sum_{j=1}^{2} \frac{1}{|r_e - R_j|} + \frac{1}{|R_1 - R_2|} + r_e.E(t). \tag{4}$$

And finally, computation of the HHG spectrum would be viable through

$$D(\omega) = \left| \int_0^T \langle\psi|a_e|\psi\rangle\, H(t) e^{-i\omega t} dt \right|^2 \tag{5}$$

which is squared magnitude of the Fourier transforms (FT) of the expectation value of the dipole acceleration a_e. Superposing of several harmonics of x component in attosecond time profile can be obtained by

(6)

$$I_x(t) = |\sum_q a_q \, exp[iq\omega t]\,|^2$$

where

$$a_q = \int a_x(t)[-iq\omega t]dt.$$

Polarization gating is based on the dependence of attosecond pulse generation efficiency on the ellipticity of laser pulse. The polarization state of the pulse changes from circular to linear and goes back to circular. In the head and tail part due to circular polarization, recombination possibility decreases dramatically. Thus, attosecond pulses can only be produced by the center portion of the laser pulse that is nearly linearly polarized.

III. RESULTS AND DISCUSSION

The calculations are performed for the superposition of a left and a right-hand circularly polarized pulse with 220 a.u. (~5 fs) time duration and separated by 220 a.u.. Laser pulses centered at 800 nm, and the peak intensity set to I=3×10^{14} W/cm^2 and Carrier-envelope phase φ=0. The calculated time profile of high harmonic emission and corresponding field components are presented in Fig.1 and Fig.2 respectively. In the Fig.3 one can see two consecutive attosecond pulses and one of them has 110 a.s. duration.

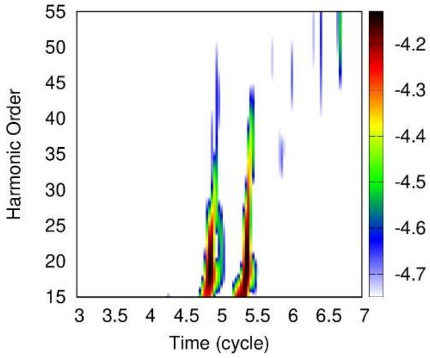

Fig.1: (Colour online) The Morlet wavelet time profile for H_2^+ molecule using polarization gating and 11000 static CS

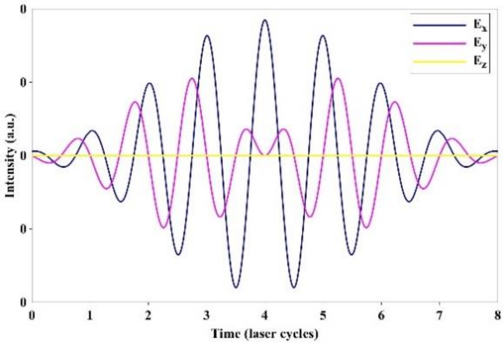

Fig.2: (Colour online) Laser field shape formed by a left and a right-hand circularly polarized Gaussian pulses at 800 nm wavelength and I=3×10^{14} W/cm^2 intensity

(7)

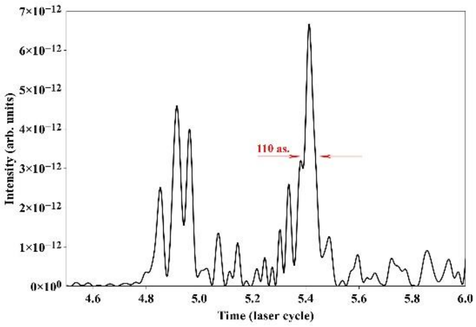

Fig.3: 110 attosecond pulse produced through polarization gating and using 11000 static CS

IV. CONCLUSION

Three-dimensional time-dependent Schrödinger is solved. The number of CS grid points is 11000 and previous to that we calculated using lower numbers of CS grid points but the best results are with final 11000 points. The generation of attosecond pulse from the HHG process in H_2^+ ion has been investigated.

In future works we can assign different amounts to the carrier-envelope-phase in order to generate single isolated attosecond pulse.

REFERENCES

[1] T. Brabec, F. Krausz, Intense few-cycle laser fields: Frontiers of nonlinear optics, Reviews of Modern Physics, 72 (2000) 545.
[2] Z. Chang, P. Corkum, Attosecond photon sources: the first decade and beyond, JOSA B, 27 (2010) B9-B17.
[3] F. Krausz, M. Ivanov, Attosecond physics, Reviews of Modern Physics, 81 (2009) 163.
[4] Z. Chang, Fundamentals of attosecond optics, CRC press2016.
[5] A. Baltuška, T. Udem, M. Uiberacker, M. Hentschel, E. Goulielmakis, C. Gohle, R. Holzwarth, V. Yakovlev, A. Scrinzi, T.W. Hänsch, Attosecond control of electronic processes by intense light fields, Nature, 421 (2003) 611.
[6] R. Kienberger, E. Goulielmakis, M. Uiberacker, A. Baltuska, V. Yakovlev, F. Bammer, A. Scrinzi, T. Westerwalbesloh, U. Kleineberg, U. Heinzmann, Atomic transient recorder, Nature, 427 (2004) 817.
[7] A. Jullien, T. Pfeifer, M.J. Abel, P. Nagel, M. Bell, D.M. Neumark, S.R. Leone, Ionization phase-match gating for wavelength-tunable isolated attosecond pulse generation, Applied Physics B, 93 (2008) 433.

[8] P. Corkum, N. Burnett, M.Y. Ivanov, Subfemtosecond pulses, Optics letters, 19 (1994) 1870-1872.
[9] H. Mashiko, S. Gilbertson, C. Li, S.D. Khan, M.M. Shakya, E. Moon, Z. Chang, Double optical gating of high-order harmonic generation with carrier-envelope phase stabilized lasers, Physical review letters, 100 (2008) 103906.
[10] H. Vincenti, F. Quéré, Attosecond lighthouses: how to use spatiotemporally coupled light fields to generate isolated attosecond pulses, Physical review letters, 108 (2012) 113904.
[11] N. Safaei, Generation of isolated attosecond pulses by polarization gating of high-order harmonic emission from H $ _2^+ $ in intense ultrashort laser fields, arXiv preprint arXiv:1703.02888, (2017).
[12] M. Eidi, M. Vafaee, A.R. Niknam, N. Morshedian, A new version of fermion coupled coherent states method: Theory and applications in simulation of two-electron systems, Chemical Physics Letters, 653 (2016) 60-66.
[13] J. Guo, X.-S. Liu, S.-I. Chu, Exploration of strong-field multiphoton double ionization, rescattering, and electron angular distribution of He atoms in intense long-wavelength laser fields: The coupled coherent-state approach, Physical Review A, 82 (2010) 023402.
[14] D.V. Shalashilin, I. Burghardt, Gaussian-based techniques for quantum propagation from the time-dependent variational principle: Formulation in terms of trajectories of coupled classical and quantum variables, The Journal of chemical physics, 129 (2008) 084104.
[15] D.V. Shalashilin, M.S. Child, Time dependent quantum propagation in phase space, The Journal of Chemical Physics, 113 (2000) 10028-10036.
[16] D.V. Shalashilin, M.S. Child, The phase space CCS approach to quantum and semiclassical molecular dynamics for high-dimensional systems, Chemical physics, 304 (2004) 103-120.
[17] D.V. Shalashilin, M.S. Child, Electronic energy levels with the help of trajectory-guided random grid of coupled wave packets. I. Six-dimensional simulation of H 2, The Journal of chemical physics, 122 (2005) 224108.
[18] M. Eidi, M. Vafaee, A. Landsman, Static Coherent States Method: One-and Two-Electron Laser-Induced Systems with Classical Nuclear Dynamics, Applied Sciences, 8 (2018) 1252.

Section:

Solid State Chemistry

Study of optical energy gap of Ag-doped ZrO_2 nanoparticles synthesized by sol-gel method

***Seyed Mohsen Mahdavi Abandansari*[a*], *HossainMilani Moghaddam*[a]**

Department of Solid State Physics, Faculty of Science, University of Mazandaran, Babolsar
Mohsen.mahdavi72@hotmail.com

Abstract:In current work the pure ZrO_2 nanoparticles and with Ag impurity were synthesized by using sol-gel method. The absorption spectra and optical energy gap of these nanoparticles were investigated. The monoclinic and tetragonal phases of these nanoparticles were confirmed by X-ray diffraction (XRD).It was found that by doping of Ag to the ZrO_2 structure, the particle size was increased. The field emission scanning electron microscopy analysis (FE-SEM) and energy-dispersive X-ray spectroscopy (EDX) demonstrated the morphology and formation of nanoparticles as well as the presence of Ag.The optical energy gap of Ag-doped ZrO_2 decreased with respect to that of pure ZrO_2.

Keywords*:* Ag, Nanoparticle, Optical properties, sol-gel method, ZrO_2

I. INTRODUCTION

The Zirconium oxide nanoparticles (ZrO_2) have high efficiency in industrial and scientific cases, because of their good natural color, high strength, high chemical stability, resistance to highly corrosive materials and chemical and microbial resistance [1].It includes high oxygen content and high ion exchange capacity and restoration activity which makes it a good catalyst. ZrO_2 has an energy gap at (5-5.5 eV) [2]. ZrO_2 has three types of cubic crystals (c-ZrO_2), tetragonal (t-ZrO_2) and monoclinic (m-ZrO_2) at different temperatures and pressures [3]. Accordingly, and considering the application of zirconium oxide nanostructures, in this research, the optical energy gap of ZrO_2 nanoparticles with $ZrO_2(NO_3)_2.xH_2O$ precursor and doped by Ag was studied under various chemical conditions.

II. METHODS

Firstly, to synthesize ZrO_2 nanoparticles, 2.3 grams of $ZrO_2(NO_3)_2.xH_2O$ were dissolved in 200 ml of deionized water at a temperature of 70℃ for one hour on a hotplate device. The pH of the solution was 3 and then, with adding 70 ml of Ammonia as a drop in 30 minute intervals, the pH of the solution reached to 10 and the solution began to precipitate. Then, the solution was allowed to shake for one hour, and washed with deionized water. The obtained material has been put in the oven at 80℃ for 12 hours; then, yielded materials was placed in a furnace at 800℃ for 2 hours. In order to add silver to ZrO_2, a few amount of $Ag(NO_3)_2.9H_2O$ (a molar 25% and 10%) was dissolved to 5 ml of deionized water at 50℃. As follows: the method is the above similar [4].

III. RESULTS AND DISCUSSION

Fig.1 shows that the pure and Ag-doped ZrO_2 nanoparticles had a monoclonal and tetragonal phases in the XRD analysis and with adding of Ag impurities, the peaks do not change. This shows that there is no change in the crystal structure. It reveals sharp, well-defined diffraction peaks. The strong and narrow diffraction peaks indicate that the sample has a good crystallinity. The size of nanoparticles was taken with using Debay-Sherer relation as given:

$$D = \frac{K\lambda}{\beta\ cos\theta} \qquad (1)$$

D is the average crystallite size (in nanometers), K is 0.9. β is the broadening of the hkl diffraction peak measured at half of its maximum intensity (in radian), λ the wavelength of the X-ray (in nanometers) is equal to 0.15418 ($k_\alpha - Cu$). θ is the Bragg diffraction angle (in degree). The crystallite size of pure ZrO_2 is 22 nm. The Ag-doped samples with the molar 25% Ag (10% Ag) is 28 (26) nm.

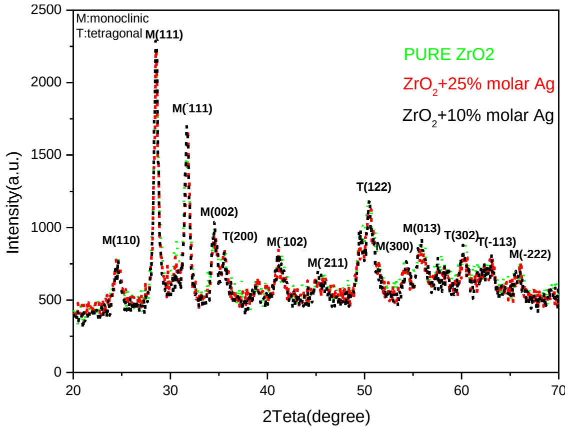

Fig.1: The acquired XRD curve for the both pure and Ag-doped ZrO_2.

FE-SEM images of pure and Ag-doped samples were shown in Fig.2 (a) and (b), respectively. It can be noticed that the formed particles are uniform and spherical. Moreover, it is indicated that with adding of Ag impurities, the particle size becomes larger. Fig.3 shows the absorption spectra of pure and Ag-doped ZrO_2 nanoparticles. The pure ZrO_2 nanoparticles had an absorption peak at 270 nm. Also, Ag-doped samples had an absorption peak at 227 nm (a molar 25% Ag) and 245 nm (a molar10% Ag).

The optical band gap of these nanoparticles has been calculated via the Tauc relation (as shown Fig.4):

$$\alpha h\nu = A(h\nu - E_g)^{0.5} \qquad (2)$$

Where $h\nu$ is the photon energy, h is Planck's constant, α is the absorption coefficient, E_g is the optical energy gap for allowed direct transition, A is the constant, The values of E_g obtained 3.88, 3.69 and 3.49 eV for pure, 25%Ag and 10% Ag-doped, respectively.

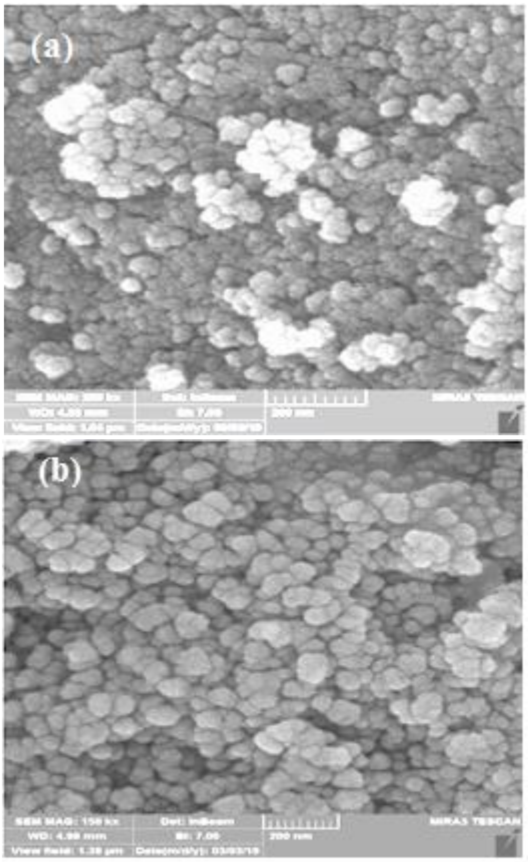

Fig.2: The FE-SEM image of (a) pure ZrO2 , (b) 25% Ag-doped ZrO2.

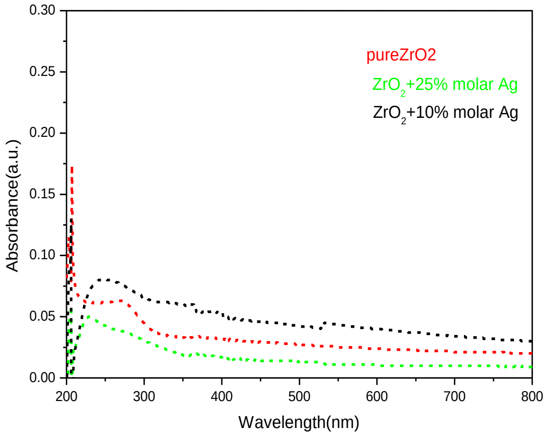

Fig.3: The absorption diagram of both pure and Ag-doped ZrO_2.

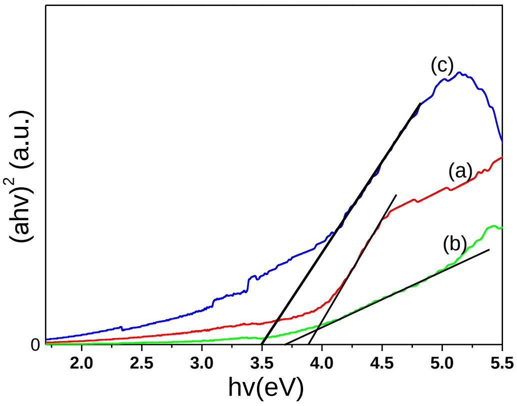

Fig.4: The optical energy gap of (a) pure ZrO2, (b) 25% Ag-doped ZrO_2, (c) 10% Ag-doped ZrO_2.

IV. CONCLUSION

In summary, pure and Ag-doped ZrO_2 nanoparticles have been successfully prepared by a sol-gel route. The increase of Ag molar ratio gives rise to better crystallinity and the increase of the size of ZrO_2 nanocrystallites. Furthermore, the doping of Ag in ZrO_2 decreased the optical energy gap.

REFERENCES

[1] U. Troitzsch, Journal of American Ceramic Society, vol. 89, pp. 3201-3210, **2006**.
[2] B. Sathyaseelan, E. Manikandan, I. Baskaran, K. Senthilnathan, K. Sivakumar, M.K. Moodley, R. Ladchumananandasivam, and M. Maaza, Journal of Alloys and Compounds, vol. 694, pp. 556-559, **2017**.
[3] D. He, Y. Ding, H. Luo, and C. Li, Journal of Molecular Catalysis A: Chemical, vol. 208, pp. 267–271, **2004**.
[4] R.F. Haaker, and R.C. Ewing, Journal of American Ceramic Society, vol. **64** (11), **1981.**

An Experimental Approach to the Surface Properties of Biodiesel Components and Their Mixtures with Some Alcohols

M.M. Alavianmehr, H. Ghazipour, H. Ghazipour*
Department of Chemistry, Shiraz University of Technology, Shiraz 71555-313, Iran
Email: halehgh@gmail.com, alavianmehr@sutech.ac.ir

Abstract: The surface tensions were measured for pure and binary mixtures of methyl caprate and ethyl myristate with 2-butanol and 1,2butandiol over the 0 to 1 composition range and at nine different temperatures between 293.15 K and 333.15 K with an interval of 5 K and at atmospheric pressure. Surface tension was measured by capillary rise method using a homemade capillary apparatus, in which the liquid/vapor equilibration can be accomplished and maintained practically. Concentration dependent surface entropy and surface energy of the solutions were calculated and studied.
The magnitude of surface tension data have been used to discuss the intermolecular forces in mixtures.

Keywords: Biodiesel, Capillary rise method, Equilibrating liquid/vapor Surface, Surface entropy, Surface tension

I. INTRODUCTION

Biodiesel fuel can be an appropriate substitute to petroleum based fuels in the transportation sector. Liquid biofules can be directly used in combustion engines unlike other natural energies. (geo thermal energy, solar power, etc.), but physicochemical properties such as surface tension are different from those of the petroleum-based diesels. These properties change the engine injection timing and influence combustion and exhaust emission. Therefore reliable data for surface tension and other physicochemical properties of biodiesels and their methyl/ethyl ester components are required for design of equipment to be used in industry of oil and fuel. [1,2]

These measurements reports surface tensions (γ) for pure and binary mixtures of methyl caprate and ethyl myristate with 2butanol and 1,2butandiol over extended range of temperature.

II. METHODS

Methyl caprate, Ethyl myristate, 2butanol and 1,2butandiol were used in this study.

The surface tension of pure liquids and their binary mixtures was measured by means of a capillary apparatus Fabricated in our laboratory.

III. RESULTS AND DISCUSSION

The capillary rise method is one of the accurate methods of measuring surface tension, though it is very susceptible to experimental errors. Good temperature control, stable thermal equilibrium, high purity chemicals, and ultra clean glassware could substantially reduce the sources of error to a minimum. [3] The capillary apparatus containing solution sample was sealed under vacuum, and thus the solution and its atmosphere is isolated from atmospheric gases. As the temperature increases, the pressure of the vapor over the solution surface is increased too. However, it does not alter much the surface tension measurement because the differential mode of the capillary apparatus balances the fluctuation of vapor in both sides. This suggests that the measurement should be done well below boiling point to prevent large fluctuation characteristics of high temperature.

By measuring the capillary height (h) and the solution density (ρ), the surface tension (γ) is calculated:

$$2\gamma\cos\theta = r\rho g\left(h+\frac{r}{3}\right) \qquad (1)$$

Where r is the capillary radius, ρ is the liquid density, and g is the acceleration of gravity. The second terms in parenthesis is due to the first order height correction, and takes into account the weight of liquid above the meniscus surface in the capillary, which is assumed to be spherical.

The plot of surface tension as a function of temperature for methyl caprate + 2butanol mixture at different mole fractions is shown in Fig.1.

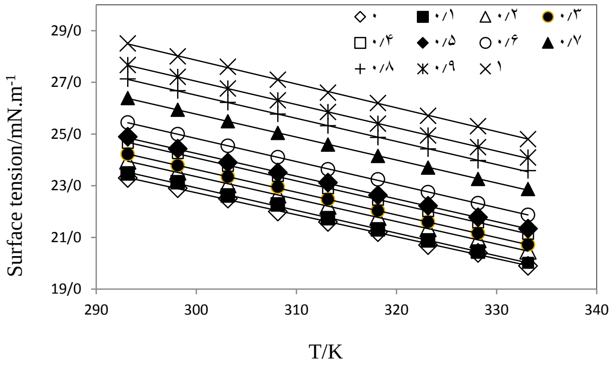

Fig.1: Surface tension of methyl caprate + 2butanol mixtures versus temperature at different mole fractions. Mole fraction of the methyl caprate is shown in the legend.

As above-mentioned figure show the surface tension of binary mixtures at all mole fractions decreases with temperature rather linearly.

The surface tension of methyl caprate (1) + 2butanol (2) and ethyl myristate (1) + 2butanol (2) mixtures at same mole fraction (x1=0.1) are compared. This comparison indicates that methyl caprate and ethyl myristate have the same effect on surface tension of 2butanol as a solvent.

IV. CONCLUSION

Using the capillary rise method, the surface tension of pure and binary mixture of methyl caprate and ethyl myristate with 2-butanol and 1,2butandiol have been measured. Their temperature dependence also was measured from which the surface thermodynamic functions, surface entropy and surface energy, were studied.

REFERENCES

[1] M. S. Graboski and R. L. McCormick, Progress in energy and combustion science, vol. 24, pp. 125-164, **1998.**

[2] A. Demirbas, Progress in energy and combustion science, vol. 31, pp. 466-487, **2005.**

[3] G. Douhéret, M. I. Davis, J. C. R. Reis and M. J. Blandamer, ChemPhysChem, vol. 2, pp. 148-161, **2001**.

Application of Persimmon Tree Leaves for Dye Removal

Gh. Kouchakzadeh*
Department of Chemistry, Islamic Azad University, Khorramabad branch, Khorramabad, Iran
Email:gh_kouchakzadeh@yahoo.com

Abstract*:* In recent years, there is a growing interest in using low cost adsorbents. Tree leaves, wool fiber, nanoclay are available adsorbent materials. In this work, persimmon tree leaves as adsorbent can well remove neutral red dye from solutions. Nowadays dyes are present in wastewater of different industries and lead to environmental pollution. Desired amount of persimmon tree leaves in dye solutions could remove dye up to 97%. Adsorption isotherms and the thermodynamic parameters were calculated. The thermodynamic studies indicated to the adsorption reaction was a spontaneous and exothermic process.

Keywords: Adsorption capacity, Freundlich isotherm, Langmuir isotherm, Neutral red dye, Persimmon tree leaves.

I. INTRODUCTION

Dyes apply in various fields widely. They are used in different industrials such as leather industry, textile industry, Pharmacy and other affiliated industries. Industrial wastewater is usually one of the major pollutants of the environment [1-2]. Among different methods of removal of pollutants, adsorption technique is widely used because of its simple operation and high efficiency in removal of pollutants [3]. Numerous adsorbents such as alumina, carbon nanotubes, zeolite, plant root, natural and modified bentonite have been studied for removal of hazardous materials from wastewater [4]. In this work, persimmon tree leaves were used as adsorbent. The removal of dye carried out with high percentage by persimmon tree leaves. Removal percentage was 97.19 in 25 mg/L dye solution and 25°C.

II. METHODS

The persimmon tree leaves were dried in room temperature after collection. Neutral red dye and the using materials were purchased from Merck. For study of the adsorption isotherms, 20 ml of 25 mg/L dye solution contacted with the desired amount of adsorbent. Initial absorption of solution and equilibrium absorption were measured at λ_{max}= 490 nm by UV- vis spectrophotometer.

III. RESULTS AND DISCUSSION

Effect of *p*H

An important parameter for the adsorption is *p*H of aqueous solutions. Effect of *p*H on the dye removal at room temperature was studied by the different values of *p*H of solution from 2.0 to 7.0 at 25°C. Dye sorption percentage was calculated by Eq. (1):

$$sorption\% = \frac{C_0 - C_e}{C_0} \times 100 \qquad (1)$$

where C_0 and C_e are initial and equilibrium concentrations of dye solution in mg/L respectively. The values of dye sorption% for solutions from *p*H =2.0 to *p*H=7.0 are shown in table 1.

Table1: The values of dye sorption% for solutions by persimmon tree leaves with different *p*Hs

*p*H	2	3	4	5	6	7
Sorption %	61.61	78.72	85.55	90.17	89.83	55.38

This result showed that optimum *p*H for dye solutions was *p*H=5 and maximum amount of dye removal carried out in *p*H=5.

Effect of value of adsorbent

Considering optimum *p*H, solutions with concentrations of 25 mg/L were prepared and different amounts of adsorbent were weighted (0.02, 0.04, 0.06, 0.08, 0.1 and 0.2g) at 25°C. Dye removal percentage was calculated for them. When the value of adsorbent was 0.1 g, dye sorption% was 97.19%; thereby the amount of o.1g adsorbent was recognized as optimum value of adsorbent.

Table 2: The values of dye sorption% for solutions by persimmon tree leaves with different values of adsorbent

Adsorbent(g)	0.02	0.04	0.06	0.08	0.1	0.2
Sorption%	72.80	89.76	95.38	96.85	97.19	95.55

Effect of contact time

The sorption of neutral red dye on persimmon tree leaves at *p*H=5 and the amount of adsorbent= 0.1g as a function of contact time were studied. Dye removal was carried out in different shaking times (10, 20, 30, 40, 50, 60 min) at 25°C. The results of sorption% for contact time were shown in table 3. Accordingly, optimum contact time was 10 min.

Table 3: The values of dye sorption% for solutions by persimmon tree leaves with different contact times

Time(min)	10	20	30	40	50	60
Sorption %	96.41	95.77	94.07	86.04	93.32	94.14

Effect of temperature

Temperature is one of the most effective parameters that can affect the adsorption behavior. The effect of temperature was studied by different temperatures of solutions from 25°C to 40°C. Results showed that dye adsorption percentage has decreased with increasing the temperature from 97.19% to 81.75%.

Adsorption isotherms and thermodynamic parameters

The equilibrium adsorption isotherm can provide information about the surface properties and adsorption behavior. In this research, Langmuir and Freundlich models were used for dye removal in solutions.

The amount of dye per unit mass of tree leaves, q_e, at the equilibrium time was calculated by Eq. (2):

$$q_e = \frac{(C_0 - C_e)V}{m} \qquad (2)$$

where C_0 and C_e are initial and equilibrium concentrations of dye solution in mg/L respectively, V is the volume of dye solution in L and m is the mass of the persimmon tree leaves in g. Adsorption equilibrium data of solutions in 25°C were correlated with the Langmuir and Freundlich isotherms.

$$\frac{1}{q_e} = \frac{1}{q_m} + \left(\frac{1}{q_m K_L}\right)\left(\frac{1}{C_e}\right) \qquad (3)$$

$$ln q_e = \frac{1}{n} \ln C_e + \ln K_F \qquad (4)$$

In Eq. (3) the values of q_m and K_L represent the maximum adsorption capacity of adsorbent (mg/g) and Langmuir constant (L/mg), respectively. In Eq. (4) K_F and n are the Freundlich constants [5].

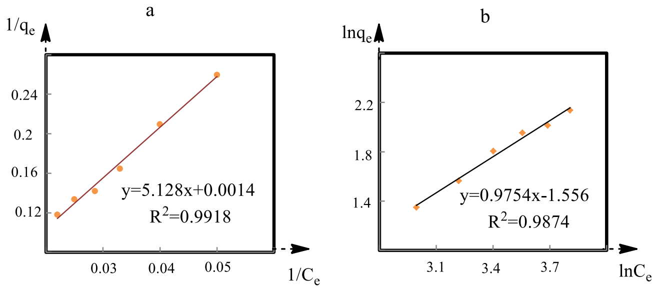

Fig.1: Adsorption isotherms in 25°C a) Langmuir isotherm b) Freundlich isotherm

Fig. 1 represented results of isotherms of dye removal by persimmon tree leaves. The based on a comparison of the correlation coefficient R^2 values, Langmuir model fitted adsorption result better than Freundlich model.

A significant parameter resulting from Langmuir equation is separation factor, R_L. The R_L equation is given as follows:

$$R_L = \frac{1}{1 + C_0 K_L} \qquad (5)$$

According to R_L value, adsorption is more favorable when $0 < R_L < 1$ [6]. The separation factor for all concentrations was evaluated and the value range was from 0.995 to 0.988. These results can confirm a favorable adsorption process.

According to adsorption isotherms equations in Fig. 1, maximum adsorption capacity of adsorbent, q_m, Langmuir constant, K_F and n were calculated. Table 1 shows its results. If n values are in the rang $1 < n < 10$, the adsorption process is favorable.

Table2: parameters of adsorption isotherms for dye removal by persimmon tree leaves

T (k)	**Langmuir model**		**Freundlich model**	
	q_m (mg/g)	K_L(L/mg)	n	K_F
298	714.28	2.73×10^{-4}	1.025	0.211

The value of n>1 in Freundlich model also represent a favorable adsorption.

Thermodynamic parameters such as ΔH, ΔG and ΔS can represent that the adsorption process is spontaneously carried out and it is an exothermic process. The values of ΔH, ΔG and ΔS were calculated by Eq. 6 and 7. The change in enthalpy was -114.83 kJ/mol and the values of ΔG and ΔS were -5.23 kJ/mol and -367.79 J/(mol K) respectively.

$$\Delta G = -RT ln K_d \qquad (6)$$

$$\Delta G = \Delta H - T\Delta S \qquad (7)$$

where R is gas constant and K_d is equilibrium constant that can calculated to $K_d = \frac{C_0 - C_e}{c_e}$.

CONCLUSION

Adsorption of neutral red dye on persimmon tree leaves is investigated under optimal conditions. First pH of solutions, desired value of adsorbent, equilibrium time and desired temperature were determined. Then adsorption experiments carried out under this condition. The results showed that persimmon tree leaves can be an excellent adsorbent for dye removal. The maximum adsorption capacity (q_m) that obtained from the Langmuir isotherm, was 714.28 mg/g at

25°C. Results of dye removal fitted in Langmuir model (R^2 values=0.9918) better than Freundlich model (R^2 values=0.9874). Thermodynamic parameters such as ΔH, ΔG and ΔS were calculated. The negative values of ΔG indicated that process of dye removal was spontaneous. Also, the value of ΔH indicated the exothermic nature of the process of dye removal.

REFERENCES

[1] Gh. Kouchakzadeh, Z. Derikvand, J. Iranian Chem. Res., 5 (1), pp. 13-18, **2012**.

[2] M. Zarrabi, M. Samarghandi, M. Noori Sepehr, E. Mohammadi, and et al., Journal of Health Ardebil, 2 (1), pp. 19-30, **2011**. [Persian]

[3] G. Zhao, J. Li, X. Wang, Chemical Engineering Journal, 173, pp. 185-190, **2011**.

[4] X. Yang, Sh. Yang, Sh. Yang, J. Hu, X. Tan, X. Wang, Chemical Engineering Journal, 168, pp. 86-93, **2011**.

[5] J. xu, L. Wang, Y. Zhu, Langmuir, 28,pp. 8418-8425, **2012**.

[6] M. Mohammadi, Kh. Shamsi, A. Dargahi, P. Sekhavati, J. Adv. Environ Health Res., 5, pp. 101-106, **2017**.

Studying the Effect of Nitric Acid on the Physical Chemistry Properties of the Prepared Extrudates Catalyst Support from Boehmite Powder of Nephleensinite Ore Mines

Zahra Shahidian[1,*], Fatemeh Tavakolzadeh[1], Sara Beshkoofeh[1], Babak hemshadi[1]
[1] Iranian Institute of Research and Design in Chemical Industries (Acecr), Karaj, Iran
*E-mail: *z_shahidian@yahoo.com*,

Abstract: In this research, for the first time, the extrudates gamma alumina prepared from Boehmite powderof the Nephleensinite ore mine. In order to enhance the physical properties of the catalyst support, the prepared extrudats were treated in high concentration nitric acid at different times, and the effect of treatment times on the basic properties as the Surface Area (S.A.) and Average Pore Diameter (A.P.D.) were studied. These effects were studied by using X-ray diffraction (XRD), N_2-adsorption/desorption (BET) and Scanning Electron Microscope (SEM) techniques. The sample 3 with 72 hr aging time was selected as the optimized sample.

Keywords*:* acidic aging time, extrudates gamma alumina, acidic treatment, catalyst support

I. INTRODUCTION

The production of alumina is done under two general methods of using Bauxite and extraction from Nephlinsinite ore throughout the world, Nephleinsinite is a type of igneous ore that contains useful compounds of K_2O, Na_2O, Al_2O_3 and SiO_2 which become diverse commercial products in the course of various processes. Appropriately, Alumina production from bauxite is the most commonly used aluminum production methods. However, the economics of making alumina from Nephlinsinite are more cost effective because of the supply of cement, sodium carbonate, potassium carbonate, potassium sulfate and silicate. Since the cost of using Nephleinsinite is 15 to 20 percent cheaper than Bauxite, the technology of alumina production from Nephleansinite is perfectly considered and expanding in most of the countries over the globe. So that, in order to improve the physical properties of the catalyst support, the extrudates were stored in a concentrated nitric acid solution at different times. The effects of nitric acid on the catalyst support were studied by using XRD, BET and SEM techniques.

II. EXPERIMENTAL SECTION

In this research, Boehmite powder was produced from Nefalinsinat Azar Shahr ore mine as a support powder and all the other raw materials, including nitric acid and hydroxyethyl cellulose, were used with laboratory purity (Merck Germany). Therefore, the PW1800 was utilized to perform the XRD test. The Belsorp mini II device was used to perform the BET tests.

a) General Method for preparing the Gamma Alumina Catalyst support

In order to prepare the extruded catalyst support, firstly; Boehmite powder is mixed with 5% by weight of hydroxyethyl cellulose powder (HEC) and then spray enough water on it. Afterwards, the mixture is well belended to obtain a homogeneous paste. The paste was passed through the extruder and the extrudates were dried for 2 hours. Then they kept at 120 ° C for 1 night in an oven. Later, they were calcined in the furnace with a temperature of 100 ° C / hr to 600 ° C.

b) Studying aging time

After preparation of the extrudates catalyst support, 65% nitric acid solution was prepared in four containers so as to evaluate the effect of aging time. Alternatively, extrudates were stored in each of these containers for 72, 48, 24 and 120 hours, and then extrudates were kept in oven for 1 night at 120 ° C.

III. RESULTS AND DISCUSSION

a) The effects of aging times on the extrudates properties

The effect of aging time was investigated on catalyst support by nitric acid concentration for five times.The results are shown in Table 1. All prepared samples except sample 4 had a high mechanical strength. Because sample 4 had a fragile texture, the BET test was not done at it.

The maximum Pore Volume (P.V.) and A.P.D. of the catalyst support are resulted in 65% nitric acid with 72 hr aging time. Besides, longer aging time will lead to a reduction in the mechanical strength of the catalyst support. Therefore, sample 3 was selected as an optimized sample.

Table 1. The BET and mechanical results of untreated catalyst support and treated samples

Sample Name	Aging time(hrs)	S.A (m^2/gr)	P.V.(cc/gr)	A.P.D.
Untreated	0	231	0.54	9.06
Number 1	24	221	0.6	10.88
Number 2	48	216	0.67	12.39
Number 3	72	226	0.76	13.49
- Number 4	120	–	–	–

b) XRD Analysis

The crystalline structure of the untreated and the optimized sample (sample No.3) was investigated using XRD analysis. It can be observed that both samples have γ-Al_2O_3 structure. Furthermore, aging in nitric acid did not affect its crystalline phase in spite of its effect on the properties of the tissue of the sample. In Table 2, the XRD analysis of these two samples is presented properly.

Table 2 - XRD analysis results of two untreated and an optimized sample

Optimized sample(No 3)		**Untreated sample**	
JCPDS Card no. 004-0858	**d spacing (observed)**	**JCPDS Card no. 004-0858**	**d spacing (observed)**
2.75	2.7806	2.750	2.734
2.43	2.4095	2.430	2.453
2.300	2.2746	2.300	2.289
2.000	1.9746	2.000	2.014
1.400	1.3984	1.400	1.410

c) Scanning Electron Microscopy Studies

Figure 1 shows the SEM images for both of the untreated (left) and the optimized sample (right), the SEM results show that with nitric acid treatment no agglomeration was ocurred.

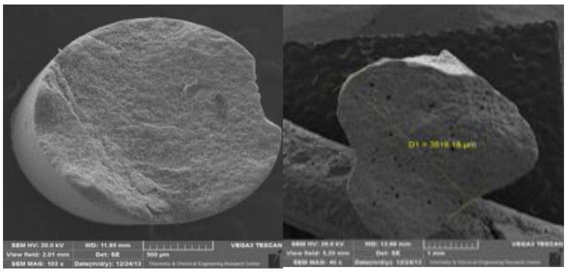

Figure 1. SEM images of untreated and optimized sample

IV. CONCLUSION

- Aging the extrudates in nitric acid cause to pilling effect. By increasing the aging times in nitric acid, the P.V. and A.P.D. of extrudates are increased.
- Due to the corrosive nature of nitric acid,the mechanical strength propreties of the extrudates which are aged more than 72 hr are reduced.
- Aging in nitric acid does not change the crystalline phase of catalyst support; the the gamma alumina crystalline phase remains appropriately.
- The extrudates catalyst support obtained from the aging in nitric acid has optimized S.A. properties. They can be used as a catalyst support in the desulfurization processes of heavy oil fractions containing large sulfur molecules.

REFERENCES

[1] M. Absi-Halabi, A. Stanislaus, and H. Al-Zaid, Applied Catalysis A: General, vol. 101, pp 117-128, **1993**.
[2] J. Ancheyta, deactivation of heavy oil hydroprocessing catalyst, John Wiley & Sons, Inc., Hoboken, New Jersey, **2016**.
[3] A. Stanislaus, K. Al-Dolama, M. Absi-Halabi, Journal of Molecular Catalysis A: Chemical, vol. 181, pp 33-43, **2002**.
[4] US 2009/0104108 A1.
[5] J. G. Speight, The desulfurization of heavy oils, Marcel Dekker, Inc., New York, **1999**.

Efficient eletrocatalytic hydrogen evolution reaction on MoS_2 nanosheets coated carbon cloth

S. Yousefzadeh[a*], ***N. Morovati***[a]
Department of Physics, Faculty of Science, Sahand University of Technology, Tabriz, P.O. Box 51335-1996, Iran
Email:Yousefzadeh@sut.ac.ir

Abstract: In this work, MoS_2 nanosheets were fabricated by two steps sonication and deposited on activated carbon cloth by binder free electrophoretic technique. Scanning electron microscopy (SEM) confirmed the presence of the MoS_2 nanosheets on carbon cloth. The electrochemical measurements exhibited overpotential of -248 mV for the MoS_2 nanosheets on carbon cloth with time deposition of 60 min.

Keywords: MoS_2 nanosheets, Hydrogen evolution reaction (HER), Electrophoretic deposition, Overpoential.

I. INTRODUCTION

In recent years, production of clean and sustainable energy is considered as a main challenge for human society. Among renewable energies, hydrogen is an appropriate candidate due to its high energy density. Hydrogen can be generated by electrocatalytic water splitting, denoted as hydrogen evolution reaction (HER). Platinum (Pt) and Pt based catalyst are the most efficient catalysts for HER and benefits from high stability and low overpotential in hydrogen production [1]. But these materials are very scarce and expensive and can't be used in large scale. Therefore, alternative low cost substance with high stability should be introduced in the HER. Carbides [2], nitrides [3], graphite composites [4] and intermediate metal dichalcogenides (TMDs) [5] have been attended as comparable materials with Pt. MoS_2 is one of the most prominent members of the TMDs for the HER, with a graphite-like structure and catalytic active edges. In order to achieve a structure with high active edge sites, exposed to the electrolyte for improved HER efficiency, the MoS_2 morphology can be engineered or arranged in three dimensional (3D) structures.

In this work, the MoS_2 nanosheets with highly active edge sites were synthesized by two steps sonication process. For the construction of the 3D structure, the MoS_2 nanosheets were deposited on carbon cloth by the electrophoretic method. Carbon cloth was used as a conductive, flexible and stable substrate. Electrochemical measurements were performed for evaluation of electrocatalytic hydrogen production.

II. METHODS

For synthesis of the MoS_2 nanosheets, MoS_2 bulk powder was sonicated in two steps. First, 200 mg of MoS_2 powder was stirred in 100 ml of a solution of water and ethanol (v:v 1:1) for one hour and then, bath sonicated for 320 min at room temperature. The obtained black suspension was centrifuged at 4000 rpm for 5 minutes and rested for 24 hours. After 24 hours, the 2/3 of supernatant was separated from the solution and tip sonicated in ice bath for one hour (probe diameter 3 Millimeter with 0.5 seconds on and 0.5 seconds off cycles. The tip sonicated solution was centrifuged at 8500 rpm for 20 min to achieve MoS_2 nanosheets.

The MoS_2 nanosheets were deposited on electrochemically activated carbon cloth (ACC) at an applied voltage of 100 V between carbon cloth and graphite during 60 and 20 min in MoS_2 nanosheets dispersion. The obtained electrodes were named as MoS_2(20)/ACC and MoS_2(60)/ACC. To improve hydrophilicity of carbon cloth, its activation was performed by using a potentiostate (SAMA500) and three electrodes cell (Pt as counter electrode, Ag/AgCl as reference electrode and carbon cloth as working electrode) in a mixture of %65 HNO_3 and %98 H_2SO_4 acid as electrolyte under potential of 3 V for 300 sec.

The linear sweep voltammetry (LSV) measurement has been utilized at scan rate of 5 mV/s via three-electrode cell with an Ag/AgCl, a Pt plate and MoS_2 nanosheets coated on the ACC as the reference, counter and working electrode, respectively. All the electrodes were put into 0.5 M H_2SO_4 aqueous solution as electrolyte.

III. RESULTS AND DISCUSSION

Fig. 1(a) showed electrochemically activated carbon cloth that constitute of carbon fibers. After deposition of the MoS_2 nanosheets, the surface of the ACC substrate has been covered with MoS_2 nanosheets. Based on SEM images, amount of the MoS_2 nanosheets increased by increasing of deposition time.

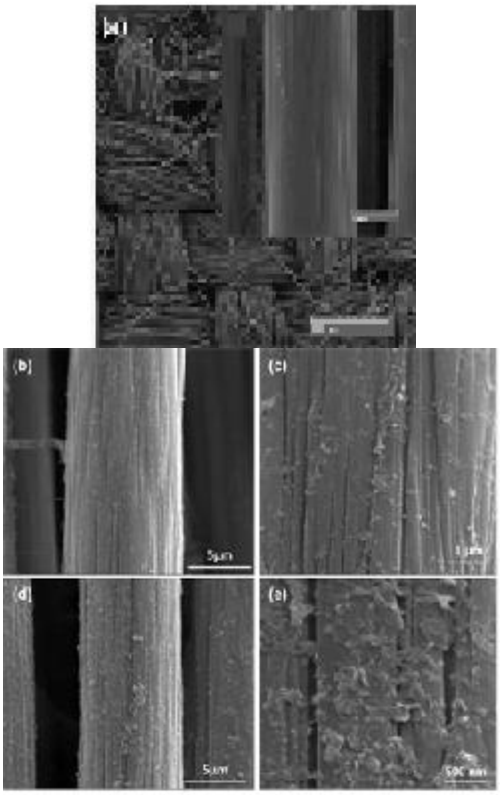

Fig.1: SEM images of (a) ACC, (b and c) MoS_2(20)/ACC and (d and e) MoS_2(60)/ACC electrodes.

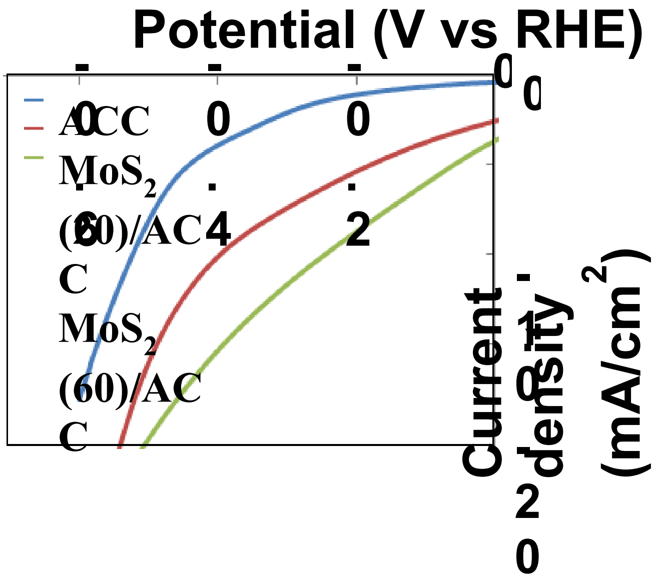

Fig.2: LSV curves of the ACC, MoS_2(20)/ACC and MoS_2(60)/ACC samples.

The HER activity of the MoS_2 plane is resulted from its edge sites. The MoS_2 nanosheets in film form possess the maximal active edge sites on a given geometric surface. The LSV curves for the ACC, MoS_2(20)/ACC and MoS_2(60)/ACC samples have been illustrated in Fig.2. As can be seen, the overpotential of the MoS_2(20)/ACC and MoS_2(60)/ACC electrode is clearly lower than those of ACC. At current density of −10 mA/cm^2, the overpotentials of the MoS_2(20)/ACC and MoS_2(60)/ACC are −399 and −248 mV versus reversible hydrogen electrode (RHE), respectively. Based on SEM images and LSV curves, higher deposition time gives rise to high amount of catalyst deposition on ACC and therefore, high HER efficiency. Furthermore, activated carbon cloth acted as stable and conductive substrate. The electrophoretic deposition approach introduces facile, binder-free, and cost-effective procedure for preparation of the MoS_2/ACC. The MoS_2/ACC electrodes possess great potential for reliable and large-scale catalytic applications.

IV. CONCLUSION

In this study, highly active and low cost MoS_2/ACC electrodes have been fabricated via simple electrophoretic method. This result could be further extended to other catalytic applications.

REFERENCES

[1] S. Elmas, W. Beelders, S. J. Bradley, R. Kroon, G. Laufersky,
M. Andersson, and T. Nann, ACS Sustainable Chemistery & Engineering, vol. 5, pp. 10206-10214, **2017**.
[2] W. Gao, Y. Shi, Y. Zhang, L. Zuo, H. Lu, Y. Huang, W. Fan and T. Liu, ACS Sustainable Chemistery & engineering, vol. 4, pp. 6252-7230, **2016**.
[3] X. Tan, H. A. Tahini and S. C. Smith, ACS Catalysis, vol. 6 ,pp.7071-7077, **2016**.
[4] Y. Shi, W. Gao, H. Lu, Y. Huang, L. Zuo, W. Fan and T. Liu, ACS Sustainable Chemistery & engineering, vol. 5, pp. 6357-7449, **2017**.
[5] Y. Zhang, L. Zuo, Y. Huang, L. Zhang, F. Lai, W. Fan and T. Liu, ACS Sustainable Chemistery & Engineering, vol. 3, pp. 3012-3496, **2015**.

Investigating the Effect of Pantaoprazole as an Environment-friendly Inhibitor for Corrosion Protection of Mild Steel

H. Tajabadipour[a]***, H. Mohammadimanesh***[a]***, M. Shahidi Zandi***[b]*******
[a]*Department of Chemistry, College of Science, Yazd University, Yazd, P.O. Box 89195-741, Iran*
[b]*Department of Chemistry, Kerman Branch, Islamic Azad University, Kerman, P. O. Box 7635131167, Iran*
Email:meshahidizandi@gmail.com

Abstract: The corrosion of mild steel in 0.5 M sulphuric acid solution in the absence and presence of different concentrations of pantoprazole was studied using Tafel polarization and electrochemical impedance spectroscopy (EIS) techniques. Results show that the addition of inhibitor to acid solution leads to decreasing the corrosion rate. The inhibitor behaves as a mixed type inhibitor because it affected both cathodic and anodic branches of the polarization curves. The results of Tafel polarization and EIS indicated that the adsorption of pantoprazole on mild steel in sulphuric acid solution followed Langmuir isotherm. There is a good agreement between the inhibition efficiencies which are obtained from polarization and EIS measurements.

Keywords: Corrosion inhibitor, Electrochemical impedance spectroscopy (EIS), Mild steel, Pantoprazole, Tafel polarization.

I. INTRODUCTION

Acid solutions are widely used in various and important industrial processes such as acid pickling, acid cleaning, acid descaling and oil well acidizing. Because of the general aggressiveness of acid solutions, inhibitors are commonly used to reduce corrosion rate of metallic materials. A corrosion inhibitor is a substance which, when added to an environment in a small concentration, effectively reduces the corrosion rate of a metal exposed to that environment [1]. However, because of numerous destructive effects that they have created in the environment, the use of these compounds as inhibitor has been questioned recently, especially by environmentalists. Thus, the development of novel non-toxic or low-toxic corrosion inhibitors from natural sources has been considered as an important issue [2-4]. Recently studies have paid attention to the development of drugs as environment-friendly inhibitors for metallic corrosion.

In this paper, the inhibition effect of pantoprazole on the corrosion of mild steel is investigated in 0.5 M H_2SO_4 solution by using potentiodynamic polarization and electrochemical impedance spectroscopy (EIS) measurements.

II. METHODS

The working electrode used here is made of mild steel (Ck45) with surface area of 100 mm^2. The sample, as the working electrode, was attached to a copper wire at one side, and other side was sealed by epoxy resin. A potentiostat/galvanostat Autolab 302N supported by Nova 1.9 software was used for performing electrochemical tests. The counter electrode was prepared from a rod of platinum with surface area of 100 mm^2 and reference electrode was a saturated (KCl) Ag/AgCl electrode.

A sinusoidal potential perturbation of 10 mV versus OCP in the 100 kHz-10 mHz frequency range was used in the EIS measurements. Tafel curves were recorded at a scan rate of 1 mV/s.

III. RESULTS AND DISCUSSION

A. *Potentiodynamic polarization*

The Tafel curves of mild steel in 0.5 M H_2SO_4 solution in the absence and presence of different concentrations of pantoprazole are shown in Fig. 1. The relevant parameters are listed in Table 1. Corrosion current density (i_{corr}) decreased by increasing the concentration of inhibitor. This drug behaved as a mixed inhibitor since the corrosion potential has not shifted to any direction markedly.

Table 1 shows the values of corrosion inhibition efficiency (IE) expressed by the following equation:

$$IE_p(\%) = \frac{i_{corr} - i'_{corr}}{i_{corr}} \times 100 \qquad (1)$$

where i_{corr} and i'_{corr} are corrosion current densities in the uninhibited and inhibited solutions, respectively. These values indicate that the drug acts as an effective inhibitor.

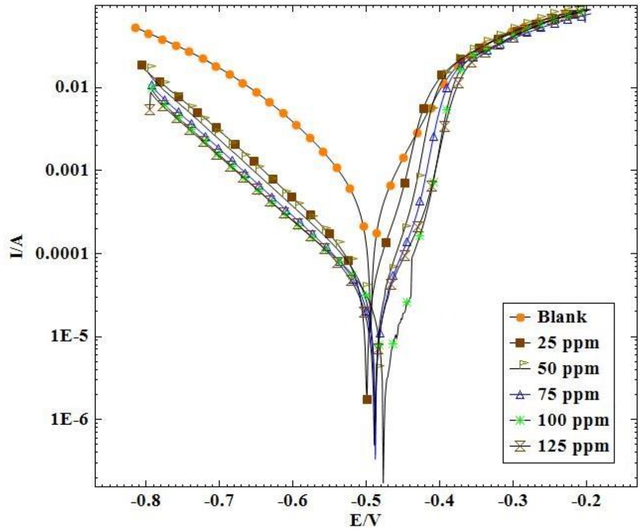

Fig.1: Polarization curves for mild steel in 0.5 M H_2SO_4 containing different concentrations of pantoprazole

Table1: Polarization parameters for mild steel in 0.5 M H_2SO_4 containing different concentrations of pantoprazole

C /ppm	i_{corr}/μA.cm^{-2}	-E_{corr}/mV	IE$_P$(%)
0	711	495	-
25	82	499	88
50	48	487	93
75	38	488	95
100	22	477	97
125	16	489	98

B. *Electrochemical impedance spectroscopy*

Fig. 2 shows Nyquist curves for mild steel in 0.5 M H_2SO_4 in the absence and presence of different concentrations of pantoprazole. EIS parameters are listed in Table 2. It is evident that R_{ct} values increased by increasing the concentration of inhibitor.

The values of IE in Table 2 were computed using the following equation:

$$IE_{EIS}(\%) = \frac{R'_{ct} - R_{ct}}{R'_{ct}} \times 100 \qquad (2)$$

where R_{ct} and R'_{ct} are the charge transfer resistance before and after addition of the inhibitor to the corrosive media, respectively. The IE values acquired from the EIS method (Table 2) are completely consistent with those acquired from the polarization method (Table 1) and actually confirm each other.

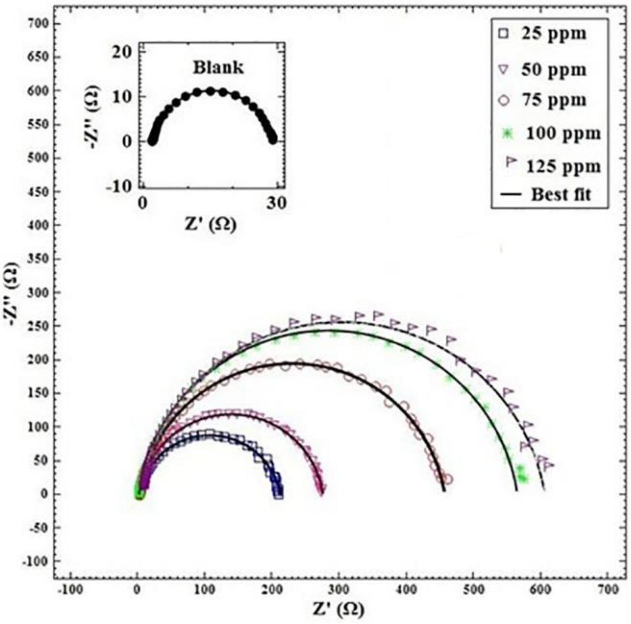

Fig.2: Nyquist plots for mild steel in 0.5 M H_2SO_4 containing different concentrations of pantoprazole

Table2: Impedance parameters for mild steel in 0.5 M H_2SO_4 containing different concentrations of pantoprazole

C /ppm	R_{ct}/Ω.cm^2	IE$_{EIS}$(%)
0	27	-
25	210	87
50	271	90
75	455	94
100	563	95
125	604	96

IV. CONCLUSION

The adsorption and inhibition effects of pantoprazole on the corrosion behavior of mild steel in 0.5 M H_2SO_4 were studied using electrochemical techniques such as Tafel and EIS. The data acquired from potentiodynamic polarization and EIS measurements indicated that the adsorption of pantoprazole on mild steel in 0.5 M H_2SO_4 follows the Langmuir isotherm. Due to easy application, reasonable cost, low toxic properties and high solubility in acidic media, Pantoprazoles could be offer as promising candidate for corrosion inhibition

REFERENCES

[1] G. Golestani. M. Shahidi, D. Ghazanfari. Appl. Surf. Sci. vol. 308, pp. 347-362, **2014**.
[2] M.R. Gholamhosseinzadeh, R. Farrahi-Moghaddam. Progress in Color, Colorants and Coatings vol. 12, pp. 15-23, **2019**.
[3] Z. Golshani, S.M.A. Hosseini, M. Shahidi Zandi, M.J. Bahrami. Mater. Corros. In Press **2019**.
[4] M.M. El-Deeb, E.N. Ads, J.R. Humaidi. Int. J. Electrochem. Sci vol. 13, pp. 4123-4138, **2018**.

Synthesis of new nanocomposite vanadium containing phosphomolybdovanadate / polyvinyl alcohol as a nanocatalyst for germination of barley seeds

Mohammad Ali Rezvani [* a] ***and Hossein Rezvani*** [*b]

[a] *Department of Chemistry, Faculty of Science, University of Zanjan, Zanjan, Iran*
[b] *Scientific Staff of Golestan Research and Education Center of Agricultural and Natural Resources Organization, Agricultural Research and Education Organization, Gorgan, Iran.*
**Corresponding author: E-mail address: marezvani@znu.ac.ir hosinrezvani@yahoo.com*

Abstract*:* In this work, a new organic-inorganic hybrid nanocomposite $PMoV_2$/PVA was synthesized on the basis of Keggin-type polyoxometalate $(N(tBu)_4)_4HPMo_{10}V_2O40$ abbreviated as $PMoV_2$) and polyvinyl alcohol (PVA). We prepared this nanocomposite by reaction of $PMoV_2$ with PVA in the presence of water, *via* a sol–gel method. The results of XRD, and SEM analysis method indicated the successful composition of the materials. The XRD studies showed that the average crystallite size of the composite particles was estimated to be about 38 nm, which confirmed by the results of SEM. The influence of the new a new organic-inorganic hybrid nanocomposite $PMoV_2$/PVA in the germination of barley seeds was investigated. In order to compare, several polyoxometalates with different concentrations used to obtain their effects on growth factors of barley seeds. From the obtained results, it is found that by applying new nanocomposite $PMoV_2$/PVA with 10 µM and 100 µM concentrations the most preferred results achieved.

Keywords: organic-inorganic hybrid nanocomposite, polyvinyl alcohol, Keggin-type polyoxometalate, barley seeds.

I. INTRODUCTION

Polyoxometalates (POMs) are well-defined oxoanionic clusters of early transition metals that have attracted growing interest for the development of advanced functional materials [1]. POMs are a type of intriguing catalysts that can be applied for a wide range of technologically relevant applications owing to reasonably high thermal stability, and reversible electron transfer ability under mild conditions [2]. Furthermore, these POMs have several advantages, including high flexibility in the modification of the acid strength, ease of handling, environmental compatibility, non-toxicity, and experimental simplicity [2, 3]. Keggin type polyoxoanions have been widely studied as homogeneous and heterogeneous catalyst for the oxidation of organic compounds. The evolution of this cluster`s chemistry is dependent upon the synthesis of new solids possessing unique structures and properties, although this still remains a challenge [3]. However, the application of this type of catalysts still suffers from some drawbacks, particularly the low surface area (1–10 m2/g) leading to the low efficiency and the high solubility, causing recycling difficulty and environmental problem [4, 5]. To overcome this disadvantage there is a need for the development of supported and heterogeneously active forms of POM [6]. Organic polymers are very easy to process due to their excellent toughness and durability and they are suitable candidates as matrices for assembling polyoxometalates. In this investigation, polyvinyl alcohol (PVA) is used to play this important and useful role as great matrices [7].

II. METHODS

sodium metavanadate was dissolved by boiling in 50 ml of water and then mixed with Na2HPO4 .The solution cooled and concentrated sulfuric acid added, after obtaining a red color solution, Na_2MoO_4•2H2O which was dissolved in 100 ml of water, added while it was stirring vigorously, followed by the slow addition of concentrated sulfuric acid. The hot solution cooled to room temperature and extracted with 500 mL of diethyl ether. Then, 0.1 g of PVA dissolved in 35 ml of hot distilled water and the temperature was fixed at 60 °C. After that, 0.1 g of (N(tBu)4)4 HPMo10V_2O_{40} was added slightly to the solution and the mixture stirred for 2 h. The jelly solution dried at 50°C for 2h. Different random experiments were done with factorial method on petri dishes on different concentrations which were 0.1, 1.0, 10 and 100 µM and as the same with several types of polyoxometalates. In this test, petri dish was used in diameter 9 cm and placed the sterile whatman filter paper at the bottom of that. To disinfect, the seeds were soaked for 30 seconds in hypochlorite 10% solution and washed with distilled water immediately. Then, in each petri dish, 25 barley seeds were placed. Then they moved to germinator with 60% relative humidity and temperature in 25/20 days/nights and length of 12 hours of light. Germinated seeds were counted to determine germination rate daily. In germinators, Barley seeds were soaked with solutions of these compounds.

RESULTS AND DISCUSSION

XRD patterns of $PMo_{10}V_2$, PVA and PMo10V2/PVA are shown in Fig. 1 and were collected in the range 0°-70° 2θ. XRD patterns (a), (b) and (c) in Fig. 1 corresponded to $PMo_{10}V^2$, PVA and PMo10V2/PVA respectively. It is obviously seen that in the XRD patterns of keggin type polyoxometalate special peak have appeared. The existence of sharp peaks in 0°-10° can prove the structure of synthesized PMoV as a keggin type. Beside, this focusing on 15°-20° and 30° is important to be sure about the structure. According to previous reporting, the XRD pattern of pure PVA must have a sharp peak in 19.7° [6]. Fig. 1 consists of required information of PVA and $(N(tBu)_4)_4HPMo_{10}V_2O_40$ (PMoV). It can be seen that the diffraction of PVA is overlapped by PMoV so the intensity around 20° decreased. Then PMoV introduced to PVA with a good interaction between them.
The SEM images, Fig. 2 (a, b, c and d), of (N(tBu)4)4HPMo10V2O40/PVA present the self- assembly of polyoxometalate with PVA. The cone-like structures are a confirmative for enough stirring rate and exact temperature and are led to this appropriate nano shape. The presence of keggin type of $PMoV_2$ on PVA, as substrate, indicates an interaction between them that was according to our expectations and can satisfy to be as an efficient catalyst for next project. The corresponding particle size distribution of the nanocatalyst is presented in Fig. 2. It is clear that, as expected, the size of $PMoV_2$/PVA particles are in the range of 38-44 nm, which proves the results of XRD analysis.

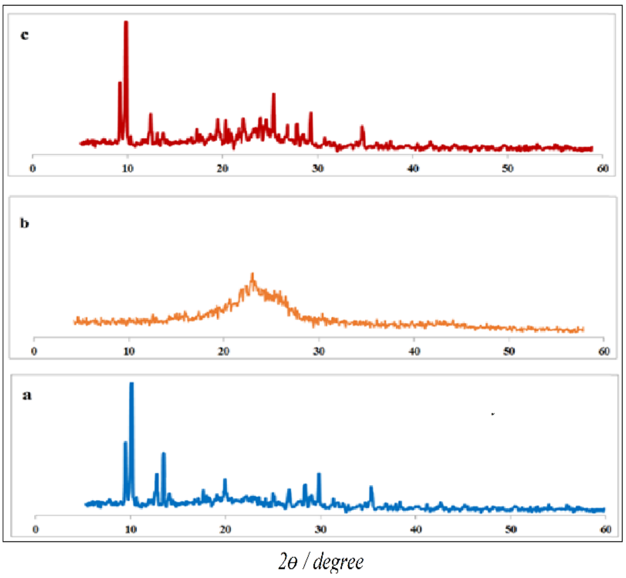

Fig. 1. XRD patterns of (a) $PMoV_2$, (b) PVA, and (c) $PMoV_2$@PVA nanocatalyst.

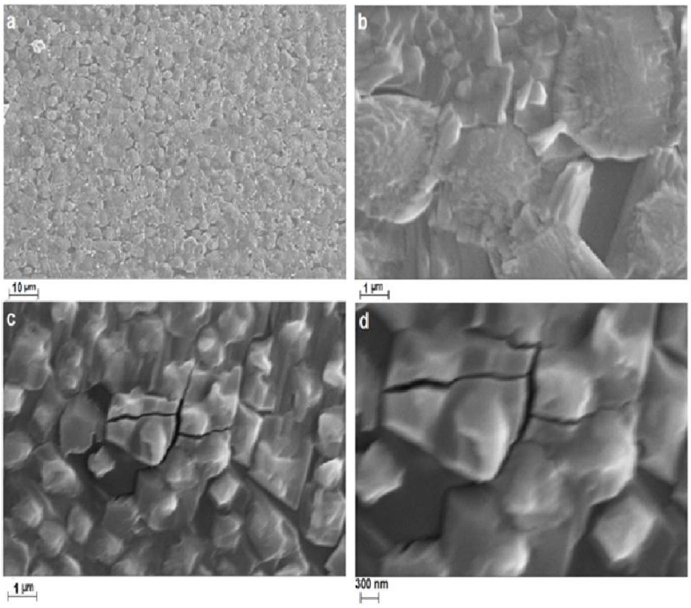

Fig.2. SEM images of $PMoV_2$@PVA nanocatalyst.

Table 1: Effect of different polyoxometalate on germination yield of barley seeds[a]

Entry	polyoxometalate	Germination Yield (%)							
		0.1 μM		1.0 μM		10 μM		100 μM	
		5th day	8th day	5th day	8th day	5th day	8th day	5th day	8th day
1	Blank	81	83	81	83	81	83	81	83
2	$PMoV_2$@ PVA	87	86	83	86	81	83	89	96
3	$Fe_2W_{18}Fe_4$	77	77	83	84	84	83	87	94
4	$H_3PW_{12}O_{40}$	89	89	77	77	91	91	86	86
5	$H_3PMo_{12}O_{40}$	76	76	88	89	88	92	82	88

[a] Different random experiments were done on petri dishes on four concentration levels which were 0.1, 1.0, 10, 100 μM and as the same with several types of polyoxometalates.

In order to investigate the effect of different polyoxometalates on the barley germination properties, a series of test were performed, and the comparative results were listed in Table 1. In this regard, the prepared $PMoV_2$, $PMoV_2$@PVA, and some different types of POMs were used. In this study, a comparison has been made between Keggin-type and sandwich-type of polyoxometalates. The obtained results show that the $PMoV_2$-type of polyoxometalate has a greater effect than sandwich of polyoxometalate. Of course, with doping $PMoV_2$-type of polyoxometalate on the PVA polymer, its efficiency has increased.

IV. CONCLUSION

In summary, the new nanocomposite $PMoV_2$@PVA prepared successfully and for the first time the influence of this new organic-inorganic hybrid nanocomposite was investigated in the germination of barley seeds. The characterization analysis demonstrated that dispersion of Keggin-type $PMoV_2$ particles on the surface of the PVA polymer support under sol-gel method was performed fine. The XRD studies showed that the average crystallite size of the composite particles was estimated to be about 38 nm, which confirmed by the results of SEM. From the obtained results, it is found that by applying new organic-inorganic hybrid nanocomposite $PMoV_2$@PVA with 10µM and 100µM concentrations the most preferred results achieved. $PMoV_2$@PVA nanocomposite have a very effective effect on seminal roots elongations, barley shoot length, coleoptile, firest leaf and biomass production. Of course the effect of supported organic-inorganic hybrid polyoxometalate ($PMoV_2$@PVA) is more than unsupported polyoxometalates. The unsupported polyoxometalates did not stimulate significantly growth of seedlings, but a positive influence was observed with increasing of concentration. The iron nanocomposite, $PMoV_2$@PVA, stimulated especially action in elongations of coleoptile and seminal roots and the growth of first leaf, while the concentration of iron composite in seedlings was slightly variable in 0.1 - 100 µM range.

REFERENCES

[1] M. A. Rezvani, S. Khandan, M. Aghmasheh, J. Taiwan Inst. Chem. Eng. 77, 321-328, **2017.**

[2] M. A. Rezvani, M. Shaterian, F. Akbarzadeh, S. Khandan, Chem. Eng. J., 333, 537-544, **2018**.

[3] J. Xiao, L. Wu, Y. Wu, B. Liu, L. Dai, Z. Li, Q. Xia, H. Xi, Appl. Energy, 113, 78-85, **2014**.

[4] J. He, P. Wu, Y. Wu, H. Li, W. Jiang, S. Xun, M. Zhang, W. Zhu, H. Li, ACS Sustainable Chem. Eng., 5, 8930-8938, **2017**.

[5] M. A. Rezvani, M. Alinia Asli, S. Khandan, H. Mousavi, Z. Shokri Aghbolagh, Chem. Eng. J., 312, 243-251, **2017**.

[6] M. A. Rezvani, Z. Shokri Aghbolagh, H. H. Monfared, S. Khandan, J. Ind. Eng. Chem., 52, 42-50, **2017**.

[7] M. A. Rezvani, S. Khandan, N. Sabahi, Energy Fuels, 31, 5472-5481, **2017**.

New nanocomposite base on sandwich-type polyoxometalate $Fe_2W_{18}Fe_4$ as a nanocatalyst for germination of barley seeds

Hossein Rezvani[a] and Mohammad Ali Rezvani*[b]

[a] Scientific Staff of Golestan Research and Education Center of Agricultural and Natural Resources Organization,
Agricultural Research and Education Organization, Gorgan, Iran.
[b] Department of Chemistry, Faculty of Science, University of Zanjan, Zanjan, Iran
**Corresponding author: Fax: +982 415 152 617; E-mail address: marezvani@znu.ac.ir*

Abstract*:* In this article, a new nanocomposite $Fe_2W_{18}Fe_4@FeTiO_3$ was synthesized on the basis of $(Na_9K[(FeW_9O_{34})_2Fe_4(H_2O)_2]\cdot 32H_2O$, abbreviated as $Fe_2W_{18}Fe_4$) and nanoceramic $FeTiO_3$. The results of XRD, and SEM analysis method indicated the successful composition of the materials. The XRD studies showed that the average crystallite size of the composite particles was estimated to be about 42 nm, which confirmed by the results of SEM. The influence of the new nanocomposite $Fe_2W_{18}Fe_4@FeTiO_3$ in the germination of barley seeds was investigated. In order to compare, several polyoxometalates with different concentrations used to obtain their effects on growth factors of barley seeds. From the obtained results, it is found that by applying new nanocomposite $Fe_2W_{18}Fe_4@FeTiO_3$ with 10 µM and 100 µM concentrations the most preferred results achieved.

Keywords: new nanocomposite, nanoceramic, sandwich-type polyoxometalate, iron titanate, barley seeds.

I. INTRODUCTION

Polyoxometalates (POMs) are self-assembled polynuclear molecules with structures and topology reminiscent of metal oxides clusters, which are known since the beginning of the XIXth century. These inorganic metal-oxygen building blocks are relevant in terms of catalysis because of their structural and compositional diversity, redox potential, surface charge, and acidity [1-3]. Among their different structures, sandwich-type transition metal POMs have been developed for catalyzing processes [4]. The POM compounds are soluble in most of the polar solvents, causing difficulties in the separation and recovery, which is an important restriction for catalytic systems [6]. To confront this limitation, many approaches were proposed to architect the POM-based heterogeneous catalysts. A feasible strategy is loading POM clusters on the surface of the appropriate supports. Thus, it is the substantial factor to choose the type of support [5]. In consideration for application of the POM-based heterogeneous catalysts, in this work, we have proposed to follow the effect of Fe2W18Fe4@FeTiO3 nanocomposite on the germination of the barley seeds. To the best of our knowledge, this is the first report of the synthesis and use of Fe2W18Fe4@FeTiO3 nanocomposite for germination of the barley seeds [3-6]. In most researches, polyoxometalates were used as a catalyst. Some experiments shown that different type of these compounds also have some sort of effects on growth factors and germination components of seeds. At this manuscript the effect of polyoxometalates on barley seedling growth factors has been examined. In order to compare, several polyoxometalates with different concentrations used to obtain their effects on growth factors of barley seeds.

II. METHODS

FeTiO3 powder (0.10 g) was dispersed in 50 mL of distilled water and sonicated using ultrasonic water bath (frequency 35 kHz mains connection 230 V) for 30 min. The synthesized Fe2W18Fe4 (0.03 g) was added slowly to the colloidal suspension of FeTiO3 under continuous sonication conditions at 35 °C for 60 min. The final suspension was centrifuged (2000 rpm) for 20 min and the precipitation separated from the solution. The remained solid product (Fe2W18Fe4@FeTiO3) was filtrated, washed several times with water. Different random experiments were done with factorial method on petri dishes on different concentrations which were 0.1, 1.0, 10 and 100 µM and as the same with several types of polyoxometalates. In this test, petri dish was used in diameter 9 cm and placed the sterile whatman filter paper at the bottom of that. To disinfect, the seeds were soaked for 30 seconds in hypochlorite 10% solution and washed with distilled water immediately. Then, in each petri dish, 25 barley seeds were placed. Then they moved to germinator with 60% relative humidity and temperature in 25/20 days/nights and length of 12 hours of light. Germinated seeds were counted to determine germination rate daily. In germinators, Barley seeds were soaked with solutions of these compounds.

III. RESULTS AND DISCUSSION

The powder X-ray diffraction patterns of (a) Fe2W18Fe4, (b) FeTiO3, and (c) Fe2W18Fe4@FeTiO3 nanocatalyst was comparatively examined by XRD analysis (Fig. 1). As shown in Fig 2a, the intense diffraction peaks at 2θ values of 17.8, 24.3, 27.2, 29.4, 31.7, 35.3, 45.5, 56.5, and 75.3° are related to the pattern of synthesized tetranuclear sandwich-type Fe2W18Fe4, indicating the presence of WO3 species according to JCPDS card No. 00-054-0508. The XRD diffraction peaks of FeTiO3 at 25.5, 27.3, 32.6, 35.6, 36.6, 41.1, 48.9, 52.4, 54.3, 56.2, 60.1, 64.3, 65.6, 69.4, 72.2, 74.4, and 76.8° are attributed to the phases of TiO2 and FeO, corresponding to the JCPDS card No. 01-071-0650 and 01-074-1886, respectively (Fig. 1b) [4]. The Fe2W18Fe4@FeTiO3 nanocatalyst exhibited similar reflections to the pattern of FeTiO3 support and the peaks of Fe2W18Fe4 did not observe clearly. This phenomenon demonstrated the fine dispersion of POM particles on the surface of the solid support [5].

SEM images were acquired to get further insight into the morphology of the samples. The irregular and agglomerated particles of Fe2W18Fe4 with different sizes are depicted in Fig. 2a. Regarding the electronic microscopy studies, the FeTiO3 sample has an unusual twisted morphology (Fig. 2b). Compared to the morphology of the Fe2W18Fe4 and FeTiO3 materials, the Fe2W18Fe4@FeTiO3 implies the well-dispersed nanoscale particles (Fig.2c). The corresponding particle size distribution of the nanocatalyst is presented in Fig. 2d. It is clear that, as expected, the size of Fe2W18Fe4@FeTiO3 particles are in the range of 40-50 nm, which proves the results of XRD analysis.

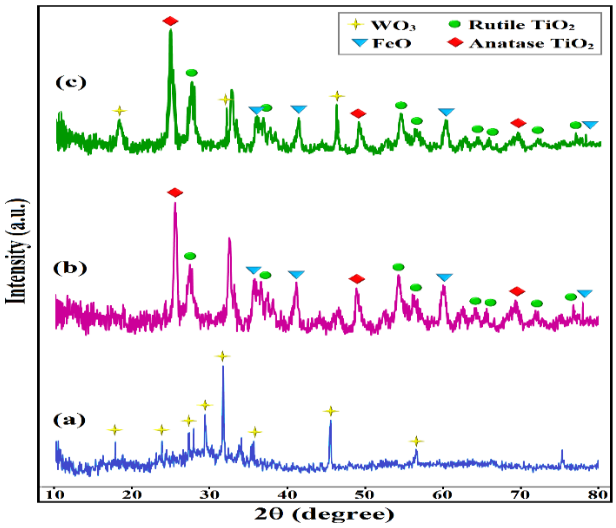

Fig. 1. XRD patterns of (a) Fe2W18Fe4, (b) FeTiO3, and (c) Fe2W18Fe4@FeTiO3 nanocatalyst.

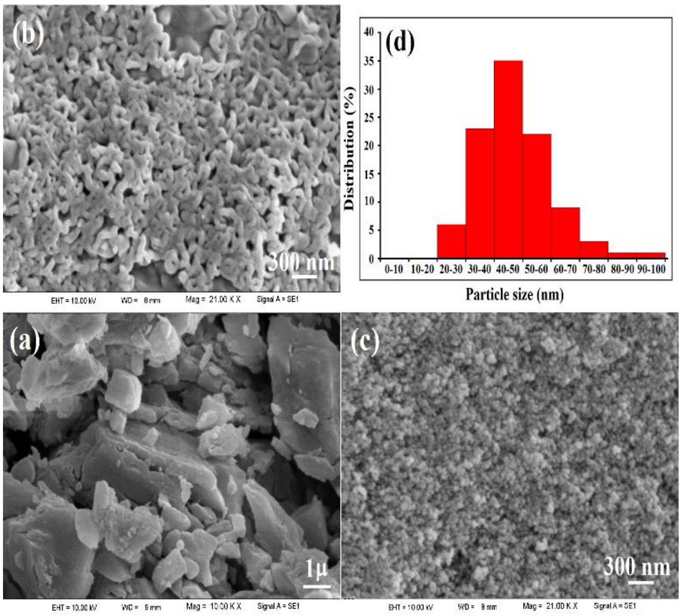

Fig.2. SEM images of (a) Fe2W18Fe4, (b) FeTiO3, (c) Fe2W18Fe4@FeTiO3, and (d) the particle size distribution histogram of the Fe2W18Fe4@FeTiO3 nanocatalyst.

Table 1: Effect of different polyoxometalate on germination yield of barley seeds[a]

Entry	polyoxometalate	Germination Yield (%)							
		0.1 µM		1.0 µM		10 µM		100 µM	
		5th day	8th day	5th day	8th day	5th day	8th day	5th day	8th day
1	Blank	81	83	81	83	81	83	81	83
2	$Fe_2W_{18}Fe_4$@ $FeTiO_3$	85	85	84	85	82	82	90	97
3	$Fe_2W_{18}Fe_4$	77	77	83	84	84	83	87	94
4	$H_3PW_{12}O_{40}$	89	89	77	77	91	91	86	86
5	$H_3PMo_{12}O_{40}$	76	76	88	89	88	92	82	88

[a] Different random experiments were done on petri dishes on four concentration levels which were 0.1, 1.0, 10, 100 µM and as the same with several types of polyoxometalates.

In order to investigate the effect of different polyoxometalates on the barley germination properties, a series of test were performed, and the comparative results were listed in Table 1. In this regard, the prepared Fe2W18Fe4, Fe2W18Fe4@FeTiO3, and some different types of POMs were used. In this study, a comparison has been made between Keggin-type and sandwich-type of polyoxometalates. The obtained results show that the sandwich-type of polyoxometalate has a greater effect than Keggin-type of polyoxometalate. Of course, with doping sandwich-type of polyoxometalate on the FeTiO3 nanoceramic, its efficiency has increased.

IV. CONCLUSION

In summary, the new nanocomposite Fe2W18Fe4@FeTiO3 prepared successfully and for the first time the influence of this new nanocomposite was investigated in the germination of barley seeds. The characterization analysis demonstrated that dispersion of sandwich-type Fe2W18Fe4 particles on the surface of the FeTiO3 solid support under ultrasonic irradiation was performed fine. The XRD studies showed that the average crystallite size of the composite particles was estimated to be about 42 nm, which confirmed by the results of SEM. From the obtained results, it is found that by applying new nanocomposite Fe2W18Fe4@FeTiO3 with 10μM and 100μM concentrations the most preferred results achieved. Fe2W18Fe4@FeTiO3 nanocomposite have a very effective effect on seminal roots elongations, barley shoot length, coleoptile, firest leaf and biomass production. Of course the effect of supported polyoxometalate (Fe2W18Fe4@FeTiO3) is more than unsupported polyoxometalates. The unsupported polyoxometalates did not stimulate significantly growth of seedlings, but a positive influence was observed with increasing of concentration. The iron nanocomposite, Fe2W18Fe4@FeTiO3, stimulated especially action in elongations of coleoptile and seminal roots and the growth of first leaf, while the concentration of iron composite in seedlings was slightly variable in 0.1 - 100 μM range.

REFERENCES

[1] M. A. Rezvani, S. Khandan, M. Aghmasheh, J. Taiwan Inst. Chem. Eng. 77, 321-328, **2017.**

[2] M. A. Rezvani, M. Shaterian, F. Akbarzadeh, S. Khandan, Chem. Eng. J., 333, 537-544, **2018**.

[3] J. Xiao, L. Wu, Y. Wu, B. Liu, L. Dai, Z. Li, Q. Xia, H. Xi, Appl. Energy, 113, 78-85, **2014**.

[4] J. He, P. Wu, Y. Wu, H. Li, W. Jiang, S. Xun, M. Zhang, W. Zhu, H. Li, ACS Sustainable Chem. Eng., 5, 8930-8938, **2017**.

[5] M. A. Rezvani, M. Alinia Asli, S. Khandan, H. Mousavi, Z. Shokri Aghbolagh, Chem. Eng. J., 312, 243-251, **2017**.

[6] M. A. Rezvani, Z. Shokri Aghbolagh, H. H. Monfared, S. Khandan, J. Ind. Eng. Chem., 52, 42-50, **2017**.

Mechanism of Adsorption of Congo Red on the Surface of Filter Paper in NaCl and 2-propanol Solutions

*M. Rafi and B. Samiey**

Department of Chemistry, Faculty of Science, Lorestan University, Khoramabad 68137-17133, Lorestan, Iran
Email: babsamiey@yahoo.com , samiey.b@lu.ac.ir

Abstract: Adsorption of CR on the surface of filter paper was studied in the presence of 0.1 M NaCl and aqueous ethanol solutions. Here, effects of ionic strength, different percentages of ethanol on the equilibrium binding constants (*K*) and adsorption capacities (q_e) of CR on the surface of filter paper were analyzed by the ARIAN model at 308, 318 and 328 K. Results of analysis showed that this was a two-region process and maximum adsorption capacity of filter paper for CR decreased with increase in concentration of ethanol and increased in the presence of 0.05, 0.25 and 0.5 M NaCl solution. Maximum adsorption capacity of process in 0.5 M NaCl solution was 121.4 mg g^{-1} at 328 K.

Keywords: ARIAN model, Congo red, Temkin, 1-Propanol, 2-Propanol, Filter paper.

I. INTRODUCTION

Dyes are used for dyeing in many industries like leather, paper, tanning, food and treatment of their sewages is a great challenge. Lots of these compounds exert dangerous effects on human and animal health and their degradation is difficult. There are various techniques for treatment of effluents produced by factories and industries. Some of these methods are filtration [1], coagulation [2], adsorption [3], ion exchange [4] etc. Among these methods, adsorption is very efficient and costly-economic method. On the other hand, in many cases substances are painted through adsorption of dyes on their surface. Congo red (CR), disodium (4-amino-3-[4-[4-(1-amino-4-sulfonato-naphthalen-2-yl)diazenylphen yl] phenyl]diazenyl-naphtha lene-1-sulfonate), is an anionic dye and has many applications.

In this work, adsorption of CR on filter paper was studied at 308-328 K in the presence of NaCl and ethanol. These compounds affected the process by changing dielectric constants and ionic strength of CR solutions. The ARIAN model as an efficient model was used to analyze isotherms.

II. METHODS

Materials. Congo red (CR) and NaCl were purchased from BDH and chromatography paper (grade 1 Chr) was prepared from Whatman.

Methods. A series of glass bottles including 0.1 g of filter paper were charged by 20 ml of CR solutions that their concentrations were in the range of $1\times10^{-5} - 2\times10^{-4}$ M. The contact time was 20 h to attain the equilibrium conditions. The contents of CR in the solutions were determined by photometry. Tests were carried out in a shaking water bath at 308, 318 and 328 K and at 148 rpm. In adsorption tests, q_t (mg g^{-1}), was calculated by a mass balance relation as follows

$$q_e = \frac{(c_0 - c_e)Mv}{1000w} \qquad (1)$$

where c_0 and c_e are the initial concentration of adsorbate and its concentration in M at a given time *t*, respectively, *v* is the volume of solution (ml), *w* is the weight of the used adsorbent (g) and *M* is the molecular weight of adsorbate (mg mol^{-1}).

Adsorption Thermodynamics Modeling. The ARIAN model is used to analyze the adsorption isotherms. ARIAN is an abbreviation for "*adsorption isotherm regional analysis model*" [5-7] and means Iranain. The ARIAN model is used for investigating adsorption isotherms up to four regions. In this model, it is assumed that region I obeys the Henry

$$q_e = Kc_e \qquad (2)$$

where *K* is the equilibrium binding constant of adsorbate on the surface and adsorption increases linearly with its concentration. Region II begins from the *ssc* (an abbreviation for *starting second region concentration*) point. In this region only monolayer adsorption occurs and can be studied by a suitable isotherm like the Langmuir, Temkin equations and etc. The Temkin equation is given by

$$q_e = c_1 \ln(c_2 c_e) \qquad (3)$$

where c_1 is a constant and c_2 is adsorption equilibrium constant.

In region III, new surface aggregates of molecules form. The *stc* (an abbreviation for *starting third region concentration*) point defines starting this region. Data of this region are investigated by the bilayer isotherm, Eq. (4), and isotherms derived from it, Eqs. (5) and (6). In region III, by assuming adsorption happens mostly in the first and second layers, we have

$$\frac{c_e}{q_e}=\frac{1+c_eK_{sa}+xc_e^2K_{sa}}{q_{mon}K_{sa}+2q_{mon}xc_eK_{sa}} \qquad (4)$$

where K_{sa} and x are the adsorption equilibrium constants of adsorbate species in the first layer surface aggregates and that of adsorbate molecules in all layers excluding the first layer, respectively. q_{mon} and q_e are the monolayer and equilibrium adsorption capacity, respectively. If adsorbate molecules are adsorbed mostly on the first layer Eq. (4) is written as

$$\frac{c_e}{q_e}=\frac{1}{q_{mon}K_{sa}}+\frac{c_e}{q_{mon}}+\frac{xc_e^2}{q_{mon}} \qquad (5)$$

which is used for surface low bilayer coverage and is called LBC isotherm which is an abbreviation for "*l*ow *b*ilayer *c*overage" isotherm. If the adsorption process results in the monolayer formation [4], Eq. (4) is reduced to

$$\frac{c_e}{q_e}=\frac{1}{q_{mon}K_{sa}}+\frac{c_e}{q_{mon}} \qquad (6)$$

where Eq. (6) is called the Langmuir-type isotherm. The region IV starts from where the adsorption capacity reaches the maximum, showing a plateau on the isotherm, or where the isotherm begins to go down. The second situation in region IV is named the reverse desorption and obeys from the reverse desorption isotherm [4]. Depending upon the characteristics of adsorption sites and adsorbate, two or more sub-regions may be observed in regions II or III or IV of an isotherm. Each sub-region is called a section and to distinguish them, they are characterized by English capital letters and shown as IIA, IIB, IIC, IIIA, IIIB etc.

III. RESULTS AND DISCUSSION

In this work, effects of temperature, ionic strength and change in dielectric constant of solutions were studied.

As shown in Table 1, an increase in percentages of ethanol, decreased the equilibrium binding constants (K) and maximum experimental adsorption capacities ($q_{e,\max}$) of CR on the surface of filter paper compared to those in pure water. With respect to electrostatic-ion dipole nature of interaction of sulfonate groups of CR with –OH groups of cellulose, this observation resulted from decrease in dielectric constants of solutions with an increase in their ethanol percentages. Also, dissolution of ethanol in water is an exothermic process and this in turn makes the adsorption process more exothermic with an increase in solvents ethanol content, Table 1. The $q_{e,\max}$ values of the process range from 16.4 to 29.1 mg g^{-1}.

On the other hand, adsorption of CR on the surface of filter paper in 0.05, 0.1 and 0.5 M NaCl solutions were endothermic which can be attributed to the endothermic contribution of endothermic nature of dissolution of NaCl in water, Table 2. Also, K and $q_{e,\max}$ values of the process increased with an increase in NaCl concentration, Table 2. Surrounding of sulfonate groups of CR with ionic atmosphere of Na$^+$ and Cl$^-$ ions fortifies interaction between CR molecules and –OH groups of cellulose surface. The $q_{e,\max}$ values of the process were in the range of 67.5-120.7 mg g^{-1}.

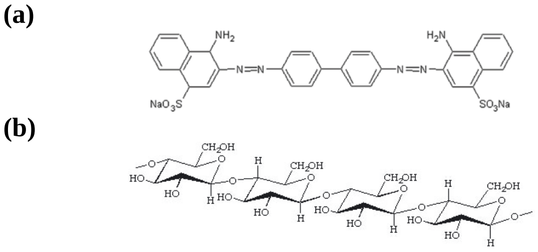

Fig.1: Molecular structure of (a) CR and (b) cellulose

Table1: K, ΔH and ΔS values for adsorption of CR on filter paper for the first region at 308-328.

First region					
	K from Henry law at			ΔH	ΔS
	308 K	318 K	328 K		
Ethanol					
0	1.5×10^5	1.3×10^5	1.1×10^5	–10.9	63.0
2.5%	61529	47331	11516	–69.8	–133.0
5%	73558	56021	44546	–21.1	24.7
7.5%	47275	38224	29410	–19.9	24.9
10%	45526	33605	19209	–36.1	–27.4
NaCl					
0.05M	1.5×10^5	1.7×10^5	6.5×10^5	61.0	295.1
0.25M	1.4×10^6	1.7×10^6	1.8×10^6	10.6	152.1
0.5M	1.5×10^6	1.8×10^6	1.9×10^6	10.0	150.5

Units of ΔH and ΔS are in kJ mol^{-1} and J mol^{-1} K^{-1}, respectively.

Table2: K, ΔH and ΔS values for adsorption of CR on filter paper for the second region at 308-328.

Second region		
K from Temkin isotherm at	ΔH	ΔS

	308 K	318 K	328 K		
Ethanol					
0	1.3×10^4	1.4×10^4	1.5×10^4	6.4	99.5
2.5%	28688	15901	11691	–37.8	–37.4
5%	26331	14015	10513	–38.7	–41.4
7.5%	9691	9431	8621	–4.9	60.7
10%	12866	10343	8230	–18.7	17.8
NaCl					
0.05M	1.3×10^5	1.5×10^5	1.6×10^5	8.7	126.4
0.25M	1.5×10^5	1.7×10^5	1.72×10^5	5.8	118.1
0.5M	2.9×10^5	3.2×10^5	3.4×10^5	7.4	126.4

Units of $q_{e,\max}$, ΔH and ΔS are in mg g^{-1}, kJ mol^{-1} and J mol^{-1} K^{-1}, respectively.

IV. CONCLUSION

Adsorption of CR on the surface of cellulose happened through interaction of sulfonate groups of CR with –OH groups of cellulose. Adding ethanol decreased K and $q_{e,\max}$ values of the process and made it exothermic while process in the presence of NaCl was endothermic and its K and $q_{e,\max}$ values increased with an increase in NaCl concentration.

REFERENCES

[1] M. F. Hamoda, I. Al-Ghusain and N. Z. Al-Mutairi, Desalination. vol. 164, pp. 203–211, **2004**.

[2] I. Uzuam, Dyes and Pigments. vol. 70, pp. 76-83, **2006**.

[3] M. Ghaedi, A. Najibi, H. Hossainian, A. Shokrollahi and M. Soylak, Toxicol. Environ. Chem. vol. 94, pp. 40–48, **2011**.

[4] G. Al-Enezi, M. Hamoda and N. Fawzi, J. Environ. Sci. Health. A. vol. 39, pp. 455–64, **2004**.

[5] B. Samiey and S. Golestan, Cent. Eur. J. Chem., vol. 8, pp. 361–369, **2010**.

[6] B. Samiey and S. Abdollahi Jonaghani, J. Pollut. Eff. Cont. vol. 3, e2, **2015**.

[7] M. Rafi, B. Samiey and C-H Cheng, Materials**.** vol. 11, e496, **2018**.

Silica Gel Dyeing by Adsorption of a Series of Triphenylmethane Dyes on its Surface

M. Rafi and B.Samiey*

Department of Chemistry, Faculty of Science, Lorestan University, Khoramabad, 68137-17133, Lorestan, Iran
Email: babsamiey@yahoo.com , samiey.b@lu.ac.ir

Abstract: In this work, both the binding constants (*K*) of some triphenylmethane dyes on the silica gel surface and its dyeing and the effect of temperature on *K* values were studied by the ARIAN model. These dyes included malachite green (MG), fuchsine acid (FA), methyl green (MEG), brilliant green (BG) and crystal violet (CV) and the dyeing process was carried out in aqueous media at 308, 318 and 328 K. The results showed that in all cases the process was two-region and endothermic. Here, the role of amine and $-SO_3^-$ functional groups of dyes in their interactions with silica gel surface was discussed. Maximum adsorption capacities of silica gel for MG, FA, MEG, BG, and CV dyes were 4.2, 5.4, 5.9, 6.9 and 7.5 mg g^{-1} at 328 K, respectively.

Keywords: ARIAN model, Brilliant green, Crystal violet, Malachite green, Fuchsine acid, Methyl green.

I. INTRODUCTION

Dyes are used for dyeing in many industries like leather, paper, tanning, food and treatment of their sewages is a great challenge. Lots of these compounds exert dangerous effects on human and animal health and their degradation is difficult. There are various techniques for treatment of effluents produced by factories and industries. Some of these methods are ion exchange [1], coagulation [2], adsorption [3], filtration [4] etc. Among these methods, adsorption is very efficient and costly-economic method. On the other hand, some substances are painted through adsorption of dyes on their surface. Malachite green oxalate (MG), brilliant green (BG), crystal violet (CV), methyl green (MEG) (as cationic dyes) and fuchsine acid(FA) (as an anionic dye) are members of triphenylmethane dyes family and have many applications.

In this study, adsorption of MG, BG, CV, MEG and FA on the surface of silica gel was investigated at 308–328 K in water. Adsorption of theses dyes was happened by their functional groups. The ARIAN model as a new efficient model was used to study resulted isotherms.

II. METHODS

Materials. Malachite green oxalate, brilliant green, crystal violet, fuchsine acid, methyl green and silica gel 60 for column chromatography (mean pore diameter 60A°) were purchased from Merck.

Methods. 10 ml of dye solutions with concentrations in the range of $4\times10^{-6}-9\times10^{-5}$ M was poured in a series of glass bottles including 0.033 g of silica gel. The contact time was 6 h to attain the equilibrium conditions. The concentrations of dyes in the solutions were measured by photometry method. Tests were carried out in a shaking water bath at 308, 318 and 328 K and at 120 rpm. In adsorption tests, q_t (mg g^{-1}), was calculated by a mass balance relation as follows

$$q_e=\frac{(c_0-c_e)Mv}{1000w} \tag{1}$$

where c_0 and c_e are the initial concentration of adsorbate and its concentration in M at a given time *t*, respectively, *v* is the volume of solution (ml), *w* is the weight of the used adsorbent (g) and *M* is the molecular weight of adsorbate (mg mole^{-1}).

Adsorption Thermodynamics Equations. The ARIAN model is used to analyze the adsorption isotherms. ARIAN is an abbreviation for "*adsorption isotherm regional analysis model*" [5-7] and means Iranain. The ARIAN model is used for investigating adsorption isotherms up to four regions. In this model, it is assumed that region I obeys the Henry

$$q_e=Kc_e \tag{2}$$

where *K* is the equilibrium binding constant of adsorbate on the surface and adsorption increases linearly with its concentration. Region II begins from the *ssc* (an abbreviation for *starting second region concentration*) point. In this region only monolayer adsorption occurs and can be studied by a suitable isotherm like the Langmuir, Temkin equations and etc. The Temkin equation is given by

$$q_e=c_1\ln(c_2c_e) \tag{3}$$

where c_1 is a constant and c_2 is adsorption equilibrium constant. In region III, new surface aggregates of molecules form. The *stc* (an abbreviation for *starting third region concentration*) point defines starting this region. Data of this

region are investigated by the bilayer isotherm, Eq. (4), and isotherms derived from it, Eqs. (5) and (6). In region III, by assuming adsorption happens mostly in the first and second layers, we have

$$\frac{c_e}{q_e}=\frac{1+c_eK_{sa}+xc_e^2K_{sa}}{q_{mon}K_{sa}+2q_{mon}xc_eK_{sa}} \tag{4}$$

where K_{sa} and x are the adsorption equilibrium constants of adsorbate species in the first layer surface aggregates and that of adsorbate molecules in all layers excluding the first layer, respectively. q_{mon} and q_e are the monolayer and equilibrium adsorption capacity, respectively. If adsorbate molecules are adsorbed mostly on the first layer Eq. (4) is written as

$$\frac{c_e}{q_e}=\frac{1}{q_{mon}K_{sa}}+\frac{c_e}{q_{mon}}+\frac{xc_e^2}{q_{mon}} \tag{5}$$

which is used for surface low bilayer coverage and is called LBC isotherm which is an abbreviation for "*l*ow *b*ilayer *c*overage" isotherm. If the adsorption process results in the monolayer formation [4], Eq. (4) is reduced to

$$\frac{c_e}{q_e}=\frac{1}{q_{mon}K_{sa}}+\frac{c_e}{q_{mon}} \tag{6}$$

where Eq. (6) is called the Langmuir-type isotherm. The region IV starts from where the adsorption capacity reaches the maximum, showing a plateau on the isotherm, or where the isotherm begins to go down. The second situation in region IV is named the reverse desorption and obeys from the reverse desorption isotherm [4]. Depending upon the characteristics of adsorption sites and adsorbate, two or more sub-regions may be observed in regions II or III or IV of an isotherm. Each sub-region is called a section and to distinguish them, they are characterized by English capital letters and shown as IIA, IIB, IIC, IIIA, IIIB, etc.

III. RESULTS AND DISCUSSION

Here, the adsorption of five members of triphenylmethane dyes family on the surface of silica gel was investigated. These dyes painted silica gel and it was important to study the character of their interactions with silica gel. Due to the microporous character of silica gel, dyes interacted with its external surface. Results showed that maximum adsorption capacities of the process increased with an increase in temperature. Analysis of adsorption isotherms by the ARIAN model showed that in all cases equilibrium binding constants of the process increased with an increase in temperature and the dyeing process was endothermic, Tables 1 and 2. These dyes interacted through their positively-charged amine groups with oxygen atoms of silica gel surface. Presence of negatively-charged sulfonate groups in FA resulted in its smaller *K* values compared to those of MG, MEG, CV and BG dyes

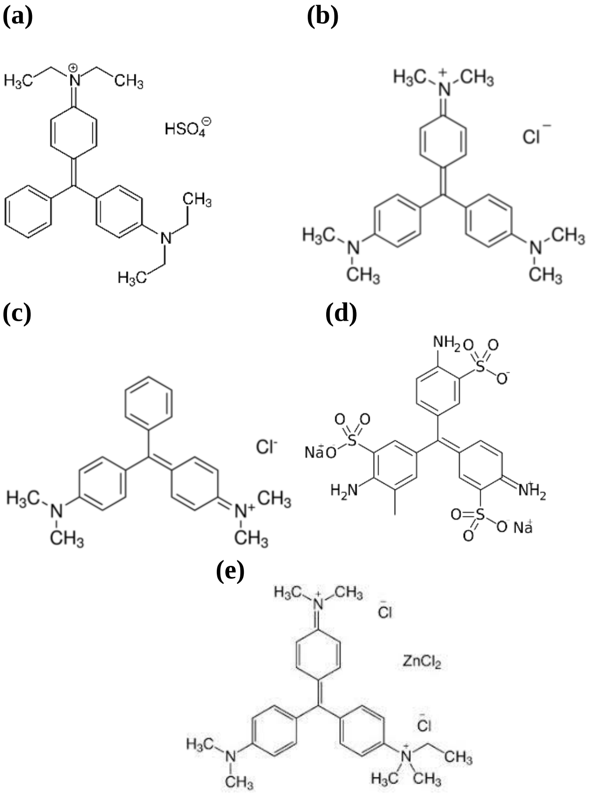

Fig.1: Molecular structure of (a) BG, (b) CV, (c) MG, (d) FA and (e) MEG

Table1: K, ΔH and ΔS values of adsorption of BG, CV, MG, FA and MEG on silica gel for the first region at 308-328.

First region					
	K from Henry law at				
Dye	**308 K**	**318 K**	**328 K**	ΔH	ΔS
BG	3.15×10^4	7.28×10^4	8.95×10^4	4.4	230.1
CV	1.13×10^6	1.17×10^6	1.20×10^6	2.5	124.0
MG	6.71×10^4	7.82×10^4	1.05×10^5	18.7	152.9
FA	1.77×10^4	4.54×10^4	6.55×10^4	55.2	261.1
MEG	9.92×10^4	3.91×10^6	2.42×10^7	231.6	849.7

Units of ΔH and ΔS are in kJ mol^{-1} and J mol^{-1} K^{-1}, respectively.

Table2: *K*, ΔH and ΔS values of adsorption of BG, CV, MG, FA and MEG on silica gel for the second region at 308-328.

Second region					
	K from Temkin isotherm at				
Dye	**308 K**	**318 K**	**328 K**	ΔH	ΔS
BG	5.91×10^5	8.42×10^5	9.63×10^5	20.6	177.6
CV	4.53×10^5	7.54×10^5	1.11×10^6	37.7	230.7
MG	9.80×10^5	9.96×10^5	1.02×10^6	1.7	119.7
FA	3.77×10^5	5.60×10^5	5.69×10^5	208.8	778.6
MEG	2.11×10^6	8.36×10^6	6.08×10^7	140.8	577.3

Units of $q_{e,\max}$, ΔH and ΔS are in mg g^{-1}, kJ mol^{-1} and J mol^{-1} K^{-1}, respectively.

IV. CONCLUSION

Adsorption of a number of triphenylmethane dyes including MG, FA, MEG, BG and CV were studied at 308, 318 and 328 K. Analysis of experimental data by the ARIAN model showed that all of these interactions were endothermic. Adsorption of these dyes happened through interaction of their amine groups with oxygen atoms of the silica gel surface. Also, presence of $-SO_3^-$ groups in FA resulted in its smaller *K* values compared to those of other dyes.

REFERENCES

[1] K. Brezinski, B. Gorczyca and , M. Sadrnourmohammadi, WQRJ. vol. 54, pp. 142–160, **2018**.

[2] C. Y. The, P. M. Budiman, K. P. Y. Shak and T. Y. Wu, Ind. Eng. Chem. Res. vol. 55, pp. 4363–4389, **2016**.

[3] H. Xu, Y. Zhang, Y. Cheng, W. Tian, Z. Zhao and J. Tang, Adsorp. Sci. Technol. vol. 37, pp. 217-235, **2019**.

[4] A. I. Zouboulis and I. A. Katsoyiannis, Water. vol. 11, e45, **2019**.

[5] B. Samiey and S. Golestan, Cent. Eur. J. Chem. vol. 8, pp. 361–369, **2010**.

[6] B. Samiey and S. Abdollahi Jonaghani, J. Pollut. Eff. Cont. vol.3, e2, **2015**.

[7] M. Rafi, B. Samiey and C-H Cheng, Materials**.** vol.11, e496, **2018**.

Study of optical energy gap of AL-doped ZnO_2 nanoparticles synthesized by sol-gel method

Javad Adabi Firuozjaie[a*], ***HossainMilani Moghaddam***[a]

Department of Solid State Physics, Faculty of Science, University of Mazandaran, Babolsar
javadadabi72@gmail.com

Abstract: In current work the pure ZnO_2 nanoparticles and with Al impurity were synthesized by using sol-gel method. The absorption spectra and optical energy gap of these nanoparticles were investigated. The monoclinic and tetragonal phases of these nanoparticles were confirmed by X-ray diffraction (XRD).It was found that by doping of Al to the ZnO_2 structure, the particle size was increased. The field emission scanning electron microscopy analysis (FE-SEM) and energy-dispersive X-ray spectroscopy (EDX) demonstrated the morphology and formation of nanoparticles as well as the presence of Al. The optical energy gap of Al-doped ZnO_2 decreased with respect to that of pure ZrO_2.

Keywords*:* Al, Nanoparticle, Optical properties, sol-gel method, ZnO_2

I. INTRODUCTION

Zinc oxide is an important and multi-functional semiconductor compound. Characteristics such as transparent and piezoelectric conductivity have led to the consideration of this material against other semiconducting oxides [1, 2]. It has also been shown that zinc oxide exhibits high conductivity and high optical passage in a certain region, and because of its wide band gap (eV3 / 3) and high energy (meV60) energy, this potential has potential In the field of light diodes, solar cells, gas sensors and optoelectronic components.
Also, due to the hardness of 4.5 units as a soft material, it has a melting point, boiling point, heat capacity and high drift, and its lowering makes it suitable for ceramic manufacturing.[3]

II. METHODS

Nanoparticles of zinc oxide with aluminum impurity (3%, 2%, 0% = x) AlxZn1-xO are produced using simultaneous deposition method. For this purpose, zinc nitrate powder and aluminum nitrate are used as raw materials and sodium hydroxide is used as a reducing agent. 100 ml of aqueous solution of zinc nitrate is added to the 0.1 molar solution and 3.2% of 0.1 molar solution of aluminum nitrate. The solution is also heated to 80 ° C for 2 hours. The amount of 100 ml of a 0.1 mol solution of sodium hydroxide solution in 1 hour was added dropwise to the solution to form a gel and finally the precipitates passed through the filter and centrifuged and dried at 500 ° C Wear centigrade.

III. RESULTS AND DISCUSSION

Fig.1 shows that the pure and Ag-doped ZnO_2 nanoparticles had a monoclonal and tetragonal phases in the XRD analysis and with adding of Al impurities, It reveals sharp, well-defined diffraction peaks. The strong and narrow diffraction peaks indicate that the sample has a good crystallinity. The size of nanoparticles was taken with using Debay-Sherer relation as given:

$$D = \frac{K\lambda}{\beta\ cos\theta} \qquad (1)$$

D is the average crystallite size (in nanometers), K is 0.9. β is the broadening of the hkl diffraction peak measured at half of its maximum intensity (in radian), λ the wavelength of the X-ray (in nanometers) is equal to 0.15418 ($k_\alpha - Cu$). θ is the Bragg diffraction angle (in degree). The crystallite size of pure ZnO_2 is 23 nm. The Al-doped samples with the molar 25% Al (10% Al) is 29 (27) nm.

FE-SEM images of pure and Al-doped samples were shown in Fig.2 (a) and (b), respectively. It can be noticed that the formed particles are uniform and spherical. Moreover, it is indicated that with adding of Al impurities, the particle size becomes larger. Fig.3 shows the absorption spectra of pure and Al-doped ZnO_2 nanoparticles. The pure ZnO_2 nanoparticles had an absorption peak at 228 nm. Also, Al-doped samples had an absorption peak at 263 nm (a molar 20% Ag) and 265 nm (a molar10% Al).

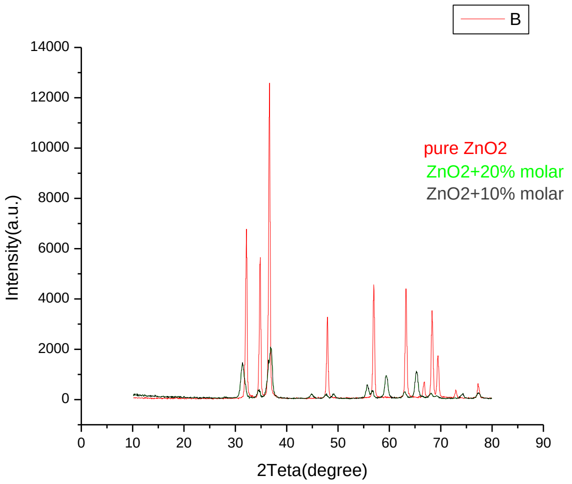

Fig.1: The acquired XRD curve for the both pure and Al-doped ZnO_2.

The optical band gap of these nanoparticles has been calculated via the Tauc relation (as shown Fig.4):

$$\alpha h\nu = A(h\nu - E_g)^{0.5} \qquad (2)$$

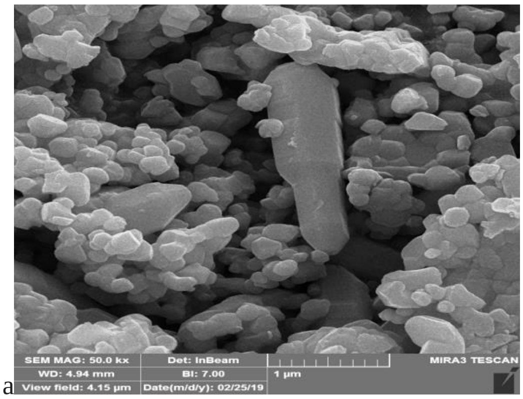

a

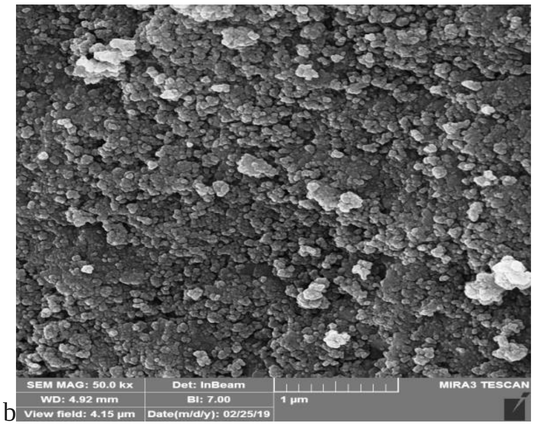

b

Fig.2: The FE-SEM image of (a) pure ZnO2 , (b) 20% Al-doped ZnO2.

Where $h\nu$ is the photon energy, h is Planck's constant, α is the absorption coefficient, E_g is the optical energy gap for allowed direct transition, A is the constant, The values of E_g obtained 3.88, 3.69 and 3.49 eV for pure, 25%Al and 10% Al-doped, respectively.

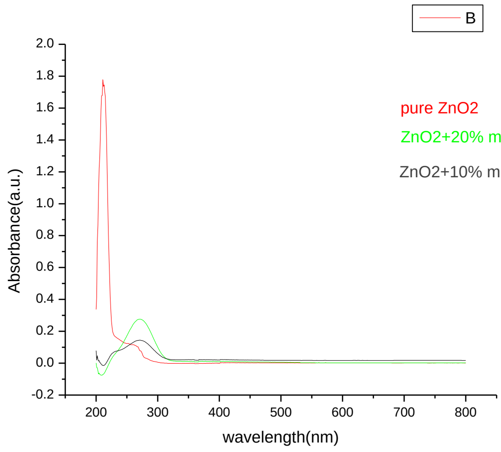

Fig.3: The absorption diagram of both pure and Al-doped ZnO_2.

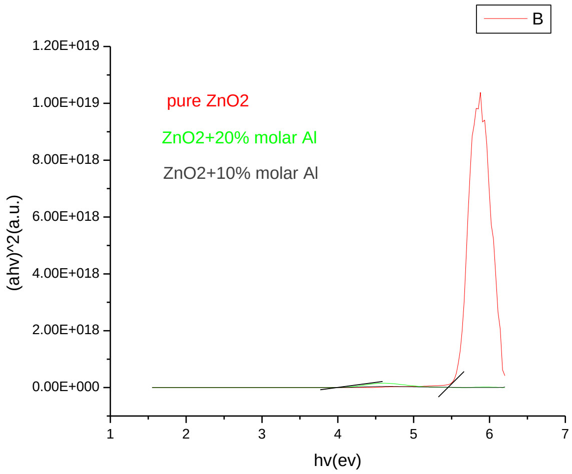

Fig.4: The optical energy gap of (a) pure ZnO2, (b) 20% Al-doped ZnO_2, (c) 10% Al-doped ZnO_2.

IV. CONCLUSION

In summary, pure and Al-doped ZnO_2 nanoparticles have been successfully prepared by a sol-gel route. The increase of Al molar ratio gives rise to better crystallinity and the increase of the size of ZnO_2 nanocrystallites. Furthermore, the doping of Al in ZnO_2 decreased the optical energy gap.

REFERENCES

[1] U.Ozgur, Ya. L. Alivov, C. Liu, A. Teke, M. A. Reshchkov, S.Dogan, V. Avrutin, S. J. Cho, H. Morkoc,"A comprehensive review of ZnO materials and devices" J. Appl. Phys. 98 (2005) 041301.

[2] R. Triboulet, J. Perriere,"Epitaxial growth of ZnO films", Prog. Cryst. Growth Charact. Mater. 47 (2003) 65.D. He, Y. Ding, H. Luo, and C. Li, Journal of Molecular Catalysis A: Chemical, vol. 208, pp. 267–271, **2004**.

[3] R.F. Haaker, and R.C. Ewing, Journal of American Ceramic Society, vol. **64** (11), **1981.**

۲۹ الی ۳۱ مرداد ۱۳۹۸
بیست و دومین کنفرانس شیمی فیزیک انجمن شیمی ایران
22nd Iranian Physical Chemistry Conference
گروه شیمی دانشگاه زنجان

The Effect of Laser Polishing on Titanium Surface in Nitrogen Media

***Ensiyeh Shabanlu*[a]*, Babak Jaleh*[a]**, Behnaz Feizi Mohazzab*[a]**
Department of Physics, Faculty of Science, Bu-Ali Sina University, Hamedan 65174, Iran
Email: bkjaleh@yahoo.com

Abstract*:* Laser ablation of titanium in nitrogen gas media using a fiber laser was studied. Titanium samples were irradiated using a fiber laser. The formation of titanium nitride (TiN) on the surface of laser ablated sample was verified by XRD. Then, laser polishing was applied in order to improve the surface roughness. After that, the effectiveness of laser polishing by remelting on the variation of TiN surface morphology was examined by SEM. It was concluded that laser polishing is a useful method to improve he surface properties of the materials.

Keywords: Laser nitriding, Laser ablation, Laser polishing, Titanium, Titanium nitride.

I. INTRODUCTION

Titanium and its alloys have vast applications in biomedical and aerospace fields because of high strength and extremely good corrosion resistance [1-3]. The production of titanium alloys machines due to its low thermal conductivity and high chemical reaction of titanium, is very difficult [4-5]. To address these disadvantages, laser nitriding is an effective way to improve titanium and its alloys surface [6-7]. The process of laser nitriding is done by laser beam scanning on the surface of the Ti target in a chamber filled with nitrogen gas. When the surface of the Ti is heated up above the melting point, a plasma is generated above it. High temperatures and high pressure levels cause laser-plasma-material interactions, leading ionization and nitrogen separation. As a result, ions and nitrogen atoms are absorbed by the melted surface and TiN structure is solidly deposited on it [8-9]. Next, laser polishing, which is a potential way to reduce surface roughness, was done [10]. This method is mainly based on the melting of the surface of the target due to the heat of laser radiation that it is one of the types of laser ablation. In this method the laser beam is focused above the surface of the target and induces a plasma plume on it. The point of this method is the diverging beam in a way that the ablation of target at the peak of irregularities is more than the valleys' of it [11-13]. In this work, identification and analysis of produced TiN structure by the laser ablation process was investigated and then the effect of laser polishing was studied. The XRD (x-ray diffraction) and SEM (Scanning electron microscopy) analyses was done to study the surface structure and morphology.

II. METHODS

In this study, we cut a metal sheet of titanium (hexagonal) with thickness of 0.6mm into pieces of 17mm×17mm as samples. Before laser ablation process, the surface of these pieces should be cleaned, so they were grinded with SiC paper and then they were washed with distilled water and acetone with an ultrasonic device, respectively. The samples were placed in the nitrogen gas chamber at the pressure of 2.5 Bar (Fig. 1). Afterward, a fiber laser (RFL-P30Q) with a wavelength of 1064 nm, laser power of 27 W, laser scanning speed of 200 mm/s, 30 KHz of repetition rate, and also with step of 50 μm in x and y direction, ablated the samples in the nitrogen gas. Sample structures, before and after laser nitriding, were evaluated by XRD analysis (XRD, Unisantis XMD300) at room temperature and over the 2θ range 10º-80º. After laser polishing in the nitrogen gas at the pressure of 2.5 Bar, laser power of 20 W , scanning speed of 2000 mm/s, morphology of TiN samples were assessed by scanning electron microscope (SEM, Camscan MV2300).

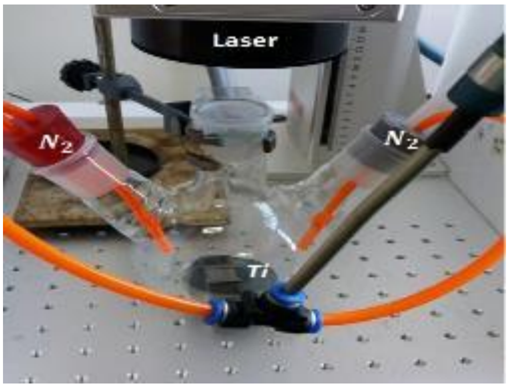

Fig. 1: Figure of laser polishing setup.

III. RESULTS AND DISCUSSION

At first, an analysis of samples was performed by X-ray diffractometer. In Fig. 2, the X-ray patterns are presented. Fig. 2(a) shows diffraction pattern of the Ti and Fig. 2(b) shows diffraction pattern laser ablated Ti the a nitrogen gas chamber at the pressure of 2.5 Bar. As are labeled, these two XRD patterns are matched with titanium hexagonal structure (ICDD Card # 01-1198). Also two peaks located at about 36.80° and 42.612° corresponding to (111) and (200) of cubic titanium nitride (ICDD Card # 06-0642). Consequently, these two picks are the evidence of the formation TiN structure during the laser ablation process. Fortunately, there is no detectable amount of oxidized Ti in XRD when laser nitriding preforms. Effect of laser polishing on the surface morphology of sample are illustrated in Fig. 3. Fig. 3(a) is showing surface SEM image of laser ablated Ti sample in the nitrogen gas chamber without any laser polishing. Macro scale photographs of laser ablated samples after the laser polishing process are presented in Fig. 3(b-f). It indicates that during laser polishing process, the surface of the laser ablated Ti reaches to the melting temperature in very short time. Fig. 3(b-f) shows laser ablated samples with one, two, three, four, and five times. Polishing on Ti leads to a smooth surface compared with the Fig. 3(a).

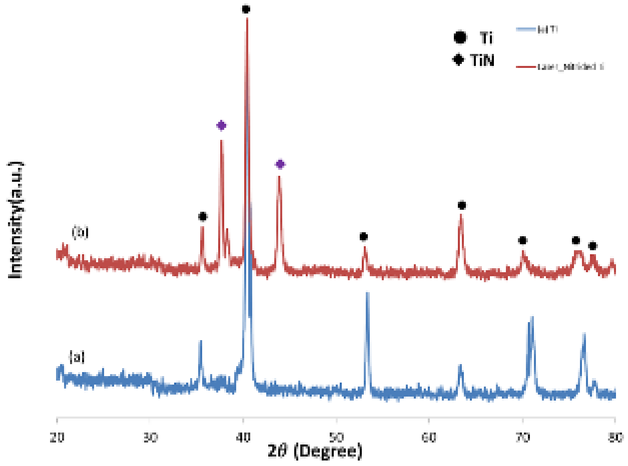

Fig. 2: XRD pattern of (a) Ti, (b) laser ablated Ti in nitrogen gas

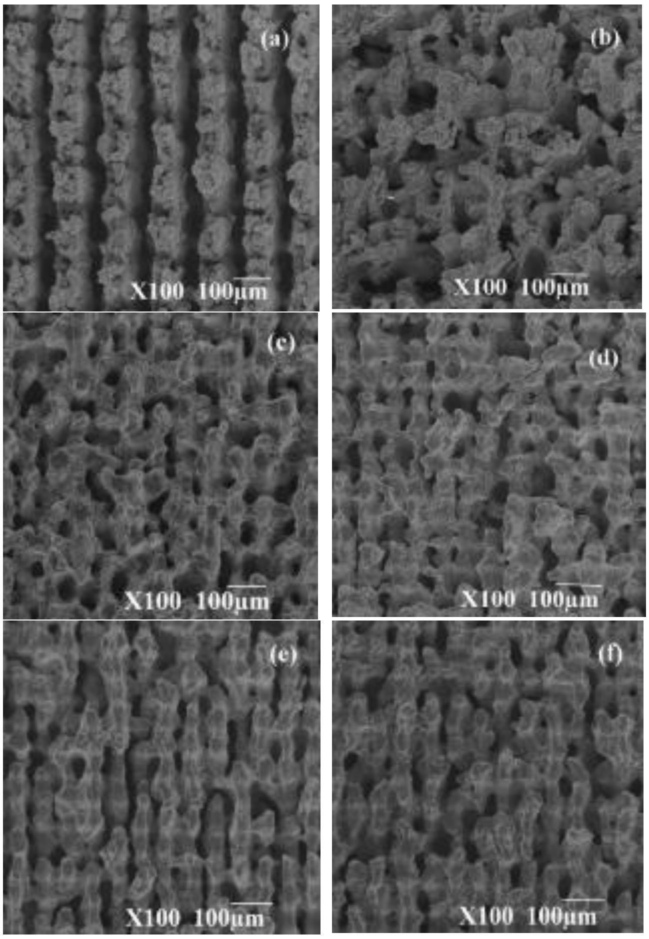

Fig. 3: Surface SEM images of (a) TiN without laser polishing, (b) one time laser polishing on TiN, (c) two times laser polishing, (d) three times laser polishing, (e) four times laser polishing, (f) five times laser polishing.

IV. CONCLUSION

We concluded that ablation of Ti and formation of TiN structure occur while implementing laser nitriding process and XRD can detect it. In addition, the SEM analyses results suggest that laser polishing leads to smooth surface compared with the laser ablated Ti without any laser polishing process. It was seen that laser polishing is a useful and applicable method to improve the surface properties of the laser ablated samples. Also, it is envisaged that corrosion resistance of samples will increase by applying laser polishing method.

REFERENCES

[1] M. Nouari, M. Calamaz, and F. Girot, Wear, 336, 772-781, 2008.
[2] JH. Qin, Q. Chen, CY. Yang, and Y. Huang, Journal of Alloys and Compounds, 654, 39-44, 2016.
[3] RC. Petersen, Metals, 4, 549-569, 2014.
[4] S. Zhang, JF. Li, J. Sun and F. Jiang, Adv Manuf Technol, 46, 2016, 69-78.
[5] S. Pervaiz, A. Rashid, I. Deiab, and M. Nicolescu, Mater Manuf Process, 29, 219-252, 2014.
[6] H. Xin, S. Mridha, and T.N. Baker, Mater, 31, 22–30, 1996.
[7] Y.S. Tian, C.Z. Chen, S.T. Li, and Q.H. Huo, Applied Surface Science, 242, 177–184, 2005.
[8] CW. Chan, S. Lee, GC. Smith, and C. Donaghy, Materials Science and Engineering, 309, 628–640, 2017.
[9]B. F. Mohazzab, B. Jaleh, O. Kakuee, and A. Fattah-alhosseini, Applied Surface Science, 478, 623–635, 2019.
[10]T. Kiedrowski, E. Willenborg, K. Wissenbach, and S. Hack, Proceedings of the Third, 297-300, 2005.
[11] E. Ukar, A. Lamikiz, F. Liébana, S. Martínez, and I. Tabernero, Materialwissenschaft und Werkstofftechnik, 46, 661-667, 2015.
[12] Q.Wang, J. D. Morrow, C. Ma, N. A. Duffie, and F. E. Pfefferkorn, Journal of Manufacturing Processes, 20, 340-348, 2015.
[13] F. E. Pfefferkorn, N. A. Duffie, J. D. Morrow, and Q.H. Wang, CIRP Annals, 63, 237-240, 2014.

Section:

Statistical Mechanics

Surface interaction energy simulation of TiO_2 and SiO_2-TiO_2 layers with Epoxy resin

Marzieh Sarafrazi[a]*, *Masood Hamadanian a,b*

[a] Department of Physical Chemistry, Faculty of Chemistry, University of Kashan, I.R. Iran
[b] Institute of nanoscience and nano technology, University of Kashan, I.R. Iran
** Email: hamadani@kashanu.ac.ir*

Abstract*:* Molecular dynamics simulation was used to calculate interaction energy between titania, titania-silica nanoparticles, and epoxy (EP) resin. Detailed simulations were performed with material studio software, Forcite module, using Build layer section, creating relatively simple surface models of epoxy resin and TiO_2, TiO_2-SiO_2. Two cell models obtained were applied to calculate the surface interaction energy. The simulated results are in good agreement with the experimental data, confirming the ability to employ the described MD method in the theoretical evaluation of the interaction between various nanofiller and the EP resin.

Keywords: Epoxy, Molecular dynamic simulation, surface interaction energy, titania

I. INTRODUCTION

Epoxy (EP), as thermosetting macromolecular material, is extensively used by industry due to their outstanding mechanical, chemical, electrical, and thermal properties [1-6]. However, it is well known that EP resins are also very fragile [7-9]. This disadvantage limits the use of EP resins in goods that require high mechanical strength [7]. Many investigations have been focused on improving mechanical properties of this polymer by adding of various types of nanofillers [8-12]. Additions of nanoparticles, such as TiO_2 [13], Al_2O_3 [14], ZnO [15], Ag [16], Nanoclay [17], CNT [18], Barium titanate ($BaTiO_3$) [19], nanoclay [20] etc. have been led to increasing of the hardness, durability, conductivity, weakening, anti-static and UV protection in nano-polymer composites [21,22]. These improvements depend strongly on the filler amounts, type and characteristics of the nanofillers [23]. However, the volume fraction and location of nanoparticles in epoxy nanocomposites are open challenges. In the study of polymer nanocomposites, the interaction energy between nanofillers and matrix is one of a determinative character on the thermal and mechanical properties of nanocomposites [24]. A strong interaction between nanofiller with polymer would be improved mechanical properties of nanocomposites. So, by determining the interaction energy, it is possible to determine the effect of various nanofiller on the mechanical properties of EP resin.

In atomistic level, this issue can be simulated by Molecular dynamics (MD) simulation method. MD is a strong tool for simulation of material properties such as Tg, the interaction between matrix and nanofiller and elastic behavior of nanocomposites [25]. In this study, titanium dioxide as one of the most widely used nanoparticles in polymer nanocomposites, and also the effect of silica nanoparticles as impurities on TiO_2, was selected. Therefore, the interaction energy between EP, TiO_2, and TiO_2-SiO_2 layers was investigated through MD simulations.

II. MOLECULAR MODELING AND SIMULATION PROCEDURE

The aim of this simulation is to calculate the surface interaction energy of EP with TiO_2 and TiO_2-SiO_2 layers. MD simulation was conducted with Material studio (MS) v8.0 packages (Accelrys, San Diego, CA) using compass (condensed phase optimized molecular potentials) force field for atomistic simulation. EP resins with crystal structure of TiO_2 and SiO_2were shown in Fig. 1. This simulation consists of several steps.

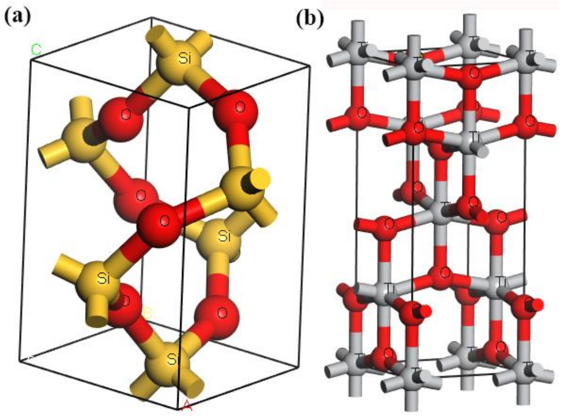

Fig. 1: Crystal structure of: a) SiO_2 and b) TiO_2

First step was a surface making. Two two-dimensional (2D) active models were constructed for the crystal structures of TiO_2 and SiO_2 on an atom-to-atom basis, and the crystal face [1 0 1] was cut. In second step the TiO_2 and SiO_2 surface was optimized (less than 5000 steps) with COMPASS (condensed-phase optimized molecular potentials for atomistic simulation studies) forcefield [26]. Followed dynamic calculation by 50 ps NVT MD simulation at 300k and 1 atm with a time step of 1 fs was used to relax the surface. Then, the supercell of TiO_2 and SiO_2 surface was created and the configuration parameters were u=v=3 and were converted from 2D to 3D. Also, combined layer of TiO_2-SiO_2 was constructed. After minimized energy with molecular mechanic (mm), dynamic run (50 ps, time step 1 fs) was used to reached an equilibration state.

Third step was a polymer building. EP structure was selected from https://pslc.ws/modelhtms/epoxypdb.htm and optimized with geometry optimization. Due to get reasonable EP polymer, amorphous cell modules must be used. Lattice parameters of this cell were the same as TiO_2 surface. Then minimized energy and dynamic run (50 ps) was used.

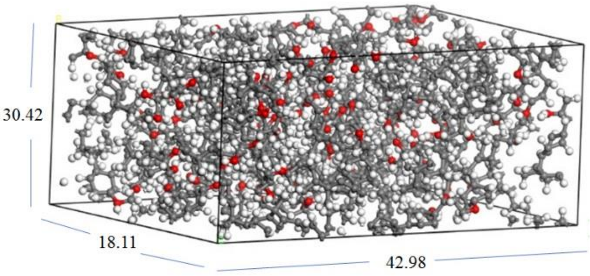

Fig. 2: Amorphous cell model of EP resin

Step four, the layer module was used to add EP resin to the surface. Fig.3 shows that the layers included EP, TiO_2 and TiO_2-SiO_2 surface and vacuum.

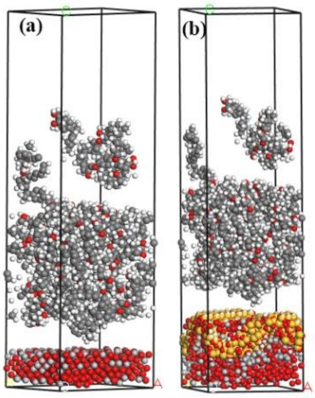

Fig. 3: Surface models of a) TiO_2/EP and b) TiO_2-SiO_2/EP

At last, MD simulation was conducted under NVT ensemble with a time step of 1 fs for 30 ps and 300 K until the system reached the equilibrium.

III. RESULTS AND DISCUSSION

Interaction energy between EP resin with surface were calculated by using the following equation:

$$E_{interaction}=E_{total}-(E_{surface}+E_{polymer}) \qquad (1)$$

Where, E_{total}, $E_{surface}$ and $E_{polymer}$ are the total energy interaction between polymer and surface, the energy of the surface without polymer and the energy of the polymer without surface, respectively. Table 1 show the interaction energy for EP polymer with surface of TiO_2 and TiO_2-SiO_2.

The value of interaction energy for EP/ TiO_2 and EP/TiO_2-SiO_2 were -60.95 and -73.82 kcal/mol. The result showed that EP/TiO_2-SiO_2 had the strongest binding ability. Lu et al. [27] investigated the effect of SiO_2-TiO_2 in the different ration of TiO_2 to SiO_2 on mechanical properties of epoxy resin. They conclude that the tensile strength of epoxy resin increased by 14% when the TiO_2-SiO_2 content up to 3wt%. This may be attributed to the fact, that $E_{interaction}$ TiO_2-SiO_2 is higher than that of titania, thus the force between its molecules is an attraction, which causes the molecules binding well, loading to good mechanical properties of the composites.

Energy component, Kcal/mol	**EP/TiO_2**	**EP/TiO_2-SiO_2**
E total	5800.4	118885.71
E surface	1908.08	115034.44
E polymer	3953.27	3925.09
E interaction	-60.95	-73.82

IV. CONCLUSION

In this study, the surface interaction energy between epoxy resin with titania and TiO_2-SiO_2 with respect ratio of titania to silica (75:25) was investigated through MD simulation method. The calculated interaction energy for EP/TiO_2 and EP/TiO_2-SiO_2 nanocomposite were -60.95 Kcal/mol and -73.82 Kcal/mol, respectively. Simulation results showed that surface interaction energy between TiO_2-SiO_2 and EP matrix had a strong bonding ability.

REFERENCES

[1] C. Y. Fei, L. Zhichao, T. Junyan, Z. Qingyu, and H. Yang, J. Nanomater, 7, 167150 (2015).
[2] C. Y. Fei, D.Q. Wang, C. Wei, and F. Tao, J. Cent. South Univ., 21, 4076-4083 (2014).
[3] S. Kumar Singh, S. Singh, A. Kumar, and A. Jain, Eng. Fract. Mech., 184, 241-248 (2017).

[4] A. P. Isfahani, M. Sadeghi, A.H. Saeedi Dehaghani, and M.A. Aravand, J. Ind. Eng. Chem., 44, 67-72 (2016).
[5] S. Zavareh, and G. Samandari, Polym. Eng. Sci., 54, 1833-1838 (2013).
[6] H. T. Chiu, S.H. Chiu, and J.H. Wu, J. Appl. Polym. Sci., 89, 959-970 (2003).
[7] X. Wang, Z. Huang, J. Zheng, and Q. Mei, Adv. Mater. Res., 221, 135-139 (2011).
[8] S. Zavareh, and G. Samandari, *Polym. Eng. Sci*., 54, 1833, (2013).
[9] H. T. Chiu, S. H. Chiu, and J. H. Wu, *J. Appl. Polym. Sci.*, 89, 959-970, (2003).
[10] M. S. Seyed Dorraji, M. H. Rasoulifard, A.R. Amani-Ghadim, M. H. Khodabandeloo, M. Felekari, M. R. Khoshrou, and I. hajimiri, *Appl. Surf. Sci.*, 383, 9-18. (2016).
[11] C. Y. Fei, D. Q. Wang, C. Wei, and F. Tao, J. Cent. South Univ., 21, 4076, (2014).
[12] A. P. Isfahani, M. Sadeghi, A. H. Saeedi Dehaghani, and M. A. Aravand, *J. Ind. Eng. Chem*., 44, 67-72, (2016).
[13] C. Yufei, L. Zhichao, T. Junyan, Z. Qingyu, and H. Yang, J. Nanomater, **7**, 167150, (2015).
[14] M. J. Kadhim, A. K. Abdullah, I. A. Al-Ajaj, and A. S. Khalil, IJAIEM, 2, 10-16, (2013).
[15] Y. Li, S. Fu, and Y. Mai, polym., 47, 2127-2132, (2006).
[16] G. Kortaberria, M. Sangermano, and I. Mondragon, Macromol. Symp., 321-322, 112–117, (2012).
[17] W. S. Chow, and Y. P. Yap, eXPRESS Polym. Lett., 2, 2–11, (2008).
[18] J. Cha, S. Jin, J. H. Shim, C. S. Park, H. J. Ryu, and S. H. Hong, Mater. Des., 95, 1–8, (2016).
[19] J. Xu, K-S Moon, P. Pramanik, S. Bhattacharya, and C. P. Wong, IEEE, 30,248-253, (2007).
[20] J. L. Suter, D. Gruen, and P. V. Coveney, Adv. Mater., 27, 1-19, (2014).
[21] H. M. El-Dessouky, and C. A. Lawrence, J. Nanopart. Res., 13, 1115–1124, (2011).
[22] A. Mirmohseni, and S. Zavareh, J. Polym. Res., 18, 509–517, (2011).
[23] M. Šupová, G. S. Martynková, and K. Barabaszová, Sci. Adv. Mater., 3, 1–25, (2011).
[24] S. Khostavan, M. Fazli, M. Ghorbanzadeh Ahangari, and Y. Rostamiyan, adv. Polym. Tech., 2019, (2019).
[25] Y.-h. Wang, W.-h. Wang, Z. Zhang, L. Xu and P. Li, Eur. Polym. J., 75, 36-45 (2016).
[26] D. R. Xin, and Q. Han, *Electron. Mater. Lett.*, 10, 535-539, (2014).
[27] S. Lu, W. Chun, J. Yu, X. Yang, J. appl. Polym. Sci.. 109, 2095-102, (2008).

Molecular Simulations of Adsorption of Hydrogen Sulfide, Carbon Dioxide, Methane and Nitrogen and Separation of Binary Mixtures (H_2S/CH_4), (CO_2/CH_4) into NUM-3a Metal–Organic Frameworks

A. Amouzad Khalili, *S. Yeganegi**

Department of Physical Chemistry, Faculty of Chemistry, University of Mazandaran, Babolsar,47416-95447, Iran
Email: amouzad125@gmail.com, sdyeganegi@gmail.com

Abstract*:* In this work, the adsorption of hydrogen sulfide, carbon dioxide, methane, nitrogen and separation of their binary mixtures (H_2S/CH_4), (CO_2/CH_4) by NUM-3a were studied using Grand Canonical Monte Carlo(GCMC) simulations The adsorption isotherms of pure gases on the studied MOF were simulated at **298K**.Comparison with experimental results showed that the simulated adsorption isotherms of hydrogen sulfide, carbon dioxide, methane and nitrogen on NUM-3a agreed well with the experimental data. The obtained results indicated that the adsorption of H_2S is higher than carbon dioxide, methane and nitrogen. As well as, the simulated adsorption selectivities NUM-3a for the CO_2/CH_4, H_2S/CH_4 were in the order $H_2S/CH_4 > CO_2/CH_4$. NUM-3a had higher selectivity for H_2S and CO_2 over CH_4 showing that this MOF can be good adsorbents for separation of H_2S, CO_2 from CH_4. Furthermore, the preferred site of adsorption for hydrogen sulfide, carbon dioxide, methane and nitrogen on the NUM-3a were also investigated.

Keywords: MOF; GCMC; Natural gas; Separation, Henry coefficient; Isosteric heat

I. INTRODUCTION

In decade recently, considerable attempts have been carried out to recognize and develop of several suitable porous materials (e.g., porous carbons[1], zeolites[2] and metal organic frameworks(MOFs) [3] in the gas storage and separation area.

Metal organic frameworks are a low-density crystalline compound with metal ion units or clusters as nodes which are connected by organic ligands as linkers to form a 3 dimensional porous solid. Metal organic frameworks have been studied in a wide variety of applications such as gas storage and separation [4], catalysis [5], drug delivery [6] and optical/electric/magnetic field.[7]. NUM-3a is a novel multi-cage-based MOF synthesis by YU et al at [8] which has four different kinds of cages with polyhedral.

NUM-3a has many interesting features such as open metal site, good thermal and solvent stability as well as adequate and tunable topology for using in sweetening of natural gas Up to our knowledge no computational study was carried out on adsorption and separation of H_2S, CO_2, CH_4 and N_2 into NUM-3a. Molecular simulation methods are strong tools to unraveling the physicochemical process at the molecular scale.

II. METHODS

I.The NUM-3a structure was taken from the Cambridge database. GCMC simulations were carried out using RASPA code. The simulations were equilibrated for 1.5×10^4 steps, and a further 10^5 steps were used to sample the desired thermodynamic properties. The obtained results were examined to ensure that the number of the moves is sufficient to achieve the equilibrium. Four types of trial moves (translation, rotation, insertion, and deletion) were randomly applied in GCMC simulations. A cut-off radius of 12.5 Å was practiced. The unit cell parameters of NU-3a are a=22.3712 Å, b=22.3712 Å, and c=95.1715 Å. The simulation box consisted of 2 × 2 × 2 unit cells of NUM-3a to fit the proposed cut-off distance. Periodic boundary conditions were applied in all three dimensions. The van der Waals (vdW) interactions was modeled as Lennard-Jones potential Eq(1)

II.The electrostatic interactions between point charges were calculated by Ewald summation technique.

III. The electrostatic potential (ESP) atomic partial charges for the clusters of NUM-3a were calculated using B3LYP functional of DFT method with 6-31G (d, p) basis set as implemented in Gaussian 09 software package.

TraPPE force field was used for Lennard- Jones potential parameters of carbon dioxide and nitrogen. H_2S was explained by a three-site model optimized by Kamath et al.In the case of methane was used OPLS FF, Three popular force fields: UFF, DREIDING and OPLS were used to model the interactions between carbon dioxide, nitrogen and methane molecules with NUM-3a atoms and obtained adsorption isotherm compared with that of experimental values [8]. The interaction between H2S and NUM-3a atoms was modeled by UFF.

III. The isosteric heat of adsorption (Q_{st}) was calculated byEq(2)

The amount of isosteric heat of adsorption is a measure of adsorbate/adsorbate and adsorbate/adsorbent interaction energies. Henry coefficient (k_H) can be used to describe the interaction between adsorbate and adsorbent in the low pressure

IV. Also, the adsorption selectivity for component i relative to component j was calculated by Eq(3)

V. RESULTS AND DISCUSSION

.

A. Figures and Tables

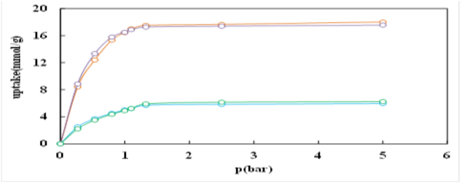

Fig 1 The calculated adsorption of CO_2 by NUM-3a using OPLS (Purple, circle), UFF (red, circle), DREIDING (blue, circle) and experimental values of YU[8] (green, circle) at 298K

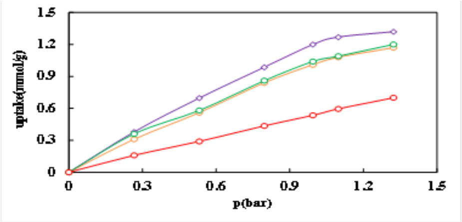

Fig2. The calculated adsorption of CH_4 by NUM-3a using OPLS (orange, circle), UFF (purple, circle), DREIDING (red, circle) and experimental values of YU[8] (green, circle) at 298K

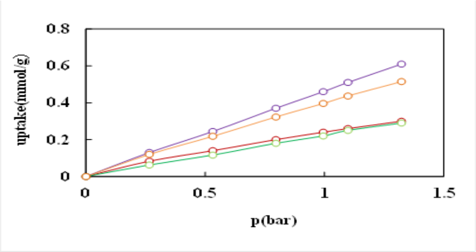

Fig3. The calculated adsorption of N_2 by NUM-3a using OPLS (orange, circle), UFF (purple, circle), DREIDING (red, circle) and experimental values of YU[8] (green, circle) at 298K

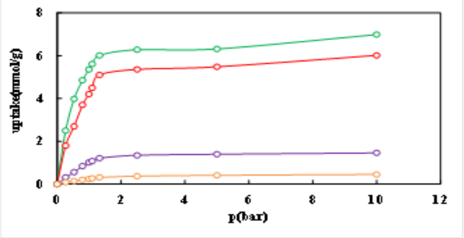

Fig4.Adsorption isotherms of H_2S (green, circle), CO_2 (red, circle), CH_4 (orange, circle), and N2 (Purple, circle) adsorption isotherms by NUM-3a at 298K

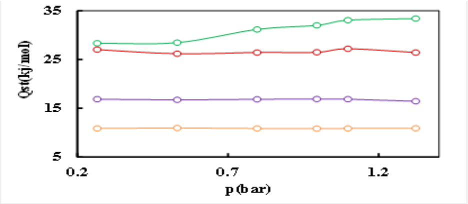

Fig5. calculated isosteric heat of adsorption of pure H_2S (green, circle), CO_2 (red, circle), CH_4 (purple, circle), and N_2 (orange, circle) at. 298K

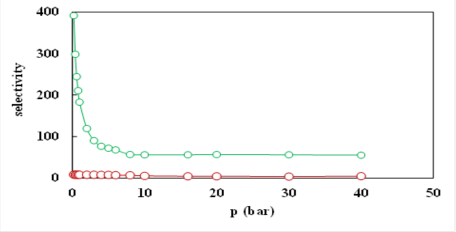

Fig.6. The adsorption selectivity of CO_2/CH_4 (red, circle), H_2S/CH_4 (green, circle) binary mixtures on NUM-3a at 298-K

Table1. Calculated of Henry's law constant K_H (mmol/(g bar)) of hydrogen sulfide, carbon dioxide, methane and nitrogen at1bar and 298K

Pressure(bar)	H_2S	CO_2	CH_4	N_2
		K_H(mmol/(g.ba)		
1.0	16.189	4.22	1.016	0.241

B. Equations

IV. $U_{LJ(r)} = 4\varepsilon\,[(\sigma/r)^{12} - (\sigma/r)^{6}]$ (1)

XI. $Q_{st} = RT - (\partial U/\partial N)_{T,V}$ (2)

$S_{ij} = (x_i/x_j)/(y_i/y_j)$ (3)

VI. CONCLUSION

In this paper, the adsorption of H_2S, CO_2, CH_4 and N_2 and their mixture on the NUM-3a were investigated using the Grand Canonical Monte Carlo (GCMC) simulation method. At the first, performance of three popular force fields, UFF, OPLS and DREIDING was evaluated for predicting the adsorption of carbon dioxide, methane and nitrogen on NUM-3a by comparing the calculated adsorption isotherms with the experimental values of YU. et al. [8] The results revealed that the simulated isotherm for carbon dioxide and nitrogen using DREIDING force field and isotherm for methane using OPLS are in good agreement with the experimental data. The result of adsorption showed that the adsorption of $H_2S > CO_2 > CH_4 > N_2$ respectively. The selectivity's of the H_2S/CH_4 and CO_2/CH_4 mixtures on the NUM-3a have the same behavior against pressure. The studied framework has higher selectivity for hydrogen sulfide over methane indicating that NUM-3a is good adsorbents for the hydrogen sulfide separation. The adsorption selectivity's are in the order $H_2S/CH_4 > CO_2/CH_4$.

REFERENCES

[1] Biswas S, Couck S, Denysenko D, et al, Microporous Mesoporous Mater.;181,:175–181, **2013**.

[2] Mofarahi M, Gholipour F, Microporous Mesoporous Mater., 200, 1–10, **2014**

[3] Yuan S, Qin J-S, Lollar CT, et al, ACS Cent. Sci, 4, 440–450, **2018**.

[4] Du L, Lu Z, Zheng K, et al. Am. Chem. Soc,135, 562–565,**2012**

[5] Wang Q, Jiang J, Zhang M, et al, Cryst. Growth Des,17, 16-18, **2016**

[6] Wang X, Chen M, Du M, Inorg. Chem, 55, 6352–6354, **2016**

[7] Wang H, Hu T-L, Wen R-M, et al, Mater. Chem.B, 1, 3879–3882, **2013**

[8] Yu M-H, Zhang P, Feng R, et al, ACS Appl. Mater. Interfaces, 9, 26177–26183, **2017**

Viscosity of Ethane at Low and Moderate Densities Using Corresponding States Correlations

***Sh. Karimi*, T. Hosseinnejad ***
Department of Chemistry, Alzahra University, Vanak, Tehran, Iran)
Email: tayebeh.hosseinnejad@alzahra.ac.ir

Abstract: At the first step of this research, we focused on the calculation of Chapman-Enskog (CE) viscosity collision integrals using different correlations in comparison with the available experimental data. The average absolute deviation (AAD) between our calculated and literature viscosity data for the dilute ethane was obtained within 1.5% in 90-600 K temperature range. We also assessed the pair interaction potential parameters to reproduce the accurate dilute viscosity values based on the corresponding state collision integrals. In the next step, Rainwater-Friend (RF) theory was applied to calculate the second virial viscosity coefficients at moderate densities up to 1.1mol.lit^{-1}. It should be mentioned that the accuracy of our calculated RF viscosities was obtained 2.1% using CE dilute viscosity values in conjunction with the corresponding states of the second virial viscosity coefficients.

Keywords: Viscosity; Pair interaction potential parameters; Collision integrals; Rainwater-Friend theory

I. INTRODUCTION

In the recent years, there is a growing need to obtain the reference values for transport properties of pure fluids such as viscosity, thermal conductivity and self-diffusion coefficient. It should be mentioned that for transport properties, a general framework with reliable accuracy and thermodynamically consistent has not been introduced and there are only many separate correlations for different transport properties that have been derived with different theoretical methods. Accurate calculation of transport properties can be obtained once the collision integrals are known from the intermolecular potential functions, using Chapman-Enskog (CE) formalism [1]. More clearly, based on CE theory, in order to obtain transport collision integrals, we require the precise knowledge of intermolecular potential energies that represents the binary interactions between two individual molecules.

In the present study, we calculated Chapman-Enskog (CE) viscosity and collision integrals of ethane using different correlations in comparison with the available experimental data. We also assessed the pair interaction potential parameters to reproduce the accurate dilute viscosity values.

In the next step, we applied Rainwater-Friend theory to calculate the second virial viscosity coefficients at moderate densities up to 1.1mol.lit^{-1} and assessed the accuracy of our obtained results in comparison with the available experimental viscosities for moderately dense ethane. It should be mentioned that Rainwater-Friend theory has been formulated for the calculation of second transport virial coefficients by modeling of two-body collisional transfer, three-monomer and monomer–dimer collisions.

II. VISCOSITY CORRELATIONS AT DILUTE AND MODERATE DENSITY RANGES

On the basis of CE formalism in the kinetic theory, viscosity in the zero-density limit can be calculated by

$$\eta_0(T) = \frac{0.021357[TM]^{1/2}}{\sigma^2 \mathfrak{S}_\eta^*} \qquad (1)$$

where $\mathfrak{S}$ is the reduced effective collision cross section and were derived from the experimental viscosity primary data, T is the temperature in Kelvin, M is the relative molecular mass, σ is a length scaling parameter in nm, and η is in units of μPa.s.

In the following, we presented the obtained correlation formula for $\mathfrak{S}$ that were fitted using appropriate statistical weights [2]:

$$\ln \mathfrak{S}_\eta^* = \sum_{i=0}^{n} a_i \ (lnT^*)^i \qquad (2)$$

where the reduced temperature T* is given by

$$T^* = \frac{KT}{\varepsilon} \qquad (3)$$

and ε/k is an energy scaling parameter in Kelvin.

The other correlation equation for the viscosity in the limit of zero density has been reported in the following [3]:

$$\eta_0(T) = \sum_{i=0}^{-8} \eta_{0,i}\, \tau^i \qquad (4)$$

with $$\tau = \frac{T_c}{T} \qquad (5)$$

It is important to note that the accuracy of correlation is 0.5% for temperatures 290 < T/K < 625, increasing to 1.0% at temperatures down to 212 K.

The viscosity second virial coefficient at moderate density can be defined as follows:

$$\eta = \eta_0[(1 + B_\eta)\rho] \qquad (6)$$

which is formulated on the basis of initial density dependence of viscosity in Rainwater-Friend theory [4]

$$B_\eta^*(T^*) = \frac{B_\eta(T)}{N_A\sigma^3} \qquad (7)$$

$$B_\eta^*(T^*) = \sum_{i=0}^{6} a_i\ (lnT^*)^{-i} \qquad (8)$$

III. RESULTS AND DISCUSSION

We calculated the viscosity collision integral of dilute ethane in 150-600 K temperature range using different corresponding states correlations.

In Figure 1, we displayed the calculated values of CE viscosity in comparison with experimental data. It should be noticed that we evaluated the ability of different interaction potential parameters to reproduce the viscosity at low density range.

In Table 1, we reported calculated viscosity collision integral in conjunction with experimental values so that the average absolute deviation (AAD) between the calculations and experiment was achieved about 1.06%.

In the next step, calculation of viscosity at moderate densities employing Rainwater-Friend (RF) theory was performed up to density 1.03 mol.lit^{-1} that showed AAD values about 2.11%

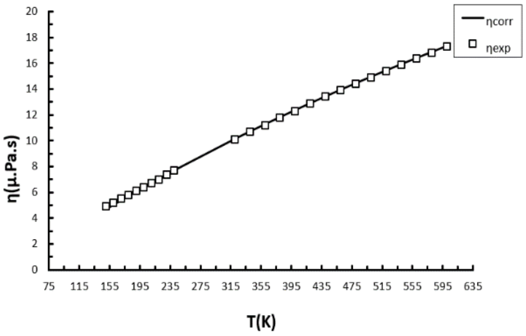

Figure 1. The CE viscosity values as a function of T in comparison with experiment

Table 1. The correlated values of viscosity collision integrals with experimental data for dilute ethane.

T*	$\mathfrak{S}^*_{corr}$	$\mathfrak{S}^*_{exp}$	Dev%
0.70	1.51	1.46	3.55
0.74	1.46	1.42	2.68
0.78	1.41	1.39	1.63
0.83	1.37	1.36	0.92
0.87	1.33	1.33	0.34
0.92	1.30	1.30	-0.13
0.96	1.27	1.27	-0.36
1.00	1.24	1.24	-0.12
1.05	1.21	1.21	0.40
1.40	1.06	1.06	0.02
1.49	1.03	1.03	-0.56
1.57	1.01	1.02	-0.16
1.66	0.99	0.99	-0.51
1.75	0.97	0.98	0.00
1.84	0.95	0.95	-0.17
1.93	0.94	0.94	-0.28
2.01	0.92	0.93	-0.32
2.10	0.914	0.91	-0.29
2.19	0.90	0.90	-0.22
2.28	0.89	0.89	-0.10
2.36	0.88	0.88	0.04
2.45	0.87	0.87	-0.35
2.54	0.86	0.86	-0.11
2.63	0.85	0.85	0.11

IV. CONCLUSION

We presented an appropriate model to calculate the viscosity of ethane at low density range based on Chapman-Enskog formalism in the corresponding states framework. The pair potential parameters were also evaluated to reproduce viscosity collision integrals. At moderate densities, we assessed the second virial viscosity coefficient correlations to calculated the viscosity values of ethane and then compared with the available experimental data. The comparison of calculated viscosity values with the experimental data shows a reliable agreement that confirms the accuracy and ability of CE and RF formalism in prediction of viscosity of dilute and moderately dense ethane.

REFERENCES

[1] J.O. Hirschfelder, C.F. Curtiss, R.B. Bird, 2nd printing, John Wiley, New York, **1964**.

[2] S. Hendl, J. Millat, V. Vesovic, E. Vogel, and W. A. Wakeham, Int. J. Thermophys. vol. 12, pp.999-1012 ,**1991**

[3] S. Hendl and E, Vogel, Fluid Phase Equilib.vol.76, pp. 259-272 ,**1992**

[4] D.G. Friend, J.C. Rainwater, Chem. Phys. Lett. vol. 107, pp. 590-594,**1984**

Corresponding States Correlations for Viscosity of Dilute n-Butane

H. Asgari*, T. Hosseinnejad

Department of Chemistry, Alzahra University, Vanak, Tehran, Iran)

Email: tayebeh.hosseinnejad@alzahra.ac.ir

Abstract: In this research, several corresponding states correlations were evaluated to calculate the viscosity collision integrals using Chapman-Enskog theory at 150-400 K range for the viscosity values of dilute n-butane.

In this line, the corresponding states correlation in conjunction with the intermolecular potential energy parameters were determined to reproduce the viscosity coefficient within the average absolute deviation (AAD) 0.69%.

Keywords: Viscosity, Collision integrals, Chapman-Enskog theory, Corresponding States.

I. INTRODUCTION

Chapman-Enskog theory as a nonequilibrium statistical mechanical approach relates the transport coefficients to collision integrals, $\Omega^{(l,s)}(T)$, as has been defined in the following reduced form [1]:

$$\Omega^{(l,s)*} = \frac{\Omega^{(l,s)}}{\pi\sigma^2} \qquad (1)$$

where σ is the collision diameter and the intermolecular potential vanishes. Moreover, l and s values in $\Omega^{(l,s)}$ represents the type of transport coefficient and depends on weighting factor in the molecular collision mechanism.

It is important to mention that for polyatomic molecules, an orientation averaged collision integral was assumed based on the approximation that the most of interactions in a collision occurs in the vicinity of the distance of closest approach that called as Mason-Monchick approximation. [2]. In this line, the knowledge of intermolecular potential functions can be regarded as an important tool for the calculation of transport collision integrals in zero density limit and also the second virial transport coefficient at moderate densities.

n-Butane (n-C4H10) is a component of natural gas and of crude oil and it is obtained from natural gas or gained in refining petroleum to produce gasoline.

In this research, we confined our attention on evaluation of several correlation equations for the corresponding states of viscosity collision integrals in comparison with experimental data. In this respect, several interaction potential energy parameters were applied to assess their accuracy in reproducing the experimental viscosity values.

II. CORRESPONDING FORMULA OF VISCOSITY COLLISION INTEGRAL

The viscosity η is usually measured as a function of temperature T and pressure p; those variables are also preferred by engineers. However, for fundamental reasons, viscosity is often correlated using temperature T and density ρ as variables.

Recently, a corresponding states formula has been introduced for the viscosity of n-butane as a function of reduced temperature and reduced density, based on the residual quantity concept, and is valid in the fluid region from the triple point to 650 K and to 100 MPa [3].

The bank of terms used for the zero-density viscosity is represented by the sum $\sum_{i=0}^{8} n_{i,0}\,(ln\tau)^i$, whose coefficients $n_{i,0}$ had to be determined in the course of the optimization procedure. Thus, the viscosity in the limit of zero density is formulated as:

$$\eta_0(\tau) = \frac{n_{PF,0}}{\tau^{\frac{1}{2}}\exp[\sum_{i=0}^{8} n_{i,0}(ln\tau)^i]} \qquad (2)$$

In the other hand, Chapman-Enskog collision integrals are related to viscosity values via the following equation:

$$\Omega^{(2,2)*} = \left[\frac{5}{16}(\pi m kT)^{1/2} f_\eta^{(n)} \Big/ \eta\,\sigma^2\right] \qquad (3)$$

and the corresponding state correlation for $\Omega^{(2,2)*}$ in temperature range, $1.0 \le T^* \le 10$, has been introduced as follows [4]:

$$\Omega^{(2,2)*} = \exp[a_0 + a_1\,(\ln T^*) + a_2\,(\ln T^*)^2 + a_3\,(\ln T^*)^3 + a_4\,(\ln T^*)^4\,], \qquad (4)$$

$b_0 = 0.46641$, $b_1 = -0.56991$, $b_2 = 0.19591$,
$b_3 = 0.03879$, $b_4 = 0.002590$,

In this line, intermolecular potential energy scaling parameters for energy and length ε/k_B and σ were applied where the collision diameter σ is defined as the separation distance when the intermolecular potential is equal to zero and ε is the potential well depth. We assessed the interaction potential energy parameters in Chapman-Enskog formalism to reproduce viscosity values within the experimental uncertainty.

III. RESULTS AND DISCUSSION

We used the correlation equations for calculation of collision integrals and viscosity values of n-butane in 150-400K temperate range up to 0.4 mol/lit density. The calculated viscosity values were compared with the available experimental data [5] to assess the accuracy of correlation equations. In Table 1, we have reported the calculated and the experimental viscosity values of dilute n-butane in conjunction with deviation percent values. It should be noted that in Table 1, the corresponding states collision integrals of Eq. 4 were applied to obtain Chapman-Enskog viscosities and the average absolute deviation percent (AAD) were obtained about 0.69% within the viscosity experimental uncertainty.

In this respect, we have analyzed different pair intermolecular potentials via calculation of reduced collision integrals and viscosity values in comparison with the available experimental data. In Fig. 1, we have displayed the reduced collision integrals of n-butane as a function of T* in combination with experimental data using σ =0.53272 nm , $\frac{\varepsilon}{k}$ =328.68 K for the potential parameters.

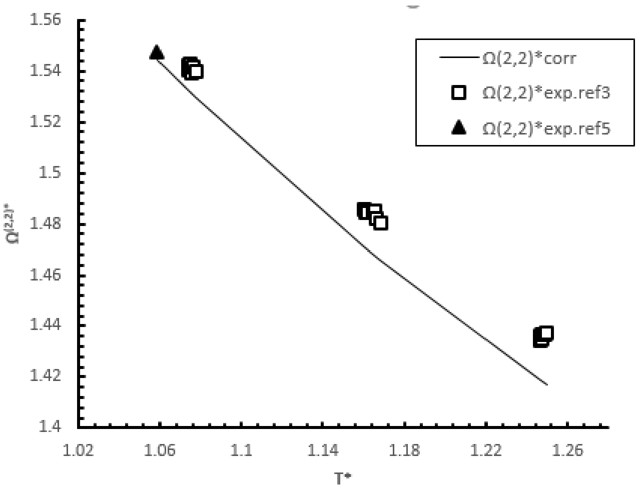

Figure 1. Reduced collision integrals of n-butane as a function of T* in comparison with the experimental data

Table 1. Experimental and calculated values for viscosity of n-butane.

T K	η_{corr} μpa.s	η_{exp} μpa.s	Dev (%)
297.8	7.32	7.37	-0.68
298.4	7.34	7.40	-0.81
298.8	7.35	7.40	-0.67
299.1	7.36	7.41	-0.75
323.1	8.00	7.98	0.23
324.8	8.05	8.05	0.03
325.4	8.06	8.06	0.08
348.0	8.66	8.64	0.20
352.9	8.79	8.74	0.51
353.0	8.79	8.73	0.64
381.5	9.52	9.43	0.93
382.8	9.55	9.45	1.11
384.1	9.59	9.49	1.01
409.1	10.22	10.10	1.21
410.4	10.24	10.11	1.33

IV. CONCLUSION

The correlation equations for the corresponding states of collision integrals and viscosity values which were obtained via different approaches were evaluated to reproduce viscosity of dilute n-butane with the accuracy within the experimental uncertainty. In this respect, the pair potential parameters were investigated in calculation of Chapman-Enskog viscosity collision integrals via comparison with experimental data.

REFERENCES

[1] S. Chapman, T.G. Cowling, The Mathematical Theory of Non-Uniform Gases, Cambridge University Press, London, **1970.**

[2] Maitland G.C., Rigby M., Smith E.B., Wakeham W.A. Intermolecular Forces: Their Origins and Determination. Oxford: Clarendon Press, **1981**.

[3] S.Herrmann, and E.Vogel, J. Phys. Chem. Ref. Data, vol. 47, No. 1, **2018.** DOI: 10.1063/1.5020802.

[4] A. Boushehri, J. Bzowski, J. Kestin and E.A. Mason, J. Phys. Chem. Ref. Data., vol.16, No.3, pp.445-466,**1987.**

[5] S.Herrmann and E.Vogel, J. Chem. Eng. Data, vol.60, No.12,pp.3703-3720, **2015.**

Using Artificial Neural Network for Modeling of Thermophysical Properties of Carbon Quantum Dot nanofluids

S.A. M Mirsaeidi[a], ***F.yousefi***[*]
Chemistry Department, Yasouj University, Yasouj, 75918-74831, Iran

**Corresponding author: Fakhri Yousefi*
Tel/fax: + 98 741 222 1711.
E-mail: fyousefi@ yu.ac.ir

Abstract: This paper presents the model including back-propagation network (BPN) and principal component analysis (PCA) to estimate the thermophisical properties of carbon quantum dot nanofluids in water, ethylene glycol and mixture of water/ethylene glycol. For optimizing to the BPN's parameters and improve the accuracy of proposed model, the PCA was coupled with the BPN.

Keywords*:* Artificial neural network, Carbon dot, Density, Viscosity, Thermal conductivity

I. INTRODUCTION

Modeling and simulating a process involves collecting information to determine how a process will behave in the future without the need for empirical work the use of modeling is acceptable for many scientific and engineering processes in scientific communities [1].
Artificial Neural Network is a powerful modeling tool that has attracted much attention in various fields of science and real-world issues today and has found great acceptance among researchers [2]. Artificial neural network has many advantages in comparison to other models such as state equation, high speed, simplicity and abundance of abilities that reduce engineering actions [3-7].
Artificial neural networks (ANNs) have significantly attracted the attention of researchers in various scientific matters because of the important advantages of high speed, ability to solve the nonlinear system, low cost and time and high precision [8]. The artificial neural networks have been based on the human brain and consist of neurons and layers such as input, hidden and output layer. The architecture, learning algorithm and transfer function can be described the ANNs. The ANN architecture presents the connections between the neurons and layers. The learning algorithm characterizes the weights and biases on the connections [9].

II. METHODS

In this study, three ANN models are applied to predict the dynamic viscosity, thermal conductivity and density of CQDs nanofluids. The temperature (*T*), volume fraction (φ), molar mass of based fluids (Mw), acentric factor (ω), critical temperature(Tc), critical pressure (Pc) and thermophysical properties of base fluids such as viscosity, thermal conductivity and density used as input parameters and thermophysical properties of nanofluides used as target.

III. RESULTS AND DISCUSSION

All experimental data point of viscosity, thermal conductivity and density are divided to three groups of training (70% of data point), validation (15% of data point), and testing data (15% of data point), respectively. The neural network programming was provided in tool box of Matlab.
Performance parameters of the network were mean square error (MSE), absolute average deviation (AAD) and coefficient of determination (R^2) described below:

$$MSE = \sum_{i=1}^{N} (X_i^{\exp} - X_i^{cal})^2$$

(1)

$$AAD(\%) = \frac{1}{N}\sum_{i=1}^{N}\left(\left|\frac{X_i^{\exp} - X_i^{cal}}{X_i^{\exp}}\right|\right)$$

(2)

$$R^2 = \frac{\sum_{i=1}^{N}(X_i^{\exp} - \overline{X})^2 - \sum_{i=1}^{N}(X_i^{\exp} - \overline{X_i^{cal}})^2}{\sum_{i=1}^{N}(X_i^{\exp} - \overline{X})^2}$$

(3)

The nets with 10, 11 and 13 neurons in hidden layer with the mean square error of 0.001204, 6.3×10^{-6} and 1.28×10^{-9} for viscosity, thermal conductivity and density of nanofluids leads to the best prediction, respectively (Fig 1).

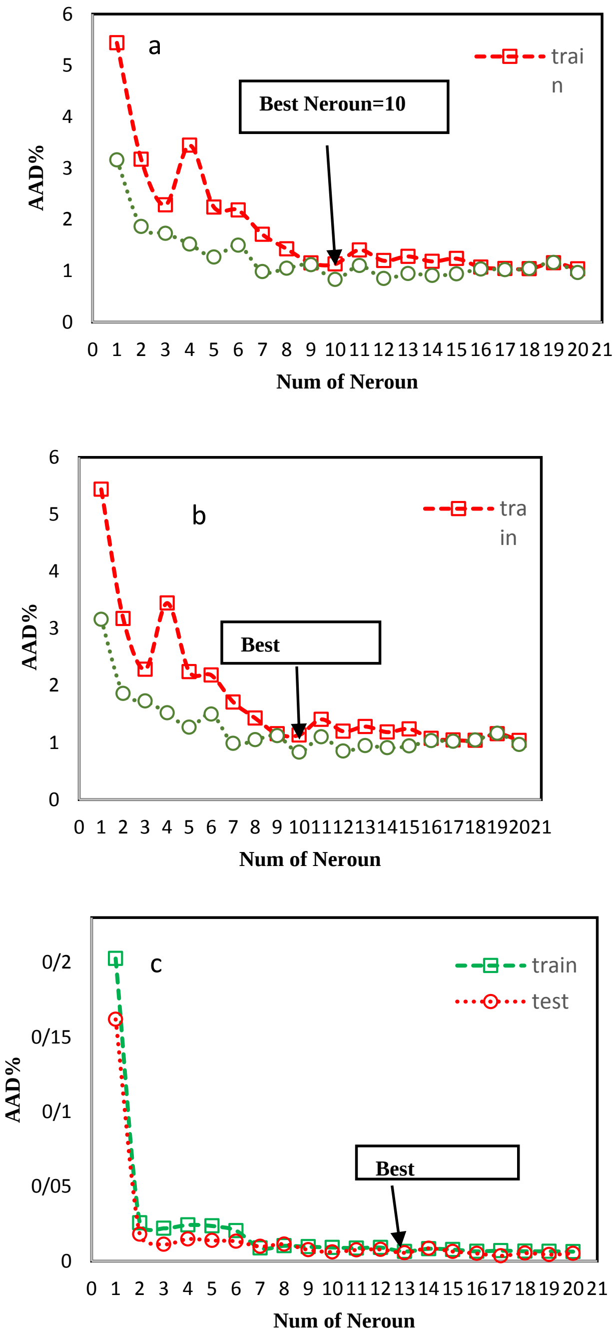

Fig 1. Effect of the number of hidden layer neurons on AAD% of the dynamic viscosity (a), thermal conductivity (b) and density (c) of nanofluids.

The analogy between predictive data and experimental data of viscosity, thermal conductivity and density of CQDs nanofluids is curried out and shown in Fig. 2. The results of Fig. 2 evaluates good compromise between the predicted data and the experimental data of viscosity, thermal conductivity and density of CQDs nanofluids with absolute average error and high correlation coefficients, AAD = 1.29% and R^2 = 0.99994 for viscosity, AAD = 0.85% and R^2 = 0.99867 for thermal conductivity and AAD = 0.01% and R^2 = 0.99999 for density of nanofluids. The neural network programming was provided in tool box of MATLAB software.

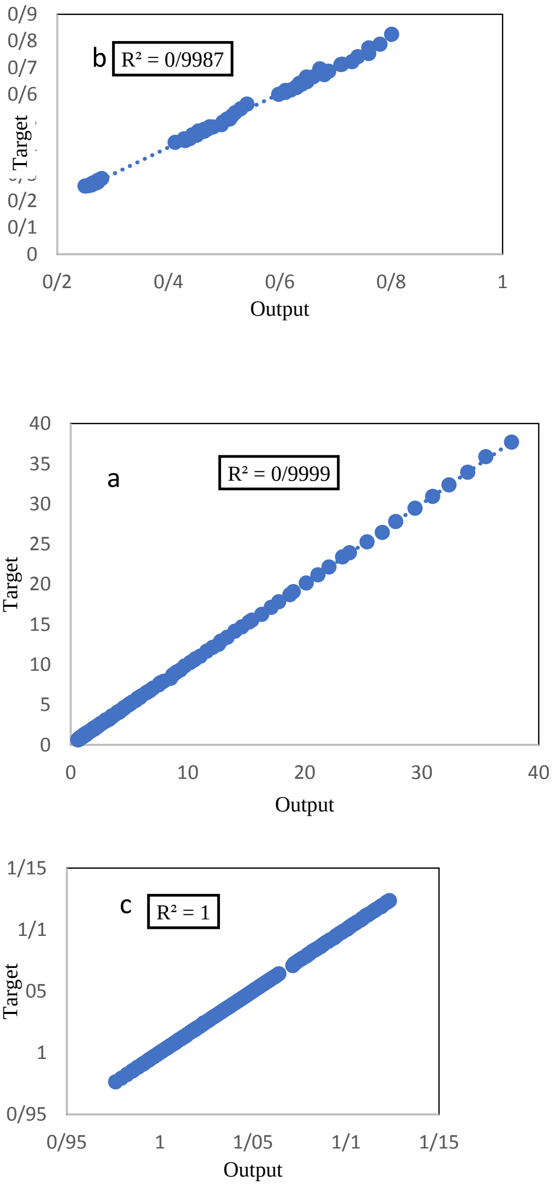

Fig 2. Modeling ability of the optimized ANN to predicate of viscosity (a), thermal conductivity (b) and density (c) of CQDs nanofluids.

IV. CONCLUSION

Three artificial neural network model applied to predict the viscosity, thermal conductivity and density of nanofluids and they are excellent agreement with experimental data with the AAD = 1.29% and R^2 = 0.99994 for viscosity, AAD = 0.85% and R^2 = 0.99867 for thermal conductivity and AAD = 0.01% and R^2 = 0.99999 for density of nanofluids.

REFERENCES

[1] A. M. Ghaedi and A. Vafaei, Advances in Colloid and Interface Science, 245 , 20–39, **2017.**

[2] I.A. Basheer and M. Hajmeer, Journal of Microbiological Methods, 43, 3–31, **2000**.

[3] J. O. Valderrama and P. A. Robles, Ind. Eng. Chem. Res,46,1338**,2007.**

[4] M. Abareshi and M. K. Goharshadi, J. Mol. Liq. 149, 66,**2009**.

[5] R. Ren, Y. Zuo, Q. Zhou, H. Zhang, and S.Zhang, J. Chem. Eng. Data 56, 27 , **2011**.

[6] F. Yousefi, H. Karimi, and M. Gomar, Fluid Phase Equilib, 355, 92, **2013**.

[7]] S. Shakeri, A. Ghassemi, M.Hassani, A.Hajian, *Int J Adv Manuf Technol*, 582, 549- 557, **2016** .

[8] M. Mohanraj, S. Jayaraj, C. Muraleedharan, *Renew. Sust. 410 Energ. Rev*, 16, 1340–1358, **2012**.

Excess Molar Volume of Ternary System of Ionic Liquids Using Artificial Neural Network

S.A. M.Mirsaeidi[a,*], *A. Kalantari*[a], *F.yousefi*[a]
[a] *Chemistry Department, Yasouj University, Yasouj, 75918-74831, Iran*

E-mail: fyousefi@ yu.ac.ir

Abstract: This paper presents the model including back-propagation network (BPN) and principal component analysis (PCA) to estimate the excess molar volume of ionic liquid ternary system. The excess molar volume of ionic liquid mixtures is tested as a function of the temperature (T), mole fractions of components (x_1 ,x_2 and x_3), molar mass of pure ionic liquids (M_1 , M_2 and M_3) and total molar mass (Mw) using artificial neural network. The obtained results by means of PCA–BPN model they have excellent agreement with experimental data with high coefficient of determination for excess molar volume is $R^2 = 0.9985$ and AAD = 1.80%.

Keywords*:* Artificial Neural Networks, Excess Molar Volume, Ionic Liquids, Principal Component Analysis

I. INTRODUCTION

Ionic liquids are compounds that are entirely made of ions. These materials have a boiling point less than 100 ° C and non-toxic nonferrous materials [1].

These materials have recently revolutionized scientific research and the chemical industry and are classified as green materials and are used to prepare nanostructures as molds, reactants and reactants [2].

Modeling and simulating a process involves collecting information to determine how a process will behave in the future without the need for empirical work the use of modeling is acceptable for many scientific and engineering processes in scientific communities [3].

Artiflcial Neural Networks are relatively crude electronic models based on the neural structure of the brain.

ANN performs a variety of tasks, including prediction or function approximation, pattern classification, clustering, and forecasting [4].

The use of artificial neural network to determine the properties of mixtures containing ionic liquids is not new and studies have already been done in this field, for example, studying the density, viscosity and refractive index of a ternary mixture containing ionic liquid, prediction of the electrical conductivity of ternary mixture containing ionic liquid, use of the neural network to determine Excess volumes and Excess enthalpies of ionic liquids, can be mentioned [5, 6].

In this paper, we used artificial neural network to provide a model for predicting the excess molar volume of a ternary methanol + methyl ethanoate +1-octyl-3 methylimidazolium bis[(trifluoromethyl)sulfonyl]imide.

II. METHODS

Structure of ANN composed of three layer namely 1-input layer containing independent variables 2- the out put layer containing independent variables and 3- one or more neuron layers that called hidden layers.

The excess molar volume of ionic liquid mixtures data of ternary mixtures of methanol + methyl ethanoate+1-octyl-3-methylimidazolium bis [(trifluoromethyl)sulfonyl] imide was collected from the refrences[7].All excess molar volume data of ionic liquid mixtures are divided to three groups of training (70% of data point), validation (15% of data point), and testing data (15% of data point), respectively. The neural network programming was provided in tool box of Matlab.

Ⅲ. RESULTS AND DISCUSSION

The mean square error (MSE), absolute average deviation (AAD %) and correlation coefficient (R^2) of training and testing data that were selected as a measure of the performance of the network, and they were given as follow:

$$MSE = \sum_{i=1}^{N} (X_i^{\exp} - X_i^{cal})^2 \qquad (1)$$

$$AAD(\%) = \frac{1}{N} \sum_{i=1}^{N} \left(\left| \frac{X_i^{\exp} - X_i^{cal}}{X_i^{\exp}} \right| \right) \qquad (2)$$

$$R^2 = \frac{\sum_{i=1}^{N} (X_i^{\exp} - \overline{X})^2 - \sum_{i=1}^{N} (X_i^{\exp} - X_i^{\overline{cal}})^2}{\sum_{i=1}^{N} (X_i^{\exp} - \overline{X})^2} \qquad (3)$$

The training data set were used to find the optimum configuration of the ANN model based on the minimizing the MSE, AARD%. Besides, R^2 value were considered as an important parameter showing the consistency and over lapping of the experimental data and predicted values for both training and test data set. the network with one hidden layer and 16 neurons for excess molar volume with an absolute average deviation of 1.80% leads to the best prediction in Fig.1.

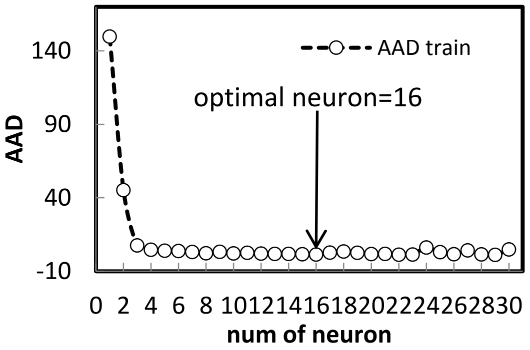

Fig. 1: Effect of the number of hidden layer neurons on *AAD*, %; *V*E

Based on testing data, the optimized neural network model was used to predict the excess molar volume of ternary mixtures of ionic liquids; the comparison between the predicted values and the experimental values is carried out and shown in figure.2

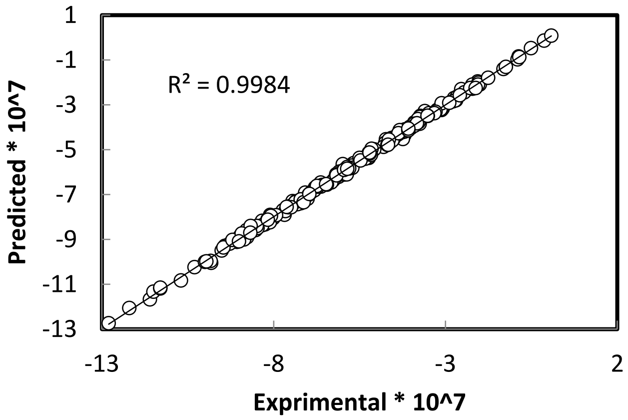

Fig.2: modeling ability of the optimized ANN to predicate excess molar volume of ternary mixtures of ionic

The results show good harmony between the predicted and the experimental values of excess molar volume of ionic liquid mixture.Figure 3 shows the error analysis of trained network over temperature variation for the excess molar volume that the MARE for predicting the network is 0.029.

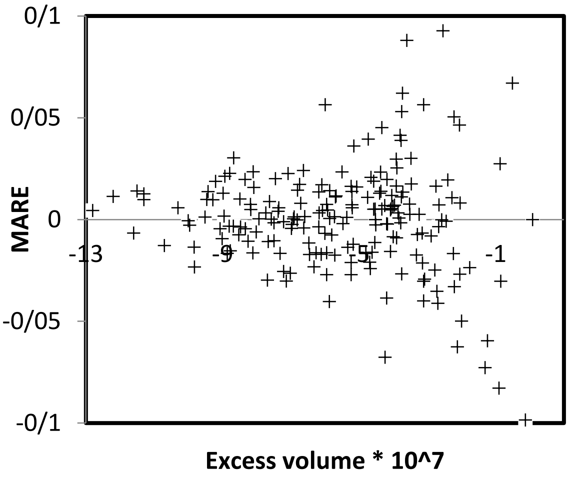

Fig.3: percentage mean absolute relative error for excess molar volume of binary mixtures of ionic liquids

The PCA–ANN was randomly compared to experimental data. Figure 4 demonestrate the plot of predicted excess molar volume as a function of the mole fraction for ternary ionic liquid mixtures methanol + methyl ethanoate+1-octyl-3-methylimidazolium bis[(trifluoromethyl)sulfonyl]imide. It can be seen from this table; the excess molar volume is negative over the entire composition range. The negative excess molar volumes indicate that a more efficient attractive interaction occurred when the ionic liquid and organic molecular liquids were mixed.

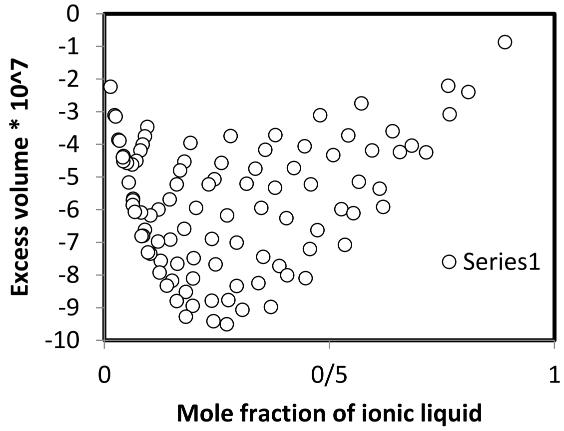

Fig.4: plot of predicted excess molar volume as a function of the mole fraction for ternary ionic liquids

III. CONCLUSION

Herein the artificial neural network and principal component analysis successfully were used to predict the excess molar volume of ionic liquid mixtures. The proposed model could calculate the excess molar volume of ionic liquid mixtures as a function of the temperature (T), mole fraction of two components (x1, x2 and x3), molar mass of two components (M1, M2 and M3) and total molar mass (Mw). The trained net of excess molar volume of ionic liquid mixtures presented good agreement between the predicted and the experimental values of excess molar volume with AAD = 1.8% and high coefficient of determination, R2 = 0.9985.

REFERENCES

[1] F. Yousefi and H. Karimi, J. Ind. Eng. Chem. 19, 498, **2013**.
[2] F.Endres. Ionic Liquids: Solvents for the Electrodeposition of Metals and Semiconductors. CHEMPHYSCHEM 3, 144-154, **2002**.
[3] A. M. Ghaedi and A. Vafaei, Advances in Colloid and Interface Science, 245 , 20–39, **2017.**
[4] He, X. & Xu, S. (2009). Process Neural Networks: Theory and Application. China: Zhejiang University Press: Prentice Hall.
[5] K. Fukumoto, M. Y. oshizawa,and H. Ohno, Journal of the American Chemical Society 127,2398-2399, **2005**.
[6] A. N. Marghmaleki, M. R. Khosravi nikou, A. Barati, Journal of Molecular Liquids, 220, 232–237, **2016**.
[7] A. E. Andreatta, A. Arce, Physical properties and phase Fluid Phase Equilib, 287 , 84-94, **2010**

Experimental and Computational Studies of Binary Mixtures of Morpholine + Cis and Trance 2-Methylcyclohexanol

R. Mirzaeei S. ranjbar., A. Soltanabadi [b]**
Faculty of Chemistry, Razi University, Kermanshah, Iran
Email: ***a.soltanabadi@razi.ac.ir***

Abstract*:* The thermodynamic properties of binary mixtures of 2-Methylcyclohexanol and morpholine were measured over the entire composition range at temperatures T = (293.15 to 313.15) K and at atmospheric pressure. From the experimental data, density and the excess molar volumes deviations were calculated. The excess molar volumes are negative over the entire mole fractions range. In the gas phase and using the density functional theory (DFT), the most stable geometric structures of 2-methylcyclohexanol…2-methylcyclohexanol, morpholine…morpholine and 2-methylcyclohexanol…morpholine have been investigated. In addition, quantum theory of atoms in molecules (AIM) were applied to analyzed hydrogen bonding (H-bonding) interactions. In the liquid phase, the molecular dynamics (MD) simulation technique was employed to calculate the densities, radial distribution functions (RDFs) and combined distribution function (CDF) of the mixtures with different mole fractions at 298.15 K and at 1 atm. For these mixtures, by molecular dynamics simulation and quantum calculations, the hydrogen bonding (H-bonding) interactions were investigated too.

Keywords Density Functional Theory, Molecular dynamic simulation, Combined distribution function; Hydrogen bond..

I. INTRODUCTION

Morpholine is heterocycle combines and both the amine and ether functional groups [1-4]. Morpholine is a common additive, in parts per million concentrations, for pH adjustment in both fossil fuel and nuclear power plant steam systems. 2-Methylcyclohexanol is a alcohol that is used as a solvent in organic reaction [5-10]. The combination of these two materials is very interesting. Because they have almost similar structure and different intermolecular interactions. This study reports the experimental data of density of binary mixtures of 2-Methylcyclohexanol + Morpholine as a function of composition at temperatures T = (293.15 to 313.15) K and at atmospheric pressure. The calculated properties from such data have been interpreted in terms of the differences in the size of molecules and the strength of specific and non-specific interactions taking place between components of the mixtures. In addition, the nature of molecular interactions between the components has been debated.

In the gas phase, the equilibrium geometries and stabilities of 2-methylcyclohexanol … 2-methylcyclohexanol, morpholine … morpholine and 2-methylcyclohexanol … morpholine were investigated using quantum mechanics. Also, in the liquid phase, using molecular dynamic simulation, the microscopic structure, and diffusivities of the pure 2-methylcyclohexanol, pure morpholine, and their mixtures are simulated. In addition, intermolecular H-bonds interactions of pairs in the gas phase by AIM and in the liquid phase by molecular dynamics simulation are discussed.

II. METHODS

2-methylcyclohexanol and morpholine were provided with high purity from Merck and were utilized without further purification. The experimental values of the densities for pure liquids and for the binary mixtures at different mole fractions were measured in the temperature range (293.15 to 343.15) K at intervals of 5 K and ambient pressure. MD simulations performed of pure 2-methylcyclohexanol, pure morpholine and mixture of 2-methylcyclohexanol + morpholine using the DL_POLY 2.20 package.

III. RESULTS AND DISCUSSION

The computed densities of pure liquids and different mole fractions from the NPT simulations for 1.0 ns at 298.15 K and at 1 atm, are given in Table 1. Where comparison to experimental data was obtainable, as can be seen that, the highest error in computing density and experimental density are 3% or better. Therefore, it can be concluded that the OPLS force field is a good force field for computing density of these materials.

Table1: The Calculated Densities, Uncertainty of Calculated Densities and Percent Error in Densities of Binary Mixtures of 2- Morpholine(1) + 2- Methylcyclohexanol at 298.15 K from Molecular Dynamic Simulation.

x_1	$\frac{\rho_{\text{expt}}}{\text{g}\cdot\text{cm}^{-3}}$	$\frac{\rho_{\text{cal}}}{\text{g}\cdot\text{cm}^{-3}}$	$E\%$
0	۰/۹۲۳۶	۹۴۳۰۲	۲/۱۳
0.13	0.93706	0.95970	- 2.42
0.38	0.95321	0.97104	- 1.87
0.48	0.96078	0.97759	- 1.75
0.77	0.98192	0.99944	- 1.78
0.85	0.98805	1.00745	- 1.96
1.0	0.99569	1.02026	– 2.45

Figure 1 show that the excess molar volumes are negative over the whole range of composition in the mixtures and increasing the temperature causes that, these values become more negative. Such behavior could be accounted to formation strong bond interactions between 2-methylcyclohexanol and morpholine in comparison ideal mixture or the diffusion of dissimilar molecules in each other.

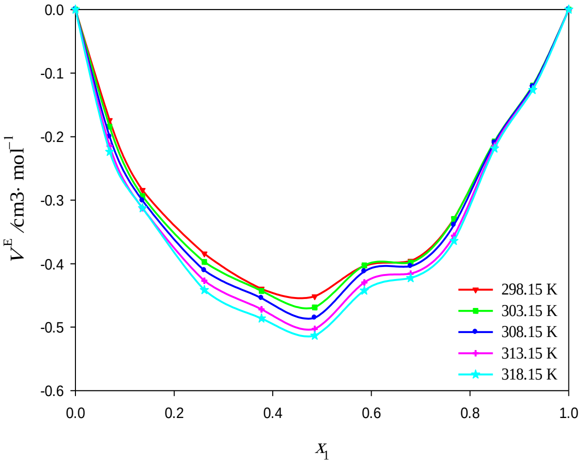

Figure 1. The excess molar volumes, of binary mixture of 2-Methylcyclohexanol + morpholine versus mole fraction of 2-Methylcyclohexanol, , at the various temperatures and at atmospheric pressure. Error bars are smaller than the symbol size.

The optimized structures of Morpholine, Cis 2-methylcyclohexanol and Trance 2-methylcyclohexanol are presented in Figure 2

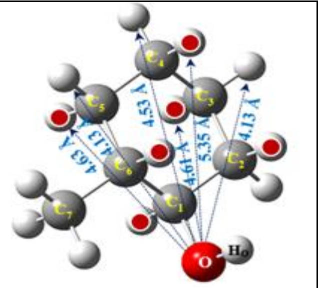	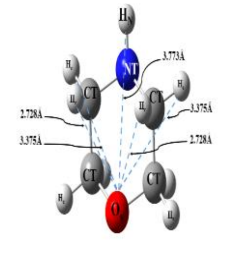
2-Methylcyclohexanol	Morpholine

Figure 2. The optimized structures of 2-Methylcyclohexanol, morpholine using Gaussian program at B3LYP level of DFT with 6-31++G** basis set. Equatorial hydrogens are indicated by small red circles

H-Bonding Interactions in the Liquid Phase: The information about these short-range structures can be obtained from analysis of the atom-atom RDF or g (r). A RDF characterizes the average density of certain particles at a distance r from an arbitrary central atom. if distance two atom a and b is less than the sum of the van der Waals radii of a and b atoms, hydrogen bonding are formed (threshold distance). The threshold distance for O···H_O, O…H_O and N···H_N are 2.48, 2.48 Å and 2.52 Å respectively. Fig. 3 shows intermolecular interactions of the O of 2-methylcyclohexanol (cis and trance) and the H_N of morpholine in various molar fractions and 298.15 K. For the pair, there is one set peaks. This set peaks (is focused at 2.0 Å) represents the interaction of O with H_N, which is located in the nearest shell, and it can be attributed to H-bonding. Also, due to H-bonding strength, each peak in this set has a specific intensity. Based on MD simulations, it may be concluded that a mixture with x_1=0.48, the maximum molecular association, occurs.

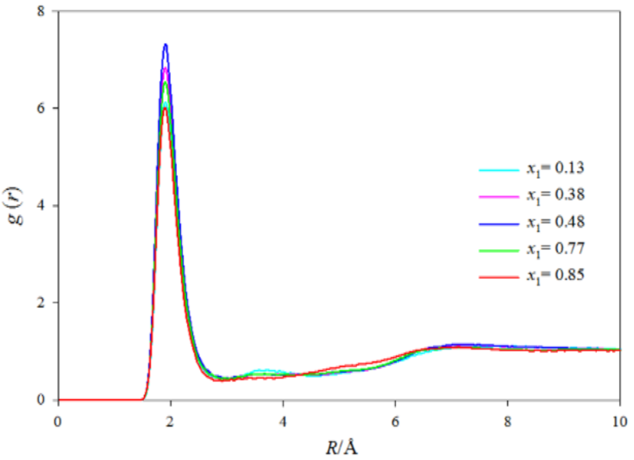

Fig. 3. The simulated radial distribution functions of H_N of morpholine and O of 2-methylcyclohexanol at the various mole fractions using the DL_POLY 2.20 program and OPLS force field at 298.15 K and at 1.0 atm.

IV. CONCLUSION

In this study, densities at T = (293.15-313.15) K were measured for the binary mixtures of 2-methylcyclohexanol with 2-methylcyclohexanol. From these measured data, excess molar volumes and deviations in viscosities were calculated. The excess molar volumes have been derived from the experimental densities data and the patterns are negative throughout the composition rang. Molecular dynamics simulations of the mixtures containing morpholine (cis and trans) + 2-methylcyclohexanol at 298.15 K and at 1 atm are carried out. The obtained densities exhibit the well trend with the experimental and provide further knowledge into the molecular level behavior. The structures of molecules have been investigated through the radial distribution function. The result of molecular dynamic simulation was agreement with quantum results experimental results. Due to the large number of molecules in the hydrogen bonded form of O…HN, the most of the thermodynamics properties of these solutions result from of this hydrogen bond.In this study, it is clarified that the OPLS force field gives sensible densities and microscopic structures of the solvents.

REFERENCES

[1] Walker, D.P, Eklov, B.M, Synthesis vol. 44, p. 2859. **2012**
[2] Abellan, T, Chinchilla, R, Galindo, N, Najera, C., and Sansano, J.M., J. Heterocycl. Chem., , vol. 37,467, **2000**
[3] Bera, S. and Panda, G, ACS Comb. Sci, , vol. 14, 1. **2012**
[4] Segat-Dioury, F, Lingibé, O, Graffe, B, Sacquet, M.-C, and Lhommet, G., Tetrahedron, , vol. 56, p. 233, **2000**
[5] Trabocchi, A, Krachmalnicoff, A, Menchi, G, and Guarna, A, Tetrahedron, vol. 68, p. 9701. **2012**
[6] Montague D G, Gibson I P, Dore J C. J Mol Phys. 44, 1355, **1981**
[7] Wertz D L, Kruh, R K. J Chem Phys, 47, 388, **1967**
[8] Zachariasen, J Chem Phys., 3, 158–160. **1935**
[9] [Harvey, G G. J Chem Phys. 6, 111-114. **1938**
[10] Wertz D L, Kruh, R K. J Chem Phys. 47, 388 – 390. **1967**

Molecular Dynamics Simulations of the Structure the Graphene–Dicationic Ionic liquid interface

A. Shamshiri., A. Soltanabadi ^{b*}
Faculty of Chemistry, Razi University, Kermanshah, Iran
Email: a.soltanabadi@razi.ac.ir

Abstract*:* Molecular dynamics simulations performed for dicationc ionic liquid 1,3 bis[3-methylimidazolium 1-yl] bis trifluoromethylsulfonyl amide ($C_6[mim]_2[ntf_2]_2$) with graphene walls. The calculated RDFs show that anions (ntf_2^-) are well organized around the imidazolium rings. By comparing peaks of RDF anion with graphene, we find that oxygen atoms of anion more interact than others atoms with graphene plates. The calculated diffusion coefficient and transference numbers show that the anions have the major role in carrying the electric current in system.

Keywords: Dicationic ionic liquid, Molecular dynamic simulations, Radial distribution function, diffusion coefficient

I. INTRODUCTION

Supercapacitors (also called electric double-layer capacitors or ultracapacitors) are electrochemical capacitors that store energy through reversible ion adsorption onto active materials that have high specific surface area.[1] Because of their many advantageous properties, such as high power density, high capacitance, and long cycle life (>100000 cycles), these systems play an important role in electrical energy storage. To generate a high specific capacitance, the specific surface area of the electrode materials needs to be as high as possible to accommodate a large number of electrolyte ions at the electrode/ electrolyte interface thereby promoting the electrical double-layer capacitance. Graphene, an atom-thick 2D nanostructure, is a promising material for supercapacitor electrodes owing to its low mass density, excellent electronic conductivity, and high surface area [2].

Geminal dicationic ionic liquids (DILs) [3] are a new family of ILs and consist of a doubly charged cation that is composed of two singly charged cations linked by an alkyl chain (also called a spacer) and paired with two singly charged anions. Some applications of DILs have also been explored, such as stationary phases for gas chromatography, solvents for high-temperature organic reactions, electrolytes in secondary batteries and dye sensitized solar cells. Therefore, an estimation of the structure and electronic properties of the ions in DILs is important for designing new DILs for the specific applications. For example, an estimation of the transport properties of the ions in the DILs is important for designing new DILs for electrolytes. In this work we have adopted the imidazolium force field of Canongia-Lopes et al. [4] for cation ($C_6(mim)_2^{+2}$) and anion (ntf_2^-). In this paper, using molecular dynamic simulation, the microscopic structure, diffusivities and transport number of the ($C_6[mim]_2[ntf_2]_2$) whit graphene walls are simulated.

II. METHODS

MD simulations performed of ($C_6[mim]_2[ntf_2]_2$) with graphene walls using the DL_POLY 2.20 package. Figure 1 shows that the structures of $C_6(mim)_2^{+2}$ and ntf_2^- were optimized at the B3LYP/6-31+G* level using Gaussian 09.

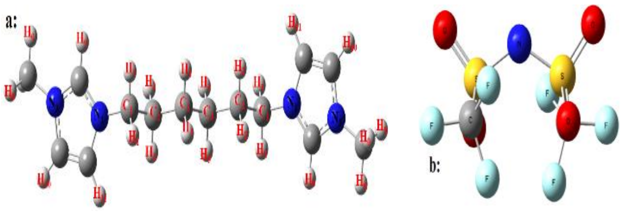

Figure 1. Schematic structure of dication $C_6(mim)_2^{+2}$ and anion (ntf_2^-) in DILs simulated in this study.

For each simulation, 120 dicationic $C_6(mim)_2^{+2}$ and 240 anions (ntf_2^-) were placed in the simulation box. The initial structures was created by randomly placing the specific number of dicationic ionic liquid and ntf_2^- in a cubic simulation box. Simulations were done at P = 1.0 atm and T = 450. K. The simulation have been continued until the energy of the system converged. Figure 2 shows the snapshot of simulation box after 1.0 ns. The radial distribution function (RDF) was done NVT simulations with 0.5 ns equilibration followed by a 1.0 ns production in which the positions of particles were recorded every 0.1 ps.

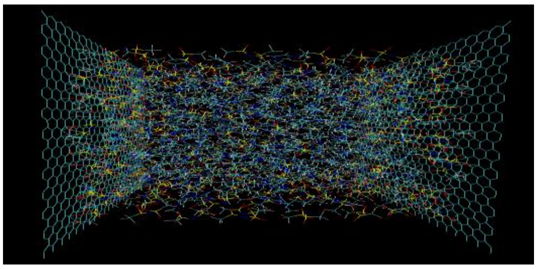

Figure 2. The snapshot of geminal dicationic ionic liquids ($C_6[mim]_2[ntf_2]_2$) in simulation box after 1.0 ns.

III. RESULTS AND DISCUSSION

We investigated the liquid structure by calculating various radial distribution functions (RDFs or g(r)) of ions over the 10.0 ns of the trajectories at 450 K and 1 atm. To determine how the molecules are arranged around each other, RDFs anion-cation was calculated and shown in figure 3. The RDF of anion-cation show that sharp peak at about 5.0 Å. The anion–anion RDFs are presented in Figure 3 show a first peak around 8 Å. The RDFs of cation–cation in Figure 3 show peaks at about 4.9. Å. In summary, these three peaks can be concluded that anion is very well organized around the cation.

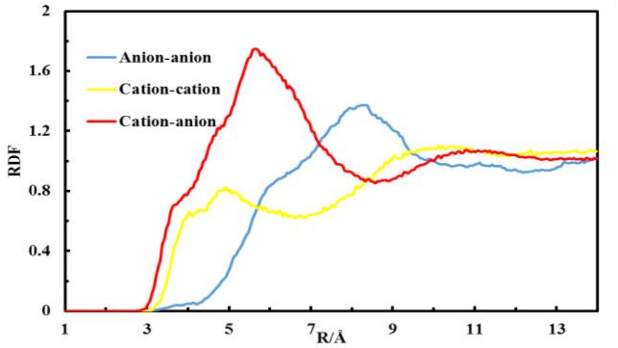

Figure 3. Calculated radial distribution functions for cation–anion, cation–cation and anion–anion correlations for $[C_6(mim)_2(ntf_2)_2]$ ionic liquids at 450 K and 1 atm.

To elaborate the more detailed structure of anions around the imidazolium ring, we have calculated the RDFs of fluorides in anion and hydrogen atoms (H_9, H_{10}, and H_{11} in Figure 1a) of the midazolium rings and shown in Figure 4. The well-defined peaks at about 2.8 Å in Figure 4 indicate the strong interactions between these hydrogens and fluorides atoms of the anions.

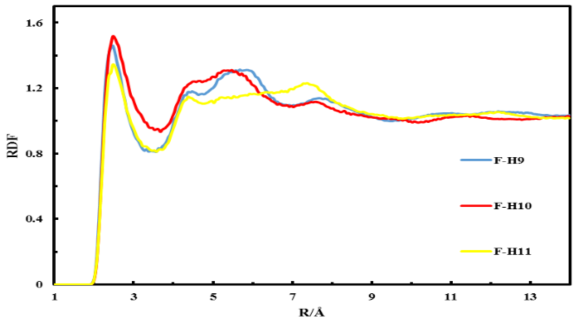

Figure 4. Radial distribution function of fluoride atoms of anion ntf_2^-around the rings atom H8, H9, and H10 for $[C_6(mim)_2(ntf_2)_2]$ at 450 K and 1 atm. The labels are defined according to Figure 1.

To determine the arrangement of anion and cation with graphene plate, we calculated RDFs of anions and cations atom whit graphene for $C_9(mim)_2(ntf_2)_2$. Figure 5a and 5b show that RDFs of anion atoms whit graphene and cation atoms whit graphene respectively.

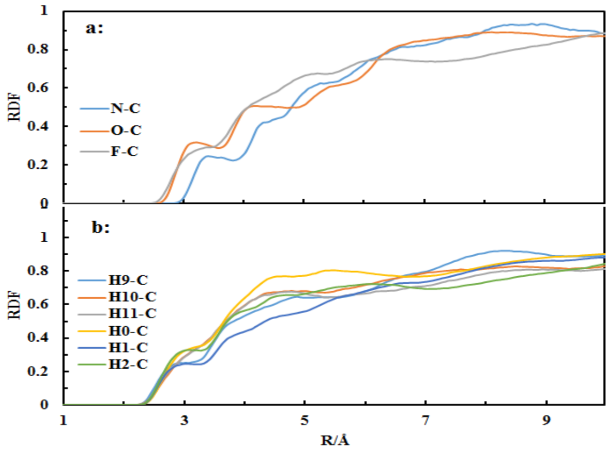

Figure 5. Calculated radial distribution functions for a: nitrogen oxygen and fluoride of anion whit graphene plate b: H_0 H_1, H_2, H_9, H_{10}, and H_{11} of cation whit graphene for $[C_6(mim)_2(ntf_2)_2]$ ionic liquids at 450 K and 1 atm.

By comparing peaks of RDF anion with graphene in the figure 5a, we find that oxygen atoms of anion more interact than others atoms with graphene plates. By comparison RDFs in figure 5a and 5b, we find that the hydrogen atoms of cation are closer to graphene than the other atoms. The self-diffusion coefficients of anions and cation for DILs calculated and shown in Table 1. Table 1 show that self-diffusion coefficients of anions more than cation. Also DILs can be used as electrolytes in the electrochemical processes and devices [5]. In most practical electrolyte applications, the relative contributions of the charged species to the transfer of the total charge are also important. For the component 1:2 electrolytes, MX_2 consisting of ions M^{2+} and two X^-, such as the dicationic ionic liquids of interest in this study, transference numbers may be estimated from the diffusion coefficients of the cation and anion

$$t_+ = \frac{D_+}{D_+ + 2D_-}, .t_- = \frac{2D_-}{D_+ + 2D_-} \qquad (1)$$

The transference numbers were calculated and shown in Table 1. The calculated transference numbers of cation and anion in DILs show that transference numbers anions more than cation.

Table 1. Calculated diffusion coefficient and transference numbers for the cations and anions in $C_6(mim)_2(ntf_2)_2$ at 450 K and 1.0 atm

DILs	$D_+(10^{-10}m^2/s)$	$D_-(10^{-10}m^2/s)$	t_+	t_-
$C_6(mim)_2(ntf_2)_2$	1.42	1.66	0.3	0.7

IV. CONCLUSION

The calculated RDFs show that anions tend to spend most of their time around the rings rather than alkyl chain atoms and the anions are very well organized around the cationic rings. By comparison RDFs of cation and anion, we find that oxigen atoms in anion more interact than other anions atoms with graphene plates. Because of the large transfer numbers for anions in DILs, anions have a major role in the transfer of electric current.

REFERENCES

[1] P .Simon, Y. Gogotsi, Materials for Electrochemical Capacitors. Nat. Mater, vol. 7, pp. 845–854. **2008.**
[2] A. Geim, K. Novoselov, The Rise of Graphene. Nat. Mater, vol. 6, pp. 183–191. **2007.**
[3] J. L, Anderson, R. Ding, A. Ellern, D. W. Armstrong, J. Am. Chem. Soc, vol. 127, pp. 593−604, **2005.**
[4] J. N. Canongia-Lopes, J. Deschamps, A. H. Pádua, J. Phys. Chem. B, vol. 108, pp. 2038−2047, **2004.**
[5] V, González-Pedro, V. Giménez, S. Azaceta, J. Am. Chem. Soc, vol. 133, pp. 20156−20159, **2011.**